SEDHYD 2019

Proceedings of SEDHYD 2019: Conferences on Sedimentation and Hydrologic Modeling

Volume 5
Poster Session, Computer Modeling Session

Proceedings of SEDHYD 2019: Conferences on Sedimentation and Hydrologic Modeling, 24-28 June 2019 in Reno, NV.

These engineering and scientific proceedings provide much of the latest information on sedimentation and hydrologic modeling (applied research and state of-the-practice) from Federal agencies, universities, and consultants. SEDHYD is the successor to the Federal Interagency Conferences on Sedimentation and Hydrologic Modeling. The Subcommittee on Sedimentation convened the first Federal Interagency Sedimentation Conference (FISC) in 1947. Subsequent FISC conferences were convened in 1963, 1976, 1986, 1991, 1996, and 2001. The Subcommittee on Hydrology convened their first Federal Interagency Workshop, "Hydrologic Modeling Demands for the 90s," in 1993. Subsequent to that workshop, the Subcommittee on Hydrology convened the Federal Interagency Hydrologic Modeling Conferences (FIHMC) in 1998 and 2002. Subsequently, the Subcommittees on Sedimentation and Hydrology began convening the Federal interagency conferences together in 2006 and again in 2010, and 2015. Beginning in 2019, the SEDHYD Conference was hosted by SEDHYD, Inc., a non-profit organization.

Since 1947, the Sedimentation and Hydrologic Modeling Conferences have provided over 3,000 technical papers and extended abstracts and provided engineers and scientists with the opportunity to learn and exchange information about the latest developments and research related to sedimentation and hydrologic modeling. As a continuation of these conferences, SEDHYD provides an interdisciplinary mix of scientists and managers from government agencies, universities, and consultants to present recent accomplishments and progress in research and on technical developments related to sedimentation processes, hydrologic modeling, and the impact of sediment on the environment.

The SEDHYD conference provides a mixed set of formats that include formal technical presentations, poster sessions, field trips, workshops, computer model demonstrations, and a student paper competition. The SEDHYD conference also provides excellent networking opportunities.

The SEDHYD 2019 Conference site was at the Peppermill Hotel and Resort in Reno, Nevada. Reno is situated in a high desert just east of the beautiful Sierra Nevada Mountains. The city lies on the western edge of the Great Basin, at an elevation of 4,400 feet (1,300 meters) above sea level. The Reno downtown area (along with Sparks) occupies a valley informally known as Truckee Meadows. The area offers spectacular desert landscapes and ecosystems, as well as numerous indoor and outdoor recreational opportunities.

SEDHYD 2019 Planning Committee

Planning Committee Position	Volunteer	Organization
SEDHYD Conference Chair	Jerry Webb	West Consultants
SEDHYD Operations Chair	Jennifer Bountry	Reclamation
SEDHYD Technical Program Chair	Chandra Pathak	USACE
SEDHYD Technical Program Chair (YP)	Will Farmer	USGS
SEDHYD Technical Program	Jerry Bernard	NRCS, retired
Sedimentation Conference Chair	Tim Randle	Reclamation
Sedimentation Program Chair	Eddy Langendoen	ARS
Sedimentation Program Chair (YP)	Joel Sholtes	Mesa State
Hydrologic Modeling Conference Chair	Claudia Hoeft	NRCS
Hydrologic Modeling Program Chair	Jim Barton	USACE, retired
Hydrologic Modeling Program Chair (YP)	Jessica Driscoll	USGS
Student Program Coordinator	Amanda Cox	MWRRC
Proceedings Coordinator	Bob Boyd	BLM
Proceedings Coordinator	Peter Doran	BLM
Poster & Computer Model Demonstration Coordinator	Eddie Brauer	USACE
Short Course Coordinator	Jeff Bradley	ASCE, West Consultants
Short Course Coordinator (YP)	Kevin Denn	USACE, St. Paul Dist.
Field Trip Coordinator	Steve Berris	USGS
Field Trip Coordinator (YP)	Jena Huntington	USGS
Web site Coordinator	Darren Nezamfar	USACE
Registration Coordinator	Penni Baker	USACE
Registration Volunteer	Kathy Randle	
Young Professionals Coordinator	Caroline Ubing	Reclamation
Young Professionals Coordinator	Sara Horgen	Reclamation
Exhibit Coordinator	Molly Wood	USGS
Exhibit Coordinator	Tim Straub	USGS
AV Equipment Coordinator	Jeff Harris	West Consultants
Planning Committee	Jo Johnson	NRCS
Planning Committee	Jon Fripp	NRCS
Planning Committee	Paul Boyd	USACE
Planning Committee	Meg Jonas	USACOE, retired
Planning Committee	Robert R Mason	USGS
Planning Committee	Victor Hom	NOAA

SEDHYD, Inc.

SEDHYD, Inc. Position	Volunteer
SEDHYD President & Board Chair	Jerry Webb
SEDHYD Vice President & Board Member	Jerry Bernard
SEDHYD Treasurer & Board Member	Don Frevert
SEDHYD Secretary & Board Member	Matt Romkens
SEDHYD Board Member	Doug Glysson

Table of Contents

Table of Contents

Table of Contents

Table of Contents

Poster Session

A Tool for Beaver Dam Analogue Design

F. Douglas Shields, Jr, cbec eco-engineering, University, MS, doug2shields@gmail.com
Michael M. Pollock, NOAA Fisheries-Northwest Fisheries Science Center, Seattle, WA, michael.pollock@noaa.gov
Rocco Fiori, Fiori Geosciences, Klamath, CA, rocco@fiorigeosci.com

Introduction

Beaver populations can be powerful tools in restoring stream and riparian habitats since their dams control and influence fluxes of water, sediment and nutrients. Beaver dam analogues (BDAs) are channel-spanning structures built by humans that mimic or reinforce natural beaver dams, and in many cases are intended to be eventually utilized and enhanced by beaver. BDAs are constructed by driving posts in a row perpendicular to the channel, weaving a mat of willow stems to create a weir supported by the posts and placing a berm of sediment, stone and plant material on the upstream face of the weir. A typical cross-sectional view, facing upstream, is provided in Figure 1. Variations on this basic design also occur. Like natural beaver dams, BDAs are temporary features on the landscape with functions that change in response to the effects of flowing water, sediment, and beaver activity (Pollock et al. 2017).

Although early BDA design and construction has relied on professional judgment, quantitative design can reduce the risk of premature failure and suboptimal use of available resources. To support and assist designers, we present a macro-enabled Excel spreadsheet that may be used to perform simple analyses leading to computation of three safety factors. Material quantities and simple cost estimates are also presented as output. Key computational modules include hydrologic flow frequency analyses to support selection of design discharge and uniform flow computations to assess pre-construction hydraulics. Uniform flow hydraulics are performed using an adapted version of the popular cross-section hydraulic analyzer spreadsheet (xsecAnalyzerVer17.xlsm) developed by the USDA-NRCS. The design tool also includes spreadsheets to assist the user in inputting geometry of the channel cross-section and the basic BDA geometry. Post-construction hydraulics are based on critical flow over the BDA crest at design discharge. Using estimates of bed material size input by the user, the design tool computes estimates of scour depth downstream from the BDA and then uses Brom's approach for noncohesive sediments to compute the required minimum embedment for the posts.

The BDA design tool is a macro-enabled Microsoft Excel file with separate sheets for various components of design as shown below. Completion of the analysis produces a set of safety factors and rough estimates of material volumes and construction costs. Support for users is in the form of default input values, tables of wood properties, soil properties and beaver dam dimensions, and a users' manual. The authors aspire to an improved version of the tool upon receipt of suggestions from reviewers.
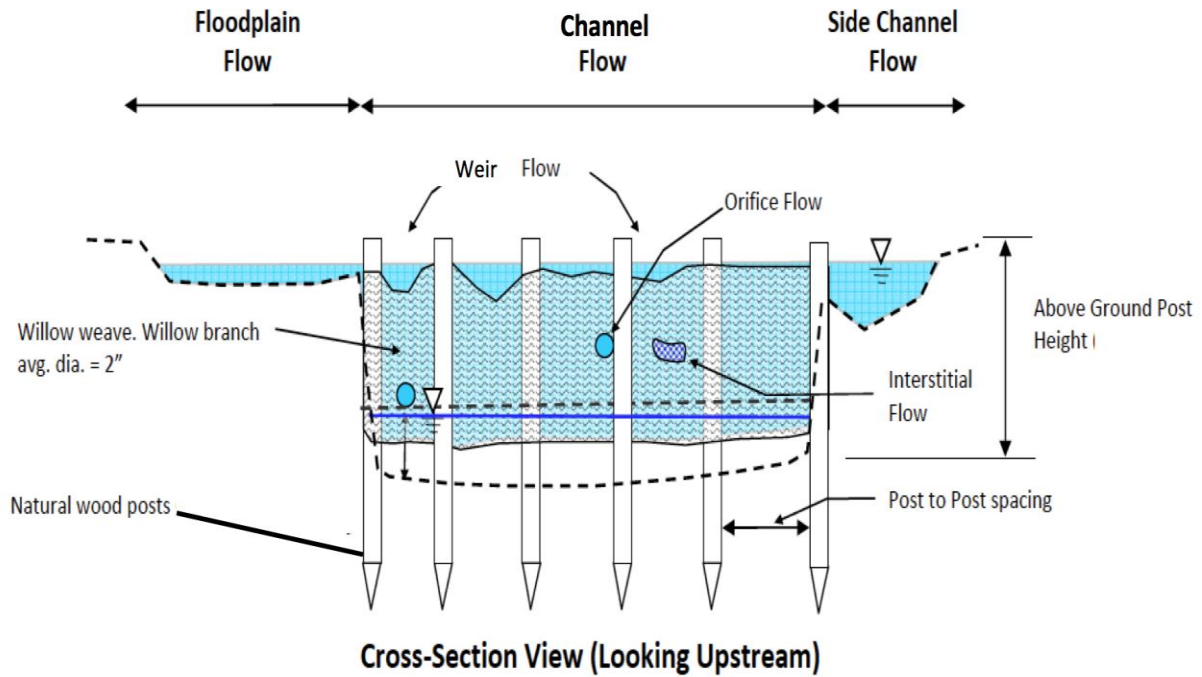
Figure 1. Typical components of beaver dam analogue. Flow passes the structure over its crest as weir flow, through discrete openings as weir flow, through small gaps or openings as interstitial flow and around the structure as floodplain or side channel flow.

Hydrology and hydraulics

Flow frequency distributions are generated within the design tool from annual series supplied by user, Streamstats regression formula, or entered by user based on estimate or other information. The user then selects a design discharge. Pre-BDA hydraulics are computed based on the USDA-NRCS uniform flow spreadsheet, xsecAnalyzerVer17.xlsm (http://go.usa.gov/0Eo), which is embedded in BDA Design Tool. Post-BDA hydraulics assume critical flow over BDA crest. The user must supply estimates of the percent of the design discharge passing the BDA over the crest, or as floodplain, side channel flow, or interstitial flow.

Table 1. Design Tool Contents

Worksheet	Description and function
Design summary	Tabulates metadata and safety factors for vertical movement and post breakage and overturning
Hydrology	Select design discharge and compare return interval to desired design life
Structure dimensions	User specifics structure height, width, slide slopes, etc.
Channel geometry	User provides cross section for BDA site. Sheet provides a cross section plot to visualize and check.
Uniform flow computations	Pre-BDA hydraulics at design discharge from NRCS sheet, Xsecanalyzer
Hydraulics	Post-BDA hydraulics assuming critical flow over weir crest
Scour and downstream rock sizing	Scour depth related to hydraulics and rock sizing using empirical formula (D'Agostino and Ferro 2004)
Upstream rock sizing	Cobble or coarse gravel is normally placed on upstream face. Size needed to remain stable even if underflow occurs is computed using four formulas to rock chutes. User selects desired result.
Impact force	Force BDA due to impact of floating log
Posts-overturning and breakage	Minimum post embedment depth to resist overturning computed using Brom's (1964) method for pilings in noncohesive material.
Posts-vertical forces	Post skin friction compared to buoyant force using method from Knutson and Fealko (2014)
Material volumes	Quantities primarily based on dimensions specified by user in Structure dimensions worksheet
Cost estimate	Based on material volumes and unit costs provided by user
Soil properties	Bulk density, friction angle. Coefficient of lateral earth pressure, etc.
Wood properties	Unit weight, modulus of rupture
Natural beaver dam dimensions	Tabulated from 16 publications

Post embedment depth

The tool computes the post embedment depth needed to resist the horizontal loading forces: fluid drag, hydrostatic force, and impact from floating logs. Dimensions which must be either specified by the user or computed are indicated in Figure 2. An iterative approach is used to compute the post embedment depth because the minimum post embedment depends on the resisting moment, which depends on the embedment depth. Moments due to each type of horizontal loading force are summed about the buried tip of the post. Drag and hydrostatic forces are assumed to act at a point midway between the water surface and the stream bed. Impact forces are assumed to act at the elevation of the crest of the weir. Moments are summed for the entire BDA but divided by the number of posts in order to get the moment acting on each post. The minimum required post embedment depth is computed using the method presented by Broms (1964) for posts in noncohesive soils or sediments.

Experience suggests that BDAs often fail when downstream scour undermines the structure, triggering underflow and enlarging the opening through the structure by progressive erosion. Embedment depth must be great enough to ensure post stability after formation of a downstream scour hole (Figure 2). The tool uses the empirical equation by D'Agostino and Ferro (2004) to

relate flow hydraulics, bed sediment size, and equilibrium scour depth. The effect of downstream bed sediment size on required post embedment as calculated by the tool is shown in Figure 3.

Profile View
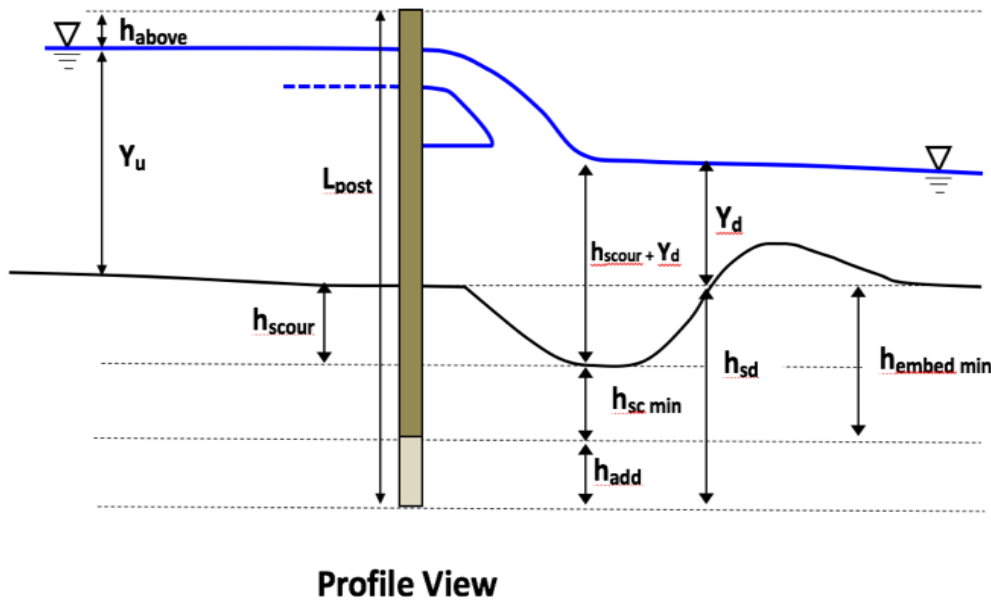
Figure 2. Definition sketch for post depth calculations. L_{post} = total length of post = h_{add} (additional embedment to increase safety factor) + $h_{sc\ min}$ (minimum embedment given computed downstream scour depth) + h_{scour} (downstream scour depth) + Y_u (upstream flow depth) + h_{above} (height of post above upstream design water surface elevation). The sum of h_{scour} and $h_{sc\ min}$ = $h_{embed\ min}$, and Y_d = downstream flow depth.
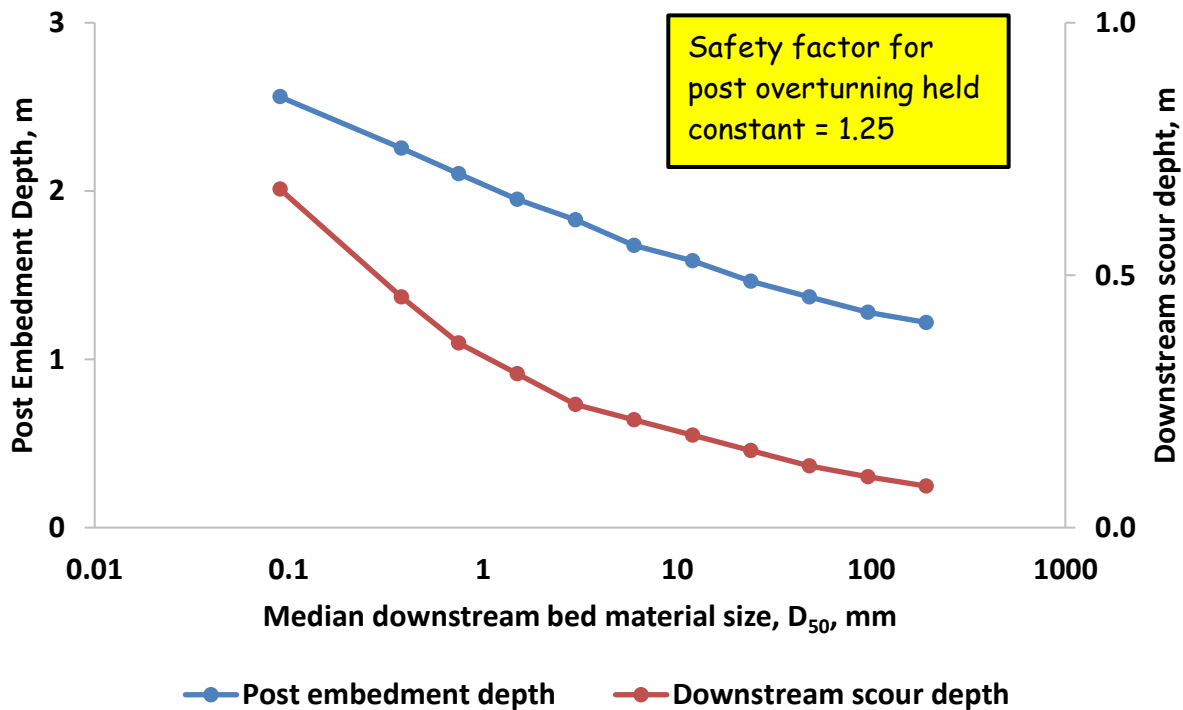
Figure 3. Post embedment and downstream scour depth as a function of bed material size

Conclusion

The BDA design tool may be used by practitioners to facilitate design of resilient, cost-effective structures with appropriate levels of failure risk. The current version is on hold pending obtaining funds to incorporate peer comments and finalize documentation. It should be viewed as model awaiting revision and refinement to reflect ongoing user experience and feedback as it is applied under a variety of hydrogeomorphic and ecological conditions.

References

Broms, B. B. 1964. "Lateral resistance of piles in cohesionless soils," Journal of the Soil Mechanics and Foundations Division, 90(3), 123-158.

D'Agostino, V. and Ferro, V. 2004. "Scour on alluvial bed downstream of grade-control structures," Journal of Hydraulic Engineering, 130(1), 24-37.

Knutson, M. and J. Fealko. 2014. Large woody material risk-based design guidelines. U.S. Department of the Interior, Bureau of Reclamation, Pacific Northwest Region Resource and Technical Services, Boise, Idaho.

Pollock, M.M., Jordan, C. Lewallen, G. and Woodruff, K. Castro, J. 2017. The Beaver Restoration Guidebook. Working with Beaver to Restore Streams, Wetlands, and Floodplains. Funded by North Pacific Landscape Conservation Cooperative.

Bloomsbury Dam Removal: Simulating Flood Risk Downstream of Passive Sediment Releases with a One-Dimensional Sediment Transport Model

Extended Abstract

Jacob Helminiak, Hydraulic Engineer, USACE – Philadelphia District, Philadelphia, PA, Jacob.E.Helminiak@usace.army.mil
Stanford Gibson, Research Hydraulic Engineer, USACE – Hydrologic Engineering Center, Davis, CA, Stanford.Gibson@usace.army.mil

Introduction

Bloomsbury Dam is a run-of-the-river concrete/masonry structure located on the Musconetcong River in northwest New Jersey (Figure 1). At approximately 8 feet high, it impounds approximately 15,000 cubic yards (CY) of accumulated sediment, nearly 98% coarse sand and gravel. The U.S. Army Corps of Engineers (USACE), Philadelphia District (NAP) completed sediment transport modeling to inform removal planning for Bloomsbury Dam, scheduled for 2020. NAP favored passive release of sediment (no management), given the quality, course gradation, and manageable volume of the impounded sediment. However, low-lying homes less than 1,000 feet downstream required analysis of potential timing and persistence of temporary increases in water surface elevation and flood risk downstream of the dam.

Figure 1. Bloomsbury Dam Removal Site

Methods

NAP used the Hydrologic Engineering Center's - River Analysis System (HEC-RAS), a one-dimensional (1D) hydraulic model capable of simulating sediment transport, to estimate timing of sediment evacuation from the impoundment as well as extent and persistence of downstream deposition. NAP simulated dam removal assuming water years with varying runoff conditions (e.g. wet, dry, average) with multiple applicable (coarse sand/gravel) transport functions to bound a range of potential outcomes. Both instantaneous and staged (phased) removal scenarios were simulated. All simulations used the quasi-unsteady flow capabilities within HEC-RAS. Sediment coring/probing and sieve analysis were used to characterize/quantify impounded sediment, with visual observation and pebble counts used for downstream bed material characterization.

The uncertainty associated with sediment data and variability associated with sediment equations makes calibration particularly important in sediment modeling studies. However, because dam removals are usually events without precedent in the system, a dam removal model cannot be calibrated within the range of modeled conditions. However, some model "credibility" tests can help analysts make relative distinctions between appropriate algorithms.

The modeling team tested the appropriate algorithms by simulating existing conditions geometry (with dam) with the selected annual hydrologies and sediment transport routines. NAP favored transport functions that produced neither erosion nor significant deposition at a stable downstream riffle (assessed via multiple repeat photos since 2008). Dam removal results were then evaluated based on the relative difference from the non-removal baseline to control for data or algorithm bias.

NAP computed post-removal water surface elevations (WSELs) for full removal and no removal at the downstream homes of concern and compared them to approximate elevations of residential basement impacts. Then, the modeling team exported updated HEC-RAS cross-sections (i.e. a new geometry file) at the time of maximum deposition for each run. NAP used this maximum deposition (minimum channel capacity) geometry file to create a fixed-bed, steady-flow model of the reach in the most flood-prone conditions, and modeled the standard frequency flows (e.g. 10%, 2% and, 1% annual exceedance probability) to determine maximum potential increases in flood risk.

Results

NAP performed a sensitivity analysis, exploring combinations of all applicable transport functions, with the active layer sorting method (USACE, 2019). While most of the dam removal simulations showed no persistent downstream deposition (most eroded within 6-months to 1-year, Figure 2), some iterations predicted several feet of deposition downstream that unacceptably increased flood risk and persisted for years after the removal (Figure 2). For example, the Yang transport function - a total load transport function generally applicable to sand and gravel grain sizes (USACE, 2016) –did not fully erode the predicted post-removal deposits during even the longest simulations (15 water years). Simulations using Meyer-Peter and Muller (MPM), a bed-load only function, and Laursen-Copeland (LC), a total load function (both generally applicable to sand/gravel grain sizes), eroded downstream deposits within months of the simulated removal (USACE, 2016).
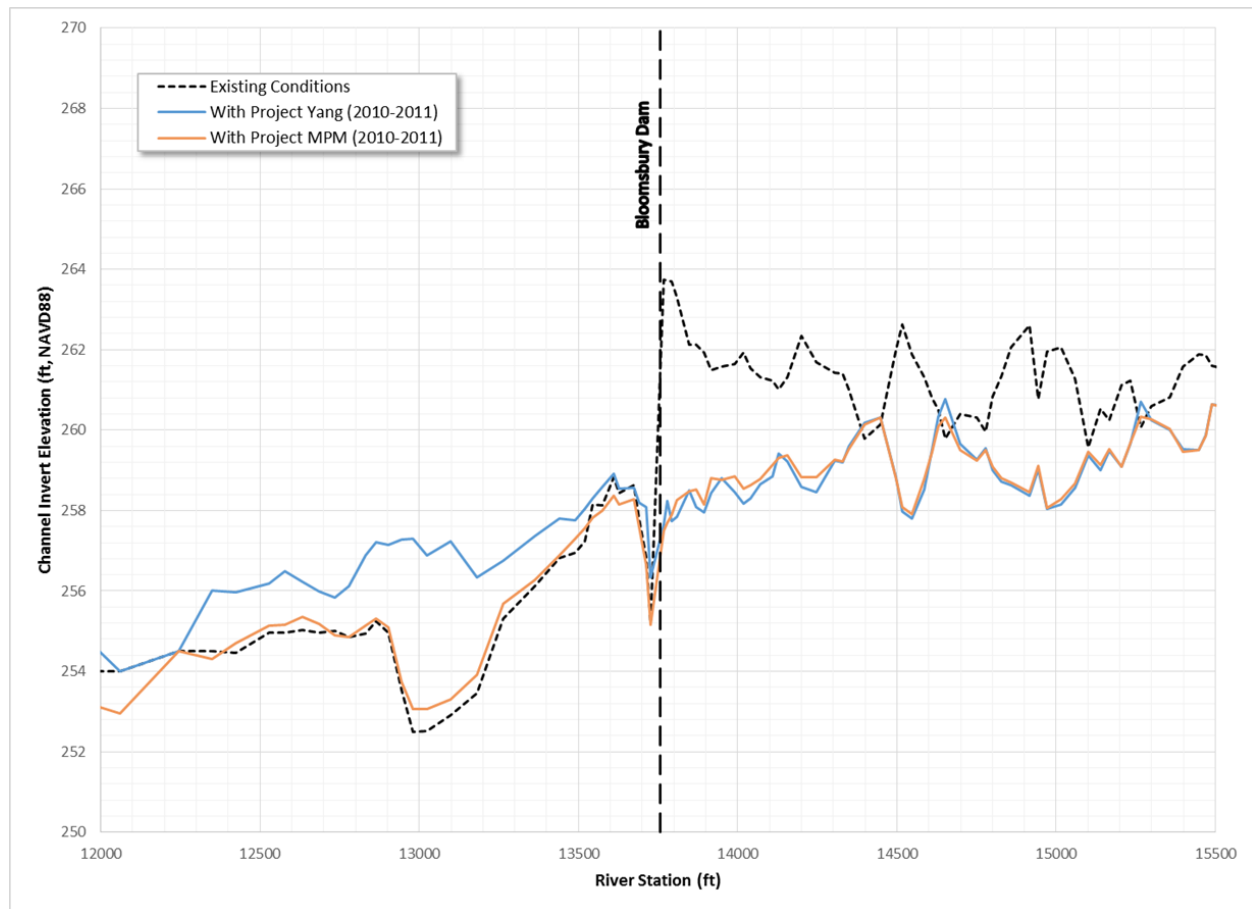
Figure 2. Portion of final longitudinal profile results from sediment transport simulations with two transport functions (using active layer sorting method). Note persistent deposition of several feet with Yang transport function simulation.

River stage increased the most during lower flows (in-channel, below any impacts to adjacent low-lying homes), with influence of the dam removal deposits tailing off at larger events that access the wider floodplain area (Figures 3 and 4). Uncertainty surrounding the analysis and equivocal model results, (e.g. predicted downstream persistence of deposition) led to a conservative staged, or phased, removal approach for the design.

The proposed staged dam removal approach removes the dam a few (vertical) feet at a time, reducing the sediment impact from each intervention. Lowering the dam gradually delivers less sediment downstream after each partial-removal-event and gives the river more time to transport it downstream. This reduces the downstream flood risk and facilitates the opportunity for adaptive management. Downstream deposits can be monitored and the further dam lowering delayed until the river transports the deposits to a location downstream of at-risk homes. However, multiple mobilizations and monitoring will increase the cost of the staged removal alternative, as compared to an instantaneous full removal.

Given uncertainty, equivocal model results, and regionally conservative regulatory climate, selecting the more conservative staged removal alterative is prudent. However, there is reason to doubt some of the model predictions. Many moderate size dam removals, including larger

removals with substantial unconsolidated sand/gravel and cobble loads, erode through their downstream deposits within a year (Healy et al., 2003, Pearson et al., 2011, Costigan, et al., 2014, , Major et al, 2017, Collins et al., 2017, Gibson et al, 2019). The repeated cross sections (Healy et al., 2003) from the Big Rapids dam removal in central Michigan (Figure 5) suggest that a dam like Bloomsbury should erode the downstream deposits in less than a year with no persistent, elevated flood risk, even with average stream flows.
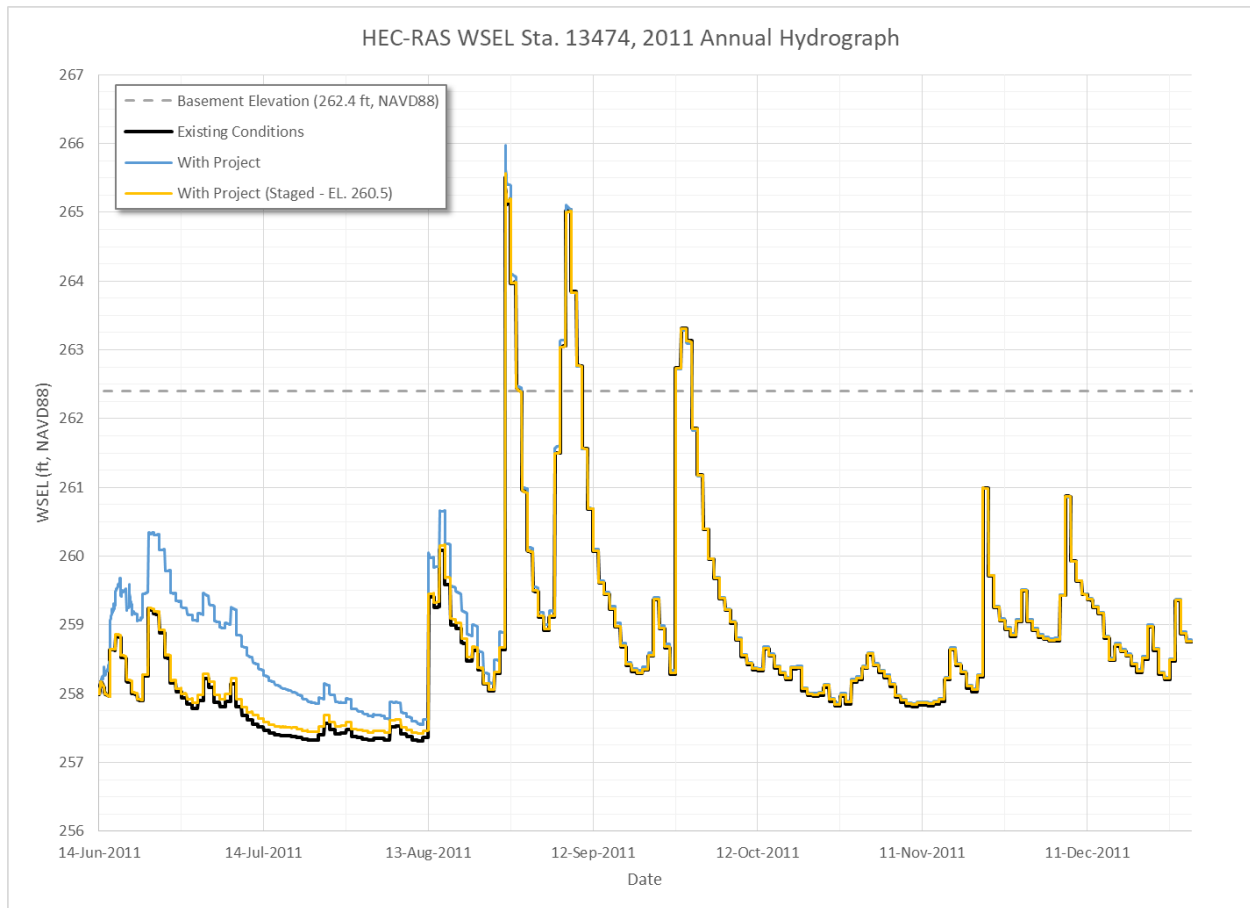
Figure 3. WSEL comparison for wet year simulation, both full removal, and staged removal, Laursen-Copeland transport function.
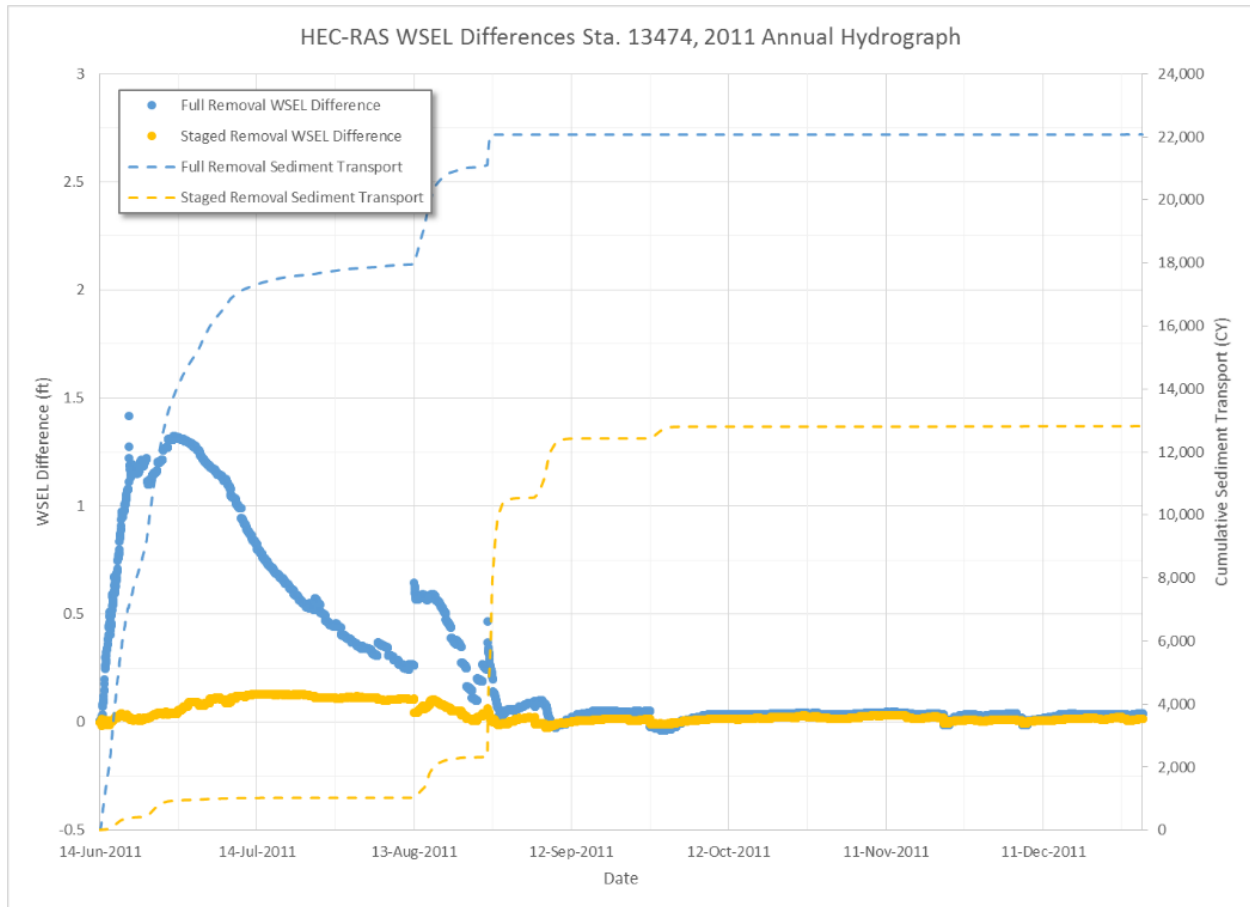
Figure 4. WSEL comparison for wet year simulation, both full removal, and staged removal, Laursen-Copeland transport function.
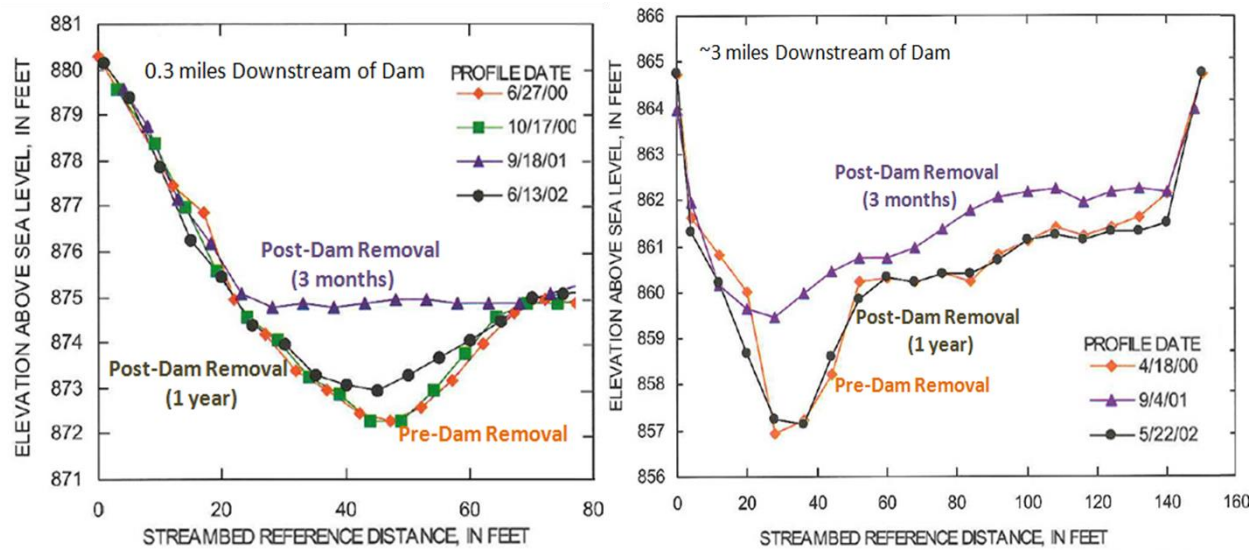
Figure 5. Cross sections collected downstream of a dam removal demonstrating the classic river response, rapid deposition followed by incision back to the initial bed elevation, with no persistent channel change (Figure modified from Healy et al., 2003)

Numerical Limitations of the Active Layer Approach in Dam Removal Simulations

The Bloomsbury Dam Removal model is not the first sediment transport model to predict suspicious, persistent downstream deposition. Over-predicting the depth and duration of downstream deposits is a systemic bias of "active layer" sediment transport models downstream of dam removals, particularly in coarse sediment. Several dam removal models have demonstrated this bias, and the US Bureau of Reclamation reviewers report that over prediction of persistent downstream deposits, particularly in pools or slow-moving water, is the most common failure mode of dam removal models (Greimann, personal communication).

Dam removal models can over predict the persistence of downstream deposition because of a numerical artifact of active layer transport methods, which is sometimes called "the floating clast problem". Active layer algorithms are the standard approach to mobile bed modeling and have many computational advantages. Active layer models mix sediment at each computational node in a computational layer close to the surface. However, dam removals demonstrate an unintended consequence of this numerical simplification. During pulses of fine impounded sediment onto coarse downstream bed material (common to dam removals), current active layer mixing algorithms artificially mix the coarse downstream bed material into the finer sediment deposits. This numerical mixing artificially incorporates the coarse, initial, bed material into the finer removal deposits, allowing the coarser particles to "float" to the top of the sediment column. When the deposits erode, those coarse, bed particles form an armor layer higher than the former bed elevation, causing persistent numerical bed change.

Future Work and Implications

NAP and HEC plan to monitor the dam removal in 2020, collecting repeated cross sections downstream of the dam to determine whether the deposits downstream of the dam persist or if the river quickly returns to the original bed elevation. The study team will then revisit the model, and develop a hindcast model of a similar dam previously removed in Big Rapids, MI, to further evaluate model results. The study team is working on numerical methods and algorithms that can improve active layer performance in these situations and avoid artificial armoring and the floating clast problem.

Regulatory agencies throughout the North Atlantic Division (NAD), and particularly in New Jersey where the Bloomsbury Dam is located, have only recently considered passive sediment management techniques during dam removal projects. Better understanding of potential downstream sedimentation impacts, including persistence and timing of sediment deposition and concentrations, would help inform future dam removal projects, lend more confidence to downstream simulated results, and, in turn, likely reduce project costs incurred through conservative design decisions, and increase likelihood of stakeholder consensus. Additionally, these tools will also be useful for reservoir flushing analyses which also send fine pulses downstream and can encounter similar biases.

Acknowledgments

References

Collins, MJ et al. 2017. "Channel response to sediment release: Insights from a paired analysis of dam removal." Earth Surface Processes and Landforms 42: 1636–1651.

Costigan, K.H., Ruffing, C.M., Perkin, J.S., and Daniels, M.D. 2014 "Rapid response of a sand dominated river to installation and removal of a temporary run-of-the river dam," River Research and Applications, 10.1002/rr.2843

Gibson, S.A., Ramos, K., Dahl, T., Webber, J.B., Vuyovich, C., 2019 (in press) "Comparing Ice jam hindcasting models to tree scar data," American Society of Civil Engineers – Journal of Cold Regions Engineering.

Healy, D.F., Rheaume, S.J., and Simpson, J.A. 2003, Water-Resources Investigations Report 03-4136, "Environmental Effects of the Big Rapids Dam Remnant Removal, Big Rapids, Michigan, 2000-02".

Major, JJ, East, AE, O'Connor, JE, Grant, GE, Wilcox, AC, Magirl, CS, Collins, MJ, Tullos, DD, 2017. "Geomorphic responses to dam removal in the United States–a two-decade perspective," In D Tsutsumi. and Laronne J., editors, Gravel-Bed Rivers: Processes and Disasters. Wiley and Sons, pp. 355– 383.

Pearson, AJ, Snyder, NP, Collins, MJ. 2011. "Rates and processes of channel response to dam removal with a sand-filled impoundment." Water Resources Research 47: W08504. DOI:10.1029/2010WR009733.

U.S. Army Corps of Engineers, Philadelphia District, 2019 (in prep). "Design Documentation Report for Removal of Bloomsbury Dam."

U.S. Army Corps of Engineers, Hydrologic Engineering Center, 2016. "HEC-RAS Hydraulic Reference Manual, version 5.0."

Changes in the Columbia River Gorge: The Eagle Creek Fire

Jarod K. Norton, Project Manager, USACE, Portland, OR, Jarod.K.Norton@usace.army.mil
Rachel O. Stolt, Hydraulic Engineer, USACE, Portland, OR, Rachel.O.Stolt@usace.army.mil
David P. May, Hydraulic Engineer, USACE-ERDC, Portland, OR David.P.May@erdc.dren.mil
Christopher P. Haring, Research Physical Scientist, USACE-ERDC, Vicksburg, OR, Christopher.P.Haring@usace.army.mil

Abstract

On September 2, 2017 a wildfire ignited in the Columbia River Gorge National Scenic Area, burning approximately 48,580 acres over two months. The two areas most severely burned were the Eagle Creek and Tanner Creek Basins. The confluences of both of these creeks with the Columbia River is at roughly River Mile 146, near the Bonneville Dam. Due to the severity of the burn the US Forest Service (USFS) conducted Soil Burn Severity (SBS) observations immediately following the fire to gather information on changes to the soil structure, water repellency, and root burn severity. Predictions from the USFS indicate that the affected basins could produce up to 4 times the annual runoff, as well as large sediment and debris pulses. These pulses have the potential to impact the Vancouver to The Dalles Federal Navigation Channel and US Army Corps of Engineers (USACE) facilities at Bonneville Dam. A number of agencies have concerns related to the mobilization of debris and sediment. The Oregon Department of Transportation (ODOT) is responsible for Interstate 84, the main east-west highway in Oregon. The interstate runs between the burned area and the Columbia River. The USFS manages most of the area that was impacted, which is extremely popular for recreation.

The USACE Portland District (Portland District) is currently evaluating potential impacts as a result of these fires. Portland District is exploring the use of LiDAR, in-stream measurements, field observations, Civil Air Patrol flights, Unmanned Aircraft System (UAS) monitoring, and hydrosurveys to predict the mobilization of sediment. This may increase Portland District's dredging need if shoaling in the Federal Navigation Channel occurs. It may also interrupt navigation locks if sediment and debris begin to move into the mainstem Columbia River. A number of Federal and State operated fish facility intakes are also threatened by increases in debris and sediment.

This paper will discuss the state of the Columbia River Gorge National Scenic Area prior to the Eagle Creek Fire, and how the fire has changed the present condition. It will also use the data that has been collected to date to project future impacts to the area, and actions that may be taken to help minimize impacts to federal and state infrastructure.

Figure 1. The Eagle Creek Fire.

Figure 2. The Bridge of the Gods in the foreground of the Eagle Creek Fire.

Introduction

In early September 2017 wildfires ignited in the Columbia River Gorge National Scenic Area; after a short period of time they merged into what is now referred to as the Eagle Creek Fire. The fire burned 48,580 acres in Oregon, and eventually jumped the Columbia River and sparked the Archer Mountain Fire near Skamania, WA that burned roughly 300 acres (Figure 3). The Eagle Creek and Tanner Creek basins in Oregon were the most severely affected, and the impacts to these basins may have a tremendous influence on local, state, and federal interests in the upcoming years.
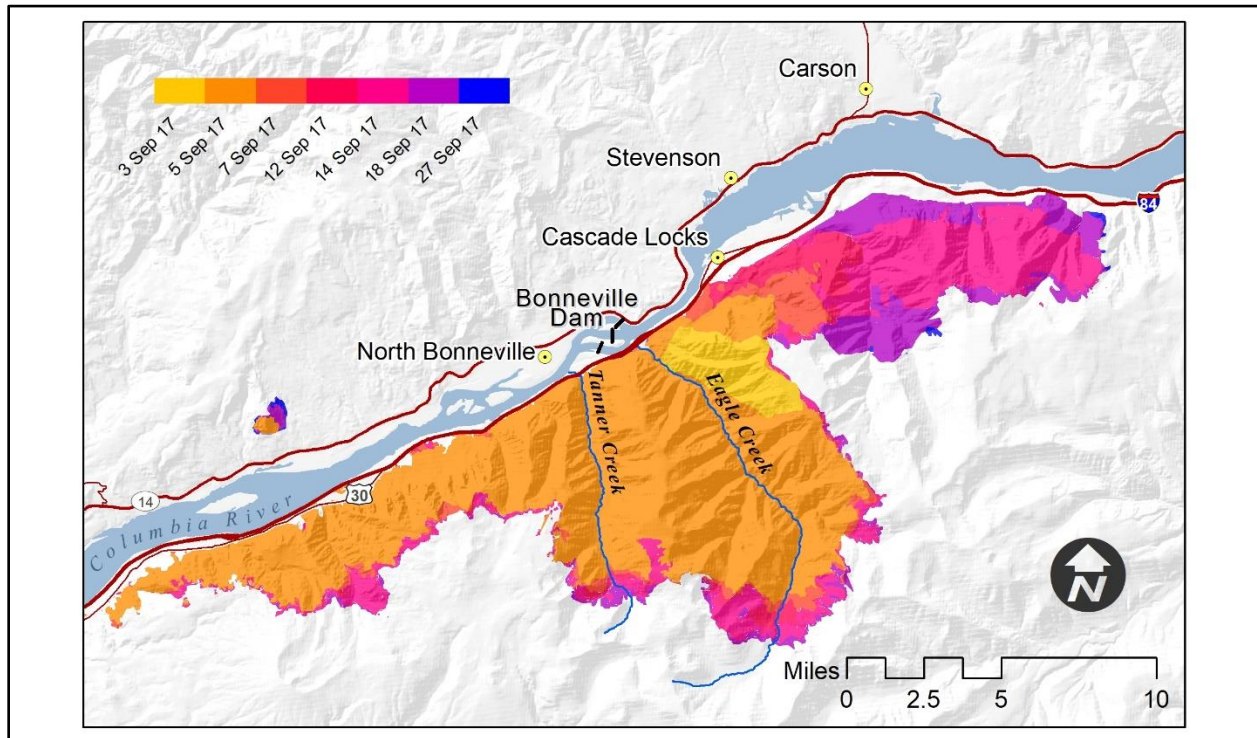
Figure 3. The Eagle Creek Fire Progression.

The Eagle Creek confluence with the Columbia River is just upstream of the Bonneville Dam navigation locks, while Tanner Creek flows adjacent to the Bonneville Fish Hatchery and meets the Columbia River immediately downstream of Bonneville Dam. Bonneville Fish Hatchery is the Oregon Department of Fish and Wildlife's largest hatchery. The impacted area includes large State and Federal infrastructure, numerous fish facilities, as well as the towns of Cascade Locks, Hood River, and Stevenson, WA. During the course of the wildfire, mandatory evacuations displaced residents and forced the closure of the Interstate 84. The fire also forced the closure of the Vancouver to The Dalles Federal Navigation Channel from River Mile 126 to River Mile 146. Areas all over the Pacific Northwest suffered from degraded air quality during this wildfire, and the post-burn recreational trails and service roads remain closed over a year later.

Federal and State agencies in charge of maintaining infrastructure have a significant interest in the post-wildfire impacts to the region. The agencies are primarily concerned about the mobilization of sediment and debris as a result of the fire, including lost vegetation and destabilized tributary basins to the Columbia River.

The areas upstream of Bonneville Dam are of great concern to the USACE due to the massive amount of economic, recreational, and navigation interest that Bonneville Dam and the Federal Navigation Channel support. Over $24B in commerce moves through the Columbia-Snake River System annually. The Columbia River Federal Navigation Channel supports the largest wheat and barley export in the nation, the world's second largest soy export, over 40,000 jobs, and over $930M in commercial investments. The Vancouver to The Dalles Federal Navigation Channel and Bonneville Dam, are located adjacent to the Eagle Creek Fire. Bonneville Dam provides an estimated $95M in power generation annually. The navigation channel supports 8.5M tons of annual commerce, worth $1.4B annually (Channel Portfolio Tool, 2019).

Pre-Fire Conditions

The Columbia River Gorge National Scenic Area spans roughly 70 miles from Troutdale, OR to The Dalles, OR. It consists of expansive conifer forests, large cliffs, steep talus slopes, high-gradient headwater streams, and lower-gradient trunk streams. A number of large waterfalls and picturesque creeks make the area a highly sought after location for recreation. Prior to the fire the large expansses of vegetation absorbed the annual precipitation. Figure 4 illustrates the steep gradient in the basins, along with the average precipitation.
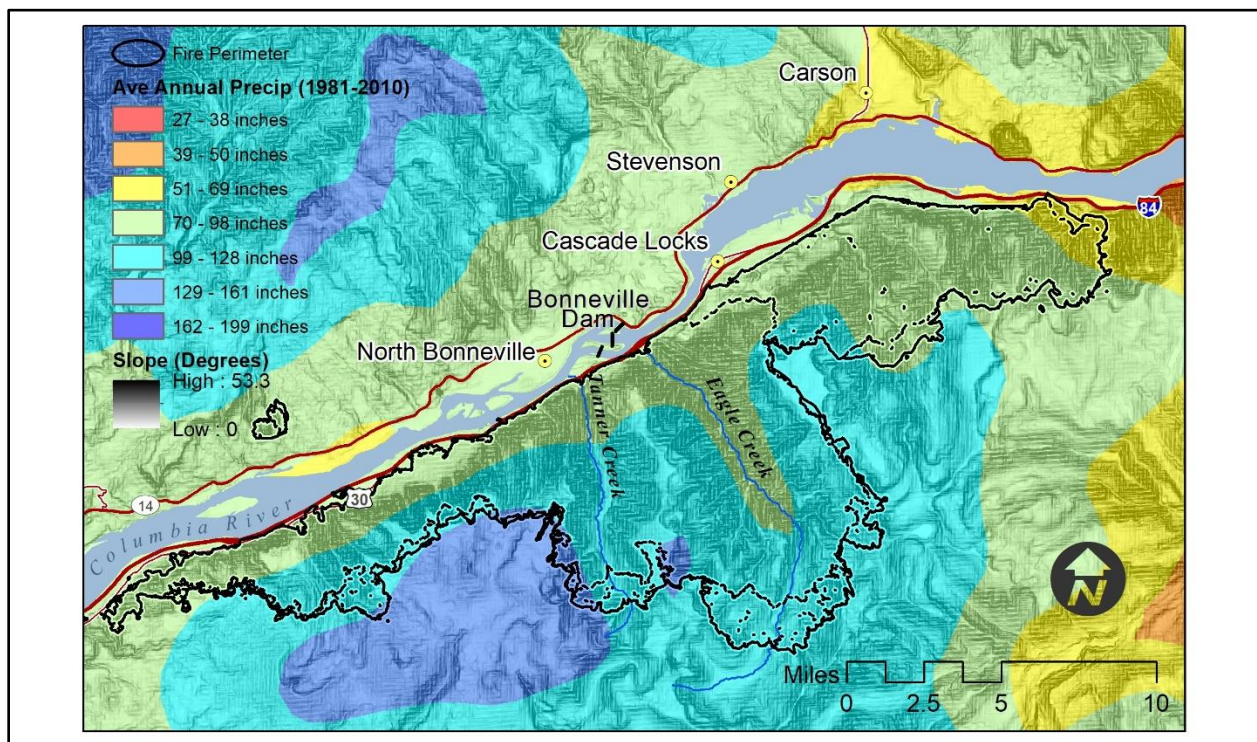
Figure 4. Slope Severity and Average Precipitation in the Eagle Creek Fire Area.

The basins in the region support a diverse number of critical species, including ESA-listed Salmonids. The tributaries provide influxes of cold water into the Bonneville Pool that warms significantly in the summer months. The tributaries also provide spawning habitat and cold water refugia for egress juvenile salmonids and returning adults. The spawning and refugia extents are limited to the lower few miles of most of these tributaries, as large waterfalls prevent upstream passage. The Columbia River Gorge is also home to a unique population of low-

elevation American Pika *(Ochotona princeps)*. This species is typically found in high elevation talus and boulder fields, but a small population exists in certain portions of the gorge.

Post-Fire Conditions

The USFS deployed a specialized team immediately following the wildfire. A Burned Area Emergency Response (BAER) assessment was conducted following the wildfire. The team observed for potential increased post-fire impacts immediately following the burn. They evaluated for geologic and hydraulic hazards including debris flows, landslides, rockslides, rock fall, and flooding associated with debris dam bursts (BAER, 2017).

The fire removed a majority of the existing vegetation in the burned basins. The BAER report (2017) included a fisheries evaluation on both naturally occurring species, and hatchery operation impacts. Based on evaluations of previous wildfires it was determined that there will be an acute effect on fish populations in the cold water tributaries, however the overall impact of the fire may enhance salmonid habitat. These acute impacts may last 5-10 years while riparian areas re-establish themselves. In the short-term it is expected that increases in water temperature and turbidity will occur due to a loss of vegetation and the decrease of shade in previously established riparian zones. The most heavily burnt basins are at high risks to realizing effects to critical habitat for ESA listed species. Significant impacts to water intakes for the Cascade Hatchery, located on Eagle Creek, are expected. Eagle Creek provides the only water source for the hatchery, which incubates millions on salmonid eggs. All contingency plans for other water sources are obsolete due to damage to roads and bridges along planned routes.

Figure 5. View of the Eagle Creek Fire from Bonneville Dam.

In addition to the BAER assessment, USACE Portland District submitted a Dredging Operations Technical Support (DOTS) request to the USACE Engineering Research and Development Center (ERDC). This request allows for teams of scientists to engage specific issues for a brief duration. The team typically provides recommendations to the requesting USACE district. The Eagle Creek Fire DOTS Team, consisting of Geologists, Soil Scientists, Biologists, and Geographers; many who have worked on sedimentation impacts as a result of wildfires in the past, observed the post-burn area from February 5th to February 8th 2018. The team was led into the area by representatives from ODOT and USFS. Similar to the BAER Team, access was limited to a few drainages where hazards to the team were minimal. The team was able to access via Forest Road 777, portions of the Historic Columbia River Highway, and a few open hiking trails.

Post-fire experience indicates that the 3 to 5 years following the fire is the period where sediment and debris mobilization is most likely to occur. The largest concern is the gradual buildup of debris dams in steep tributaries, which pool large amounts of water and debris behind them (Figure 6). Eventually these debris dams burst and pulse the contents of their reservoirs downstream. Depending on the size of the debris dams, the result of these pulses may force large walls of water and debris that could threaten life-safety and critical infrastructure, such as Interstate 84, the Federal Navigation Channel, and Bonneville Dam Facilities.

Figure 6. Debris building in Multnomah Creek.

Data Collection

Large portions of the burned area are still too hazardous to access for in-situ data. Many of the drainages remain too unstable to safely observe due to the risk of slides, as well as falling rock and trees. The BAER Specialists were able to provide the most detailed observations on the ground, and their report represents the most in-depth analysis of the area. However, Portland District is working on other methods to quantify and project impacts that may result from the fire.

In addition to qualitative observations, the Portland District entered into an agreement with the Civil Air Patrol to secure small aircraft flights of the area. This perspective gives the team another qualitative tool to view of the scale of the burn, the proximity of the burn to critical infrastructure, as well as severity of the burn mosaic. Analyzing the burn mosaics (Figure 7) allows the team to focus on the specific areas within the wildfire that were most severely affected.

Figure 7. Burn Mosaic of the Eagle Creek Drainage from BAER Report 2017.

The Portland District is working to install gages at the mouths of Eagle and Tanner Creeks to measure changes in flow that may signal increases over the expected annual discharge. Periodic grab samples will be done in conjunction with suspended sediment measurements to track changes in flow. Routine sediment testing has been done in the area and will provide a baseline data set. This may give advanced warning of debris flows that would threaten infrastructure in the short or long term.

Through an agreement with the National Center for Airborne Laser Mapping (NCALM) at the University of Houston LiDAR data of the wildfire has been collected. LiDAR will allow Portland District, and others, to quantify changes to the topography over time. A USACE data set from 2014 provides a pre-fire baseline. It is expected that LiDAR data will be collected twice a year, pre and post precipitation season. LiDAR is expected to provide information on slope changes,

and coupled with Civil Air Patrol flights, may be able to detect debris dams and new pinch points.

USACE UAS aerial imaging and hydrosurveys are being conducted at the mouths of Multnomah, Horsetail, Oneonta, Tumalt, McCord, Mofatt, Tanner, and Eagle Creeks to monitor changes to the creek deltas.

Future Considerations

The ability to actively manage the burned area is constrained by the Columbia River Gorge National Scenic Area and USFS. The areas are managed to remain natural and pristine. Active management to remove debris dams and to shape slopes to prevent influxes of sediment are not allowed.

Similar USACE DOTS Teams have analyzed the 2011 Las Conchas Wildfire in New Mexico. This was the second largest fire in New Mexico's history, burning over 156,000 acres. The team was able to actively manage the areas of this fire. This included mitigating for debris flows through the construction of catchments, brush mattress and watling, rootwad toe protection, stream meanders, and deflection systems. In New Mexico the team was able to use on site material to construct erosion control structures, using manual labor and light equipment (Figure 8). It's possible that if imminent threats to life and safety are discovered in the Eagle Creek Basins that similar structures may be allowed to mitigate risks of loss of life and infrastructure.

Figure 8. Erosion Control Structures in New Mexico.

Conclusion

There are a large number of Federal, State, and local agencies that are all interested in learning how the fire will change the area. Due to limited resources and access it is clear that

collaboration between all parties will provide the greatest understanding of how the area has been altered, and how each agency can adapt to meet their missions in the changed environment.

It's unclear exactly how the Eagle Creek Fire will impact the region. The largest immediate impacts have been to ODOT as they stabilize Interstate 84 and clean debris from the roadways. Based on previous wildfires it's likely that major impacts, should they occur, will be seen 3-5 years post-fire. We are beginning to enter that window and evaluations are needed to track changes to the basin in order to predict the possibility of catastrophic debris flows.

Portland District has just begun to engage on monitoring efforts, and is working with partner agencies in order to share and built the available information. Following the wildfire annual precipitation has been relatively low when compared to historic levels. USACE, ODOT and other partners are anticipating that debris has slowly been building in some localized areas, but likely need a large rainfall event to mobilize large debris flows and destabilize slopes. Following a major rainfall event it is likely that changes to the basin will represent the new baseline for the area and provide interested parties with an idea of how severe impacts to their infrastructure will be in the near-term.

Figure 9. Post-Fire Multnomah Falls.

References

Eagle Creek Fire Burned Area Emergency Response (BAER) Recreation Specialists Report. United States Forest Service. October 2017.

Dredging Operations Technical Support (DOTS) Consultation. U.S. Army Corps of Engineers, Engineering Research and Development Center. Eagle Creek Fire, Oregon. February 2018.

Dredging Operations Technical Support (DOTS) Consultation. U.S. Army Corps of Engineers, Engineering Research and Development Center. Santa Clara Creek, Santa Clara Canyon, Espanola, New Mexico. May 2017

United States Army Corps of Engineers (USACE) Waterborne Commerce Statistics Center (WCSC) Data for the Columbia River between Vancouver, Washington and The Dalles, Oregon. USACE Channel Portfolio Tool (CPT). January 2019.

Characterization of Hydrology and Sediment Transport Following Drought and Wildfire in Cache Creek, California

Michelle Stern, U.S. Geological Survey, Sacramento, CA, mstern@usgs.gov

Dr. Alan Flint, U.S. Geological Survey, Sacramento, CA, aflint@usgs.gov

Dr. Lorraine Flint, U.S. Geological Survey, Sacramento, CA, lflint@usgs.gov

Introduction

A hydrologic model has been developed to assess wildfire effects on hydrology and sediment transport in the Cache Creek watershed of northern California (Figure 1). The worst drought in California in over 1,200 years occurred between 2012-2017 (Griffin, 2014), depleting surface water and groundwater supply and drying out the soils past wilting point. In the summer of 2015, the Jerusalem and Rocky fires burned roughly 40,000 acres within the Cache Creek watershed below Clear Lake (Figure 1). The fires varied in intensity across the watershed, resulting in spatially variable changes of soil properties and vegetation cover, with unknown changes in hydrology and sediment transport in the area. Post-fire effects on hydrology and sediment transport can be challenging to model, however numerous studies in other watersheds have shown increased runoff and erosion and reduced saturated hydraulic conductivity of soils, especially in the high burn severity class (DeBano, 1966; DeBano and Krammes, 1966; Robichaud, 2000a, 2000b; Johansen et al., 2001; Pierson et al., 2001, 2002).

To fully characterize the post-fire effects in the Cache Creek watershed, an hourly model of streamflow and sediment transport was developed using the Hydrological Simulation Program – FORTRAN (HSPF). This model requires air temperature, precipitation, and potential evapotranspiration as climate inputs. Hourly station data are sparse in the area and may not capture the variability of elevation and local climatology patterns within the watershed. Since uncertainty in climate data can be a major source of error in modeling, it is important to reduce this uncertainty as much as possible. A technique used to spatially-interpolate daily-climate station data has been shown to improve the characterization of local and regional climate patterns on a daily scale in areas with sparse data (Flint et al., 2014). This technique was applied to available hourly observed data to produce spatially-varying climate inputs for the Cache Creek hydrologic model.

A daily HSPF model of the Sacramento River Basin (Stern et al., 2016) was developed to estimate sediment transport in the Sacramento River, and its tributaries, which include the Cache Creek watershed below Clear Lake. The Sacramento River Basin HSPF model was developed at a larger scale than appropriate for characterizing a single watershed the size of Cache Creek below Clear Lake, so the new Cache Creek HSPF model was extracted to create a smaller domain. It was then refined temporally from daily to an hourly time step and refined spatially to create smaller sub basins for calibration.
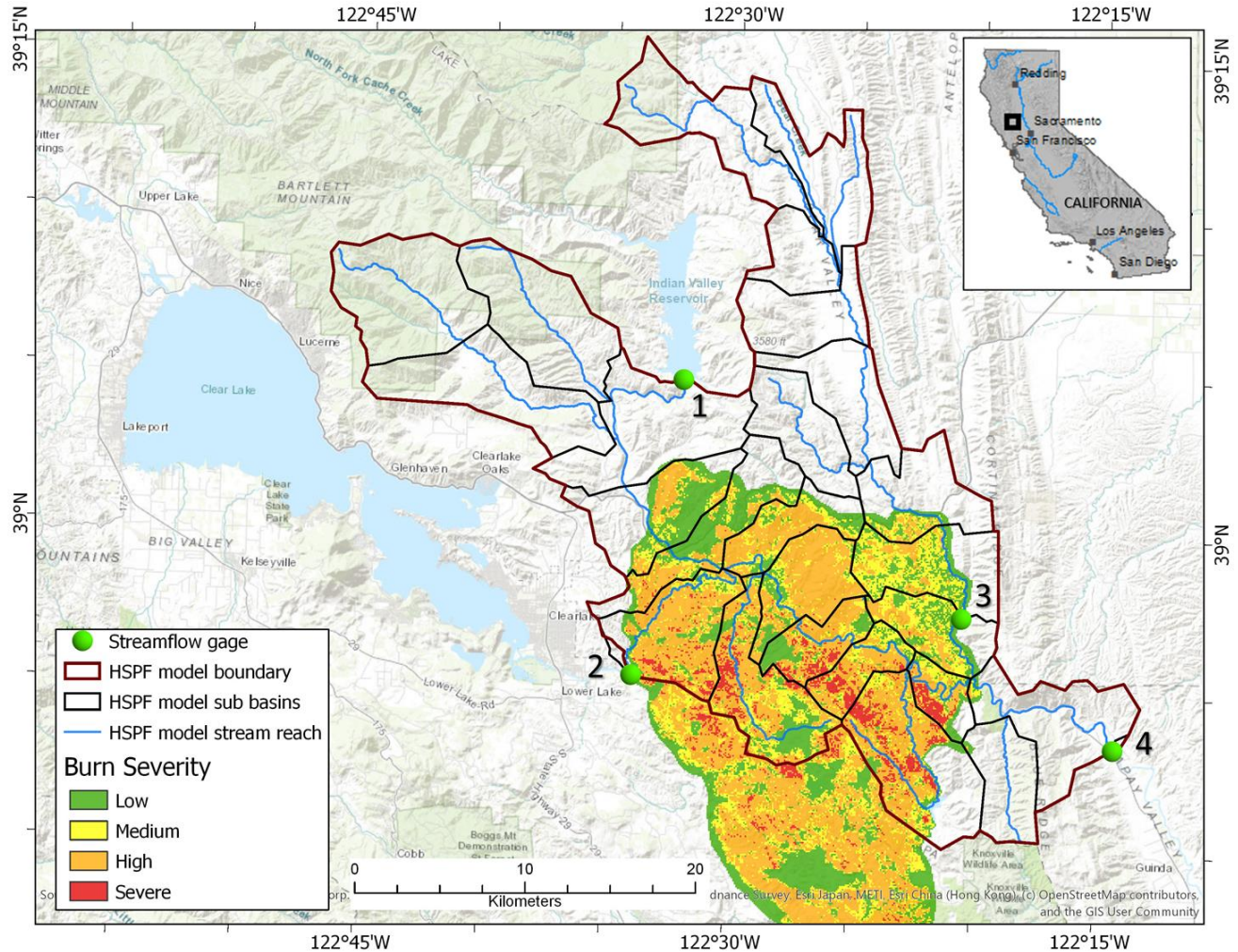
Figure 1. Location of Cache Creek HSPF model (red outline), model sub basins (black outline), burn severity, and gage locations (green circles)

Methods

The Cache Creek HSPF model was developed to run as a continuous multi-year simulation with hourly time steps starting on June 1, 2014 and ending on September 30, 2017. Hourly climate inputs (precipitation, air temperature, and potential evapotranspiration (PET)) were developed as unique time series for each model sub basin by averaging gridded results from spatial interpolation methods over the area of each sub basin. The spatial interpolations were done using a 270-meter grid spacing and provided an improved representation of spatially varying precipitation and air temperature compared to methods such as Thiessen polygons and inverse-distance-weighting. The gridded climate inputs (precipitation and air temperature) and 270-meter elevation data were used to develop gridded estimates of PET.

Gridded climate inputs

To develop hourly grids for precipitation and air temperature for the Cache Creek watershed, an existing FORTRAN-based program was modified to input hourly station data and spatially interpolate the hourly data across the watershed using a digital elevation model (DEM) and the Parameter-elevation Regressions on Independent Slopes Model (PRISM, http://prism.oregonstate.edu/). Hourly PET was developed for the study area using hourly air

temperature grids and the Priestley-Taylor evapotranspiration equation based on calculated topographic shading, simulated solar radiation, estimated atmospheric parameters, and estimated cloudiness (Flint et al., 2013).

Hourly climate (air temperature, precipitation, and PET) grids were developed in four steps:

1) Hourly and daily station data were downloaded from Remote Automated Weather Stations (RAWS; http://www.raws.dri.edu/), California Irrigation Management Information System (CIMIS; http://wwwcimis.water.ca.gov/cimis/welcome.jsp), and the National Climatic Data Center (NCDC; http://www.ncdc.noaa.gov) for stations located within and surrounding the Cache Creek watershed.

2) The daily and hourly station data were checked for errors and then spatially distributed across the study area using a Gradient and Inverse Distance Squared (GIDS) weighting method (Nalder and Wein, 1998). For every active station, GIDS developed regressions for each time step including the northing, easting, and elevation at each station to adjust for local gradients such as lapse rates, inversions, or rain shadows.

3) Gridded PRISM climate maps (http://prism.oregonstate.edu/) were downloaded and clipped to the watershed boundary. PRISM is a knowledge-based analytical model that uses point data of measured precipitation and air temperature that is then integrated with a digital elevation model, expert knowledge of complex climatic extremes, such as rain shadows, temperature inversions and coastal effects to produce digital grids of monthly or daily precipitation, and minimum and maximum air temperatures. Monthly PRISM grids were used in a two-step scaling method with climate GIDS maps (Step 2) to develop daily grids, then the daily grids were used to scale hourly climate GIDS maps.

   a. Step 3.1: The daily GIDS maps from step 2 were summed (for precipitation) or averaged (for air temperature) into monthly maps to calculate a ratio $(PRISM/GIDS)_m$ for each grid cell using the monthly PRISM data. Next, the daily GIDS maps were multiplied by that ratio to create daily maps that exactly sum (for precipitation) or average (for air temperature) to match the monthly PRISM maps.

   b. Step 3.2: The hourly station data were used to develop hourly GIDS maps. The hourly GIDS maps were summed or averaged into daily maps used to develop a ratio $(PRISM/GIDS)_d$ with the daily PRISM-adjusted grids from the previous step. This resulted in hourly gridded precipitation and air temperature grids. This method captures the temporal variability at each climate station yet preserves the regional monthly spatial structure of the PRISM dataset.

4) PET grids were developed using the air temperature grids and a FORTRAN algorithm that applies the Priestley-Taylor equation (Priestley and Taylor, 1972). In this step, topographic shading parameters, including slope and aspect, are calculated using the DEM and are used for simulating short-wave radiation. The algorithm also accounts for atmospheric effects (such as cloudiness and turbidity) on simulated short-wave radiation.

Calibration of Cache Creek HSPF model

The refined Cache Creek HSPF model was initialized using the previously calibrated parameters and calibrated using available streamflow and sediment data at an hourly time step. Hydrologic and sediment calibration data were downloaded from the U.S. Geological Survey (USGS) National Water Information System (NWIS; https://waterdata.usgs.gov/nwis). Two hourly stream gage locations were available in the model period and within the study area for calibration and two locations provided continuous hydrology input from Clear Lake and Indian

Valley Reservoir (Figure 1, Table 1). The Cache Creek at Rumsey gage was originally operated by the Department of Water Resources (DWR) and data were downloaded from the California Data Exchange Center (CDEC, http://cdec.water.ca.gov) until the gage was taken over by USGS on September 23, 2015. Sediment data were only available at the Cache Creek at Rumsey gage (4, Table 1).

Table 1. Stream gage stations used for HSPF modeling

Gage number	Site ID	Site Name	Boundary/Calibration	Sediment samples
1	11451300	N Fk Cache C nr Clearlake Oaks	Boundary	
2	11451000	Cache C nr Lower Lake	Boundary	
3	11451715	Bear C ab Holsten Chimney Cyn nr Rumsey	Calibration	
4	11451800	Cache C at Rumsey	Calibration	n = 163 Daily, 10/1/2015 – 4/30/2017
4	RUM	Cache C at Rumsey Bridge	Calibration (pre-09/2015)	

Hydrologic calibration was performed using data from water year 2015 (October 2014 - September 2015), and validated using the same parameters for water year 2016. The model was run through water year 2017 to characterize the effects of wildfire on hydrology and sediment transport. The HSPF model was run at an hourly time step from June 1, 2014 through September 30, 2017 to ensure a model initiation period of four months prior to the target simulation period used for calibration and analysis. The initiation period provides a model "spin up" to establish antecedent conditions at the start of the target period.

Results

Statistical metrics were calculated at daily and hourly time steps to describe the agreement of modeled with observed data and included: coefficient of determination (R^2), mean squared rror (MSE), Nash-Sutcliffe Efficiency statistic (NSE), and root mean squared error (RMSE). Statistics were calculated at two gage locations, Bear Creek (3, Figure 1) and Cache Creek (4, Figure 1), for the calibration (water year 2015), validation (water year 2016), and the simulation period (water years 2015-2017, Table 2).

Table 2. Calibration, validation, and simulation period statistics for two gage locations. R^2 = coefficient of determination, MSE = mean squared error, NSE = Nash Sutcliffe Efficiency, RMSE = root mean squared error (in cubic feet per second), WY = water year

		Hourly				Daily			
		R^2	MSE	NSE	RMSE	R^2	MSE	NSE	RMSE
Calibration	Bear Creek	0.68	20.2	0.58	4.5	0.73	4,645	0.62	68.2
(WY 2015)	Cache Creek	0.67	238.9	0.48	15.5	0.79	170,238	0.53	412.6

Validation	Bear Creek	0.35	23.5	0.28	4.9	0.37	5,609	0.28	74.9
(WY 2016)	Cache Creek	0.72	108.8	0.71	10.4	0.80	56,142	0.79	236.9
wy2015-2017	Bear Creek	0.41	47.8	0.36	6.9	0.44	28,071	0.36	167.5
	Cache Creek	0.87	197.0	0.87	14.0	0.92	156,844	0.92	396.0

Results indicate a satisfactory model fit at Bear Creek and Cache Creek for the calibration year, with hourly R^2 values of 0.68 and 0.67, respectively (Table 2). Hourly NSE values were 0.58 and 0.48 for Bear Creek and Cache Creek, respectively. Daily R^2 values were 0.73 and 0.79 for Bear Creek and Cache Creek and were improved significantly for the entire simulation period for Cache Creek with daily R^2 and NSE values of 0.92. Figure 2 shows the modeled and observed hourly time series of flow, indicating a good overall representation of observed data. Storm hydrographs were also viewed during calibration because one of the main goals of the study is to quantify sediment loads, which are much higher in peak flows.
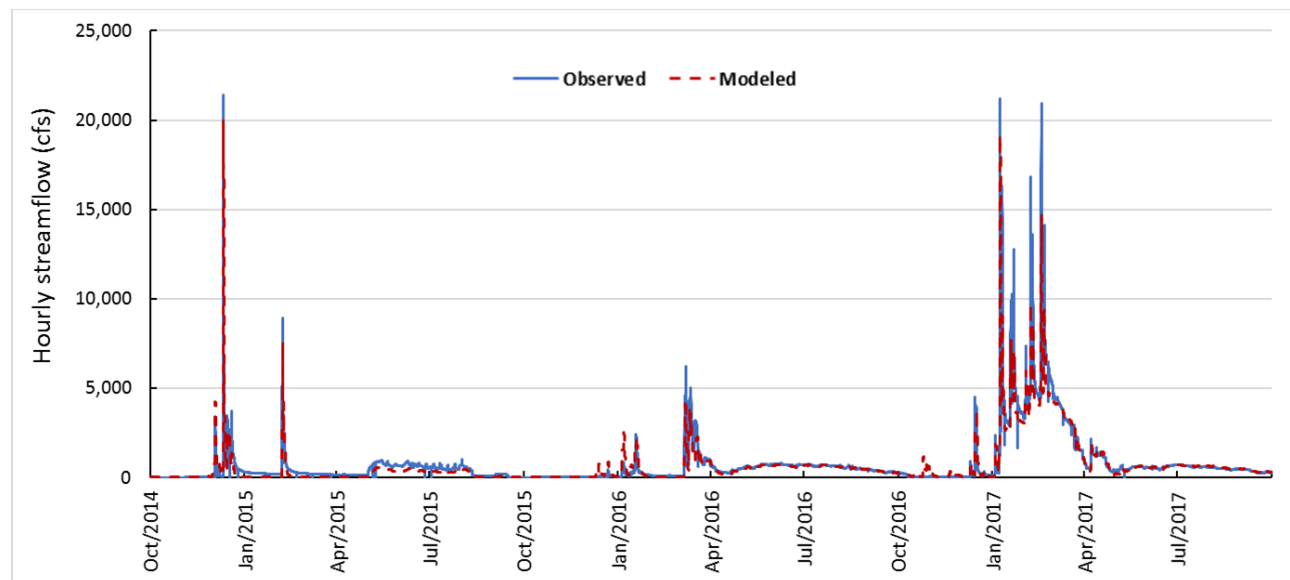
Figure 2. Observed hourly streamflow (blue) and modeled (red dashed) for the Cache Creek at Rumsey gage, for the model simulation period

Six storms were chosen to determine magnitude and timing of peak streamflow events, two from each of the three years in the simulation period (Table 3). Statistical results from the storm events indicate satisfactory timing and magnitude for simulating the major peak stormflow events in the simulation period. The modeled peak flows generally underpredicted observed peak flows; however, the modeled storm volumes were only slightly under or over the observed storm volumes. The HSPF model better represented the second storm of water years 2016 and 2017 than the first storms of either year or the storms in water year 2015.

Table 3. Statistics for six storms at Cache Creek at Rumsey. in = inches, cfs = cubic feet per second, hr = hour, R^2 = coefficient of determination, NSE = Nash Sutcliffe Efficiency

Water Year	Start Date	End Date	n(days)	Storm precipitation (in)	Modeled peak flow (cfs)	Observed peak flow (cfs)	Maximum storm intensity (in/hr)	R^2	NSE
2015	12/10/2014	12/14/2014	5	4.7	19,981	21,418	0.39	0.68	0.48
	2/6/2015	2/11/2015	6	4.4	7,563	8,916	0.32	0.41	0.29
2016	3/5/2016	3/9/2016	5	3.6	4,416	6,245	0.46	0.35	0.50
	3/10/2016	3/13/2016	4	2.2	4,017	5,010	0.22	0.78	0.71
2017	1/6/2017	1/12/2017	7	7.7	19,163	21,225	0.35	0.62	0.69
	2/17/2017	2/22/2017	6	4.9	14,698	20,950	0.23	0.82	0.91

Sediment transport

Sediment transport was calibrated using a "weight of evidence" approach, due to little available sediment data in the study area. Sediment parameters were initially set using the existing Sacramento River Basin model for this sub-watershed area and were changed iteratively through the calibration process. To simulate a fire across the landscape, sediment parameters were changed for sub basins that were burned in the Jerusalem and Rocky fires (Figure 1). For the burned areas, vegetation cover was reduced to zero, and soil detachment and wash off parameters were increased for water year 2016. These parameters were changed for water year 2017 to indicate partial watershed recovery.

Available sediment discharge (tons/day) and suspended sediment concentration (SSC, mg/l) data were compiled (Table 1). Instantaneous and daily data from the Cache Creek at Rumsey location were compared with simulated hourly and daily sediment transport results, respectively. R^2 values for daily SSC and sediment discharge were 0.70 and 0.75, respectively. Instantaneous SSC and sediment discharge samples were compared to the nearest modeled time series value and resulting R^2 values were 0.56 and 0.46, respectively. After aggregating to monthly values, R^2 of SSC and sediment discharge were 0.91 and 0.98, respectively.

Discussion

Results from this study indicate that post-drought and post-fire effects in the Cache Creek watershed were inconclusive for runoff; however, sediment transport was sensitive to the watershed disturbances and required changes in the model parameterization to better characterize sediment transport post-fire and post-drought. Changing hydrologic parameters post-fire did not result in improved calibration to observed streamflow, indicating that increased runoff caused by the effects of fires on soils and vegetation were not distinguishable. However, the watershed is baseflow-dominated and the period before the fire was an extended drought which complicated the watershed response to fire. Wildfires commonly occur after periods of extended drought and in a three-year simulation, distinguishing between post-drought and post-fire effects was not possible. Although there were no perceived changes in modeled runoff, it was necessary to adjust sediment parameters to simulate post-fire sediment transport. Sediment parameters were changed to increase erosion and decrease vegetation cover in areas affected by wildfire. Modeled sediment results indicate that suspended sediment concentrations increased relative to streamflow in the post-fire conditions, whereas sediment discharge followed the trends of flow between pre-fire and post-fire years. The modeled flow and

sediment results can be used to estimate concentrations and loads of water quality constituents that are correlated with flow and or sediment and could be a major concern, especially following the combined effects of drought and wildfire. The watershed responses to wildfire and drought examined in this study can be used to help land managers consider best management practices to manage sediment and water quality constituents after a watershed disturbance.

References

DeBano, L.F., 1966. "Formation of non-wettable soils: Involves heat transfer mechanism," (Vol. 132). Pacific Southwest Forest & Range Experiment Station.

DeBano, L.F. and Krammes, J.S., 1966. "Water repellent soils and their relation to wildfire temperatures," International Association of Scientific Hydrology Bulletin, 11, pp. 14-19.

Flint, A.L., Flint, L.E., and Stern, M.A., 2014. "Spatial downscaling and mapping of daily precipitation and air temperature using daily station data and monthly mean maps," Poster presented at 2014 Fall Meeting, AGU, San Francisco, Calif., 15-19 Dec.

Flint, L.E., Flint, A.L., Thorne, J.H., and Boynton, R., 2013. "Fine-scale hydrological modeling for climate change applications; using watershed calibrations to assess model performance for landscape projections," Ecological Processes 2:25.

Griffin, D. and Anchukaitis, K.J., 2014. "How unusual is the 2012–2014 California drought?," Geophysical Research Letters, 41(24): pp. 9017-9023.

Johansen, M.P., Hakonson, T.E., and Breshears D.D., 2001. "Post-fire runoff and erosion from rainfall simulation: contrasting forests with shrublands and grasslands," Hydrological Processes 15: 2953– 2965.

Nalder, I.A. and Wein, R.W., 1998. "Spatial interpolation of climatic normals: test of a new method in the Canadian boreal forest," Agricultural and Forest Meteorology, 92(4), pp.211-225.

Pierson, F.B., Robichaud, P.R., and Spaeth, K.E., 2001. "Spatial and temporal effects of wildfire on the hydrology of a steep rangeland watershed," Hydrological Processes 15: 2905– 2916.

Pierson, F.B., Carlson, D.H., and Spaeth, K.E., 2002. "Hydrologic impacts of fire on steep intermountain sagebrush–steppe rangeland," International Journal of Wildland Fire 11: 145–151.

Priestley, C.H.B. and Taylor, R.J., 1972. "On the assessment of surface heat flux and evaporation using large-scale parameters," Monthly weather review, 100(2), pp.81-92.

Robichaud, P.R., 2000a. "Forest fire effects on hillslope erosion: what we know," In Watershed Management Council Networker, vol. 9, no. 1, Fire Effects. Watershed Management Council: Davis, CA; 9–13.

Robichaud, P.R., 2000b. "Fire effects on infiltration rates after prescribed fire in northern Rocky Mountain forests, USA," Journal of Hydrology, pp. 220–229.

Shuttleworth, W.J., 1993, Evaporation, in Maidment, D.R. (Ed.), 1993. Handbook of Hydrology. McGraw-Hill, Inc.

Stern, M., Flint, L., Minear, J., Flint, A., Wright, S., 2016. "Characterizing changes in streamflow and sediment supply in the Sacramento River basin, California, Using Hydrological Simulation Program—FORTRAN (HSPF)," Water; 8(10):432.

Characterization of Shallow Groundwater in Detroit: Environmental, Hydraulic, and Health Considerations

Authors: Brendan F. O'Leary (brendanfoleary@gmail.com), Sadaf Teimoori, and Carol J. Miller, Civil and Environmental Engineering, Wayne State University, 5050 Anthony Wayne Dr., Detroit, MI 48202

Abstract: Groundwater plays a critical role in the vitality of the Great Lakes Basin, supplying drinking water, industrial water supply, cooling water for power generation, and irrigation water for farms in rural areas and landscape in urban areas. It also is interconnected with surface water features, including the lakes, streams, and reservoirs of the region. Therefore, the quality of the groundwater is crucial and has potential economic, health, and social implications for the region. The traditional focus of environmental and health concern, especially in urban areas, has been on surface water rather than groundwater, following the "out of sight, out of mind" mentality. The lack of data on groundwater (especially shallow, near-surface) flow, quality, and transport in urban centers is a threat to the health of the Great Lakes Basin. Two approaches are being used to evaluate groundwater in southeast Michigan. The first approach is constructing a neighborhood scale urban water budget at Recovery Park. This water budget model will contribute to evaluating urban groundwater flow in urban settings with limited groundwater data. The second approach is compiling a regional groundwater model within four major watersheds to address the general groundwater flow direction in the Detroit region. Both the regional and neighborhood scale models will help develop and evaluate the potential risks posed to urban environments and human health.

Continuous River Bed Monitoring at Hydroelectric Intakes Using Dual-Axis Sonar Scanners

Dan Haught, Fluvial geomorphologist, Northwest Hydraulic Consultants, Sacramento, CA, dhaught@nhcweb.com

Andre Zimmermann, Principal Geomorphologist, Northwest Hydraulic Consultants, Vancouver, BC, Canada, azimermann@nhcweb.com

Introduction

Bedload transport, particularly coarse gravel, is of interest to hydroelectric facilities that must monitor and manage their facilities. Yet bedload transport is naturally stochastic and both transport and supply driven. Traditional bedload measurements have proven difficult in events that transport substantial bedload, while modeling bedload transport accurately remains a contemporary challenge. Here we show through several deployments, at two sites, how we utilize the Dual-Axis Sonar (DAS) to monitor both bed elevation and debris management on a variety of hydroelectric dams. The observations, in lieu of models, provide a robust direct method in which to manage hydroelectric facilities in real-time. The results can also be used with models and other direct measurements to provide valuable information to support model development and operational rules for rarely occurring high consequence scenarios.

In general, observations from the sites prove more useful than general sediment operational rules and have enabled operators to produce more power at times of the year when the sediment supply rates are slower. At times of high bedload transport, adjustment of operations can be made when sluicing needs to be more aggressive to prevent sediment clogging trash racks and damaging turbine runners. The sonar data has also been used in real-time to adjust dredging activities at sites with scans as frequent as every 10 minutes.

Site Descriptions and Instrument Setup

We have utilized DAS scanners at four sites, two of which are described herein. The Northern British Columbia site is located at a run-of-the-river hydroelectric facility on McLymont Creek, a tributary to the Iskut River, and is operated by AltaGas. The hydrology is dominated by a snowmelt and glacier melt freshet, but also impacted by fall rain storms that cause the largest floods on the river and are particularly flashy. Bed material is coarse gravel and cobble.

The second site located in Southwestern Washington is operated by Lewis County Public Utility District (LCPUD) and is on the Cowlitz River. Though the Cowlitz also relies on snowmelt fall rain storms result in the largest floods. The sediment load at Cowlitz is considerably finer and composed largely of sand that can deposit in the reservoir created by the facility. The operational rules of the reservoir require the water levels to be drawn down during floods, which can result in a dramatic increase in sediment loading at the site as the sand in the reservoir is dewatered, and the river transitions from reservoir conditions to riverine conditions.

Dual-Axis Sonar Setup:

We deploy DAS scanners developed by Kongsberg Mesotech. The sonar uses a 330 kHz frequency and max range of 300m, with an applicable range dependent on the sonar settings.

The scanner covers 360° in the horizontal and ranges from 10° to -90° in the vertical. The step size varies between 0.225° and 7.2° which determines the total time to complete a scan. The scans can take between a few minutes to a day in duration, with most scans set to run every half hour to two hours, depending on the desired resolution and extents. The system is integrated with the plant control networks so that plant operators can respond to changes in bed elevation quickly. Figure 1 (left) shows the DAS deployment at the Cowlitz Hydroelectric facility and the instrument mount that was hung off a debris prevention boom (left). Figure 1 (right) = shows an image of the head pond empty, which lends perspective to the scans described below.

Figure 1. Images showing the DAS deployment at the Cowlitz Hydroelectric facility.

Continuous River Bed Monitoring:

Bedload Transport Events

To monitor bedload at a site, we scan the bed over a predetermined time. Time intervals are based off the resolution needed. Most deployments range from 30 minutes to a couple hours. Longer scans are collected to create base digital elevation models (DEM), while shorter scans are done in smaller areas. Figure 2 shows an event from the McLymont facility during peak discharge (Figure 2 top). The DEM shows bedforms moving through the head pond from left to right (Figure 2 bottom left), along with the change in elevation from the prior scan (Figure 2 bottom right). To provide facility managers and operators information on the river bed dynamics, we average spatially specific areas (~4 m²) as point data to provide time-series of the elevation changes, in addition to the DEMs. Between the more temporally resolute time-series data and the more spatially dynamic bed scans, managers and engineers are able to track the river bed and identify issues in both the short and long term. Management decisions can be made in real-time, while engineers and managers gain more insight into the local processes that come with longer data sets, allowing for more efficient management practices.

The data from the sonars has enabled us to continuously track dunes and gravel bars. Additionally, we gain information on sediment transport around a multitude of structures where both long-term (aggradation/degradation) and short-term (scour) sediment transport processes

are of interest. Figure 2 shows dunes moving left to right towards the intake of the facility that is at the bottom of the image.
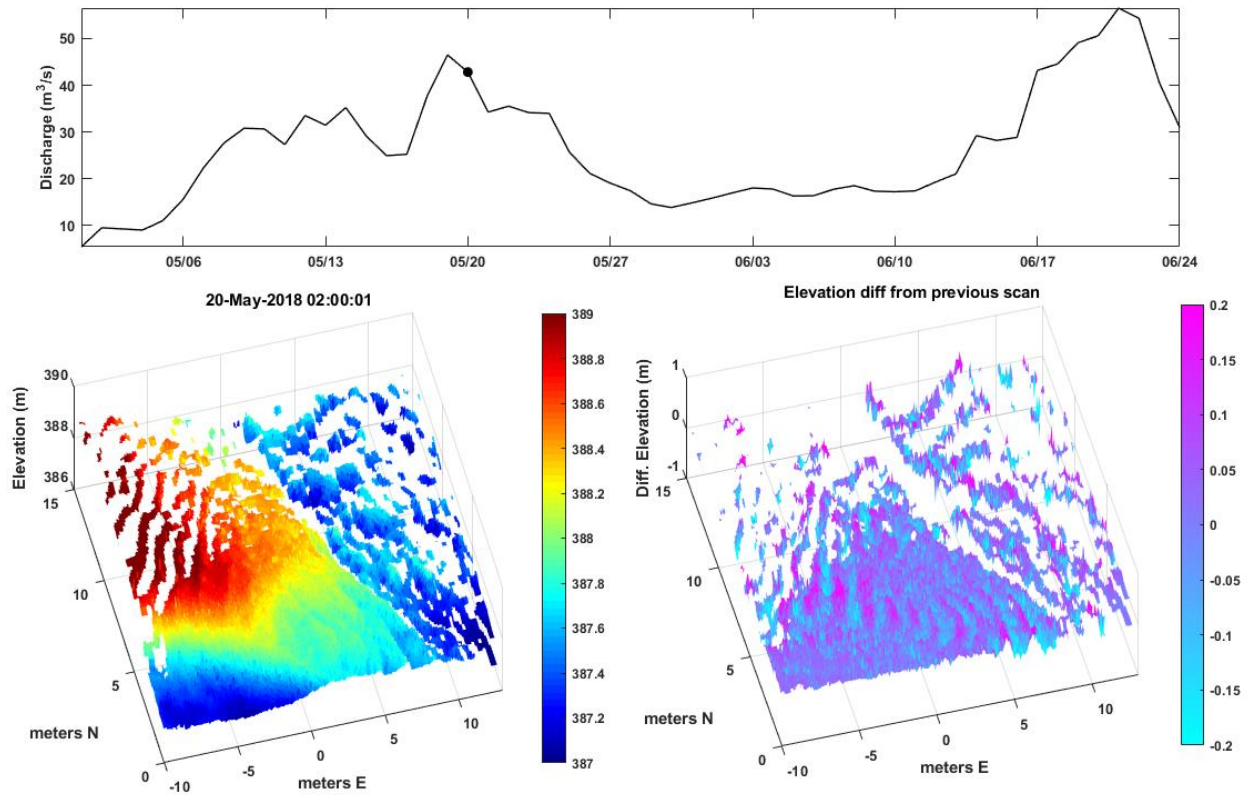
Figure 2. Time series showing the discharge (top), the DAS scan DEM (bottom left), and the difference between the DEM and the scan prior (i.e. change in elevation over two hours).

Sediment and Debris Monitoring

Our monitoring setup and analysis provides important information to dam managers and operators with respect to the effectiveness of debris prevention and efficient sluicing. Figure 3 shows a scan of the Cowlitz River hydroelectric facility. This scan was fit to a model of the structure. The scan captures a large log, large rock that is positioned near the gates, and the existing concrete divide wall used to direct flow and sediment through the sluice gates. The DEM captured by the scan can also be seen in the empty headpond shown in Figure 4. At this facility the intent of the sonar is to track bed elevations in front of the sluice gates and power generation intakes and watch for sediment and debris accumulation during floods while the reservoir is being drawn down and converted to a river.
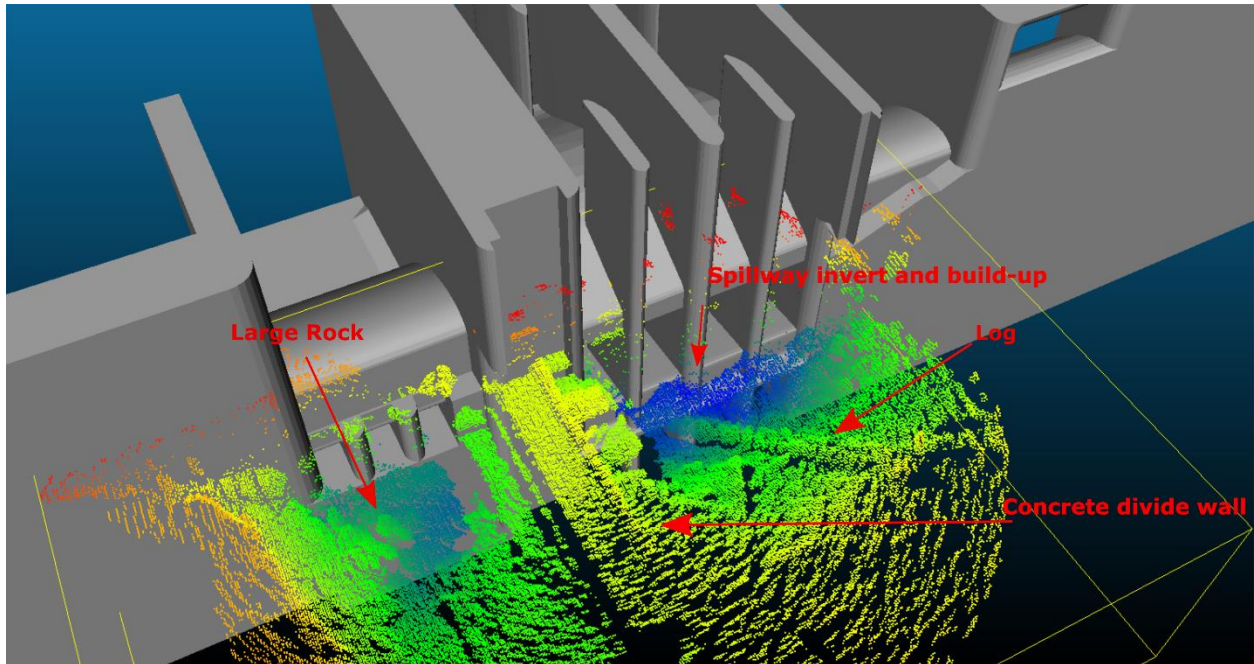
Figure 3. DAS scan from Cowlitz Hydroelectric facility showing the structure and the bathymetry of the head pond.

Figure 4. Photo of the hydroelectric structure during drawdown illustrating many of the same structures that the scan shows.

Conclusion

The DAS installs that we have completed to date clearly show the passage of dunes, gravel bars, logs and woody debris as well as the location of rocks and concrete structures. We use these scans to select areas of interest where we spatially average the data over small areas to produce single points that we track in time. This simple analysis provides dam operators with both spatial and temporal information on sediment transport and debris build-up. The points that are tracked in time are commonly imported into the Programable Logical Controller (PLC) and alarms are set for when the bed elevation exceeds a preset threshold. Additionally, we show how this monitoring can capture sediment transport processes that have proven difficult to model or measure directly. Differentiating the scans both spatially and temporally could allow for estimates of transport rates, while hydraulic and bed sediment information could better develop local transport models. Analyzing these methods to provide sediment fluxes is the next frontier and would provide exceptionally high-quality direct measures of sediment transport in large rivers with complicated hydraulics.

Regional Patterns and Spatial Clusters of Nonstationarities in Annual Peak Instantaneous Stream Flow

Bryan Baker, Hydraulic Engineer, Remote Sensing-GIS Center of Expertise, Cold Regions Research and Engineering Lab, U.S. Army Corps of Engineers, Hanover, NH, bryan.e.baker@usace.army.mil
Aaron Sant-Miller, Senior Lead Data Scientist, Booz Allen Hamilton, Washington, DC, sant-miller_aaron@bah.com and aaron.m.sant-miller@usace.army.mil

Introduction

When designing and evaluating water resources infrastructure and water management plans, practitioners often lean on traditional methods for defining risk, reliability, and return period. In many cases, these techniques assume stationary hydrologic conditions, which implies natural systems fluctuate within an unchanging envelope of variability. In other words, these methods assume hydrologic processes are relatively unchanging in time; events arise from a time series with a probability distribution whose statistical properties are fixed (Brillinger 2001). If stationarity is taken to be true, one can conditionally assume that historic trends reflect future expectations, where more historic data leads to stronger conclusions about the future.

Yet, increasingly, scientific evidence suggests that this principle is no longer universally applicable. In many cases, climate change and human watershed modifications have impacted components critical to the design and evaluation of hydrologic projects (e.g., Milly et al. 2008; Villarini et al. 2009a; Villarini et al. 2009b; Vogel et al. 2011; Prosdocimi et al. 2014; Slater et al. 2015; Villarini and Slater 2017). Not only is there evidence of historical impacts, but these impacts are continuing to occur today, requiring the validation of the stationarity assumption when using traditional techniques. If practitioners cannot validate this principle, analytic outputs that quantify risk or future changes in hydrologic behavior may be inconsistent with the true reality. Therefore, it is recommended that an additional step be added into the analytical workflow – a test for nonstationarity (Brekke et al. 2009, 2011). By detecting nonstationarities in flow records, engineers may adjust their approach to make more informed risk-based decisions under more volatile conditions.

Many organizations are proactively developing analytic methodologies and technical tools to better detect, evaluate, and consider nonstationarities in flows. The United States Army Corps of Engineers (USACE) is one of those organizations, as USACE offers their Nonstationarity Detection Tool to the public for research and engineering analysis. This tool, and tools like it, can analyze particular locations of interest and provide a foundation for more in-depth case studies, as shown below in USACE's study of geospatial patterns of nonstationarity in unimpaired stream flow.

Nonstationarity Detection

By definition, a nonstationarity is a statistically significant change or shift in hydrologic behavior, where hydrologic processes subsequently behave differently than they did before (Villarini et al. 2009a; Villarini et al. 2009b). This is an appropriately broad definition; there are

many types of nonstationarities, each with different tests and techniques for their detection. Below, these types will be outlined, as well as various statistical tests used to uncover them.

Families and Types of Nonstationarities

Generally speaking, there are two families of nonstationarities: 1) those that are abrupt or sudden, and 2) those that are smooth or gradual (Friedman et al. 2018). Each family must be treated differently, where unique statistical assumptions are used to account for different windows of time and different thresholds for volatility. Within these two families, there are three types of nonstationarities that may occur: 1) a change in the first moment of the data, or the mean, 2) a change in the second moment of the data, or the variance, and 3) a change that results in a new distribution for the data (Friedman et al. 2018).

Here, it is worth noting that methods designed to detect changes in the mean will not detect changes in the variance; these tests are designed and optimized to isolate one specific type of change point or nonstationarity. For this reason, general best practices recommend the application of multiple tests, which helps build greater fidelity around analytic conclusions. In a complete nonstationarity analysis, the flagging of a nonstationarity involves not just the detection of a change point from one test, but also test consensus (i.e., multiple different tests detect the same kind of change), nonstationarity robustness (i.e., several types of changes are detected all at once), and nonstationarity magnitude (i.e., changes should have both statistical significance and practical impact) (Friedman et al. 2018). When a nonstationarity is detected that is robust, with consensus and with significant magnitude, adaptive planning on hydrologic behavior should be undertaken (Friedman et al. 2018).

Nonstationarity Detection Methods

The United States Army Corps of Engineers (USACE) has evaluated a number of statistical tests used to identify nonstationarities, recommending ten methods for abrupt changes and two methods for smooth changes. Accordingly, these are the methods used in this study (Friedman et al. 2018). In Figure 1 below, these statistical tests are both enumerated and defined, where some tests can be tailored for either abrupt or smooth nonstationarity detection (e.g., the Lombard-Wilcoxon Test and the Lombard-Mood Test).

1. Mean-based Tests

Detects a nonstationarity where there has been a significant change in the average value of the data
Examples:
1. *Lombard Wilcoxon*: Nests the Wilcoxon score function within the Lombard test statistic to detect both smooth and abrupt shifts in mean by time
2. *Pettitt*: Nonparametric test that identifies changepoints in the mean by tests whether two samples come from the same population
3. *Mann-Whitney*: Nonparametric test on mean shift, that tests if randomly selected value is from one sample is greater than or less than a randomly selected value at from the comparison sample (seen as the nonparametric counterpart to the t-test)
4. *Bayesian CPD:* Parametric (Gaussian) test that uses product partitions to identify change points within a sequence using MCMC sampling by assuming a sequence can be broken into partitions with a constant mean, where changes in the mean between partitions are change points.

2. Variance-based Tests

Detects a nonstationarity where there has been a significant change in the variance of the data
Examples:
1. *Mood*: A nonparametric case of a Pearson's Chi-test that evaluates change points based on volatility in medians between defined samples
2. *Lombard Mood*: Nests the Mood score function within the Lombard test statistic to detect both smooth and abrupt shifts in variance by time

3. Distribution-Based Tests

Detects a nonstationarity where there has been a significant change in the underlying distribution of the data, which can be caused by a change in the parameters of the same distribution or from one distribution type to another (test shape, location, and modality)
Examples:
1. *Cramer-Von-Mises*: Parametric goodness of fit test that compares two empirical distributions by evaluating a test statistic of distributional distance
2. *Kolmogorov-Smirnov*: Nonparametric test that compares two empirical distributions by evaluating a test statistic of distributional distance
3. *LePage*: Simultaneously tests the equality of both the location and scale parameters, where inequality in one suggests distributional shift
4. *Energy Divisive*: Nonparametric test based on hierarchical clustering, where change points are iteratively identified and can be diagrammed as a binary tree. The statistical significance is examined by means of a permutation test that combines bisection and multivariate divergence measures

Figure 1. USACE applied nonstationarity tests

As shown in Figure 2 below, abrupt changes occur at a single point in the record, functionally separating the data into two subsets differ either in mean, variance, or statistical distribution. It is worth noting that a record may have multiple abrupt changes, separating it into several subsets of data. On the other hand, while smooth nonstationarities may be less visually apparent at low temporal resolution, the long-term impacts can be just as significant (see Figure 2 below).
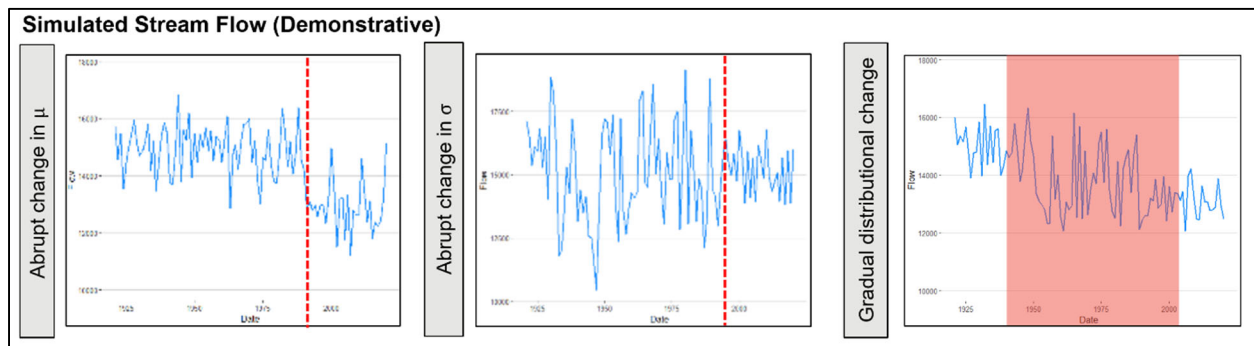
Figure 2. Detected nonstationarities in simulated stream flow data (Left: an abrupt change in mean, Center: an abrupt change in variance, and Right: a smooth change in distribution)

Case Study: Geospatial Analysis of Unimpaired Gages

Summary

As previously discussed, scientific evidence increasingly suggests that the stationarity principle is not universally valid, where climate change and human watershed modifications have impacted stream flow behavior. Though there are well-founded associations between nonstationarity and these underlying drivers of instability, moving from correlation to attribution can be challenging. In the following case study, the data set was restricted to stream gages that were unimpaired (i.e., unimpacted by human watershed modifications). Doing so functionally introduces a limited scientific control, offering more refined analytic conclusions.

Historically, most similar studies have considered all gages, regardless of impairment, and few have considered these relationships, systematically, across the continental United States (e.g., Villarini et al. 2009a; Villarini et al. 2009b; Sadri et al. 2016). By reducing the data set in this way, this study aims to offer a more simplified causal analysis and, potentially, evidence suggesting further studies linking climate change effects to nonstationarities.

Data and Inputs

For this study, a reduced sample of unimpaired gages (N = 333) was drawn from the Gages-II data set provided by USGS (Falcone 2011; Ryberg and Vecchia 2012). Only gages with over 40 years of record were used. From this sample, instantaneous daily stream flow values were transformed into a time series of annual peak flows for more stable nonstationarity analysis. Doing so helps control for the natural volatility in hydrologic systems, increasing the efficacy of applied statistical tests. The transformed time series data was then passed through the suite of USACE nonstationarity detection tests. When two or more tests flagged the same year in a time series, implying statistical consensus, that gauge was identified as nonstationary (n = 77, or 23 percent of the gages in the sample). Figure 3 below shows a geospatial rendering of the unimpaired gages considered in this study, where those meeting the aforementioned conditions are coded accordingly.
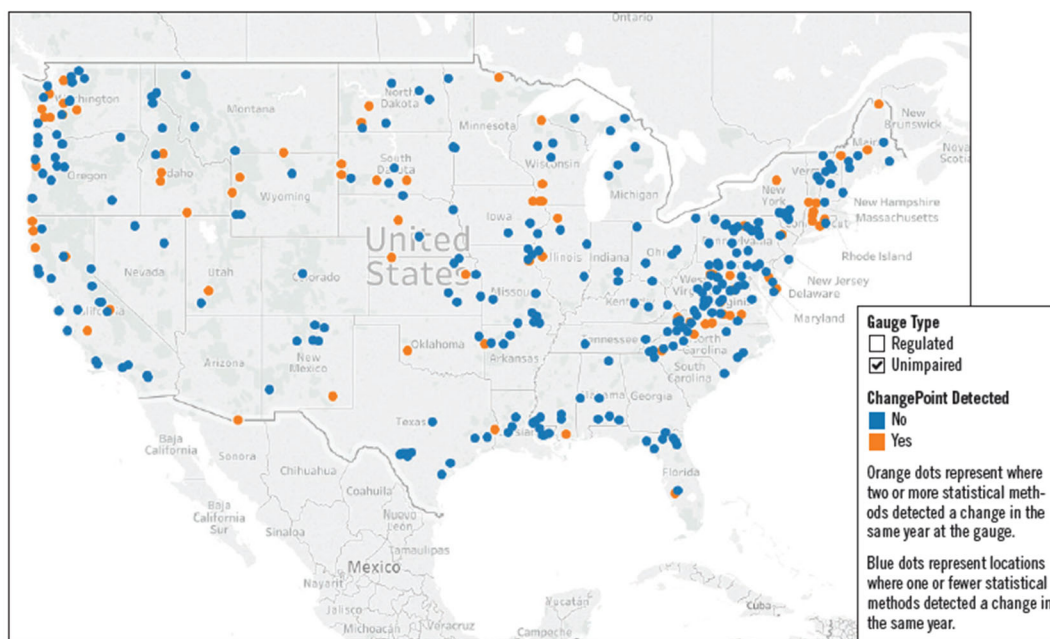
Figure 3. Geospatial rendering of detected nonstationarities

Methodology and Approach

Broadly speaking, the aim of the study was to uncover previously hidden geospatial patterns of nonstationarities in the continental United States. The implemented methodology was designed to remain agnostic of gauge characteristics, isolating detected patterns to just geospatial distance. In other words, stream flow characteristics and geographic factors other than location were not directly considered. Using unsupervised machine learning techniques (i.e., algorithms that process untagged data without structured variable relationships to consider, learning

hidden associations based on data similarity and difference alone), unimpaired gages were geospatially clustered together. For each identified cluster, the proportion of gages with a nonstationarity was calculated so that regional nonstationarity frequency could be compared to the norm across the entire sample and to the frequency in other geographic locations. It is worth noting that this analysis does not determine causality but does identify the association between a known output metric (i.e., the presence of a nonstationarity with consensus) and the natural structure of the data (i.e., geospatial clusters determined by latitude and longitude) (Hastie et al. 2001).

The Density-based Spatial Clustering of Applications with Noise (DBSCAN) was selected as the optimal algorithm for this use case (Ester et al. 1996). At its foundation, DBSCAN was designed for spatial datasets, making it a natural choice. Additionally, the algorithm maintains flexibility through its implementation; rather than forcing an explicit number of clusters or a specific shape of cluster, DBSCAN builds clusters of any shape or size. If there are data points in low density areas, the algorithm tags them as noise, ignoring them when fitting the optimal clusters. This can combat the inherent challenges posed when mining a small dataset, as the algorithm builds fewer but more dense clusters. Standalone gages that are geospatially distant from others in the data set, which is common in this sample, can be ignored and treated as outliers from the larger trends uncovered.

Results

In the selected dataset of unimpaired gauges, the DBSCAN algorithm uncovered six geospatially-unique clusters across the continental United States. For ease in identification and discussion, these clusters are labeled as 1) the West coast cluster, 2) the North West cluster, 3) the Northern Midwest cluster, 4) the Midwest cluster, 5) South cluster, and 6) the North East cluster. All six of these clusters are reasonably dense, geospatial disparate, and agnostic to noise.

When nonstationarity proportions were calculated, results revealed two significant deviations from the cohort norm (see Figure 4 and Table 1 below). In the Northern Midwest cluster, 50 percent of the unimpaired gages were nonstationary, while only 10 percent of the gages in the South cluster were nonstationary. Both of these measures deviate from the expected proportions, as 23 percent of the unimpaired gages across the United States had a nonstationarity. None of the other four geospatial clusters significantly deviate from this sample norm. This suggests that there may be a relationship between geospatial location and the likelihood that a stream's behavior violates the stationarity assumption, which may be explained by observed shifts in these areas for both seasonal and heavy precipitation (e.g., Hayhoe et al., 2018).
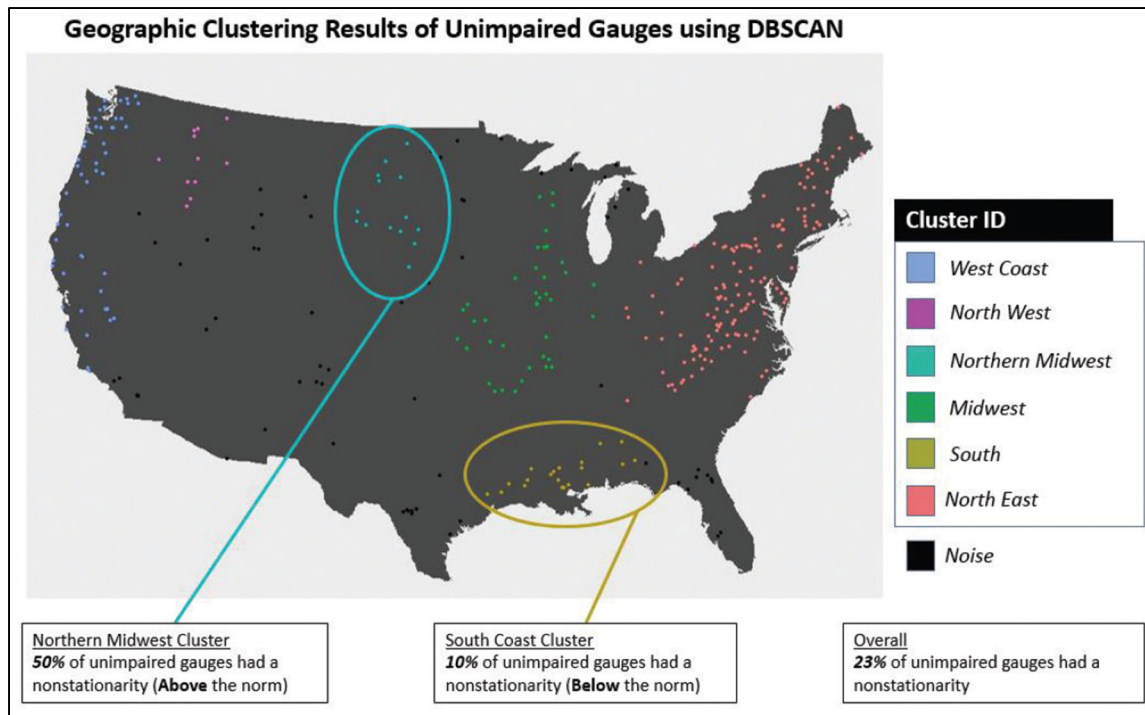
Figure 4. Geographic clustering results of unimpaired gages using DBSCAN

Table 1. Percent of unimpaired gages with a nonstationarity, by DBSCAN generated clusters

Cluster ID	West Coast	North West	Northern Midwest	Midwest	South	North East
Percentage	29%	27%	50%	23%	10%	22%

Conclusions and Future Directions

Though this analysis does suggest a relationship between geospatial location and stream flow propensity for nonstationarity, it does not confirm there is a formal linkage or that this relationship can be attributed to a known causal factor. Rather, the methods employed and their preliminary statistical conclusions act as a prompting for a deeper analysis with more data. To create a more robust analytic data set, organizations can work to reconstruct unimpaired flow records at regulated gages. With larger data sets, similar studies can lead to stronger conclusions. Additionally, to better attribute these findings to their underlying drivers, future studies should consider other hydrologic and climate characteristics. By associating nonstationarity patterns in stream flow with changes in temperature and precipitation, further work may uncover previously hidden patterns that link analytic findings to scientifically-founded causal relationships. In its entirety, though this study is illuminating, it most importantly acts as a suggestion for more: deeper analysis of geospatial patterns of nonstationarity and their causes.

References

Barry, D. and J.A. Hartigan. 1993. "A Bayesian analysis for change point problems," Journal of the American Statistical Association, 88, 309–19.

Brekke, L., Kiang, J.E., Olsen, J.R., Pulwarty, D.R., Raff, D., Turnipseed, D.P., Webb, R.S., and White, K.D. 2009. "Climate change and water resources management: A federal perspective," USGS Circular 1331, (http://pubs.usgs.gov/circ/1331/).

Brekke, L., White, K., Olsen, J.R., Townsley, S., Williams, D., Hanbali, F., Hennig, C., Brown, C., Raff, D., and Wittler, R. 2011. "Addressing Climate Change in Long-Term Water Resources Planning and Management - User Needs for Improving Tools and Information," U.S. Army USACE of Engineers Civil Works Technical Series Report CWTS-10-02, U.S. Army USACE of Engineers Washington, DC and U.S. Department of the Interior Bureau of Reclamation Washington, DC, (http://www.usbr.gov/climate/userneeds/).

Brillinger, D.R. 2001. Time Series: Data Analysis and Theory, 540 pp., Soc. for Ind. and Appl. Math., Philadelphia, Pa.

Chow, V.T. 1964. Handbook of Applied Hydrology: A Compendium of Water-Resources Technology, New York: McGraw-Hill Book Co.

Conover, W.J. 1999. Practical Nonparametric Statistics, Third edition, New York: Wiley.

Erdman, C. and Emerson, J.W. 2007. "bcp: An R package for performing a Bayesian analysis of change point problems," Journal of Statistical Software, 1–13.

Ester, M., Kriegel, H.P., Sander, J., and Xu, X. 1996. "A density-based algorithm for discovering clusters in large spatial databases with noise," AAAI Press, Pp: 226-231, doi:10.1.1.121.9220.

Falcone, J. 2011. "GAGES-II: Geospatial Attributes of Gages for Evaluating Streamflow," U.S. Geological Survey Report. https://doi.org/10.3133/70046617.

Friedman, D., Schechter, J., Sant-Miller, A.M., Mueller, C., Villarini, G., White, K.D., and Baker, B. 2018. "US Army Corps of Engineers Nonstationarity Detection Tool User Guide," US Army Corps of Engineers: Washington, DC.

Hastie, T., Tibshirani, R., and Friedman, J. 2001. The Elements of Statistical Learning, New York, NY, USA: Springer New York Inc.

James, N.A. and Matteson, D.S. 2015. "ecp: An R Package for Nonparametric Multiple Change Point Analysis of Multivariate Data," Journal of Statistical Software, 62.7.

Milly, P., Betancourt, J., Falkenmark, M., Hirsch, R.M., Kundzewicz, Z.W., Lettenmaier, D.P., ans Stouffer, R. J. 2008. "Stationarity is dead: Whither water management?" Science, 319 (5863), 573-574. doi:10.1126.

Pettitt, A.N. 1979. "A non-parametric approach to the change point problem," Journal of the Royal Statistical Society Series C, Applied Statistics 28, 126-135.

Pinson, A., Julien, P., Baker, B., and White, K. In Press. "Projected Changes in Sedimentation at Seven USACE Reservoirs on the Southern Plains," Federal Interagency Sedimentation and Hydrologic Modeling Conference 2019.

Pohlert, T. 2015. "trend: Non-Parametric Trend Tests and Change-Point Detection," R package version 0.0.1. doi:10.13140.

Prosdocimi, I., Kjeldsen, T.R., and Svensson, C. 2014. "Non-stationarity in annual and seasonal series of peak flow and precipitation in the UK," National Hazards and Earth Systems Sciences, 14, 1125–1144.

Quessy, J.F., Favre, A.C., Said, M., and Champagne, M. 2011. "Statistical Inference in Lombard's Smooth-Change Model," Envirometrics, 882-93.

R Core Team. No Date. R: A language and environment for statistical computing. Vienna, Austria: R Foundation for Statistical Computing.

Repetto, R. 2012. America's Climate Problem: The Way Forward, Routeledge, Abingdon, UK.

Hayhoe, K., D.J. Wuebbles, D.R. Easterling, D.W. Fahey, S. Doherty, J. Kossin, W. Sweet, R. Vose, and M. Wehner, 2018: Our Changing Climate. In Impacts, Risks, and Adaptation in the United States: Fourth National Climate Assessment, Volume II [Reidmiller, D.R., C.W. Avery, D.R. Easterling, K.E. Kunkel, K.L.M. Lewis, T.K. Maycock, and B.C. Stewart (eds.)]. U.S. Global Change Research Program, Washington, DC, USA, pp. 72–144. doi: 10.7930/NCA4.2018.CH2

Ross, G. J. 2015. "Parametric and Nonparametric Sequential Change Detection in R: The cpm Package," Journal of Statistical Software, 66.3.

Ryberg, K.R. and Vecchia, A.V. 2012. "waterData—An R package for retrieval, analysis, and anomaly calculation of daily hydrologic time series data, version 1.0." U.S. Geological Survey. Bismarck, N.D.: U.S. Geological Survey. Retrieved September 18, 2015, from http://pubs.usgs.gov/of/2012/1168/of12-1168.pdf.

Sadri, S., Kam, J., and Sheffield, J. 2016. "Nonstationarity of low flows and their timing in the eastern United States," Hydrology and Earth System Sciences, 20, 633–649. doi:10.5194/hess-20-633-2016

Slater, L.J., Singer, M.B., and Kirchner, J.W. 2015. "Hydrologic versus geomorphic drivers of trends in flood hazard," Geophysical Research Letters 42(2): 370-376.

Slater, L. J., and Villarini, G. 2017. "On the impact of gaps on trend detection in extreme streamflow time series," International Journal of Climatology, DOI: 10.1002/joc.4954.

U.S. Army Corps of Engineers. 1987. Hydrologic analysis of interior areas, Washington, D.C.: U.S. Army Corps of Engineers. Retrieved September 18, 2015, from http://www.publications.usace.army.mil/Portals/76/Publications/EngineerManuals/EM_1110-2-1413.pdf.

U.S. Army Corps of Engineers. 1994. Flood-runoff analysis, Washington, D.C.: U.S. Army Corps of Engineers. Retrieved September 18, 2015, from http://www.publications.usace.army.mil/Portals/76/Publications/EngineerManuals/EM_1110-2- 1417.pdf.

U.S. Army Corps of Engineers. 2017. Guidance for detection of nonstationarities in annual maximum discharges, Washington, D.C.: U.S. Army Corps of Engineers.

Verstraeten, G., Poesen, J., Demaree, G., and Salles, C. 2006. "Long-term (105 years) variability in rain erosivity as derived from 10-min rainfall depth data for Ukkel (Brussels, Belgium): Implications for assessing soil erosion rates," Journal of Geophysical Research 111, D22109.

Villarini, G., Smith, J.A., Serinaldi, F., Bales, J., Bates, P.D., and W.F. Krajewski. 2009a. "Flood Frequency Analysis for Nonstationary Annual Peak Records in an Urban Drainage Basin," Advances in Water Resources, 32:1255-1266.

Villarini, G., Serinaldi, F., Smith, J.A., and Krajewski, W.F. 2009b. "On the stationarity of annual flood peaks in the continental United States during the 20th century," Water Resources Research, 45, W08417, doi:10.1029/2008WR007645.

Vogel, R.M., Yaindl, C., and Walter, M. 2011. "Nonstationarity: Flood magnification and recurrence reduction factors in the United States," Journal of the American Water Resource Association, 47, 464–474.

Yue, S., Pilon, P., and Cavadias, G. 2002. "Power of the Mann-Kendall and Spearman's rho tests for detecting monotonic trends in hydrological series," Journal of Hydrology 259: 254–271.

Design, Calibration and Deployment of a Hydrophone Based Bed Load Monitoring Surrogate

Bradley T. Goodwiller, Research and Development Engineer II, 145 Hill Drive, National Center for Physical Acoustics, University of Mississippi, University, Mississippi 38677, USA, btgoodwi@olemiss.edu

Daniel G. Wren, Research Hydraulic Engineer, 598 McElroy Drive, National Sedimentation Laboratory, USDA Agricultural Research Service, Oxford, Mississippi 38655, USA

JR Rigby, Research Hydrologist, 598 McElroy Drive, National Sedimentation Laboratory, USDA Agricultural Research Service, Oxford, Mississippi 38655, USA

Robert C. Hilldale, Civil Engineer, (Hydraulics), P. O. Box 25007, Sedimentation and River Hydraulics Group, US Bureau of Reclamation, Denver, Colorado 80225, USA

Abstract

The use of sediment generated noise (SGN) has been studied as a potential surrogate method for determining bedload transport rates. Laboratory and preliminary field experiments have shown multiple characteristics of this acoustic signal that correspond with properties of the bedload in transport. A portable passive-acoustic data collection system was designed by researchers at the National Center for Physical Acoustics at the University of Mississippi along with researchers at the National Sedimentation Laboratory in Oxford, Mississippi. The system uses two hydrophones (High Tech Inc 96 MIN-Exportable) to record the sound generated by coarse bedload movement. A portable data recorder (Zoom H4N) streamed the continuous acoustic data to audio files that were then processed. The data collection hardware was placed in a waterproof container. The system is compact, robust, portable and can operate for long periods of time with minimal user input. A custom hydrophone case was designed to allow multiple mounting techniques, thus providing adaptability to a wide range of gravel-bed fluvial systems. The data collection system was deployed on Halfmoon Creek near Leadville, Colorado, during the summer of 2015, collecting nearly one month of continuous acoustic data. The system was also deployed on the Elwha River near Port Angeles, Washington and on the Trinity River in Weaverville, California. Multiple analysis techniques have been tested on the data sets and compared with similar measurements made in laboratory flumes and tanks. Design of the system and its calibration will be presented as well as multiple deployment techniques.

Introduction

Passive acoustic methods for monitoring bed load transport have been explored for some time. Several methods of determining bedload based on gravel impacts with instrumented plates have been investigated world-wide (Rickenmann and McArdell 2007; Rickenmann, Turowski et al. 2014; Hilldale, Carpenter et al. 2015). The acoustic properties of bed load discharge of single-sized particles were investigated in a laboratory flume (Johnson and Muir 1969), as well as the

acoustic properties of impacting glass spheres and gravel of mixed sizes (Thorne 1985). These and other laboratory studies have consistently shown that the sound generated by impacting gravel particles can be used to determine a relationship between gravel transport and acoustic energy. Recent field studies have been conducted using hydrophones to detect gravel movement in the Trinity River (Barton 2006; Barton, Slingerland et al. 2010). To continue this research, a passive acoustic system was tested at four different field sites: Trinity River in Weaverville, CA; the Elwha River in Port Angeles, CA; the Walnut Gulch Watershed near Tombstone, AZ at the Lucky Hills sub-watershed; and Bear Creek in Evergreen, CO. Following these deployments, a more robust and portable system was developed (Figure 1). The system uses two HTI 96-MIN Exportable hydrophones. The voltage generated by these hydrophones is digitized and recorded using a Zoom H4N wave recorder. The data collection components are housed in a weatherproof case, and the hydrophones are placed in a custom case that provides a variety of mounting options.
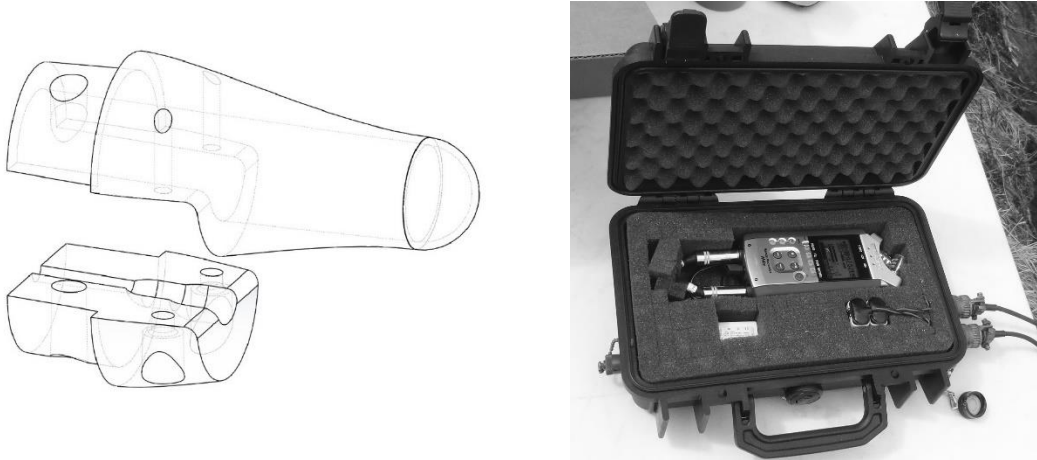
Figure 1. Left: Casing for the hydrophone with collar that fits inside a 1" PVC coupler. Right: Zoom H4N and connections housed in a weatherproof case

Deployments

The portable system was deployed on Halfmoon Creek, a small mountain stream near Leadville, Colorado. The deployment lasted one month in the summer of 2015, and the hydrophone system collected nearly continuous data during this deployment. In conjunction with the acoustic data collection, physical samples were collected using portable bedload traps (Bunte, Abt et al. 2004; Bunte, Swingle et al. 2007). The hydrophones were mounted on metal poles driven into the stream bed upstream of the bedload traps. A fairing with a teardrop cross-section was placed over the poles to reduce flow noise from the surface disturbance. The hydrophone cables were strung across the creek to the data collection box on the bank (Figure 2).
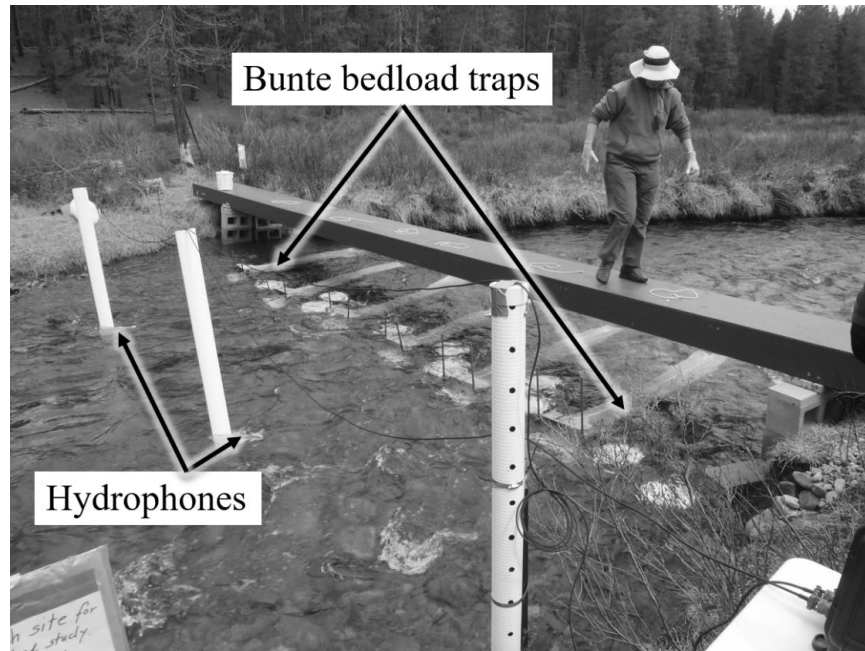
Figure 2. Hydrophone and bedload trap installation on Halfmoon Creek

In the summer of 2016, the system was deployed on the Elwha River in Port Angeles, Washington. At the time of deployment, the Elwha River was not wadeable. For this reason, the hydrophones were mounted to a modified kayak (Figure 3). The data collection box was mounted on top of the kayak, which was tethered to a line strung across the river. The deployment was made in conjunction with physical sampling by Graham Matthews and Associates. Three different hydrophone systems were deployed. One kayak was mounted in a stationary position, while another was moveable (this system was moved laterally in order to be directly upstream of the physical sampling raft). The third hydrophone system was mounted directly to the physical sampling raft.

Figure 3. Data recording system and hydrophones mounted on a modified kayak being deployed on the Elwha River

In the summer of 2017, the system was deployed on the Trinity River in Weaverville, CA during the scheduled dam release and gravel augmentation. The same raft configuration was used on the Trinity as the Elwha. However, due to the high flow of the Trinity during the time of testing, the raft could not be safely placed in the middle of the river. Instead the raft had to be floated in an eddy behind a tree to which the raft was tethered (Figure 4).

Figure 4. Hydrophone raft deployed on the Trinity River

A summary of some properties of the three deployments is shown in Table 1.

Table 1: Physical and hydraulic properties of the three deployments

	Halfmoon Creek	**Elwha River**	**Trinity River**
Location	Leadville, Colorado	Port Angeles, Washington	Weaverville, California
Deployment Dates	May 20 - June 16, 2015	May 21 - 26, 2016	April 25 - 28, 2017
Discharge Range (m³/s)	0.61-5.5 (21.6-195 cfs)	44-48 (1,560 - 1,680 cfs)	245-374 (8,650 - 13,200 cfs)
Water Depth Range (m)	0.130 - 0.475	Not Available	~0.75
Approx. Width (m)	8.7 (at low flow)	45	40
Bed Type	Gravel	Gravel	Gravel
River Access	Wadable	Partially Wadable	Not Wadable

Conclusions

The development of a user-friendly portable hydrophone system was a success. Approximately 272 GB of acoustic data were collected on Halfmoon Creek, 32 GB on the Elwha River, and 30 GB on the Trinity River. The system is adaptable to many different situations and requirements. The data collection is straightforward and requires minimal operator input. In addition, when connected to an external 12 V battery, the system can operate until the memory is full (approximately 36 hours).

Analysis of the data from all three deployments is ongoing. Preliminary results indicate that raw RMS voltage may not be a valid metric for determining bed load transport, as it is highly correlated with flow discharge but not very well correlated with bedload discharge. The flow noise must be removed from the data before an accurate method of estimating bed load transport can be determined. Various analysis techniques are being investigated to isolate the SGN from the total acoustic recording.

References

Barton, J.S. (2006). Passive Acoustic Monitoring of Coarse Bedload in Mountain Streams. Geosciences. Pennsylvania, Pennsylvania State University. **Doctor of Philosophy**.

Barton, J.S. and Slingerland R.L. (2010). "Monitoring Course Bedload Transport with Passive Acoustic Instrumentation: A Field Study." U.S. Geological Survey Scientific Investigations Report.

Bunte, K. and Abt, S.R. (2004). "Measurement of Coarse Gravel and Cobble Transport Using Portable Bedload Traps." Journal of Hydraulic Engineering **130**(9): 879-893.

Bunte, K. and Swingle, K.W. (2007). Guidelines for Using Bedload Traps in Coarse-Bedded Mountain Streams: Construction, Installation, Operation, and Sample Processing. F. S. United States Department of Agriculture, Rocky Mountain Research Station. Fort Collins, CO. General Technical Report RMRS-GTR-191.

Hilldale, R., Carpenter, W.O. (2015). "Installation of Impact Plates to Continuously Measure Bed Load: Elwha River, Washington, USA." Journal of Hydraulic Engineering **141**(3): 06014023.

Johnson, P. and Muir, T.C. (1969). "Acoustic Detection of Sediment Movement." Journal of Hydraulic Research **7**(4).

Rickenmann, D. and McArdell, B.W. (2007). "Continuous measurement of sediment transport in the Erlenbach stream using piezoelectric bedload impact sensors." Earth Surface Processes and Landforms **32**(9): 1362-1378.

Rickenmann, D. and Turowski, J.M. (2014). "Bedload transport measurements with impact plate geophones: comparison of sensor calibration in different gravel-bed streams." Earth Surface Processes and Landforms **39**(7): 928-942.

Thorne, P. D. (1985). "The Measurement of Acoustic Noise Generated by Moving Artificial Sediments." Journal of the Acoustical Society of America **78**(3): 1013-1023.

Development of an Operational Plan to meet Water Level Rates of Change Objectives Downstream of a Control Structure

Tim Calappi, Hydraulic Engineer, U.S. Army Corps of Engineers, Detroit, MI, tim.j.calappi@usace.army.mil

Katherine Labuhn, Hydraulic Engineer, U.S. Army Corps of Engineers, Detroit, MI, katherine.a.labuhn@usace.army.mil

Charles Sidick, Hydraulic Engineer, U.S. Army Corps of Engineers, Detroit, MI, charles.l.sidick@usace.army.mil

James Selegean, Hydraulic Engineer, U.S. Army Corps of Engineers, Detroit, MI, james.p.selegean@usace.army.mil

Abstract

The St. Marys Rapids are a productive ecosystem many species rely on to fulfill some portion of their lifecycle. Management of Lake Superior outflow alters conditions in the rapids and affects habitat quality. This work investigates various strategies associated with gate operation at the Compensating Works used to control the flow through the rapids. The Lake Superior Board of Control strives to keep water level rates of change to less than 10 cm per hour; however, very little is known about water level response to gate changes in the rapids. A two-dimensional model was constructed of the St. Marys River to help understand the water level response within the rapids. Preliminary results are used to develop general guidelines for use while more specific recommendations are developed. Results show water level rates of change are more sensitive during relatively low discharge and provide guidance on the duration of the gate movements to meet the 10 cm per hour water level rate of change.

Introduction

The St. Marys River drains Lake Superior into Lake Huron, figure 1. The St. Marys Rapids are near Sault Sainte Marie, Michigan, which is separated from its twin city Sault Sainte Marie, Ontario by the river. This Great Lake connecting channel is an important ecological corridor, helping to fulfill many processes including, most notably, the movement and maintenance of fish populations. The river also plays an important role as a waterway for commerce, hydropower, water supply and recreational fishing and boating. Originally, due to the sudden drop in elevation in an area known as the St. Marys Rapids, navigation between Lake Superior and Lake Huron was not possible. By 1920, the outflow from Lake Superior was completely controlled for navigation and hydropower and the Compensating Works was built at the head of the rapids. The 16-gate structure straddles the international border and has eight gates on either side, with each set of gates owned and operated by respective governments.

Figure 1. Map of the Great Lakes with the project area circled

The St. Marys Rapids, at the outlet of Lake Superior is a vital habitat for a wide range of aquatic species including Lake Whitefish (*Coregonus clupeaformis*), walleye (*Sander vitreus),* lake sturgeon (*Acipenser fulvescens*) and several species of salmonids. The regulation of the outflows from Lake Superior through the Compensating Works (i.e., a series of sluice gates) can lead to rapid changes in hydraulic characteristics, potentially creating adverse conditions for downstream biota. Helping alleviate this concern, the U.S. Army Corps of Engineers (USACE) Detroit District constructed four remotely operated gates on the United States side of the Compensating Works. The gates are capable of being opened slowly (over many hours) until a desired discharge is achieved. Currently, gates are manually operated and changes are made quickly. Both the U.S. and Canadian gates were changed on the same day, usually before noon. In an effort to optimize habitat availability in the St. Marys Rapids and meet new water level rate-of-change requirements, a two-dimensional, Adaptive Hydraulics model was developed. Model uses include quantifying available habitat in the rapids for various species for a given gate setting, as well as evaluating water level rates of change. The goal of this work is to gain a preliminary understanding of water level rates of change associated with gate changes at the Compensating Works and various water levels on Lake Superior.

As required by the Lake Superior Regulation Plan, the International Lake Superior Board of Control must maintain a minimum flow through the main portion of the St. Marys Rapids equivalent to one-half gate open at the Compensating Works. The main portion of the rapids is immediately downstream of the Compensating Works. The minimum flow is achieved by partially opening four gates, which helps distribute the water more evenly across the rapids. The one-half gate setting has been used almost exclusively during the recent period of low water levels in Lake Superior (occurring from 1997 through 2013). By May 2014, the water level on Lake Superior had risen enough that the regulation plan frequently required multiple gate openings. Conditions in the rapids are dictated by the gate openings on the Compensating Works and the rate at which the gate settings are changed. In a pilot study of available habitat in the St. Marys Rapids, Calappi, et. Al., (2017), determined the areal extent of habitat for four indicator species under various gate operation scenarios. This report, however, did not address how to implement the rate of change recommendation the Lake Superior Board of Control strives to meet.

This work examines general conditions associated with multiple gate openings; it provides some initial guidance on how to best use the new, remotely operated gates at the head of the St. Marys Rapids to best maintain water level rates of change to less than the recommended 10 cm-per-hour rate described by Bain et. Al., (2010). Upon completion of more thorough modeling, these types of results can help determine how altering gate movement strategies can best meet water management and ecosystem function objectives in the St. Marys Rapids. However, operational costs also need further investigation. For example, an audible alarm may be required while a remotely operating gate is moving, potentially disrupting the community during long duration gate movements. Additionally, an operator may be required to observe the gate movement via closed circuit monitoring. Given these costs, excessively long gate changes may not be feasible.

Given the remote nature of the rapids and access difficulties, there is no permanent gauge record on this portion of the river. One season of data were collected with temporarily installed pressure sensors at multiple points within the rapids to provide limited model calibration data, (Calappi, et. Al., 2017). With limited data, natural resource managers were unable to determine if gate operations were in compliance with the 10 cm-per-hour recommended water level rate of change. Given the once-per-month gate changes and slow hydrologic response of Lake Superior, hydrodynamic modeling was used to gain a more expedient understanding of rates of change in the rapids as a function of gate operation and Lake Superior water level.

Methods

As an initial approach, steady state model scenarios were run with Lake Superior at a 75th-percentile and 50th-percentile annual average water level. When Lake Superior is at relatively low water level, the Compensating Works discharge is typically fixed at the half-gate setting and need not be considered. Lake Huron was fixed at the median annual average. Hydropower and

navigation uses were held constant and Compensating Works gate openings were the only change for a given Lake Superior water level. Gate settings on each of the 16 gates can vary widely from month-to-month, and it is important for operational staff to understand the time-scale for which a given change in gate opening must be made to remain in compliance with the recommended water level rate of change. Each gate can be partially opened to meet a given month outflow requirement. Gate openings can be uniform across the structure or each gate can be open a different amount. Given the new water level rate of change recommendations and operational constraints of changing a gate setting, each government can change gate settings on the same day as with historic practices, or on different days to help limit the water level rate of change for significant gate changes. However, regulators/operators can not define a significant change in gate setting, relative to the water level rate of change recommendation, without this or similar work. Simplistic model runs help fill this knowledge gap in the near-term and through adaptive management, operational practices may change as additional modeling is performed.

Ten model runs were made with Lake Superior at the 75th- percentile water level and each of the gates on the Compensating Works open 10cm to 100cm. Model runs were made for each 10cm increment of gate opening, 45 gate changes in all; nine settings with a 10 cm difference in the gate opening. For example, moving all gates from 100 cm open to 90 cm open, and all combinations down to a 10 cm closure with the gates starting at a 20 cm opening. Similarly, eight combinations of 20 cm gate changes, seven combinations of 30 cm gate changes, etc.

Water depths in the rapids were compared between each of the gate openings. Two analyses are performed for each gate combination: First, find the maximum change in depth in the rapids between the two gate settings. This defines the maximum length of time for 100 percent of the rapids to be in compliance with the rate of change recommendation. For example, for a maximum of 1-meter change in depth between two gate settings, each of the gates would be simultaneously changed at a constant rate for 10 hours. While this is not operationally feasible, it does provide the regulators/operators an idea of the time scale required for the gate change. The second calculation determines a one hour range in time for at least 95 percent of the rapids to be in compliance with the recommendation.

Results

Each of the gate openings from 10 cm to 100 cm were run and analyzed. Results capturing the variability in a 10 cm gate change are shown in figure 2. The location of the rapids are defined in figure 2 (a) and (b). The depth change shown in Figure 2 (c) through (f) show the average water level rate of change if the gate change lasted one hour. Blank space on the map indicates this portion of the rapids are in compliance with the 10 cm per hour water level rate of change recommendation while red indicates water level rates of change greater than 10 cm per hour and green indicates changes on the order of 80 cm per hour. The sample calculations below each
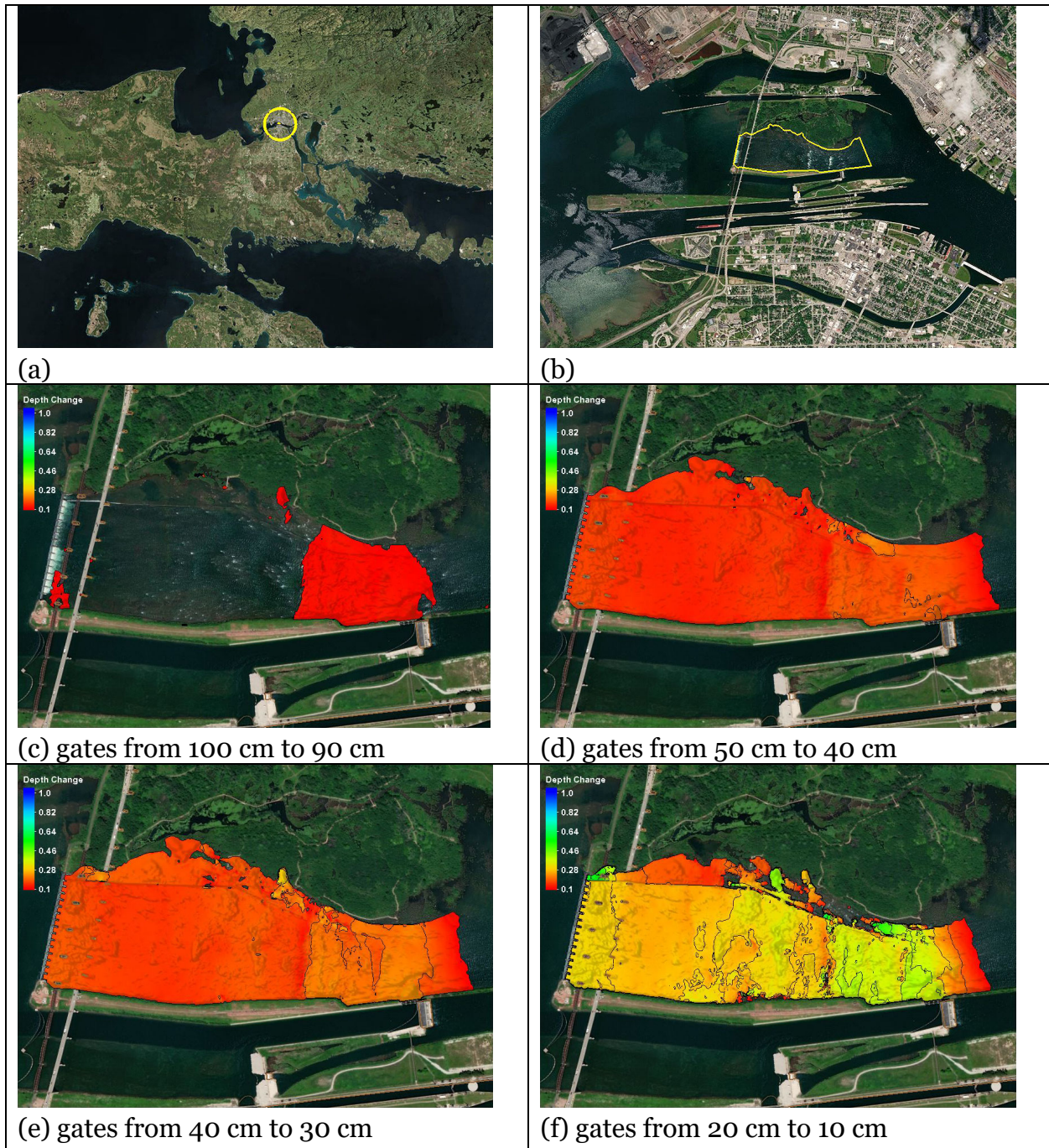
Figure 2. Average rate of change, over one hour, corresponding to a 10 cm gate change. Each gate on the compensating works was changed 10 cm. The corresponding average water level rate of change is shown to be a function of the gate opening. Blank space on the map represents areas within compliance of the 10cm per hour water level rate of change.

show a 10 cm change in gate setting, but they have differing effect on the water level rate of change within the rapids depending on the amount of the gate opening. These results show the dependency of rate of change on the total flow in the rapids and suggest further analyses at the lower end of the flow range.

The second analysis aims to determine a length of time over which a gate change should be conducted to achieve 100 percent compliance with the recommendation versus how long it takes to achieve 95 percent compliance. That is, at what length of time are there diminishing marginal returns, and under what conditions (if any) is 100 percent compliance worth the operational costs.

Table 1: Minimum required time for gate changes on the Compensating Works to meet 10 cm per hour water level rate of change recommendations. Time required for the entire rapids to be in compliance with the recommendation and time for 95 percent of the rapids to be in compliance with the recommendation.

Lake Superior Water Level	Compensating Works gate openings for uniform gate openings across the structure							
	Gated moved from 60 cm open to 50 cm open		Gate moved from 30 cm open to 20 cm open		Gate moved from 40 cm open to 10 cm open		Gate moved from 100 cm open to 60 cm open	
	10 cm gate change		10 cm gate change		30 cm gate change		40 cm gate change	
% area compliant with the 10 cm water level rate of change	100%	95%	100%	95%	100%	95%	100%	95%
When Lake Superior is at the a 75th percentile water level	3 hours	1 to 2 hours	9 hours	2 to 3 hours	11 hours	8 to 9 hours	19 hours	5 to 6 hours

Table 1 shows the expected duration for the gate changes for both 100 percent and an approximate 95 percent compliance of the recommendation within the rapids for select gate changes. A 10 cm gate change achieves 100 percent compliance from 3 to 9 hours depending the amount of the gate opening. However, both 10 cm gate changes have similar response times to achieve 95 percent compliance. Table 1 also shows it can take longer to achieve 95% compliance for a smaller gate change than it does to achieve 95% compliance for a large gate change but at the upper end of the flow regime. That is, during high flows, larger gate changes can be made and over shorter durations when compared to gate changes at the lower flow regime.

A closer look at a 10 cm gate change and a 40 cm gate change in figure 3 and figure 4, respectively, show the spatial extent of compliant/non-compliant areas within the rapids. In both of these cases the benefit of extending the duration of the gate change for an additional hour appears significant. These data were not available to natural resource managers during the formulation of the rate of change recommendation. These figures highlight areas within the rapids susceptible to high rates of change in water level, however, further analysis of the habitat is required. For example, figure 3 (b) shows minimal areal extent of the rapids exceeding the rate of change recommendation; if the area highlighted in figure 3 (b) happens to be a particularly productive portion of the rapids, perhaps seeking 100 percent compliance is worthwhile. This level of analysis is beyond the scope of this initial work, however, is possible as shown in Calappi et. Al. (2017).

(a) 60 percent compliant, two hours   (b) > 95 percent compliant, three hours

Figure 3. Area of rapids non-compliant with the recommended water level rate of change for a gate change from 30 cm to 20 cm open: (a) the gate change occurs over a two hour window and (b) over a three hour window

(a) ~90 percent compliant, five hours   (b) > 95 percent compliant, six hours

Figure 4. Area of rapids non-compliant with the recommended water level rate of change for a gate change from 100 cm open to 60 cm open: (a) the gate change occurs over a five hour window and (b) over a six hour window

Conclusions and Future Work

As expected, this work has shown water level rates of change are faster at the lower gate settings and take longer to achieve 95% compliance as shown in Table 1. Additional work is required to further define gate operation over the lower end of the discharge range. Future iterations of this work will consider dynamic gate changes. These results will be compared to the steady state results, shared with the natural resource management community and evaluated against the current recommendation.

This work is preliminary in nature and was performed to provide quick insight regarding water level rate of change to the regulators and natural resource managers. Further definition of required conditions in the St. Marys Rapids will help inform more insightful analyses. For example, the International Lake Superior Board of Control uses the 10 cm per hour maximum rate of change recommendation to help guide operational decisions. However, no guidance is provided for a range of water levels (gate settings) where this recommendation is important.

Lake Superior outflow is governed by an adaptive management plan and regulators have used the 10 cm per hour water level rate of change since 2014. This new hydrodynamic and ecosystem modeling already underway by Calappi et. Al. (2017) will help form a basis for further collaboration with natural resource managers so new rates of change, more specific locations where these rates apply or the conditions under which water managers should consider water level rates of change, can be identified for a more optimal regulation of the rapids.

References

Bain, M., K. Arend, G. Steinhart, A. Moerke, and P. Varnakovida. 2010. St. Marys River biological status and hydrologic performance indicators. Environmental Working Group International Upper Great Lakes Study. http://www.iugls.org/DocStore/ProjectArchive/ECO_Ecosystem/ECO15_Bain_StMarys RiverEcosystemPIs/Reports/ECO15-R1_Bain_et-al_StMarysRiverSummary.pdf.

Calappi, T., Labuhn, K., Fowler, S., Suedel, B., Wilkens, J., Savant, G., Bachand, M., Guénard, G., 2018. Analyzing the St. Marys Rapids for suitable fish habitat – in review, TR-17-19322. ERDC http://acwc.sdp.sirsi.net/client/default

Effects of Rain-on-Snow Events on Suspended-Sediment Loading in the Truckee River Basin, California: Implications for Water Quality and Aquatic Habitat

Brian Hastings, Geomorphologist, Balance Hydrologics, Truckee, California, bhastings@balancehydro.com
David Shaw, Geologist, Balance Hydrologics, Truckee, California, dshaw@balancehydro.com

Introduction

Mountain drainages in the eastern Sierra Nevada are defined as snowmelt-dominated hydrologic systems in which the annual flood typically occurs in the spring with peak snowmelt runoff (Kattelmann 1996). In recent decades, however, mid-winter rain-on-snow events have resulted in the highest annual peak floods in the Truckee River Basin. McCabe et al. (2007) highlighted an increase in rain-on-snow events in high elevation areas of the western United States over the last 35 years and suggested very little is known about the relative importance of rain-on-snow events on fluvial processes including sediment transport or loads. In our research, we measured suspended-sediment loads in the Truckee River and several different tributaries and quantified loads for rain-on-snow driven events and compared them to loads for spring snowmelt runoff events.

Background

The Truckee River harbors several aquatic species of concern, including the federally-listed Lahontan cutthroat trout, that rely on clean gravels to support spawning habitat and macro-invertebrate food sources. The Truckee River is also a primary source of water for both municipal water supply, and irrigation for downstream communities in Nevada. Water quality is vital for continued uses. In Lake Tahoe, the delivery of fine-grained sediment from tributary basins is listed as a major cause of water-clarity deterioration in the lake (Simon 2008). The Middle Truckee River, between Lake Tahoe downstream to the Nevada-California state line was listed as impaired by fine-sediment concentration in 1994. A result, a Total Maximum Daily Load (TMDL) was established in 2008 under the Clean Water Act, Section 303(d). Kulchawik et al. (2014) evaluated bed sedimentation in the Middle Truckee River, downstream of Lake Tahoe, over a multi-year period and found fine sediment filling pool habitat and an overall fining of the bed with an increase in the sand fraction of fluvial sediment. Herbst et al. (2013) found that fine sediment in the Middle Truckee River reduced macroinvertebrate species diversity, altered food web function, and modified the abundance and types of aquatic life that inhabit the river.   Given these resources, management actions to control fine sediment sources and reduce potential increases to fine sediment loading in the Truckee River Basin are imperative in preparation for conditions under current and future climate change conditions.

Sierra Nevada rivers are most often viewed as snowmelt-dominated systems, and habitat is most affected by fine sediment, so regional studies have primarily focused on the role snowmelt runoff has had on the annual suspended-sediment load (Dana et al. 2004, Langlois et al. 2005). However, a few studies (Costa and O'Connor 1995, Kattelmann 1996, Inman and Jenkins 1999) have shown that the majority of suspended sediment load carried by a river in eastern California is usually transported during one or few extreme events. Under current climate change models for the Sierra Nevada Mountains of California, average precipitation is not expected to change; however, minimum and maximum temperatures are expected to rise and result in more precipitation as rain instead of snow (Coats 2010, Jepsen et al. 2016). This is likely to increase the frequency of rain-on-snow events, often characterized as extreme events. Extreme or episodic events, while typical in mountain drainages of the eastern Sierra Nevada, have implications for channel geomorphology, aquatic habitat and water quality if they become more frequent. We examine suspended-sediment load dynamics between rain-on-snow event and snowmelt runoff events in order to better understand how changing climate and potentially more frequent extreme events may affect fine-sediment loading and habitat under present and future conditions.

Methods

This research originated from several separate monitoring projects funded to support implementation of the TMDL for fine sediment in the Middle Truckee River watershed. Funders included the Truckee River Watershed Council, California Department of Water Resources (DWR), National Fish and Wildlife Foundation (NFWF), California Department of Fish and Wildlife (CDFW), Town of Truckee, and Placer County.

Near-continuous streamflow and turbidity gaging stations were installed on 3 perennial tributaries to the Truckee River near Truckee, California (Cold Creek, Middle Martis Creek, and West Martis Creek). In addition, a near-continuous turbidity instrument was co-located with U.S. Geological Survey (USGS) streamflow gaging station on the mainstem Truckee River near Truckee, California (USGS 10338000). The mainstem Truckee River flows out of Lake Tahoe, and though the contributing watershed includes Lake Tahoe, runoff and sediment delivery to the gaging station is most influenced by the 119 km² watershed downstream of the lake, since the lake outflow is regulated by the Tahoe City Dam. Within this effective watershed, elevations range between 1792 m and 2745 m. Tributary stations are located downstream of the mainstem Truckee River station and include watersheds that range between 10.6 km² and 32.6 km² and between 1780 m and 2728 m in elevation (Figure 1).
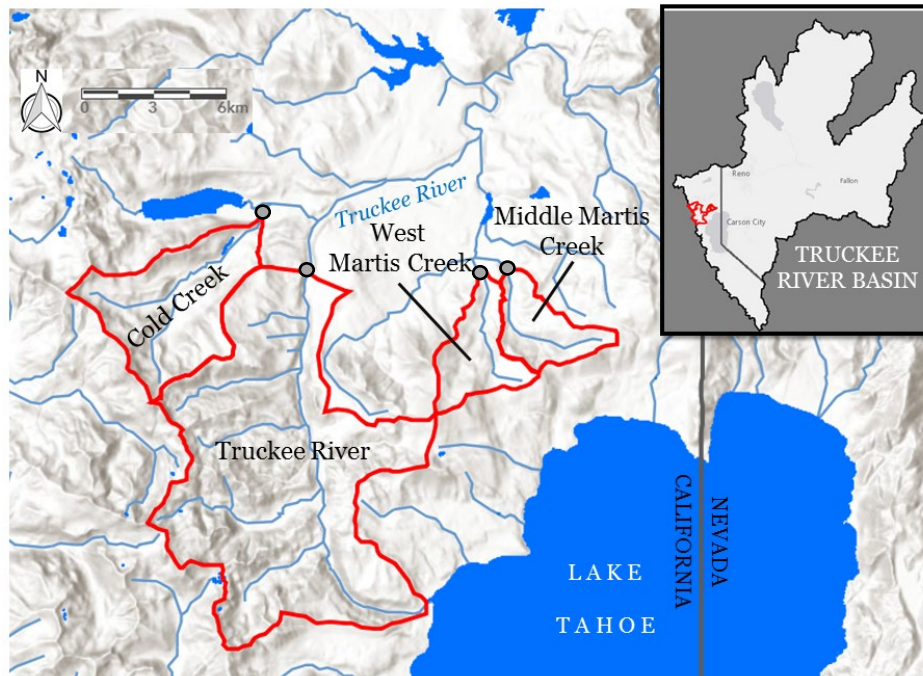
Figure 1. Study Location, Truckee River Basin, California

Data were collected between water year 2011 (WY2011) and WY2017, but not all stations were operated during the same period. Total precipitation and snowpack in WY2012, WY2013, WY2014, WY2015 was below average, so these are considered as dry years; WY2016 was an average precipitation year, and WY2011 and WY2017 were above-average (wet) years. Near-continuous turbidity was measured at all stations. Suspended-sediment samples were collected over a range of hydrologic conditions, during different times of the year, and over multiple years to develop correlations between instantaneous turbidity and suspended-sediment concentration to calculate estimated suspended-sediment loads. Sampling emphasis was placed on peak flows occurring during rain-on-snow events and snowmelt runoff. In some instances, discharge-based suspended-sediment rating curves were also used to compute loads.

Results and Discussion

Data evaluated under this study were collected during water years that ranged from extremely dry (WY2014 and WY2015, 23% of long-term, average annual runoff) to extremely wet (WY2017; 180% of long-term, average annual runoff) as measured at a long-term USGS streamflow gaging station (Sagehen Creek near Truckee, California; USGS 10343500). We measured between 2 and 5 rain-on-snow events in each water year with durations lasting from several hours to a several days. Duration of snowmelt runoff periods ranged between 37 days (WY2012) and 102 days (WY2017) (Figure 2).
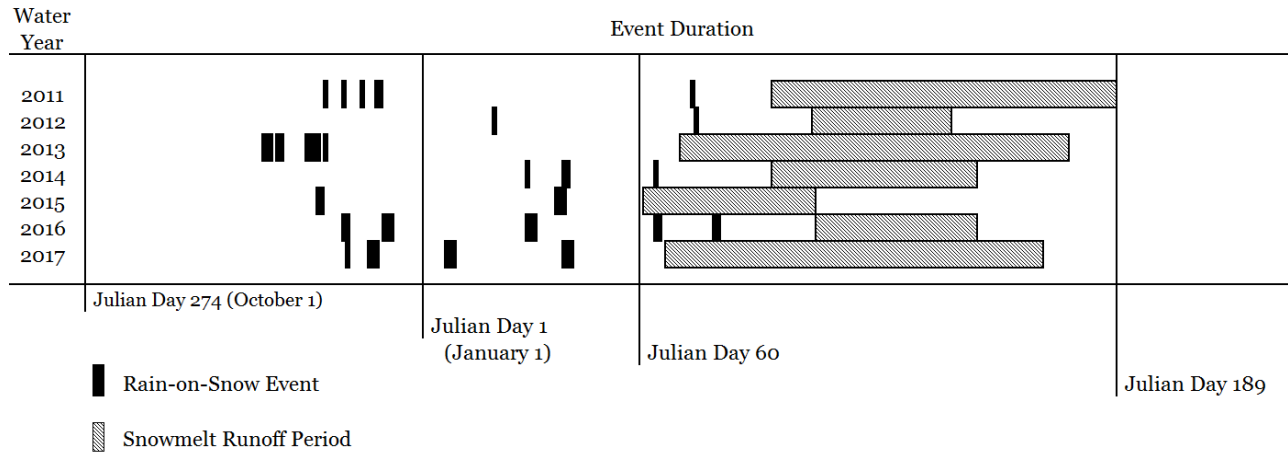
Figure 2. Duration and frequency of rain-on-snow events and snowmelt runoff periods, Truckee River Basin, water years 2011-2017

Suspended-sediment loads during rain-on-snow events exceeded suspended-sediment loads measured during snowmelt runoff periods in 4 of the 7 years at one or more stations in this study (Figure 3). For instance, the Truckee River exhibited higher suspended-sediment loads from rain-on-snow events relative to loads measured from snowmelt runoff in 3 of the 4 years measured. In those years, loads measured from rain-on-snow events exhibited a 2- to 25-fold increase over loads measured from snowmelt runoff.
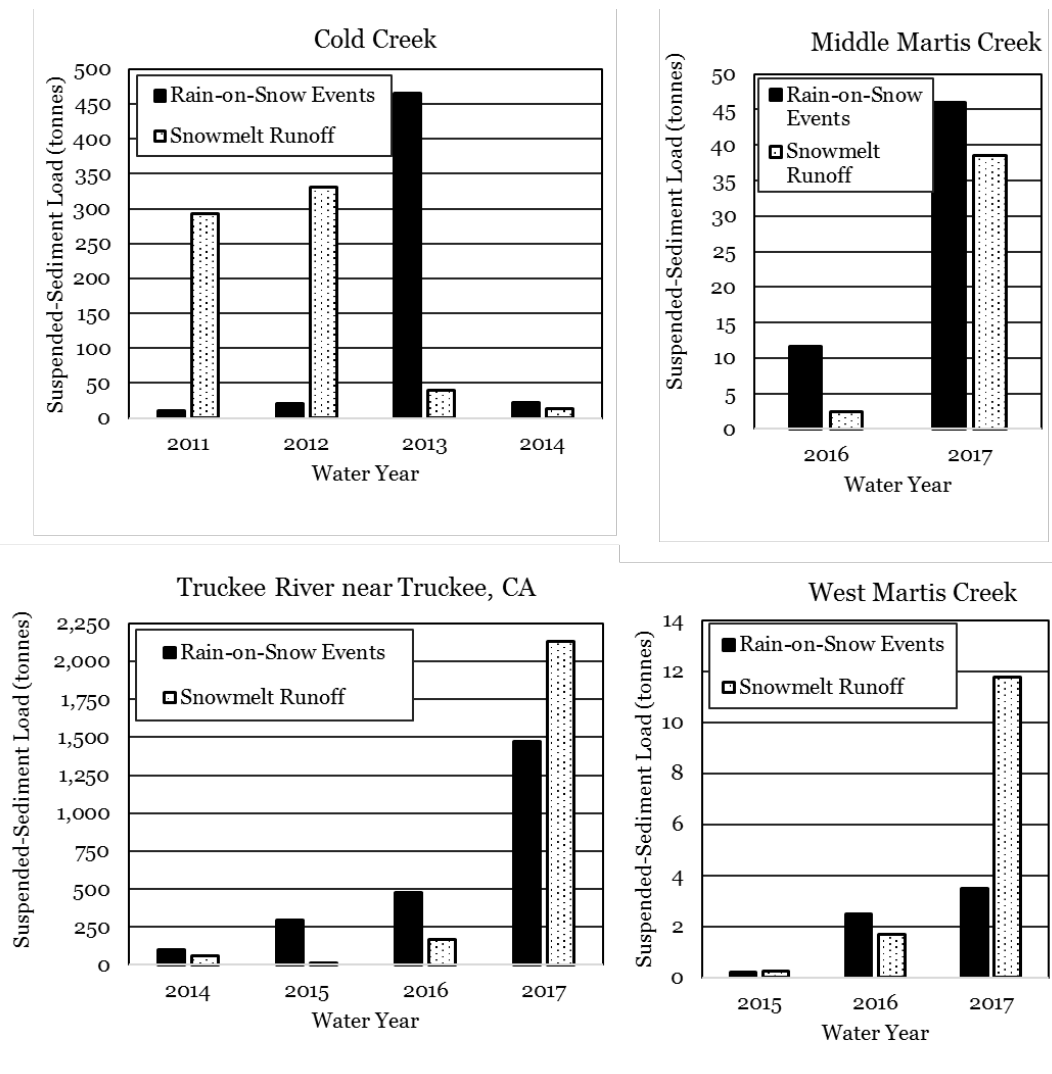
Figure 3. Suspended-sediment loads measured from the Truckee River and 3 tributaries for rain-on-snow events and snowmelt runoff periods, water years 2011-2017

Suspended sediment loads were generally higher during snowmelt runoff events in years with above average snowpack and annual runoff (WY2011 and WY2017). Water year type does not, however, correlate with loads in Cold Creek. Across all 4 years when suspended-sediment was measured in Cold Creek, the highest load was measured in WY2013, one of the drier years. In this case, a single rain-on-snow event on December 2, 2012 (WY2013) generated 348 tonnes of suspended-sediment, an order of magnitude greater than the load measured for the entire snowmelt runoff period in WY2013 (39 tonnes). This single event load also exceeded loads measured from snowmelt runoff in a wet year (293 tonnes, WY2011). This event was an atmospheric river with warm temperatures and abundant rainfall recorded over a period of days with the bulk of the precipitation recorded on December 2. Soil saturation and rapid snowmelt resulted in a mid-winter flash flood in high elevation drainages and likely increased channel and bank erosion.

Across all stations, suspended-sediment yields ranged between 0.02 tonnes/km^2 and 14.3 tonnes/km^2 for all rain-on-snow events, and between 0.02 tonnes/km^2 and 17.9 tonnes/km^2 for all snowmelt runoff periods. Because not all streams were monitored over the same years,

comparisons across watersheds is difficult. The Truckee River exhibited the highest yields when compared to tributaries measured in the same years, even though the Truckee River is a regulated system.

While this study included measurements over multiple years, it is important to consider sediment loading on a decadal scale, especially under climate change scenarios. If rain-on-snow events become more frequent, the sum of loads measured from these events are likely to exceed loads measured from snowmelt runoff. Management strategies, therefore, targeted at extreme events are likely to be most effective in protecting and restoring aquatic habitat in snowmelt-dominated systems. Possible management actions in tributary watersheds may include: a) identification and mitigation of sediment sources, b) enforcement of construction and post-construction best management practices, c) regulation of new developments such that they avoid disturbance of sensitive soils, d) riparian enhancements to reduce bank erosion, and e) floodplain restoration and enhancements to sequester fine sediment.

In addition to controlling sources of fine sediment in tributaries, changes in dam operations may be useful in managing fine sediment transport and deposition on the Truckee River bed. The Truckee River Operations Agreement (TROA), implemented in 2015, provides operations flexibility and efficiency to provide environmental benefits. It may be possible under TROA to mimic flushing events after rain-on-snow events if snowmelt runoff peak flows are insufficient to scour pools and bed habitat of fine sediment deposition.

References

Coats, R. 2010, "Climate change in the Tahoe Basin: regional trends, impacts and drivers," Climate Change, 102: 435-466.

Costa, J.E. and J.E. O'Connor. 1995. "Geomorphically effective floods," *In* Natural and anthropogenic influences in fluvial geomorphology, the Wolman volume, edited by J.E. Costa, A.J. Miller, K.W. Potter, and P.R. Wilcock, 45–56. Geophysical Monograph 89. Washington, DC: American Geophysical Union

Dana, G.L., Panorska, A.K., Susfalk, R.B., McGraw, D., McKay, W.A., and Dornoo, M. 2004, "Suspended sediment and turbidity patterns in the Middle Truckee River, California for the period 2002-2003," Pub. No. 41196, Division of Hydrologic Sciences, Desert Research Institute, Reno, Nevada, 64 p.

Herbst, D.B., Medhurst, B., and Bell, I.D. 2013, "Benthic macroinvertebrate response to sediment deposition as criteria for evaluating and monitoring the extent of habitat degradation on the Middle Truckee River, California," Sierra Nevada Aquatic Research Laboratory report, prepared for Truckee River Watershed Council, Truckee, California, 28 p.

Inman, D.L. and Jenkins, S.A. 1999, "Climate change and the episodicity of sediment flux of small California rivers," Journal of Geology, 108: 251-270.

Jepsen, S.M., Harmon, T.C., Meadows, M.W., and Hunsaker, C.T. 2016, "Hydrogeologic influence on changes in snowmelt runoff with climate warming: Numerical experiments on a mid-elevation catchment in the Sierra Nevada, USA," Journal of Hydrology, 533: 332-342.

Kattelmann, R. 1996. "Hydrology and Water Resources," *In* Sierra Nevada Ecosystem Project: final report to Congress, vol. II, Assessments and scientific basis for management options. Davis: University of California, Centers for Water and Wildland Resources, 855-920.

Kulchawik, P., Shaw, D., and Donaldson, E. 2014, "Middle Truckee River Total Maximum Daily Load (TMDL): Bed conditions monitoring report, water years 2011-2014," Balance Hydrologics consulting report prepared for Truckee River Watershed Council, Truckee, California, 58 p.

Langlois, J.L., Johnson, D.W., and Mehuys, G.R. 2005, "Suspended sediment dynamics associated with snowmelt runoff in a small mountain stream of Lake Tahoe (Nevada)," Hydrological Processes, 19: 3569-3580.

McCabe, G.J., Clark M.P., and Hay, L.E. 2007. "Rain-on-snow events in the western United States," American Meteorological Society Articles, March 2007: 319-328.

Simon, A. 2008. "Fine-Sediment Loadings to Lake Tahoe," Journal of the American Water Resources Association 44:618-639.

Exceedance Flows for Sediment Yield Determination: Michigan Harbors

Extended Abstract

John H. Barkach, M.S. Department of Civil and Environmental Engineering, Wayne State University, Detroit, MI, jbarkach@glec.com

Carol J. Miller, Ph.D., Department of Civil and Environmental Engineering, Wayne State University, Detroit, MI, ab1421@wayne.edu

James P. Selegean, Ph.D., USACE, Detroit, MI, James.P.Selegean@usace.army.mil

Emily A. Bradley, USACE, Detroit, MI, Emily.A.Bradley@usace.army.mil

Wayne State University and the USACE-Detroit District are researching sediment delivery to the Great Lakes from the 60 largest watersheds located in Michigan. These 60 Michigan watersheds range in size from Falls River with a contributing watershed area covering 45 miles2 to the Saginaw River watershed covering 6,132 miles2. Together, these 60 watersheds cover 51,172 miles2 or 86% of the total land cover of the State of Michigan. Of these 60 watersheds, 30 watersheds discharge into USACE harbors and navigation channels that are managed by the USACE-Detroit District (see Figure 1).

Many of the watershed sediment delivery equations have been developed for application at a much larger watershed scale (Syvitski, 2002; Syvitski and Milliman, 2007; Cohen et al., 2011; and, Cohen et al., 2014). The sediment delivery equations developed by Syvitski and Milliman (2007) focused on watersheds that contain large rivers that discharge to the world's oceans with annual mean river discharges exceeding 1,060 cubic feet per second (cfs). In comparison, the average annual flow rate of Michigan rivers that discharge to the Great Lakes, and these 30 USACE harbors and navigation channels in particular, are typically much smaller and range in size with mean flow rates of 161 cfs (Au Gres River) to 4,410 cfs (Saginaw River). Of the 60 watersheds evaluated by Wayne State University, 78% have mean flow rates that are less than 1,060 cfs.

Bankfull is a very important concept with respect to assessment of watershed sediment transport. Bankfull is the elevation where the river spills into the flood plain and is a relief valve for the river (ASCE, 2008; USACE, 1995). At bankfull, the average cross-sectional bed shear force is greatest, and the river performs the most work (e.g. moves the most sediment). If the river cannot spread out onto the flood plain to release energy, the river may incise and de-stabilize banks (bank failure or mass wasting). The frequency of bankfull flow within a river system varies, but the recurrence interval typically ranges from 1.5 to 2.0 years (Biedenharn et al, 2008).

Figure 1. Federal Harbors of the Great Lakes

With respect to estimation of watershed sediment delivery, many researchers have applied either dimensional analysis or regression analysis using mean river flow (Syvitski, 2002; Syvitski and Milliman, 2007; Cohen et al., 2011; and, Cohen et al., 2014). Estimation of a river's mean and exceedance flows is in many ways one of the most important variables needed to estimate watershed sediment delivery.

Calculations for the mean river flow and 1.5 year and 2.0 year recurrence interval flows at the river outlet were completed by the State of Michigan Department of Environmental Quality (MDEQ) in collaboration with this project. In addition, contributing drainage area for each of these watersheds is a known parameter. Therefore, it is possible to develop regression formulas which relate these exceedance flows to the contributing area, as shown in Figure 2.
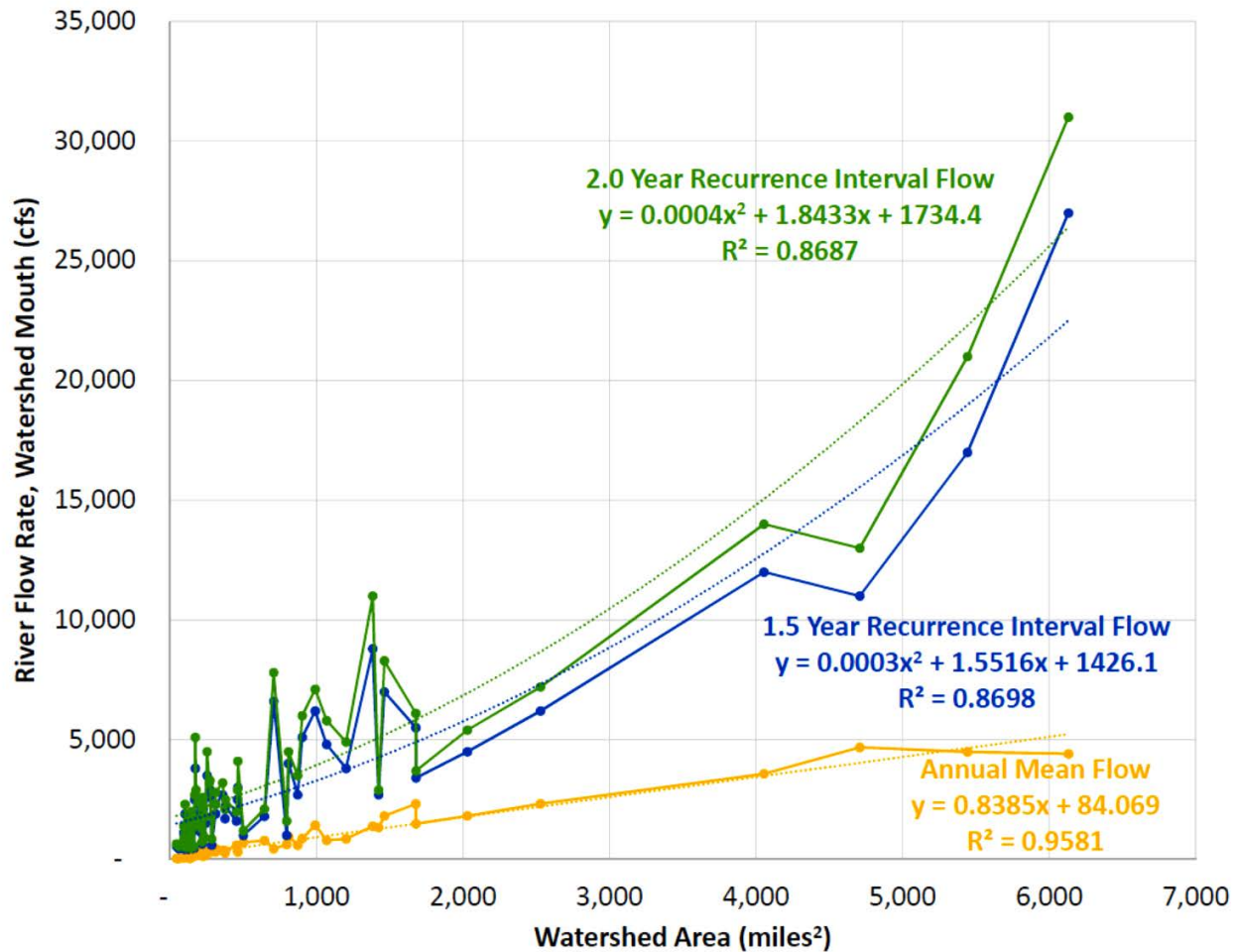
Figure 2. Mean Flow, and 1.5 Year and 2.0 Year Recurrence Interval Flows at the River Mouth

Review of Figure 2 and the corresponding correlation coefficient (R^2) values reveals that there is a strong correlation between the annual mean flow (as well as the corresponding 1.5 year and 2.0 year recurrence interval flows) to watershed area, although there are significant differences in land use, topography, and surficial geology within these 60 watersheds. The strong correlation between watershed area and river discharge at the outlet to the corresponding Great Lake or connecting channel likely explains the high correlation between watershed sediment yield and watershed area that have been reported by the USACE (2008 and 2010) and others (USACE, 1995; Borah et al, 2002; Syvitski JPM, 2002; Syvitski and Milliman, 2007; Cohen et al., 2011; and, Cohen et al., 2014).

Estimation of a river's mean and exceedance flows (particularly channel forming flows) is one of the most important steps in estimating watershed sediment delivery. With respect to estimating watershed sediment delivery to the Great Lakes and connecting channels, there are two likely reasons why the correlations between watershed area and mean flow, and 1.5 year and 2.0 year exceedance flows are so strong. First, Michigan's extensive glacial heritage has resulted in relatively small differences in topography at the watershed scale in comparison to the elevation of the receiving water (the corresponding Great Lake or connecting channels); these multiple glacial events have resulted in the low gradient streams that are common in Michigan and throughout the Great Lakes watershed.

Second, although the percentage of developed land greatly affects mean flow and flood flows within Michigan's urban watersheds, the average and median percentage of developed land in the 60 Michigan watersheds that are presented in this paper are relatively small (9.71% and 6.07%, respectively), with watershed land use dominated by forest land, wetlands, and agriculture. A recent study prepared for the MDEQ (Stantec, 2014) found a similar relationship between drainage area and annual mean flow for 28 watersheds ranging in size from 16.3 to 545 miles^2 that are located in southern Michigan, with correlation coefficients ranging from 0.84 to 0.94. These reasons likely explain why there is a strong correlation between the annual mean flow (and the corresponding 1.5 year and 2.0 year recurrence interval flows) to watershed area, despite differences in land use, topography, and surficial geology within these 60 Michigan watersheds.

Acknowledgments

References

Biedenharn DS, Watson CC, and Thorne CR. 2008. Fundamentals of Fluvial Geomorphology. IN: Chapter 6, Sedimentation Engineering, Processes Measurement, Modeling, and Practice, edited by Marcelo H. Garcia, Ph.D. American Society of Civil Engineers, Practice No. 110. ASCE, Reston, Virginia.

Borah DK, Drug EC, and Yoder D. 2008. Watershed Sediment Yield. IN: Chapter 17, Sedimentation Engineering, Processes Measurement, Modeling, and Practice, edited by Marcelo H. Garcia, Ph.D. American Society of Civil Engineers, Practice No. 110. ASCE, Reston, Virginia.

Cohen S, Kettner AJ, Syvitski, JP, Fekete BM. 2011. WBMsed, a distributed global-scale riverine sediment flux model: Model description and validation. Computers and Geosciences. Volume 53, pages 80-93.

Cohen S, Kettner AJ, Syvitski, JP. 2014. Global suspended sediment and water discharge dynamics between 1960 and 2010: Continental trends and intra-basin sensitivity. Global and Planetary Change; Volume 115, pages 44-58.

Stantec. 2014. Michigan Lake Plain Regional Reference Curves Project, Revised Bankfull Discharge for Selected Michigan Rivers and Regional Hydraulic Geometry Curves for Estimating Bankfull Characteristics in Southern Michigan Rivers Study. Prepared for the Michigan Department of Environmental Quality and the Bay County Drain Commissioner. Stantec, Ann Arbor, Michigan. Report Number: 2011-0100.

Syvitski JPM. 2002. Supply and flux of sediment along hydrological pathways: research for the 21st century. Environmental Computation and Imaging Group, Institute of Arctic and Alpine Research, University of Colorado. Elsevier, Global and Planetary Change. Volume 39, pages 1-11.

Syvitski JP and Milliman JD. 2007. Geology, Geography, and Humans Battle for Dominance over the Delivery of Fluvial Sediments to the Coastal Ocean. Journal of Geology, The University of Chicago. Volume 115, pages 1-19.

U.S. Army Corps of Engineers. 1995. Sedimentation Investigations of Rivers and Reservoirs. Department of the Army, Washington DC. Manual No. 1110-2-4000. Revision date: October 31, 1995.

U.S. Army Corps of Engineers. 2008. Fluvial Sediment Budget Development for the Great Lakes Region, Great Lakes Tributary Modeling Program (516(e)). Engineer Research and Development Center, USACE-Detroit District, Great Lakes Hydraulics and Hydrology Office, Detroit, Michigan. Report Date: July 2008.

U.S. Army Corps of Engineers. 2010. Ontonagon River Watershed 516e Sediment Study. USACE-Detroit District, Great Lakes Hydraulics and Hydrology Office, Detroit, Michigan. Report Date: August 2010.

Fire Potential Modeling and its Impact in New Mexico

Emma Kelly, Resource Management Coordinator, United States Bureau of Reclamation, Albuquerque Area Office, Albuquerque, NM, ekelly@usbr.gov

Dagmar Llewellyn, Hydrologist, United State Bureau of Reclamation, Albuquerque Area Office, Albuquerque, NM, dllewellyn@usbr.gov

Rachel Meier, GIS Specialist, The Nature Conservancy, New Mexico Chapter, Santa Fe, NM, rachel.meier@tnc.org

Introduction

Anticipated high-severity wildfires in northern New Mexico and southern Colorado, and subsequent post-fire flooding, pose enormous threats to the region's watersheds and downstream communities that depend on them for water supply.[1]

Throughout the past century, forest management has worked within the suppression paradigm, with the goal to extinguish a fire as quickly as possible. New Mexico's forests are well adapted to fire and many of their ecosystems are considered fire-dependent. Normal forest conditions would see frequent low-severity fires throughout the landscape that would burn and clear the understory brush of a forest but allow older growth trees to survive. With active fire suppression, the forests have grown denser with many layers that create ladder fuels. These ladder fuels result in a larger high-severity fires that cause more damage to the forests and watersheds than would low-severity fires.[2]

Forest thinning provides a benefit to water supply through a reduction in forest canopy coverage. Watershed resiliency will increase as the water supply and sedimentation rate increase and mitigating drought and flooding impacts occur.[3]

Fire-potential modeling developed by The Nature Conservancy's (TNC) New Mexico Chapter has guided forest and watershed treatments throughout the state, including in the Bureau of Reclamation's San Juan – Chama Project region in northern New Mexico and southern Colorado. This extended abstract discusses the modeling techniques utilized for this risk assessment, the implementation practices it has initiated, and the collaborative approach taken by agencies and partners to accomplish this work. This fire-potential modeling takes fuels data, topography, weather data and soil type into account when assessing fire risk. This modeling has helped TNC and their subsidiary project, the Rio Grande Water Fund (RGWF), establish four upland headwater priority areas that are critical to New Mexico's water supply. One of these priority areas is the Bureau of Reclamation's San Juan – Project's headwaters region. These four priority areas have been the subject of substantial forest and watershed restoration treatments

[1] "Navajo Blanco Watersheds Resilience Strategy for the San Juan Chama Project Source Watersheds," Navajo-Blanco Working Group, https://static1.squarespace.com/static/5a6d11100100277c343e6176/t/5b8580734fa51aaa9a33bb90/1535475901562/SJCP_Strategy_2017_03_13.pdf, (March 2017).

[2] The Rio Grande Water Fund, https://www.nature.org/en-us/about-us/where-we-work/united-states/new-mexico/stories-in-new-mexico/new-mexico-rio-grande-water-fund/, (February 2019).

[3] Fire Learning Network, https://www.conservationgateway.org/conservationpractices/firelandscapes/firelearningnetwork/pages/fire-learning-network.aspx, (February 2019).

1

by various agencies and entities over the last four years, including tree thinning, mastication, prescribed fire, and riparian restoration. These techniques are utilized to offset the potential for catastrophic fire and its effects, a serious threat to New Mexico's water supply. Impressive collaborative effort has been involved in this work. The Rio Grande Water Fund has brought together almost 100 partners from federal, state, tribal and municipal agencies, non-governmental organizations, and businesses to collaborate on how to secure New Mexico's water future. As the major water management agency in the state, the Bureau of Reclamation is just one of many organizations involved in this effort. This abstract outlines the partnership between federal agencies and local initiatives, a relationship that has great potential benefit to increase the effectiveness of hydrological modeling and forecasting.

Background

In New Mexico the forests in the San Juan River and Rio Chama Watersheds are the primary source of water for the state where snow is retained within the canopy until the spring melt. A forest's ability to adequately perform these storage functions depends on its overall health. High-severity fires greatly hinder this process, as they cause extensive watershed damage and create hydrophobic soils. Heavy rainfall after a fire can be severe and the resulting debris flows can be a dangerous and detrimental after-effect from high-intensity burns.

The San Juan – Chama Project and other watersheds impacted by these dangerous forest conditions are the key drivers for Reclamation's engagement with TNC's Rio Grande Water Fund. These watersheds are critical to Reclamation's mission of water delivery and TNC is pioneering the effort to protect them.

Modeling Techniques

TNC worked with experts from the US Geological Society (USGS), USDA Forest Service (USFS), Rocky Mountain Research Station (RMRS) and RGWF Advisory Board members to develop a model that would aid in the identification of forested watersheds most at risk of catastrophic damage from high severity wildfire. Models including the FlamMap model from the USGS, the FSIM model from RMRS, and a debris flow model developed by the USGS Landslide Hazards Program. These models together estimated spatial variation in burn probability, fire severity, and debris flow hazard across the state of New Mexico and collectively present the debris flow threat in unburned, forested watersheds within the RGWF boundary.

Important layers incorporated in the models used include: topography (slope, aspect, elevation) from LANDFIRE, fuels data such as canopy cover, vegetation type and density from LANDFIRE, weather data from Remote Automatic Weather Stations (RAWS) and burn severity data from the Monitoring Trends in Burn Severity (MTBS) program. The FlamMap model produces outputs describing the spatial probability of crown fire. The USGS' post-fire debris flow model estimates the probability and volume of material resulting from post-fire debris flows. Finally, the FSIM model provides estimates of annual burn probability of the landscape. Combined outputs from these models depict areas at greatest risk of high severity wildfire and significant post-fire debris flow potential.

Figure 1 depicts a rapid assessment of burn probability coupled with probability of debris flow after a wildfire in the Rio Grande Water Fund region. This modeling was developed by TNC as

2

part of the Southwest Forest Assessment Project. Using layers of percent slope, burn severity, soil type and percent rainfall expected, the assessment classifies the overall fire risk within the RGWF footprint and allows for comparisons between landscapes and identification of focal areas like the San Juan-Chama Headwaters region.
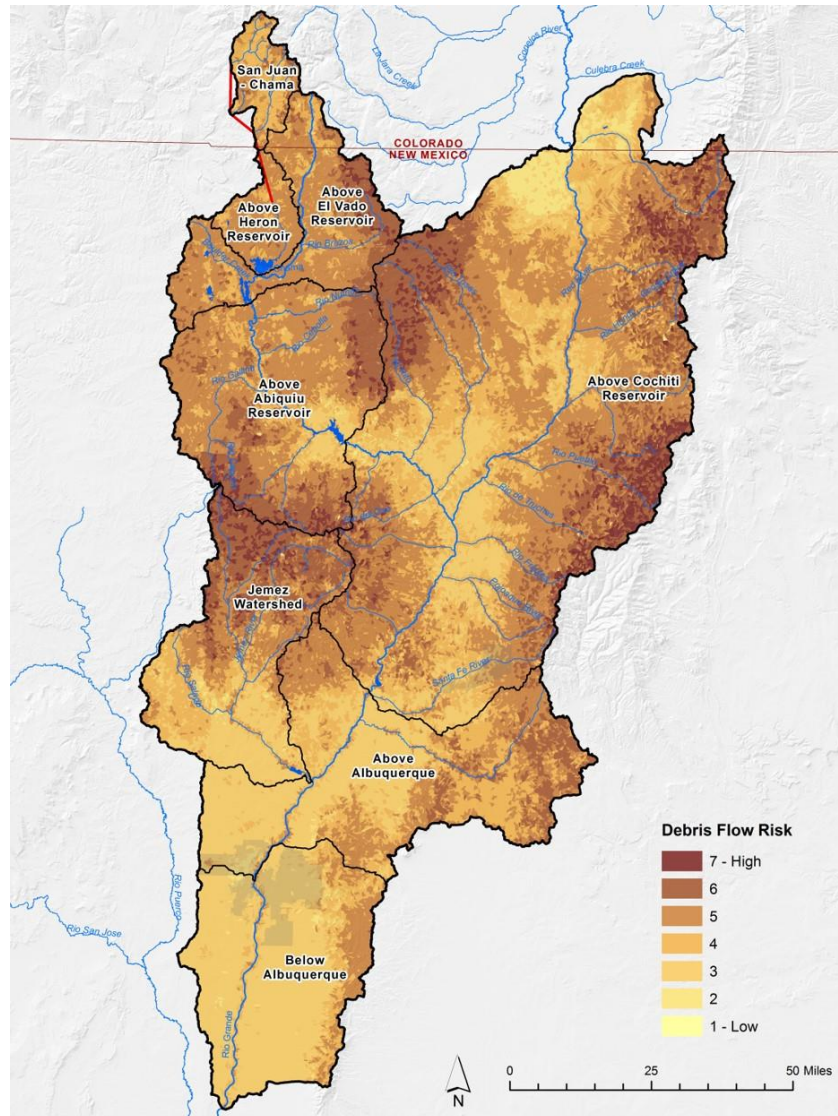
Figure 1. Results of a rapid assessment of burn probability coupled with probability of debris flow after a wildfire in the Rio Grande Water Fund region. (RGWF).

Implementation Practices

Overview

Various forest treatments, including thinning, mastication, and prescribed fire, have been completed throughout the RGWF's four focus areas in New Mexico and more are planned. Recent work in the San Juan – Chama Project region has included thinning and forest treatments in critical, yet accessible, terrain. RGWF funding has allowed for more than 300

3

acres of treatments on private land in southern Colorado and northern New Mexico. Attention was paid to areas that were deemed accessible and in critical need of treatment, with further emphasis given to access roads where critical infrastructure lies.

Treatment Types

There are a variety of treatment practices happening all over New Mexico that have been guided by the RGWF's wildfire and debris flow potential modeling. Below is an overview of some (but not all) of the methods used. Treatment can be an effective tool to protect critical water supplies and ensure water quality.[4]

Thinning: Thinning reduces stand density and remove fuels from the forest. Generally, forest thinning involves strategically zeroing out smaller diameter woods from forests to clear the understory of forests and allow for regrowth of grasses. Larger trees can be removed as well.[5]

Mastication: Like thinning, mastication removes fuels from the forest. This technique essentially mulches the forest. Vegetation is reduced into small chunks either mechanically or manually. Small trees, brush, and slash is ground, chipped, and broken apart to reduce ladder fuels to prevent crown fire spread in the event of a fire.[6]

Prescribed Fires: Across the American West, historic natural fire regimes have been disturbed in the past century due to active fire suppression. Many western forested ecosystems, including the Pecos River Basin headwaters region, are considered to be "fire-dependent," meaning they rely on fire as an agent to keep them healthy. Trees are stressed by overcrowding. Historically, fire has been the natural tool to reduce the spread of insect pests and disease, remove non-native species, recycle nutrients back to the soil, and to provide forage for game.

According to the US Forest Service, "Prescribed fire is a planned fire used to meet management objectives." Prescribed fires are planned and administered by fire-management specialists in order to reintroduce fire onto the landscape. Burn plans are written with extreme caution and awareness of climate, weather, and forest type. Often, prescribed fires will be executed on lands that have already undergone thinning or mastication treatment as fuel reduction has already taken place.[7]

Managed Fire: Managed fires are similar to prescribed fires and are used to clear the forest's overgrown understory while allowing older growth trees to remain. This increasingly-used tactic starts when a fire occurs naturally. Rather than suppressing the fire, the response agency (usually Forest Service or BLM) allows the fire to burn with active and attentive management. These types of fires are done with extreme sensitivity to the current climate, weather, and forest conditions. They are also well staffed with firefighter response teams to properly manage the fire. However, because managed fires are by nature more unpredictable than a prescribed fire, a range of fire severity can be seen in a managed fire footprint.[8]

---

[4] Silvio Simonit, "The Impact of Forest Thinning on the Reliability of Water Supply in Central Arizona" PLoS ONE, (April 2015).

[5] Donna Childress, "Tree Thinning 101," Woodland Magazine, Forest Foundation, (Fall 2014).

[6] "What is Forest Mastication?" Diversified Resources Inc. https://www.driforest.com/what-is-forest-mastication/ (February 2019).

[7] "Wildland Fire: What is a Prescribed Fire?" National Park Service, https://www.nps.gov/articles/what-is-a-prescribed-fire.htm, (February 2017).

[8] Fire Use for Resource Benefit, United States Department of Agriculture Forest Service, https://www.fs.usda.gov/detail/sequoia/home/?cid=fsbdev3_059508, (February 2019).

Collaborative Approach

Collaboration and coordination between stakeholder groups are critical for continued effective water supply protection projects in New Mexico. Below are two examples of innovative groups that are pioneering the effort in the state.

The Rio Grande Water Fund

Founded in 2014, the Rio Grande Water Fund has established itself as a leader in forest and watershed protection in the state. The RGWF works by gathering key stakeholders throughout the state to raise and distribute money for forest and watershed treatment efforts in its four focus areas, including the San Juan – Chama Watershed area.[9]

This innovative approach to fundraising and project development engages stakeholders across the state in planning and implementing watershed protection measures. The Water Fund has more than 70 member organizations that have signed its charter document and is actively working to engage even more agencies and businesses.

Using this collaborative approach, the RGWF has treated 108,000 acres with thinning, controlled burns, and managed natural fires. There are currently 300,000 acres of land that are currently being planned for treatments. The RGWF is working progressively towards a goal of restoring 600,000 acres over a 30-year period. The Fund has accumulated $4.55 million in private funding and has leveraged $40 million in public funding.

The RGWF has been incredibly effective at engaging partners and honing in on critical regions within the upper Rio Grande watershed to help ensure that New Mexico's water future is secure.

The San Juan – Chama Watershed Partnership

Also founded in 2014, the San Juan – Chama Watershed Partnership is a partnership of local, county, state, tribal, and federal agencies, non-government organizations, and local individuals that come together to support a watershed for a healthy ecosystem, a vibrant economy, and sustainable communities for the people who live and depend on this watershed. The Partnership's region is made up of the three sub-watershed basins that make up the San Juan - Chama Project: the Rio Blanco, the Navajo River, and the Little Navajo River in southern Colorado, and the entire Rio Chama watershed basin in northern New Mexico.[10]

The Partnership's members engage with the Water Fund and other entities in the area to further watershed protection efforts and to encourage collaboration to enable effective local cooperative decision-making. The Partnership's flagship event hosted every Spring, the Rio Chama Congreso, gathers stakeholders in the region for a day long forum that connects individuals, non-government organizations, and agencies with one another to discuss resource management challenges and solutions. In 2018, over 80 individuals attended the Rio Chama Congreso to discuss the nexus between wildfire and water in the region.

---

[9] Rio Grande Water Fund, The Nature Conservancy, https://www.nature.org/en-us/about-us/where-we-work/united-states/new-mexico/stories-in-new-mexico/new-mexico-rio-grande-water-fund/, (February 2019).
[10] San Juan – Chama Watershed Partnership, https://www.sanjuanchama.org/, (February 2019).

5

Next Steps

As outlined above, agencies and non-government entities alike have begun extensive work in New Mexico's critical watersheds. The RGWF is on track to have 100 signatories by 2020, the San Juan – Chama Watershed Partnership is becoming more active in their region, and there appears to be more fire mitigation collaboration efforts happening throughout the state.

Notably, 2019 New Mexico State Legislature passed the Forest and Watershed Restoration Act into law in March 2019. This act establishes a board that provides criteria to evaluate forest and watershed restoration projects and provides approved projects with funding from the New Mexico Irrigation Works Construction Fund and the Improvement of the Rio Grande Fund. This indicates that state leadership understands the challenges New Mexico faces with regards to water security and is prioritizing the treatment and restoration its critical watersheds.

References

Albuquerque Bernalillo County Water Utility Authority Website (2017).

Donna Childress, "Tree Thinning 101," Woodland Magazine, Forest Foundation, (Fall 2014).

Fire Learning Network, https://www.conservationgateway.org/conservationpractices/firelandscapes/firelearningnetwork/pages/fire-learning-network.aspx, (February 2019).

Fire Use for Resource Benefit, United States Department of Agriculture Forest Service, https://www.fs.usda.gov/detail/sequoia/home/?cid=fsbdev3_059508, (February 2019).

Harpold, A., Biederman, J., Condon, K., Merino, M., Korgaonkar, Y., Nan, T., Sloat, L., Ross, M., Brooks, P. *Changes in snow accumulation and ablation following the Las Conchas Forest Fire, New Mexico, USA* (Ecohydrology Vol. 7, Iss. 2)

"Navajo Blanco Watersheds Resilience Strategy for the San Juan Chama Project Source Watersheds," Navajo-Blanco Working Group, https://static1.squarespace.com/static/5a6d11100100277c343e6176/t/5b8580734fa51aaa9a33bb90/1535475901562/SJCP_Strategy_2017_03_13.pdf, (March 2017).

Rio Grande Water Fund, The Nature Conservancy, https://www.nature.org/en-us/about-us/where-we-work/united-states/new-mexico/stories-in-new-mexico/new-mexico-rio-grande-water-fund/, (February 2019).

San Juan – Chama Watershed Partnership, https://www.sanjuanchama.org/, (February 2019).

Simonit S, Connors JP, Yoo J, Kinzig A, Perrings C (2015) The Impact of Forest Thinning on the Reliability of Water Supply in Central Arizona. PLOS ONE 10(4): e0121596. https://doi.org/10.1371/journal.pone.0121596

Sun G, Caldwell PV, McNulty SG. (2015) Modelling the potential role of forest thinning in maintaining water supplies under a changing climate across the conterminous United States. Hydrological Processes. Doi:10.1002/hyp.10469

Vaughan D, Makes K (2015) Characteristics of Colorado Forestry Contractors and Their Role in Current Forest Health Issues. Forest Prod. J. 65(5/6):217-225. doi:10.13073/FPJ-D-14-00095

"Wildland Fire: What is a Prescribed Fire?" National Park Service, https://www.nps.gov/articles/what-is-a-prescribed-fire.htm, (February 2017).

"What is Forest Mastication?" Diversified Resources Inc. https://www.driforest.com/what-is-forest-mastication/ (February 2019).

Fires and Floods: A Case Study of the Relative Magnitudes and Persistence of Geomorphic Effects at the Watershed Scale

Lee H. MacDonald, Senior Research Scientist, NREL, and Professor Emeritus, Department of Ecosystem Science and Sustainability, Colorado State University, Fort Collins, Colorado, USA; lee.macdonald@colostate.edu

Daniel J. Brogan, Department of Civil and Environmental Engineering, Colorado State University, Colorado State University, Fort Collins, Colorado, USA; buckhtr@gmail.com

Peter A. Nelson, Associate Professor, Department of Civil and Environmental Engineering, Colorado State University, Colorado State University, Fort Collins, Colorado, USA; peter.nelson@colostate.edu

Stephanie K. Kampf, Associate Professor, Department of Ecosystem Science and Sustainability, Colorado State University, Fort Collins, Colorado, USA; stephanie.kampf@colostate.edu

ABSTRACT

Fires and floods are important drivers of geomorphic change. This paper compares the relative changes in the channels and valley bottoms resulting from a high severity fire and extreme floods in two 15 km² catchments—Hill Gulch and Skin Gulch—in the northern Colorado Front Range. In Skin Gulch a very high-intensity summer thunderstorm just one week after the fire caused an extreme peak flow and much more sediment deposition than observed in Hill Gulch. Overall, summer thunderstorms caused deposition in the valley bottoms while the intervening baseflows and spring snowmelt eroded some of this deposited sediment. Fifteen months after burning both watersheds experienced sustained high flows resulting from a long-duration rainstorm where multi-day rainfalls had a several-hundred-year recurrence interval. This flood greatly altered the expected post-fire trajectory, as it removed nearly all of the post-fire sediment as well as much of the older valley bottom deposits. The flood greatly enlarged the channel and reworked much of the valley bottom, leaving a much coarser channels and floodplains. We argue that this coarsening and the removal of the deposited sediment have greatly decreased the geomorphic sensitivity of both watersheds to future floods, and effectively truncated the typical post-fire depositional sequence. Both the post-fire and flood-induced geomorphic changes were much larger in Skin Gulch than Hill Gulch, and this can be attributed to several factors, including the much greater deposition in Skin Gulch shortly after the fire; reduced geomorphic sensitivity in Hill Gulch resulting from a large erosional flood in 1976; and the spatial distribution of burn severity and summer thunderstorms that resulted in lower peak flows and less post-fire deposition in Hill Gulch. The results suggest that fires in the Rocky Mountains can trigger significant hillslope runoff and erosion along with downstream channel changes, but large floods can cause larger and more persistent downstream channel changes regardless of whether a catchment has recently burned.

INTRODUCTION

Fires and floods are important drivers of geomorphic change, and in both cases the changes are largely driven by rainfall magnitude and intensity. There are, however, some key differences

with respect to the initial conditions and relative sensitivity of the landscape before floods and after fires, the spatial scales of their effects, and the typical duration of the resulting high flows and their associated potential for geomorphic work as defined by Costa and O'Connor (1995).

The hydrologic and geomorphic effects of fires have been relatively well studied at the hillslope scale, but we have much more limited data on post-fire effects at larger scales. In summer 2012 we began intensively monitoring the effects of the High Park Fire throughout two 15 km² catchments—Hill Gulch and Skin Gulch—in the northern Colorado Front Range (Figure 1). Two extreme storms allowed us the unique opportunity to compare the immediate effects of fires and floods in and between our two study watersheds. The first extreme storm was a very high intensity convective storm that occurred over a portion of upper Skin Gulch that had burned at high severity, and this caused tremendous amounts of hillslope erosion and downstream deposition (Brogan et al., 2016); no comparable convective storms and resulting depositional events occurred in Hill Gulch (Brogan et al., 2019a). The second storm was a multi-day mesoscale rain event in September 2013, fifteen months after the High Park fire, and this caused major flooding and the destruction of highways and structures along nearly all the major creeks and rivers draining the Colorado Front Range (e.g., Gochis et al., 2014; Yochum et al., 2017). Our comparison of the relative effects of fires and floods was further facilitated by the fortuitous documentation of the effects of an exceptional flood in lower Hill Gulch in summer 1976 by the landowner living adjacent to the stream. Hence the objectives of this paper are to: 1) characterize the hillslope erosion and downstream channel and valley bottom changes following the High Park Fire; 2) compare these post-fire changes to the measured effects of the September 2013 mesoscale flood; and 3) compare the downstream post-fire channel changes in each watershed to the effects of the 1976 flood.
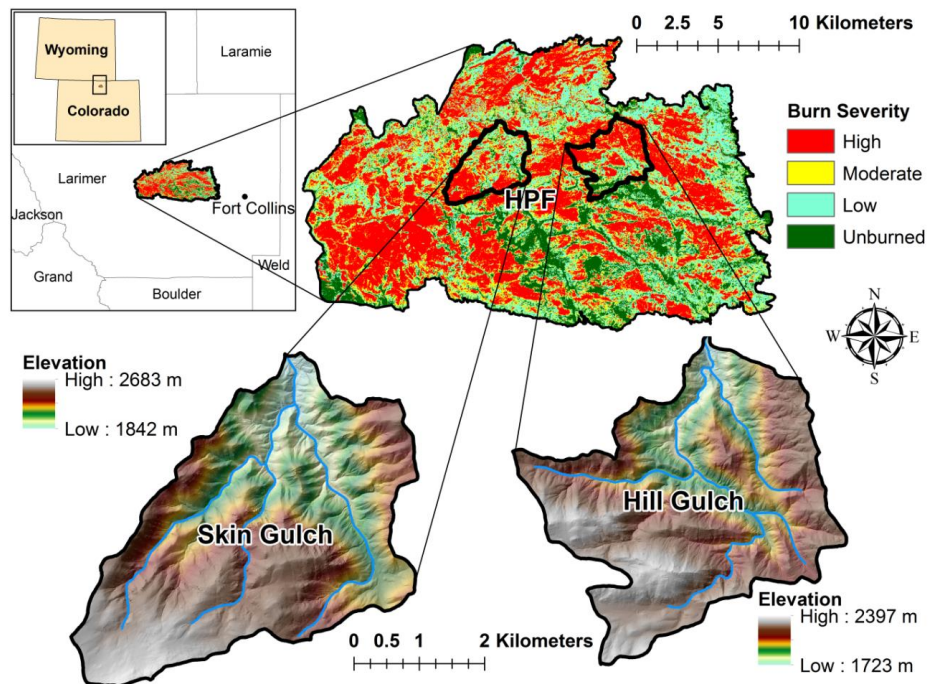

Figure 1. Location and burn severity of the 2012 High Park Fire in northern Colorado just west of Fort Collins, and maps of our two study watersheds where we intensively monitored channel changes using both field methods (cross sections and longitudinal profiles) and post-fire erosion and deposition in the valley bottoms by differencing five sequential lidar datasets.

METHODS AND SITE DESCRIPTION

Most of our field-based monitoring began in mid- and late summer 2012, with the exception of one short downstream cross-section in Skin Gulch surveyed just four days after the fire and two days before the large convective storm. Monitoring at the hillslope scale included repeated surface cover measurements and measuring sediment production from 29 convergent hillslopes loosely organized into five groups, with each group having one or two tipping bucket rain gauges (Kampf et al., 2017; Schmeer et al., 2018). To document downstream channel change we established and intensively monitored 10-11 cross sections and longitudinal profiles in each watershed (Brogan et al., 2019a). We also quantified the volumes of deposition, erosion, and net change for 50-m valley bottom segments throughout each watershed by differencing high-resolution digital elevation models derived from five aerial lidar datasets collected between October 2012—four months after the High Park Fire—and June 2015 (Brogan et al., 2019b). Peak flows for the largest floods were estimated from high water marks and 2D hydraulic modeling (Brogan et al., 2017; Brogan et al., 2019a).

Mean annual precipitation in the watersheds is about 450-550 mm yr^{-1}, with about one-third of this as snow. Most of the summer rainfall comes in short-duration, high-intensity convective storms, and these are the events that drive almost all of the post-fire hillslope erosion (Benavides-Solorio and MacDonald, 2005). Prior to the fire the vegetation in each watershed was over 80% coniferous forest, and this was primarily ponderosa pine with some douglas-fir and lodgepole pine on north-facing slopes and at higher elevations. Bedrock is primarily schist and gneiss, and soils are predominantly shallow, coarse-textured sandy loam soils with scattered rock outcrops. Mean slopes and total relief in each watershed are nearly identical at about 24% and 650 m, respectively (Brogan et al., 2019b). About 65% of each watershed burned at high or moderate severity, and prior to the fire both watersheds had minimal or no flow during the summer. Hence the main channels were typically less that one meter wide, and 70-80% of the channels were steeper than 0.065 m m^{-1} (Brogan et al., 2019b).

RESULTS

Modeled Peak flows for the high-intensity summer thunderstorm that occurred in Skin Gulch—without accounting for sediment bulking—were up to 30 m^3 s^{-1} km^{-2} (Brogan et al., 2017). None of the sediment fences or rain gages had been installed at this point, but field observations, the deposition of imbricated boulders one meter in diameter, and the one downstream cross-section clearly showed the extreme magnitude of this flood (Figure 2). The subsequent but smaller convective storms in summer 2012 caused additional hillslope erosion and downstream deposition; overall deposition was qualitatively much greater in Skin Gulch than Hill Gulch. Spring snowmelt cut new and sometimes deeper channels through these deposits but most of the deposited sediment remained in place (Brogan et al., 2019a). Summer 2013 brought a new cycle of convective storms, hillslope erosion, and downstream deposition, and the cross-section data indicated that the mean increase in cross-sectional area of 1.4 m^2 in Skin Gulch was nearly double the value in Hill Gulch (Brogan et al., 2019a).

Mean total precipitation for the September 2013 mesoscale flood was about 260-280 mm, with approximately 175 mm falling over a two-day period (Kampf et al., 2016). The estimated recurrence of these multi-day rainfalls was more than one hundred years. In contrast, the peak

Figure 2. Deposition of sediment and woody debris from the high-intensity summer thunderstorm in Skin Gulch one week after burning.

rainfall intensities were no more than about 34 mm hr^{-1}, so hillslope erosion from the mesoscale flood was generally less than from the summer convective storms (Kampf et al., 2016). In contrast to the limited hillslope erosion, the sustained high flows caused tremendous scour in the downstream channels and valley bottoms, removing nearly all of the post-fire sediment deposits and a considerable amount of pre-fire sediment (Figure 3). In Skin Gulch the mean increase in cross-sectional area for all but the lowest cross-section was nearly 8 m^2 and the mean thalweg incision was nearly 0.7 m. In Hill Gulch the mean increase in cross-sectional area and mean thalweg incision in all but the lowest cross-sections were only about one-sixth of the values in Skin Gulch (Brogan et al., 2019a). The net volumetric change was also about 50% larger in Skin Gulch than Hill Gulch (Brogan et al., 2019b). The preferential removal of finer sediments caused the mean D_{84} at the cross-sections to nearly double to 126 and 110 mm in Skin and Hill Gulch, respectively.

Figure 3. a) Channel downstream of cross section 4 in Skin Gulch in summer 2013, and b) September 2013 after the mesoscale flood showing the tremendous channel widening, scour, and substrate coarsening. Red circle is centered on the same tree in each picture.

Following the large September flood there were only relatively minor amounts of hillslope erosion (Schmeer et al., 2018) as vegetative regrowth increased infiltration rates and reduced rainsplash, overland flow, sheetwash, and rilling. The lower amounts of hillslope runoff and erosion, when combined with the downstream channel enlargement and bed coarsening from the September 2013 flood, meant that there were only minor changes in channel cross sections and longitudinal profiles from October 2013 through summer 2015.

Historic photographs from the bottom of Hill Gulch showed that the 1976 Big Thompson flood caused tremendous scour and coarsening in the channel and valley bottom near the mouth of the watershed (Figure 4). These changes and the overall appearance of the channel are remarkably similar to the changes and condition of Skin Gulch following the combined effects of the High Park Fire and 2013 flood. Since Hill Gulch was unburned prior to the 1976 flood, this means that a large flood is sufficient to cause tremendous channel and valley bottom geomorphic change, regardless of whether it is burned or unburned. This view is supported by the well-documented disastrous effects of the 1976 flood in the Big Thompson canyon, which killed 142 people and nearly completely destroyed Highway 34 (Simons et al., 1978). The September 2013 flood also caused large amounts of damage and reservoir sedimentation throughout the Colorado Front Range (Yochum et al., 2017), even though nearly all of the watersheds with major damage had not had been recently burned.
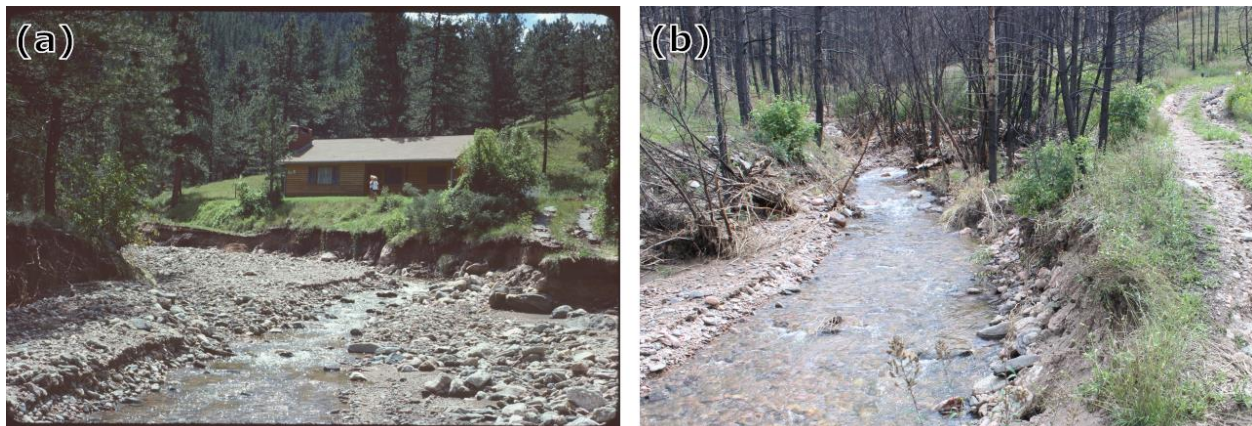
Figure 4. Lower portion of Hill Gulch after (a) the 1976 flood and (b) the September 2013 flood. The house in (a) was burned by the 2012 High Park fire.

DISCUSSION AND CONCLUSIONS

It is an intriguing question as to why the September 2013 flood did not have nearly as large an effect in Hill Gulch as in Skin Gulch, and there are several possible explanations. First, the peak flows in Hill Gulch, as estimated from high water marks and 2D hydrodynamic modeling, were only 25-40% of the estimated peak flows in Skin Gulch due to some combination of differences in rainfall, watershed topology, and different synchronization of flows based on the location of areas burned at high and low severity (Brogan et al., 2019a). Second, and perhaps more importantly, there was much more readily-available post-fire sediment deposited in Skin Gulch, with much of this stemming from the extreme convective storm in July 2102. For many channel segments the volumes of eroded sediment during the mesoscale flood were proportional to the volumes of post-fire sediment deposited after the fire from summer convective storms.

However, there was a much poorer correlation between the volumes of eroded and deposited sediment in lower Skin Gulch because so much of the post-fire sediment was deposited prior to the first lidar flight (Brogan et al., 2019b). Peak flows during the September 2013 flood also were estimated to be substantially lower in Hill Gulch than Skin Gulch (Brogan et al., 2019a). Finally, we believe that the extreme 1976 flood in Hill Gulch scoured out much of the available sediment, and the intervening 37 years was not enough to replenish the sediment supply in the valley bottoms given the relatively low background erosion rates.

The implication of our work, when placed in the larger temporal context of the 1976 flood and the larger regional context of the 1976 and 2013 floods, is that fires can cause tremendous localized effects in terms of hillslope erosion and downstream deposition. However, there are inherent limitations on the larger scale geomorphic effects of fires in the Colorado Front Range and similar environments. First, most of the post-fire runoff and erosion is driven by summer convective storms (Benavides-Solorio and MacDonald, 2005), and high intensity rains occur over only a limited area at a given point in time. Second, fires typically burn in headwater regions, so it is rare that most of a large watershed is burned. Third, wildfires are typically a mosaic of burn severities and substantial areas within a fire perimeter are either unburned or burned at low severity, so these areas do not generate large amounts of surface runoff or erosion. In contrast, floods like those in 1976 and 2013 are driven by larger-scale storms that drop large amounts of rain over a substantial portion of a larger watershed, and it is the downstream accumulation of this runoff that drives the severe downstream channel changes that were observed from both the 1976 and 2013 floods. Fires and floods are therefore a contrast between smaller-scale, higher-intensity storms on highly sensitive burned areas, and larger-scale sustained storms on landscapes that are much less sensitive due to the vegetative and litter cover. Hence fires may cause the highest peak flows and erosion rates at the hillslope and small watershed scales of perhaps up to 10-20 km^2, but in watersheds larger than around 100-200 km^2 the accumulation of runoff, sometimes combined with more sustained high flows, can result in substantially more downstream sediment transport and geomorphic change than after wildfires.

We would posit that these results are generally applicable to much of the western United States as well as many other fire-prone areas, but there are exceptions. Localized high intensity storms after the 550 km^2 Hayman Fire caused substantial amounts of downstream deposition in the sediment retention basin built on the 73 km^2 Turkey Creek watershed after the 2002 Hayman wildfire, but sediment accumulations per unit area were far less in the 240 km^2 Goose Creek watershed. After the 1996 Buffalo Creek fire and the 2002 Hayman fire the volume of post-fire sediment deposited into Strontia Springs Reservoir on the South Platte River was estimated to be equivalent to only a couple of decades of normal sediment inputs. In some environments like southern California, post-fire debris flows coming from exceptionally steep, rapidly-uplifting mountain fronts may be of greater importance for downstream deposition than rainfall-induced floods on unburned areas. The problem is that people have settled on the resulting alluvial fans without recognizing the potential danger (Montgomery, 2018). The broader lessons from the large floods in Colorado and the post-fire debris flows in southern California are that planners must recognize the hazards posed by extreme events, and a process-based geomorphic understanding is essential for explicitly identifying areas at risk from runoff, erosion, and deposition from fires and floods. Cities and counties then need the political will to enact zoning restrictions to minimize future losses of life and property.

REFERENCES

Benavides-Solorio, J. and MacDonald, L.H. 2005. "Measurement and prediction of post-fire erosion at the hillslope scale, Colorado Front Range," International Journal of Wildland Fire 14:1-18.

Brogan, D.J., MacDonald, L.H., Nelson, P.A., and Morgan, J.A., 2019a. "Channel geomorphic complexity and sensitivity to fires and floods in mountain catchments," Geomorphology 337: 53-68.

Brogan, D.C., Nelson, P.A., and MacDonald, L.H. 2017. "Reconstructing extreme post-wildfire floods: a comparison of convective and mesoscale events," Earth Surface Processes and Landforms 42:2502-2522; doi: 10.1002/esp.4194.

Brogan, D.J., Nelson, P.A., and MacDonald, L.H. 2019b. "Spatial and temporal patterns of sediment storage and erosion following a wildfire and extreme flood," Earth Surface Dynamics, in press.

Costa, J.E., and O'Connor, J.E.1995. "Geomorphically effective floods," in Natural and Anthropogenic Influences in Fluvial Geomorphology 45–56. doi:10.1029/GM089p0045.

Gochis, D., Schumacher, R., Friedrich, K., Doesken, N., Kelsch, M., Sun, J., Ikeda, K., Lindsey, D., Wood, A., Dolan, B., Matrosov, S., Newman, A., Mahoney, K., Rutledge, S., Johnson, R., Kucera, P., Kennedy, Sempere-Torres, D., Steiner, M., Roberts, R., Wilson, J., Yu, W., Chandrasekar, V., Rasmussen, R., Anderson, A., and Brown, B. 2014. "The great Colorado flood of September 2013", Bulletin of the American Meteorological Society.

Kampf, S.K., Brogan, D.J., Schmeer, S., MacDonald, L.H., and Nelson, P.A. 2016. "How do geomorphic effects of rainfall vary with storm type and spatial scale in a post-fire landscape?" Geomorphology 273: 39-51.

MacDonald, L.H., 2018. "Post-fire debris flow problems aren't new and likely to get worse", Conversations, 16 January 2018, 5 pp.

Montgomery, D., 2018. "Deadly California mudslides show the need for better maps and zoning that better reflect landslide risk", Conversations, 16 January 2018.

Schmeer, S., Kampf, S.K., MacDonald, L.H., Hewitt, J., and Wilson, C. 2018. "Empirical models of annual post-fire erosion on mulched and unmulched hillslopes", Catena 163:276-287.

Simons, D.B., Nelson, J.D., Reiter, E.R., and Barkau, R.L. 1978. "Flood of 31 July 1976 in Big Thompson Canyon, Colorado", National Academy of Sciences, Washington, D.C. 85 p.

Yochum, S.E., Sholtes, J.S., Scott, J.A., Bledsoe, B.P., 2017. "Stream power framework for predicting geomorphic change: The 2013 Colorado Front Range flood", Geomorphology doi:10.1016/j.geomorph.2017.03.004.

Five Years of Sedimentation behind Two Large Run-of-River Dams in the Brazilian Amazon

Trey Crouch, PhD Candidate, University of Florida, Gainesville, FL, treycrouch@ufl.edu
David Kaplan, Associate Professor, University of Florida, Gainesville, FL, dkaplan@ufl.edu
Edgardo Latrubesse, Professor, Nanyang Technological University, Singapore, elatrubesse@ntu.edu.sg
**Landerlei Santos**, PhD Candidate, Sao Paulo State University, Sao Paulo, Brazil, lahn_almeida@hotmail.com

Extended Abstract

Sedimentation behind run-of-river (ROR) dams is expected to be limited and quickly stabilized, because of the preserved energy gradient available to move sediment through these systems. However, this depositional expectation may not hold behind reservoirs along large, tropical rivers with high sediment loads. Estimations of sedimentation for environmental licensing and design for the Madeira Hydroelectric Complex (MHC) in the Brazilian Amazon was done following standard engineering practices. These studies used empirical and one-dimensional sediment retention and transport models to determine relatively uniform sedimentation along the reservoirs, with wedge shaped sedimentation at the foot of the dams, and no upstream delta (Furnas 2005). Environmental and operational licenses were granted, and dam designs were finalized based on the conclusion that after 20 years, reservoir sediment retention would discontinue (Furnas 2005). On-going monitoring reports, required to maintain dam operation, have been made public through the Brazilian Institute of Environment and Renewable Resource Natural Resources (IBAMA, acronym from Portuguese). Since the construction of the dams, monitoring of established control cross-sections show the predicted sedimentation at the foot of the dam, but sedimentation has not been horizontally uniform along the reservoir. Major sedimentation in the now flooded, pre-dam floodplains (as high as 10-15m) has blocked off passage of smaller tributaries. While the environmental and design studies did acknowledge the shortcomings of the initial methodologies used (including the use of one-dimensional sedimentation modeling that did not capture the observed non-uniform horizontal deposition), third party reviews concluded that estimates also lacked a rigorous uncertainty analysis and attention to unsteady flow conditions (Dunne 2007; Molina et al 2008). Moreover, these studies also do not take into account non-stationary climate and upstream anthropogenic activities. The above justifies a non-stationary and uncertainty bounded quantification of sedimentation behind the MHC.

The above-mentioned monitoring reports are rich with additional information that has yet to be synthesized to aid in estimating sedimentation under a non-stationary future. Here we synthesize and validate monitoring data with independent measurements taken by our research group in May of 2018. We first present the study reach and findings from the MHC Environmental Impact Assessment (EIA), design documents, and monitoring programs. We then report on preliminary results of our field-based data collection to validate and complement the EIA and monitoring data. Finally, a two dimensional modeling framework is proposed as future work to model the cumulative effects of changing climate and upstream development on the life expectancy to the MHC reservoirs.

Study Reach

Figure 1 shows the reach of the Madeira River where the MHC was constructed. The MHC is comprised of two large, ROR dams - Jirau (commissioned in 2013-2016) and Santo Antonio (2012) - with a combined installed potential of >7000MW. The Madeira River carries 430 MT of sediment per year (Vauchel et al, 2017) - nearly 50% of the Amazon's total sediment flux - with suspended concentrations ranging between 120 - 3500 mg/l (PCE 2005). Of the yearly total sediment load, it is estimated that 94.3% is transported as suspended sediment (PCE 2005).
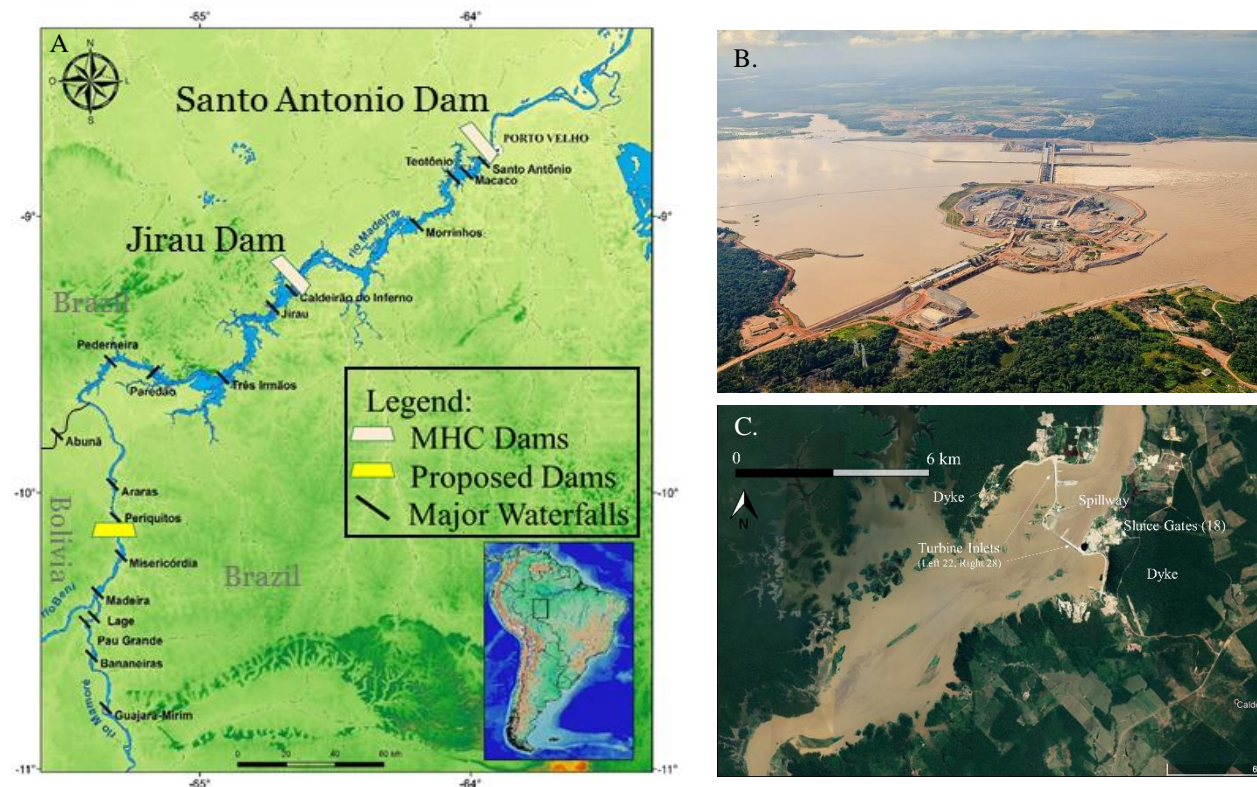
Figure 1. A. Santo Antonio and Jirau dam locations along the Madeira River in Rondonia, Brazil (Modified from Cella-Ribeiro et al 2013); B. Santo Antonio Dam under construction (skyscrapercity.com); C. Jirau Dam with major components and scale for reference (Google Earth).

Combined, the reservoir is greater than 200 km long, with a surface area greater than 500km^2, and a total storage volume > 4km^3. The EIA analysis concluded that sedimentation would reach an equilibrium after about 22 years and result in the loss of about half of the combined reservoir capacity due to trapping of approximately 2.06 km^3 of sediment. Monitoring and 3D computer and a physical models now show that sedimentation will stabilize in just six to seven years, rather than the 20 years predicted in the EIA, implying the reservoirs have almost stopped long-term deposition as of 2018, due to the concentration of flow toward the main channel as floodplains fill with sediment. These conclusions, however, were made without including the extensive upstream dam development plans, increasing land use cover change, or changes in climate change (Forsberg et al. 2017).

Preliminary Results from 2018 Survey

Explicit comparisons of 2018 cross-sections to pre-dam surveys show that at the upstream reaches of the reservoir, sedimentation does not exceed natural seasonal fluctuations, which were observed as high as 5 m during pre-dam monitoring. Closer to the Jirau dam, higher sedimentation is observed above pre-dam bank-full elevations on what was previously floodplain, consistent with the monitoring programs reported cross-sections. Some cross-sections also exhibit high in-channel deposition closer to the dam.

Initial surface suspended sediment concentration (SSSC) results of the grab samples taken up and downstream of the MHC, show an overall decline in sediment concentration along the two in-series reservoirs. From these preliminary observations, it is hard to make any concrete estimations of trapping efficiency. However, if well-mixed, turbulent hydraulic conditions are initially assumed we can infer that sediment is falling out of suspension progressively downstream relative to upstream values. As stated by Annandale et al. (2015), suspended sediment concentration estimates from surface grab samples is not adequate for robust sediment transport estimations, because of the variability of vertical concentration profiles. Additionally, suspended sediment sampling should be done using isokinetic samplers to avoid oversampling sands (Ewards and Glysson 1999). During the May, 2018 field campaign, isokinetic depth and point-integrated samples were collected for surface sample bias-correction and correlation to total cross-section-averaged concentrations. Grain size distribution (GSD) of our samples compared to pre- and post-dam monitoring samples will also provide better sedimentation interpretations. These data will be further compared and validated against the Santo Antonio and Jirau dam company's monitoring program data to assure data is complementary for the proposed modeling.

Conclusion and Future Work

From the initial SSSC results, it appears that average sediment concentrations are declining from upstream to downstream through the reservoirs. Comparison to the MHC's monitoring programs support this finding, although our independent results from the point and depth-integrated samples and GSD will be used for further evaluation. Additionally, bed material was collected to assess bed material GSD for better constraining channel hydraulic modeling. Further synthesis and comparison of our data with the monitoring data is required to predict future sedimentation in the reservoirs under non-stationary climate and upstream development conditions.

Preliminary inspection of the May 2018 field data shows no significant sedimentation along the first 90 km of the 120 km long reservoir. Further downstream, closer to the dam, many sections do not exhibit in-channel deposition outside of natural season fluctuations, while others do. Deposition, however, is noticeably higher, >10m, on what was previously the channel floodplain. Due to the one-dimensional nature of the sediment transport modeling conducted for the EIA and design studies, this horizontal sedimentation variability was not captured, meriting the 3D and physical modeling that was done by the dam companies. Both the physical and computer models suggest sedimentation is close to stabilization under stationary conditions, only a few years after flooding.

From initial reservoir monitoring, it is apparent that direct comparison of cross-sections of pre and post-dam measurements is difficult because of the control section locations, natural dynamism of the channel bed, and the run-of-river dam design. With this in mind, for the proposed future work, related to quantifying sedimentation behind MHC under non-stationary hydrology and sediment loads, at least a two-dimensional sediment transport model will be

needed to better model non-uniform floodplain deposition. We propose the use of the SRH-2D model, because of the 2-dimensional mobile bed sediment transport module. Exploration of measurement and model parameter uncertainty will be used together with non-stationary boundary conditions to independently quantify the useful life-span of the reservoirs.

References

CNEC WorleyParsons Engenharia S.A., Energia Sustentavel do Brasil. 2013 Programa de Monitoramento Hidrossedimentológico: USINA HIDRELÉTRICA JIRAU. 1st Relatório Semestral (Licença de Operação nº 1097/2012).

CNEC WorleyParsons Engenharia S.A., Energia Sustentavel do Brasil. 2016 8º RELATÓRIO SEMESTRAL Licença de Operação nº 1097 / 2012 Programa de Monitoramento idrossedimentológico

Dunne, T. 2007. Response to analyses of flow and sedimentation at the sites of proposed Rio Madeira hydroelectric projects, 8 July 2007, Report to International Rivers, Berkeley, California, USA.

Edwards, T. E., and Glysson, G. D. (1999). "Book 3, Chapter C2: Field methods for measurement of fluvial sediment." Techniques of Water-Resources Investigations , U.S. Geological Survey, Reston, Va.,
http://water.usgs.gov/osw/techniques/EdwardsTWRI.pdf (Oct. 5, 2005).

Forsberg BR, Melack JM, Dunne T, Barthem RB, Goulding M, Paiva RCD, et al. (2017) The potential impact of new Andean dams on Amazon fluvial ecosystems. PLoS ONE 12(8):e0182254

Latrubesse, Edgardo M, Eugenio Y Arima, Thomas Dunne, Edward Park, Victor R Baker, Fernando M Horta, Charles Wight, et al. 2017. "Damming the Rivers of the Amazon Basin." Nature Publishing Group 546 (7658). Nature Publishing Group: 363–69. doi:10.1038/nature22333.

Molina Carpio, Jorge, Fabiola Ledezma, and Philippe Vauchel. 2008. Estudio del rio Madera: remanso hidraulico y sedimentación

SENAMHI-ENDE, 2007. Secciones transversales en los ríos Madera y Abuná. Topografía y batimetría. Noviembre 2007.

Santo Antonio Energia (SAE). 2015. 7º Relatório De Acompanhamento Dos Programas Ambientais Após Emissão De Licença De Operação 1044/2011 e 1º Relatório Consolidado Pós-Lo Tomo I - Acompanhamento Dos Programas Ambientais Período De Setembro De 2011 A Fevereiro De 2015

PCE; SantoAntonia Energia. 2015 Uhe santo antônio. 4ª Etapa do programa de levantamentos e monitoramento hidrossedimentológico do rio madeira e do reservatório da uhe santo antônio,

PCE. Estudos Sedimentológicos do Rio Madeira 2005. Appendix from Madeira Hydroelectric Complex EIA Volume 6 of 8. Accessed at http://licenciamento.ibama.gov.br/Hidreletricas /Santo%20Antonio%20(Rio%20Madeira)/

Vauchel, P. Estudio de la crecida 2014 en la cuenca del río Madera. HYBAM-IRD 2014.

Vauchel, P.; Santini, W.; Guyot, J-L.; Moquet, J. S.; Martinez, J-M.; Espinoza, J.C.; Baby, P.; Fuertes, O.; Noriega, L.; Puita, O.; Sondag, F.; Fraizy, P.; Armijos, E.; Cochonneau, G.; Timouk, F.; de Oliveira, E.; Filizola, N.; Molina, J.; Ronchail, J. 2017. A reassessment of the suspended sediment load in the Madeira River basin from the 368 Andes of Peru and Bolivia to the Amazon River in Brazil, based on 10 years of data 369 from the HYBAM

monitoring programme. J. Hydrol. 2017, 553, pp. 35-48. DOI 370
10.1016/j.jhydrol.2017.07.018

Flows for Fish: Analyzing Restoration Flow Releases in the San Joaquin River, CA for Salmonid Habitat

Emily Thomas, Hydrologic Engineer, U.S. Bureau of Reclamation, Sacramento CA, ethomas@usbr.gov

Regina Story, Civil Engineer, U.S. Bureau of Reclamation, Sacramento CA, rstory@usbr.gov

Introduction

The San Joaquin River Restoration Program (SJRRP) is an interdisciplinary effort to restore a naturally reproducing and self-sustaining population of salmon and other native fish to the San Joaquin River below Friant Dam, near Fresno, California, while also reducing or avoiding adverse water supply impacts to the water users served by Friant Dam. Friant Dam was completed in 1942 to provide water for irrigation and municipal supply, and for flood control, with a storage capacity of 520,500 acre-feet. Two canals, with a combined length of 187 miles, serve as the primary conveyance of Friant Dam waters to water users. Upon completion of the dam, the majority of the waters of the San Joaquin River were diverted into the canals, leaving over 60 miles of river below Friant Dam dewatered. As a result of this operation, anadromous fish populations downstream of the dam were extirpated.

Following a lawsuit challenging the renewal of the long-term water service contracts between the United States and the Friant water users, the Natural Resources Defense Council and the Departments of the Interior and Commerce reached agreement on the terms and conditions of the San Joaquin River Restoration Settlement (Settlement) in October 2006. The San Joaquin River Restoration Settlement Act authorized federal implementation of the Settlement in March 2009. The Bureau of Reclamation's SJRRP Office coordinates implementation of the Settlement.

To achieve the goals of the Settlement, the SJRRP has multiple restoration objectives, including providing suitable salmonid rearing habitat and water temperatures through the release of Restoration Flows from Friant Dam. These two objectives are closely linked to channel capacity. When the Settlement was signed, portions of the San Joaquin River below Friant dam had zero channel capacity, constrained by deteriorated levee conditions and seepage impacts to adjacent agricultural fields. While the SJRRP is directed by the Settlement to build channel capacity to 4,500 cfs between Friant Dam and the Merced River confluence (Figure 1), financial constraints necessitated evaluation of an interim channel capacity that could be achieved with currently available funding. While the long-term goal of achieving 4,500 cfs capacity in the San Joaquin River remains, this analysis evaluates a range of lower channel capacities to assess a suitable interim channel capacity which will support biological objectives within the appropriated funding. To inform this selection, rearing habitat-flow and temperature-flow relationships were analyzed for flow rates between 1,000 cfs and 4,000 cfs under six different viable flow release strategies.
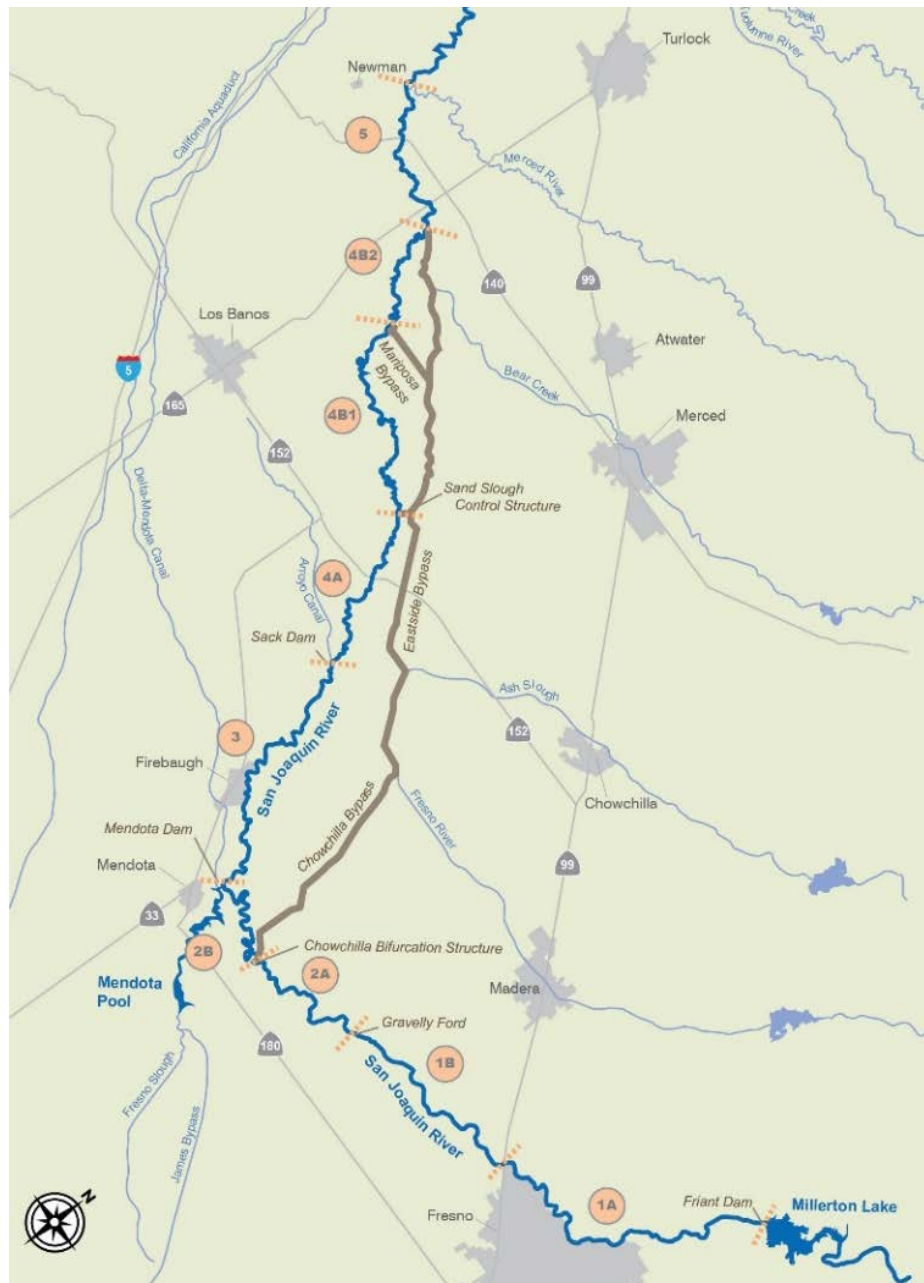
Figure 1. Map of SJRRP Restoration Area from Friant Dam to the confluence with the Merced River

Methods

To assess suitable rearing habitat at each flow rate, the two-dimensional depth averaged hydraulic model SRH-2D (Lai, 2008) was used to simulate hydraulic conditions in four reaches of the San Joaquin River. This model uses elevation data applied over a model domain and calibrated hydraulic roughness to simulate depth and velocity across the model grid cells for different boundary conditions. Models were run in 500 cfs increments from 1,000 cfs through 4,000 cfs in each reach. From each run, water depth and velocity were computed at each node. These nodes were rasterized into 5 feet by 5 feet cells, then cells were filtered by suitable juvenile

rearing habitat criteria for depth and velocity. Depth and velocity habitat suitability indices (HSI) were determined from previous floodplain habitat work on the San Joaquin River (Reclamation, 2012a). Note that unlike previous work, this analysis did not filter by vegetation cover, and instead clipped the low flow channel from the suitable area to remove any in-channel cells with suitable depths and velocities that were unlikely to have vegetation cover present.

Temperature output from the Programmatic EIS/R SJR HEC-5Q model (Reclamation, 2012b; Resource Management Associates, 2007) was also analyzed in support of evaluating flow scenarios. The temperature model extends from January 1980 to September 2003 and determines temperature and flow data per node on a diurnal time scale by superimposing the SJRRP's Restoration Flow hydrographs from the Settlement over historical flow data. Water temperature data were smoothed into 7-day, daily running averages to align with known temperature tolerances for salmonid life stages. The objective was to determine when critical and lethal temperatures for salmonids were exceeded at key locations in the Restoration Area. Analysis of each day provided an estimate of temperature per day of the water year given trends of a selected flow range. This provided a relationship between flow and temperature to evaluate the flow scenarios.

Results

Findings from SRH-2D, filtered by the HSI criteria, suggest that rearing habitat is present in all reaches analyzed at flows as low as 1,000 cfs. However, at low flow rates, rearing habitat is limited to channel margins; floodplains and side channels are not inundated until flows in excess of 1,000 cfs (Figure 2). The relationship between flow and suitable habitat is not linear, and varies by reach due to the diversity of floodplain configurations found along the San Joaquin River. Additionally, as flow rate increases and inundates more floodplain, the channel margin habitat becomes unsuitable due to increasing water depth and velocity. Thus, there is not a demarcation where suitable habitat increases sharply with increasing flow, and there is a variety of rearing habitat available at flow rates far lower than the maximum 4,000 cfs flow envisioned in the Settlement.
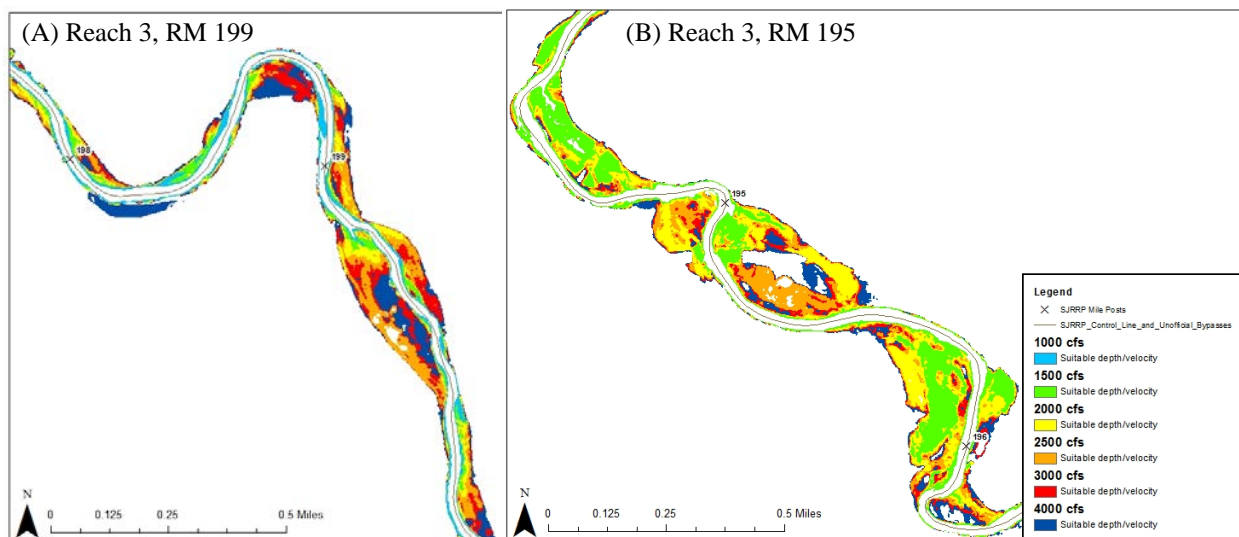
Figure 2. Inundated Area at a Series of Flow Rates in a Sample Section of Reach 3 of the San Joaquin River, Near (A) River Mile 199 and (B) River Mile 195

A comparison of hydraulically suitable rearing habitat by reach shows a general increase in rearing habitat with increased flow rate in all reaches; however, this increase plateaus near 2,500 to 3,000 cfs in three of the four reaches analyzed (Figure 3). The outlier, Reach 2B, shows increasing hydraulically suitable area with larger flows throughout almost all flow rates analyzed. This reach is the site of a planned large-scale levee setback and floodplain regrading project, and has been designed to maximize floodplain habitat. While this project has not yet been constructed, the topography used in this analysis reflects the designed grading, and is therefore the most favorable reach for suitable rearing habitat.
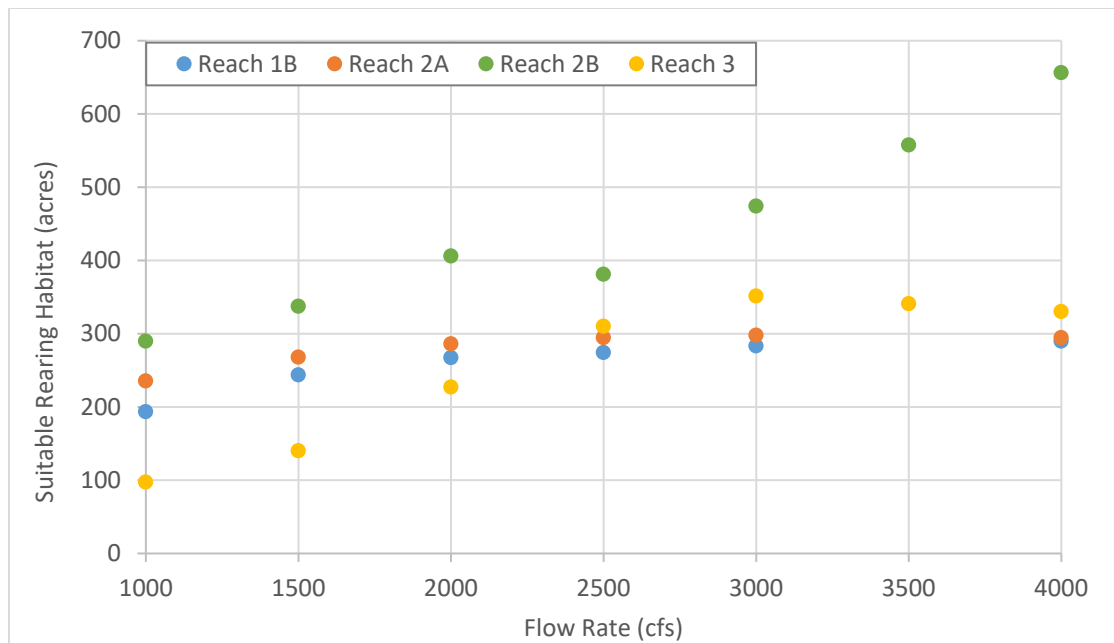
Figure 3. Hydraulically Suitable Rearing Habitat (acres) vs. Flow Rate (cfs) for Reach 1B through Reach 3 of the San Joaquin River

Results from the temperature analysis indicate that beyond mid to late April, the flow rate required to maintain water temperatures below the 68 °F lethal threshold for adult salmonids in critical migration reaches becomes difficult to attain (Figure 4). Adult salmonid upstream migration typically occurs from March through June, and juvenile salmonid downstream emigration typically occurs from November through June. These results indicate that temperature limits the optimal window for adult salmonid upstream migration, however temperatures would be suitable for at least part of the spring migration period. For emigrating juveniles, maintaining water temperatures below the 75 °F lethal threshold in all reaches can be accomplished through the end of May with flows at or below the range of channel capacities considered. Reach 5 is expected to be constraining with the highest temperatures in the system because it is furthest downstream. Even if the channel capacity existed to convey flows for managing temperature later into the summer months, there would not likely be volume available for such flows (and the requisite ramp-down after high flows to prevent fish stranding) unless other objectives such as floodplain rearing were sacrificed for temperature control.
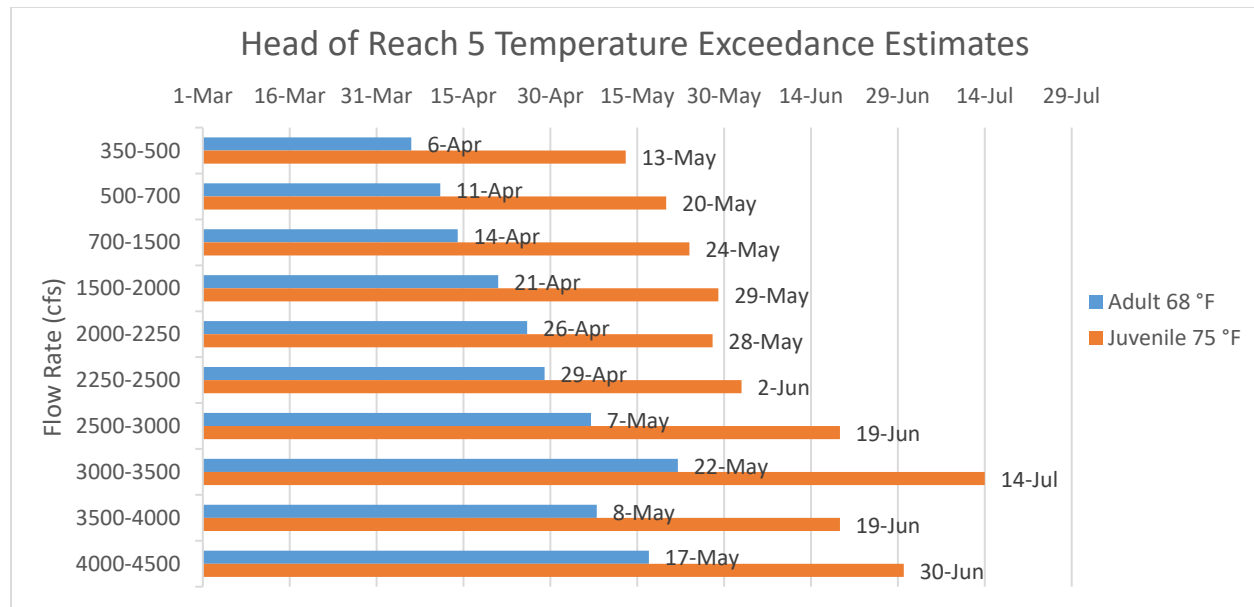
Figure 4. Estimated Dates of Temperature Exceedance at the Head of Reach 5 across different Restoration Flow rates, per Salmon Life Stage

Conclusions

While suitable rearing habitat area generally increases with higher flow rates, some rearing habitat is present at flow rates as low as 1,000 cfs. Less significant rearing habitat gain is made by increasing flow rates higher than 3,000 cfs in the unmodified reaches of the San Joaquin River. This analysis suggests that an interim channel capacity range of 2,500 cfs to 3,000 cfs will provide similar rearing habitat area as the ultimate 4,000 cfs channel capacity in the unmodified river reaches, and is likely to meet near-term rearing habitat objectives.

Adequate springtime water temperatures are most constrained in Reach 5, the lowermost section of the Restoration Area. The lethal threshold for adult Chinook salmon of 68 °F during upstream migration is expected to be more of a constraint than the lethal threshold for juvenile Chinook salmon of 75 °F during downstream emigration. There is a fair amount of uncertainty in the accuracy of the temperature model; however, the model is still valuable for comparing different flow scenarios and understanding the relationship between flow and water temperature. Temperature monitoring will be necessary to verify modeled results with in-situ data, as will an evaluation of reservoir management strategies to optimize releases for temperature control.

This analysis allowed the SJRRP to compare rearing habitat area and temperature across flow rates, ultimately leading to a selection of a 2,500 cfs interim channel capacity. Further description of this analysis is available in an SJRRP Technical Memorandum, *Analysis of Physical Flow Characteristics Supportive of Chinook Salmon to Inform Channel Capacity Selection in the Funding Constrained Framework* (SJRRP, 2018).

Acknowledgements

References

Lai, Y. 2008. SRH-2D version 2: Theory and User's Manual, Sedimentation and River Hydraulics – Two-dimensional River Flow Modeling. U.S. Bureau of Reclamation, Technical Service Center, Denver, CO.

Resource Management Associates, Inc. and Reclamation. 2007. San-Joaquin Basin Water Temperature Modeling and Analysis. Mid-Pacific Region, U.S. Bureau of Reclamation, Sacramento, CA.

Reclamation. 2012a. Minimum Floodplain Habitat Area: for Spring and Fall-Run Chinook Salmon, Technical Report. San Joaquin River Restoration Program, Mid-Pacific Region, U.S. Bureau of Reclamation, Sacramento, CA.

Reclamation. 2012b. San Joaquin River Restoration Program Programmatic EIS/EIR. U.S. Bureau of Reclamation.

SJRRP. 2018. Analysis of Physical Flow Characteristics Supportive of Chinook Salmon to Inform Channel Capacity Selection in the Funding Constrained Framework. U.S. Bureau of Reclamation, Sacramento, CA. http://www.restoresjr.net/?wpfb_dl=2159

Large Bed Elements Rule Everything around Me: Hydraulic and Geomorphic Patterns in a Mountain River

Jason S. Wiener, PhD Candidate, University of California-Davis Department of Land Air and Water Resources, Davis, CA, jswiener@ucdavis.edu

Gregory B. Pasternack, Professor, University of California-Davis Department of Land Air and Water Resources, Davis, CA, gpast@ucdavis.edu

Introduction

One major component differentiating the landform structure and steering conditions of mountain rivers from lowland gravel-or-sand bedded rivers is the abundance of boulders and bedrock outcrops, collectively referred to as large bed elements (LBEs). LBEs exert a strong influence on channel hydraulics, sediment transport, landforms, and geomorphic processes (Grant et al. 1990; Thompson 2001; Yager et al. 2007; Papanicolaou and Tsakiris 2017). Ecologically, LBEs function to provide cover, refugia, and biologically important flow patterns for aquatic biota (Raleigh et al. 1984; Crowder and Diplas 2006; Branco et al. 2013). Despite LBE importance, methods to systematically map and analyze these features at scales relevant to river management, such as reach (10^2-10^3 channel widths [W]) or segment (10^3-10^4 W) scales, are lacking (Carbonneau et al. 2004; Resop et al. 2012). Additionally, there are few studies in natural rivers analyzing interactions between planform spatial configurations of LBEs and 1-m scale hydraulic patterns (i.e., velocity magnitude and direction as well as bed shear stress) (Pasternack and Senter 2011). This leaves many important questions on these topics open. In particular, as discharge increases from baseflow to flood flow and in-channel LBEs become submerged, does the set of flow directions (i.e., the flow pattern) become more aligned with thalweg-parallel streamlines, thereby suggesting that LBEs are a less significant control on hydraulics and morphodynamics? Further, do zones of similar flow direction persist in their locations as coherent patches and what hydraulic-morphodynamic mechanisms result from different patterns of flow direction persistence?

Hydraulic-Morphodynamic Conceptual Models

Conceptually, within a flow field, LBEs drives strong lateral streamline deviations from thalweg-parallel flow paths that would dominate in the absence of these features. Streamline deviations are often strong enough to form complete 360° recirculations, or eddies. Morphology driven directing of flow paths is sometimes referred to as topographic steering (Brown and Pasternack 2014). Theoretically the spatial persistence of zones with coherent flow directions (flow-direction zones) across discharges, particularly zones with flow recirulations, have implications for interannual to decadal scale storage and transport of sediments (Rathburn and Wohl 2003; Melis 2011).

Assuming sediment transport capacity differs between flow-direction zones, if zones persist, erosion and deposition will be highly spatially stratified. We coin the term "chutes-and-traps" to refer to the hydraulic-morphodynamic mechanism active under this scenario. Here the term "chutes" refers to flow-direction zones that have relatively high sediment transport capacity, are

relatively aligned with thalweg-parallel streamlines, and remain spatially fixed independent of discharge. These chutes are envisioned to act as efficient conveyor belts for local material transport with little sediment storage potential. "Traps" are the opposite of chutes, having low transport capacity and greater potential for sediment accumulation and storage. Such areas may be analogous to what is referred to in the scientific literature as pocket water (Bisson et al. 1982; Hawkins et al. 1993). The chutes-and-traps mechanism represents a scenario where uni-scalar topographic steering dominates.

Contrarily, if flow-direction zones do not persist but rather shift between erosional or depositional likelihoods, then sediment can be eroded or deposited, respectively, for different locations at different times depending on where the shear stress peak is present at any given flow. We coin the term "stage-dependent dynamic mobility" to refer to the hydraulic-morphodynamic mechanism active under this scenario. In this mode multi-scalar topographic steering dominates. This is somewhat analogous to the flow convergence routing mechanism, but differs by having greater spatial complexity to erosion and deposition zones as well as a greater role for LBE and bedrock outcrops in controlling morphodynamics compared to what happens in flow convergence routing.

Study Design and Hypothesis Testing

This study presents four new concepts and methods for scientific investigation of LBEs and channel hydraulics to answer the two questions posed above and ascertain the spatial context and discharge domain of the two alternate mechanisms proposed above (chutes and traps vs. stage-dependent dynamic mobility): (1) a novel process to delineate LBEs, (2) a process-based approach to map unique flow-direction zones aided by two-dimensional (2D) hydrodynamic modeling, (3) a framework for evaluating hydraulic properties within flow-direction zones, (4) and a framework for studying the abundance and persistence of flow directions (flow pattern) and potential LBE interactions.

Within this framework, metrics documenting the abundance and submergence of LBEs were defined and quantified. In this study, LBEs are considered ubiquitous features in the river corridor if they occupy > 15 % of the area of the river corridor becoming wetted between successive study discharges (i.e., the inundation corridor). This domain focuses analyses, in this case the abundance of LBEs, within a series of nested but individually isolated portions of the river corridor that become successively inundated and geomorphically active with increasing discharge.

Flow pattern metrics extracted include the percent wetted area occupied by seven different flow-direction zones as well as measures of total flow direction persistence and relative persistence of each flow-direction zone's area between discharges. In this study, if the percent of the wetted channel occupied by non-thalweg-parallel flow-direction zones is > 50%, then that discharge is considered to have highly non-uniform flow patterns with greater control from LBEs and other landform non-uniformity compared to valley-scale topographic steering. It is hypothesized that flow patterns will become increasingly aligned to the thalweg-parallel bulk flow direction as LBEs become submerged.

In addressing this study's second question, if, over the range of discharges studied, relative persistence of all flow-direction zones is > 50% then the study site has high persistence

indicating flow-independent chute-and-trap transport dynamics dominate. At the other extreme, if relative persistence of all zones is < 10% then the stage-dependent dynamic mobility mechanism described above dominates. Alternately, flow-direction zones may differ greatly in their degree of relative persistence allowing both mechanisms to be active, or relative persistence of all flow-direction zones may be between these thresholds resulting in a mixture of the mechanisms, both of these outcomes are referred to herein as "variable-scale topographic steering". It is hypothesized that variable-scale topographic steering will be the dominant mechanism present in the study site.

This overall hypothesis is further refined to include a stage-dependent spatially nested version of the variable-scale topographic steering mechanism that manifests in an iterative manner within the previously defined inundation corridors of the river channel. In this refined model, beginning with flow patterns mapped in the baseflow inundation corridor (region inundated at baseflow), some but not all of the flow-direction zones will have moderate (50% > persistence > 10%) to high (persistence >50%) relative persistence over the full range of discharges studied. For the remaining flow-direction zones in the baseflow inundation corridor that do not have moderate-to-high persistence, stage-dependent shifts in these flow directions will drive more transient topographic steering and sediment transport dynamics consistent with the dynamic mobility mechanism. Outside the baseflow inundation corridor, flow-direction zones in the study's other inundation corridors will initially have moderate-to-high relative persistence but as these regions experience greater and greater discharges, trends in flow-direction zone persistence will follow the same pattern as the baseflow inundation corridor, thus representing the stage-dependent nested variation of the mechanism.

Methods

We used a confined 13.2-km segment of the mountainous Yuba River (Northern California) as the study site to test our concepts (Figure 1). The study site is a complex, low sinuosity, boulder-bedded, 5th order mountain river confined within a steep-walled bedrock and forested hillside canyon. Airborne Light Detection and Ranging (LiDAR) data collected in September 2014, using near infrared and green lasers, were supplemented with surveyed and remotely sensed topographic data, cumulatively resulting in ~21 million ground points covering the entirety of river corridor (e.g. channel bed, adjacent hillslopes, and LBEs). These data were used to create a digital elevation model (DEM) of the river corridor with a 0.46 m x 0.46 m resolution raster. Steady state hydrodynamics in study site were simulated at ~ 1-m resolution using the free, public two-dimensional (2D) model known as Sedimentation and River Hydraulics—Two-Dimensional model (SRH-2D) v. 2.2 (Lai 2008). For this study a total of 4 simulations were considered ranging from an approximate baseflow discharge of 1.54 m^3/s to a ~3.5-yr flood of 343.6 m^3/s.
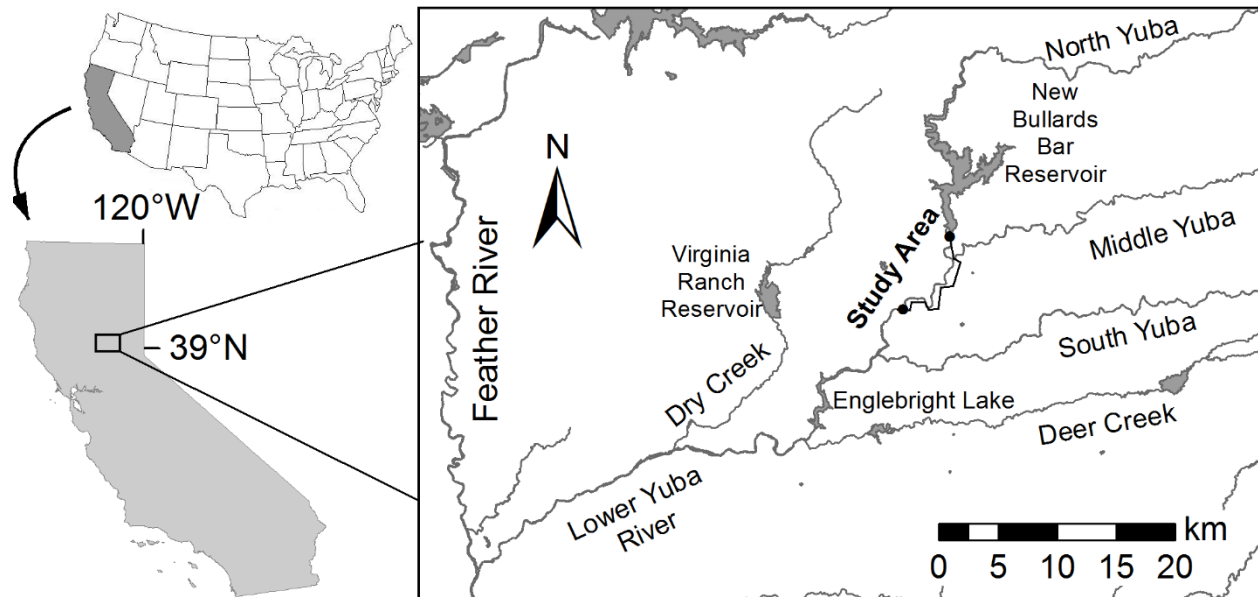
Figure 1. Map of study site, Yuba River, CA.

Delineation of LBEs in the river corridor was accomplished using point cloud processing and topographic differencing techniques (Wiener and Pasternack 2016). Initially, the point cloud comprising the complete topographic surface was re-processed using a ground classification algorithm (Isenburg 2016) implemented with 'coarse' classification filter settings. The resultant points, representing a 'smoothed' surface, were used to create a new DEM at the same 0.46 m resolution as the complete topographic surface. Differencing the smoothed and complete DEMs yields a preliminary mapping of the elevation of surface roughness features. Applying a minimum vertical threshold to these data instantaneously maps LBE polygons features meeting the imposed criteria across the entire study domain.

Once delineated the area of LBEs within each discharge simulation's wetted area were calculated including the areas just within those areas that became inundated between discharges (Figure 2). The ratio of submerged vs. total number of LBEs interacting with each discharge (% LBE submergence) was calculated as the number of LBE features that were completely covered by a discharge's wetted area polygon over the number of features intersecting the wetted polygon (Eq. 1). The total number of LBEs per river km within the baseflow and flood-flow wetted areas were also calculated.

$$\% \, LBE \, Submergence = \frac{\#\,covered\,LBEs}{\#\,intersected\,LBEs} \qquad\qquad \text{(EQ. 1)}$$
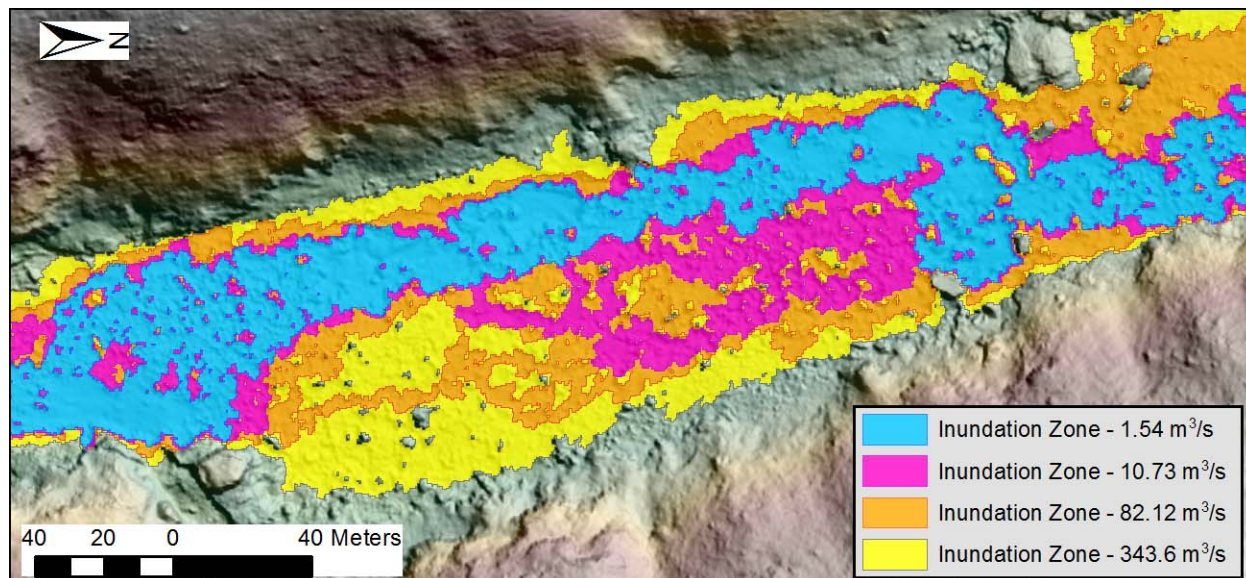
Figure 2. Typical output from 2D model simulations showing inundation corridors occurring as strips between successive simulations. Flow is from right to left in graphic.

The process for delineating flow patterns for each flow simulation is conceptually briefly described below (for full details see Wiener and Pasternack 2018). Initially, a thalweg approximating the longitudinal path of greatest momentum (~depth*velocity^2) was delineated using simulated hydraulic results (Pasternack 2011). From this output a streamwise-specific coordinate system was created demarcating the bank-parallel bulk flow direction at points spaced longitudinally ~0.91m along the thalweg profile. To reference predicted velocity directions to the thalweg-parallel bulk flow direction each modeled velocity direction was paired with a point along the thalweg profile at the nearest location. The difference between the paired thalweg direction and velocity direction were calculated using a custom algorithm ultimately resulting in a final flow direction angle at each model output location. Flow directions were classified into seven bins defining spatially explicit zones of parallel, laterally convergent, laterally divergent, and upstream recirculating flow (Table 1) (Figure 3).

Table 1. Flow-direction Zone Classification Scheme

Flow Direction Range (°)	Description
-180 to -90	Divergent upstream recirculating flow
-90 to -45	Strongly divergent flow
-45 to -15	Weakly divergent flow
-15 to +15	Parallel flow
+15 to +45	Weakly convergent flow
+45 to +90	Strongly convergent flow
+90 to +180	Convergent upstream recirculating flow
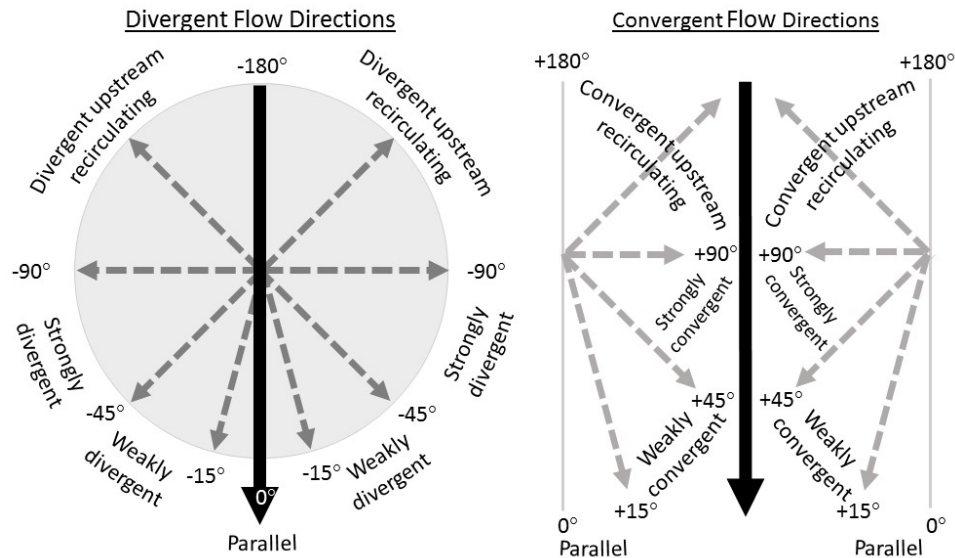
Figure 3. Conceptual graphic of divergent and convergent flow-direction zones relative to bulk flow direction. Dark arrows represent thalweg-parallel bulk flow direction. Dashed gray lines represent theoretical velocity flow direction angles typically at threshold between zones.

For each 2D model simulation, the percentage of wetted area occupied by each flow-direction zone was calculated and compared between simulations. Spatially averaged values of predicted bed shear stress were quantified for each zone. Spatial persistence of flow-direction zones between discharges was assessed through areal intersection of classified results. For each discharge comparison, persistence was defined as the percent area of each zone from the starting, lower discharge simulation remaining present in the ending, higher discharge simulation. From these intersections a total persistence metric was defined as the percent of a starting discharge's wetted area with persistent flow directions between discharges. A second, relative persistence metric, was defined as the percent areal persistence of each zone between discharges compared to the area of that zone in the starting discharge. Intersections were made for all possible discharge combinations such that the lowest simulated discharge was compared to the three larger discharges but the second largest discharge was only compared to the largest discharge. This was done individually between discharges (e.g. 1.54 m³/s to 10.73 m³/s, 1.54 m³/s to 82.12 m³/s, ect.) as well as in a stepwise manner, intersecting results from the first intersection with the next higher flow and so on. Intersection results for starting discharges above baseflow were also clipped to the inundation corridor associated with the starting flow (Figure 2). To simplify interpretation of the zone-averaged hydraulics and persistence analyses, the seven zones were aggregated into four zones: |90°| to |180°| for recirculating flow, -90° to -15° for divergent flow, -15° to +15° for parallel flow, and +15° to +90° for convergent flow.

Results

A total of 52,926 individual LBEs were mapped within the study site (Figure 4). Qualitative assessment of the mapped LBEs against available data; aerial imagery, DEM, and DEM hillshade indicated a visually accurate mapping given the systematic approach and spatial scale of the effort. The average number of LBEs per river km was 967 within the baseflow wetted area and 2561 per km in the ~3.5 flood wetted area. LBEs were abundant in the baseflow channel as well as areas inundated by successively higher discharges (Table 2). In fact the area of wetted channel overlapping LBEs monotonically increased with discharge from ~15% of the baseflow wetted area to ~29% of the area inundated between 82.12 m³/s and 343.60 m³/s. This confirms

LBEs as ubiquitous features within the studied portion of the river corridor. Higher discharges have the potential to interact with more LBEs, however greater flow depths resulted in the percentage of submerged LBEs monotonically increasing with increasing discharge (Table 2).
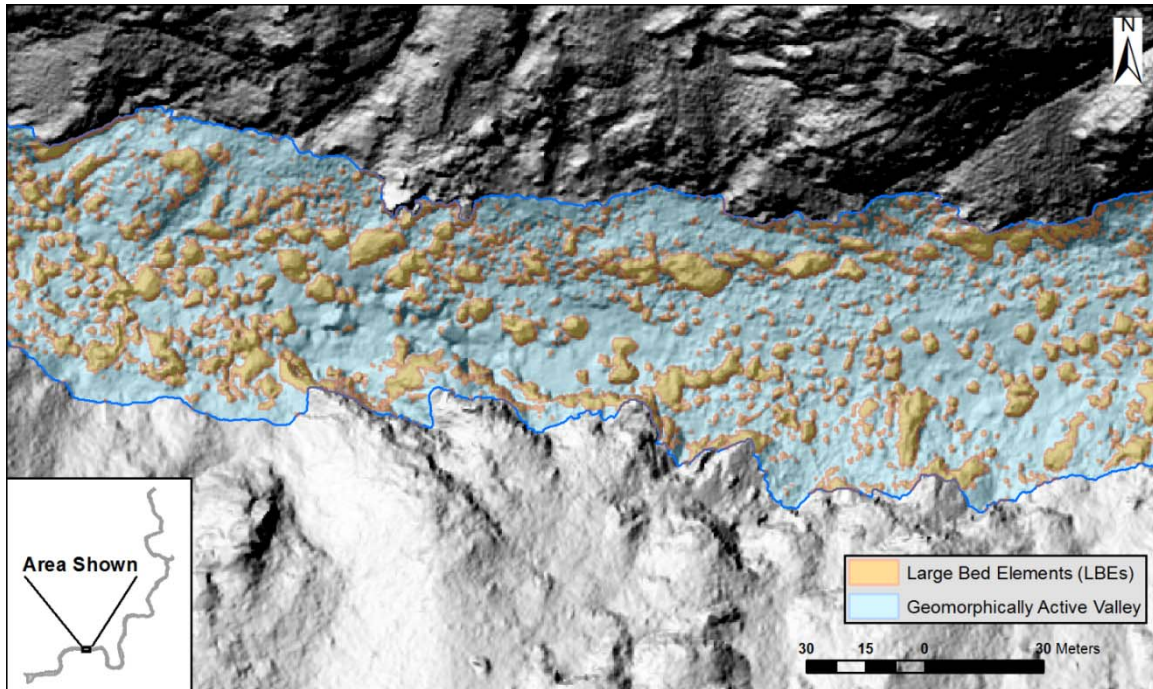
Figure 4. Example of mapped large bed elements overlain on DEM hillshade.

Table 2. LBE area and submergence metrics

Simulated Discharge (m³/s)	Area of LBEs[1]			Number of LBEs[2]		
	LBE Area (km²)	Inundation Corridor Area (km²)	Inundation Corridor as LBE (%)	Emergent LBEs (-)	Submerged LBEs (-)	Submerged LBEs (%)
1.54	0.039	0.257	15.3	7904	6192	43.9
10.73	0.020	0.076	25.9	6992	11374	61.9
82.12	0.033	0.119	27.5	6250	19334	75.6
343.60	0.036	0.125	29.0	5888	28368	82.8

[1]Metrics are for inundation corridor.

[2]Metrics are for entire wetted area.

The percentage of wetted area occupied by different flow-direction zones remained consistent across simulated discharges (Figure 5). Flow aligned to the thalweg-parallel streamlines (parallel flow) was most common, occupying between ~31-41% of wetted areas. The next most abundant flow-direction zone was weakly divergent flow (~23-31%) followed by weakly

convergent flow (~10-14%). Recirculating flow zones were generally the least prolific in each simulation (~2-8%). Across discharges the majority of the wetted channel (~59-70%) was characterized by flows that differed from the dominate flow path by at least 15°, meaning all simulated discharges studied had highly non-uniform flow patterns. This complexity was driven by the multiple-scales of topographic non-uniformity present, which can be envisioned as the successive interaction of higher flows with new LBEs, bed and bank morphologies, and riparian vegetation. The continued abundance of LBEs within new inundation corridors provides strong evidence for these interactions (Table 2).
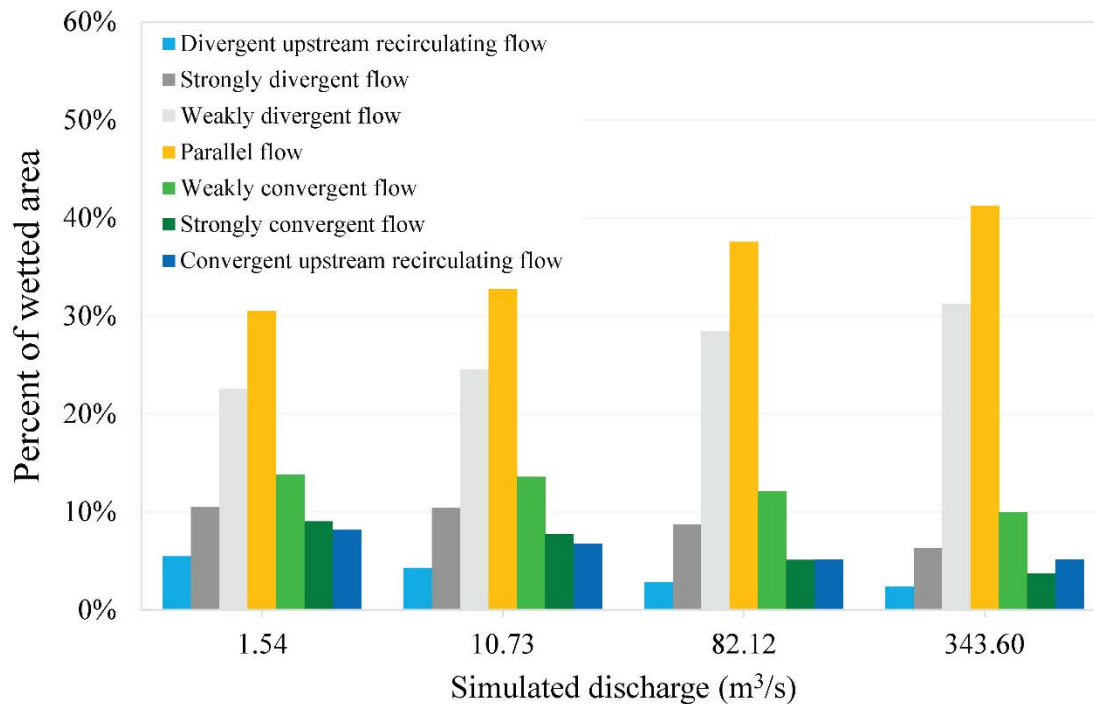
Figure 5. Percent of wetted area mapped as different flow-direction zones.

Aggregated flow-direction zones exhibited different capacities for sediment transport based on spatially averaged values of bed shear stress (Figure 6). Pair-wise comparison of the distribution of average bed shear stress values for all zones using the nonparametric Mann–Whitney rank-sum U test found nearly all zones to have different distributions at the 95% confidence level ($p \leq 0.05$). Only average bed shear stresses within convergent and divergent zones from the 10.73 m^3/s simulation could not be said to come from the same distribution at the specified confidence level. Zones of recirculating flow, which are envisioned as more depositional environments, had the lowest average values of bed shear stress. Parallel flow directions had the highest average bed shear stress for all simulations followed by divergent and then convergent flow-direction zones. The rate of increase in average bed shear stress was greatest for parallel and divergent zones and least for recirculating flow zones. Parallel flow directions in particular support a high potential for channel change as the flow field remains fixed and in a predominately downstream trajectory (Brown and Pasternack 2014).
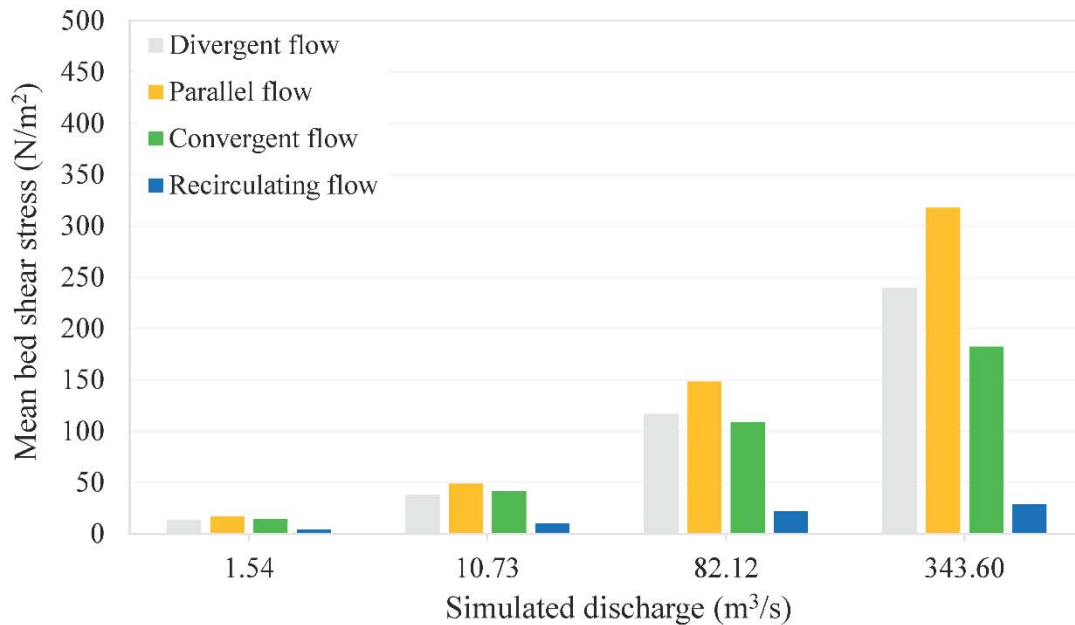
Figure 6. Mean bed shear stress for consolidated flow-direction zones.

Total and relative persistence results varied depending on the discharges being compared, the portion of channel analyzed, and between flow-direction zones. Across all discharge comparisons total persistence was between ~19-55% of the starting discharge's entire wetted area and between ~19-51% of the starting area when only considering inundations corridors. The amount of total persistence was highest between successive intersections (i.e., between 1.54-10.73 m³/s, 10.73-82.12 m³/s, and 82.12-343.60 m³/s).

The relative persistence of flow-direction zones across discharge intersections are depicted in Figure 7. Only results from the stepwise intersections are presented as this method more closely represents conditions experienced in the field. No discharge intersections resulted in all zones having high relative persistence (persistence >50%) or all zones having low relative persistence (10% > persistence). Therefore, neither the chute-and-trap or dynamic mobility mechanisms solely dominates. Intersections between successive discharges resulted in all flow-direction zones having moderate-to-high relative persistence. The differences in flow magnitude between successive discharges were non-trivial, ranging between ~4-8 times of one another (e.g. 343.60 m³/s is 4.2 time larger than 82.12 m³/s and 82.12 m³/s is 7.7 time larger than 10.73 m³/s). This supports that during periods where discharge fluctuations remain within these ranges, erosion and deposition probabilities are spatially stratified. For example, sustained dry summers typical in the study site region may include long periods where discharge is between 1.54-10.73 m³/s. The highest relative persistence values between successive intersections were consistently for parallel and divergent flow-direction zones, with values often exceeding 50%, typically followed by zones of convergent flow and lastly by zones of recirculating flow.

The amount of relative persistence consistently decreased with increasing disparity between the discharges used in the comparisons. However, for all intersections, relative persistence of parallel and divergent flow-direction zones remained moderate-to-high, staying above 25%. Persistence of convergent and recirculating flow-direction zones were more variable ranging between ~3-35% and ~5-39%, respectively (Figure 7). Non-persistent between discharge

transitions for parallel and divergent flow-direction zones were typically to one-another (i.e. parallel-to-divergent and divergent-to-parallel) with smaller percentages transitioning to convergent or recirculation zones. Non-persistent transition patterns for convergent and recirculating zones were more variable.
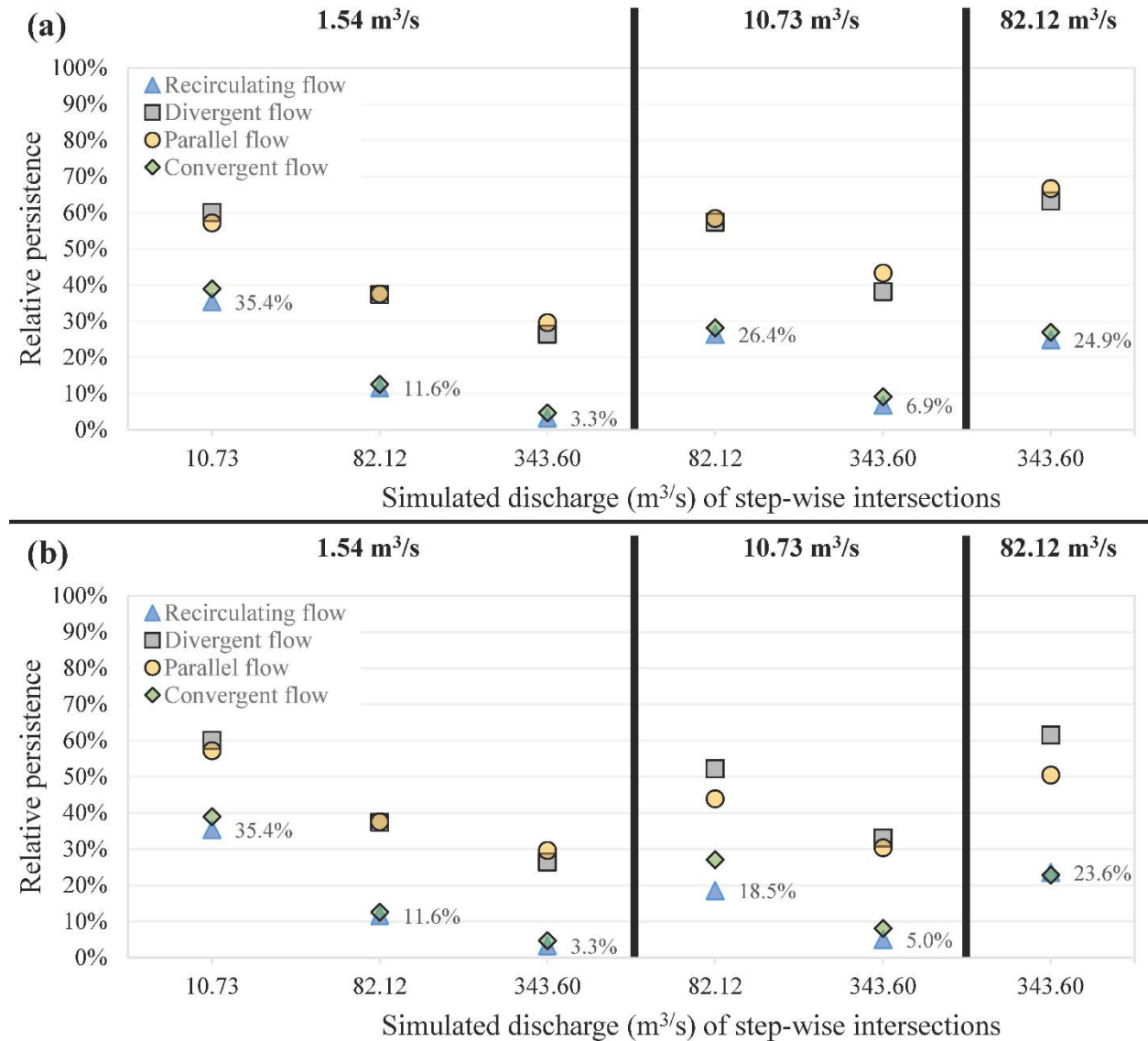
Figure 7. Relative persistence of consolidated flow-direction zones within the entire wetted area (a) and within inundation corridors (b) for step-wise intersections of each starting discharge, indicated in the header, to all other discharges. Numbers shown are persistence of recirculating flow-direction zones.

In the baseflow inundation corridor, results from the complete series of discharge intersections found moderate persistence of parallel and divergent flow-direction zones (29.4% and 26.4%, respectively) and low relative persistence of zones of convergent or recirculating flow (4.6% and 3.3%, respectively). Thus, at the highest simulated discharge only ~3% of the baseflow wetted area classified as recirculating flow remained unchanged. Although a small percentage, these areas in particular have the potential to support long term storage of fine sediment and act as prolonged habitat refugia (Melis 2011). Contrarily, comparatively large percentages of the baseflow wetted

area remain aligned with the thalweg-parallel bulk flow direction through this level of flood simulation. The inundation corridor of the 10.73 m³/s discharge simulation behaved similarly to the baseflow inundation corridor, the only difference being consistent higher relative persistence values for each flow-direction zone (Figure 7b). Lastly, within the 82.12 m³/s discharge inundation corridor all flow-direction zones had moderate-to-high relative persistence, however this result is based on intersection with only one higher discharge. Outside of the wetted extent of the 82.12 m³/s discharge within the 343.6 m³/s simulation inundation corridor the distribution of flow direction zones is similar to those shown in Figure 5.

Discussion and Conclusion

This study raised and addresses two primary questions regarding the abundance and persistence of stage-dependent flow patterns in a mountain river and provides inference on the interaction of LBEs on the observed hydraulic patterns as well as how these patterns may influence sediment transport dynamics. Findings from the study support the original hypotheses. First, LBEs were found to be to be widely abundant (overlapping greater than 15% of simulated discharge inundation areas) in multiple spatial domains in the river corridor. The presence of such topographic non-uniformity is considered influential in the finding that all discharge simulations, from baseflow to a~ 3.5-yr flood event, were characterized as having highly non-uniform flow patterns. The degree of non-uniform flow patterns decreased with increasing discharge, as simultaneously a larger percentage of LBEs in contact with the increasingly wetted area became submerged. This trend would likely continue at even higher discharges as the river canyon fills, submerging LBEs faster than new LBEs enter the wetted area, and as valley-scale topography becomes more important in steering flow than LBEs. The degree of flow pattern complexity and non-uniformity is relevant in mediating the potential for widespread channel change, particularly in supply-limited channels, as less complex, more uniform and parallel flow conditions have been found to have greater potential for erosion (Lisle et al. 2000; Brown and Pasternack 2014).

The assumption that flow-direction zones exhibit unique capacities for sediment transport was confirmed for all studied discharges with only one exception. Pairing this finding with flow-direction zone persistence results confirmed neither of the conceptualized mechanisms, chute-and-trap or stage-dependent dynamic mobility, universally dominates. Instead, different parts of the channel experienced different persistent or shifting that were consistent with the hypothesized variable-scale topographic steering conceptual model. Areas of the channel that began as zones of parallel and divergent flow had the highest probability of persisting and also had the highest probability as end-members for non-persistent transitions. Zones of recirculating flow had lower probabilities of persistence but some recirculation zones did remain stationary across the full range of discharge while many experienced a stage-dependent cycle of transition to more transport dominant flow directions. Visual inspection found many of the persistent recirculation zones occurred along the channel periphery or in the wake of LBEs.

Patterns of flow-direction zone persistence within each inundation corridor varied but followed similar trends. Across the range of simulated discharges, flow patterns in the baseflow inundation corridor became increasingly aligned with thalweg-parallel flow directions. Overall the baseflow inundation corridor transitioned from initially experiencing moderate-to-high relative persistence for all flow-direction zones to ultimately being characterized by moderate-to-low relative persistence and greater potential for transient sediment transport dynamics. Outside the baseflow inundation corridor, this same transition repeats in each successive inundation corridor with the exception that through a ~3.5-yr event larger portions of the

numerously created pockets of persistent flow-direction zones are sustained along the periphery of the expanding wetted area (Figure 7). This trend represents the spatially nested component of the stage-dependent variable-scale topographic steering mechanism. Through the rising and falling limbs of multiple hydrographs, this mechanism results in many possible combinations for spatial patterns of in-channel and overbank sediment mobilization and deposition often influenced by the presence of LBEs. Due to anthropogenic controls on sediment delivered to the study site, this theoretical mechanism of storage and subsequent transport is important in both the short and long-term sediment balance of the study site.

One limitation of this study involves 2D hydrodynamic modeling's inability to represent the shear stresses associated with velocity fluctuations. Values of bed shear stress used in this study are based on model predicted mean velocities. Instantaneous velocity fluctuations resulting from flow accelerations and decelerations, shear layers, and other hydromorphic phenomena create turbulence generation and strong instantaneous shear stresses that significantly influence sediment entrainment (MacVicar and Roy 2007; Thompson and Wohl 2009). The inability to account for these processes constrains this study's findings on the relative roles of the different flow direction zones in sediment transport and identifies the need for methods to include velocity fluctuations in computationally efficient 2D modeling software.

Ultimately, this study's analyses, based predominantly on submeter-to-meter resolution of topographic and 2D model results, includes several new or innovative methods for the investigation of landform structure and hydraulics in a mountain river. A new systematic and objective procedure is presented for delineation and mapping of LBEs across large spatial domains. Coupling 2D modeled hydraulics with a unique flow-direction analysis framework informed the basis for a conceptual model of discharge-LBE-sediment transport interactions in the study site.

Acknowledgements

References

Bisson, P. A., J. L. Nielsen, R. A. Palmason, and L. E. Grove. 1982. A system of naming habitat types in small streams, with examples of habitat utilization by salmonids during low streamflow. Pages 62-73 in N. B. Armantrout, ed. Acquisition and utilization of aquatic habitat inventory information. American Fisheries Society, Western Division, Bethesda, MD.

Branco, P., Boavida, I., Santos, J. M., Pinheiro, A. and Ferreira, M. T. 2013, Boulders as building blocks: improving habitat and river connectivity for stream fish. Ecohydrolgy, 6: 627-634.

Brown, R. A., & Pasternack, G. B. 2014. Hydrologic and topographic variability modulate channel change in mountain rivers. Journal of Hydrology, 510(Supplement C), 551-564.

Carbonneau, P., Fonstad, M. A., Marcus, W. A., & Dugdale, S. J. 2012. Making riverscapes real. Geomorphology, 137(1), 74-86.

Crowder, D. W., & Diplas, P. 2006. Applying spatial hydraulic principles to quantify stream habitat. River Research and Applications, 22(1), 79-89.

Grant, G. E., Swanson, F. J., & Wolman, M. G. 1990. Pattern and origin of stepped-bed morphology in high-gradient streams, Western Cascades, Oregon. GSA Bulletin, 102(3), 340-352.

Hawkins C. P., Kershner J. L., Bisson P. A., Bryant M. D., Decker L. M., Gregory S. V., McCullough D. A., Overton C. K., Reeves G. H., Steedman R. J., & . Young M. K .1993. A Hierarchical Approach to Classifying Stream Habitat Features, Fisheries, 18:6, 3-12.

Lai Y.G., 2008. "SRH-2D version 2: Theory and User's Manual Sedimentation and River Hydraulics – Two-Dimensional River Flow Modeling". U.S. Department of the Interior, Bureau of Reclamation, Technical Service Center, Sedimentation and River Hydraulics Group. Denver, Colorado.

Lisle, T. E., J. M. Nelson, J. Pitlick, M. A. Madej, and B. L. Barkett. 2000. Variability of bed mobility in natural, gravel-bed channels and adjustments to sediment load at local and reach scales, *Water Resour. Res.*, 36(12), 3743−3755.

MacVicar, B. J., and A. G. Roy .2007. Hydrodynamics of a forced riffle pool in a gravel bed river: 1. Mean velocity and turbulence intensity, Water Resour. Res., 43, W12401.

elis, T. S., Topping, D. J., Rubin, D. M., & Wright, S. A. 2007. Research Furthers Conservation of Grand Canyon Sandbars (2007-3020). Retrieved from http://pubs.er.usgs.gov/publication/fs20073020

(Thanos) Papanicolaou, A. and Tsakiris, A. G. 2017. Boulder Effects on Turbulence and Bedload Transport. In Gravel-Bed Rivers (eds D. Tsutsumi and J. B. Laronne).

Pasternack, G.B., 2011. 2D Modeling and Ecohydraulic Analysis. Createspace, Seatle, WA.

Pasternack, G. B. and Senter, A.E. 2011. 21st Century instream flow assessment framework for mountain streams. California Energy Commission, PIER. CEC-500-2013-059.

Raleigh, R. F., Hickman, T., Solomon, R. C., & Nelson, P. C. (1984). Habitat Suitability Index Models: Rainbow trout (82/10.60). Retrieved from http://pubs.er.usgs.gov/publication/fwsobs82_10_60

Rathburn, S., & Wohl, E. 2003. Predicting fine sediment dynamics along a pool-riffle mountain channel. Geomorphology, 55(1−4), 111-124.

Resop, J. P., Kozarek, J. L., & Hession, W. C. 2012. Terrestrial Laser Scanning for Delineating In-stream Boulders and Quantifying Habitat Complexity Measures. Photogrammetric Engineering & Remote Sensing, 78(4), 363-371.

Thompson, D. M. 2001. Random controls on semi-rhythmic spacing of pools and riffles in constriction-dominated rivers. Earth Surf. Process. Landforms, 26: 1195-1212.

Thompson, D. M. and Wohl, E. E. 2009. The linkage between velocity patterns and sediment entrainment in a forced-pool and riffle unit. Earth Surf. Process. Landforms, 34: 177-192.

Wiener, J., Pasternack, G.B. 2018. Geomorphology and Physical Fish Habitats of the Yuba River between New Bulards Bar Dam and Colgate Powerhouse. Prepared for Yuba County Water Agency. University of California, Davis, CA.

Yager, E. M., J. W. Kirchner, and W. E. Dietrich. 2007. Calculating bed load transport in steep boulder bed channels, Water Resour. Res., 43, W0718.

Modeling Lateral Erosion During Reservoir Drawdown

Authors: Tessa Artruc (artruct@oregonstate.edu), Desiree Tullos, Ben Leshchinsky, Jonathan Istok

Abstract: Reservoir drawdown is a management technique increasingly used to maintain aging infrastructure, decommission dams, and promote the flushing of fish and sediment. Typically, models of the reservoir's geomorphic response have been limited to 1D incisional erosion without the incorporation of lateral widening. The proposed research aims to understand how the drawdown rate may affect the magnitude, timing, and mechanism of lateral erosion processes in a reservoir. It is hypothesized that an increased drawdown rate (the water level is reduced over a relatively shorter period of time) will increase the volume and rate of lateral erosion and will be dominated by geotechnical failure. Field observations will be coupled with a hydrodynamic and bank stability model to conduct numerical experiments of the processes leading to erosion with varying drawdown scenarios. Bishop's Method will be utilized in a limit equilibrium model to evaluate planes of slope failure at various water levels, in addition to shear stress transfer at the bank toe for hydraulic failure. The incorporation of retrogressive bank erosion in this model will be a new contribution to address sequential slumping, which is expected to play a critical role in improving the accuracy of modeling reservoir erosion. High frequency surveys and sediment testing from Lake Mills and Lake Aldwell on the Elwha River in Washington will provide input data for robust verification of the model. Predicting the characteristics of erosion in a reservoir is essential in managing the impacts of sediment on downstream ecosystems and infrastructure.

Monitoring the Effect of Deep Drawdowns of a Flood Control Reservoir on Sediment Transport and Dissolved Oxygen, Fall Creek Lake, Oregon

Liam Schenk, Hydrologist, U.S. Geological Survey, Klamath Falls, Oregon, lschenk@usgs.gov

Heather Bragg, Hydrographer, U.S. Geological Survey, Portland, Oregon, hmbragg@gmail.com

Introduction

Annual reservoir drawdowns at Fall Creek Lake, Oregon, have occurred for eight consecutive years from December 2012 to November 2019. The annual drawdowns are the result of the 2008 Biological Opinion of the US Army Corps of Engineers (USACE) Willamette Valley Project operations, which directed the USACE to carry out interim operational measures that would provide volitional downstream passage for endangered species act (ESA)-listed Chinook salmon. At Fall Creek Lake, the USACE modifies its operations by lowering the reservoir elevation to 690-ft, approximately 40 feet below the normal winter low-pool elevation. This action results in a run-of-river scenario through the dam allowing juvenile Chinook salmon to safely pass through the regulating outlets. Monitoring of juvenile Chinook salmon in screw traps at the outlet of the dam has shown variable timing in out-migration associated with reservoir elevation, and that most of the juvenile fish exited the reservoir when the pool elevation passed 700-ft (Taylor and others, 2015). The annual drawdown has therefore been effective in providing safe downstream fish passage and has also had the collateral effect of transporting large quantities of suspended sediment to the downstream reaches of Fall Creek and the Middle Fork Willamette River. The US Geological Survey (USGS) has calculated time-series of suspended sediment concentrations (SSC) and suspended sediment loads (SSL) before, during, and after the drawdowns for six of the last nine drawdown years (water years [WY] 2013-2018), which have lasted between 5-14 days. The transport and deposition of sediment from the drawdowns has affected side-channel habitat below the dam by depositing large quantities of sand-size material resulting in streambed aggradation in several locations. The results from the USGS monitoring effort have provided important information to USACE on how the modification of their operations has affected sediment transport in the river reaches below the dam.
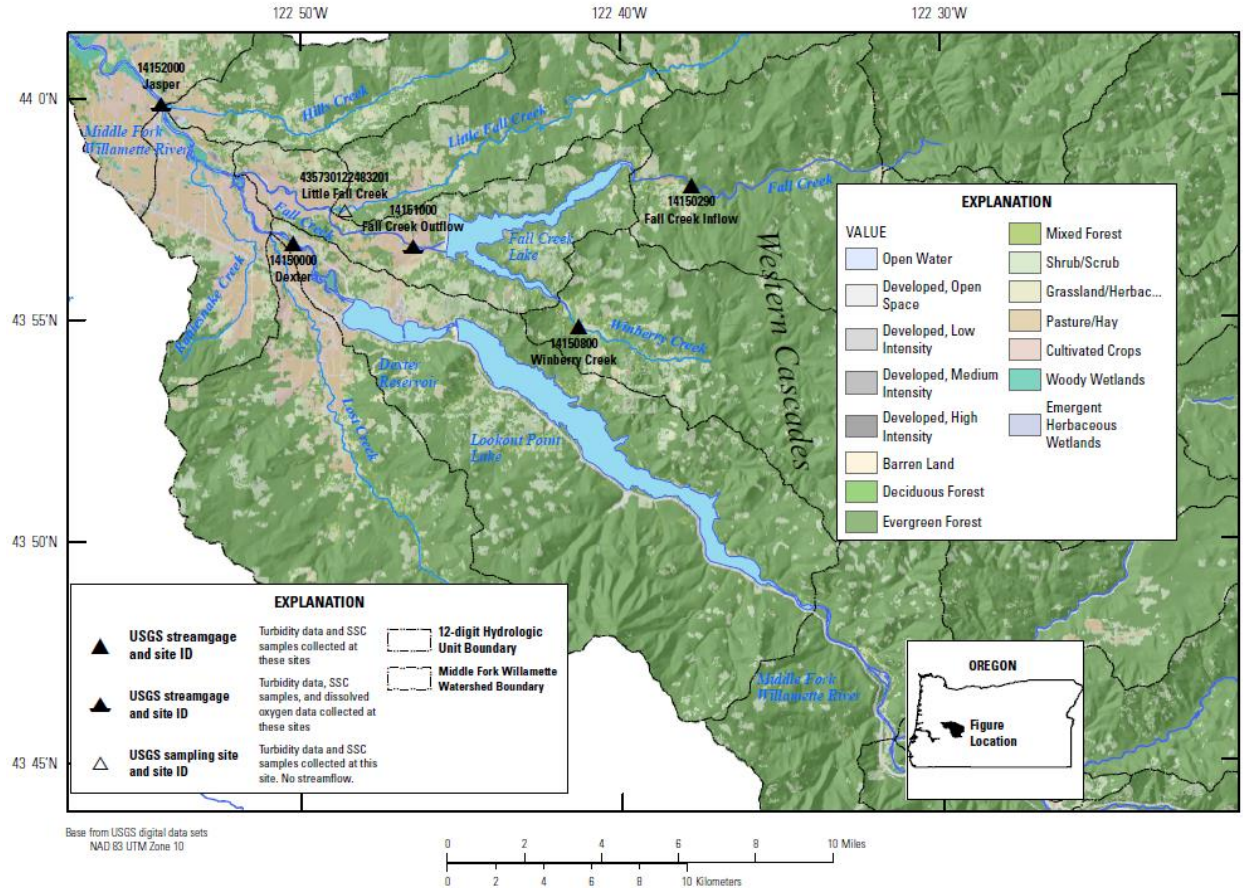
Figure 1. Project Area Map

Data Collection and Analysis Methods

The USGS monitored turbidity, dissolved oxygen, and suspended sediment over a range of hydrologic conditions and sediment transport during the drawdown operations at Fall Creek Lake (Figure 1). Monitoring in all years typically began in November and ended in February or March. USACE conducted a drawdown operation in water year (WY) 2012, during which no sediment samples or turbidity data were collected. USGS began monitoring in WY 2013, when six monitoring stations were established for the lake and at strategic locations downstream, including the two main inflows to Fall Creek Lake, Fall Creek below Fall Creek Dam (Fall Creek Outflow in Figure 1), Little Fall Creek (a tributary to Fall Creek), and two sites on the Middle Fork Willamette River (Dexter and Jasper). Results from the WY 2013 monitoring, including a short-term sediment budget are presented in Schenk and Bragg (2014). During WY 2014-2018, only the stations at Fall Creek Outflow and Jasper were monitored. Turbidity sensors measuring in Formazin Nephelometric Units (FNUs) and dissolved oxygen sensors were deployed on Hydrolab multi-parameter instruments (sondes), and Equal-Width-Increment (EWI) suspended-sediment concentration (SSC) samples were collected at all sites. Automatic pump samplers were installed at several sites to provide additional SSC data. Correction coefficients (box coefficients) were calculated to adjust the pump sample concentrations to cross section EWI samples. All samples were analyzed for SSC (in milligrams per liter [mg/L]) and percent finer than 63 microns (% fines) at the USGS Cascades Volcano Observatory sediment lab. Each discrete SSC sample was assigned

an associated turbidity and streamflow (in cubic feet per second [cfs]) value from the continuously monitored instream data.

Site-specific regression models were developed from discrete turbidity, streamflow, and SSC data. Sample data for sites downstream of the dam were divided into pre-drawdown, drawdown, and post-drawdown analysis periods. Log10-transformed and untransformed turbidity and streamflow data were used to create both simple and multiple linear regression models which were based on residual plots and summary statistics. Model development followed USGS guidelines outlined in Rassmussen et al. (2009). The preferred models were used to compute continuous SSC records for each of the sites. Continuous suspended-sediment loads were computed from the SSC and streamflow records. For WY 2013, suspended-sediment loads were computed for all six stations. For WY 2014-2018, suspended-sediment loads were only computed for Fall Creek outflow, during and after the drawdown, for comparison to SSL calculated in WY 2013. SSC samples, turbidity data, and dissolved oxygen data were collected at the Jasper site in WY 2014-2018, but poor mixing of suspended sediment in the channel made turbidity-SSC relations difficult since the turbidity sensor was deployed on the right edge of water, where SSC concentrations were higher than the left edge of water during storm events and the drawdown periods. As a result, this poster will focus on data at Fall Creek outflow (USGS site 14151000), where SSC, turbidity, and dissolved oxygen data were consistently collected for six consecutive drawdown operations.

Suspended Sediment Loads

SSL computed for the drawdowns in WY 2013-2018 do not represent all the sediment removed from behind Fall Creek dam since the dam was constructed in 1966. Operational drawdowns at Fall Creek Lake have occurred on multiple occasions from 1974 to 1988, and in WY 2012 prior to USGS monitoring efforts. Therefore, sediment loads presented here should be viewed within the context of other drawdowns that have occurred without any knowledge of sediment transport in those years.

SSL below Fall Creek dam were highest in WY 2013, the first year of USGS monitoring and the second consecutive drawdown since 1988. During the 6-day drawdown in December 2012, approximately 50,000 tons of sediment were measured downstream of the dam (Figure 2). That year's drawdown also resulted in approximately 16,300 tons of sediment deposited in the reaches between Fall Creek Lake and the Middle Fork Willamette at Jasper, which is 10 miles downstream of the lake (Schenk and Bragg, 2014). Due to unusually cold weather that froze the surface layer of sediment within the reservoir, SSL during the WY 2014 drawdown was particularly low. The area received 8–10 inches of snow followed by air temperatures consistently below freezing for most of the drawdown period concurrent with low streamflow, resulting in a total sediment load of approximately 5,220 tons during the 10-day drawdown period (Figure 2). SSL from WY2015-2018 were approximately 10,000 tons each year and show an overall decrease regardless of average streamflow during the drawdown period or the duration of the drawdown in those years, suggesting that streamflow has not been greatly influencing the SSL since WY 2015.
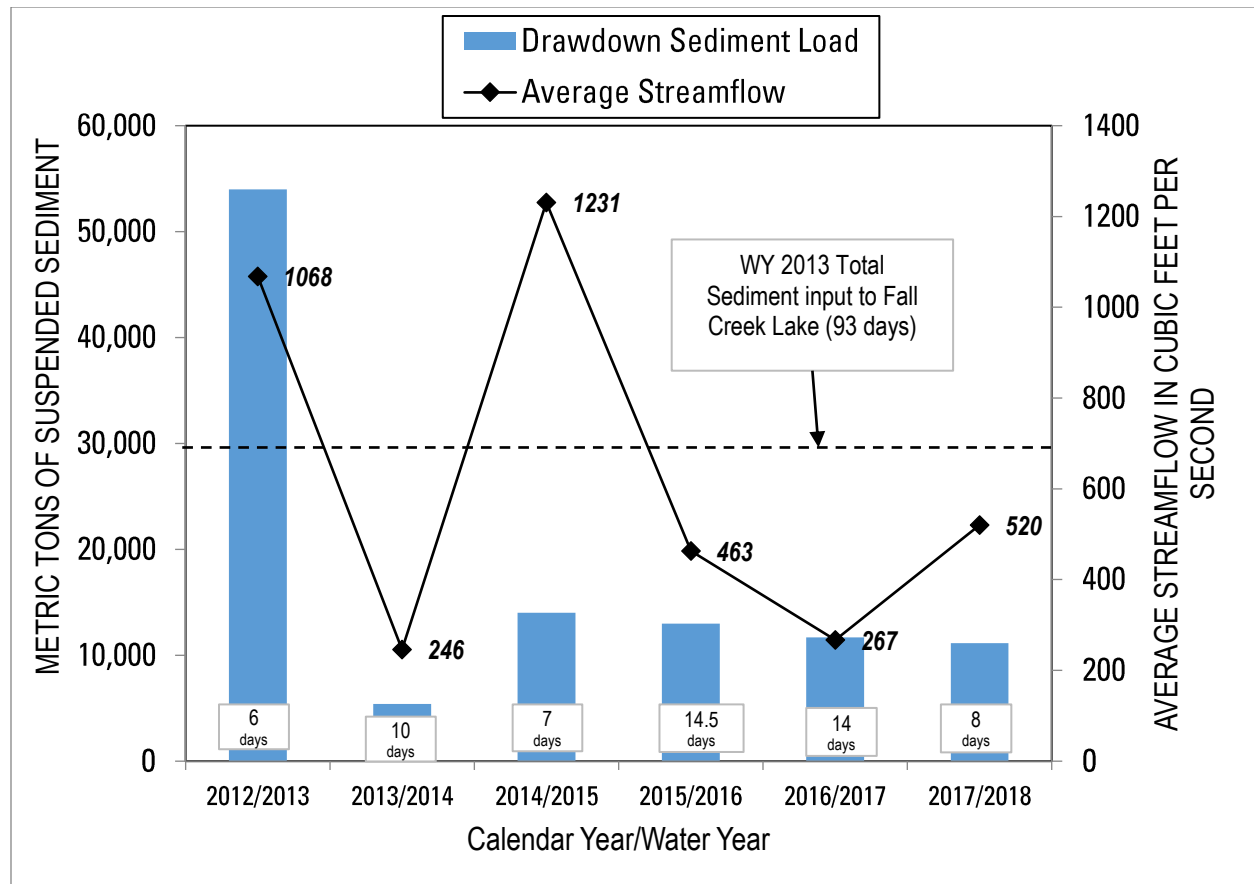
Figure 2. Sediment loads WY 2013-2018

The WY 2013 drawdown resulted in a change in sediment trap efficiency of the lake, from 74% pre-drawdown to 67% post-drawdown (Schenk and Bragg, 2014). Total inflow SSL for the monitoring period in WY 2013 (93 days) was approximately 30,000 tons compared to an average of approximately 10,000 tons from each drawdown in WY 2015-2018. Assuming the annual inflow SSL to Fall Creek Lake is greater than 30,000 tons, this suggests that the drawdown operations have reached a point where a small percentage of the SSL entering the lake over a given water year are being transported out of the lake during the drawdown. One explanation of the reduced sediment loads is the channel morphology within the reservoir during the drawdown. Geomorphic studies have shown that the stream channel within the reservoir during the drawdown is highly constrained, does not erode much of the channel banks during the drawdown periods, and therefore does not access much of the sediment deposited on the areas that are topographically higher than the streambed (Keith and others, 2018), where much of the sediment from the basin is likely deposited throughout the year.

Changes in Sediment Characteristics

Turbidity monitoring and percent fines data from SSC samples have given insight into how sediment characteristics change during the operational drawdowns. In every year of USGS monitoring, the slope and intercept terms of the turbidity-SSC regressions shifted considerably from pre-drawdown to drawdown time frames, resulting from changes in turbidity response to

grain size distribution in the SSC samples. Turbidity sensors will have different responses to fine grained versus coarse grained (sand-size) material in suspension, with fine grained samples having more light scattering and higher turbidity values versus less light scattering and lower turbidity values for sand-sized material (Merten and others, 2014). Turbidity-SSC relations from this study follow this theory up to turbidities in the 200 FNU range as shown in Figure 3, which shows how the slopes of the regressions change with the percentage of sand-sized material in the SSC samples. At turbidities above 200 FNU, the regression lines shift from the theoretical turbidity sensor response, which may be the result of the presence of both fines and sand-size material in the samples. The lab studies conducted by Merten and others (2014) evaluated samples with an equal distribution of grain sizes, which may lead to inconsistencies with the theoretical turbidity response from our environmental samples. Because of the grain-size shift during the drawdowns, multiple regression equations were used each year in short durations to reflect the changes in sediment characteristics. Regression equations also changed year-to-year during the drawdowns, so new evaluations of turbidity-SSC relations were required for each individual monitoring period.
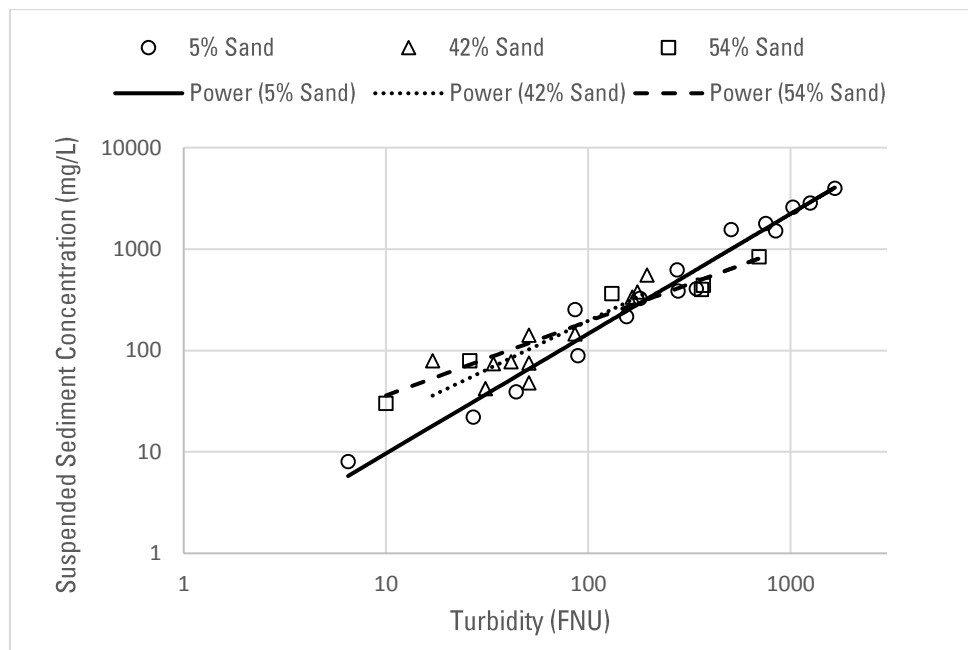
Figure 3. Regression lines for Turbidity-SSC models based on grain size

The shift in grain-size distribution in SSC samples as measured by the percent of fine-grained material less than 0.063mm (percent fines) occurred toward the end of the drawdown and after the reservoir began refilling in all the monitoring years. In the first few days of every drawdown, percent fines in the SSC samples was typically between 90-100%. Toward the end of every drawdown, and after the drawdown had ended, the percent fines in the samples decreased, reflecting an increase in sand-sized material in the samples. The sand-sized material was more readily deposited in side channel habitat downstream of the dam, and in areas of low velocity within the stream channels. The cause of the increase in grain size is unclear, and our monitoring

efforts have found that the increase in sand-sized material in SSC samples occurs regardless of streamflow or of the regulating outlet gate positions during the drawdowns, suggesting that stream energy and gate management is not affecting the transport of sands in suspension. Particle settling velocity as described by Stokes Law dictates that coarse-grained material will fall out of suspension first as stream velocity decreases, followed by fine-grained particles (Guy, 1970). When Fall Creek Lake is drawn down to streambed, the fine-grained sediment is likely accessed first, followed by the coarser sediment. However, the shift in particle size in the SSC samples occurs toward the end of the drawdowns regardless of the drawdown length. It is possible that a combination of fines and sands are transported through the dam at the start of the drawdown, and that much of the sands are deposited in the channel just downstream of the dam outlet. Those sands could then be transported when the regulating outlets are closed at the end of the drawdown and much of the fines have already moved downstream.

Drawdown Influence on Dissolved Oxygen

Another collateral effect of the drawdowns is short-term decreases in dissolved oxygen concentrations concurrent with the first pulse of fine-grained sediment at the start of the drawdown. Dissolved oxygen data were collected using Hydrolab sondes in all years of USGS monitoring except WY 2014 when no dissolved oxygen data were collected. In most years, excessive sensor fouling resulted in data loss when the first pulse of sediment was released from behind the dam. After modifications to the deployment structure for the sondes was implemented in WY 2016, data integrity improved, and a minimum dissolved oxygen concentration of 0.7 mg/L was recorded coincident with the peak in turbidity at the start of the drawdown. The dissolved oxygen minimum value was verified by independent sensors deployed by the field crew (Schenk and Bragg, 2017, Figure 4). The low dissolved oxygen event was short, with concentrations remaining below 5 mg/L for approximately one hour. This quick expression of oxygen demand suggests that the demand is chemical in nature and is likely the result of rapid oxygenation of reduced sediments trapped behind the dam. Concurrent studies of the drawdowns by Oregon State University confirm this hypothesis, having shown spikes in reduced nitrogen represented by ammonia concentrations at the onset of the drawdowns, and have also suggested that the oxygen demand of the sediments is "modest" (Johnson and others, 2017).
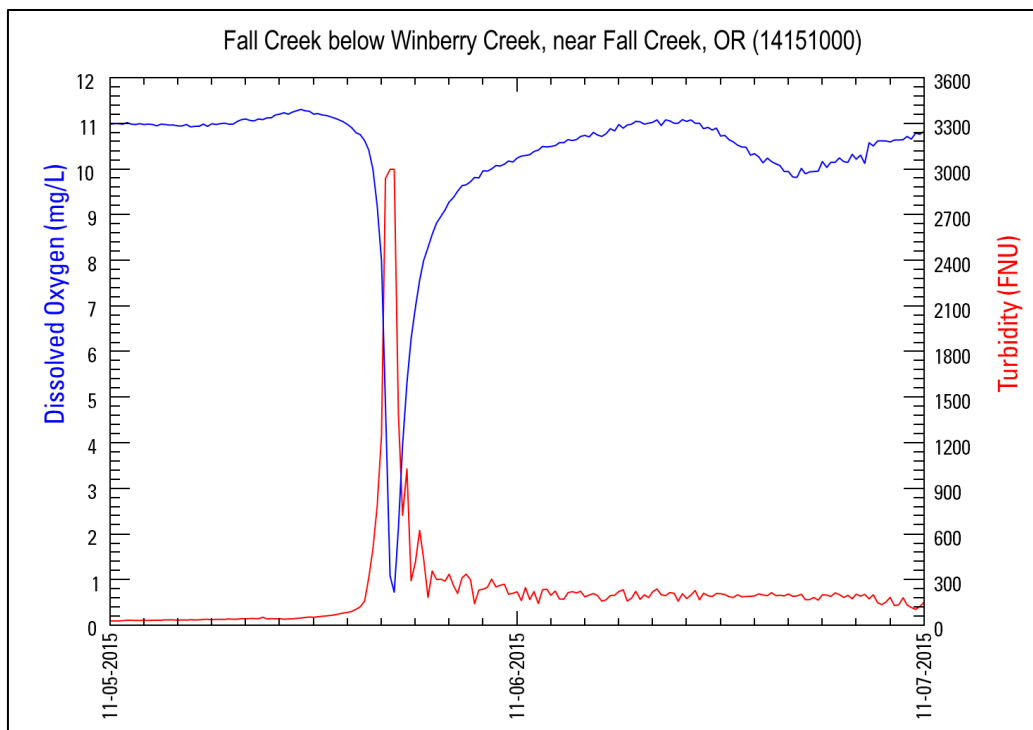
Figure 4. Dissolved oxygen concentrations during the WY 2016 drawdown

Summary

The streambed drawdown of this flood control reservoir has successfully met the goal of providing volitional passage of ESA-listed juvenile chinook salmon through the regulating outlets of Fall Creek dam. The collateral effect of large sediment transport events and short-term low dissolved oxygen events has been well documented through six years of data collection efforts by USGS. Sediment loads were highest in the first year of drawdown monitoring, which was also the second consecutive year of the drawdowns and have been steadily decreasing from 2015-2018 through various hydrologic regimes, suggesting that sediment supply is now the controlling factor in sediment loads compared to the effect that streamflow appeared to have on sediment transport in the first two years of monitoring (WY 2013-2014). The transport of sand-sized material that occurs toward the end of the drawdowns and when the reservoir is refilling has caused sediment deposition and aggradation in off-channel habitats, backwaters, and low-velocity zones within the channel margins downstream of the dam. In some locations, emergent vegetation has inhibited the sediments from being mobilized at the highest flows allowed in the channel. Short term periods of anoxia have resulted from the first release of reduced sediments from behind the dam at the start of the drawdowns. The oxygen demand is typically expressed over short time frames (approximately 1 hour when measured at a fixed location) and occurred after most of the juvenile chinook salmon had passed through the dam. The effect of the drawdowns on sediment transport and dissolved oxygen are specific to this flood control reservoir, but the results of this effort can help inform drawdown operations that may be considered at other reservoirs. Some application of these results could be used to evaluate such operations, but site-specific investigations would best inform implementation of those actions.

References

Guy, Harold P., 1970. "Fluvial Sediment Concepts", U.S. Geological Survey Techniques of Water Resources Investigations, Chapter C1, https://pubs.usgs.gov/twri/twri3-c1/pdf/twri_3-C1_a.pdf

Johnson, S., Hamilton, S., Murphy, C., Arismendi, I. 2017. "Water quality ramifications of draining a reservoir to facilitate salmon passage". Willamette Fisheries Science Review presentation to the U.S. Army Corps of Engineers, February 2017, Corvallis, Oregon, available at http://pweb.crohms.org/tmt/documents/FPOM/2010/Willamette_Coordination/WFSR/.

Keith, M., Gordon, G., Stratton, L., White, J., Schenk, L., Wallick, R., Mangano, J., Taylor, G. 2018. "Geomorphic Impacts to Fall Creek and the Middle Fork Willamette River from Annual Drawdowns at Fall Creek Dam". Willamette Fisheries Science Review presentation to the U.S. Army Corps of Engineers, February 2018, Corvallis, Oregon, available at http://pweb.crohms.org/tmt/documents/FPOM/2010/Willamette_Coordination/WFSR/.

Merten, G.H., Capel, P.D., Minella, J.P.G. 2014. "Effects of Suspended Sediment Concentration and grain size on three optical turbidity sensors". Journal of Soils and Sediments., 14: 1235-1241., https://link.springer.com/article/10.1007/s11368-013-0813-0

Rasmussen, P.P., Gray, J.R., Glysson, G.D., and Ziegler, A.C. 2009. "Guidelines and procedures for computing time-series suspended sediment concentrations and loads from in-stream turbidity-sensor and streamflow data," U.S. Geological Survey Techniques and Methods, book 3, chap. C4, 52 p., https://pubs.usgs.gov/tm/tm3c4/

Schenk, L.N., Bragg, H.M. 2014. "Assessment of suspended-sediment transport, bedload, and dissolved oxygen during a short-term drawdown of Fall Creek Lake, Oregon, winter 2012-13," U.S. Geological Survey Open-File Report 2014-1114, 80 p., http://dx.doi.org/10.3133/ofr20141114.

Schenk, L.N., Bragg, H.M. 2017. "Suspended-Sediment and Dissolved Oxygen Monitoring during Operational Drawdowns of Fall Creek Lake, 2012-2017". Willamette Fisheries Science Review presentation to the U.S. Army Corps of Engineers, February 2017, Corvallis, Oregon, available at http://pweb.crohms.org/tmt/documents/FPOM/2010/Willamette_Coordination/WFSR/.

Taylor, G., Garletts, D., Helms, C., Pierce, T., Dalgliesh, J., Berling, T., Rayfield, K. 2015. "Fall Creek Overview: Adult Returns and Juvenile Outmigration Data". Willamette Fisheries Science Review presentation to the U.S. Army Corps of Engineers, February 2015, Corvallis, Oregon, available at http://pweb.crohms.org/tmt/documents/FPOM/2010/Willamette_Coordination/WFSR/.

Optimized Reservoir Refill

Tom Chisholm, Civil Engineer, U. S. Army Corps of Engineers Northwestern Division, Portland, OR tom.a.chishom@usace.army.mil

Introduction

Refilling reservoirs in regions with seasonally varying water supply can be one of the most challenging aspects of reservoir operation planning. Refill operations aim to strike a balance between storing sufficient water to meet demand for water during ensuing periods of lower water supply while maintaining sufficient space in reservoirs to prevent flooding caused by high inflow events occurring when projects approach full. The operational challenge becomes finding the optimum balance between these two competing objectives. The following describes attempts to use mathematical optimization to find this optimum balance.

Application

To address uncertainty in future water supply, regulators use multiple scenarios, called ensemble stream flow predictions (ESP). Hydroregulation models regulate ESP traces. Historically, a regulator calculated a refill operation using engineering procedures and judgment for the median ESP trace. The resulting operation was then tested using the full suite of ESP traces. The optimization approach described herein allows automatic calculation of an optimum refill operation for each ESP trace. These optimum operations are then statistically analyzed to determine operational directives provided to dam operators. The optimization approach results in more repeatable results obtained with less regulator effort.   The procedure may be implemented repeatedly as revised ESP traces become available.

The optimization procedure starts by running a constraint driven reservoir regulation model with pre-computed refill percentages. The implementation described herein used the Reservoir System Simulation (HEC-ResSim) model (HEC 2013). The HEC-ResSim flow at the potential flooding location is extracted from HEC-ResSim as a sum of discharge from the dam being analyzed and discharge from other sources. The discharge from the dam being analyzed is then optimized using the Frontline Systems Analytic Solver (Frontline Systems 2018) on an ESP trace by ESP trace basis resulting in a cumulative distribution plot of optimum project elevations. Frontline Systems developed the solver that comes with Microsoft Excel and Analytic Solver is similar but more capable.

Test System

Numerical experiments investigated optimization based operation of a reservoir system. Analyses use an artificial system of two dams one upstream of the other. Both dams have a capacity of 600 kaf. Inflow to the reservoir system occurs into the upstream reservoir, between the reservoirs, and downstream of the lower reservoir. Inflows use daily flow from ESP data produced by the Northwest River Forecast Center in Portland, OR and issued 7 January 2019 (https://www.nwrfc.noaa.gov/misc/downloads/). Using data beginning 6 months after forecast date minimizes impacts of current conditions on ESP traces. Analyses use the portion of ESP projections extending from 1 July 2019 to 30 June 2020. Data from three northwest river systems provided inflow traces. These included the Slocan River near Crescent Valley, BC (SLCQ2W 123229000) modeled as flowing into the upper reservoir (upstream reservoir inflow),

the Yakima River near Parker, WA (PARWW 125050003) modeled as the incremental flowing into the lower reservoir (between reservoir inflow), and the Grande Ronde River at Troy, ID (TRYO3W 133330000) modeled as the incremental below the lower reservoir (downstream of lower reservoir inflow). Much of the upstream reservoir inflow comes from high elevation so it occurs during the early summer freshet. Between reservoir inflow and downstream of lower reservoir inflow come from more southerly areas so their freshets occur earlier and their runoff is more evenly distributed throughout the year. The Yakima River has the largest annual average runoff of 3942 kaf and the Grand Ronde has the least with 2190 kaf. The Slocan is slightly larger than the Grande Ronde with 2438 kaf.

Analysis

Flood management attempts to minimize peak flow for a flood season. The obvious objective of optimization is thus to minimize maximum discharge of the season. In practice minimizing peak flood implies maintaining constant flow during a flood season. Two measures of constant flow are 1) sums of absolute values of daily flows minus average flows and 2) sums of squares of flows. These were tested on a one reservoir system with the reservoir fed by the Yakima River traces and Grande Ronde River traces serving as incremental flow downstream of the reservoir.

Specifying peak flow in the objective function implies that flow on only one date specifies the objective function, although the date can vary as the optimizer searches for the optimum solution. This can lead to unrealistic solutions in time periods that are not flow peaks. Therefore, using max flow as the objective functions leads to undesirable solutions.

Specifying even flow effectively minimizes peak flow. The absolute value of the flow minus the average flow evenly weights all deviations from average. However, it results in a function with a discontinuous derivative, which adversely impacts efficiency of gradient solvers. Squaring flow or the difference between flow and average flow yields a value that increases quadratically as flow increases. Therefore, their sum over a time period is minimized by even flows. Both appear best suited for optimization based minimization of peak flows.

Optimization software frequently limits problem sizes, providing an incentive to simplify problems. One simplification for the test system would be to optimize reservoir operations one at a time. Thus a comparison was done of 1) optimizing the upstream reservoir then the downstream reservoir 2) optimizing the downstream reservoir then the upstream reservoirs and 3) optimizing both concurrently. These approaches were compared for a high water trace (1973-1974) and a low water trace (1972-1973). All scenarios optimized to produce virtually identical maximum flows. Not surprisingly, if the reservoirs are optimized separately the solution flexes the first reservoir optimized more aggressively then the second. In larger water conditions, operations are more similar because flexibility in both reservoirs is used to the maximum extent possible. In smaller water years the first reservoir optimized is flexed as much as possible and the second reservoir is only flexed as much as necessary to achieve objectives. Optimizing both reservoirs concurrently produces more balance between reservoirs. Optimizing reservoirs separately results in a numerically simpler problem and appears to produce acceptable results if the analyst is aware of this behavior. Optimizing concurrently in most cases appears to be the desired approach.

If an optimizer is not available or the analyst does not wish to use one this section describes a simplified approach that uses a root finding algorithm such as bisection. Remembering that minimizing peak flow for a period is achieved by releasing constant flow throughout the period

one can divide the sum of inflows and change in reservoir storage for the period by the length of time to obtain a discharge for the entire period. In most cases this operation is physically infeasible: to support it the reservoir must draft below empty or fill beyond full or water must flow upstream into the reservoir.   However, modeled reservoir elevation is readily constrained to ensure physical reasonableness. In this case the reservoir releases the desired average flow except when it can't. The problem becomes adjusting the desired discharge to minimize the sum of the squares of the discharge. This problem has one free parameter, the desired discharge, and one value to minimize, the sum of the squares of the discharge. Numerically it is an easy problem to solve. The result is not as optimal as that produced by a solver. In a test example the objective function found using the simplified example was 14% larger than the optimized solution. However, in one example of 70 traces it reduced solution time from over an hour to less than 5 minutes.

Conclusion

Modeling reservoir operations using the constraint driven HEC-ResSim but applying a solver to determination of reservoir refill operation appears to offer promise.   Minimizing squares of project discharge is computationally more robust than other tested approaches. Alternate numerical approaches including individually optimizing reservoirs and using a root finding based approach yield less desirable but useful solutions.

References

Frontline Systems. 2018. "Frontline Solvers Reference Guide", Incline Village, NV.

HEC (Hydrologic Engineering Center). 2013. "HEC-ResSim Reservoir System Simulation, User's Manual". Davis, CA.

P-6 Comparison Tests -A Point-Integrating Suspended Sediment Sampler Comparison

Kurt Spicer, Supervisory Hydrologic Technician, U.S. Geological Survey, Vancouver, WA
krspicer@usgs.gov

Introduction

Federal Interagency Sedimentation Project (FISP) Memo 2011.01 introduced the US P-6 point-integrating suspended-sediment sampler (in 100 and 200 lb. versions yclept P-6 100 and P-6 200, respectively) as the next-generation replacement for the P-61, P-63, and P-72 series point-integrating samplers (FISP 2011). The memo describes the new sampler and provides details of flume and tow-tank hydraulic efficiency testing that verified nozzle hydraulic efficiencies within a range of 0.93 to 1.12. The tests showed a nozzle hydraulic efficiency of near 1.0 at 3.5 ft/sec flume flow velocity. Tow tank tests showed hydraulic efficiency varying from approximately 1.10 at 1.5 ft/sec to 0.95 at about 5.5 ft/sec, then remaining in a range between 0.93 to 0.96 up to 16 ft/sec. These results fall within the acceptable range of 0.9 to 1.1. The memo describes field testing performed by the U.S. Army Corps of Engineers' Coastal and Hydraulics Laboratory but lists only sampled ranges of flow velocity and depth, as well as total number of samples and sample frequency time. Field comparison sampling with a different point sampler is not mentioned. An important consideration of long-term time series sample data is to document potential bias due to changes in sampling equipment. Such sampler comparison tests were made between earlier versions of FISP-issued (and other) suspended-sediment samplers (FISP 1944). Notes from a Spring 2012 FISP meeting (FISP 2012) include a remark about acquiring side-by-side sampler testing, but subsequent testing was of limited value due to a very low amount of suspended sediment (Jim Selegean, USACE written communication 2018). Additional comparison testing between a P-6 200 and a P-63 was completed in 2015, but those data have not been published with narrative description (Lane Simmons, USGS written communication 2018). Presented here are results of field comparison sampling using a P-6 100 (hereinafter P-6) and a US-P-61-A1 (hereinafter P-61) under different conditions on two rivers near Mount St. Helens, Washington, during 2018. Sample analyses focused on suspended-sediment concentration (SSC) and particle size.

Study sites

Samples for this study were collected at two USGS gage sites in Southwest Washington state, Toutle River at Tower Road near Silver Lake, WA (USGS station number 14242580—USGS 2019a), and Cowlitz River at Castle Rock, WA (USGS station number 14243000—USGS 2019b). Both sites are on rivers that transport sediment derived mostly from the debris avalanche that resulted from the 1980 eruption of Mount St. Helens. Sampling at both sites was done from a bridge at the gage station (downstream side at Tower Road, upstream side at Castle Rock).

Methods

Comparison sampling can be done various ways, but no method under field conditions can achieve perfect comparison due to temporal and spatial variation in SSC, particle size distribution, and streamflow velocity. Due to limited resources for this study, sampling was conducted at a single station on a bridge, so all depth-integrated (DI) samples used the same

vertical, and all fixed-point (FP, or point) samples used the same point, or points (with the exception that during the March 5 sampling at Castle Rock, bed elevation change due to dune migration engendered a 0.5-ft raise in the bottom three sampled depths, in an attempt to maintain relative distance above bed). This method limited spatial variation at the cost of accentuated temporal variation. The alternate approach of collecting samples side-by-side to constrain temporal variation at the expense of spatial variation was rejected as it would have required more people to operate two sampling rigs simultaneously. Samplers were deployed from a bridge crane using an E-reel with one-eighth inch copper-core steel suspension cable. and a Hydrologic Instrumentation Facility (HIF) variable speed reel drive unit. Limited velocity data was collected with a Price meter or an Acoustic Doppler Current Profiler (ADCP) but is not presented here due to large uncertainty in its applicability for computing nozzle intake efficiencies. Prior to sampling, dry bottle tests were performed by lowering the sampler with bottle into the stream for a short time with the nozzle closed, then retrieving it to inspect for leakage. Quart glass sample bottles were used for both samplers. Next, a series of samples, either DI or point, were collected using a P-61. Then, the P-61 was swapped for a P-6, and a second series of samples was collected with that sampler, at the same transit rate, depths, and nozzle open times. Generally, samples were collected using the same transit rate (for DI samples) and the same nozzle open times (for point samples). Exceptions to this were the first two P-61 point samples collected on March 5, when subsequent nozzle-open times were altered to optimize sample volume; one DI sample collected on March 5, transit rate for which was not noted; and the first P-61 point sample on December 19, when subsequent nozzle-open time was reduced to optimize sample volume. Throughout the four separate days of sampling at both sites, the sequence of sampling, and the number of samples collected varied. All samples were analyzed at the Cascades Volcano Observatory sediment lab for sand fine split and concentration.

Data

Samples were collected on February 27 and March 5 at USGS station 14243000 Cowlitz River at Castle Rock, WA; on December 19 at USGS station 14242580 Toutle River at Tower Road near Silver Lake, WA; and on December 21, again at Cowlitz River at Castle Rock.

Samples collected on February 27 (Table 1) consisted of five fixed-point samples from each sampler at a depth of 10 feet, and nozzle-open time of 20 seconds, at station 234 ft on the upstream side of the bridge (this and subsequent references to bridge station are distance in feet from the river-left end of the bridge).

On March 5, 30 fixed-point samples and two depth-integrated samples were collected at a single vertical at station 350, off the upstream side of the bridge in Castle Rock, WA (Table 2). Sampled depths were 10, 9, 8, 5, and 1 ft below the water surface (but the bottom P-6 samples were adjusted upward 0.5 ft to adjust for gradual rise in bed elevation). Twenty-one consecutive P-61 samples were collected at the various depths and nozzle-open times in a repeating fashion. Then the sampler was changed to the P-6 and another 9 samples were similarly collected with that sampler.

On December 19, sequential comparison samples were collected at station 200 off the downstream side of the Tower Road bridge over the Toutle River (Table 3). Six DI samples were collected with a P-61, followed by six point samples with the same sampler. Then,

Table 1. P-6 and P-61 sample metadata and lab results, February 27, 2018. [%finer; percent finer than 0.0625 mm]

| Date/Time (PST) | Sampler | | Sample Type | | Transit rate (ft/s) | Transit length (ft) | Depth below water surface (ft) | Nozzle-open time interval (sec) | Lab Results | |
	P-61	P-6	DI	FP					SSC (mg/L)	%finer
2/27/18 @1301	X			X			10	20	33	18.7
2/27/18 @1305	X			X			10	20	39	18.8
2/27/18 @1310	X			X			10	20	40	17.2
2/27/18 @1314	X			X			10	20	39	19.3
2/27/18 @1316	X			X			10	20	34	18.7
2/27/18 @1334		X		X			10	20	42	18.4
2/27/18 @1336		X		X			10	20	36	18.1
2/27/18 @1339		X		X			10	20	34	18.6
2/27/18 @1342		X		X			10	20	33	15.8
2/27/18 @1345		X		X			10	20	40	19.0

Table 2. P-6 and P-61 sample metadata and lab results, March 5, 2018. [%finer; percent finer than 0.0625 mm]

| Date/Time (PST) | Sampler | | Sample Type | | Transit rate (ft/s) | Transit length (ft) | Depth below water surface (ft) | Nozzle-open time interval (sec) | Lab Results | |
	P-61	P-6	DI	FP					SSC (mg/L)	%finer
3/05/18 @1347	X			X			10	30	41	23.0
3/05/18 @1351	X			X			9	45	26	27.4
3/05/18 @1353	X			X			8	40	25	26.1
3/05/18 @1356	X			X			5	30	21	34.0
3/05/18 @1358	X			X			1	25	18	39.1
3/05/18 @1420	X			X			10	45	29	25.9
3/05/18 @1421	X			X			9	35	23	31.3
3/05/18 @1433	X			X			8	30	20	33.0
3/05/18 @1435	X			X			5	30	20	34.8
3/05/18 @1436	X			X			1	25	17	41.9
3/05/18 @1450	X			X			10	45	39	18.6
3/05/18 @1455	X			X			9	35	31	26.2
3/05/18 @1457	X			X			8	30	22	34.8
3/05/18 @1458	X			X			5	25	19	33.0
3/05/18 @1503	X			X			1	25	19	44.6
3/05/18 @1529	X			X			10	45	30	24.3
3/05/18 @1528	X			X			9	35	24	30.1
3/05/18 @1532	X			X			8	35	26	29.5
3/05/18 @1534	X			X			5	30	20	36.6
3/05/18 @1537	X			X			1	25	14	52.6
3/05/18 @1556	X			X			10	45	30	25.4
3/05/18 @1605		X		X			9	35	42	20.3
3/05/18 @1607		X		X			8	35	32	25.4
3/05/18 @1609		X		X			5	30	25	34.5
3/05/18 @1614		X		X			1	25	16	46.4
3/05/18 @1634		X		X			9.5	45	38	19.7
3/05/18 @1636		X		X			8.5	35	31	18.7
3/05/18 @1638		X		X			7.5	30	21	33.3
3/05/18 @1640		X		X			5	25	21	34.8
3/05/18 @1642		X		X			1	25	16	41.8
3/05/18 @1504	X		X		1.0	~10.5			23	38.5
3/05/18 @1559		X	X		Not noted	~10.5			23	34.8

six point samples were collected with a P-6 at the same depth and nozzle open time, followed by six depth-integrated samples using the same transit rate as used with the P-61.

On December 21, sequential comparison samples were collected at station 234 ft off the upstream side of the bridge over the Cowlitz River in Castle Rock, Washington (Table 4). As at the Toutle River site two days earlier, six depth-integrated samples were collected with a P-61, followed by six point samples with the same sampler. Then, six point samples were collected with a P-6 at the same depth and nozzle open time, followed by six depth-integrated samples using the same transit rate as used with the P-61.

Table 3. P-6 and P-61 sample metadata and lab results, December 19, 2018. [%finer; percent finer than 0.0625 mm]

| Date/Time (PST) | Sampler | | Sample Type | | Transit rate (ft/s) | Transit length (ft) | Depth below water surface (ft) | Nozzle-open time interval (sec) | Lab Results | |
	P-61	P-6	DI	FP					SSC (mg/L)	%finer
12/19/2018@1336	X		X		1.5	~11.8			2,300	15.5
12/19/2018@1340	X		X		1.5	~11.8			2,573	13.9
12/19/2018@1342	X		X		1.5	~11.8			2,679	13.4
12/19/2018@1344	X		X		1.5	~11.8			2,683	13.2
12/19/2018@1346	X		X		1.5	~11.8			2,143	16.3
12/19/2018@1348	X		X		1.5	~11.8			2,960	11.5
12/19/2018@1354	X			X			7	20	2,145	16.4
12/19/2018@1356	X			X			7	15	1,987	17.7
12/19/2018@1358	X			X			7	15	2,093	16.9
12/19/2018@1400	X			X			7	15	2,341	14.9
12/19/2018@1402	X			X			7	15	2,164	16.2
12/19/2018@1404	X			X			7	15	2,163	16.2
12/19/2018@1428		X		X			7	15	1,980	17.2
12/19/2018@1431		X		X			7	15	2,201	15.9
12/19/2018@1433		X		X			7	15	2,079	16.5
12/19/2018@1435		X		X			7	15	1,962	17.5
12/19/2018@1437		X		X			7	15	1,924	17.8
12/19/2018@1439		X		X			7	15	2,009	17.2
12/19/2018@1447		X	X		1.5	~12.5			1,790	18.8
12/19/2018@1449		X	X		1.5	~12.5			2,000	16.7
12/19/2018@1451		X	X		1.5	~12.5			2,186	15.4
12/19/2018@1453		X	X		1.5	~12.5			2,273	14.8
12/19/2018@1456		X	X		1.5	~12.5			2,197	15.2
12/19/2018@1458		X	X		1.5	~12.5			2,215	15.0

Discussion

Due to the small number of samples collected during each of the four comparison sampling events (maximum number of directly comparable samples was six), rigorous statistical analysis was not conducted for these data. Graphs are presented for the three more-complex data sets collected on March 5, December 19, and December 21 to visualize sample variation.

Streamflow during sampling at Castle Rock on February 27 was steady at 16,200 ft^3/s. As the previous substantial sediment-mobilizing peak was in late December 2017, river SSC was relatively low. P-61 sample SSC ranged from 33 to 40 mg/L (37 mg/L average), and percent finer than 0.0625 mm (%finer) from 17.2% to 19.3% (18.5% average). P-6 samples collected at the same station, depth, and nozzle-open time ranged from 33 to 42 mg/L (37 mg/L average),

and %finer from 15.8% to 19.0% (18.0% average). Under these relatively low SSC and stable flow conditions, the two samplers produced nearly identical results.

One week later, on March 5, streamflow at Castle Rock had almost halved, and was slowly declining at about 8,300 ft3/s. Much of the decline in flow between February 27 and March 5 was due to a series of dam-regulated flow reductions on the Cowlitz River above its confluence with the Toutle River. This significant reduction in clean-water flow from the upper Cowlitz River, combined with a small rise on the Toutle River on March 1, resulted in similar SSC for the two sample sets. March 5 samples were collected to document variation in SSC and particle size distribution with depth, and to show temporal variation. Figure 1 shows six series of five repetitive different-depth point samples progressing from near-bed to near-surface. Although the first one or two samples collected with the P-6 appear slightly high compared to the immediately preceding P-61 sample, these data points also show close similarity of SSC and %finer values. A possible contributing factor to the higher SSC values in the first two P-6 samples is that the river bed elevation appeared to have aggraded since sampling commenced, presumably due to dune migration, so the P-6 samples at times 1605 and 1607 may have been nearer the bed than previous same-depth samples. For the final set of samples with the P-6, sample locations were raised 0.5 ft to adjust for the change.

Table 4. P-6 and P-61 sample metadata and lab results, December 21, 2018. [%finer; percent finer than 0.0625 mm]

| Date/Time (PST) | Sampler | | Sample Type | | Transit rate (ft/s) | Transit length (ft) | Depth below water surface (ft) | Open-nozzle time interval (sec) | Lab Results | |
	P-61	P-6	DI	FP					SSC (mg/L)	%finer
12/21/2018@1335	X		X		1.0	~10.5			228	25.2
12/21/2018@1338	X		X		1.0	~10.5			217	25.7
12/21/2018@1341	X		X		1.0	~10.5			200	28.1
12/21/2018@1342	X		X		1.0	~10.5			227	23.9
12/21/2018@1344	X		X		1.0	~10.5			200	27.8
12/21/2018@1346	X		X		1.0	~10.5			237	23.7
12/21/2018@1349	X			X			7	17	244	22.5
12/21/2018@1350	X			X			7	17	232	25.5
12/21/2018@1352	X			X			7	17	265	22.3
12/21/2018@1354	X			X			7	17	224	26.1
12/21/2018@1356	X			X			7	17	231	24.3
12/21/2018@1357	X			X			7	17	261	22.2
12/21/2018@1413		X		X			7	17	275	20.3
12/21/2018@1415		X		X			7	17	248	22.8
12/21/2018@1417		X		X			7	17	212	27.3
12/21/2018@1418		X		X			7	17	244	22.8
12/21/2018@1420		X		X			7	17	239	23.6
12/21/2018@1422		X		X			7	17	207	27.2
12/21/2018@1424		X	X		1.0	~10.5			234	25.2
12/21/2018@1426		X	X		1.0	~10.5			209	27.3
12/21/2018@1428		X	X		1.0	~10.5			198	29.3
12/21/2018@1430		X	X		1.0	~10.5			270	21.3
12/21/2018@1431		X	X		1.0	~10.5			190	30.0
12/21/2018@1433		X	X		1.0	~10.5			225	25.6
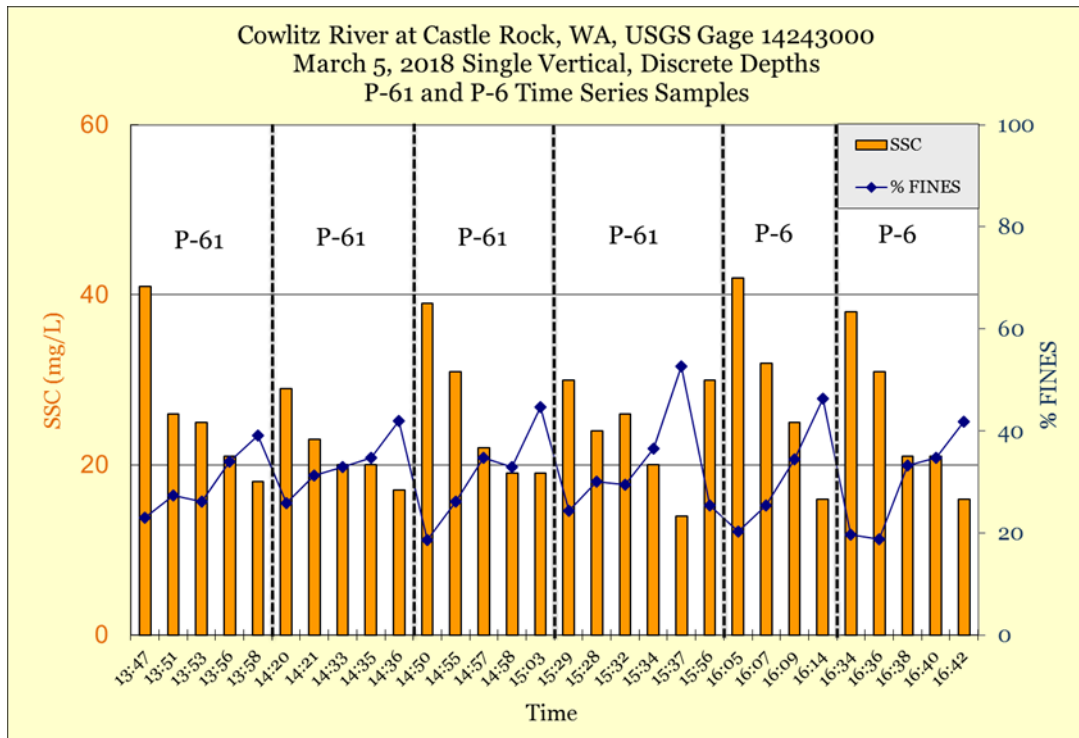
Figure 1. Cowlitz River at Castle Rock point sample SSC and %finer results. Samples taken successively at various depths, from near bed to near surface, repetitively.

Sample collection on December 19, at the Toutle River gage, occurred at streamflow of 5,800 ft³/s during a slow recession from a peak about 24 hours previous (sharp rise in 14 hours from 2,000 ft³/s to 10,000 ft³/s). Figure 2 shows sample concentrations; 15-minute values of turbidity (scaled by multiplying raw value by 35) and discharge (both provisional) show a general declining trend in streamflow and SSC. Average values of the four sets of samples are plotted as well; these data show about 10% greater spread in SSC range for P-61 DI samples against later P-6 DI samples, and a 2% (on average) greater amount of sand in the P-6 samples. In the interval between P-61 DI and P-6 DI sampling, notes indicate stream depth increased approximately 0.7 ft (presumably a bed elevation change). Point samples show a tighter grouping for both samplers, with only about 3.5% difference from low to high SSC. Average %finer values between the two sets of point samples differed by less than one percent. Visual comparison shows that in context of declining streamflow and turbidity trends, the two samplers produced reasonably equivalent results.

Sample collection on December 21, at the Cowlitz River in Castle Rock gage, occurred at streamflow of about 14,800 ft³/s during continued slow recession from the peak on December 18. Figure 3 shows sample SSC and 15-minute streamflow values that indicate a general declining trend. Average values of the four sets of samples are plotted as well. Opposite to data from two days previous, here the P-6 DI sample grouping is wider than the P-61 DI set (P-6 range about 20% greater than P-61 range). However, average SSC and %finer values for the two DI sample sets differed by only a percentage point. Point samples showed similar differences in range and average, with P-6 sample SSC having about 20% greater range, but close agreement with the P-61 in both mean SSC and mean %finer values.
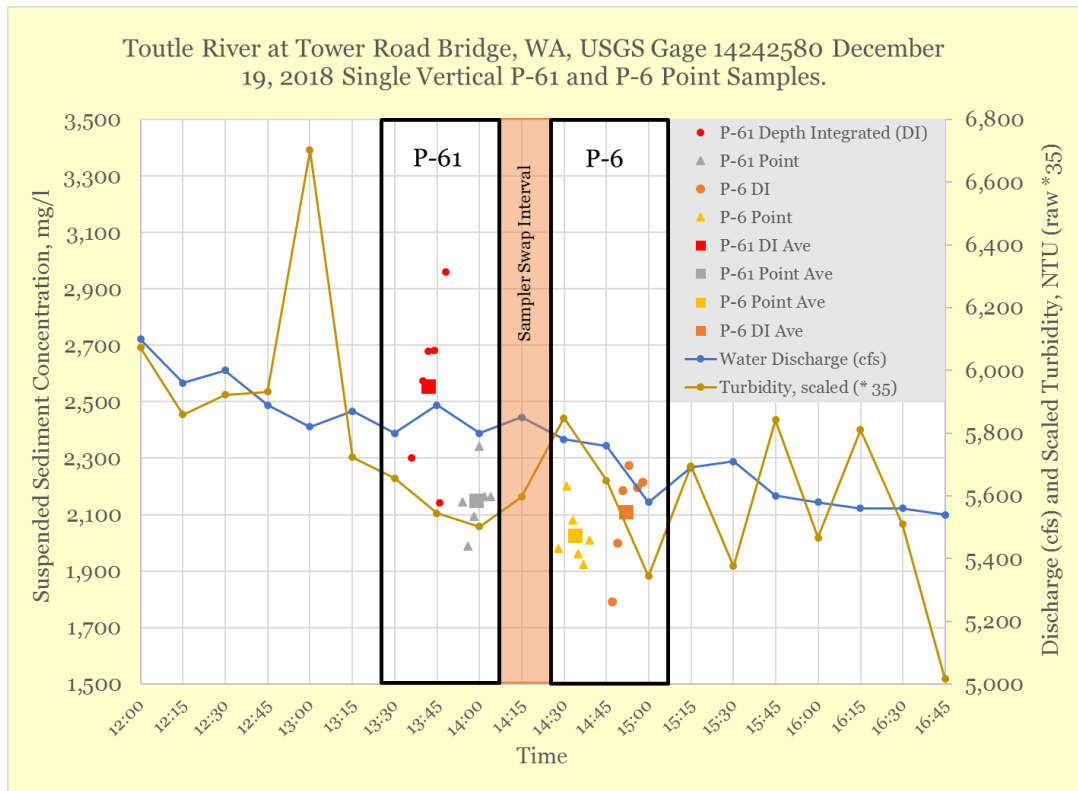
Figure 2. Toutle River at Tower Road DI and point sample SSC. Samples taken at same vertical and depths.
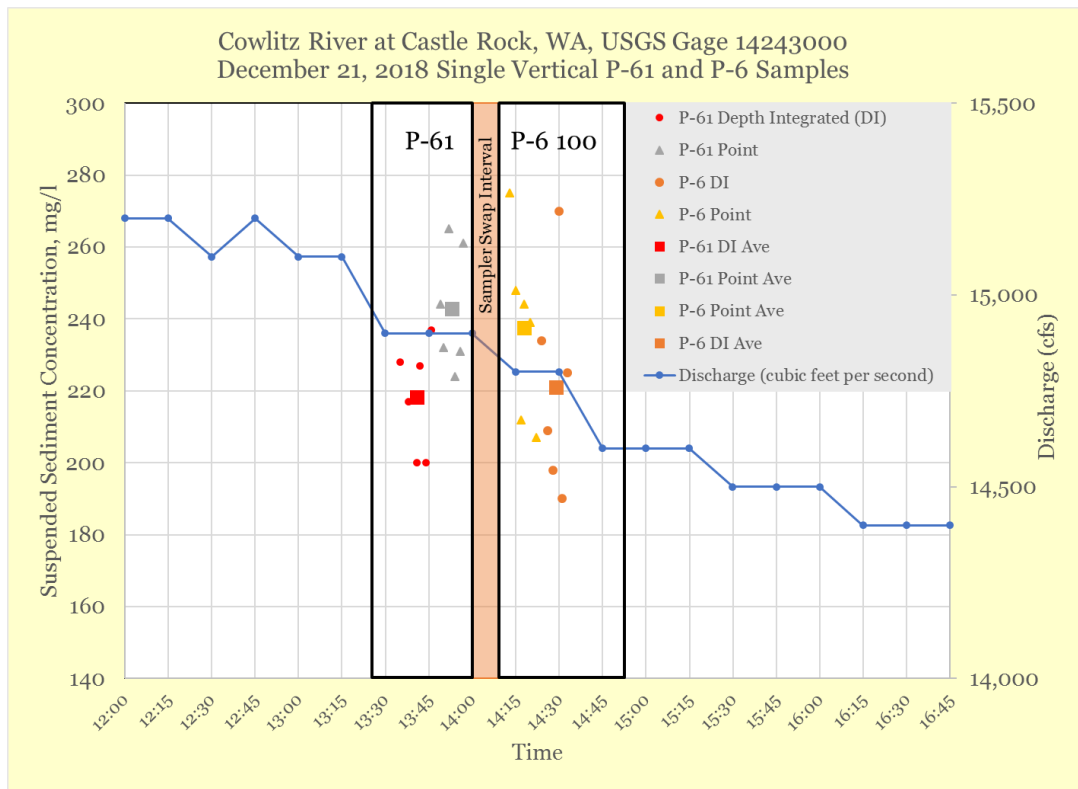

Figure 3. Cowlitz River at Castle Rock DI and point sample SSC. Samples taken at same vertical and depths.

Conclusions

Collectively, these sample sets show general agreement over a range of flow and concentration values. Despite the lack of perfect congruence in time and place, the results indicate that the two samplers produce reasonably consistent results. While this was the expected result of the study, these data document the compatibility of use between the two samplers and serve to bolster confidence that adoption of the P-6 will not introduce bias in any time series of samples collected with the P-61.

Acknowledgements

References

Federal Interagency Sedimentation Project. 1944. "Comparative field tests on suspended-sediment samplers progress report", Report C, 58 p.; https://water.usgs.gov/fisp/docs/Report_C.pdf.

Federal Interagency Sedimentation Project. 2011. "US P-6 Point integrating suspended-sediment sampler", Technical Memorandum 2011.01, 9 p.; https://water.usgs.gov/fisp/docs/FISP_Tech_Memo_US_P-6.pdf.

Federal Interagency Sedimentation Project. 2012. "Minutes of the FISP Technical Committee—Spring 2012", 9 p.; https://water.usgs.gov/fisp/docs/FISP_TechCom_Minutes_Spring2012.pdf.

U.S. Geological Survey. 2019a. "USGS Current conditions for USGS 14242580 Toutle River at Tower Road near Silver Lake, WA", https://waterdata.usgs.gov/nwis/uv?site_no=14242580.

U.S. Geological Survey. 2019b. "USGS Current conditions for USGS 14243000 Cowlitz River at Castle Rock, WA", https://waterdata.usgs.gov/nwis/uv?site_no=14243000.

Paleoflood Hydrology of the Deadwood River, Idaho

Jeanne Godaire, Geologist, Bureau of Reclamation, Denver, CO, jgodaire@usbr.gov
Caroline Ubing, Hydraulic Engineer, Bureau of Reclamation, Denver, CO, cubing@usbr.gov
Amanda Stone, Hydraulic Engineer, Bureau of Reclamation, Denver, CO, astone@usbr.gov
Jennifer Bountry, Hydraulic Engineer, Bureau of Reclamation, Denver, CO, jbountry@usbr.gov

Introduction

Most conventional estimates for the frequency of large floods are based on extrapolations from stream gaging records, commonly with record lengths shorter than 100 years. While flood frequency can be estimated to about two times the record length, estimates greater than 200 years can be vastly improved by including historical flood information and paleoflood data. In the United States, peak discharge estimates of historical (pre-systematic record) floods may extend flood frequency estimates up to several hundred years. In the Deadwood River Basin, Idaho, streamgage records are relatively short, or are relatively long but have been regulated for the majority of the period of record by Deadwood Dam. The addition of paleoflood data provided a long term perspective on extreme floods for a 10-mile valley segment on the Deadwood River and helped direct the flood frequency curve at low annual exceedance probabilities (AEPs), which is critical when assessing hydrologic risk posed by infrastructure to downstream populations.

Setting

The Deadwood River has its headwaters in the Sawtooth and Boise Mountain Ranges in western Idaho and has a basin area of 226 mi². From its headwaters at elevations near 9,000 ft, the Deadwood River flows south into Deadwood Reservoir, located upstream from Lowman, Idaho (Figure 1). Downstream of Deadwood Dam in the study reach, several minor tributaries flow into Deadwood River before the river reaches its confluence with the South Fork Payette River west of Lowman, Idaho. The Deadwood River watershed lies within a relatively wet region of the mountains. The range of mean annual precipitation (MAP) within the watershed is 28 to 66 inches. All annual peak floods during the period of measurement record occur during the months of April, May, and June, indicating that this system is driven by snowmelt or rain-on-snow floods.

Granitic bedrock of the Idaho Batholith forms the canyon walls that bound the river. The character of channel alluvium varies within the study reach, ranging from a cobble-boulder channel bed in high-gradient reaches and sand-pebble channel bed in low-gradient reaches. Channel morphology consists of irregular meanders separated by straight reaches of varying lengths. This morphology is likely controlled by a combination of the varying resistance of local bedrock to erosion and tributary alluvial fans that contribute bouldery and cobbly sediment to the channels.
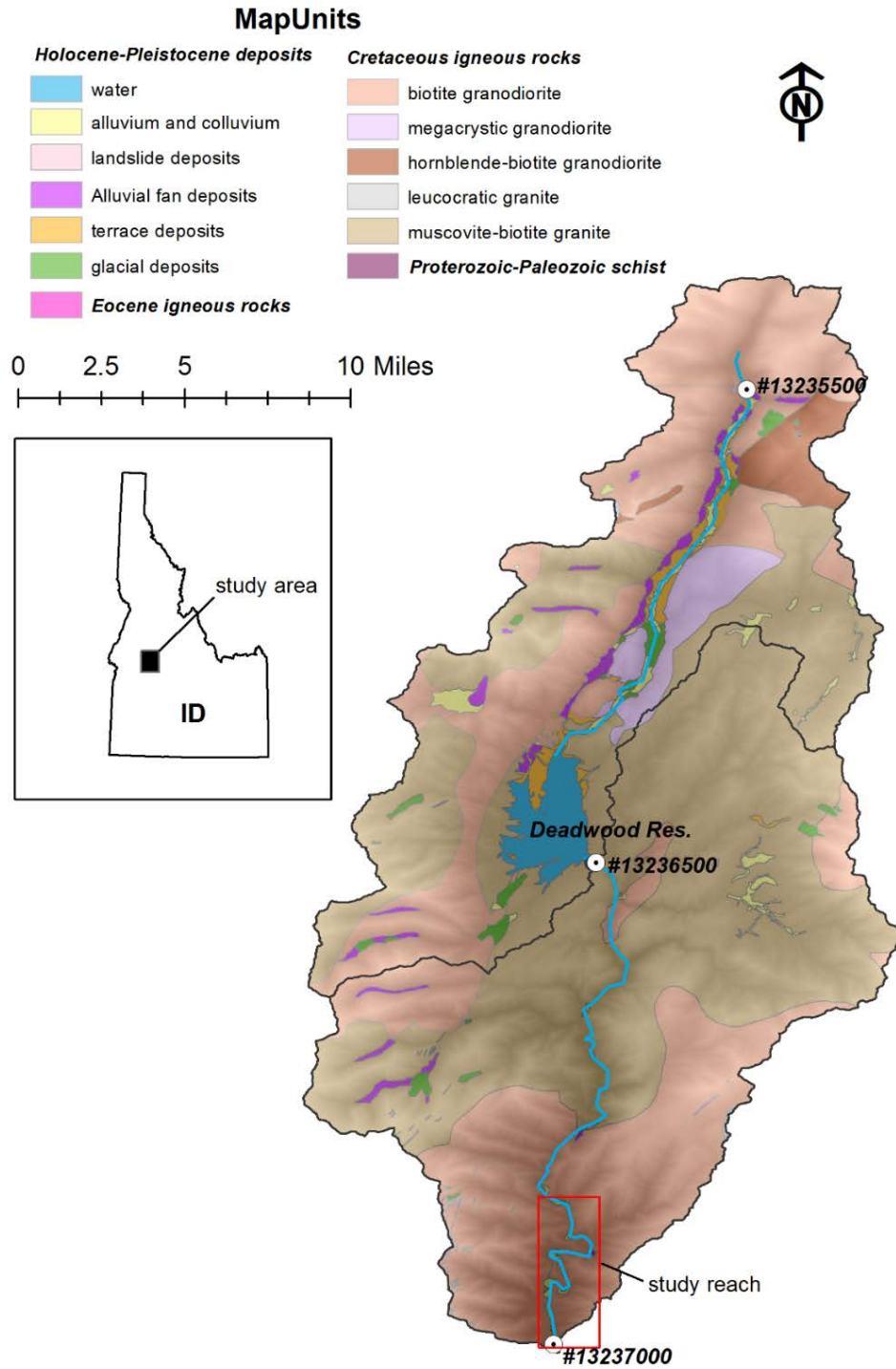
Figure 1 Overview of the upper Deadwood River watershed, showing location of Deadwood River study reach (red box), general geology, and stream gages (white circles). The hydromet gage, DEDI, is located downstream of Deadwood Dam.

Methods

This study utilizes stream terraces formed along the Deadwood River to develop pre-systematic record hydrologic data regarding extreme floods in the Deadwood River basin. Nonexceedance bounds, which provide a credible limit to the magnitude and frequency of extreme floods in the geologic record, can be developed by estimating the stage and corresponding range of discharges that have not been exceeded over the time period of terrace stabilization (Levish, 2002).

Soils were described following USDA standards (Soil Survey Division Staff, 1993) and modified terminology from Birkeland (1999). Charcoal samples were collected from the soil profiles, identified and submitted for radiocarbon analysis to obtain age estimates for the period of surface stabilization. Surface horizons at each pit were sampled to characterize surface sediment grain size for shear stress estimates in the hydraulic modeling that would be required to mobilize the surface sediment. The samples were submitted to the Colorado State University Soil Laboratory for particle size analysis (hydrometer, ASTM, 2014), sand fraction (1mm, 0.5mm, 0.125mm, and 0.0039 mm sieve sizes) and gravel fraction (> 2mm sieve sizes)

The SRH-2D (Lai, 2008) hydraulics model (version 2.2) was used to estimate peak discharges for paleoflood and non-exceedance bounds. This model solves the two-dimensional (2D) depth-averaged dynamic wave equations using a finite volume numerical scheme. SRH-2D utilizes an implicit scheme for time integration to achieve solution robustness and efficiency and makes use of a flexible mesh (Lai, 2010) that can incorporate various mesh resolutions and roughness zones. This zonal modeling concept allows for greater modeling detail in areas of interest that ultimately leads to increased modeling efficiency through a compromise between solution accuracy and computing demand. For the topographic base, Light Detection and Ranging (Lidar) data collected during August 2015 were used to develop a terrain and grid. Although Lidar does not include bathymetric data, the terrain accurately represents the dominant channel and valley topography necessary for floodplain and terrace inundation analysis. While channel erosion and aggradation is likely to occur during floods, the model assumes that the current topography represents an equilibrium condition for the purposes of this analysis due to the armored bed condition and likely presence of shallow bedrock in the channel.

To account for hydraulic model and topographic uncertainty, a range of flows is developed for each site. For paleoflood sites, the range is developed using the wetting flow or the discharge required to just inundate a surface, and the flow that covers the site with up to 2 ft of water. For non-exceedance flows, the range is developed using the wetting flow as a minimum and the flow that exceeds the Shield's critical stress value (τ^*) up to the discharge that covers the site with approximately 2 ft of water.

The Expected Moments Algorithm (EMA; Lane, 1995; Lane and Cohn, 1996) is a moments-based parameter estimation procedure that was designed to incorporate numerous sources of information – including systematic, historical, and paleoflood data – into flood frequency analysis. The core assumption of EMA is that a Log-Pearson type III (LP3) distribution can be used to model peak discharge data. PeakfqSA version 0.998 (England, et al. 2018) was utilized to analyze the data using the EMA method described above. In order to estimate a series of annual peak flows at Deadwood Dam given the low number of observed unregulated peaks, nearby gage data was used in combination with the Hydromet estimated daily unregulated inflows to develop a systematic peak record.

Results

Paleoflood Hydrology

The soil/stratigraphic sites within the study reach were selected based on the presence of stream terrace deposits that appeared to be near or above the highest stage of historical floods as recorded at USGS gaging stations and whose morphological character appeared to have minimal disturbance to their surfaces. Eight soil/stratigraphic sites were analyzed along the 10-mile long model reach. Two main terrace levels are described in the study and are approximately 4-7 ft (T2) and 6-11 ft (T1) above the river. The younger (T2) terrace is prevalent along the study reach and shows evidence for historical inundation with irregular topography and surface channelization. The older (T1) terrace is a broad, planar surface along the study reach and shows evidence for surface stability through development of a surface soil, with no evidence of recent inundation.

One non-exceedance bound for the T1 terrace was developed from data gathered during this study by combining non-exceedance data from five of the eight individual study sites. Although the data from each study site could be used independently, the combination of model output and radiocarbon data from multiple sites provides a more robust estimate by accounting for the uncertainty of age and discharge estimates for alluvial deposits that would be mapped as correlative terraces along the river. Terraces at each of the five sites have similar planar surface morphology and soil development, with all soils exhibiting Bw horizon development, which includes changes in color and structure.

To develop the age estimate for the non-exceedance bound on the T1 terrace, the 2σ distribution of the relevant radiocarbon ages from the soil profiles were plotted in Oxcal v. 4.2 (https://c14.arch.ox.ac.uk/oxcal.html; Bronk Ramsey, 2009). The upper and lower age outliers were discarded to obtain a range of 3,175 to 1,415 Cal BP using a total of 7 radiocarbon ages. Based on the median age of the radiocarbon data, the preferred age estimate is 2,740 Cal BP. The discharge estimate was obtained by combining the discharges from the 5 sites that inundated the terrace surface as a lower bound and that exceeded critical shear stress and/or inundated the surface by an approximate 2-ft depth as an upper bound. Peak discharges using this method ranged from 7,000 to 15,000 ft³/s for the non-exceedance bound.

Flood Frequency Analysis

In order to utilize the data in flood frequency analysis for estimating the hazard at Deadwood Dam, the age estimate is modified by adding 65 years to account for the 1950 datum in the radiocarbon calibration curve while the discharge estimate is transposed to the drainage area of Deadwood Dam using an exponent of 0.94 in Berenbrock (2002). The modified estimate ranges from 4,000-7,000 ft³/s with an age estimate of 1,480 to 3,240 years.

The final systematic record consists of 90 years of peak discharge data with temporal range Water Years 1927-2017. The median estimate from EMA adequately represents both the systematic and the paleoflood data. The systematic data is entirely contained within the EMA confidence limits. Using 90 years of systematic data and paleoflood non-exceedance bound, the confidence limits are very reasonable, especially for events as rare as annual exceedance probability (AEP) of 1/10,000 (Figure 2).

The range in discharges for the non-exceedance bound developed along the Deadwood River spans the value of the envelope curve (6,000 ft³/s) and plots above most of the historical peak

data derived from reservoir inflow curves and regional systematic gage records (Figure 3). This implies that the envelope curve and non-exceedance data provide a reasonable limit of flood magnitude for a drainage area of the Deadwood River near Deadwood Dam (110 mi²) for at least the last ~3,000 years.
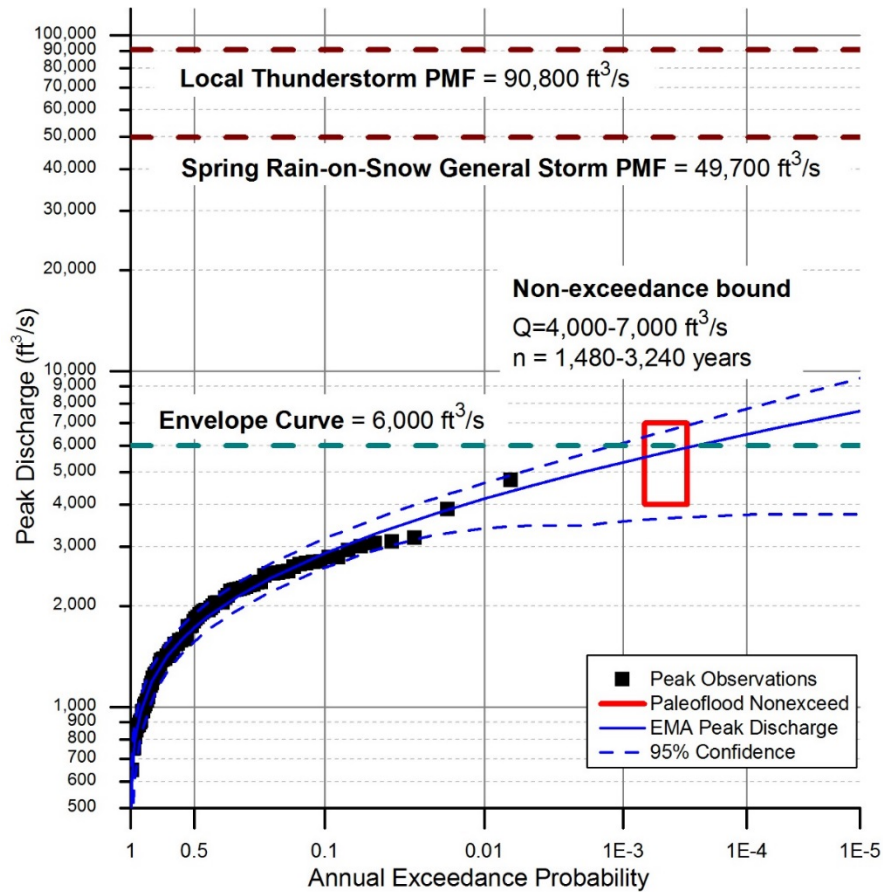
Figure 2. EMA peak discharge frequency curve, Deadwood River at Deadwood Dam, Idaho
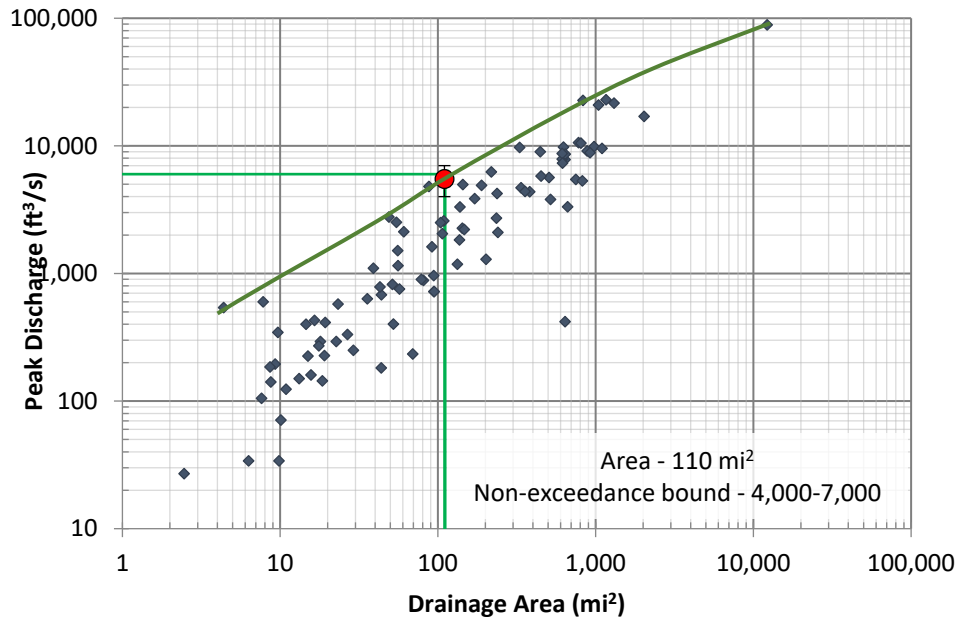
Figure 3. Regional envelope curve in the vicinity of the Deadwood River. Red square shows the non-exceedance bound and uncertainty. Blue symbols represent peak discharges from regional streamgage records.

References

Berenbrock, C., 2002. "Estimating the Magnitude of Peak Flows at Selected Recurrence Intervals for Streams in Idaho," U.S. Geological Survey Water-Resources Investigations Report 02-4170, 59 p.

Birkeland, P.W., 1999. Soils and Geomorphology. Oxford University Press, New York, 448 p.

Bronk Ramsey, C., 2009. "Bayesian analysis of radiocarbon dates," Radiocarbon, v. 51, no.1, p.337-360.

England, J.F., Jr., Cohn, T.A., Faber, B.A., Stedinger, J.R., Thomas, W.O., Jr., Veilleux, A.G., Kiang, J.E., and Mason, R.R., Jr., 2018, Guidelines for determining flood flow frequency—Bulletin 17C: U.S. Geological Survey Techniques and Methods, book 4, chap. B5, 148 p., https://doi.org/10.3133/tm4B5.

Lai, Y.G., 2008. SRH-2D version 2: Theory and User's Manual. U.S. Department of the Interior, Bureau of Reclamation Technical Service Center, Denver, CO.

Lane, W.L., 1995. "Method of moments approach to historical data, informal handout,"Bulletin 17B Working Group, Hydrology Subcommittee, Interagency Advisory Committee on Water Data, 2 p.

Lane, W.L., and T.A. Cohn, 1996. "Expected moments algorithm for flood frequency analysis," North American Water and Environment Congress, edited by C.T. Bathala, American Society of Civil Engineers, Anaheim, California.

Levish, D.R., 2002. "Paleohydrologic bounds--non-exceedance information for flood hazard Assessment," in House, P.K., Webb, R.H., Baker, V.R., and Levish, D.R., (eds.), Ancient Floods, Modern Hazards, Principles and Applications of Paleoflood Hydrology: Washington, D.C., American Geophysical Union, Water and Science Application 5, p. 175-190.

Soil Survey Division Staff, 1993. Soil survey manual. Soil Conservation Service, U.S. Department of Agriculture Handbook 18.

Process-Based Evolution Models of Steep River Channels by Migration of Bedrock Steps

Authors: Aaron A. Hurst (Aaron.Hurst@colorado.edu), Robert S. Anderson, & John P. Crimaldi

Abstract: Bedrock erosion is an important driver of landscape evolution, as it governs the base level lowering rate in mountainous landscapes. In many settings, the lateral migration of bedrock steps or small knickpoints accomplishes most of the vertical erosion in bedrock channels. However, most models of channel evolution focus on abrasion without accounting for the entrainment of blocks at the downstream edges of bed steps. Therefore, the magnitude of channel erosion and the detailed geometry of bedrock channels are not captured well. The diverse erosional components of bedrock channels prevent treatment as a continuum, and so to address this we present our first attempts to incorporate bedrock step migration in channel evolution models by explicitly tracking the extraction of individual blocks on a channel bed comprised of discrete blocks of prescribed size and aspect ratio. We base their probability of entrainment on the physics of block toppling and sliding. In the required force balance, we include the effects of a pressure difference between the upstream and downstream faces of the block. We inform the pressure fields and the probability of toppling and sliding of blocks with Computational Fluid Dynamics (CFD) experiments. In particular, for a prescribed water discharge, we explore the effects of the block aspect ratio on the forces that promote block motion. Varying the aspect of a block in the lee of a step affects the pressure fluctuations downstream of the block by altering the length of the recirculation zone. Low fluctuations in this pressure enhance block entrainment. Both abrasion and plucking of the bed are prevented in the topographic lows in the channel where sediment preferentially accumulates. Together, these rules allow self-organization of the bed into small-scale knick zones that propagate upstream. The location and longevity of the knick zones are governed by joint spacing (block size) and lithology. The propagation of the knick zone stalls at larger block sizes and more resistant lithologies. This work illustrates the roles of block size and aspect ratio, and hence of the geological setting, in governing the pace and the shape of evolving bedrock channels.

Refining the Baseline Sediment Budget for the Klamath River, California

Chauncey Anderson, Hydrologist, U.S.G.S. Oregon Water Science Center,
2130 SW 5th Ave., Portland, OR, 97201, chauncey@usgs.gov, 503-251-3206
Scott Wright, Hydrologist, U.S.G.S. California Water Science Center,
6000 J Street, Placer Hall, Sacramento, CA, 95819, sawright@usgs.gov, 916-278-3024
Liam Schenk, Hydrologist, U.S.G.S. Oregon Water Science Center,
2795 Anderson Ave., Suite 106, Klamath Falls, OR, lschenk@usgs.gov, 541.273.8689 x208
Katherine Skalak, Research Hydrologist, U.S.G.S. Earth Systems Processes Division,
430 National Center, Reston, VA, 20192, kslakak@usgs.gov, 703-648-5435
Jennifer Curtis, Geologist, U.S.G.S. California Water Science Center,
716 W. Cedar St. Unit E Eureka, CA, 95501, jacurtis@usgs.gov, 707 834 7818
**Amy East**, Research Geologist, U.S.G.S. Pacific Coastal and Marine Science Center,
2885 Mission St., Santa Cruz, CA 95060, aeast@usgs.gov, 831-460-7533
Adam Benthem, Hydrologist, U.S. Geological Survey, New England Water Science Center,
430 National Center, Reston, VA 20192, abenthem@usgs.gov, (703) 648-5208

Abstract

Four dams in the Klamath River Hydroelectric Project (KHP) in Oregon and California (Figure 1) are currently scheduled to be removed over a period of a few weeks or months, beginning in January 2021. The Klamath dam removal will be the largest in the world by almost all measures, and is an unprecedented opportunity to advance science of river responses to such events. The KHP contains approximately 10-12 million cubic meters of mostly fine sediment and model estimates suggest approximately 1/3-2/3 of this volume is expected to be eroded from reservoirs. Much of this sediment is expected to be eventually transported by the river to, or through, the Klamath River Estuary, a distance of more than 300 kilometers.

To improve the success of restoration activities following dam removal, agencies must understand the baseline conditions for biological, chemical, and physical processes, prior to the removal. We expect large changes in water quality (turbidity, suspended sediment, dissolved oxygen, temperature, and algal toxins) and in fish habitat in the Hydroelectric Reach and the main-stem of the Klamath River to the ocean. For example, modeled sediment concentrations in the Klamath River during dam removal were estimated exceed 10,000 – 15,000 mg/L, depending on streamflows, location, and the dam removal process, and to remain > 100 – 1000 mg/L for months at a time. Final time to achieve background concentrations post dam removal may take over two years (Reclamation, 2011). Plans to assess many of these changes post-dam removal are still being formulated.
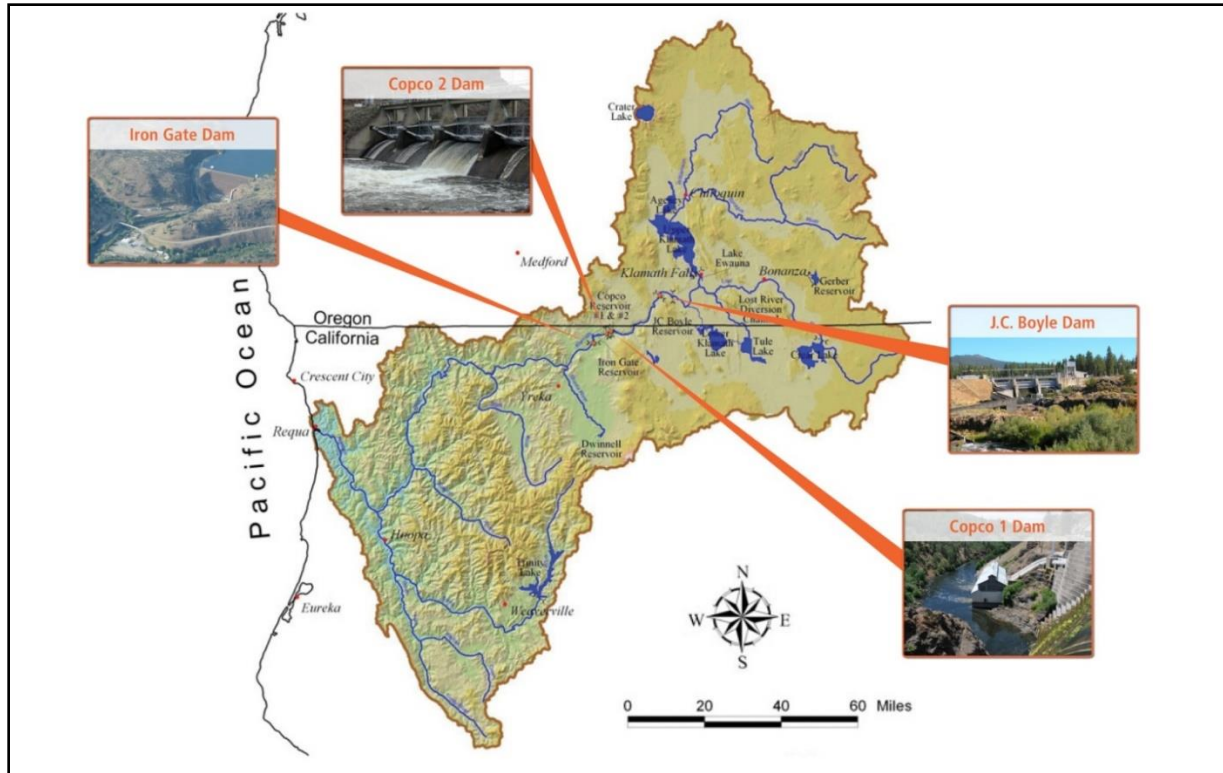
Figure 1. Map showing the Klamath River Basin in Oregon and California, including the locations and photographs of the four dams in the Klamath Hydroelectric Project (KHP) currently slated for removal in January, 2021 (source: Interior, 2012)

A sediment budget for the Klamath River downstream of the KHP aids understanding of the river's physical response to hydrologic events prior to dam removal. Accordingly, we are establishing a network of sites on the mainstem and key tributaries to estimate fine sediment loading to the river and downstream transport, including to the Klamath River Estuary in Requa, California.

Numerous other potential sediment sources contribute to the Klamath River's total sediment budget (Figure 2). These include 4 major tributaries downstream of the KHP, the Shasta, Scott, Salmon and Trinity Rivers, as well as background loading from the mainstem above the KHP (above Keno Dam), and possibly from tributaries within the KHP itself. Based on limited data on suspended sediment in the Klamath River Basin, primarily from monitoring from ~1980 – 2000 (Reclamation, 2011), the sediment volume released from the dam removal is hypothesized to be equivalent to the annual sediment load (or more) from the Trinity River, and about a third of the total annual load to the estuary, depending on the hydrology of the dam removal year. Sediment export from the estuary to the marine area has not been measured previously. Additionally, recent wildfire areas could increase contributions from smaller streams or along mainstem reaches. Recent data on the sediment contributions from most sources is limited, and additional baseline data prior to dam removal would enable better understanding of the effects of reservoir sediment releases after dam removal.
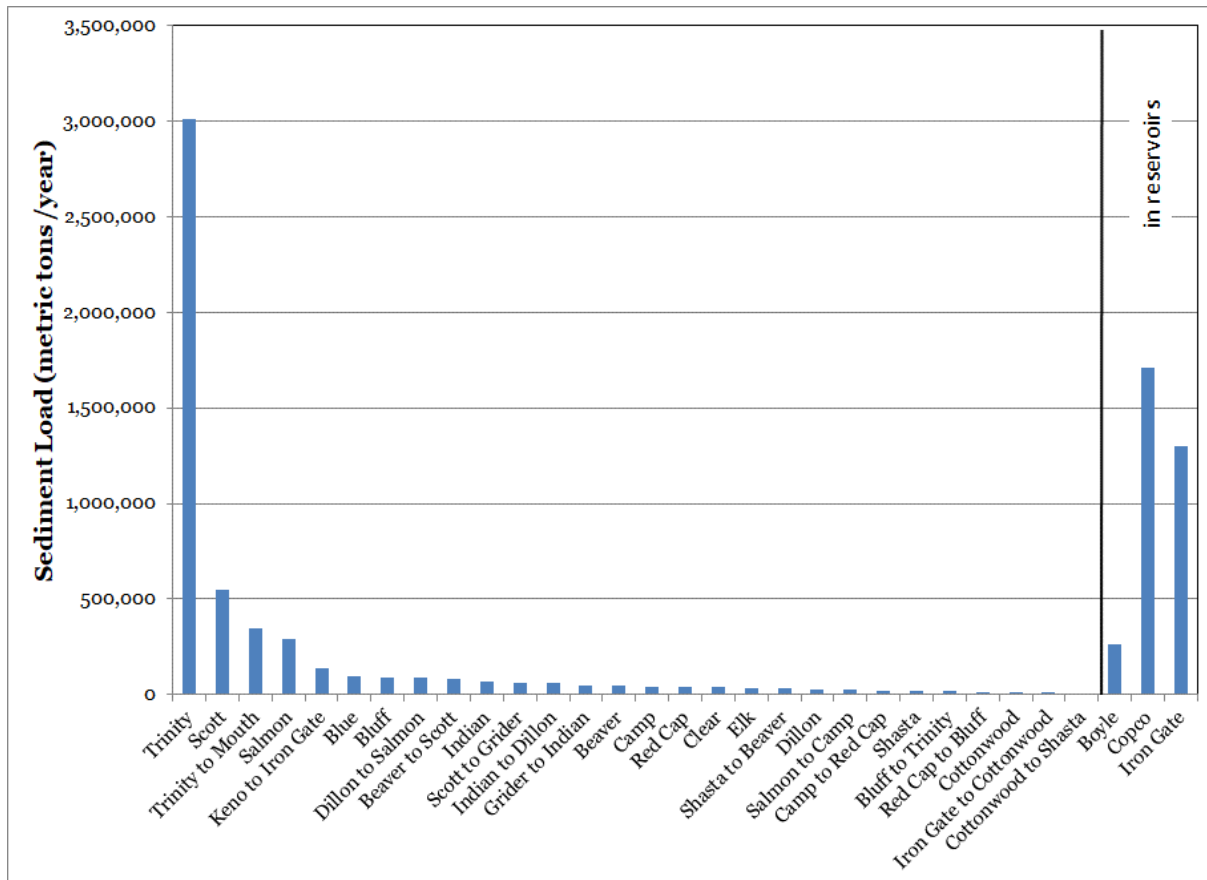
Figure 2. Annual sediment loads for individual reaches and tributaries of the Klamath River from Keno, OR, to the mouth. Also shown are the total amounts of sediment stored in the three major reservoirs in the hydroelectric reach. Source: Reclamation (2011).

A baseline sediment budget will be constructed for the entire length of the river from the KHP to the estuary. Sediment transport will be estimated using a fine-sediment network developed from existing streamgages, supplemented by additional equipment and sampling enabling continuous estimation of sediment concentrations using surrogate methods (Rasmussen et al., 2009; Landers et al., 2016). Strategic sub-reaches will be identified for detailed mapping and process-related studies for geomorphic change, textural change associated with deposition, sediment sourcing, and understanding the role of prior large events in the basin. Where possible, additional data, collected for other studies or by other entities, will used to augment data collected for our purposes. For example, recent (2018) Light Detection and Ranging (LiDAR) and bathymetric surveys completed for the Klamath River will be used to help identify strategic subreaches for intensive geomorphic analysis, define critical geometries, and quantify baseline conditions prior to dam removal. Data gathered for the sediment budget will also support studies linking changes in sediment processes with other expected changes, such as temperature regimes, nutrient delivery, food webs, and fish disease.

References

Landers, M.N., Straub, T.D., Wood, M.S., and Domanski, M.M. 2016. Sediment acoustic index method for computing continuous suspended-sediment concentrations. U. S. Geological Survey Techniques and Methods book 3, chap. C5. 63 p. http://dx.doi.org/10.3133/tm3C5.

Rasmussen, P., Gray, J.R., Glysson, G.D., and Ziegler, A.C. 2009. Guidelines and procedures for estimating time-series of suspended-sediment concentrations and loads from in-stream turbidity sensors and streamflow data. U. S. Geological Survey Techniques and Methods book 3, chapter C4. 57 p. http://pubs.usgs.gov/tm/tm3c4/.

Reclamation. 2011. Hydrology, Hydraulics and Sediment Transport Studies for the Secretary's Determination on Klamath River Dam Removal and Basin Restoration. Technical Report No. SRH-2011-02. Prepared for Mid-Pacific Region, US Bureau of Reclamation, Technical Service Center. Denver, CO. https://klamathrestoration.gov/.

U.S. Department of Interior. 2012. Klamath Dam Removal Overview Report for the Secretary of Interior – An Assessment of Science and Technical Information. U.S. Department of Interior and U.S. Department of Commerce, National Marine Fisheries Service. 420 pp. https://klamathrestoration.gov/

A Physically Based Method of Combining ADCP Velocity Data with Point Samples to Compute Suspended-Sand Discharge – Application to the Rhone River, France

Guillaume Dramais, PhD student, IRSTEA, Lyon, France,
visiting scientist at US Geological Survey, Flagstaff, Arizona, guillaume.dramais@irstea.fr
Benoît Camenen, Scientist, IRSTEA, Lyon, France, benoit.camenen@irstea.fr
Jérôme Le Coz, Scientist, IRSTEA, Lyon, France, jerome.lecoz@irstea.fr
David J. Topping, Research Hydrologist, US Geological Survey, Flagstaff, Arizona, dtopping@usgs.gov
Christophe Peteuil, Senior Engineer, CNR, Lyon, France, c.peteuil@cnr.tm.fr
Gilles Pierrefeu, Senior Engineer, CNR, Lyon, France, g.pierrefeu@cnr.tm.fr

Abstract

Measuring suspended-sand flux in rivers is a challenge since sand concentrations are highly variable in time and space throughout a river cross section. Most of the present methodologies rely on point or depth-integrated sampling (Nolan et al., 2005, Topping et al., 2016). The standard method estimates mean concentration and multiply it by discharge to compute the suspended-sand discharge. Here, we demonstrate methods of combining point suspended-sediment samples with ADCP (Acoustic Doppler Current Profiler) high-resolution depth and velocity measurements to improve vertical and lateral integration of concentration and flux. A preliminary version of this method is applied to data collected in the Rhône River in Lyon, France, during a 10-year flood in January 2018. Two options for vertically integrating the measured suspended-sediment concentrations were tested whereas lateral integration was based on nearest-neighbor interpolation only, as a baseline option. Sand flux results are similar, thus suggesting that vertical integration options may be less critical than lateral integration options that will be implemented and tested in future work.

Introduction

Estimation of suspended-sand discharge in rivers

Measuring suspended-sediment discharge in rivers is a multi-step process that requires accurate measurement of water discharge and suspended sediment throughout the river cross section. Measuring suspended-sediment concentrations that are representative of sediment conditions in a river is difficult for several reasons and many sources of uncertainties affect the final results. Because the suspended sediment is highly variable in space and time a large number of samples may be required to be representative of the suspended-sediment conditions in the cross section, especially if the suspended load is dominated by sand. Suspended sand (particles with diameter $d>63\mu m$) is not homogeneously distributed throughout the cross section; concentrations generally increase toward the river bed (*i.e.* graded suspension). Conversely, washload, which is

made of particles finer than sands (clays and silts, i.e., particles with d<63μm), is mixed more homogeneously throughout the cross-section and may be characterized with relatively fewer samples.

The cross-sectional suspended sediment discharge, Q_s [kg/s], is defined as the mass of suspended sediment passing through a specific river cross section per unit time:

$$Q_s = \int_{y=0}^{B} \int_{z=0}^{H} c(y,z) v(y,z) \mathrm{d}z \mathrm{d}y \qquad (1)$$

where v [m/s] and c [g/L] are the time-averaged velocity and suspended-sediment concentration, respectively. B and $H(y)$ [m] are the surface width and vertical depth of flow, respectively.

To compute the suspended-sand discharge in the cross section the standardized method consists of estimating the mean concentration with the sample results and multiplying it by discharge measured or computed in the river reach. The limited number of samples involves interpolating the concentration in the cross section. The aim of the proposed method is to improve vertical and lateral integration of concentrations using high-resolution ADCP depth and velocity measurements.

Methods for computing sand discharge measurement

The most popular method in the USA to compute sediment discharge is to measure the velocity-weighted suspended-sediment concentration in the cross-section using depth-integrating sampling (Edwards and Glysson, 1999) and then to multiply this concentration by the water discharge as:

$$Q_s = C \times Q \qquad (2)$$

with Q_s [kg/s] the instantaneous suspended-sediment discharge, C [g/L] the velocity-weighted suspended-sediment concentration in the river cross section and Q [m³/s] the water discharge at the same time. The method endorsed by the USGS (Porterfield, 1972; Edwards and Glysson, 1999) is described in the ISO 4363 (2002) standard as the "Conventional method" or "discharge-weighted method". In the rest of this study the method is identified as the standardized method. It is based on the computation of a velocity-weighted suspended-sediment concentration for the cross-section. The method involves dividing the cross-section by verticals into n segments. The verticals are chosen according to two methods: Equal-Width Increment method (EWI) or the Equal-Discharge Increment method (EDI). Using these methods, samples of the water–suspended-sediment mixture are collected at the local velocity in each vertical. Depth-integrated or point integrated sampling methods are used to eliminate the effect of turbulent fluctuations in concentration because they are time-averaged (Topping et al., 2011). The velocity-weighted sediment concentration averaged over the flow depth at each vertical is either that measured by a depth-integrating sampler or, when point-integrating samplers are used, a velocity-weighted spatial average of the concentrations measured at various depths. Depending on the method used to sample the cross section (EWI or EDI), samples are combined or analyzed separately for concentration. Both the mean-section and the mid-section methods from the ISO 748 (2009) standard can be applied to calculate the segmental sediment discharge. For the suspended-sand discharge the standard recommends including in the calculation the percentage of the mass of sediment coarser than a given diameter.

Limitations of the methods: In the standardized method there is no specific focus on the near-bed zone which cannot be sampled, where although sand concentrations are highest,

velocities are lowest. In the proposed method the near-bed concentrations are extrapolated using a physically-based vertical profile calibrated with point samples and ADCP velocity profiles. Because the depth-integrating samplers cannot describe vertical gradients in suspended-sand concentration, we use a point sampler in this study. The point-sample method is better suited to compute suspended-sand profiles and to extrapolate concentration throughout the vertical. The estimation of sand concentration might be improved with additional spatial information that can be provided by ADCP measurements and analyses of velocities and concentration profiles, to laterally integrate each ADCP ensemble. One other issue is that the lateral integration is done in the standardized method with a constant concentration integrated on the several segments defined above, with no constraints from depth, velocity and sediment transport along the cross-section.

Objectives

ADCP measurements from a moving boat are today a commonly used method for measuring streamflow (Mueller, 2009). The development of this method allowed a vast reduction in time spent making discharge measurements while providing large datasets with high-resolution measurements of depth, water velocity, and acoustic backscatter. We propose in this study to use this spatial information together with point suspended-sediment samples to work on the estimation of the suspended-sand discharge through the cross section. The velocity field and the bathymetry measured with the ADCP are used for the sediment discharge estimation including the extrapolation in unmeasured zones and interpolations between samples. For each cell of the ADCP, sand concentration is estimated based on a physical interpretation of both flow field and sand-concentration measurements. Some computing options for the vertical integration are tested here and applied to data collected during a flood on the Rhône River (France). We compare these computation options with the standardized method to validate this approach. The lateral integration, which is an important issue, is discussed but not yet implemented in our study.

Methodology

General methodology

The method we propose is based on typical ADCP discharge measurements and point suspended-sediment samples. The calculation procedure is based on an estimation of the concentration on a grid taken from ADCP data exports. The discharge grid from down-looking ADCPs is made of m ensembles of n cells distributed throughout the cross section. The top and bottom discharges (which are unmeasured) are extrapolated during the acquisition. These extrapolations are done according to the measurements and the user settings (Figure 1). The general idea is to assign a concentration for each cell such that, when multiplied by the ADCP discharge in this cell, it yields a good estimate of the sand flux through each cell. The total suspended-sand discharge Q_s [kg/s] can be computed such as:

$$Q_s = \sum_{j=0}^{m+1} \sum_{i=0}^{n+1} C_{ij} q_{ij} \qquad (3)$$

where C_{ij} [m/s] and q_{ij} [m³/s] are the concentration and discharge at the cell (i,j). The unmeasured zones near the edges ($j = 0, j = m + 1$), the bottom ($i = 0$) and top ($i = n + 1$)

layers are included in the computation. Thus, the interpolation and extrapolation of concentration through the verticals and between them is the main source of error.
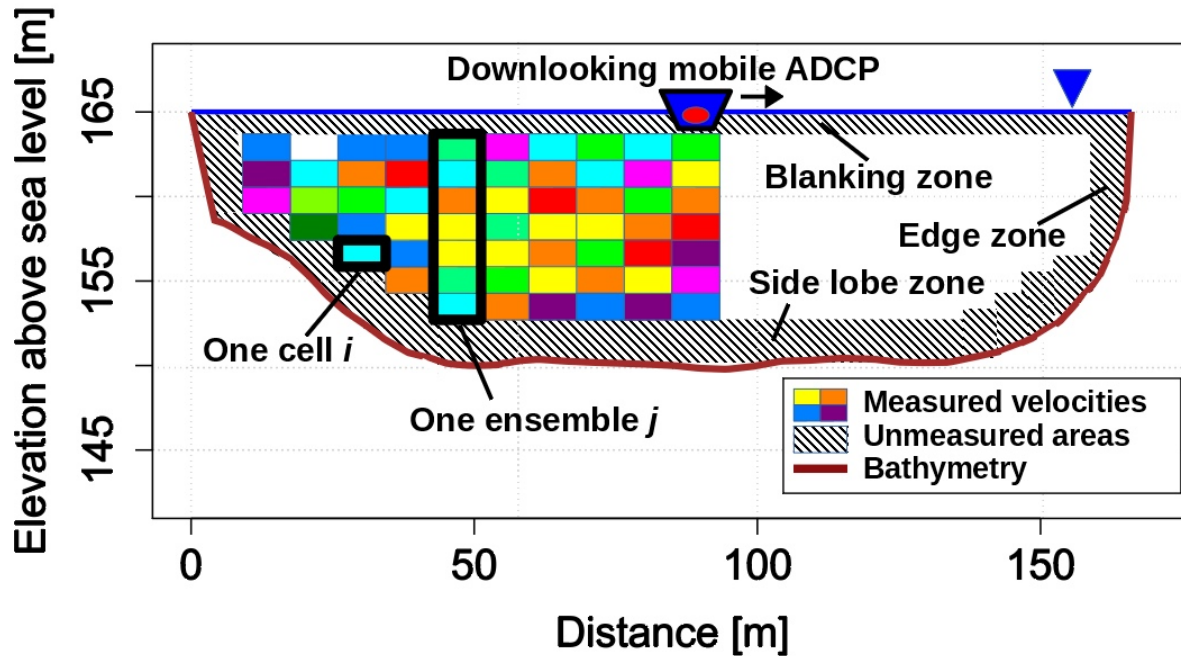
Figure 1: ADCP cross-section measurement sketch

The suspended-sand discharge φ_{ij} [kg/s] through one ADCP cell ij is:

$$\varphi_{ij} = q_{ij} \times C_{ij} = v_{ij} \times w_j \times h_{ij} \times C_{ij} \tag{4}$$

where v_{ij} [m/s] is the normal velocity, w_j [m] is the width, h_{ij} [m] is the ADCP bin size, and C_{ij} [g/L] is the time- and spatial-averaged sand concentration in the ADCP cell ij (j^{th} ensemble, i^{th} vertical cell).

In both processing options presented below, we apply the same lateral integration option, based on the mid-section method, using the concentrations around each vertical within 1/2 distance of the adjacent verticals. As for the measurement of water discharge with ADCPs, the final suspended-sediment discharge is the average of at least 4 ADCP transects computed with the sediment concentration data.

Adaptation of standardized method for depth-integrating point samples

This method is used to convert point-sample suspended-sediment concentrations to velocity-weighted suspended-sediment concentrations at each vertical j.

The flux per unit area φ'_{ij} [kg/m²/s] at each point (i, j) is calculated by multiplying the suspended-sediment concentration at each point C_{ij} [kg/m³] by the time-averaged velocity at each point v_{ij} [m/s] as:

$$\varphi'_{ij} = C_{ij} \times v_{ij} \tag{5}$$

The time-averaged velocity at each point v_{ij} is calculated using the nearest-neighbor method described above.

The velocity-weighted suspended-sediment concentration C_p [kg/m³] is then calculated for sub-section p centered on each vertical j is calculated as:

$$C_p = \frac{\sum_{i=1}^{N_{samples}} \varphi'_{ip} \times (z_{i+1} - z_{i-1})}{\overline{v_p}\, \overline{h_p}} \tag{6}$$

with $\overline{v_p}$ [m/s] and $\overline{h_p}$ [m] being the mean velocity and the mean depth of the sub-section p, respectively.

Finally, the suspended-sand discharge Q_s [kg/s] is calculated as:

$$Q_s = \frac{Q}{W} \sum_{p=1}^{N_{subsections}} C_p w_p \tag{7}$$

with Q being the water discharge [m³/s], W [m] the river width, and w_p the width of sub-section p (computed using the mid-section procedure).

Nearest-neighbor method

In this simple method, the nearest measured suspended-sediment concentration is applied to each ADCP cell. The post-processing steps for the estimation of C_{ij} are as follows:

- Every point suspended-sediment sample and every ADCP cell is located in the cross-section coordinate plane (in an elevation down from the water surface (z) and width (y) scale). In this plane we calculate for each cell (even in the unmeasured zones) with coordinates (y_{ij}, z_{ij}) the distance dm [m] to all the samples with coordinates (y_s, z_s) as:

$$dm = \sqrt{(y_s - y_{ij})^2 + (z_s - z_{ij})^2} \tag{8}$$

  The concentration of the nearest sample is assigned as the concentration of each cell ij. This results in a complete concentration grid including the unmeasured parts.
- As an exception to the rule, the concentration applied on the edge sub-section is the concentration of the nearest surface sample.
- Each cell discharge measurement q_{ij} from the water discharge grid is multiplied by each cell concentration C_{ij} from the concentration grid to obtain a suspended sand discharge, for each cell, according to equation 4.

This nearest-neighbor method splits each sub-section p around a vertical in as many horizontal slices as there are samples. If only one depth-averaged concentration per sampling vertical is available, only one slice is made and the computing method is the same as the standardized method.

Physically based method

To provide a better approach to assigning concentrations to individual cells in each vertical, based on the point suspended sediment sample concentrations, we also developed a physically based method using Rouse mechanics to interpolate sediment concentrations in the z dimension at each vertical. Velocity profiles can be represented by a logarithmic vertical profile in the inner

region (Smart, 1999):

$$\frac{u(z)}{U^*} = \frac{1}{k} \ln\left(\frac{z}{z_0}\right) \tag{9}$$

where u is the local, time-average velocity, U^* [m/s] the shear velocity, k the Von Kármán's constant, and z the distance from z_o, the Nikuradse roughness parameter. U^* is computed as a function of the depth-averaged velocity and z_0:

$$U^* = \sqrt{C_D} \times U \tag{10}$$

with the current friction coefficient $C_D = \left\{\frac{k}{(1+\ln(z_0/h))}\right\}^2$

Because $U = q_j/(w_j h_j)$, the only parameter to estimate is z_0. This estimation was based on ensemble-averaging.

An exponential relationship was employed to characterize the Rouse-style reduction in suspended-sand concentration with distance from the bed (Camenen et al., 2008):

$$C(z) = C_R \exp\left(\alpha \frac{z}{h}\right) \tag{11}$$

This equation was fit to the point-sample data at each vertical and then applied to each sub-section p around each vertical, allowing the reference concentration at a z_o level: C_R [g/L] and the coefficient α to be determined.

Equation 11 was then used to predict the suspended-sand concentration profile over the water column.

The sediment flux at each elevation $\phi_p(z)$ in each sub-section k is then computed by multiplying equations (9) and (11), as follows.

$$\phi_p(z) = C_{p(z)} u_{p(z)} = U_p^*/k \, \ln\left(\frac{z}{z_{0p}}\right) C_{Rp} \exp\left(\frac{\alpha_p z}{h}\right) \tag{12}$$

Equation 12 is then integrated vertically and subsequently laterally to compute the suspended-sand discharge through the cross-section.

As a modification to this method, it is possible to compute a sediment flux for each ADCP vertical j, to improve the lateral integration. Indeed, it is then possible to have a model for the sand flux vertical profile:

$$\phi_j(z) = C_{j(z)} u_{j(z)} = U_j^*/k \ln\left(\frac{z}{z_{0j}}\right) C_{Rj} \exp\left(\frac{\alpha_j z}{h}\right) \tag{13}$$

For each vertical j for the ADCP grid, one can estimate U_j^*, z_{0j}, C_{Rj} and α_j using an interpolation between each measured vertical or assuming on the edge some relationship to water depth with,

$$U_j^* \propto \sqrt{h}, C_{Rj} \propto h \tag{14}$$

The suspended-sand concentration for each cell can then be estimated as:

$$C_{ij} = \frac{1}{q_{ij} w_j h_{ij}} \int_{z_{i,j}}^{z_{i+1,j}} \phi_j(z) dz \tag{15}$$

with $h_{ij} = z_{i,j+1} - z_{i,j}$ and w_j the height and the width of the cell ij, respectively

This option is not yet implemented in the code and will be tested to improve the lateral integration.

Application to a flood on the Rhône River, France

Field survey and dataset

The Rhône River is one of the major rivers of Europe, heading at the Rhône Glacier in the Alps, and running through southeastern France (Figure 2). The Rhône river drains a catchment of about 95,000 km². The mean annual discharge is 1700 m³/s. The river has been largely modified since the middle of the 20th century (sediment dredging, levees, dams on the river and on its tributaries). Despite large modifications, the Rhône River remains the main tributary of the Mediterranean Sea by mean sediment flux. It is mostly a gravel-bed river in France. The study site is in the city of Lyon. The dataset results from 4 surveys carried out during a 10-year recurrence-interval flood in January 2018. The range of investigated discharges varied from 1,900 to 2,700 m³/s during the successive phases of the flood (Figure 3).
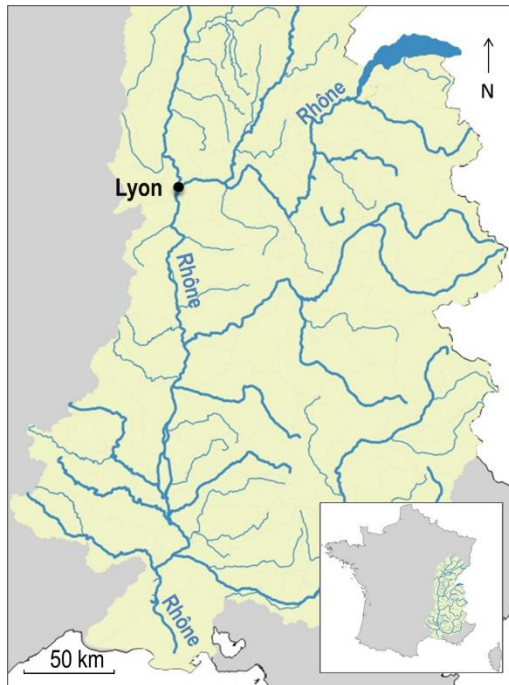
Figure 2: The Rhône River catchment
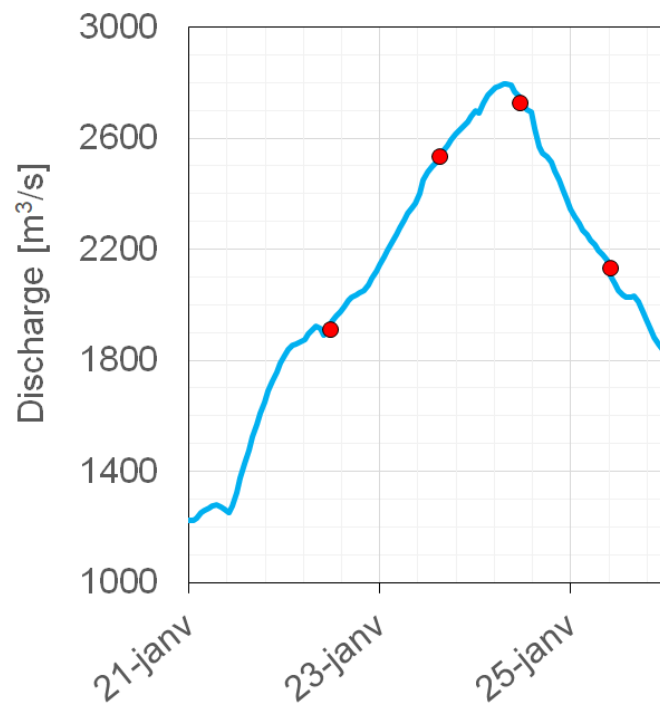
Figure 3 : Discharge during the 2018 flood (blue line) and sampling surveys (red dots)
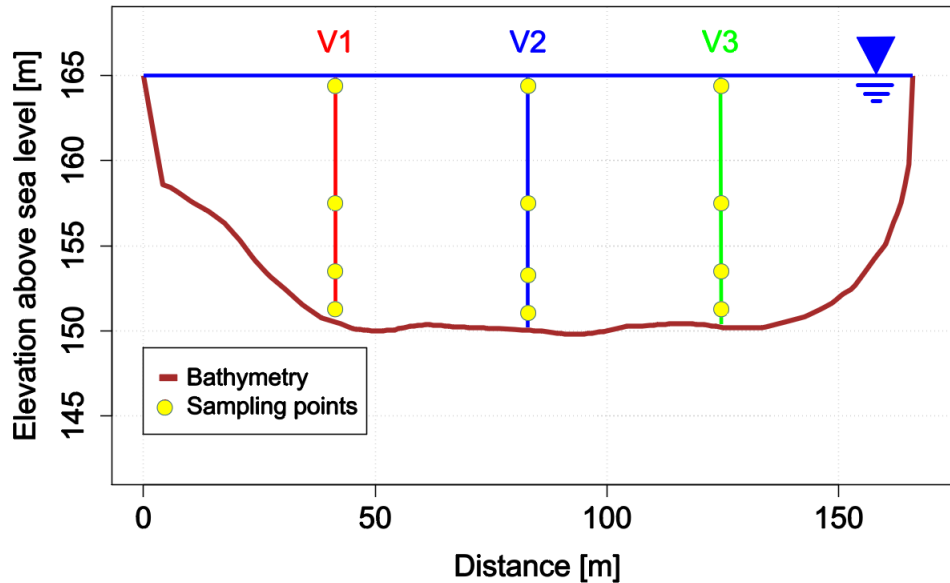
Figure 4 : Samples and verticals position sketch

Each suspended-sediment sampling survey consisted of a set of 12 point-samples distributed throughout a cross-section. Three verticals were sampled following the EWI option. The sampler was a 2-liter Van Dorn bottle that could be opened at both ends. This sampler was deployed as follows. Upstream from the sampled cross section, the open bottle was lowered from a boat into the river on a cable until it reached the target depth. During this phase the boat drifted downstream to the cross-section where the cable became vertical. To achieved the verticality of the cable, the boat's drifted velocity must be higher than the sampler's drifted. Sampling commenced by closing the bottle by sending a weighted trigger (messenger) down the cable. We also took ADCP velocity and discharge measurements (600 and 1200 kHz) at the same time according to our standard procedure.

Sediment characteristics

Analyses of the suspended-sediment samples were conducted in the laboratory by sieving and filtering according to the ASTM D3977 (2013) standard. Both sand and silt concentrations were measured on each point sample in each set. Our analyses on the Rhône samples showed that silt and clay-sized sediment (d<63μm) were well mixed in the cross section during the surveys and could be considered as washload. We observed substantial gradients in the profiles of sand concentration (Figure 5) and grain size. The amount of sand in suspension was relatively small compared to most sandy rivers, but it was substantial for the Rhône River. The median grain-size (d50) of the sand-size sediment was between 100 and 350 μm and the grain size first fined and then coarsened during the event.
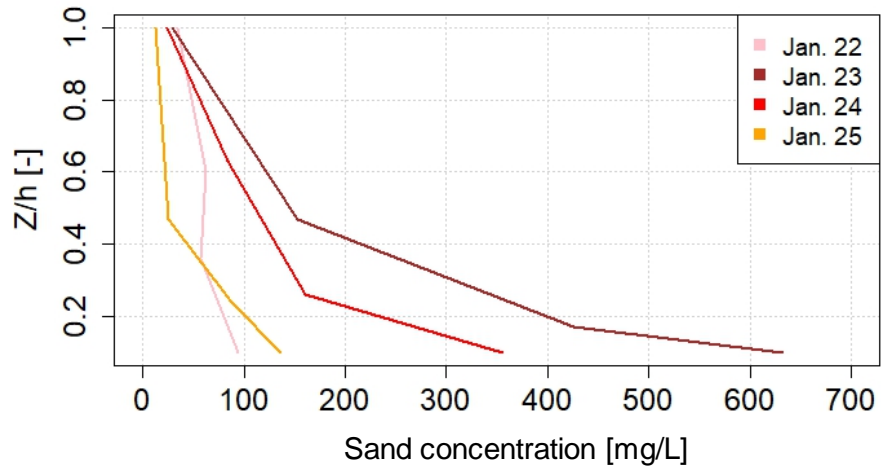
Figure 5: Evolution of the sand concentration profiles on the middle vertical (V2) during 4 days of the flood

Estimation of sediment fluxes

33 ADCP transects were computed for the flood event. Figure 6a shows an example of the concentration grid computed with ADCP and sand-concentration data using the nearest-neighbor interpolation method applied to individual point samples. The figure 6b shows an example of the velocity-weighted sand concentration grid computed for each ADCP cells.
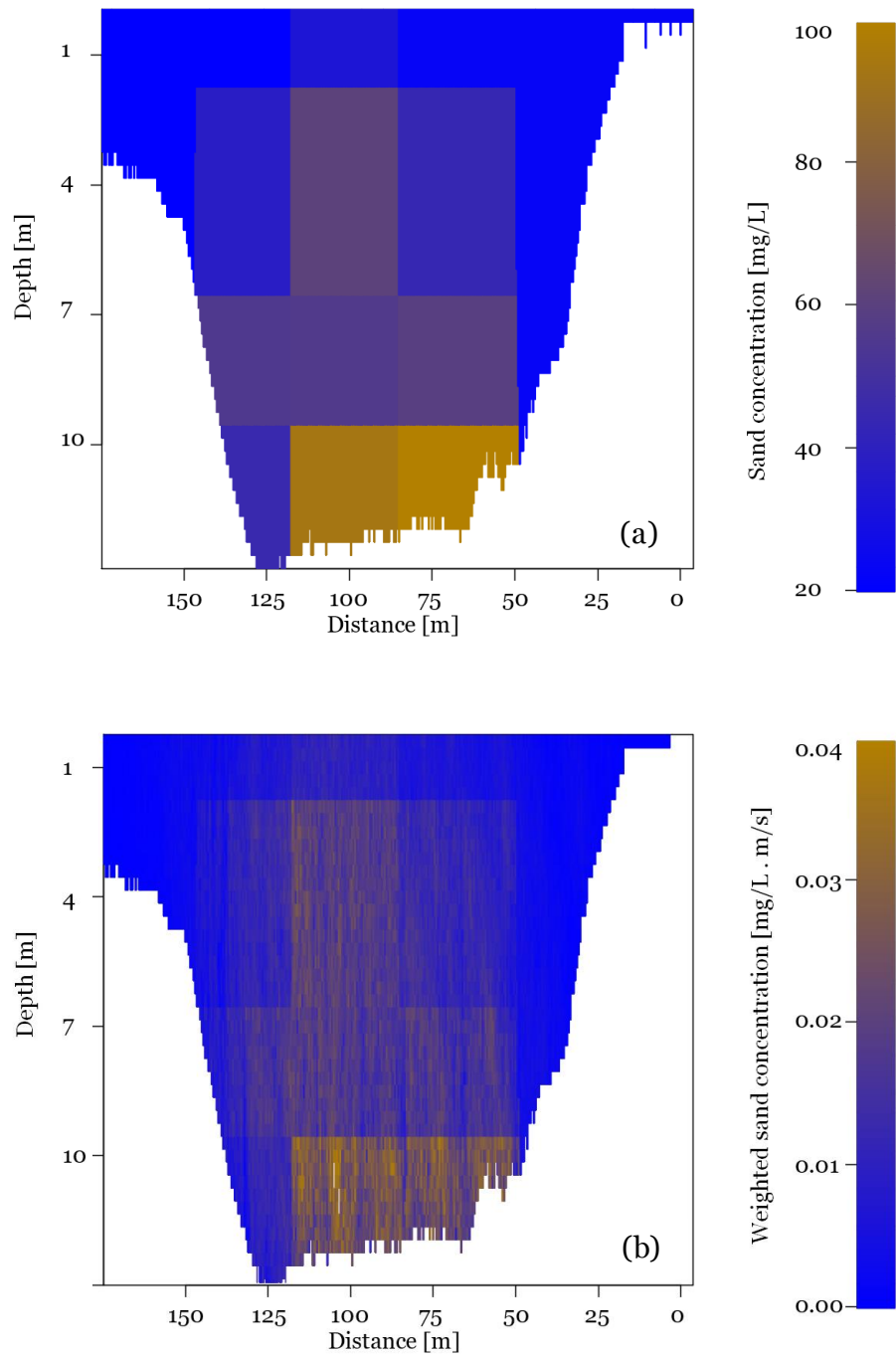
Figure 6: The nearest-neighbor method applied to individual point samples in the Rhône River at Lyon: (a) Sand concentration assigned to sub-sections according to the sample positions and ADCP data; (b) Velocity weighted sand concentration calculated for each ADCP cell.

Results from using the physically based method to estimate sand fluxes, highlighting the three main steps of this method, are illustrated in Figure 7: the logarithmic velocity law fit to the ADCP velocity data (Figure 7a), the Rouse-based exponential fit to the point-sample sand

concentrations (Figure 7b), and the flux profiles (Figure 7c) resulting from the combination of the velocity and concentration profiles.
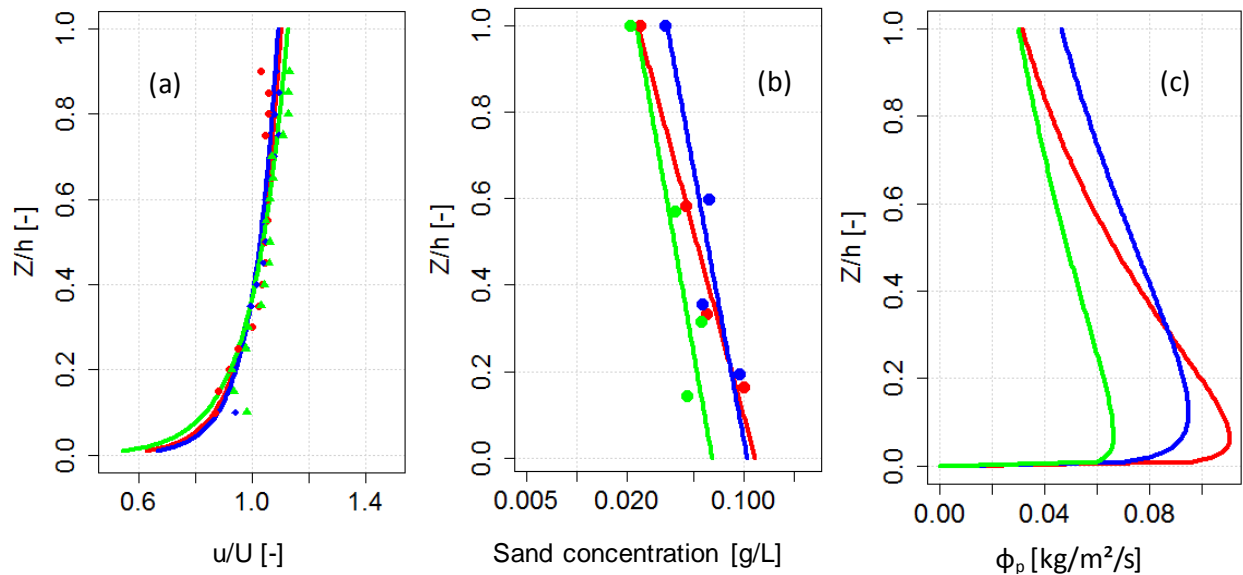
Figure 7: "Physically based method" applied to the Rhône River dataset (2018/01/22) (a) fitted ADCP velocities, (b) exponential profile (semi log scale), (c) Flux profile. Colors represent verticals numbers according to **Figure 4**.

Table 1 shows a summary of the results for the different post-processing options. For each day, the sand-flux and water-discharge results are the average of the computation of several ADCP transects. The same dataset (ADCP measurements and point sample concentration) is used for all the computations. The standardized method is considered as the reference. Results are quite similar. The nearest-neighbor method gave results that were only slightly lower than the standardized method, about -14% for the largest difference. The physically based method gave results close to the standardized method, with the largest difference also being -11%. The farthest right Q_s column is a simplified case with a single vertical in the middle of the river, which produced mostly overestimations owing to the higher concentrations and velocities in the center of the river cross section, thus illustrating the need for multiple verticals.

Table 1. Results of the different computation options for suspended-sand discharge

Date	Q$_{water}$	**Qs** Standard	Qs Nearest neighbor	Deviation versus Standard	Qs Physically-based	Deviation versus Standard	Qs Standard Single vertical	Deviation versus Standard
	[m³/s]	**[kg/s]**	[kg/s]	[%]	[kg/s]	[%]	[kg/s]	[%]
2018/01/22	2000	**104**	102	-2	108	4	130	25
2018/01/23	2650	**505**	482	-5	510	1	587	16
2018/01/24	2720	**378**	333	-14	338	-11	368	-3
2018/01/25	2150	**87**	82	-6	87	0	104	20

This comparison shows that the same dataset and different computing methods yield results that are only slightly different. Although the physically based method is very sensitive to the velocity and sediment-concentration profile calibrations, it provides a better estimate of the

concentration through the entire water column at each vertical, especially near the bed where it is difficult to measure velocity and suspended-sediment concentration.

Conclusions

In this study, we developed a method to combine ADCP data with suspended-sediment-concentration data to compute the suspended-sand discharge. We applied this method to field surveys carried out on the Rhône River during a 10-year flood. This method is a reliable procedure to estimate suspended-sand discharge through the cross section. The nearest-neighbor and physically based methods provided us with results consistent with the standardized method. The results show that little difference is found among vertical integration, but they lay the groundwork for the next step on lateral integration, which is what will really take advantage of the resolution of ADCP data for lateral integration as already done for vertical integration. Our study site of Perrache on the Rhône River is quite simple with a quasi-trapezoidal cross-section. To test our method in more complicated channel geometries, we need to conduct further tests of our method at other sites. Our results suggest that the computed suspended-sand discharge is relatively insensitive to the method used for vertical integration. We expect more difference with the lateral integration options we plan to test in the future. A first step in improving the lateral integration in our method will be to combine the suspended-sand concentration profiles from the physically-based method with each ensemble of the ADCP grid to improve the concentration estimations. We then propose to further improve the lateral integration by using the fluid-corrected backscatter from the ADCP (Boldt, 2015; Topping and Wright, 2016) to better interpolate the suspended-sand concentrations between the locations of the point samples.

References

ASTM, 2007. Standard test method for determining sediment concentration in water samples. D3977-97R07, West Conshohocken, PA, USA. 6 p.

Boldt, J. 2015. "From mobile ADCP to high resolution SSC: a cross calibration tool", SEDHYD conference 2015, Reno, NV, USA. 3 p.

Camenen, B. and Larson, M. 2007. "A General Formula for Non-cohesive Suspended Sediment Transport", Journal of Coastal Research, 24-3, pp. 615-627.

Edwards, T. K. and Glysson, G. D. 1999. "Field methods for measurement of fluvial sediment", U.S. Geological Survey Techniques of Water-Resources Investigation, 118 p.

Gitto, A.B. Venditti, J. Kostaschuk, R. and Church, M. 2017. "Representative point-integrated suspended sediment sampling in rivers", Water Resources Research, 53: pp. 2956-2971.

ISO 4363, 2002. "Measurement of liquid flow in open channels – Methods for measurement of characteristics of suspended sediment". International Organization for Standardization, Geneva, Switzerland, 32 p.

ISO 748, 2009. "Hydrometry — Measurement of liquid flow in open channels using current-meters or floats". International Organization for Standardization, Geneva, Switzerland, 46 p. using point velocity measurements, 50 p.

Muller, D. S., Wagner, C. R. 2009 "Measuring discharge with Acoustic Doppler Current Profilers from a moving boat", U.S. Geological Survey Techniques and Methods 3A−22, 72 p.

Nolan, K. M., Gray, J. R., and Glysson, G. D. 2015. Introduction to suspended-sediment sampling. USGS. Scientific Investigations Report 2005-5077.

Smart, G. 1999. "Turbulent velocity profiles and boundary shear in gravel bed rivers", Journal of Hydraulic Engineering. pp 106-116.

Topping, D. J. Rubin, D.M. Wright, S.A. and Melis, T. S. 2011. "Field evaluation of the error arising from inadequate time averaging in the standard use of depth-integrating suspended-sediment samplers". US Geological Survey Professional Paper, 1774, 95 p.

Topping, D. J. and Wright, S. A. 2016. "Long-term continuous acoustical suspended-sediment measurements in rivers - Theory, application, bias, and error", USGS Professional Paper, 1823, 97 p.

Testing hydraulic efficiency of three pressure-difference samplers while varying flows and bag properties (mesh size, weave density, fill level)

Kristin Bunte, Research Scientist, Department of Civil and Environmental Engineering, Colorado State University, kbunte@engr.colostate.edu
Taylor Hogan, Student, Department of Civil and Environmental Engineering, Colorado State University, tayhogan@colostate.edu
Mathew Klema, Grad. Student, Department of Civil and Environmental Engineering, Colorado State University, Matthew.Klema@colostate.edu
Christopher Thornton, Prof., Department of Civil and Environmental Engineering, Colorado State University, thornton@engr.colostate.edu

1. Introduction

Pressure-difference bedload samplers have a flared opening that is designed to accelerate flow velocity as it enters the sampler in order to counteract a deceleration of flow that occurs during the sampling process as the sampler bag fills with captured bedload and mesh pores become clogged by small particles. The ratio of flow velocity at the sampler entrance to the flow velocity measured when no sampler is present denotes a sampler's hydraulic efficiency. Maintaining a hydraulic efficiency of 100% in a sampler over all flows as well as for different nets and their varying levels of fill and clogging is considered an ideal (though probably unattainable) goal.

To meet the various sampling tasks in sand and gravel-bed streams, pressure-difference samplers are used with a variety of sampler bags that differ in length, shape, and netting fabric. While several studies have noted effect of bag clogging on hydraulic or sampling efficiency (Druffel et al., 1976; Johnson et al., 1977; Edwards, 1980; O'Leary and Beschta, 1981; Beschta, 1981), only a few preliminary studies (Bunte et al. 2009, 2015) started to investigate how netting properties, including fabric details such as thread and mesh width, affect a sampler's hydraulic efficiency. Ultimately, effects on the hydraulic efficiency extend to sampling efficiency which is the ratio of a transport rate measured in the sampler to the transport rate that occurs in the sampler's absence. This study evaluated the effects of various netting properties on the hydraulic efficiency of three pressure-difference samplers. The details of this study and its results are described in Bunte et al. (2017).

2. Methods

2.1 Flume experiments

Flume experiments for this study were conducted in a large flume at the Engineering Research Center at Colorado State University. The flow was 6 ft wide and 2.2 ft deep for all runs, ensuring that all samplers were well submerged and wall effects were minimized near the flume center. Three pressure-difference samplers with 1.4 expansion ratios were tested: The Toutle River 2 (TR2) sampler with a 12-by-6 inch opening, the similarly shaped but smaller Elwha sampler with the 8-by-4 inch opening, and the BL-84 sampler with its square 3-by-3 inch opening (Figure 1). Bags with four different mesh widths were tested for the TR2: 0.55, 1, 2, and 3.6 mm (Figure 2). Three bags with mesh widths of 0.55, 1, and 3.6 mm were tested for the Elwha sam-

pler and two bags with 0.25 and a 0.5 mm bag for the BL-84. The custom-sewn bags available for the study differed in size and shape; their bag surface areas were equalized by adjusting the clamping location at the bag ends. Each bag was tested empty, and two of the bags for each sampler were tested filled to 30 and 50% of its volumetric capacity with gravel. In addition to the gravel fill, those bags were also tested clad with an inner plastic liner that blocked 30 and 50% of the net surface and simulated bag clogging by organic debris or sediment particles.
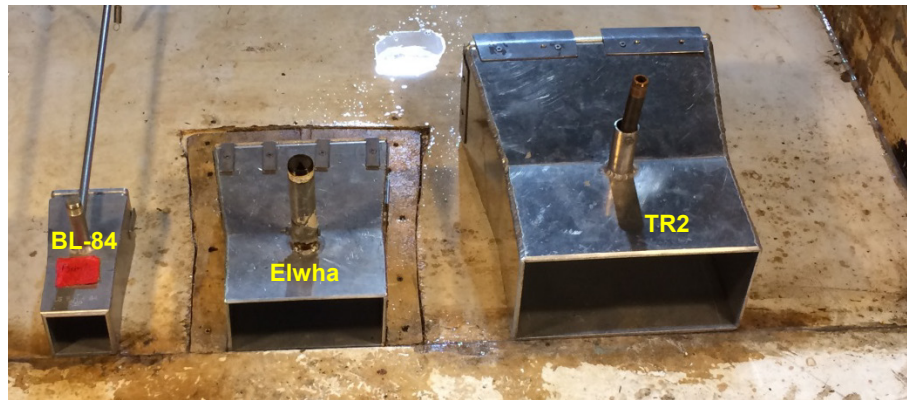
Figure 1: The three pressure-difference samplers used for testing (viewed from the front and with no bags attached).
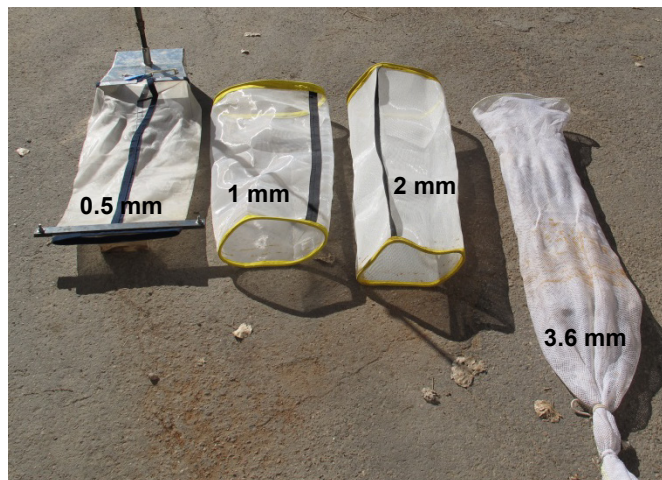
Figure 2: Bags with four different mesh widths were used for testing with the TR2 sampler. The 0.55 mm net is shown attached to the TR2 sampler and with a clamp at the end.

Each sampler and its different net configurations were tested with three target velocities of 1.5, 2.5, and 3.5 ft/s. Together with runs for each sampler when no net was attached and measurements of flow velocity in the absence of a sampler, testing amounted to about 80 runs. Flow velocities were measured using an ADV at 7-9 locations along a line about 1 inch in front of each sampler per run. Velocity was either measured at a constant height of 2" above ground ($v_{x,2}$) or computed for that height from measured velocity profiles.

2.2 Data analyses

2.2.1 Relation between mesh width and the density of the netting weave:
The study examined the relation between mesh width w, i.e., the distance from the edge of one

thread to the next, and the density of the netting weave that may be characterized by the fabric's percent open area (%Ao). The %Ao is determined by a ratio of thread width d to mesh width w and computed as %Ao = $w^2 \cdot 100/(\underline{w}+d)^2$. A net's %$Ao$, and hence the net's throughflow capacity, generally increases with mesh width, as was shown for wide range netting material with mesh widths between 0.5 and 10 mm, but thread width contributes as well such that a thinly-threaded net with a 0.5 mm mesh width may have the same %Ao as a thickly-threaded net with a 2 mm mesh width (Figure 3).
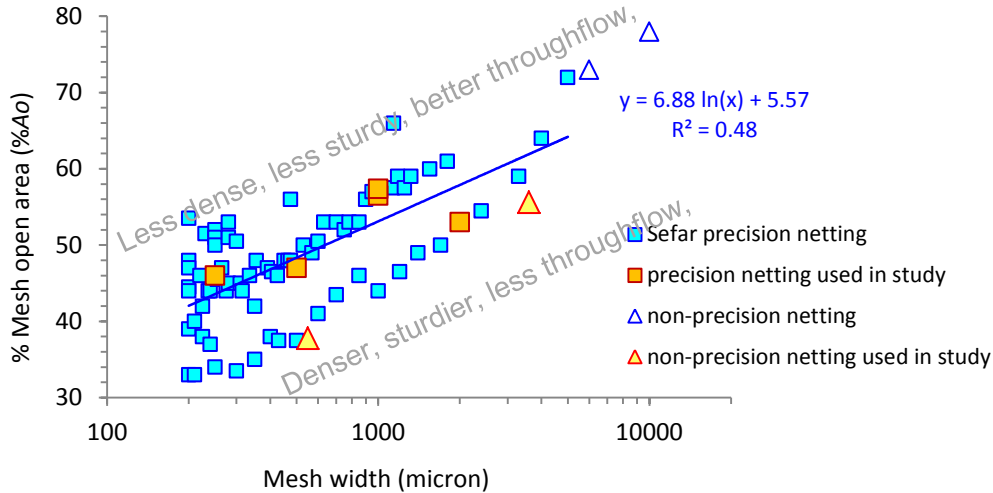
Figure 3: Relation of % mesh open area (%Ao) to mesh width w for Sefar precision netting. Data from the Sefar (2006) product catalogue. Data for the netting used in this study and for other netting materials are included.

A net's throughflow rate is not only determined by the %Ao but also by other blockages of the sampler bag such as bag surface area blocked by seams, by gravel fill, and by clogged mesh pores. The various sources of net blockage are likely additive, hence, this study mathematically combined the various bag parameters (bag size, seam width, %Ao, and the degree of bag clogging or filling) into a single parameter denoted as the final percent bag open area

$$\%Ao_{final} = (\%Ao_{tot} - \%Ao_{clogged} - \%Ao_{seam}) \cdot (\%Ao) \qquad \text{Eq. (1)}$$

where %Ao_{tot} is set to 100. For a net that is 50% clogged, has 4% of its surface covered by seams, and has a %Ao of 57, the %Ao_{final} is computed as (100-50-4)·57% = 26.2. Measured flow velocities and computed hydraulic parameters were then related to the %Ao_{final}.

2.2.2 Matrix of velocity measurements condensed to single parameters:

Flow velocities measured at multiple locations along the front of the samplers during the various runs were condensed into a few hydraulic parameters that could subsequently be related to the combined parameter for net openness %Ao_{final}. Velocities measured at 2 inches above ground ($v_{x,2}$) or interpolated for that height from measured velocity profiles were analyzed as lateral averages over all locations measured directly in front of the sampler entrance ($v_{xin,2}$), within the central part of the sampler width ($v_{xctr,2}$), as well as the ratio of inside to outside of the sampler ($x_{xin,2}/v_{xout,2}$). Discharge passing through the sampler (Q_{in}) was computed from the velocity profiles. Hydraulic efficiency (HE) was computed from the flow velocity measured right in front of the sampler opening ($v_{xin,2}$) divided by the $v_{xin,2}$ measured at the same locations when no sampler was in the flume and was accordingly termed $HE_{in,2}$.

3. Results

3.1 Relations of flow velocity and discharge to *%Ao$_{final}$*

For each sampler and each target velocity, flow velocity in front of the sampler ($v_{xin,2}$) was positively related to the percent bag open area (*%Ao$_{final}$*) (Figure 4). Logarithmic functions best described the trend of the relations that were characterized by an initial steep increase from low to moderate values of *%Ao$_{final}$* (basically from clogged to empty bags) and subsequent flattening from moderate to high values of *%Ao$_{final}$* (basically from empty nets to a sampler with no net attached).
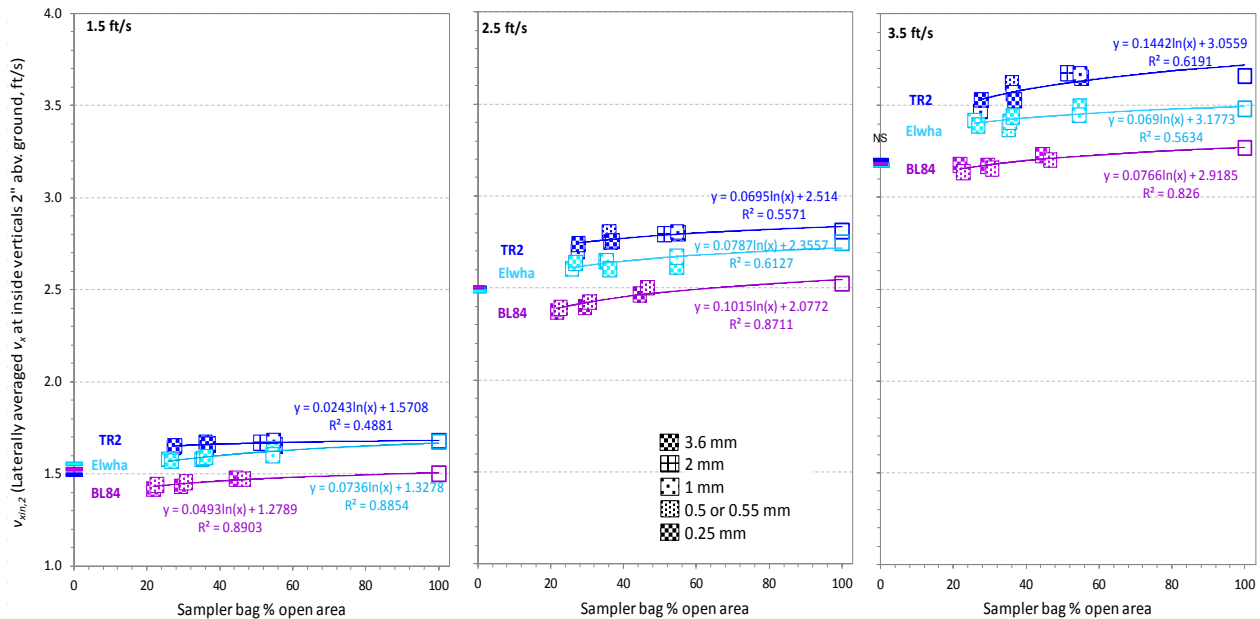

Figure 4: Logarithmic regression functions fitted to the relations of $v_{xin,2} = f$(*%Ao$_{final}$*) computed for the $v_{xin,2}$ averaged over the measurement locations directly in front of the sampler entrance. To improve the visual comparison of $v_{xin,2}$ among target velocities and samplers, all data were plotted in the same scale for $v_{xin,2}$. The legend in the center panel indicates mesh width and refers to all panels.

Figure 4 shows that sampler type (i.e., the size of the entrance area), target velocity, and the *%Ao$_{final}$* all affected $v_{xin,2}$. The relative magnitude with which those three parameters affected $v_{xin,2}$ as well as the other hydraulic parameters was analyzed by comparing the $v_{xin,2}$ associated with a specified percentage of net openness, which was selected as 50% *Ao$_{final}$*. The velocity $v_{xin,2}$ was mostly controlled by the target velocity of a run, while sampler entrance area and net openness had minor influences. Several studies had reported that HE increases with ambient velocity (e.g., Kuhnle, 1992), while other studies reported that HE differs among pressure-difference samplers (Hubbell et al., 1987; Pitlick, 1988; Gray et al., 1991; Ryan and Porth, 1999; Childers, 1991, 1999; Ryan, 2005; Vericat et al., 2006). An unexpected discovery in this study was the effect of sampler width on $v_{xin,2}$. The BL-84 and the Elwha samplers differ by just one inch in sampler height, but the notably larger $v_{xin,2}$ for the Elwha suggested that $v_{xin,2}$ was not only influenced by a sampler's protrusion into fast flow but also by the sampler's width.

3.2 Hydraulic efficiency

Similar to the results obtained for near-bed flow velocity $v_{xin,2}$, hydraulic efficiency computed from $v_{xin,2}$ ($HE_{in,2}$) increased with sampler entrance area, with target velocity, and with the % bag open area %Ao_{final} (Figure 5). Hwever, while target velocity had exerted a large influence when measured $v_{xin,2}$ was compared among samplers, the dominating influence of the target velocity parameter dropped out when analyzing the effect of HE, because hydraulic efficiency is calculated as a velocity ratio. Instead, all three parameters, sampler entrance area, target velocity, and %Ao_{final} each exerted relatively equal controls on hydraulic efficiency. However, the way in which the three parameters affected HE was complex and not uniform among the samplers.
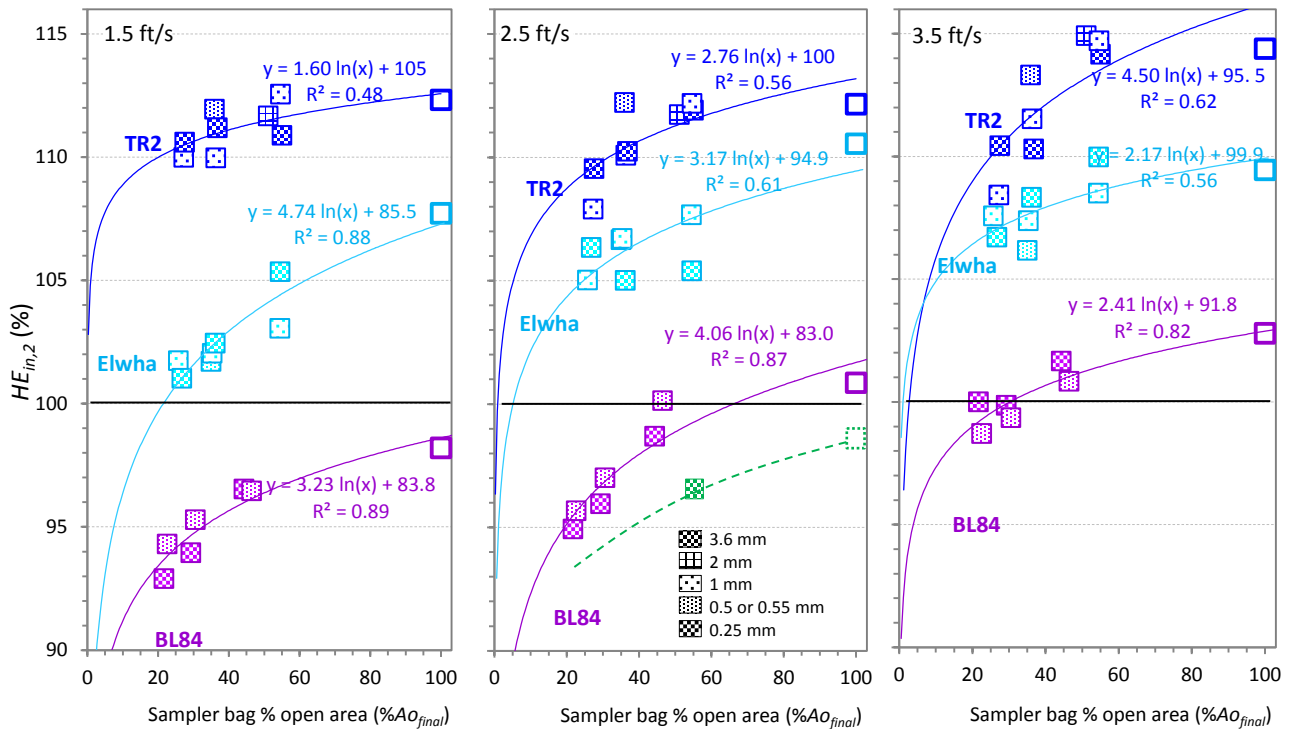
Figure 5: Hydraulic efficiency $HE_{in,2}$ for the three samplers and three target velocities. All panels are plotted in the same scale. The legend in the center panel refers to all panels. The green data point in the central panel indicates $HE_{in,2}$ measured for a bedload trap with an empty 3.6 mm net.

3.2.1 Sampler size affects *HE* most, target velocity and %Ao_{final} come next:
Absolute values of hydraulic efficiency for the TR2 and Elwha samplers were within 101 to 115%, showing that flow was sucked into those two pressure-difference samplers for all target velocities and all net configurations, even for clogged nets. The $HE_{in,2}$ for the BL-84 was below 100% (93-98%) for the slowest flow tested and ranged around 100% in the fastest test runs.

A TR2 sampler half filled with gravel had a higher hydraulic efficiency than an Elwha with empty bags, and an Elwha with half-clogged nets has a higher efficiency than an empty BL-84 sampler, showing that on average, sampler entrance size affected hydraulic efficiency slightly more than target velocity, while the overall percent bag openness (%Ao_{final}) ranked third. A single test run with an unflared bedload trap (Bunte et al., 2004, 2007) yielded a hydraulic efficiency of 97%, showing that a sampler's expansion ratios affects hydraulic efficiency much more than either target velocity, sampler entrance area, or bag opening.

3.2.2 Complex effects of %Ao_{final} on hydraulic efficiency: The effects of %Ao_{final} on hydraulic efficiency were complex and differed among samplers, among bags, and among target velocities. Coarse-meshed nets (with Ao_{final} >50%) that were empty did not reduce hydraulic efficiency for the TR2 sampler, but clogged nets did, indicating that the choice of bag mattered little for the TR2 sampler as long as the bag was not filled to 50%, especially not in faster flow and not for the shape-retaining 1-mm bag. For the BL-84 sampler, the choice among coarse nets was likewise less important for hydraulic efficiency than avoiding filling the bag to 50%, especially in slower flow. By contrast for the Elwha sampler, gravel fill and the sheer presence of a coarse net equally reduced $HE_{in,2}$, particularly at slower flow.

3.2.3 Bag clogging vs gravel fill: Comparison of runs in which bag were filled to 30 and 50% of their volumes with gravel to those in which 30 and 50% of the bag volume was clogged showed that bag clogging reduced hydraulic efficiency notably more than gravel fills of similar volumes. This is because water could easily exit the bags above the gravel wedges, whereas complete clogging of the backward portion of the net caused turbulence and redirection of the flow within the net and that reduced $HE_{in,2}$. Further, net shape was found to exert a notable influence on how net openness affected hydraulic efficiency.

3.2.4 From hydraulic efficiency to sampling efficiency: In order to use multiple bedload samplers interchangeably, or to compare results between studies that used different samplers, all samplers should have the same HE, and ideally, that value should be near 100% for a wide range of sampler bag configurations.

However, HE is not a straightforward measure of sampling efficiency. Instead, the relation between flow hydraulics at the sampler entrance and bedload transport is highly complex, and even estimating a possible relation requires several assumptions. Consequently, rather than assuming a direct or fixed relation between HE and sampling efficiency, the sediment transport mode and processes at the sampler entrance need to be evaluated. A high HE more likely causes pronounced over-sampling under specific conditions: 1) When sand and fine gravel or organic material is transported in suspended mode rather than as true bedload, 2) When sandy or fine gravel bed material is entrained due to turbulence and vortices at the sampler entrance, such as when pushing the sampler through the water column t the stream bed, and then sucked into the sampler, 3) When gravel particles are dislodged during sampler placement on the bed and then sucked into sampler (Bunte et al., 2019, *this volume*).

5. References

Beschta, R.L., 1981. "Increased bag size improves Helley-Smith bed load sampler for use in streams with high sand and organic matter transport," Erosion and Sediment Transport Measurement. IAHS Publ. no. 133: 17-25.

Bunte, K., Abt, S.R., Potyondy, J.P., and Ryan, S.E. 2004. "Measurement of coarse gravel and cobble transport using a portable bedload trap," J. Hydraulic Engineering 130(9): 879-893.

Bunte, K., Swingle, K.W., and Abt, S.R. 2007. "Guidelines for using bedload traps in coarse-bedded mountain streams: Construction, installation, operation, and sample processing," General Technical Report, RMRS-GTR-191, Fort Collins, CO, U.S.D.A. Forest Service, Rocky Mountain Research Station, 91 pp.

Bunte, K. and K. Swingle, 2009. Testing bedload traps with a 1.18 mm mesh width netting. Report submitted to Stream Systems Technology Center, USDA Forest Service, Rocky Mountain Research Station, Fort Collins, CO, 32 pp.

Bunte, K., K.W. Swingle, S.R. Abt, and D.A. Cenderelli, 2015. "Effect of bedload sampler netting properties on hydraulic and sampling efficiency," Proc. 3rd Joint Federal Interagency Conference on Sedimentation and Hydrologic Modeling, April 19-23, 2015, Reno, Nevada, USA, p. 1869-1880.

Bunte, K., Klema, M., Hogan, T., and Thornton, C. 2017. "Testing the Hydraulic Efficiency of Pressure Difference Samplers While Varying Mesh Size and Type," Report submitted to the Technical Committee of the Federal Interagency Sedimentation Project, 116 pp., April 2017.

Bunte, K., Swingle, K.W., Ettema, R., Abt, S.R., and Cenderelli, D.A. 2019. "Helley-Smith sampler's mismeasurement of gravel transport rates and particle sizes," Proc., SEDHYD 2019, 11th Federal Interagency Sedimentation and 6th Hydrologic Modeling Conference, June 24-28, 2019, Reno, NV. USA

Druffel, L., Emmett, W.W., Schneider, V.R., and Skinner, J.V. 1976. "Laboratory hydraulic calibration of the Helley-Smith bedload sediment sampler". U.S. Geol. Survey Open-File Report 76-752, 63 pp.

Childers, D. 1991. "Sampling differences between the Helley-Smith and BL-84 bedload samplers," Proc. Fifth Federal Interagency Sedimentation Conference, March 18-21, 1991, Las Vegas, NV, p. 6.31-6.38.

Childers, D. 1999. "Field comparison of six-pressure-difference bedload samplers in high energy flow," U.S. Geol. Survey, Water Resourc. Investigat. Rep. 92-4068, Vancouver, WA, 59 pp.

Edwards, R.E., 1980. "Sediment Transport and Channel Morphology in a Small Mountain Stream in Western Oregon," M.S. Thesis, Oregon State University, Corvallis, OR, 114 pp.

Gray, J.R., Webb, R.H., and Hyndman, D.W. 1991. "Low-flow sediment transport in the Colorado River," Proc. Fifth Federal Interagency Sedimentation Conference, March 18-21, 1991, Las Vegas, Nev., p. 4.63-4.71.

Hubbell, D.W., Stevens Jr., H.H., Skinner, J.V., and Beverage, J.P. 1987. "Laboratory Data on Coarse-Sediment Transport for Bedload-Sampler Calibrations," U.S. Geol. Survey Water-Supply Paper 2299: 1-31.

Johnson, C.W., Engleman, R.L., Smith J.P., and Hansen, C.L. 1977. "Helley-Smith bed load samplers," J. Hydraulics Division, ASCE, 103 (HY10): 1217-1221.

Kuhnle, R.A. 1992. "Fractional transport rates of bedload on Goodwin Creek," In: Dynamics of Gravel Bed Rivers. P. Billi, R.D. Hey, C.R. Thorne and P. Tacconi (eds.), John Wiley, Chichester, p. 141-155.

Pitlick, J.C., 1988. "Variability of bed load measurement," Water Resources Research 24(1): 173-177.

O'Leary, S.J. and Beschta, R.L. 1981. "Bed load transport in an Oregon Coast Range stream,". Water Resources Bulletin 17(5): 886-894.

Ryan, S.E., 2005. "The use of pressure-difference samplers in measuring bedload transport in small, coarse-grained alluvial channels," Proc. Federal Interagency Sediment Monitoring Instrument and Analysis Workshop, September 9-11, 2003, Flagstaff, Arizona, J.R. Gray, ed.: U.S. Geological Survey Circular 1276, 78 p.

Ryan, S.E. and Porth, L.S. 1999. "A field comparison of three pressure-difference bedload samplers," Geomorphology 30: 307-322.

Sefar 2006. "Open Mesh Fabrics. Precision Woven Synthetics Monofilament Fabrics," Sefar Filtration Inc., http://techlist.sefar.com/cms/newtechlistpdf.nsf/vwWebPDFs/openmesh_EN.pdf/$FILE/openmesh_EN.pdf

Vericat, D., Church, M. and Batalla, R.J. 2006. "Bed load bias: Comparison of measurements obtained from using two (76 and 152 mm) Helley-Smith samplers in a gravel bed river," Water Resources Research 42, W01402, doi:10.1029/2005WR004025.

The National Hydrography Dataset (NHD) and National Hydrography Dataset Plus High Resolution (NHDPlus HR)

Alan Rea, P.E., Hydrologist, U.S. Geological Survey, Boise, Idaho, ahrea@usgs.gov
Susan G. Buto, Physical Scientist, U.S. Geological Survey, Carson City, Nevada, sbuto@usgs.gov

Extended Abstract

The National Hydrography Dataset (NHD) is the U.S. Geological Survey's geospatial dataset used to portray surface water in The National Map. The NHD represents the drainage network with features such as rivers, streams, canals, lakes, ponds, coastline, dams, and streamgages. The NHD also includes a linear referencing system based on reach codes that functions like a street address, and network connectivity information that, combined, enable analysis and discovery of information upstream or downstream of a point of interest.

Although the reach-code addressing system has been implemented in the NHD for many years, the USGS currently is working to improve user tools to make it easier to derive reach-code addresses, and also to develop systems that use reach-addressed data to aid in data discovery and hydrographic network-based search capabilities. These improvements should both make it easier to reference data by reach address, and to use the hydrographic network to infer relationships (e.g. upstream to downstream) between data collected by many different entities and stored in many different databases distributed across the Internet. This model for federated data storage, coupled with open data standards to enable interoperability should greatly enhance the ability for the water resources community to discover and use data collected by others.

The National Hydrography Dataset Plus (NHDPlus) enhances the NHD by incorporating two other USGS datasets; seamless elevation data from the 3D Elevation Program (3DEP), and delineations of drainage divides from the Watershed Boundary Dataset (WBD). The NHDPlus comprises an integrated suite of hydrologic geospatial data sets, including a hydrographic stream network, polygonal catchment areas representing incremental drainage areas for each stream network element, and Digital Elevation Model (DEM) derivatives including flow direction and flow accumulation grids. The USGS and U.S. Environmental Protection Agency (USEPA) collaborated to produce two versions of the National Hydrography Dataset Plus (NHDPlus V1 and NHDPlus V2), using the Medium-Resolution NHD at 1:100,000 scale, 30-meter elevation data from 3DEP, and WBD (Moore and Dewald 2016). The USGS is now developing the NHDPlus High Resolution (NHDPlus HR).

The NHDPlus HR is created using the High-Resolution National Hydrography Dataset (NHD) at 1:24,000 scale or better, 1/3 arc-second (10-meter resolution) seamless 3DEP data, and nationally complete Watershed Boundary Dataset (WBD). It contains numerous components in both vector and raster formats, including snapshots of the NHD, WBD, and 3DEP data at the time the NHDPlus HR was built, as well as:
- A set of value added attributes that enhance stream network navigation, analysis, and display
- An elevation-based catchment area for each flowline in the stream network
- Catchment characteristics, including 1971-2000 mean annual precipitation and mean annual temperature (after PRISM 2006, and McKenney et al. 2006), mean annual runoff (after McCabe and Wolock 2011), and mean latitude
- Cumulative drainage area characteristics
- Mean annual flow (1971-2000) and velocity estimates and minimum/maximum elevations and slopes for each flowline in the stream network

- Several raster datasets such as flow direction, flow accumulation, elevation, and hydro-enforced elevation

A first "Beta" version of NHDPlus HR has now (2019) been developed for approximately ¾ of the Nation, including most of the conterminous U.S., plus parts of Alaska. A status map is shown in Figure 1. The USGS invites users to use the NHDPlus HR Beta version in their applications, and to provide feedback so that the data may be improved. A new web-based "Markup Application" is provided to allow users to easily identify issues in either NHD or WBD, or in the derived NHDPlus HR data. These issues are automatically made available to data stewards who help to maintain the datasets, as well as USGS in-house editors, and the issues will be evaluated and fixed as appropriate in a timely manner. After these data improvements have been accomplished for an area, the NHDPlus HR for the area will be "Refreshed," and a new NHDPlus HR generated. In this way the data will iteratively and continuously be improved.

Figure 1. Map showing NHDPlus High Resolution Availability (updated 4/4/2019)

NHDPlus HR catchment areas create a seamless, scalable hydrography framework to map and model the flow of water and related characteristics across the landscape to the stream network. Many additional landscape characteristics may be computed for each catchment in addition to the pre-computed catchment characteristics delivered with the NHDPlus HR. Computed catchment characteristics can be readily accumulated and summarized for every stream segment. As an example, the StreamCat dataset (Hill et al. 2016) includes 517 metrics that have been computed for each of the approximately 2.65 million stream segments and their associated catchments from the NHDPlus V2. The LakeCat dataset (Hill et al. 2018) similarly includes 272 metrics for 378,088 lakes in the conterminous U.S., again, based on the NHDPlus V2. In another example, Schwarz and Wieczorek (2018), provide an improved routing table, correcting some routing errors in the

NHDPlus V2 network, and Wieczorek et al. (2018) provides numerous landscape attributes linked to this improved routing of the spatial features in the NHDPlus V2. While such extensive collections of landscape characteristics have yet to be developed for NHDPlus HR, it is reasonable to expect that they will be.

Many applications have been built upon the previous versions of NHDPlus, and it is anticipated that even more will make use of the NHDPlus HR. The NHDPlus HR geospatial framework can provide key information necessary for modeling of sediment transport and fate, among many other applications. Combined with the NHD reach addressing system described above, this system provides a strong foundation upon which all sorts of water resource models and analyses can be based.

References

Hill, Ryan A., Marc H. Weber, Scott G. Leibowitz, Anthony R. Olsen, and Darren J. Thornbrugh, 2016. The Stream-Catchment (StreamCat) Dataset: A Database of Watershed Metrics for the Conterminous United States. Journal of the American Water Resources Association (JAWRA) 52:120-128. DOI: 10.1111/1752-1688.12372.

Hill, Ryan A., Marc H. Weber, Rick Debbout, Scott G. Leibowitz, Anthony R. Olsen. 2018. The Lake-Catchment (LakeCat) Dataset: characterizing landscape features for lake basins within the conterminous USA. Freshwater Science doi:10.1086/697966.

McCabe, G. J., and D. M. Wolock (2011), Independent effects of temperature and precipitation on modeled runoff in the conterminous United States, Water Resour. Res., 47, W11522, doi:10.1029/2011WR010630.

McKenney, D.W., Papadopol, P., Campbell, K.L., Lawrence, K.M., Hutchinson, M.F., 2006, "Spatial models of Canada- and North America-wide 1971/2000 minimum and maximum temperature, total precipitation and derived bioclimatic variables," Frontline Technical Notes 106, Natural Resources Canada, Great Lakes Forestry Centre, Sault St. Marie, Ontario, 9 p.

Moore, Richard B. and Dewald, Thomas G., 2016. The Road to NHDPlus — Advancements in Digital Stream Networks and Associated Catchments. Journal of the American Water Resources Association (JAWRA) 52(4): 890– 900. DOI: 10.1111/1752-1688.12389.

PRISM Climate Group, Oregon State University, http://www.prismclimate.org, created 6 Dec 2006.

Schwarz, G.E., and Wieczorek, M.E., 2018, Database of modified routing for NHDPlus version 2.1 flowlines: ENHDPlusV2_us: U.S. Geological Survey data release, https://doi.org/10.5066/P9PA63SM.

Wieczorek, M.E., Jackson, S.E., and Schwarz, G.E., 2018, Select Attributes for NHDPlus Version 2.1 Reach Catchments and Modified Network Routed Upstream Watersheds for the Conterminous United States: U.S. Geological Survey data release, https://doi.org/10.5066/F7765D7V.

The seismic view on sediment laden ephemeral flows – modelling of ground motion data for fluid and bedload dynamics in the Arroyo de los Piños

Michael Dietze, Dr, GFZ Potsdam, Potsdam, Germany, mdietze@gfz-potsdam.de

Florent Gimbert, Dr, University of Grenoble Alpes, CNRS, IRD, Institut des Géosciences de l'Environnement (IGE), Grenoble, France, florent.gimbert@univ-grenoble-alpes.fr

Jens M. Turowski, Dr, GFZ Potsdam, Potsdam, Germany, turowski@gfz-potsdam.de

Kyle A. Stark, New Mexico Institute of Mining and Technology, Socorro, NM, kyle.stark@student.nmt.edu

Daniel Cadol, New Mexico Institute of Mining and Technology, Socorro, NM, daniel.cadol@nmt.edu

Jonathan B. Laronne, Dr, Ben Gurion University of the Negev, Beer Sheva, Israel, john@bgu.ac.il

Abstract

Ephemeral streams prone to sediment laden flash floods are key to understand the modes of long term landscape evolution in semi-arid areas, pose a significant hazard to infrastructure and people and are requisite to model the stability of main stem rivers to which they deliver sediment. Key parameters of fluid and bedload dynamics are difficult to measure directly during events unless an extensive measurement infrastructure is installed in the channel. Even then, bedload samplers and pressure transducers provide spatially localised and temporally discrete data that require interpolation to gain representative information about a flash flood event.

Seismometers are potentially valuable alternatives to in-stream devices. Installed at the stream bank, they are safe from damage, continuously record high resolution data, incorporate the average behaviour of a given footprint, and record proxy signals of a series of key parameters. In order to develop these sensors as established devices for monitoring bedload transporting flows, we need to understand what they tell us by unmixing the superimposed signals of the parameters of interest. This requires comparison of data generated by seismic sensors with independent records of established devices.

In this study we exploit the excellent infrastructure of the newly activated Arroyo de los Piños sediment research facility. We make use of seismic signals of a large flash flood event recorded by a broadband seismometer station. We model the seismic spectra due to bedload and flowing water, explicitly taking into account input parameter uncertainty, and compare the results with independent measurements.

Introduction

Understanding the boundary conditions and operational modes of ephemeral streams is essential from a process geomorphology and long term landscape evolution perspective. Ephemeral streams are specifically prone to flash floods, rapidly occurring inundations due to heavy rain. Under such rapid and massive flood conditions, the stream mobilises very high

amounts of bedload (Reid & Laronne, 1995). These flow and transport mechanisms are important to better understand the geomorphic effects of such systems but also to estimate and mitigate effects on infrastructure.

Accordingly, there has been significant effort in collecting instrumental data on key parameters inherent to flow conditions and the boundary conditions determining the dynamics of flash flood events. Classic approaches involve the construction of massive concrete supported infrastructure inside the stream bed. This is necessary to maintain operation under the harsh conditions during events. Typical in-stream instrumentation to constrain flow conditions include pressure gauges, temperature sensors, and turbidity sensors. Bedload dynamics are monitored with time resolving slot samplers and acoustic sensors such as hydrophones and plate geophones (e.g., Cohen & Laronne, 2005; Rickenmann et al., 2014).

Most of these sensors, delivering direct and indirect data on the target parameters, provide point measurements or can at best be regarded as cross sectional lines of sensors. Furthermore, the in stream instrumentation approach requires careful planning of suitable deployment sites as a massive investment is involved and a characteristic reach needs to be identified. The maintenance effort is significant.

In recent years, a valuable alternative and complementary approach has gained increasing attention: out-of-stream instrumentation with seismic sensors (Burtin et al., 2008; Barrierére et al., 2015; Schmandt et al., 2017). Such sensors are installed at a safe distance to the stream and record the ground motion due to stream dynamics, along with a series of further seismic sources. Modern seismic stations can be deployed easily under rugged conditions and are able to operate autonomously for months without maintenance; some systems are even capable of near real time data telemetry. They provide continuous high resolution (> 200 Hz) time series that carry information averaging over a given footprint of tens to thousands of metres. Thus, seismic stations may provide near real time high quality proxy data of key parameters otherwise hard to obtain.

Physical models were suggested to predict the seismic frequency spectra caused by earth surface dynamics, such as turbulent fluid flow (Gimbert et al., 2014) and river bedload transport (Tsai et al., 2012; Gimbert et al., 2018). In order to make appropriate use of such models, it is important to explore robust ways to apply them inversely, i.e., to invert flow bedload and flux properties from the measured seismic data.

We make use of the excellent infrastructure of the Arroyo de los Piños sediment research facility (Varyu et al., –this issue). We explore to which extent physically based model results (Tsai et al., 2012; Gimbert et al., 2018) are consistent with seismic signals recorded next to the instrumented stream.

Study site

The United States Bureau of Reclamation identified the Arroyo de los Piños as a prime candidate to improve Rio Grande sediment dynamics modeling. Work began on a world-class sediment monitoring station on the Piños with construction being completed in early 2018. The catchment size is 32 km²; as tributary of the Rio Grande, the Piños is typical of many systems found in the southwestern United States. Flash floods carry sediment directly into the Rio Grande causing a localized influx at the point of confluence. The Piños is located at the northern

extent of the Chihuahuan Desert; characterized by violent monsoonal storms during the summer months. Most of the runoff observed in the Piños to date comes from these monsoonal storms.

Materials and methods

Instrumentation and seismic setup

A 9.1 m wide cross section of the Arroyo de los Piños has been turned into a sediment dynamics research facility by installing a concrete lined sill. Into its concrete floor a series of in stream sensors have been embedded. For details see Varyu et al. (this issue).

In addition, a Nanometrics Trillium Compact TC120s broadband seismometer has been installed on the bank, 6 m away from the stream margin. The sensor was inserted into a 50 cm deep hand dug pit, oriented to the North and levelled horizontally, mantled with sand and the pit was closed again. The ground motion signals are recorded by a Nanometrics Centaur data logger, operating at a recording frequency of 1000 Hz, with a dynamic range of 10 Vpp (gain = 4).

Data analysis

The analysis focuses on the largest flash flood event in 2018 (Figures 1, 2). The measured seismic data were prepared and analysed with the R package 'eseis' (Dietze, 2018). The continuous time series were imported for the flood event duration, and their means and linear trends were removed. The instrument response was removed, also accounting for the dynamic range of the logger, and the data was high pass filtered with a lower cut-off frequency of 1 Hz to remove the ocean signal content. Spectrograms were calculated from the tapered time series (taper size 0.5 % of the total time series length) using the sub window averaging approach (Welch, 1967) on periodogram-based spectra, each calculated from 80 % overlapping data snippets with window sizes of 40 and 20 s, respectively.

Seismic models

During flash flood events, the seismic signal at the Arroyo de los Piños facility is expected to be dominated by the effects of turbulent fluid flow and/or the seismic wave scape due to particles impacting the bed. Secondary effects may be caused by rainfall at the site, but more severely by road traffic and people walking past the sensor. A further source of seismic signals can be other rivers, such as the Rio Grande, some 250 m westwards. During this event operators arrived at the site too late to cross the river toward the station; hence, noise due to persons or vehicles was probably absent.

To explore the potential effect of fluid flow and bedload transport, we calculated seismic spectra based on the models of Gimbert et al. (2014) and Tsai et al. (2012), respectively. Both models are physically based representations of first order processes that cause ground motion as recorded by seismic stations. The two models are part of the R package 'eseis', rewritten from the original publications and validated against the corresponding Matlab script outputs. The models require a range of parameters (Table 1) to be set or estimated, in order to account for properties of the fluid, the transported sediment particles, the bed characteristics and the properties of the medium through which the seismic waves travel toward the sensor.

Since several of these parameters remain unknown or can only be provided with an associated uncertainty, we have to account for different model realisations, i.e., propagating the input parameter uncertainties through the modelling process into the model output. For such highly complex, non-linear and partly approximating models, there is no straightforward analytic approach to uncertainty implementation. Thus, we use a Monte Carlo approach (cf. Dietze, 2018). We run both models multiple times (10,000 in our case), each time with slightly different parameter values. The values are drawn from uniform random distributions. Each model output is stored and the resulting assemblage of data is used to generate average seismic model spectra and confidence intervals (quartile ranges). The spectra were calculated for different potential stages of the flood and bedload fluxes. Table 1 summarizes the model parameters along with their ranges of possible values. The parameter ranges are based on empirical field data, results of studies under comparable landscape configurations, and best knowledge estimates, as indicated in Table 1.

Table 1. Parameters and estimated uncertainty ranges for physically based models to predict the seismic spectra due to turbulent water flow and bedload sediment transport (s.d. means dimensionless).

| Paramater (unit)	Symbol	Value range/fixed	Justification
D_{50} bedload grain diameter (m)	d_s	0.007–0.009	field sample measurements
Grain diameter standard deviation (log m)	s_s	0.5–0.9	field sample measurements
Bedload sediment flux (m²/s)	q_s	see figure 4	observatory data result
Sediment density (kg/m³)	r_s	2600–2700	average rock density
Fluid density (kg/m³)	r_w	1000–1200	density of water with suspended load
Water depth (m)	h_w	see figure 4	observatory data
Channel width (m)	w_w	9–10	observatory data
Channel slope (radians)	a_w	0.016–0.020	observatory data
Distance river to station (m)	r_0	6	observatory data
Reference frequency (Hz)	f_0	1	Tsai et al. (2012), Gimbert et al. (2014)
Material quality factor at f_0 (s.d.)	q_0	10–20	Tsai et al. (2012), Gimbert et al. (2014)
Rayleigh wave phase velocity at f_0	v_0	400–600	estimate based on Dietze (2018)
Variation coefficient for v_0	p_0	0.6–0.7	Tsai et al. (2012), Gimbert et al. (2014)
Q increase with frequency (s.d.)	e_0	0.0–0.2	Tsai et al. (2012), Gimbert et al. (2014)
Greens function displacement amplitude coefficients (s.d.)	n_0	0.6–0.8, 0.8–0.9	Lagarde et al. (unpublished)

Results

Empirical data

The largest sediment laden flash flood event of 2018 was caused by 30 mm precipitation in the upstream section of the catchment around 10 am on 26 July, preceded and succeeded by smaller precipitation events. Moving southward, the main storm also caused precipitation affecting adjacent catchments and the trunk stream, the Rio Grande. Flow was recorded at the monitoring station over 5.5 hours (22:06–03:30 local time, 04:06–9:30 UTC time – UTC time unit used hereafter). Within one hour the stage rose to peak at 1.61 m and then receded during 4.5 hours (Figure 1). With the onset of flow, the bedload samplers started filling, most pronounced in the left and central device. These filled within a few minutes while the right sampler collected bedload for a few more minutes. Thus, data from these devices cannot be used for the entire flood event and have been truncated in figure 1. However, the pipe microphones, collecting surrogate data of bedload particle impacts were in operation throughout the event. The two sensors show significantly differing time series.
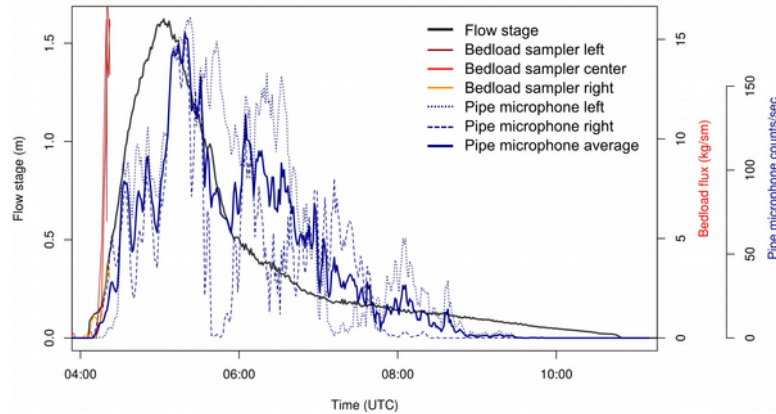
Figure 1. Sensor time series of the sediment laden flash flood in the Arroyo de los Piños. The hydrograph (black line) shows a rapid stage rise just after 4 am (UTC time) with recession lasting until 10 am on July 27 2018. Bedload flux was massive enough to fill all three Reid type basket samplers. The pipe microphone count data (left sensor dotted line, right sensor dashed line, average solid bold line), show bedload movement for about five hours.

The seismic perspective on this flash flood event (Figure 2a) shows the preceding conditions and the seismic background signals superimposed on the actual target processes. The rain events appear as vertical bands due to their broad band frequency character (Dietze et al., 2017). A 2-8 Hz frequency band is continuously present (horizontal green line in Figure 2a). The most prominent feature in the spectrogram is the flood event (Figure 2b). Its onset at 4:10 am is recorded as a sudden increase in seismic energy across almost the entire frequency space, followed by the emergence of another, even more energetic pulse around 4:20 am. Most seismic energy is carried by frequencies in the range 4–12 Hz with a gliding upward trend as the flood progresses.
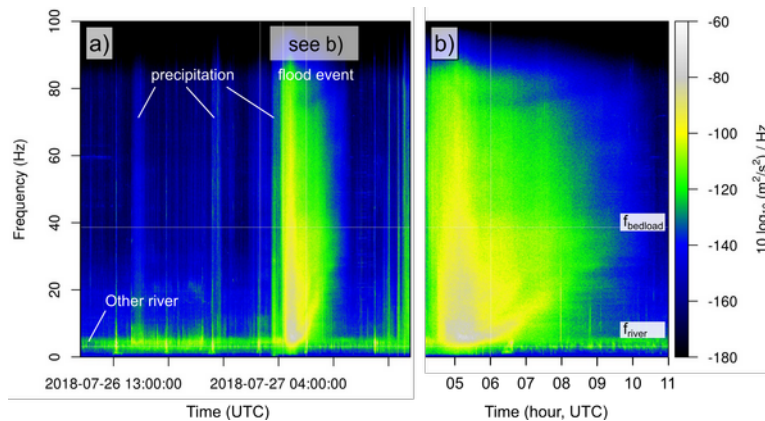
Figure 2. Seismic spectrograms (time-frequency plots) of the investigated flash flood event. a) overview including preceding phase with multiple rain events (vertical broad frequency bands) and the continuous 2-8 Hz frequency band signal generated by another continuous source (horizontal band). b) close-up of the flood event, dominated by frequencies between 4 and 30 Hz. The white bands in b) denote frequency ranges used to generate time series of seismic activity in Figure 3, assumed to be dominated by turbulent flow in the Arroyo de los Piños (f_{river}) and bedload impacts ($f_{bedload}$).

Following suggestions from the literature (e.g., Gimbert et al., 2014; Cook et al., 2018) we extract average seismic power time series from the spectral data in the two discrete frequency bands 5–8 Hz and 35–40 Hz, which supposedly are characteristic of river turbulence and bedload impacts, respectively. The resulting surrogate time series (Figure 3) show the general co-evolution of the two supposed sources of seismic energy. However, they also show that the

portion of signal caused by bedload impact behaves differently during recession than the fluvial signal source. Both time series are similar to the evolution of the independently measured data sets. The hydrograph and the 5–8 Hz band both rise from the onset of the flood at 4:06 am, peak around 5 am and fall to background values by 10 am. However, the peak of the seismic time series is broader and the falling limb shows another, secondary maximum between 6:10 and 7:00 am, which is not visible in the pressure gauge data. Seismic power characteristic for bedload flux appears to rise steeper and less uniform than the other seismic time series before it also peaks around 5 am. Overall, the data shows greater differences from the averaged pipe microphone time series, most notable it does not show the plateau-like evolution in the rising part.
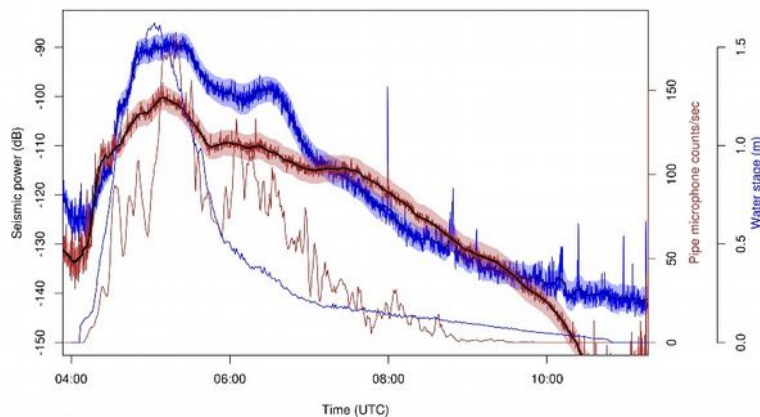
Figure 3. Seismic power time series, supposed to be characteristic for turbulent fluid flow (5–8 Hz, blue lines) and bedload particle impacts (35–40 Hz, brown lines), corresponding to the annotations in Figure 2b. The plot shows the raw seismic data (solid thin lines) and their one standard deviation ranges (polygons) as well as 200 sample wide running averages (thick lines) in dB, i.e., $10 \cdot \log_{10}(\text{m}^2/\text{s}^2/\text{Hz}^2)$. The independently measured time series of water stage (thin blue line) and bedload impact related average pipe microphone (thin brown line) are given for comparison.
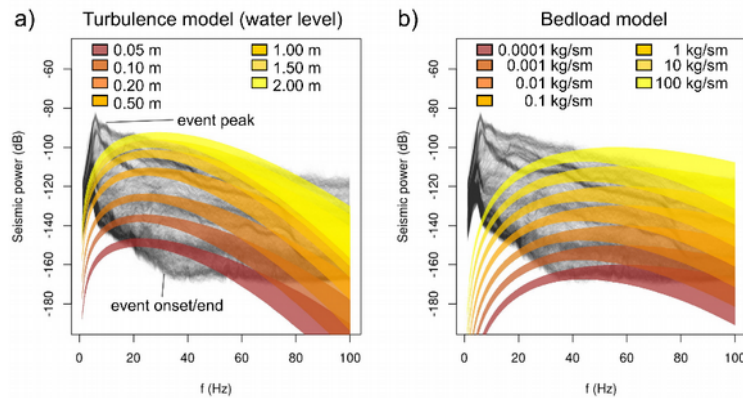
Seismic models

Turbulence signatures (after Gimbert et al., 2014) were calculated for flow depths from 0.05 to 2 m (Figure 4a), with relevant model parameters being allowed to range freely within meaningful limits (cf. Table 1). This range in depth covers most of the independently measured values (0–1.61 m) and the corresponding spectra span the majority of the energy levels of spectra measured by the broadband station (grey curves in Figure 4a). However, the shape of the modelled turbulence spectra is obviously different from the empirical one; most prominently below 20 Hz and above 60 Hz.

Bedload models (after Tsai et al., 2012) cover seven orders of magnitude, from 0.1 g/sm to 100 kg/sm. The lower value was set after exploring which flux best matches the lowest empirical spectrum. The highest value was set based on scaling the Reid type sampler values by the pipe microphone data (about 60 kg/sm). Here as well, the resulting spectra represent the range of the empirical data (grey curves in Figure 4b) but deviate significantly from those, predominantly, below 40 Hz.

Both model spectra overlap significantly and have their highest values in frequency bands different from the bands denoted in Figure 2 (5–8 Hz and 35–40 Hz). This underlines the ambiguities with separating the two sources of seismic signals by simply isolating these two

frequency bands. The overlap is caused not only by the range of individual spectra as a result of input parameter uncertainty and scatter, but also by the overall shape of the two model outputs.

Figure 4. Modelled seismic spectra caused by a) water turbulence and b) bedload transport. Shaded polygon area depicts inter quartile range of model solutions due to input parameter uncertainty. Grey curves in the background depict empirical spectra as measured by the broadband seismometer over the duration of the flash flood (i.e., corresponding to the vertical dimension of the spectrogram in figure 2).

Discussion

Clearly, there is a relation between the seismic record and fluvial dynamics. But this relation is far from straightforward. The temporal evolution of the seismic frequency bands, supposed to represent turbulence and bedload transport, deviates significantly from independently measured proxy data. Deviation may at least for the bedload proxy data be due to cross-sectional differing pipe microphone impact rates (dashed vs. dotted lines in Figure 1), caused by spatially non-uniform particle flux or cover and dampening effects. This highlights the need for a spatially averaging technique if the goal is to infer the general flow and flux characteristics, not only in a cross-sectional dimension but also along stream.

During this significant flood, two of the three Reid type basket samplers filled by a small fraction of the transported bedload. Furthermore, the pit samplers also show a spatially non-uniform evolution. These results also argue for the need of an additional, continuous and spatially averaging monitoring technique to better constrain the general event characteristics.

The seismic data indicate convolution of at least three sources of seismic signals. Although the Rio Grande would be able to cause seismic signals in the 2–8 Hz range (Cook et al., 2018), which is clearly visible before and after the flood event, it is unlikely to be the cause of the low frequency peak in the spectra as it cannot reach beyond -160 dB even under enormous flow conditions (model results not shown, based on 250 m distance to station, 80 m width, 3 m depth, coarse sand D_{50}). Thus, it is likely that other tributary channels or continuously operating seismic sources are responsible for the contamination of the data in this frequency band. The 5–8 Hz band as proxy for channel flow activity starts at a higher energy level than after the flood. This is most likely due to energy leaking from the 2–8 Hz seismic source into the 5–8 Hz frequency band. This tendency is visible in Figure 2a, where the persistent frequency band is active also hours before and after the flood event.

The observed spectra (Figure 4, grey background lines) can be explained in major parts (i.e., frequencies > 20 Hz) by a combination of the two seismic models (Tsai et al., 2012; Gimbert et

al., 2014). However, the dominant low frequency part (2–8 Hz) is not reproduced by any of the models. It may be related to local effects, such as the concrete reinforced cross section, resonating in its characteristic frequency. More investigations are needed to explore this effect, either by modelling the characteristic frequency of such a concrete body or by conducting dedicated seismic sensing of this structure. Likewise, the low power spectra, before the flood starts and just after it ended (i.e., low power spectra lines in Figure 4), only follow the flat -160 dB shape of typical "environmental noise" spectra above 40 Hz, while seismic power steadily rises below this frequency.

The convolution of channel flow turbulence and bedload flux signal is obvious when considering the Monte Carlo based seismic spectra models (Figure 4). While the turbulence spectra match the frequency range 20–60 Hz and the bedload spectra better describe the frequency range 60–100 Hz, both estimates overlap. Except for the extreme periods in water stage (1.61 m) and bedload flux (perhaps 20 kg/sm) – for which there is indeed agreement of empirical and modelled spectra – the number of potential combinations of similar likely spectra due to the two sources is high. This makes simple frequency band time series as proxies for water stage and bedload flux questionable, at least under the current setting of this observatory.

Accordingly, a more robust approach should explicitly account for the combined effect of at least two different seismic sources, thereby taking into account a wide range of frequencies along with the shape of the modelled spectra. Furthermore, uncertainty in the model parameter space should feed into the robust approach to develop a realistic estimate not only of the most likely values for key flood event metrics, but also their uncertainties. Thus, a Monte Carlo based inversion of physically based seismic models appears a prosperous approach to this problem.

Conclusion

In this ongoing study we used a seismic instrument as a high resolution, non-invasive sensor to continuously survey the spatially averaged characteristics of a sediment laden flash flood event at safe distance to the channel and its devastating effects. We compared the seismic ground motion data with other, independently constrained flood proxy data, and explored to which extent existing physically based seismic model results agree with the empirical data.

The spectral information in the seismic data (figure 2) show a distinct evolution of the signals contained in different frequency bands (figure 3), which is in general consistent with expectations from theory. While it would be appealing to extract key flood parameters by conveniently deploying a state of the art seismic station, there are several shortcomings adherent to this approach. The seismic data are by no means straightforward to interpret. The spectra emitted by at least three temporally distinct sources overlap significantly, whereby the source of a low frequency (2–8 Hz) signal is not yet resolved, but may perhaps be related to the characteristic frequency of the concrete structure of the observatory. Furthermore, the seismic station is subject to the influence of further seismic sources such as wind, rain, anthropogenic activity (though not in this particular case) and other river systems. Existing physically based model predictions fall well into the range of empirically determined data but overlap to a significant degree. Accordingly, it is vital to develop a manner to handle this mixed nature of the signals we record.

In addition, and in the light of the expected lifetime of the observatory, it might be valuable to reconfigure the seismic station components. The seismic data show that there is no need to work with broadband instrument data, as most of the signals of interest are > 1 Hz, whereas the

currently used sensor is ideal for frequencies between 0.008 and 200 Hz. Likewise, none of the models is designed for other than the vertical component data. Thus, it would be an option to replace the one three-component broadband sensor by three single-component geophones. These can be arranged in a triangular geometry with two sensors along stream and one sensor ca. 40–70 m away. Such a setup would allow for more profound insight into streamwise changes in hydraulic and sediment transport dynamics, but also allow a more robust inversion by adding a further data set at another distance to the channel, with other expected spectral properties to include to the inversion approach.

Acknowledgements

References

Barrière, J., Oth, A., Hostache, R. and Krein, A. 2015. "Bed load transport monitoring using seismic observations in a low-gradient rural gravel bed stream," Geophys. Res. Lett., 42, 2294–2301, doi:10.1002/2015GL063630.

Burtin, A., Bollinger, L., Vergne, J., Cattin, R. and Nábělek, J.L. 2008. "Spectral analysis of seismic noise induced by rivers: A new tool to monitor spatiotemporal changes in stream hydrodynamics," J. Geophys. Res., 113, B05301, doi:10.1029/2007JB005034.

Cohen, H., and Laronne, J.B. 2005. "High rates of sediment transport by flashfloods in the Southern Judean Desert, Israel", Hydrological Processes, 19, 1687-1702, doi: 10.1002/hyp.5630.

Cook, K., Andermann, C., Gimbert, F., Raj Adhikari, B. and Hovius, N. 2018. "Glacial lake outburst floods as drivers of fluvial erosion in the Himalaya," Science 362, 6410, 53-57, doi: 10.1126/science.aat4981.

Dietze, M. 2018. "The R package 'eseis' – a software toolbox for environmental seismology," Earth Surf. Dynam., 6, 669-686, doi: 10.5194/esurf-6-669-2018

Dietze, M., Turowski, J.M., Cook, K.L. and Hovius, N. 2017. "Spatiotemporal patterns, triggers and anatomies of seismically detected rockfalls," Earth Surf. Dynam., 5, 757–779, doi: 10.5194/esurf-5-757-2017.

Gimbert, F., Tsai, V.C. and Lamb, M.P. 2014. "A physical model for seismic noise generation by turbulent flow in rivers," J. Geophys. Res., 119, 2209–2238, doi: 10.1002/2014JF003201, 2014.

Gimbert, F., Fuller, B. M., Lamb, M. P., Tsai, V. C., and Johnson, J. P. L. 2018. "Particle transport mechanics and induced seismic noise in steep flume experiments with accelerometer-embedded tracers," *Earth Surf. Process. Landforms*, 44, 219–241, https://doi.org/10.1002/esp.4495.

Reid, I. and Laronne, J.B. 1995. "Bedload sediment transport in an ephemeral stream and a comparison with seasonal and perennial counterparts", Water Resources Research, 31 (3), 773-781, doi:10.1029/94WR02233.

Rickenmann, D., Turowski, J.M., Fritschi, B., Wyss, C., Laronne, J.B., Barzilai, R., Reid, I., Kreisler, A., Aigner, J., Seitz, H. and Habersack, H. 2014. "Bedload transport measurements with impact plate geophones: comparison of sensor calibration at different gravel-bed streams", Earth Surface Processes and Landforms 39, 928-942. DOI:10.1002/esp.3499

Schmandt, B., Gaeuman, D., Stewart, R., Hansen, S.M., Tsai, V.C. and Smith, J. 2017. "Seismic array constraints on reach-scale bedload transport". Geology.

Tsai, V., Minchew, B., Lamb, M.P. and Ampuero, J.-P. 2012. "A physical model for seismic noise generation from sediment transport in rivers," Geophys. Res. Lett., 39, L02404, doi: 10.1029/2011GL050255.

Welch, P.D. 1967. "The use of fast Fourier transform for the estimation of power spectra: A method based on time averaging over short, modified periodograms," IEEE T. Audio. Speech., 15, 70−73.

Turbidity Probe Testing Comparison

Teri Snazelle, Chemist, U.S. Geological Survey, Stennis Space Center, MS
tsnazelle@usgs.gov

Introduction

Turbidity is a measure of water clarity and is an important indicator of environmental health (Ziegler, 2002). Turbid water will appear cloudy from the presence of suspended solids such as soil particles, algae, microbes, and other substances in the water column. The turbidity of a body of water is determined by measuring how much the material or suspended solids in the water reduce or scatter the passage of light through the water column (American Public Health Association, 2012), however; turbidity is not a direct measurement, therefore the process of obtaining accurate measurements, and the proper interpretation of those measurements can be a challenge to the scientific community. Four commercially available turbidity sensors were field tested by the U.S. Geological Survey (USGS) Hydrologic Instrumentation Facility (HIF) to demonstrate the ability of different sensors to provide highly trending turbidity data, and to show that measurement variability can occur not only due to differences in sensor design or optical configuration, but also due to manufacturer practices in raw signal processing.

Description of Tested Sensors

The four tested turbidity sensors were the Xylem EXO, the HACH Solitax sc (Solitax), the In-Situ Aqua TROLL 600 sensor (TROLL 600), and the Observator ANALITE NEP-5000 sidescatter only sensor (NEP5000). The EXO turbidity sensor by Xylem is a nephelometric sensor that uses a near-infrared light source with a spectral range of 845-875 nm, and a single detector 90 degrees (^{0}) from the light (Xylem, 2017). The Solitax has dual infrared light sources with a spectral wavelength of 860 nm. The Solitax has a photodetector 90^0 from the light source, and another detector located 140^0 from the light for backscatter detection (HACH, 2017). The TROLL 600 turbidity sensor is another nephelometric sensor with a single LED light source with an 855 nm spectral wavelength, and a single detector 90^0 from the light (In-Situ, 2016). The ANALITE NEP-5000 is customizable; however, the probe in this study was a V3 90-degree ISO 7027-compliant sensor. The sensor has an infrared light source with spectral wavelength of 850 nm, and a single detector positioned 90^0 from the light (Observator Instruments, 2016) (Figure 1).

Figure 1. Tested turbidity sensors (right to left, and top to bottom); the EXO turbidity sensor, the HACH Solitax, the Aqua TROLL 600 turbidity sensor, and the ANALITE NEP-5000 by Observator

Procedures and Results

Test Setup

Sensor testing was conducted at USGS site 02492620 Pearl River at NSTL Station, MS from November 13, 2017 to January 2, 2018. Site 02492620 is designed with a programmable pumping system that fills a 10-gallon polyvinyl chloride (PVC) tank with water from the East Pearl River in 15-minute intervals. Each tested sensor was fitted with a nylon collar and securely mounted to the tank using a tank lid with pre-drilled holes. This installation protected the sensors from damage, minimized stray light from the tank and the other sensors, but most importantly, ensured that every turbidity sensor measured the same water at the same time.

Accuracy

Accuracy refers to the closeness of a measured value to a known value. Defining the accuracy of a turbidity sensor can be difficult because turbidity is not a direct measurement such as temperature or conductivity. Measured closeness or "accuracy" of the sensors is shown by the percent difference between the sensors' measured turbidity and corresponding discrete samples collected concurrently during the testing period (Figure 2). Discrete samples were analyzed on a calibrated bench top HACH 2100N turbidimeter operated in ratio mode with averaging and are listed in Table 1 along with the corresponding sensor measurements (HACH 2014).
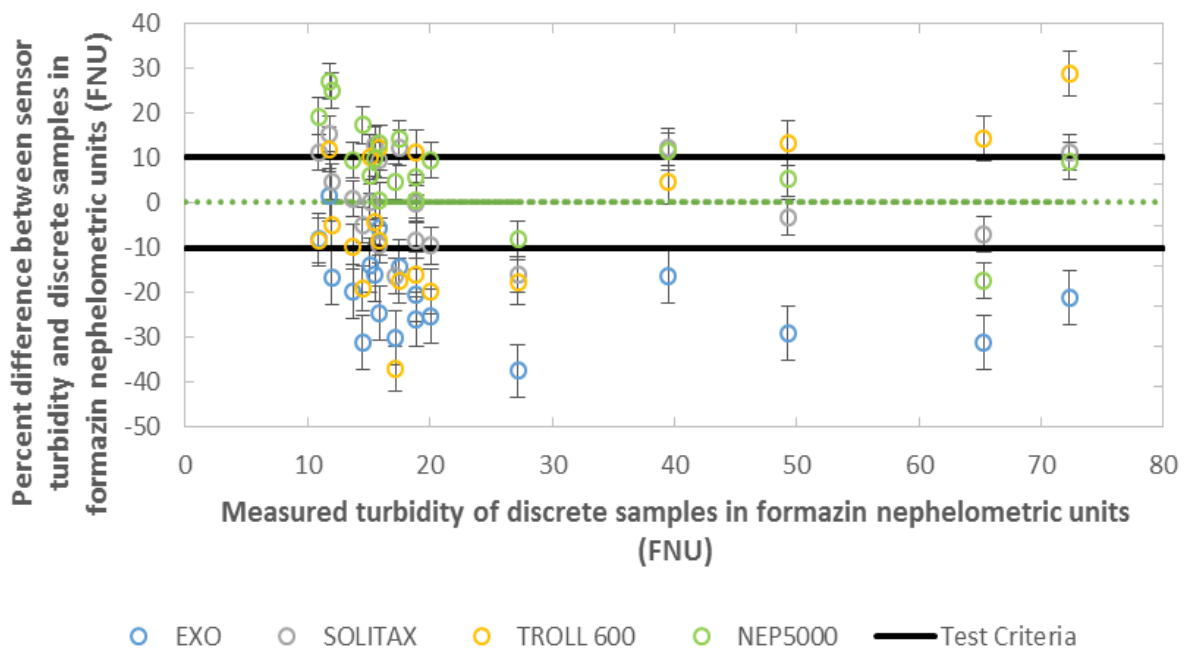

Figure 2. Percent difference between the sensors' measured turbidity in formazin nephelometric units, and the corresponding discrete sample turbidity analyzed on a HACH 2100N turbidimeter. Uncertainty was represented by the vertical error bars, and test criteria was established as plus or minus 10 percent

Table 1. Sensor turbidity data and corresponding discrete turbidity in FNU

| HACH 2100N (Discrete turbidity)	EXO	SOLITAX	TROLL 600	NEP5000
13.7	11	13.8	12.3	15
15.9	12	14.4	14.6	16
18.9	14	17.3	15.9	19
17.2	12	14.4	10.8	18
15.1	13	19.6	16.7	16
17.5	15	19.6	14.4	20
11.8	12	13.6	13.2	15
14.5	10	13.8	11.8	17
10.9	10	12.1	10.0	13
12	10	12.6	11.4	15
27.2	17	22.8	22.4	25
18.9	15	18.9	21.0	20
15.5	13	17.5	14.8	17
39.5	33	44.4	41.3	44
72.3	57	80.3	93	79
65.3	45	60.6	74.6	54
49.3	35	47.7	55.8	52
20.1	15	18.2	16.1	22
15.9	15	17.4	17.8	18

Data from the four sensors showed consistent trending even through occasional spikes in turbidity. Comparison of the continuous data to turbidity from the corresponding discrete samples showed good agreement as well (Figure 3).
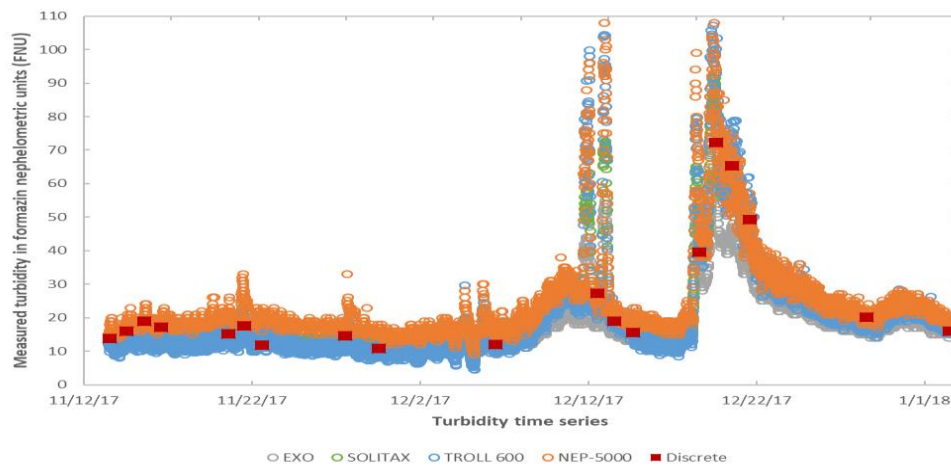
Figure 3. Turbidity time series showing the close trending of data produced by the four turbidity sensors. Red squares are the measured turbidity from discrete samples collected concurrently and analyzed on a calibrated bench top HACH 2100N turbidimeter

Discussion

A rolling filter is a moving or sliding average of raw signal designed to smooth out fluctuations in the data. Filtering or processing of raw data is a common practice, but many processes are proprietary. As shown in figure 4, Data from the EXO turbidity sensor demonstrated a low bias as compared to the HACH 2100N and to some of the other tested sensors. Xylem is forthcoming with their filtering processes and allows the user to select from three modes of filtering; default, accelerated, and rapid. For this test, the default mode was used which averages up to 40 seconds of data. In addition, Xylem applies outlier rejection protocols to the data that further processes and smooths the raw signal. The default mode for the Solitax is a 3 second averaged window. The NEP5000 is factory configured for a 5 second window, and the TROLL 600 takes three independent measurements, and depending on the variance between the measurements, either averages the data or takes the median. Variations in signal processing can cause obvious differences in data when comparing one sensor to another and shifts in continuous data may occur when the site turbidity sensor is replaced.
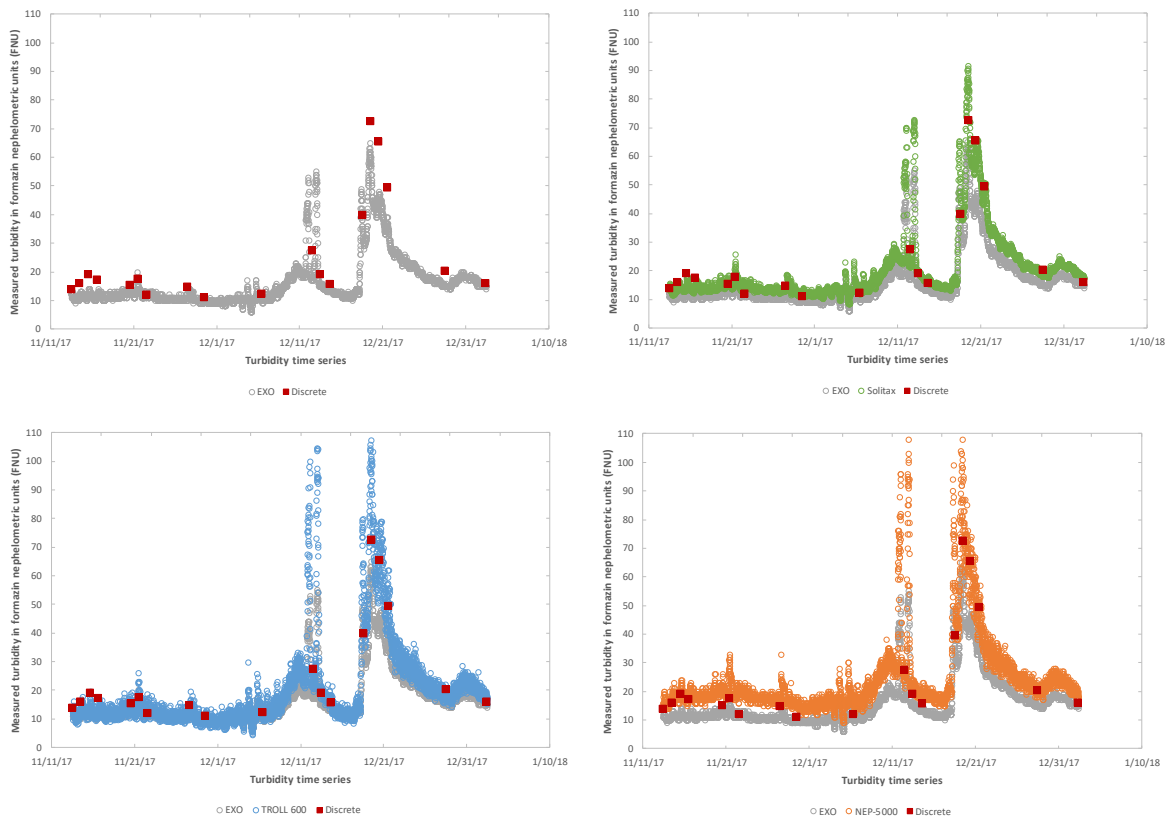
Figure 4. Four time series showing EXO data compared to discrete sample results, SOLITAX compared to EXO and discrete, TROLL 600 compared to EXO and discrete, and NEP5000 compared to EXO and discrete (left to right and top to bottom)

Conclusion

Four in situ turbidity sensors were evaluated at USGS site 02492620 for data comparability to each other and to concurrently collected discrete samples that were analyzed on a HACH 2100N bench top turbidimeter. All sensors were calibrated and/or calibration-verified prior to deployment and were serviced weekly during the evaluation period. The turbidity sensors were

deployed to ensure that the same water was measured by all sensors, while eliminating stray light as much as possible. The sensors trended closely with each other and with discrete samples collected during the evaluation period. Differences were observed between the individual sensors and the EXO site sonde turbidity, and the EXO data showed a low bias as compared to the other sensors' data.

Differences observed in sensor data were more than likely due to the differences in signal processing. Filtering or raw-data processing is not uncommon among sensor manufacturers, and many of these processes are proprietary. Xylem offers different filtering modes, but the default setting averages up to 40 seconds of filtering, and is the mode used for the site sonde turbidity sensor at USGS site 02492620. To further process and smooth the raw turbidity data, Xylem employs additional outlier rejection protocols that other manufacturers do not use. The Solitax and NEP-5000 have adjustable filter durations. The Solitax default setting is a 3 second averaging filter, and the NEP-5000 default is set for a 5 second averaging filter. The TROLL 600 takes three independent measurements, and depending on the variance between the measurements, reports either the average or the median of the three.

References

Hach Company, 2014, DOC022.97.80203, 2100N, Basic user manual, edition 5.

Hach Company, 2017, LIT2472, Solitax sc turbidity & suspended solids sensors, edition 9.
In-Situ Inc., 2016, 0096402, Aqua TROLL 600 Multiparameter Sonde Operator's Manual, revision 3.

Observator Instruments, 2016, ANALITE NEP5000 turbidity sensor datasheet, version 102016.
Xylem, 2017, EXO user manual revision g; Advanced water quality monitoring platform: Yellow Springs, Ohio, Yellow Springs Instrument (YSI) Incorporated, 154 p.

Ziegler, A.C., 2002, Issues related to use of turbidity measurements as a surrogate for suspended sediment, *in* Gray, J.R., and Glysson, G.D., eds., Proceedings of Federal Interagency Workshop on Turbidity and Other Sediment Surrogates, Reno, Nev., April 30–May 2, 2002: U.S. Geological Survey Circular 1250.

Uncertainty and Parameter Sensitivity of the KINEROS2 Physically-Based Distributed Sediment and Runoff Model.

Menberu B. Meles, USDA-ARS, Southwest Watershed Research Center, Tucson, AZ, Menberu.Bitew@ars.usda.gov
Dave C. Goodrich, USDA-ARS, Southwest Watershed Research Center, Tucson, AZ, Dave.Goodrich@ars.usda.gov
Hoshin V. Gupta, University of Arizona, Department of Hydrology and Water Resources, Tucson, Arizona, USA, hoshin.gupta@hwr.arizona.edu
I. Shea Burns, University of Arizona, School of Natural Resources and the Environment, Tucson, Arizona, USA, isburns@email.arizona.edu
Carl L. Unkrich, USDA-ARS, Southwest Watershed Research Center, Tucson, AZ, carl.unkrich@ars.usda.gov
Saman Razavi, University of Saskatchewan, Global Institute for Water Security, Saskatoon, Canada, saman.razavi@usask.ca
D. Phillip Guertin, University of Arizona, School of Natural Resources and the Environment, Tucson, Arizona, USA, dguertin@cals.arizona.edu

Introduction

Advanced hydrologic modeling tools play an important role in developing sustainable rangeland and water resource management systems, including the implementation of real-time flood forecast and warning systems (Creutin and Borga, 2003; Kitanidis and Bras, 1980a, 1980b), and assessments of climate change adaptation strategies. In the semiarid southwestern US, the highly nonlinear nature of the rainfall-runoff relationship (Yatheendradas et al., 2008; Goodrich et al., 2000; Pilgrim et al., 1988) makes understanding the sources of modeling uncertainty especially difficult. In this region, precipitation is extremely localized, and summertime convective thunderstorms are exceptionally intense (Roeske et al., 1989, Keefer et al., 2015). The resulting flash floods in the region are considered to be the deadliest natural disaster in the US, accounting more than 80% of all flood-related deaths; the average economic losses are about one billion U.S. dollars per year (American Meteorological Society, 1985). As a result of anthropogenic global warming the southwest is also expected to experience increased drought frequency (Seager et al., 2007; IPCC, 2013; Cook et al., 2014; Zhao and Dai, 2015; Feng et al., 2014). Short-term droughts can reduce agricultural crop yields, while longer-term droughts can lead to increased wildfire risks with subsequent mudslides and flooding.

The advanced, high-resolution, spatially distributed KINEROS2 (Kinematic Runoff and Erosion) modeling system (Smith et al., 1995; Semmens et al., 2005) is well suited to arid and semi-arid watersheds (Goodrich et al. 2012), providing a physically-based representation of the highly variable response typical to semiarid rainfall forcing and the consequent infiltration and runoff processes experienced in the southwest. Herein, we assess the relative importance of controls exerted by all the KINEROS2 parameters on hydrologic outputs. As advanced and realistic its representation of the hydrology of the southwest arid environment is, KINEROS2 (K2) results can only be as good as the quality of input and values of the parameter estimates. To explore how realistic the model results are, we must understand the relative influence of uncertainties and model output sensitivities from sources such as forcing inputs, initial conditions and model parameters.

The process by which we can understand the relative influence of parameters on the dynamics of hydrologic model behavior is termed sensitivity analysis (SA). In addition to helping elucidate the impact of different model structures, SA also helps the modeler to prepare for model parameterization, and to direct research priorities, by establishing which parameters contribute the most to uncertainty in the model response (Razavi and Gupta, 2015; Wei et al., 2007; Saltelli and Campolongo, 2000; Breshears et al., 1992). As discussed in Razavi and Gupta (2015) and Razavi and Gupta (2016a,b), several SA approaches such as the Morris method (Morris 1991; Campolongo et al. 2007), Sobol method (Sobol, 1990; Saltelli et al., 2008), PAWN method (Pianosi and Wagener 2015), DELSA method (Rakovec et al., 2014), and Moment-based method (Dell'Oca et al 2016), etc., can provide identical sensitivity rankings for situations having very different parameter sensitivity properties. In view of the limitations of many current SA methodologies, there is a need for robust, informative and computationally efficient sensitivity analysis (SA) techniques for developing, understanding, and applying the details of hydrologic modeling systems (Gupta and Razavi, 2018).

In this work, we implemented the Variogram Analysis of Response Surfaces (VARS) methodology (Razavi and Gupta, 2016 a, b) to assess the importance of KINEROS2 parameters, and to investigate the dynamics of parameter importance with varying rainfall depth/intensity on the Lucky Hills watershed at the Walnut Gulch Experimental Watershed, Arizona. Unlike other SA analysis tools, VARS accounts for the spatial correlation in model response as parameters are varied, is more efficient and cost effective, and has been reported to provide more reliable (stable) estimates in the face of sampling variability (Gupta and Razavi, 2018). We compare the results of the VARS method to that of the Sobol (Sobol' 1990; Saltelli et al., 2008) and Morris (Morris 1991; Campolongo et al. 2007) methods, which are included in the VARS computations as by-products.

The framework followed here is known as Global SA (GSA). We investigate the strength of influence of K2 parameters on different types of model output attributes or response surfaces. We also test how the strengths of influence of the parameters change based on the variability of rainfall intensities. The model output attributes studied are the predictive utilities of the K2 model applied to an event-scale simulated high-resolution runoff and sediment rate. We identified a total of 12 predictive utilities (response surfaces) from the K2 predicted runoff and sediment yield outputs. Most of these responses are categorized as performance-metric-free (Gupta and Razavi, 2018), such as flow rate, peak flow rate, flow duration, time-to-peak, time-to-start runoff, recession time, average sediment rate showing mass of sediment per given unit time, peak sediment rate, and total sediment mass. We also explore the influence of the parameters on selected performance-metric-based responses that represent goodness-of-model-fit to the observations; this includes the Nash-Sutcliffe efficiency coefficient (NSE, Nash and Sutcliffe, 1970), Bias (Observation−model prediction) and Kling-Gupta efficiency (KGE, Gupta et al., 2009).

The objectives of the paper are (i) to evaluate the strengths and weaknesses of the metric-free GSA methodology in regard to identifying parameter importance in the context of time-variant and total-period time-aggregate model responses, and (ii) to evaluate the impacts of rainfall intensity on the importance of parameters in modeling rainfall-runoff systems. The latter objective will aid understanding of the effects of parameter perturbation and their importance across simulation periods using K2 model outputs in southwestern USA.

Data and Methods

Using changing rainfall intensities to force the model, we investigated the impact of parameter perturbations on several targeted responses of the event-based, physically distributed, hydrologic model KINEROS2.

Data

Data from six, small to large rainfall depth rainfall-runoff events(Figure 1) from the Lucky Hills watershed were selected for the analysis. Event data are available in the DAP (Data Access Project) database as breakpoint formatted rainfall hyetographs and runoff hydrographs that include time and accumulated depth at slope breaks (Goodrich et al., 2008). DAP is a database for the Walnut Gulch Experimental Watershed (WGEW) that contains high-quality long-term hydro-climatic observations (https://www.tucson.ars.ag.gov/dap/, Nichols and Anson, 2008). Lucky Hills is a very small (4.8 hectare), specialized, experimental watershed within WGEW.
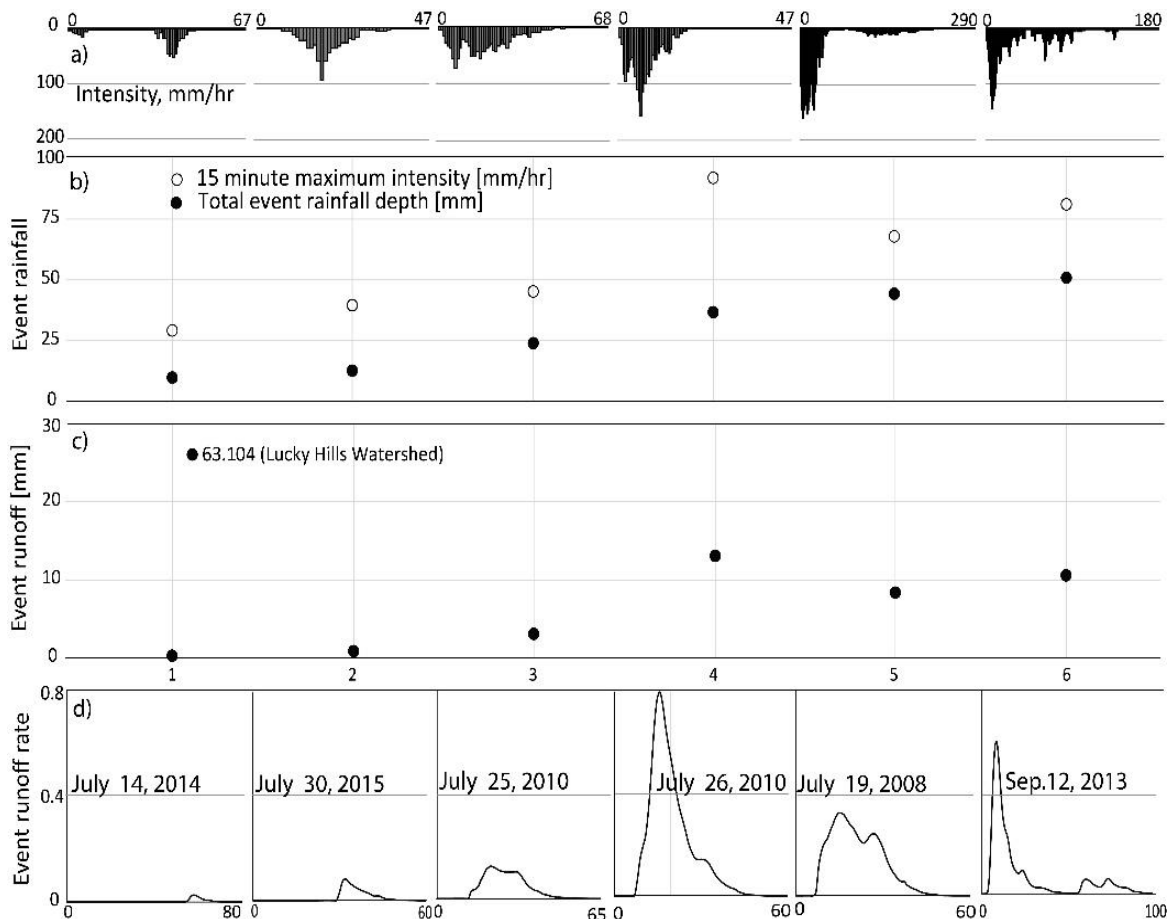
Figure 1. Six selected rainfall and corresponding runoff events in Lucky Hills, a) hyetograph in mm/hr (duration of the rainfall is given in the x-axis), b) event rainfall depth and 15-minute maximum intensity of rainfall for the selected events, c) the corresponding total runoff, and d) the corresponding hydrograph. The rainfall and runoff are sorted based on increasing depth of rainfall from left to right.

Modeling Using K2

K2 (Semmens et al., 2005; www.tucson.ars.ag.gov/agwa/kineros) is an event-based, physically distributed model developed to simulate runoff and sediment responses in southwestern arid environments. K2 simulates entire hydrographs and sedigraphs for a single rainfall event (Goodrich et al. 2012) at sub-minute time step resolution. The model represents interception and the dynamics of infiltration and infiltration-excess surface runoff, and flow routing is based on a finite difference solution of the one-dimensional kinematic wave equations over a basin conceptualized as a cascade of planes (hillslopes) and channels. The Automated Geospatial Watershed Assessment Tool (AGWA, Miller, et al., 2007; www.tucson.ars.ag.gov/agwa/) was used to support the K2 modeling effort in setting up the model, parametrization, and execution of the simulation. Initial estimates for the K2 parameter values were obtained through AGWA parametrization using input GIS layers such as a DEM, SSURGO soils, and USGS land use data layers. The DEM used in the modeling exercises was LiDAR-derived with a 1m resolution.

Our sensitivity analysis investigated seven of the model parameters reflecting infiltration, runoff, flow routing, and soil characteristics including the Saturated Hydraulic Conductivity (Ksat), Manning's coefficient (n), coefficient of variability of Ksat (CV), capillary drive coefficient (G), intercepted depth (In), sediment cohesion coefficient (C), and sediment splash coefficient (S). Target responses from flow and sediment outputs of K2 were generated iteratively using a suite of AGWA-K2 multiplier files with values between 0 and 2.

Response Surfaces

Response surfaces (model output attributes) of the target model were created based on randomly generated sets of multiplier values applied to each parameter. For each randomly generated parameter set, we computed the time series of the runoff and sediment rate, from which we extracted the 12 response surfaces used to evaluate the relative importance of the K2 parameters. These include two flow-rate related, three sediment -yield related, and four flow-time related performance-metric-free responses and three goodness-of-model-fit performance-metric-based responses. Listed together, these responses are: Average flow rate (cfs), Maximum flow rate (cfs), Flow duration (min), Time-to-peak (min), Time to runoff start-time(min), Recession time (min), Average sediment yield per event runoff (kg/ha), Maximum sediment rate (kg/sec), Total sediment yield for the event (kg/ha), Nash-Sutcliffe Efficiency coefficient, Bias, and Kling-Gupta Efficiency coefficient.

VARS Methodology

The VARS framework (Razavi and Gupta, 2015a,b) enables robust and efficient global sensitivity testing of model responses based on a star-based sampling strategy (known as STAR VARS) (Razavi and Gupta, 2016b) across the full range of parameter space. The global sensitivity of a given model response y with respect to a model property θ varying within the feasible space is characterized by its variogram γ(h) and covariogram C(h) functions:

$$\gamma(h) = \frac{1}{2}V(y((\theta + h) - y(x)) \tag{1}$$

$$C(h) = \frac{1}{2} COV(y((\theta + h) - y(x))) \tag{2}$$

where $h = \theta^A + \theta^B$ is the length of the vector $h = \{h_i, \dots h_n\}$ between any two points A and B in the factor space. Directional variograms $\gamma(h)$ and covariograms $C(h)$ provide sensitivity information across a full range of scales. These variogram based sensitivity metrics are also integrated to provide integrated summary metrics (IVARS: Integrated Variogram Across a Range of Scales) for particular scales (H_i) of interest.

$$\Gamma(H_i) = \int_0^{H_i} \gamma(h_i) dh_i \tag{3}$$

For the details of the theoretical and mathematical formulation of VARS methodology, readers are referred to Razavi and Gupta, 2015; Razavi and Gupta, 2016 a, b; Gupta and Razavi, 2018. Because of the close theoretical connection between VARS directional variograms as $h_i \to 0$ and the expected value of the square of the ratios of changes in output to changes in inputs, VARS-SA is closely associated to the Morris-based SA. Similarly, the variogram and covariogram functions are closely related to the total-order effect Sobol variance-based SA as h_i becomes large. Based on this close relationship between VARS and the Morris and Sobol' methods, the VARS methodology provides reliable estimates of the Sobol and Morris sensitivity rankings as by-products at no extra computational expense (Gupta and Razavi, 2018).

In this work, we conducted the SA based on both the total-period and time-variant analysis in VARS offline mode using the procedure described in the Razavi (2018) VARS user's manual. First, sets of the K2 parameter multipliers were randomly generated using Latin-Hypercube sampling within the feasible range of the multipliers in a STAR VARS sampling strategy (Razavi and Gupta, 2016b) to extract sensitivity information across the full extent of the parameter space. Second, we ran K2 for each set of parameters and for each of the selected rainfall events. Third, we ran VARS tool in offline mode to construct and analyze the Generalized Global Sensitivity Matrix (GGSM). First, we extracted the 12 target model responses from the K2 model simulation outputs. Each of the target surfaces were considered as a single output surface. Then we applied a conventional total-period GGSM analysis using each of the single output response surfaces. Here the variogram-based algorithm computes the overall (total time-period) relative parameters importance through Directional variograms γ(h), covariograms C(h), and IVARS generated for this analysis. Subsequently, we implemented the time-varying GGSM analysis to conduct a time variant sensitivity assessment using the entire K2 simulation outputs for each of the parameter sets. For this time variant sensitivity analysis, we examined two types of simulated time series (sediment and flow rate) for all the selected rainfall events.

$$\nabla_\Theta Y^k(t) = \begin{bmatrix} dY_t^k \big/ d\theta_1^1 & \cdots & dY_t^k \big/ d\theta_1^{N_{Pts}} \\ \vdots & \ddots & \vdots \\ dY_t^k \big/ d\theta_{N_\theta}^1 & \cdots & dY_t^k \big/ d\theta_{N_\theta}^{N_{Pts}} \end{bmatrix} \tag{4}$$

The global sensitivity matrix $\nabla_\Theta Y^k$ is a three-dimensional array of the partial derivatives of the system output Y^k as it varies with time (t = 1,…, T), with the number of parameters (N_θ) and the number of points (N_{Pts}) sampled across the feasible space. Accordingly, $\nabla_\Theta^j Y^k(t)$ (see Equation

4) is corresponding two-dimensional sub-matrix at a specific simulation time step t. The index k ={1, 2} indicates the simulation output (e.g., sediment and runoff rate) of interest. In the conventional GGSM k ={1, ... 12} represents the targeted surfaces without the simulation time dimension. For details of the analysis on the dynamic time variant VARS algorithm readers are encouraged to see Gupta and Razavi (2018).

Here we present the analysis and interpretation of both conventional GGSM of the single output response surfaces and the dynamic VARS outputs. The interpretations are based on values of the IVARS $\Gamma(H)$, and also of the percent sensitivity across the h distance vectors, where the latter is defined as the value of $\Gamma(H_i)$ for each parameter divided by the sum of $\Gamma(H_i)$ for all the parameters multiplied by 100.

Results and Discussion

Total Time-Period GSA

The relative importance of each K2 parameter identified using the VARS methodology was found to be intuitively consistent with the type of response investigated. In Figure 2, we show the relative importance of each of the K2 parameters to each of the responses, along with 90% confidence intervals of the parameter space. Clearly, the degree of importance of each parameter depends on the type of the response investigated. Further, we find a significant difference in the level and kind of parameter importance when evaluated for the different categories of performance-based and performance-metrics free responses. As expected given the dynamical aspect of the model, the time leading up to runoff generation is affected by all the flow parameters, with saturated hydraulic conductivity (Ksat), the capillary coefficient(G), and the variability of conductivity coefficient (CV) playing the most significant roles. However, for the flow time components responses such as duration, time to peak, and recession time, Manning's coefficient (n) appears to be the most dominant parameter. In surfaces that cover a small part of the simulation period such as the time to peak and time to start, almost all K2 flow parameters showed noticeable importance, but the number decreases to 3 (flow and time-related responses) or 4 (sediment related responses) in other response surfaces.

When using the Bias, NSE, and KGE performance-based flow rate metrics as responses, the saturated hydraulic conductivity was found to be most important, with the G value and n also having a significant impact. Using the performance-metric-free flow rate related responses, the Manning's coefficient is the most important parameter, although its impact reduces when the peak flow rate is used as the response. When examining the performance-metric-free sediment yield related responses, the hydrologic conductivity, soil surface roughness, and cohesion coefficient property related parameters play a significant role.
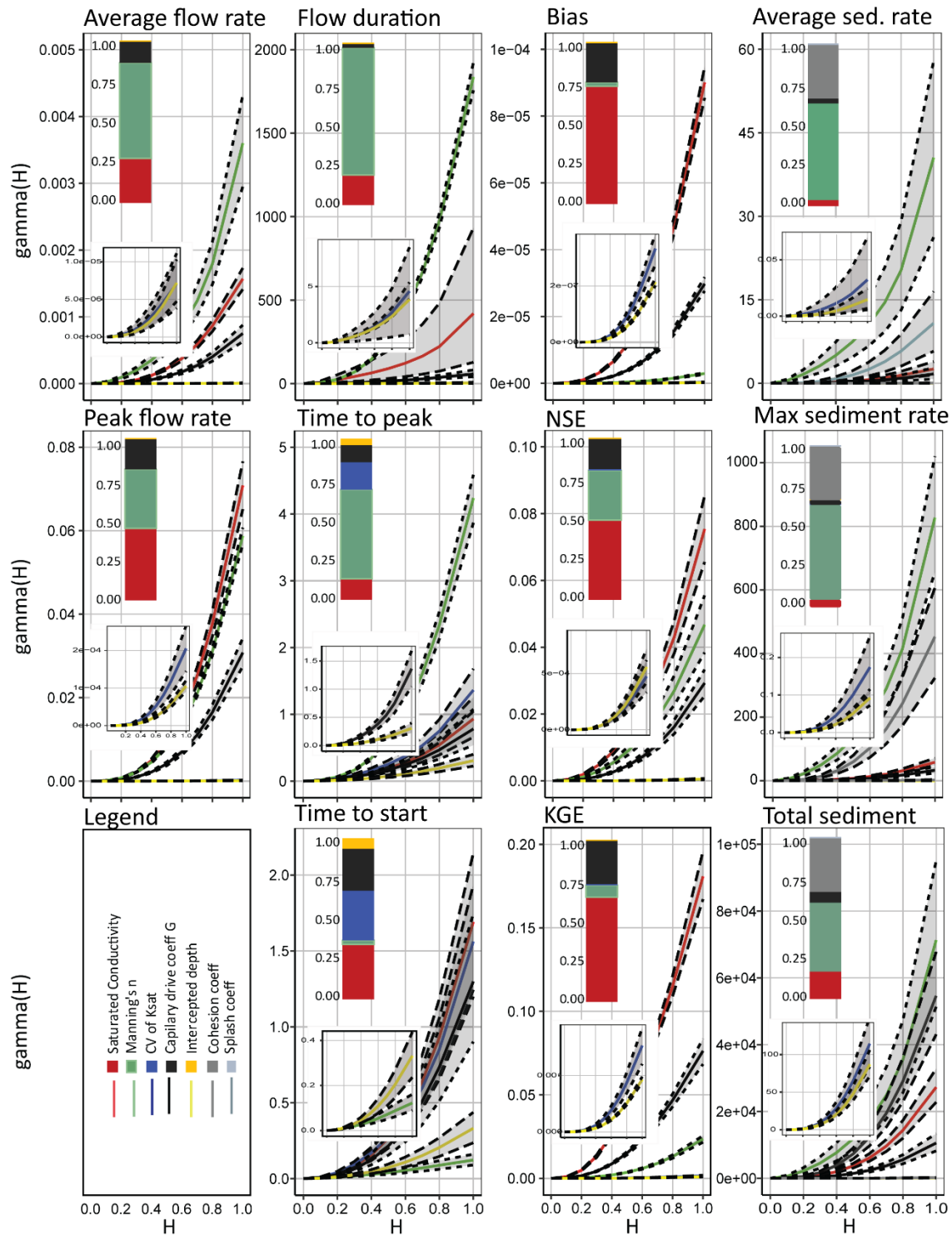
Figure 2. Bootstrap-based uncertainties (90% confidence interval) of the integrated variogram sensitivity metrics (y-axis) for 11 model outputs over the range of STAR-VARS (x-axis) for seven KINEROS2 parameter multipliers. Inter-related response surfaces grouped on columns of flow volume, time aspect of flow rates, optimization measures of flow rates compared to observed flow, and the sediment yield components from left to right, respectively. The inset in each panel shows the details of each the sensitivity of each of the parameters. The stacked bar chart shows the extent of sensitivity of the parameter multipliers to each response.

Figure 2 also shows that the ranges of the 90% confidence (uncertainty) intervals vary from one response to another. With the full VARS trial of 100 samples of the cross section for each factor (with a total of more than 6000 function evaluations) some responses such as Bias and KGE provide evidence for robustness against sampling variability. It is evident that the level of robustness also varies by parameter, even when compared for the same response (see flow duration, maximum sediment rate, etc).

Clearly, parameter importance can depend on the type of metric and the response investigated, as illustrated by Figure 3, where the parameter rankings vary significantly except for the sediment related responses. In the latter, the rankings do not change, but the magnitude of sensitivity shows noticeable change. One sees the same for the two performance-based metrics Bias and KGE. The difference in the percent sensitivity values and the ranking between "duration" and "recession time" were comparable for the dominant parameters with little variation in the two insensitive parameters (CV of Ksat and the intercepted depth). This small variation is attributable to the similarity between the flow duration and the recession time (the flow duration minus the time to peak) which is very small in the southwest arid environment because of the short-lived nature of intense rainfall.
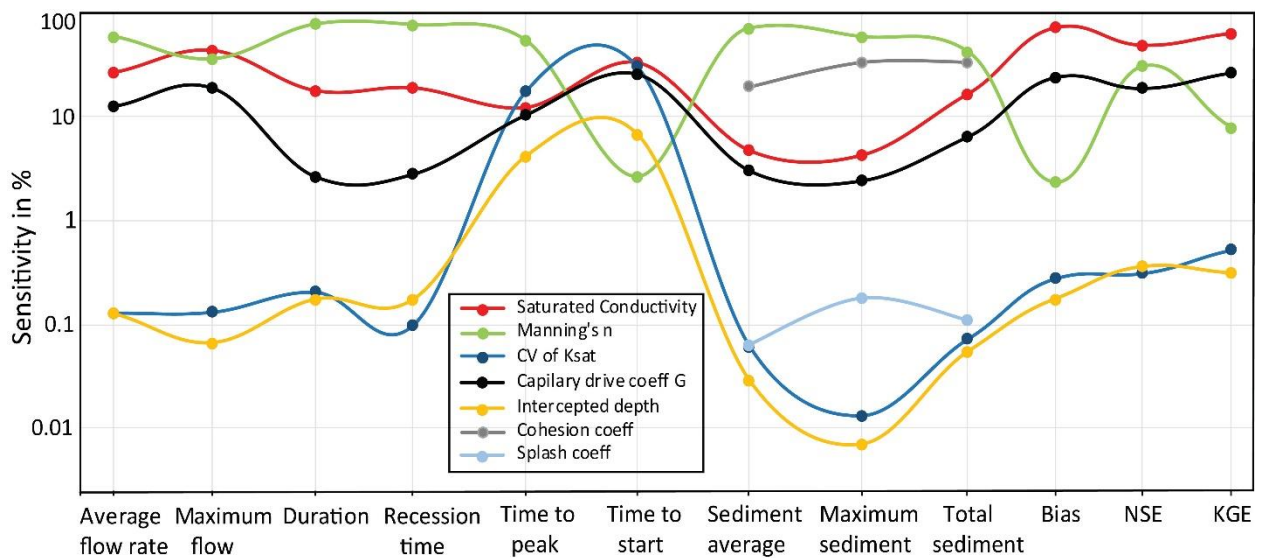

Figure 3. Comparison of sensitivity of each of the parameters across the all the responses (note that the y-axis is on a log scale).

The analysis also reveals significant variability in the sensitivity values of flow rate and sediment responses. The variability is minimal in the responses "time to peak" and "start time", which share two properties in common: 1) all the parameters play an essential role, 2) the ranges of the responses are very small.

Comparison of SA Methods

To compare the broader view of sensitivity, we used the percent of sensitivity values of three sets of sensitivity metrics (Figure 4) found in the VARS framework. The figure showed nine selected response surfaces in three groups. The Sobol and Morris performance metrics are compared in

Figure 4 because of their similarity to the VARS method and included computation within the VARS structure (Gupta and Razavi 2018).
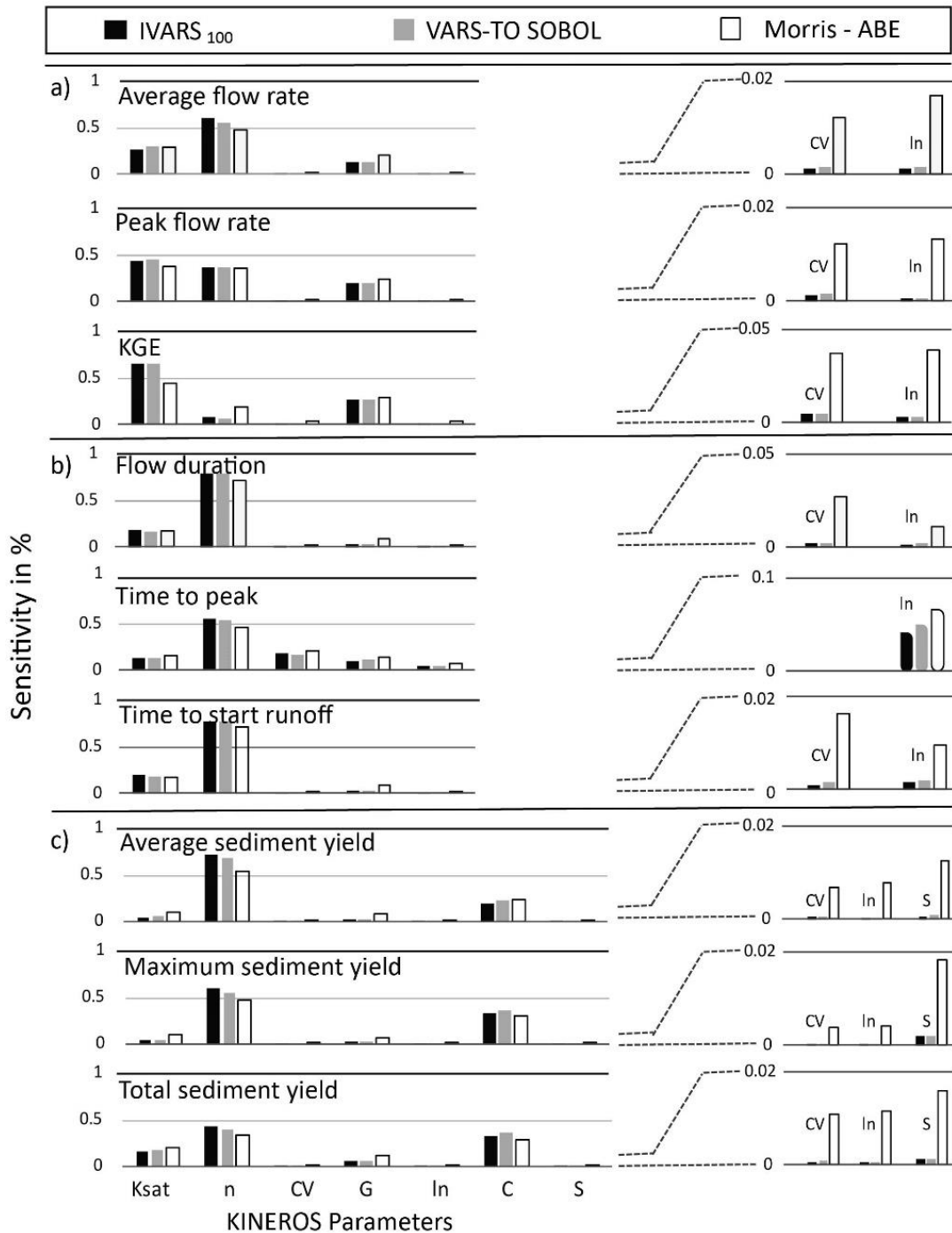

Figure 4. Comparison of the IVARS sensitivity to the variance-based Total-Order effect (TO-Sobol) and the derivative based Morris sensitivity metrics for K2 parameters across the different response surfaces. The vertical axis shows the proportion of each of the metrics as ratio of the sensitivity values obtained by dividing each of the sensitivity values by the sum of the sensitivity values of all the parameters. The right side plot shows a zoom-in of the left side plot. The comparison includes a) flow related, b) time related, and c) sediment related responses.

In this case study, the variance-based total-order (Sobol-TO) and derivative based Morris sensitivity metrics showed equal ranking to the resulting VARS metrics. Even though the ranking was similar across the different methods, the extent of sensitivities was different. The results show that both Ksat and n played a significant impact in flow rate related surfaces. In the time-related response surfaces, the parameter n showed dominance compared to other parameters. However, in the sediment response surfaces, n was the dominant parameter with the second dominant parameter being the soil cohesion coefficient (C).

Time-variant GSA

The extent of sensitivity of the parameters were smaller in the Morris method for parameters that showed essential impacts on the response surfaces such as the Ksat, n, G and C. However, among the insensitive parameters (see Figure 4, right side) the Morris metric showed significant difference compared to both IVARS and Sobol.
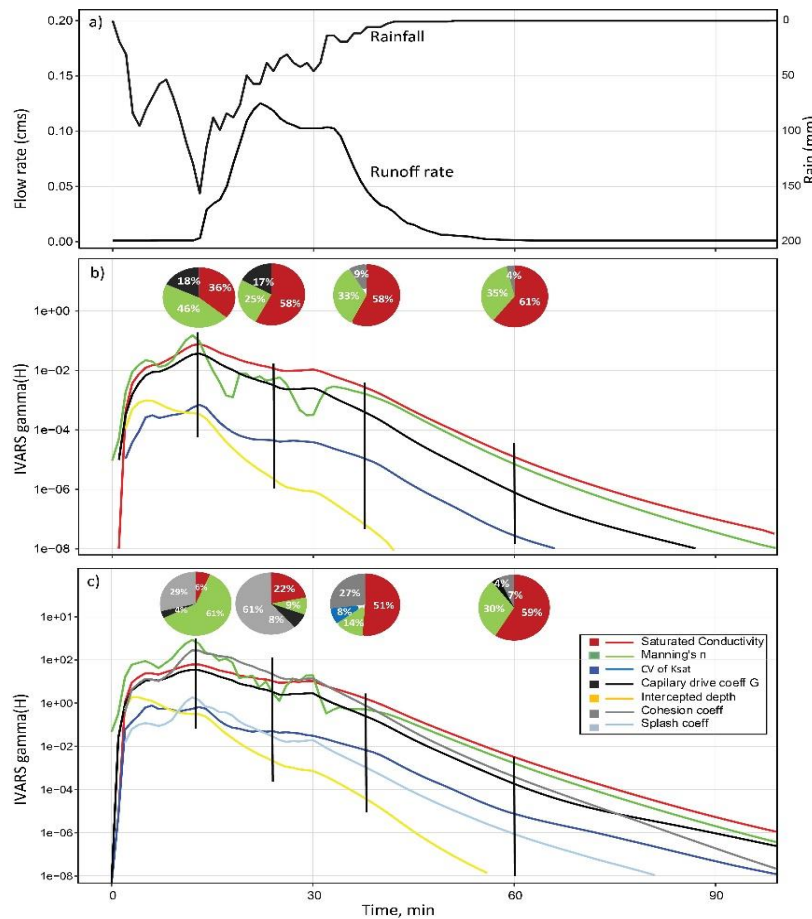

Figure 5. Time-variant sensitivity of K2 parameters for the duration flow of the event 5, a) rainfall and runoff hydrograph of event ID #5, b) the IVARS values of parameters related to flow, and c) the IVARS values of all K2 parameters. Note that the y-axis in b and c are in log scale. The pie charts on b and c represent the proportion of the sensitivity metrics at four sections of the hydrograph. These are: on the rising limb (at the time when the rainfall hit maximum intensity), peak runoff rate, time at the median of the flow rate on the recession side, and the time of the smallest flow.

Using the event #5 of July 19, 2008 (Figure 5) we showed the hyetograph and hydrograph (Figure 5a) and the corresponding high-resolution sensitivity indices of the parameters on the simulated runoff (Figure 5b) and sediment yield (Figure 5c) from the Lucky Hills watershed. In both b and c, the time-varying changes in parameter importance illustrate the integrated effects of the algorithms of K2 modeling structure and the entire system drivers (climate, surface topography, soil, and land cover properties). The GSA results were evaluated at high temporal resolution (1-minute time step) of the K2 outputs. The importance of all K2 parameters became stronger with the increasing rainfall intensity with time and decreased as the rainfall subsides. The significance of the parameter trajectories continues even after the rainfall stopped over the runoff period. The four pie charts in the subplots b and c showed the extent of the importance in percent. The relative importance of the Ksat (red) seems to increase over the event flow period on flow rate while the relative importance of the Manning's n (green) decreases then increases over time, and the capillary drive coefficient (black) decreases over time. In the simulated sediment yield (Figure 5c), most trajectories of parameter importance showed variation across the simulation period, though Ksat (red) exhibited the same increasing trajectory as for flow rate. In the time variant analysis of parameter importance, the event-based simulation capability of K2 provides a unique opportunity to study the effects of parameters and associated model forcing on the response surfaces.

Effects of Rainfall Intensity on Parameter Importance

The level of parameter importance varies according to the intensity and depth of rain received in the watershed (Figure 6). The selection of the three parameters (Ksat, n, and G) and response surfaces (average runoff rate, KGE, and time to peak) was made for illustrative purposes. The relative importance of Ksat is consistently lower for high-intensity rain regardless of the type of responses, and increases with decreasing rainfall intensity. The influence of Manning's coefficient and the capillary drive coefficient increases with increasing rainfall intensities for average runoff rate and time to peak based surfaces while its influence reverses for the performance-based KGE surface. We, therefore, conclude that rainfall intensities influence parameter importance differently on different model output attributes.
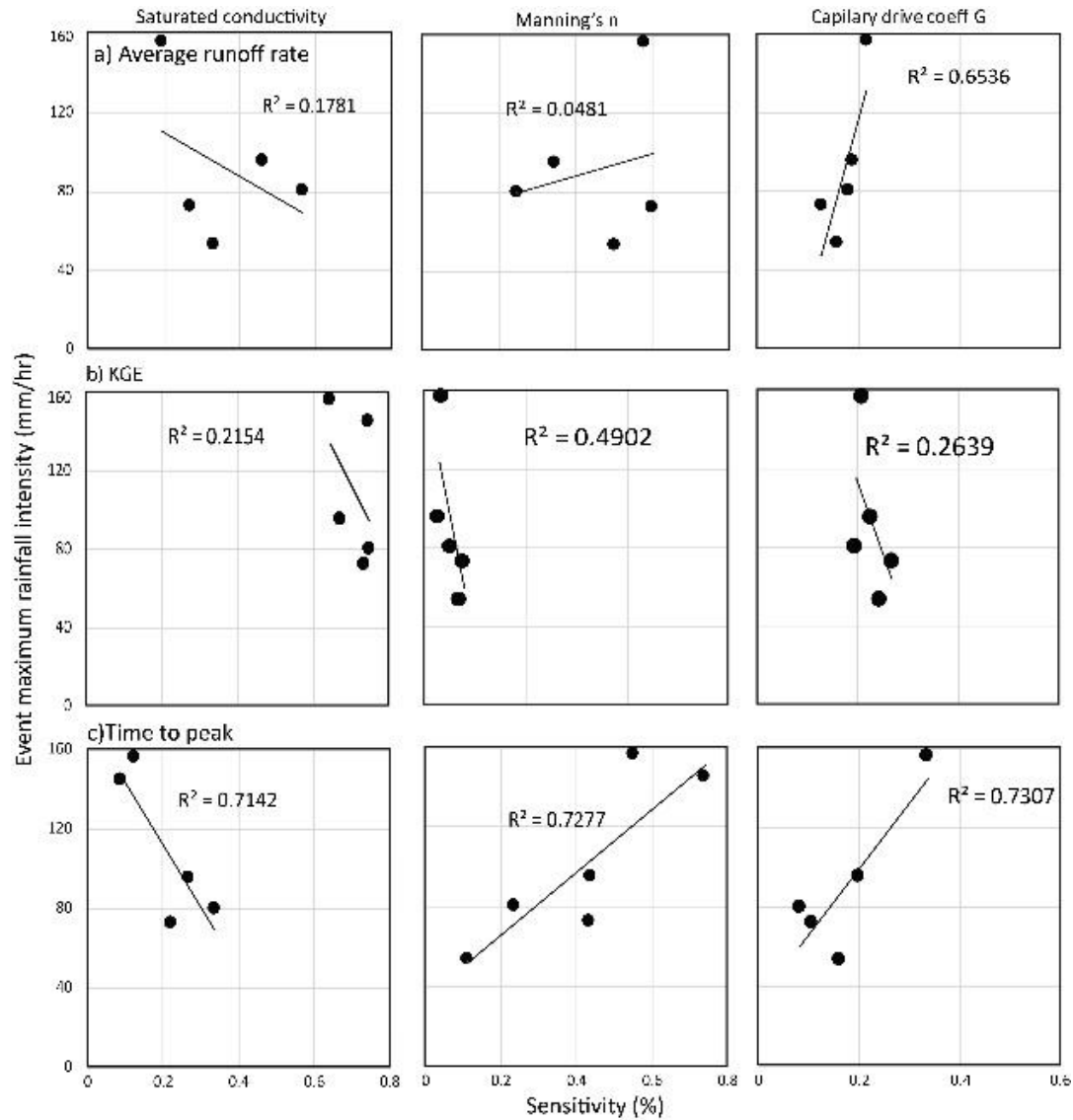
Figure 6. Comparison of the influence of rainfall intensity variation on parameter importance. Sensitivity values of selected K2 parameters (Ksat, n, and G) for a different range of event rainfall intensities. The rows indicate three selected response surfaces: a) average runoff rate, b) KGE, and c) time to peak.

Conclusions

The study revealed that the extent and rankings of parameter importance varies depending on the type of model output attributes (response surfaces) and the rainfall intensities. In flow rate and sediment related response surfaces, the VARS sensitivity metrics showed considerable variability among K2 parameters with Ksat, n, and G parameters showing the dominant impact. On the contrary, the time-based response surfaces, especially the time-to-peak and start time, showed minimum variation with all the K2 parameters showing noticeable importance. This shows, in model calibration and model parameter identification exercises, it is important to focus on the most sensitive parameters depending on the type of model attributes of interest.

In general, the coefficient of variation of the conductivity (CV), the interception (In), and Splash (S) parameters are the least sensitive parameters in K2 with an insignificant level of importance. Comparison of the variance-based total-order (Sobol-TO) and derivative based Morris sensitivity metrics showed equal ranking to the resulting VARS metrics. However, there were differences in the extent of the relative importance of the parameters given by the magnitude of VARS indices.

The time-variant global sensitivity analysis (GSA) showed the relative parameter importance and ranking varies across the flow period. The variation in the relative importance is affected by the rainfall input and continues to the end of the model period. The relative importance among the parameters also varies with the rainfall event that resulted in the runoff.

References

[IPCC] Intergovernmental Panel on Climate Change. 2013. Climate Change 2013: The Physical Science Basis. Contribution of Working Group I to the Fifth Assessment Report of the Intergovernmental Panel on Climate Change. Cambridge (UK) and New York (NY): Cambridge University Press.

Breshears D. D., T. B. Kirchner, and F. W. Whicker. 1992. Contaminant transport through agroecosystems: Assessing relative importance of environmental, physiological, and management factors. Ecological Applications 2(3): 285-297.

Campolongo F, J Cariboni and A Saltelli (2007), An effective screening design for sensitivity analysis of large models. Environmental Modelling and Software 22 (10), 1509e1518.

Cook BI, Smerdon JE, Seager R, Coats S. 2014. Global warming and 2st century drying. Climate Dynamics 43(9): 2607-2627.

Creutin, J.-D., and M. Borga (2003), Radar hydrology modifies the monitoring of flash-flood hazard, Hydrol. Processes, 17, 1453–1456, doi:10.1002/hyp.5122.

Feng S, Hu Q, Huang W, Ho C, Li R, Tang Z. 2014. Projected climate regime shift under future global warming from multi-model, multi-scenario CMIP5 simulations. Global and Planetary Change 112: 41-52.

Goodrich, D. C., et al. (2000), Preface paper to the Semi-Arid LandSurface-Atmosphere (SALSA) program special issue, Agric. For. Meteorol., 105(1–3), 3–20, doi:10.1016/S0168-1923(00)00178-7.

Goodrich, D. C., T. O. Keefer, C. L. Unkrich, M. H. Nichols, H. B. Osborn, J. J. Stone, and J. R. Smith (2008), Long-term precipitation database, Walnut Gulch Experimental Watershed, Arizona, United States, Water Resour. Res., doi:10.1029/2006WR005782.

Goodrich, D.C., Burns, I.S., Unkrich, C.L., Semmens, D.J., Guertin D.P., Hernandez, M., Yatheendradas, S. Kennedy, J.R., and Levick, L.R. (2012). KINEROS2/AGWA: Model use, calibration, and validation, Trans. of the ASABE. 55(4): 1561-1574.

Gupta HV and S Razavi (2018), Revisiting the Basis of Sensitivity Analysis for Dynamical Environmental Systems Models, Water Resources Research, 54. https://doi.org/10.1029/2018WR022668

Keefer1 O. T., Renard. K. G. Goodrich C. D., Heilman H., and Unkrich C. (2015). Quantifying Extreme Rainfall Events and Their Hydrologic Response in Southeastern Arizona, Trans. ASCE, 15(1), 1–10. DOI: 10.1061/(ASCE)HE.1943-5584.0001270.

Kitanidis, P. K., and R. L. Bras (1980a), Real-time forecasting with a conceptual hydrologic model: 1. Analysis of uncertainty, Water Resour. Res., 16(6), 1025–1033, doi:10.1029/WR016i006p01025. Kitanidis, P. K., and R. L. Bras (1980b), Real-time forecasting with a conceptual hydrologic model: 2. Applications and results, Water Resour. Res., 16(6), 1034–1044, doi:10.1029/WR016i006p01034.

Kling, H., Gupta, H., 2009. On the development of regionalization relationships for lumped watershed models: the impact of ignoring sub-basin scale variability. Journal of Hydrology 373, 337−351.

Miller, S.N., Semmens, D.J., Goodrich, D.C., Hernandez, M., Miller, R.C., Kepner, W.G., and Guertin, D.P. (2007). The Automated Geospatial Watershed Assessment Tool. J. Environmental Modeling and Software. 22:365-377.

Morris M.D (1991). Factorial sampling plans for preliminary computational experiments. Technometrics 33 (2), 161e174.

Nash JE and JV Sutcliffe (1970). River flow forecasting through conceptual models. Part I: a discussion of principles. Journal of Hydrology 10: 282 – 290.

Pianosi F and T Wagener (2015). A simple and efficient method for global sensitivity analysis based on cumulative distribution functions. Environmental Modelling & Software 67, 1e11. http://dx.doi.org/10.1016/j.envsoft. 2015.01.004.

Pilgrim, D. H., T. G. Chapman, and D. G. Doran (1988), Problems of rainfall–runoff modelling in arid and semiarid regions, Hydrol. Sci. J., 33(4), 379–400.

Rakovec O, MC Hill, MP Clark, AH Weerts, AJ Teuling and R Uijlenhoet (2014). Distributed evaluation of local sensitivity analysis (DELSA), with application to hydrologic models. Water Resources Research 50, 409e426. http://dx.doi.org/10.1002/2013WR014063.

Razavi S and HV Gupta (2015), What Do We Mean by Sensitivity Analysis? The Need for a Comprehensive Characterisation of 'Global' Sensitivity in Earth and Environmental Systems Models, Water Resources Research, doi: 10.1002/2014WR016527

Razavi S and HV Gupta (2016a). A new framework for comprehensive, robust, and efficient global sensitivity analysis: Part I - Theory. Water Resources Research 52, 423e439. http://dx.doi.org/10.1002/2015WR017558. 1132

Razavi S and HV Gupta (2016b). A new framework for comprehensive, robust, and efficient global sensitivity analysis: Part II - Applications. Water Resources Research 52, 440e455. http://dx.doi.org/10.1002/2015WR017559.1135

Razavi S and HV Gupta (in review), A General Approach to Multi-Method Sensitivity Analysis of Dynamical Systems Models, submitted to Environmental Modelling & Software.

Razavi S, R Sheikholeslami, H Gupta, and A Haghnegahdar (in review), VARS-TOOL: A Toolbox for Comprehensive, Efficient, and Robust Global Sensitivity Analysis, Environmental Modeling and Software.

Roeske, R. H., J. M. Garrett, and J. H. Eychaner (1989), Floods of October 1983 in southeastern Arizona, U.S. Geol. Surv. Water Resour. Invest. Rep., 98-4225-c.

Saltelli, S. T., and F. Campolongo. 2000. Sensitivity analysis as an ingredient of modeling. Stat. Sci. 15(4): 377-395.

Seager R, Ting M, Held I, Kushnir Y, Lu J, Vecchi G, Naik N. 2007. Model projections of an imminent transition to a more arid climate in southwestern North America. Science 316(5828): 1181-1184.

Semmens, D., D. C. Goodrich, C. L. Unkrich, R. E. Smith, D. A. Woolhiser, and S. N. Miller (2005), KINEROS2 and the AGWA modeling framework, paper presented at the GWADI International Modeling Workshop, UNESCO, Roorkee, India. Smith, R. E., D. C. Goodrich, D. A. Woolhiser, and C. L. Unkrich (1995), KINEROS2—A KINematic Runoff and EROSion Model, in Computer Models of Watershed Hydrology, edited by V. P. Singh, pp. 697–732, Water Resour. Publ., Highlands Ranch, Colo. Sobol', I. M. (1993), Sensitivity estimates for nonlinear mathematical models, Math. Model. Comput., 1(4), 407–414.

Sobol' IM (1990), On sensitivity estimation for nonlinear mathematical models, Matematicheskoe Modelirovanie.

Wei, H., Nearing, M.A., and Stone, J.J. 2007. A Comprehensive Sensitivity Analysis Framework for Model Evaluation and Improvement using a Case Study of The Rangeland Hydrology and Erosion Model. 50(3): 945–953.

Yatheendradas, S., T. Wagener, H. Gupta, C. Unkrich, D. Goodrich, M. Schaffner, and A. Stewart (2008), Understanding uncertainty in distributed flash flood forecasting for semiarid regions, Water Resour. Res., 44, W05S19, doi:10.1029/2007WR005940.

Zhao T, Dai A. 2015. The Magnitude and Causes of Global Drought Changes in the Twenty-First Century under a Low-Moderate Emissions Scenario. Journal of Climate 28(11): 4490-4512.

USGS Sediment Data-Collection Techniques Training: Selected Data Results

Heather Bragg, Hydrologic Technician, USGS, Portland, OR, hmbragg@usgs.gov
John Gray, Scientist Emeritus, USGS, Reston, VA, jrgray@usgs.gov

Introduction

Sediment Data-Collection Techniques (SW1091) training has been offered regularly through the USGS National Training Center to personnel from the USGS and its federal and state partners since at least the 1970's. The current 5-day field-oriented training class is set in Castle Rock, Washington and offers an in-depth look at the rivers and sediment draining the slopes of Mt. St. Helens. On the bridge spanning the Cowlitz River (at USGS streamgage 14243000), instructors provide hands-on training with a diverse suite of samplers and instruments, demonstrating approved methods for obtaining reliable riverine suspended-sediment, bedload, and bed-material data. The student-collected samples obtained during the first day of the course are submitted to the USGS Cascades Volcano Observatory (CVO) sediment laboratory and the results are presented and discussed before the class adjourns. These data are useful for demonstrating the mechanics of fluvial-sediment transport, evaluating various samplers and sampling techniques, and providing insights toward avoiding data-collection and processing errors. In addition to sample collection, students learn about sediment surrogates (including optical and acoustic technologies) and complete computations of sediment load. The combination of field exercises and classroom instruction provide a broad perspective of the value of measuring and analyzing sediment transport in rivers and the importance of quality sediment data.

A data report summarizing 8 years of site conditions and sample results from the Sediment Data-Collection Techniques training course is in progress. The poster presents suspended-sediment sample sets from training held March 24-28, 2014, which provides a good example of the data collection and analysis lessons students receive in this class.

Data Collection

On March 24, student attendees of the training course (under the direction of experienced instructors) collected two cross-sectional samples using the equal-discharge-increment (EDI) method and equal-width-increment (EWI) methods (Edwards and Glysson, 1999) with two different Federal Interagency Sedimentation Project (FISP) approved samplers. A complete EDI or EWI sample consists of two cross-sectional passes (typically labelled A and B sets), the results of which are then averaged to produce a single "event" result. At distinct locations in the cross-section, three additional types of FISP-approved samplers and one non-isokinetic sampler were used to collect single-vertical samples from the water column. Numerous samples were collected at each location with a specific sampler, all of which are averaged to present a single result for each. On the left bank of the river just downstream of the bridge, an automatic pumping sampler was programmed to collect samples every 15 minutes for the duration of the sampling period. All these samples are also averaged to present a single result for the sampler. Detailed field notes were recorded for each sample, including sampling time and any special observations. Table 1 provides details of the sampling methods and sampler features.

Table 1. Sample method and sampler information

Method name	Sampler name	Sampler container	Sampler intake	Integrating
EDI	DH-95	Rigid bottle	Isokinetic	Depth
EWI	DH-76	Rigid bottle	Isokinetic	Depth
Single vertical	D-74	Rigid bottle	Isokinetic	Depth
Single vertical	D-96	Collapsible bag	Isokinetic	Depth
Single vertical	DH-2	Collapsible bag	Isokinetic	Depth
Single vertical	Weighted bottle	Rigid bottle	Non-isokinetic	Depth
Single vertical	P-61	Rigid bottle	Isokinetic	Point
Point	Automatic pump	Rigid bottle	Non-isokinetic	Non-integrating

During the time of the sample collection (1:00 to 5:00 pm), streamflow at the station averaged 14,000 cubic feet per second (cfs) and turbidity measured near the pump sampler intake averaged 26 Formazin Nephelometric Unit (FNU).

Data Results and Analysis

The training attendees collected approximately 135 separate bottles during the sample collection activities which were labeled, logged into the lab sample submission portal using the SEDiment-sample LOGIN application (SedLOGIN), and delivered to the CVO Sediment Laboratory the evening of March 24, 2014. Within 2 days, the lab had provided the suspended-sediment concentration (SSC) and percent fine sediment (less than 63 microns) results for each sample. The results are summarized in Figure 1.
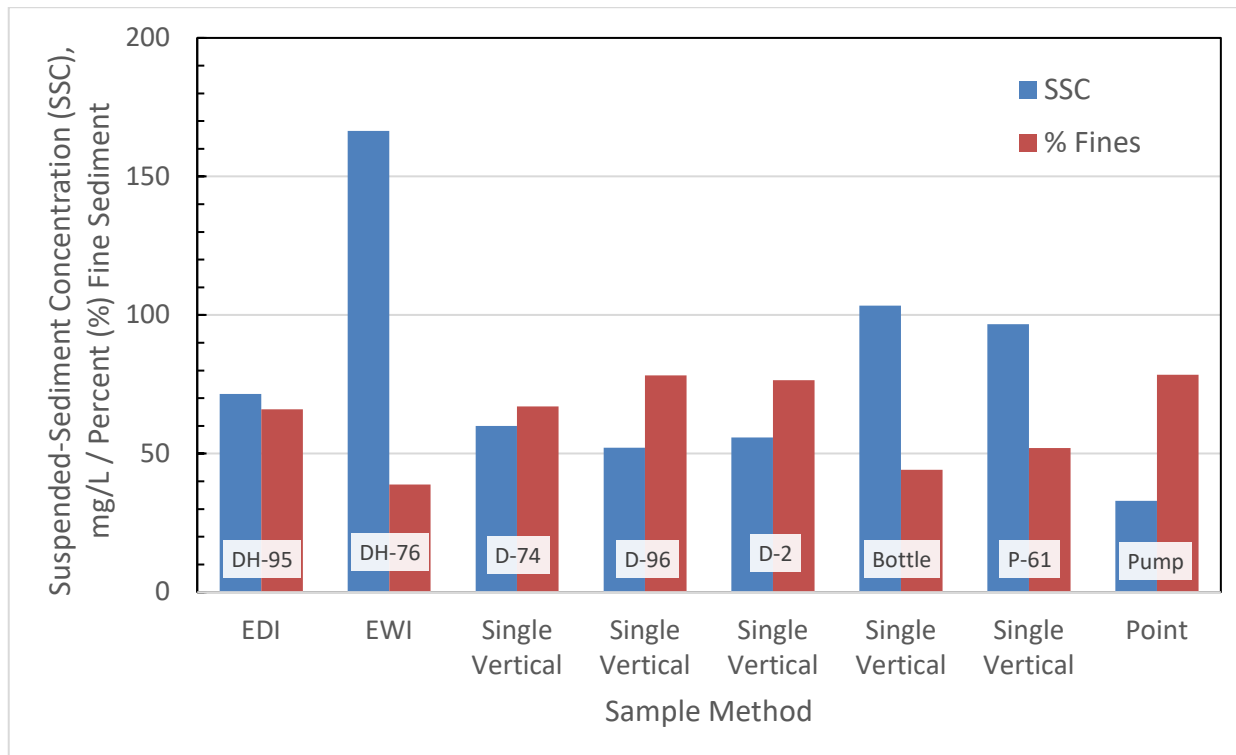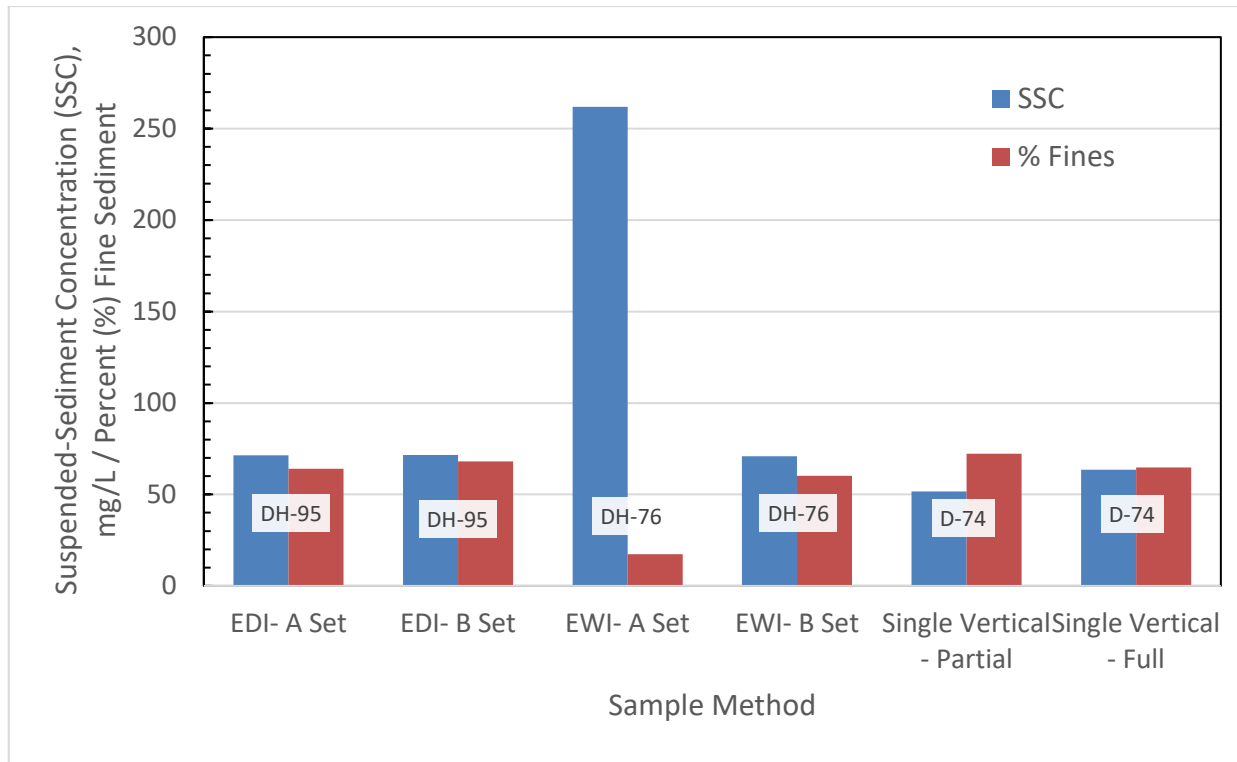

Figure 1. Suspended-sediment laboratory results by sampling method and sampler

The SSC of the compiled results range from 32 to 166 milligrams per liter (mg/L) and the percent fine sediment values range from 39 to 78 percent. Much of the variation is likely explained by sampling method. Most rivers have non-uniform velocity profiles, resulting in varying sediment concentrations in the cross-section. Unless the river is extremely well-mixed, the SSC of a single vertical sample is likely to differ from the mean obtained by an EDI or EWI sample. Non-isokinetic samplers are also understood to often produce biased SSC and percent fines results. The intakes of both the weighted bottle and pump samplers can either over- or under-sample suspended sediment. Whether biased by method or sampler, these SSC results can often be adjusted using correction factors for use in further analysis.

The two cross-sectional methods (EDI and EWI) should produce similar SSC and percent fines results, but the EWI sample collected appears to have higher sand content (lower percent fines) and much higher total SSC than the EDI sample. Examination of the individual sample results, rather than the averaged "event" results, reveals a likely problem with one of the EWI samples (Figure 2).

Figure 2. Individual suspended-sediment laboratory results by sampling method and sampler

The SSC results of the EWI samples were 262 mg/L (17 percent fines) and 71 mg/L (60 percent fines). Without the other sample results for comparison, it would be difficult to determine which of these results is more "correct," but the comparison indicates that set A was not representative of the sediment transport conditions at the time. The field notes collected at the time noted that the DH-76 sampler may have bumped the riverbed, stirring up coarse sediment that was drawn into the sampler. Inspection of the sample at the time of collection might have allowed the

opportunity to reject the questionable bottle and collect another one, but at least the field notes provide justification for removing the EWI A set from further analysis. The Sediment Data-Collection Techniques training class provides numerous real sampling scenarios such as this to the attendees, demonstrating the importance of careful sample collection and good field documentation.

References

Edwards, T.K. and Glysson, G.D., 1999, Field Methods for measurement of fluvial sediment: U.S. Geological Survey Techniques of Water-Resource Investigations, book 3, chap. C2, 89 p.

Preliminary Results of Suspended-Sediment and Total Metal Concentrations of the San Juan River near Bluff, Utah

Chris Wilkowske, Hydrologist, U.S. Geological Survey, Moab, Utah, wilkowsk@usgs.gov

Abstract

A limited set of concurrent water quality and suspended sediment samples has been collected at the U.S. Geological Survey gaging station San Juan River near Bluff, Utah (U.S. Geological Survey Station Number 09379500). Analysis of these samples appears to indicate a fair to good relationship between total, or unfiltered metals and the suspended sediment and silt-clay concentration. Based on favorable preliminary results, it is believed that continued sample collection will be successful in building a model that can be used to measure sediment and metals loads in the lower San Juan River basin. This study should still be considered in the data collection phase and requires an extended sampling effort to build robust regression models.

Introduction

Purpose and Scope

The U.S. Geological Survey (USGS) stream gage San Juan River near Bluff, Utah (USGS station number 09379500) has historically provided important data on streamflow, sediment load, and dissolved solids load to Lake Powell in southern Utah. On August 5, 2015 an unintentional release of metal laden water from the Gold King Mine occurred in the headwaters of the San Juan drainage. Emergency response to this release renewed interest in the concentration and chemical make-up of the suspended sediment at the San Juan River near Bluff. The purpose of this study is to obtain continuous estimates of suspended sand concentration, suspended sand median grain size, suspended silt-clay concentration, and total metal concentrations.

To accomplish the study goals of continuously monitoring the river, a dual frequency array of single frequency acoustic doppler velocimeters has been installed at the San Juan River near Bluff, Utah gage. The acoustic backscatter intensity and attenuation from the instruments is recorded and used along with concurrent collection of suspended sediment samples. After a sufficient period of data collection, a site-specific model can be developed to relate the desired suspended sediment parameters to the acoustic signal following the methods outlined in U.S. Geological Survey Professional Paper 1823 (Topping and Wright, 2016). Along with the suspended sediment samples, separate water quality samples are also collected and analyzed for dissolved and particulate metals concentration. Analyses from the two data sets should reveal which sediment size fraction is associated with the highest metals loads and perhaps the source of the sediment. Once a model has been developed that relates suspended sand or silt-clay concentration to metals concentration, the total annual load of suspended sediment and metals from the San Juan River can be determined.

At the time of publication of this report, only a limited data set was available. Preliminary results show a successful proof-of-concept for the project and will focus on the relationship between

suspended sediment concentration and metals concentration. The development of the hydroacoustic relationship will require an extensive data set that will take several years to develop.

Hydrologic Setting

The San Juan River as measured at San Juan River near Bluff, Utah drains an area of approximately 23,000 square miles (figure 1). The river headwaters are in the alpine zone of the San Juan mountains of southeastern Colorado. The San Juan mountains contain many areas of highly mineralized bedrock and many historic mining districts that produce elevated levels of metals concentrations in surface water (Church, 2007). From Colorado, the river drops in elevation as it flows through New Mexico and the environment becomes increasingly more arid. East of Farmington, New Mexico, the river is regulated by Navajo dam. Below Navajo reservoir, the main tributaries are the Animas River and the Mancos River which are largely unregulated. High flow at San Juan River near Bluff, Utah is dominated by two periods. Spring snowmelt runoff that normally occurs from April through June, and a summer monsoon period that occurs from July through early October. Although the river is regulated by Navajo Dam, the spring runoff includes the mostly unregulated flow from the Animas River and Mancos River. Spring runoff can also include release of storage water from Navajo Reservoir. Most of the inflow from summer monsoon events enters the main stem of the San Juan River through several large ephemeral channels downstream of Navajo Dam.

The San Juan River enters the upper end of Lake Powell, about 50 miles downstream of the gaging station, San Juan River near Bluff, Utah. The two largest historic peak flow events occurred in September as the result of widespread regional rain events. The maximum discharge prior to construction of Navajo dam was 70,000 ft^3/s on September 10, 1927. The maximum discharge after the dam was constructed in 1962 was 52,000 ft^3/s on September 6, 1970. The maximum sediment load also occurs during large summer-fall rain events. The maximum daily suspended sediment discharge for this station occurred on October 20, 1972 at 15.7 million tons. This maximum is a daily value that was computed using U.S. Geological Survey standard methods in use at the time. Specifically, a sediment-discharge relationship. However, this suspended sediment discharge is more than five times greater than the maximum observed load of the Green and Colorado Rivers.

Sources of Sediment and Metals

Church and others (1997) describe the geochemical process of metals transport in the Animas River which is in the upper part of the San Juan River drainage basin. Bedrock in this area is heavily mineralized and the area is home to several mining districts. In general, metals are transported in the aqueous phase in the upper portion of the drainage near Silverton, CO. Heading downstream towards Durango, CO, the aqueous metals loads are attenuated as the colloidal and sorbed loads increase. It is this portion of metals in colloidal form or as sorbed onto other fine-grained sediment that is of concern in the lower drainage basin. Many trace metals have been previously detected in bottom sediment from the San Juan arm of Lake Powell (Hornewer, 2014). Resuspension of these metals into the water column of Lake Powell where they can bioaccumulate is of particular concern.

The arid rangeland of the lower San Juan River basin produces a much different type of sediment load. This area is characterized by Colorado Plateau sandstone and mudstone that do not contain high concentrations of raw metals. This portion of the basin is responsible for much of the total sediment load in the river. Although they are significantly different from the mined formations in the upper basin, several metals are known to exist in substantial quantities in rocks of the Colorado Plateau; including uranium and vanadium (Newman, 1962). The Mancos Shale, which underlies much of the Mancos River basin, is known to contribute substantial amounts of sulfate and selenium in other parts of Colorado (Leib, 2008).
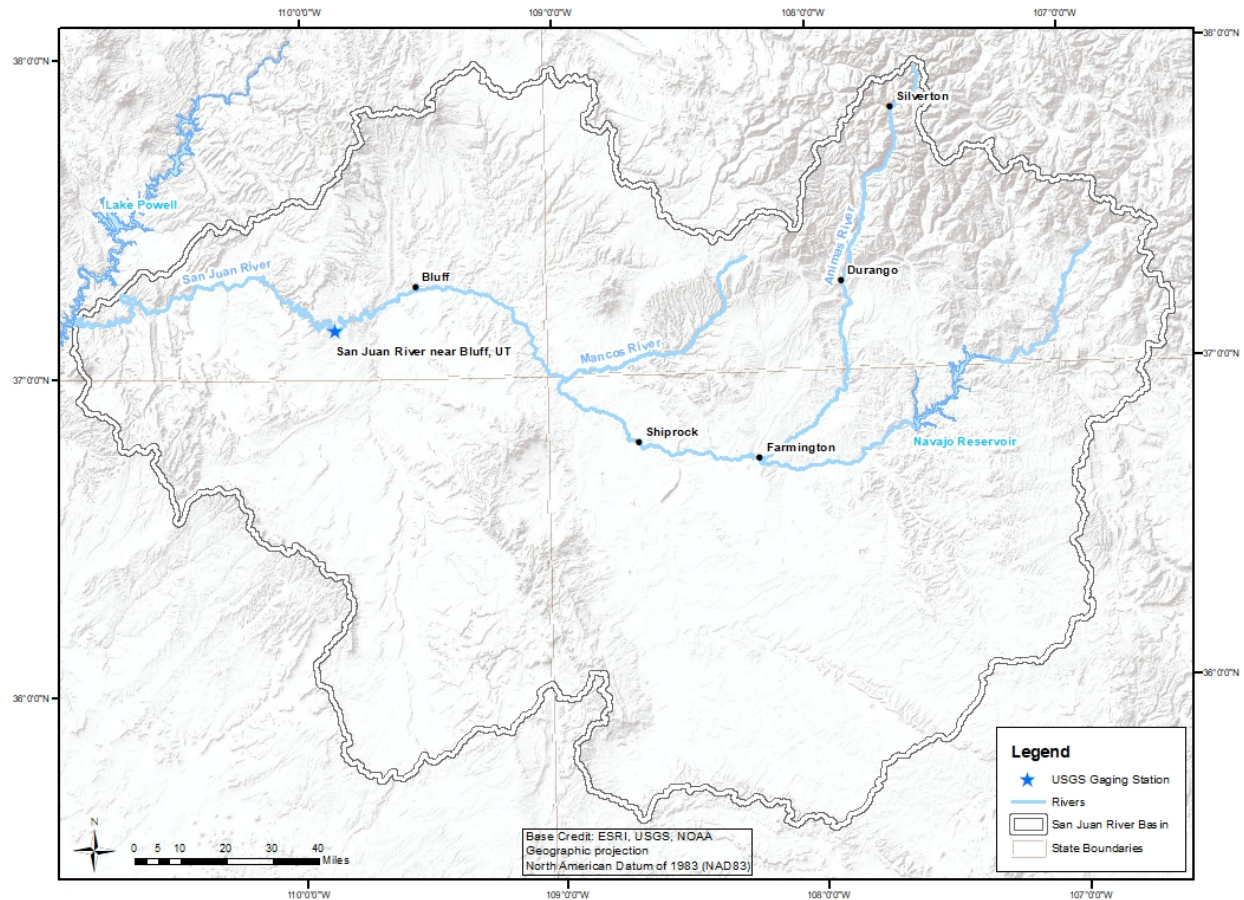
Figure 1. Map of the San Juan River Basin.

The San Juan River near Bluff, Utah gage is the last monitoring station in the drainage basin before the river enters Lake Powell. As described above, the San Juan River transports large volumes of sediment to Lake Powell. Carried along with the sediment are sorbed metals, the source of which is a mixture of the upstream mineralized bedrock, and surface runoff from the lower elevation arid lands (Church and others, 1997). Several Federal and State agencies have interest in monitoring the metals concentration in the San Juan River and in the sediment that eventually makes its way to Lake Powell. Monitoring of the San Juan River by the USGS and others has to this point consisted of traditional water quality parameter monitoring, including

water temperature, specific conductance, pH, dissolved oxygen, and turbidity. Since the Gold King Mine release on August 5, 2015, this monitoring has expanded to include collection of discrete water quality samples for metals analysis (Mast, 2018).

Mast (2018) developed regression models for metals concentrations at several sites along the San Juan and Animas rivers using water quality parameters as surrogates. The regression analysis at the San Juan near Bluff, Utah had the best surrogate realtions for total (unfiltered) metals concentration. Each of the developed regression equations used turbidity as a surrogate; however, use of the models was not recommended until additional validation samples could be collected. The data set used in the analysis did not cover the full range of turbidity and flow conditions. In many cases the turbidity value was censored as it exceeded the maximum sensor limit. Mast (2018) also recommended the use of hydroacoustic backscatter measured sediment concentrations for sites along the lower reaches of the San Juan River where the suspended sediment concentration is often too high to use turbidity as a surrogate.

Approach and Methods

Sample Collection and Analysis

Suspended sediment samples are collected at the San Juan near Bluff, Utah gaging station from a cableway located just downstream of the gage. The samples are collected as isokinetic depth integrated samples using the equal width (EWI) or equal discharge (EDI) sampling method as described by Edwards and Glysson (1999). Individual bottles from each sampling vertical were analyzed by the USGS Cascades Volcano Observatory for suspended sediment concentration and particle size analysis.

Separate water-quality samples were collected concurrently with the suspended sediment samples. These samples were also collected as an EWI or EDI sample using USGS protocols for parts-per-billion level sampling as described in the USGS National Field Manual (U.S. Geological Survey, 2006). The integrated sample used for metals analysis was composited on site using a churn splitter. The filtered and unfiltered samples were then submitted to the USGS National Water Quality Lab for analysis of a suite of major ions and trace metals. The composited sample was not used for suspended sediment analysis.

Preliminary Results

Suspended Sediment Concentrations

Samples were collected at the San Juan River near Bluff, Utah gaging station from May 10, 2018 through August 23, 2018 (table 1). Discharge during the sampling events ranged from 648 to 1,550 ft³/s (figure 2). Water year 2018 experienced a significantly less than normal spring runoff; therefore, the data only represents a limited range of flow conditions at the site. Normal peak spring runoff is on the order of 5,000 ft³/s. Several of the samples were collected from June 7-8, 2018 over a brief planned release from Navajo Reservoir. Samples were collected just before and during the rising limb of the release that lasted for one day. The sample collected on August 23, 2018 represents a typical summer monsoon event and had the highest suspended sediment concentration (4,690 mg/L) of the samples analyzed. This sample also was collected during a period of relatively low discharge and shows up as an outlier in Figure 2. However, the

historic range of measured suspended sediment concentration at this station is from 5 to 155,000 mg/L.

Table 1. Suspended sediment concentrations and particle size data for samples collected May 10 to August 23, 2018 at San Juan River near Bluff, Utah.

Sample date and time	Discharge in cubic feet per second	Percent silt-clay (<0.063 mm)	Suspended Sediment Concentration (mg/L)	Silt-clay concentration (mg/L)	Sand concentration (mg/L)
5/10/18 9:50	650	79.0	112	88	24
5/14/18 10:30	1,170	83.7	1,856	1,553	303
5/18/18 12:20	779	83.0	437	363	74
6/7/18 13:40	717	64.0	118	76	42
6/8/18 10:30	1,160	54.6	894	488	406
6/8/18 12:20	1,470	67.5	1,623	1,096	527
6/8/18 14:30	1,530	53.4	3,044	1,625	1,419
6/8/18 16:20	1,550	72.9	2,286	1,666	620
8/23/18 11:05	648	98.6	4,693	4,627	66
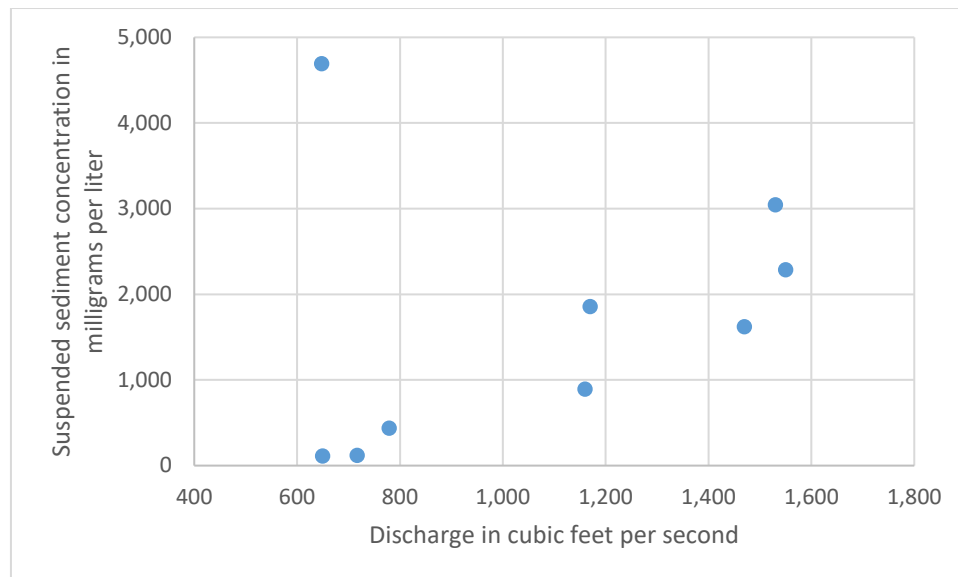
Figure 2. Distribution of suspended sediment samples and discharge.

Metals Concentrations and Potential Relationship to Suspended Sediment Concentration

The water quality analyses included both dissolved (filtered) and total (unfiltered) metals concentrations. It is believed that most of the metals transported in the lower San Juan River

basin occurs in the solid phase as either colloidal or sorbed metals onto fine sediment. The initial data appears to verify that hypothesis as much of the dissolved fraction had concentrations that were less than the detection limit. Data presented here is for total concentrations only.

Data were examined to determine whether a better relationship existed between metals concentrations and total suspended sediment, suspended silt-clay concentration, or suspended sand concentration. Again, the working hypothesis is that most of the metals transport is associated with the fine particle size fraction of the sediment load.

A cursory analysis of the sample data indicated fair to good correlation for most total metals concentrations and the silt-clay concentration (table 2). R-squared values ranged from 0.71 to 0.99 except for zinc which had and r-squared value of 0.53, and selenium which had an r-squared value of 0.63. Fair to good correlations (r-squared of 0.74 to 0.95) were also seen between the total suspended sediment concentration and the total metals concentrations except for zinc, selenium, and lithium. No correlation was found between the metals and the sand concentration. Plots of the relationship between selected metals of interest and the silt-clay concentration can be seen in figures 3 and 4.

Table 2. R-squared values for selected metals concentrations versus the suspended silt-clay, sand and total sediment concentration for samples collected from May 10 to August 23, 2018 at San Juan River near Bluff, Utah.

	As	Ba	Cd	Cr	Co	Cu	Fe	Pb	Mn	Ni	Sr	Vn	Zn	Al	Li	Se	U
Suspended silt-clay concentration	0.96	0.93	0.71	0.90	0.98	0.83	0.95	0.93	0.93	0.99	0.91	0.99	0.53	0.98	0.84	0.63	0.98
Total suspended sediment concentration	0.91	0.78	0.78	0.95	0.91	0.79	0.93	0.89	0.89	0.91	0.74	0.87	0.63	0.83	0.66	0.45	0.83
Suspended sand concentration	0.02	0.00	0.11	0.10	0.01	0.02	0.03	0.02	0.02	0.01	0.01	0.00	0.16	0.00	0.02	0.05	0.00

Figure 3 shows the relationship between the total (unfiltered) concentration of several metals of interest (aluminum, arsenic, cadmium, copper, iron, lead, manganese, and zinc) and the suspended sediment concentration. The relationships are distinguished by different sediment size partitions (suspended silt-clay concentration, total suspended sediment concentration, and suspended sand concentration).
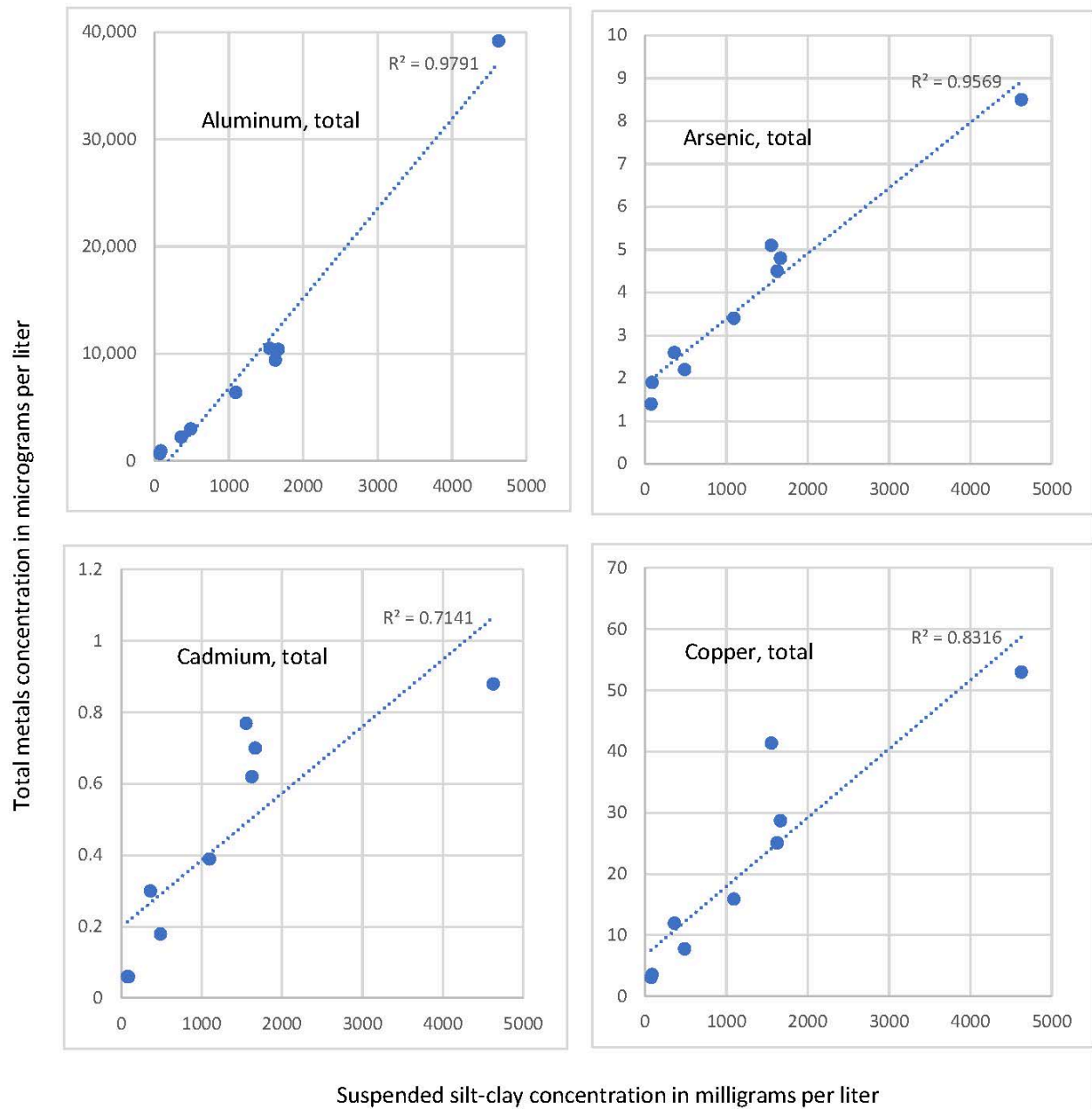
Figure 3. Relationship between suspended silt-clay concentration and the total (unfiltered) concentration of aluminum, arsenic, cadmium, and copper.
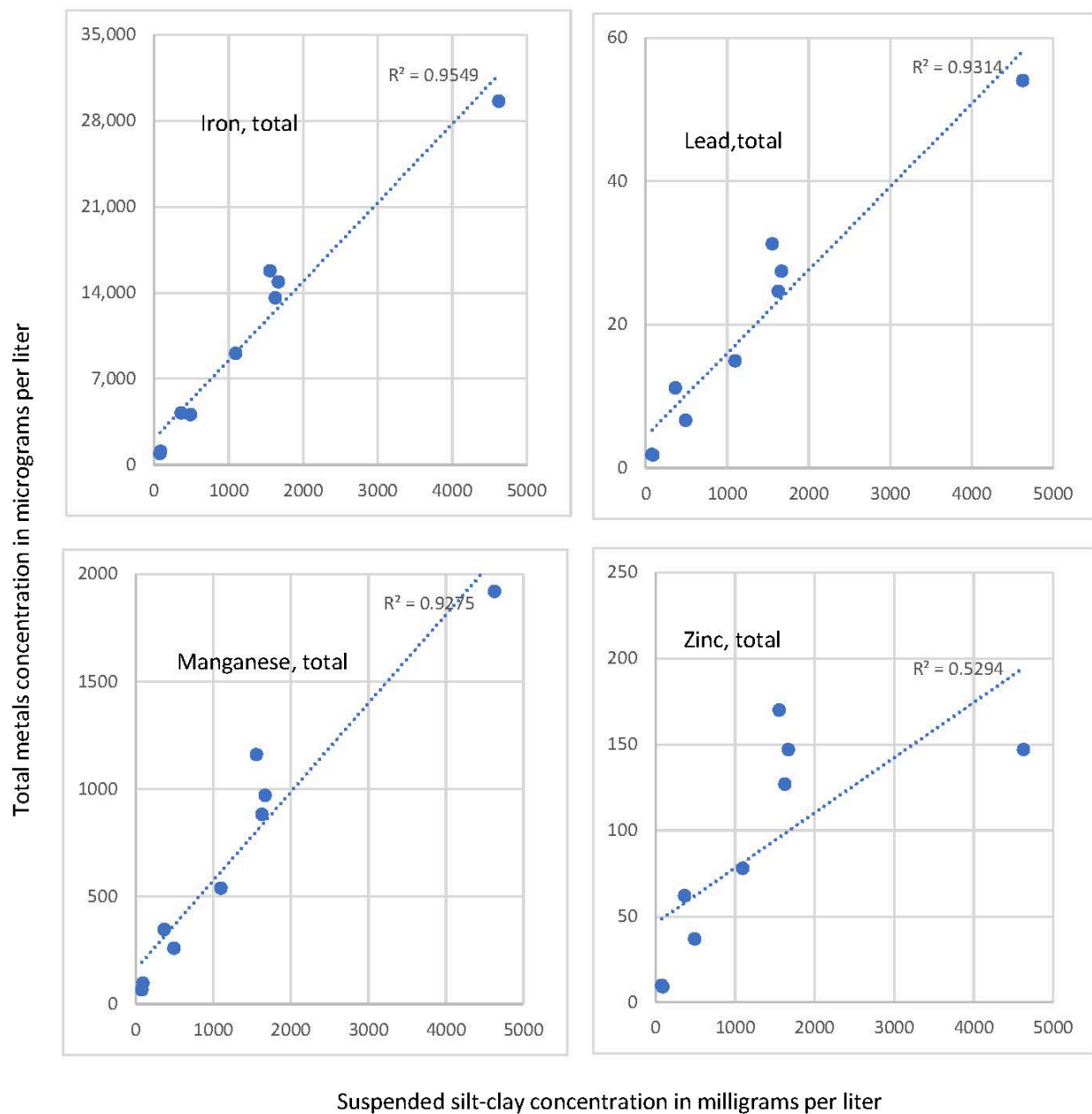
Figure 4. Relationship between suspended silt-clay concentration and the total (unfiltered) concentration of iron, lead, manganese, and zinc.

The correlations are heavily influenced by the sample with the highest suspended sediment concentration which was collected in August 2018. There are also too few samples to build a statistically valid model currently. However, the results do suggest that using suspended sediment, in particular the silt-clay fraction, as a surrogate may be a useful tool to model total metals concentrations. The lack of correlation with the sand fraction also indicates that it will be important to monitor grain size distribution when trying to related sediment concentration to metals concentration.

Summary and Additional Work

From an initial set of concurrent water quality and suspended sediment samples, it appears that a fair to good relationship exists between the two. Continued sample collection should be successful in building models that can be used to measure sediment and metals loads in the lower San Juan River basin. These models can be used to estimate sediment and metals transport to Lake Powell. Future analysis of the relationships will use more rigorous statistical methods to develop and test the regression analyses. As more data become available, an attempt will be made to differentiate the source of the sediment, and whether the sediment transported past the Bluff, Utah gage changes from the snowmelt season to the summer monsoon season.

Dual frequency hydroacoustic backscatter data is currently being collected at the San Juan River near Bluff, Utah. Once enough verification sediment samples have been collected to build a robust model, the backscatter will be used to calculate continuous suspended silt-clay and sand concentration using the method described by Topping and Wright (2016). Concurrent water quality samples will also continue to be collected, with the goal being to build the relationship between sediment and metals concentrations. Another goal of this project is to make the concentration and load data available in near real-time through the use of the U.S. Geological Survey National Real-Time Water Quality website at https://nrtwq.usgs.gov/. This near real-time data could inform water quality managers to make health related advisories about the San Juan River.

During the fall of 2018, lake sediment cores were collected from several sites in the San Juan arm of Lake Powell. The cores were collected as part of a cooperative study between the USGS and the Utah Department of Environmental Quality. These cores are currently being analyzed to address sedimentation rates and the geochemical composition of the sediment. This project will add significant insight into the fate and transport of sediment and metals to Lake Powell.

References

Church, S.E., Kimball, B.A., Fey, D.L., Ferderer, D.A., Yager, T.J., and Vaughn, R.B., 1997, Source, transport, and partitioning of metals between water, colloids, and bed sediments of the Animas River, Colorado: U.S. Geological Survey Open-File Report 97–151, 135 p., https://pubs.er.usgs.gov/publication/ofr97151.

Edwards, T.K., and Glysson, G.D., 1999, Field methods for measurement of fluvial sediment: Techniques of Water-Resources Investigations of the U.S. Geological Survey, book 3, chap. C2, 89 p.

Hornewer, N.J., 2014, Sediment and water chemistry of the San Juan River and Escalante River deltas of Lake Powell, Utah, 2010–2011: U.S. Geological Survey Open-File Report 2014-1096, 7 p., http://dx.doi.org/10.3133/ofr20141096.

Leib, Kenneth J., 2008, Concentrations and loads of selenium in selected tributaries to the Colorado River in the Grand Valley, western Colorado, 2004–2006: U.S. Geological Survey Scientific Investigations Report 2008–5036, 36 p.

Mast, M.A., 2018, Estimating metal concentrations with regression analysis and water-quality surrogates at nine sites on the Animas and San Juan Rivers, Colorado, New Mexico, and Utah: U.S. Geological Survey Scientific Investigations Report 2018–5116, 68 p., https://doi.org/10.3133/sir20185116.

Newman, William L., 1962, Distribution of Elements in Sedimentary Rocks of the Colorado Plateau- A Preliminary Report, United States Geological Survey Bulletin 1107-F, 445 p.

Topping, D. J., and Wright, S.A., 2016, Long-Term continuous acoustical suspended-sediment measurements in rivers—Theory, application, bias, and error: U.S. Geological Survey Professional Paper 1823, 98 p., http://dx.doi.org/10.3133/pp1823

U.S. Geological Survey, 2006, Techniques of Water-Resources Investigations, Book 9, National Field Manual for the Collection of Water-Quality Data, Chapter A4. Collection of Water Samples, 166 p.

Using Oblique Imagery to Measure Hypsometric Changes in Sandbar Volume Following Controlled Floods in the Grand Canyon

Ryan Lima, Ph.D. Candidate, Northern Arizona University, Flagstaff, AZ, rl587@nau.edu
Daniel Buscombe, Assistant Research Professor, Northern Arizona University, Flagstaff, AZ, Daniel.Buscombe@nau.edu
Temuulen Sankey, Associate Professor, Northern Arizona University, Flagstaff, AZ, Temuulen.Sankey@nau.edu
Paul Grams, Research Hydrologist, USGS, Flagstaff, AZ, pgrams@usgs.gov
Erich Mueller, Visiting Assistant Professor, University of Wyoming, Laramie, WY, erich.mueller@uwyo.edu

Abstract

Measuring changes in the elevation distribution of sub-aerial fine ($< 2\ mm$) sediment and estimating sandbar volume multiple times per year can improve sediment budget calculations in fluvial systems. In the Grand Canyon of the Colorado River, effects of dam operations on sandbar size and distribution is of long-term management interest. Bar-building controlled floods have been implemented in 1996, 2004, 2008, 2012, 2013, 2014, 2016, and 2018 to mitigate sandbar erosion. Annual topographic surveys provide a single measurement of sandbar change caused by the integrated effects of all flows in one year (both controlled floods and normal dam releases), but do not measure erosion and deposition caused by specific operations or individual floods. On one sandbar monitoring site in Grand Canyon, we demonstrate that imagery from autonomous digital cameras can be used to provide quantitative measures of sandbar hypsometry several times per year without costly and labor-intensive surveys. We describe methods for measuring changes in the storage of fine sediment at monthly or seasonal timescales by constructing hypsometric (area-elevation relation) curves. These curves are created and updated with sandbar area measurements from georectified images taken multiple times each day. As the water surface elevation fluctuates with daily, seasonal, and monthly discharge patterns, sandbar area and volume can be estimated using known stage-discharge relationships. We present parameters extracted from image-derived hypsometries to estimate sandbar volume and elevation relief ratio, which provides a new way to quantitatively measure monthly or seasonal changes in fine sediment storage.

Introduction

The closure of Glen Canyon Dam in 1963 significantly altered the discharge patterns and sediment supply of the Colorado River in Grand Canyon. Increases in minimum and mean discharges, increases in daily discharge fluctuation, decreases in maximum discharge, and a reduction of sediment supply have created a deficit of fine sediment (Topping et al. 2000) and reductions in the size and extent of sandbars throughout Grand Canyon (Dolan et al. 1974; Schmidt et al. 2004). The preservation of fine sediment resources downstream of Glen Canyon Dam has been a long-standing management focus. Sandbars are used for camping by nearly 25,000 people each year who float the Grand Canyon. Sandbars also form habitat used by native fish and provide a source of sand for aeolian transport to upslope archaeological resources, protecting those areas from erosion (Sankey et al. 2018)

Controlled floods have been carried out periodically since 1996 to rebuild and maintain sandbars. They are conducted following significant tributary inputs of sediment. The high flows are intended to redistribute sand from low elevations within the channel or in eddies to high elevations where sand is less vulnerable to erosion from fluctuating flows and can provide the benefits previously listed. Following the high flow events, topographic surveys are the primary method for monitoring the storage of sub-aerial fine sediment within Grand Canyon. These surveys are typically conducted once per year and provide a detailed snapshot of fine sediment storage at 44 sandbar monitoring sites (Hazel et al. 2006).

To supplement the detailed topographic surveys, daily photographic monitoring of sandbars in Grand Canyon began in the early 1990s with film cameras, which collected one image per day at just a few sandbar monitoring sites. These images revealed that sandbars undergo cycles of rapid short-term erosion followed by gradual deposition throughout the year and that short-term rates of erosion equaled or exceeded the rates of erosion and deposition measured at annual timesteps (Dexter and Cluer, 1999). These findings reiterated the need for more frequent, short-term monitoring in addition to detailed annual monitoring.

The network of remote cameras was expanded throughout the 1990s and early 2000s to monitor 43 sandbars sites, and between 2008 and 2014, film cameras were replaced with digital cameras capturing five or more oblique images each day. These remote camera systems include a solar panel, a data logger, a 12V battery, a camera, and lens sealed in weatherproof boxes. The camera systems and their specifications, referred to hereafter as 'remote cameras' are described by Bogle et al., (2013). They operate autonomously with semi-annual maintenance schedules. The sandbar imagery dataset contains over 500,000 images and is one of the most comprehensive and longest records of fluvial sandbar monitoring currently available. Recently, imagery from remote cameras has been used to qualitatively assess size changes following controlled floods, and also to quantify sandbar area at a single elevation through time (Grams et al. 2018, Tusso et al. 2015).

We describe methods for quantifying changes in fine sediment storage at sandbars in Grand Canyon using oblique imagery captured from the remote cameras. We utilize rectified oblique

imagery to: (1) isolate sandbar pixels from images, taken at multiple discharges, to compute sandbar area at different elevations; (2) examine the area-elevation relationship and (3) estimate sandbar volume at monthly or seasonal timescales. Our analysis focuses on the sub-aerial portion of sandbars, which are emergent during most flows. Since daily discharges are rarely less than 8,000 ft^3s^{-1}, our analyses are limited to the portions of the sandbar which remain sub-aerial at a discharge of 8,000 ft^3s^{-1}. The elevation of the water-surface at 8,000 ft^3s^{-1} is hereafter referred to as the reference elevation. At RM 30.7 the reference elevation is 855.475 m.

We refer to elevations in two different ways in this study; the first is in meters above sea level. This absolute elevation is useful for understanding changes in storage at a particular site. Secondly, we use discharge as a proxy for elevation based on an observed stage-discharge relationship to show the proportion of the bar inundated at different flow levels. This relative elevation-proxy provides a context for understanding changes in storage in relation to particular flow patterns and allows for comparison across sites throughout the canyon which occur at different absolute elevations.

In this study, we examine hypsometry because it provides a quantitative estimate of overall sandbar steepness and allows quick visualization of where fine sediment is stored in relation to stage-elevations. We estimate sandbar volume by creating digital elevation models (DEMs) from the segmented sandbar outline in the oblique images collected in discrete (one to four day) intervals, where three or more images showing water-surfaces across a broad range discharges.

Methods

Study Area: We chose to focus on the sandbar site located 30.7 river miles downstream of Lees Ferry, referred to, hereafter, as RM30.7 (Figure 1). This site was chosen principally because it is dynamic, but also because it is almost vegetation-free. The lack of vegetation makes automated segmentation of sandbar area simpler, which was important in the initial development of our new method. Further, RM30.7 is located just 0.7 river miles downstream of USGS gage #09383050, which provides 15-minute measurements of discharge. In 2009, the location of the camera at RM30.7 was moved and we primarily use images (up to five times per day) captured between 2009 and 2017. Images were pre-processed and processed via a sequence of analyses and methods. We describe each of the important steps below.

Image-Derived Area Measurement

Sandbar area measurements from the images involved registering and rectifying the images to known references and then segmenting the sandbars to calculate their areas.

Registration: Registration is the process of spatially matching multiple images of the same scene. This is needed because small shifts in the camera viewing angle occur during camera maintenance or as a result of environmental conditions. Batch registration was carried out to register all images taken at RM 30.7 to a single reference image using a 2-D Fast Fourier Transform (*see* Grams et al. 2018).
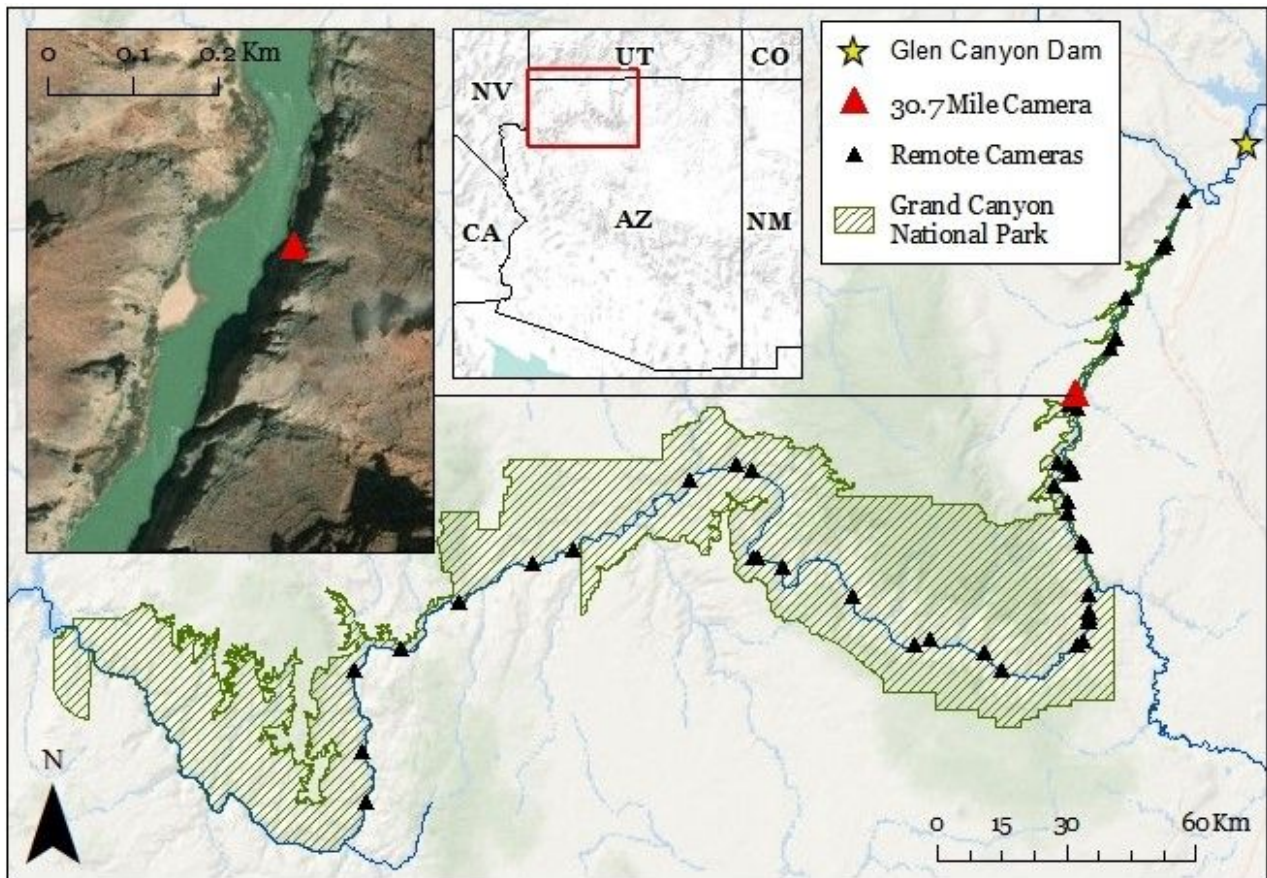
Figure 1. The Grand Canyon study region and the sandbar monitoring site at River Mile 30.7.

Rectification: Once registered, images were rectified using a homography or a transformation between two images in the same planar surface. A homography was developed by using the known location of particular rocks (i.e. hardpoints) and panels which were surveyed for their precise location and imaged with the remote cameras; collectively these are known as ground control points (GCPs). This transformation assumes all ground control points are on the same 2D plane or have the same elevation. The homography could then be applied to images so that distances in pixels could be translated into distances on Earth's surface. The homography was generated using the OpenCV package in Python 2.7. The workflow is described in Grams et al., (2018).

Segmentation: To perform segmentation, or the process of delineating pixels containing sand from non-sand pixels, we used a program called "RCSandseg", implemented in Python 2.7 and described in Grams et al., (2018). RCSandseg allows the user to define a bounding box around the sandbar and uses the GrabCut algorithm (Rother and Kolmogorov, 2004) to delineate a subject from the background. This supervised method also allows the user to correct misclassified pixels. Each segmentation requires minimal user input and takes between one and five minutes.

Area Measurement: Once the sandbars were segmented, we imported the coordinates of the sandbar shoreline from all photos, or the boundary between pixels classified as sandbar and those classified as background, into ArcMap 10.6.1 and created a polygon from the points. The area of the polygon was then calculated using the Geometry tool within ArcMap 10.6.1.

Estimating Image Water-Surface Elevation: To associate a measured water-surface elevation to an image, we first estimated the discharge pictured in each image using the time recorded in the image EXIF metadata and subtracting a lag-time to the upstream gage (USGS-09383050) from the image time. This provides an estimated time when the discharge wave in the image passed the upstream gage. Since the gage records discharge every 15 minutes, discharge was interpolated from the two discharge measurements closest (temporally) to the discharge wave. That discharge was then converted to water surface elevation using the stage-discharge relationship developed from several decades of field observations at the RM30.7 site (Hazel et al. 2007).

Volume from Image-Derived DEMs: Our first approach in estimating sandbar volume was to find periods of one to four day where images captured discharges at or below the reference elevation and also images at higher discharges > 12,000 $ft^3 s^{-1}$. A total of 22 such periods were identified between 2012 and 2015. An image from at or below the reference elevation was selected for each period along with at least two other images at higher stage elevations. A total of 68 images from those 22 intervals were selected. These images were segmented to identify the sandbar. The homography (described above) was applied to points along the boundary between the sandbar and the water providing geographic coordinates for those points. An elevation value estimated using the process described above was paired with the water's edge points based on the image time. Points were converted into polylines in ArcMap 10.6.1

Because imagery showing discharges above 20,000 $ft^3 s^{-1}$ (high-water) is rare, and the area of the sandbar which remains sub-aerial at discharges > 20,000 $ft^2 s^{-1}$ is rarely inundated, we utilized imagery from the most recent controlled flood to create a high elevation contour. This necessarily assumes that high-elevation areas of the sandbar have not changed significantly since the last flood. The high-elevation portion of the bar at RM 30.7 is closest to the valley wall at the reattachment point and thus undergoes erosion less frequently. Such images could, therefore, have been taken up to a year before the rest of the images in each set. Time-lapse of the sandbar imagery was used to visually inspect the sandbar for erosion above the high-elevation contours. Polylines were then converted to rasters using natural neighbor interpolation. This process is analogous to creating a DEM from contour lines. Volume of the raster surface was then calculated above the reference elevation plane.

Hypsometric Analysis: Hypsometry is a measure of the relationship between area and elevation, usually applied to a basin or watershed. Hypsometric curves are created by plotting the cumulative area of a basin against its relative elevation (Strahler, 1952). For a drainage basin, the shape of this curve is characteristic of the erosional processes occurring within the basin and the geologic setting. Convex hypsometries may indicate a tectonically young basin where much of the basin's mass is stored at high elevations; in such basins hillslope processes are more significant. In contrast, concave hypsometries may indicate basins where much of the mass is stored at lower elevations, but small areas of high relief still exist. In such basins, fluvial processes play a greater role (Stahler, 1952). Elevation relief ratio, shown in equation 1,

$$(1) \quad \frac{Mean\ Elevation - Min\ Elevation}{Max\ Elevation - Min\ Elevation} = Elevation\ Relief\ Ratio \text{ (Pike and Wilson, 1971)}$$

 is the normalized elevation of the mean basin area. Described by Pike and Wilson (1971), it provides a single number that can be used to compare basins irrespective of scale. Concave hypsometries result in lower elevation relief ratios (~0.2 -0.5), whereas convex hypsometries result in higher elevation relief ratios (~0.5-0.8) (Pike and Wilson 1971). This metric is useful because it distills the complexity of a curve, which may have several inflection points and different slopes, into a single number which can be compared over time at the same site and across several sites in the canyon.

These concepts are useful to the analysis and monitoring of sandbars in several ways. Like drainage basins, sandbars can have complex morphologies which are not easily quantified. Hypsometric curves, and the elevation relief ratio can provide a simple means of quantifying changes occurring to these sandbars through time. Determining the elevation relief ratio for a sandbar at a particular time might also provide insight into the dominant types of erosion, which can be expected to occur at a given site, and how that might be related to overall sandbar slope or degree of convexity. Alvarez and Schmeeckle (2013), for example, found in the laboratory that the slope angle of sandbars determines the dominant mode of erosion in response to diurnal stage fluctuations. A field test of this finding is one eventual goal of the present work.

Controlled floods in Grand Canyon generally mobilize sediment from low elevations on the channel bed and store it at higher elevations within eddies and on the river banks (Grams et al. 2015). The hypsometric curves in figure 2 were created from surveys before and after the 2008 and 2012 controlled flood. They show that a higher proportion of sandbar area occurs at higher elevations following the flood, which supports the conclusions that controlled floods are depositing sediment at higher elevations. Although controlled floods were also conducted in 2013, 2014, 2015, and 2017, sandbar topography was not measured in the field before and after these events.
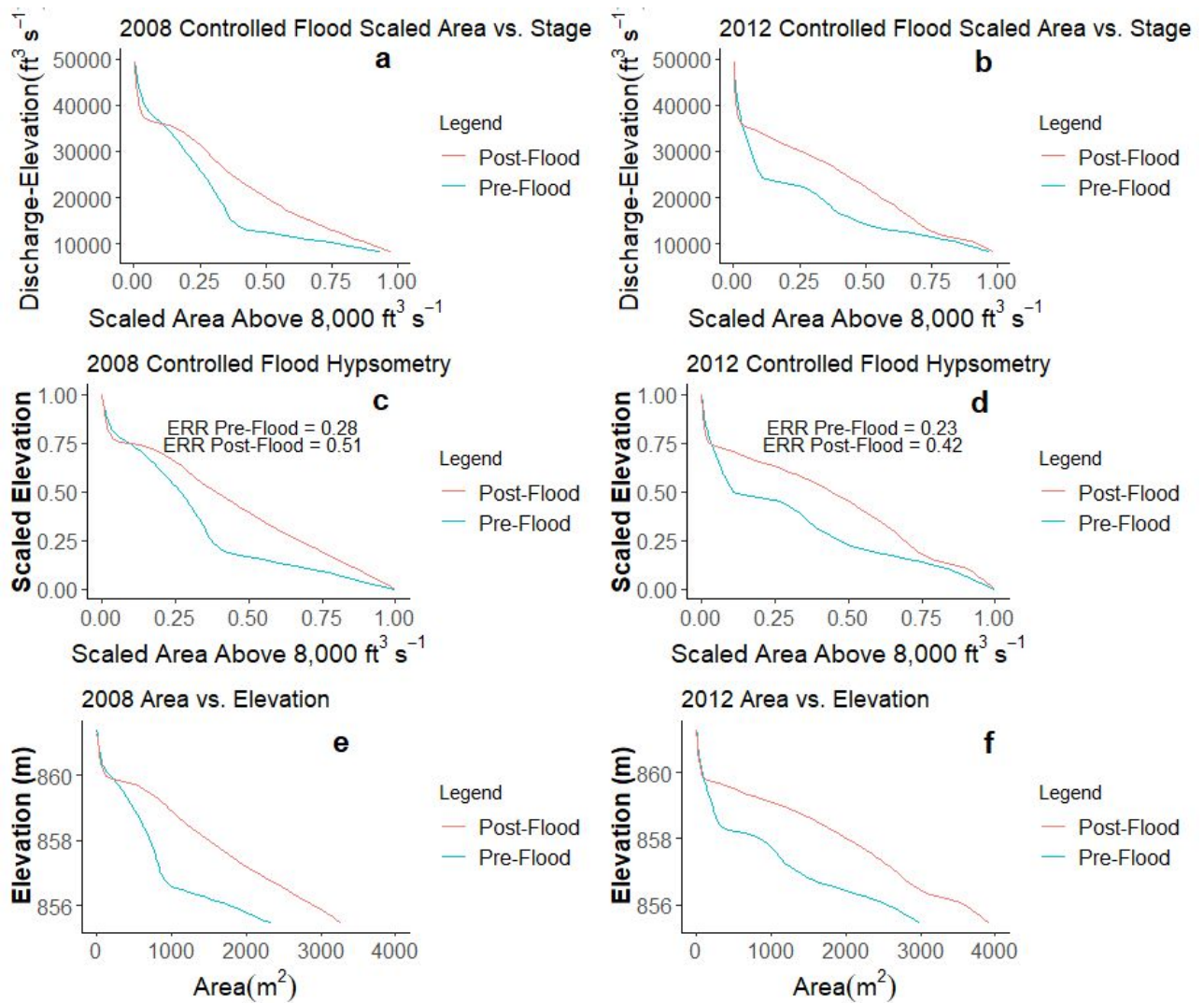
Figure 2. Relationships between the area and elevation plotted in three ways, before and after the 2008 and 2012 flood using data from topographic surveys. Panels (a) and (b) show sandbar area scaled to the sub-aerial sandbar area at a discharge of $8,000\,ft^3 s^{-1}$, plotted against the water surface elevation $ft^3 s^{-1}$ for each year. Panels (c) and (d) show normalized area and elevation showing the hypsometry for each year, where ERR is the elevation relief ratio. Panels (e) and (f) show area (m^2) by elevation (m) relationship for each year.

Maintaining campable sandbar area that is above the water-surface most of the time is a primary management concern along the Colorado River in Grand Canyon. In comparison to volume alone, a hypsometric curve provides more information about the usable area, since the steeper sandbars may be less desirable for camping and hypsometry provides insight into overall sandbar slope angle.

Results and Discussion

Surveyed Hypsometries: We built hypsometric curves using data from 42 topographic surveys of RM 30.7 collected between 1990 and 2019. The measured area was scaled as a percentage of the sandbar area at the reference elevation, and plotted against elevation. Here elevation is expressed as the water-surface elevation at a particular discharge in ft^3s^{-1} (Figure 3). We built these hypsometric curves for two reasons. First, we sought to understand the variability in sandbar morphology which has been observed over the multi-decadal topographic survey period. Second, river management would benefit from an improved understanding of the relationship between sandbar area at the reference stage, and scaled area scaled to the reference stage at various other water surface elevations. Our goal is to develop a relationship through which sandbar volume can be predicted using two oblique images, one at the reference stage and another at a higher elevation.
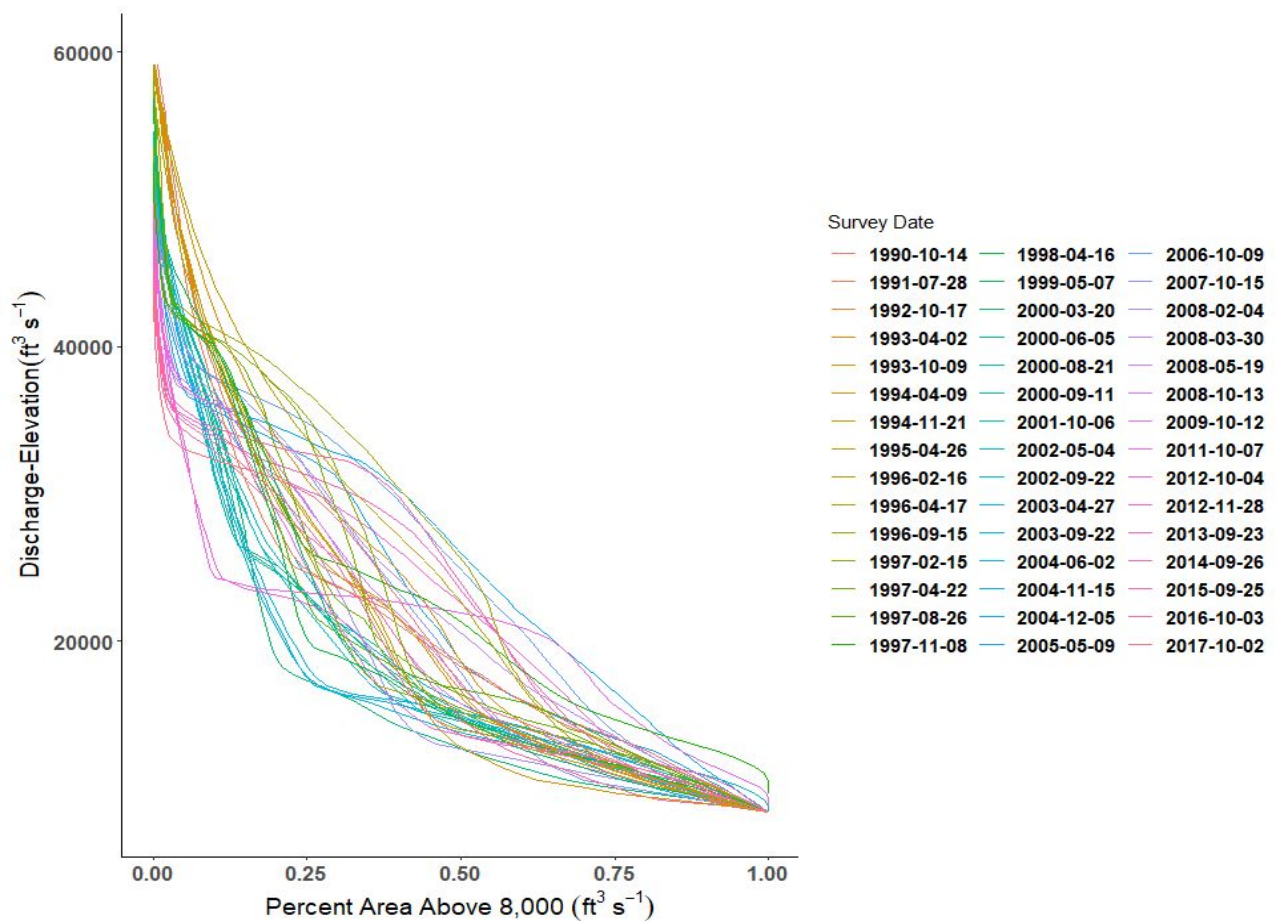
Figure 3. Relationship between survey-derived area measurements scaled to the reference elevation and the stage elevations for 42 sandbar surveys at RM 30.7.

Hypsometrically-Derived Volume: To estimate sandbar volume using the rectified oblique imagery, we first needed to determine the relationship between area at multiple elevations and volume at the reference elevation. Linear models were fit to the hypsometric relation (figure 3) using the survey-derived area measured at the reference elevation and the scaled area for each elevation with 100 ft^3s^{-1} intervals between 8,000 ft^3s^{-1} and 45,000 ft^3s^{-1} as the predictor, and volume at the reference elevation as the response (Equation 2):

$$(2) \quad V_{ref} = \beta_0 + \beta_1 A_{ref} + \beta_2 A_2 + \varepsilon$$

where the V_{ref} is the volume (m^3) at the reference elevation, the predictor variables are A_{ref}, the area (m^2) at the reference elevation, and A_2 the area (m^2) at another elevation scaled to the area at the reference elevation. β_0 is the intercept, β_1 and β_2 are the coefficients for the predictor variables, and ε is an error term. The lm() function in R was used to fit models using ordinary least squares. We examined model fits using a wide range of elevations for the second variable. Coefficients of determination in Table 1 are > 0.9 for linear models utilizing an area at the reference stage and a scaled sub-aerial sandbar area at discharges between 15,000 ft^3s^{-1} and 26,000 ft^3s^{-1}. Therefore, in a predictive capacity, if area can be measured accurately from oblique imagery,we can estimate sandbar volume within an accuracy of 90% or more, using just two images: one at the reference stage and a second at a water-surface elevation associated with flows between 15,000 ft^3s^{-1} and 26,000 ft^3s^{-1}.

Table 1. Coefficients of determination and root-mean-squared error (RMSE) for linear models relating surveyed sandbar volume at the reference elevation with (1) the surveyed area at the reference elevation and (2) the scaled area at discharges between 14,000 ft^3s^{-1} and 26,000 ft^3s^{-1} at RM30.7. Adjusted R^2_{adj} = 1-(1-R^2) $\frac{n-1}{n-p-1}$, where p = # of predictors

| A_2 Discharge (ft^3s^{-1}) Elevation	R^2	R^2_{adj}	RMSE (M^3)
14000	0.874857	0.86844	601.3845
15000	0.911225	0.906673	506.5172
16000	0.921782	0.91777	475.4492
17000	0.926187	0.922402	461.8654
18000	0.928511	0.924845	454.5362
19000	0.929401	0.92578	451.6995
20000	0.93369	0.930289	437.7633
21000	0.940267	0.937204	415.486
22000	0.958439	0.956307	346.5727
23000	0.963504	0.961632	324.7686
24000	0.919457	0.915326	482.4634
25000	0.912903	0.908437	501.7069
26000	0.906134	0.901321	520.8383

Estimating Image Water-Surface Elevation: To determine how accurate the predicted water-surface elevation is at any given date and time, we compared our results to the water-surface elevation in 14 surveys where the water's edge was surveyed at RM30.7. The surveyed elevations were compared to estimated water-surface elevations using the same dates and times (Figure 4). Our predicted water surface elevations correlated with the surveyed elevations with an $R^2 = 0.9573$ and root-mean-squared error or (RMSE) of $0.053\ m$, indicating strong agreement between our estimates and survey results.
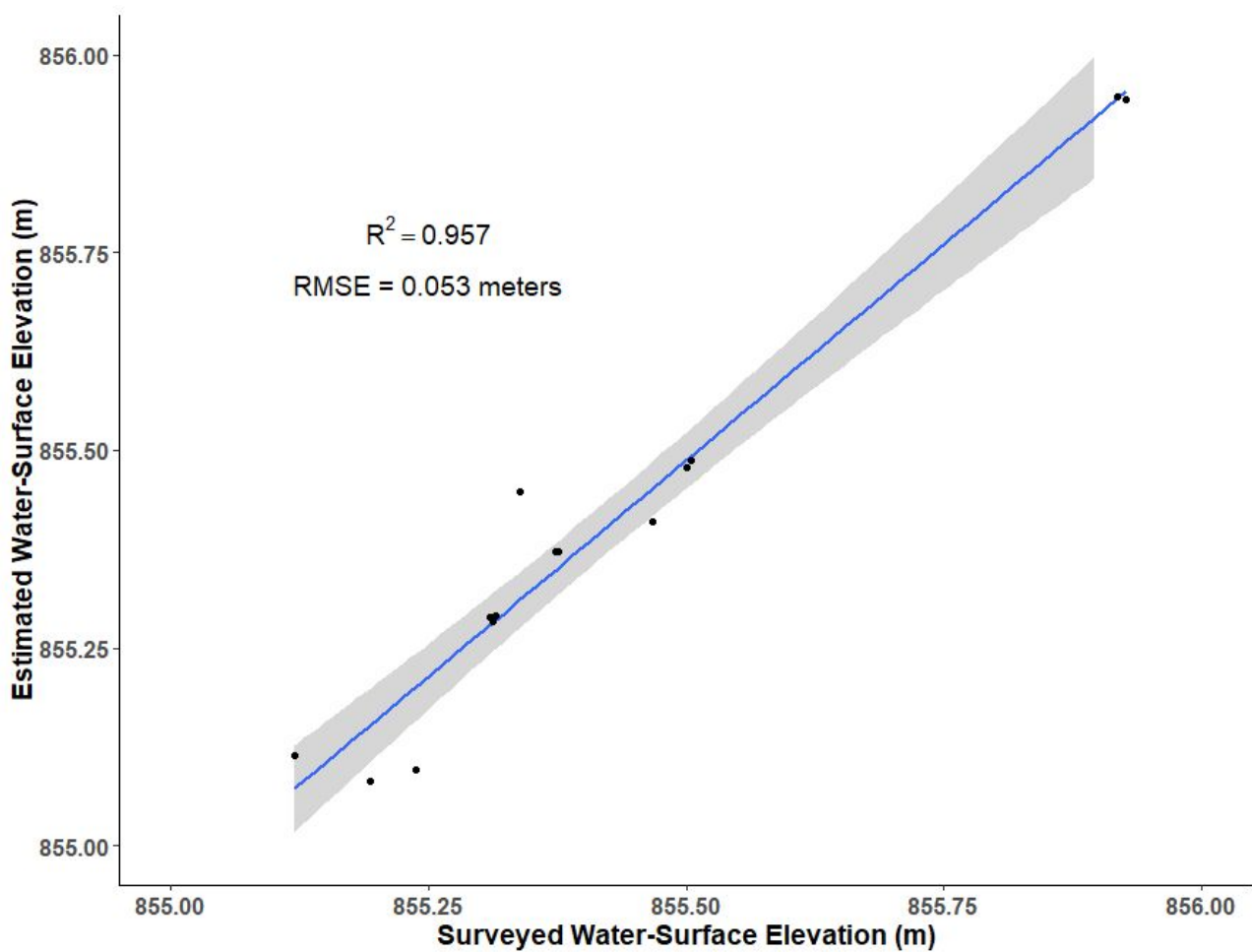

Figure 4. Comparison between estimated water-surface elevation and surveyed water-surface elevations.

Volume from Image-Derived DEMs: When comparing image-derived sediment volume estimates above the reference elevation to the survey-derived volumes above the reference elevation (Figure 5), we observe that the trends in surveyed and estimated volume over time are similar. However, four out of five of the image-derived estimates underestimated sandbar volume (Figure 5). Therefore, an offset or a correction factor could be applied to image-derived volumes if the errors are found to be within the same range in every case (Figure 6). Unfortunately, direct comparisons between the 22 image-derived volume estimations could only be made on four occasions between 2012 and 2016 when surveys occurred within a day or two of each estimate (Figure 6). More data are needed to quantifying the accuracy of image-derived volume estimates. New imagery from 2017- 2019 should allow for more accurate comparison in future work. Evaluating uncertainty is a future research goal and involves estimating the combined errors in the segmentation process, image rectification, and area estimation, and how these errors propagate into volume measurements of resulting raster surfaces.
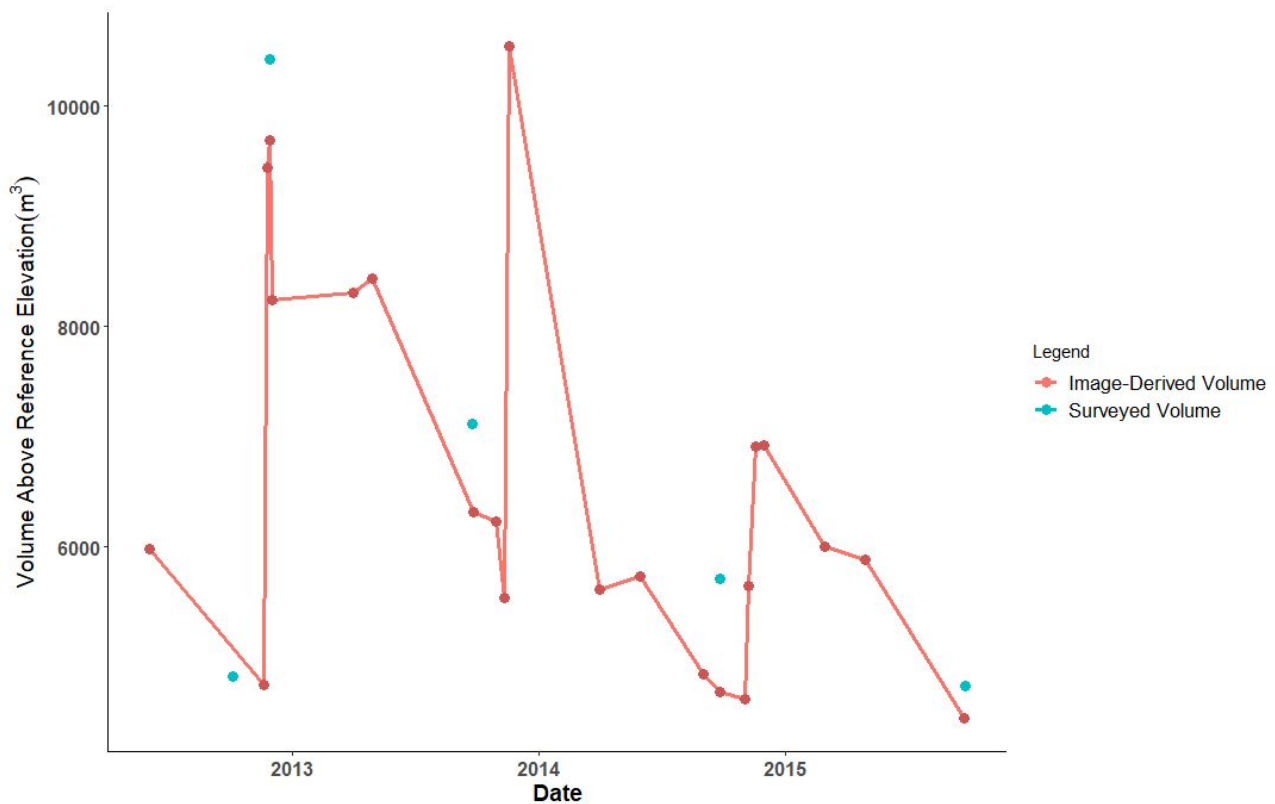

Figure 5. Comparison between the survey-derived volumes above the reference elevation (blue dots) and volumes estimated from image-derived DEMs (red line).
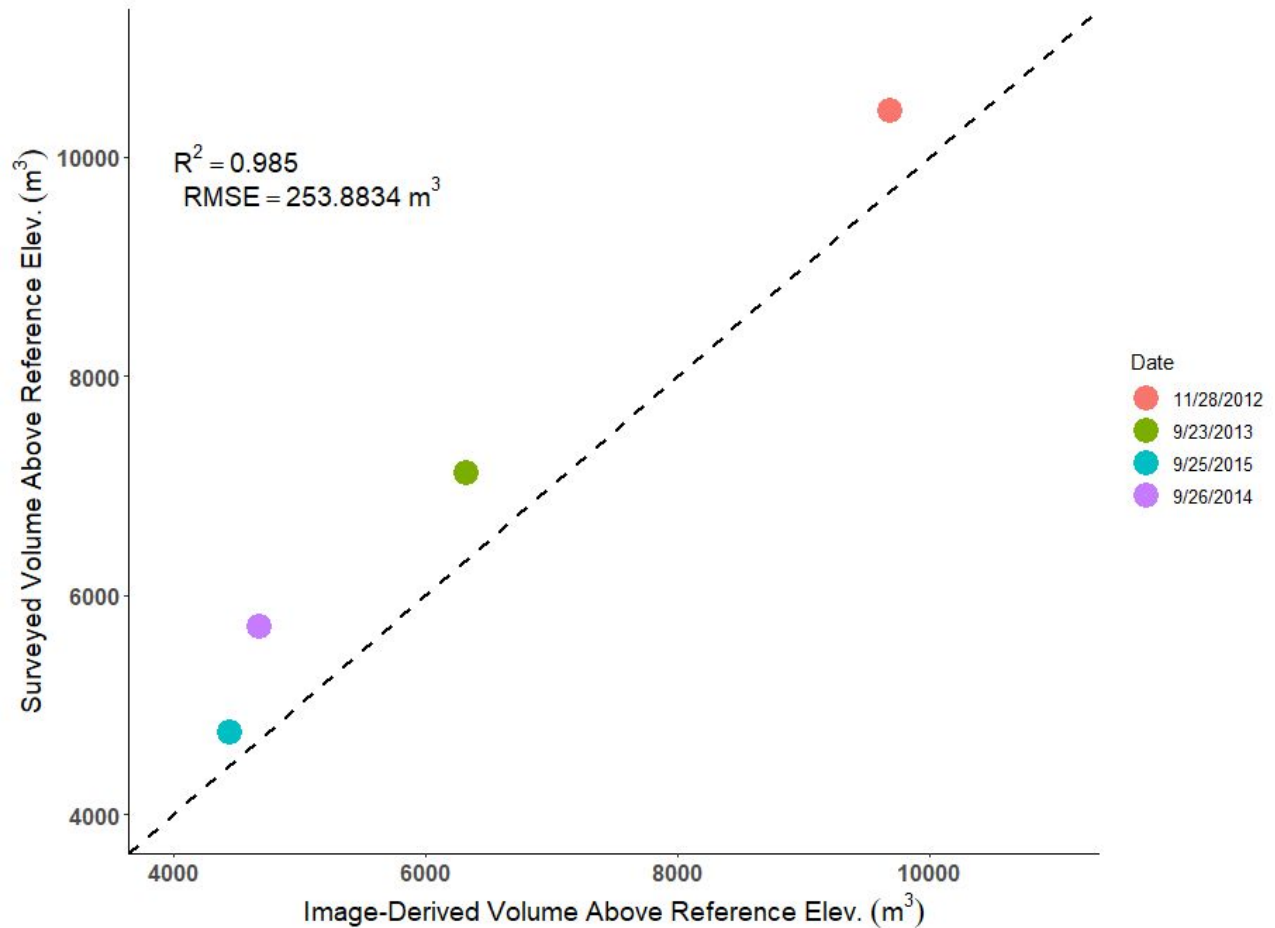
Figure 6. Comparison between survey-derived volumes above the reference elevation and image-derived volumes for four corresponding dates.

Limitations: The creation of DEMs and hypsometric curves, and their accuracy, is limited by the frequency with which an image at or very near the reference elevation is taken, along with images at discharges greater than 15,000 $ft^3 s^{-1}$ within a few days of each other. Or a period where erosion and deposition can be assumed to be negligible. The frequency of images captured at discharges greater than 20,000 $ft^3 s^{-1}$ is low, and periods, where a broad range of discharges can be captured, are limited to infrequent controlled floods. Figure 7 shows the frequency of images at various discharges at RM 30.7. Since portions of the sandbar that remain sub-aerial above 20,000 $ft^3 s^{-1}$ are rarely inundated, we assume that fluvial erosion of those portions of the bar is limited to controlled floods, and episodic mass failures likely resulting from erosion at lower elevations and backwasting. Such failure events are evident in imagery. Overall, we assume these high-elevation areas remain static in the absence of obvious episodic mass failures detected by manual inspection of imagery. To aid in future analysis, the camera systems could be programmed to take 10 images per day instead of five which would provide additional area measurements and increase the accuracy of image-derived hypsometries, and potentially the accuracy of volume estimates.
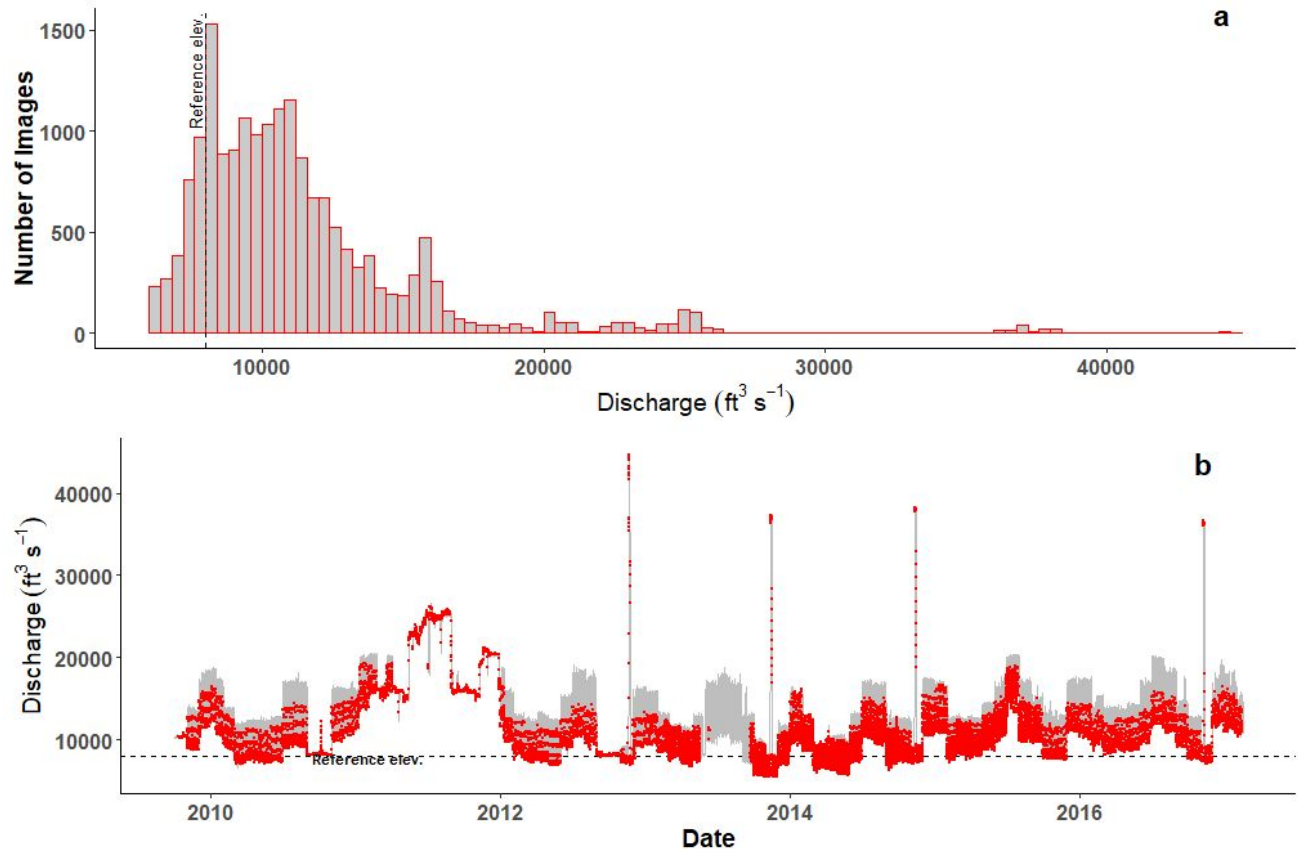
Figure 7. (a) The frequency of images at RM30.7 at different discharges; (b) image times plotted over the estimated hydrograph for RM30.7. There are 18,699 total images between 2009 and 2017.

Conclusions

Our results indicate that sandbars can be successfully delineated in oblique imagery. Segmented sandbar imagery can be used to accurately estimate sandbar area and water surface elevation. Image-extracted area measurements were successfully combined to create contours and subsequent DEMs at the RM30.7 sandbar three to five times per year from 2012 - 2016, providing a mechanism for monthly or seasonal monitoring of sandbar size and morphology. Volume measurements from image-derived DEMs showed a similar trend to surveyed sandbar volumes. Currently, there are only four occasions where surveys correspond temporally to image-derived DEMs. Therefore, more data are needed to evaluate the accuracy of volume estimates. Analysis of images in 2017 - 2019 will likely provide more corresponding surveys to test image-derived volume estimate accuracy.

Future analysis will attempt to produce hypsometric curves from oblique imagery. This technique offers an important tool for monitoring the effects of controlled floods between surveys and may provide a single value, the elevation relief ratio, which can be used to compare changes in elevational storage at individual sites and across sites within Grand Canyon. Combining the hypsometric curves and associated elevation relief ratios offer a way to monitor the variability in sandbar morphologies at particular sites.

References

Alvarez, L. V., and M. W. Schmeeckle (2013), Erosion of river sandbars by diurnal stage fluctuations in the Colorado River in the Marble and Grand Canyons: full-scale laboratory experiments., *River Res. Appl.*, *22*(July 2011), 1085–1095, doi:10.1002/rra.

Bogle, R., Velasco, M., & Vogel, J. (2013). *An Automated Digital Imaging System for Environmental Monitoring Applications*.

Dexter, L. R., & Cluer, B. L. (1999). Cyclic erosional instability of sandbars along the Colorado River, Grand Canyon, Arizona. *Annals of the Association of American Geographers*, *89*(2), 238–266. http://doi.org/Doi 10.1111/1467-8306.00144

Dolan, R., Howard, A., & Gallenson, A. (1974). Man's impact on the Colorado River in the Grand Canyon. *American Scientist*, *62*(4), 392–401. Retrieved from http://erode.evsc.virginia.edu/papers/dolan_GrCyn_impact_74.pdf

Grams, P. E., J. C. Schmidt, S. A. Wright, D. J. Topping, T. S. Melis, and D. M. Rubin (2015), Building sandbars in the Grand Canyon, *Eos (Washington. DC).*, *96*, doi:10.1029/2015EO030349.

Grams, P. E., Tusso, R. B., & Buscombe, D. (2018). *Automated remote cameras for monitoring alluvial sandbars on the Colorado River in Grand Canyon, Arizona*. *Open-File Report*. Reston, VA. Retrieved from http://pubs.er.usgs.gov/publication/ofr20181019

Hazel, J. E., Topping, D. J., Schmidt, J. C., & Kaplinski, M. (2006). Influence of a dam on fine-sediment storage in a canyon river. *Journal of Geophysical Research: Earth Surface*, *111*(1), 1–16. https://doi.org/10.1029/2004JF000193

Hazel, J. E., M. Kaplinski, R. Parnell, K. Kohl, and D. J. Topping (2007), Stage-Discharge Relations for the Colorado River in Glen, Marble, and Grand Canyons, Arizona, 1990-2005, , *7*.

Pike, R. J., and S. E. Wilson (1971), Elevation-relief ratio, hypsometric integral, and geomorphic area-altitude analysis, *Bull. Geol. Soc. Am.*, *82*(4), 1079–1084, doi:10.1130/0016-7606(1971)82[1079:ERHIAG]2.0.CO;2.

Rother, C., V. Kolmogorov, and A. Blake (2004), "GrabCut": interactive foreground extraction using iterated graph cuts, *ACM Trans. Graph.*, *23*(3), 309, doi:10.1145/1015706.1015720.

Sankey, J. B., Caster, J., Kasprak, A., & East, A. E. (2018). The response of source-bordering aeolian dunefields to sediment-supply changes 2: Controlled floods of the Colorado River in Grand Canyon, Arizona, USA. *Aeolian Research*, *32*(October 2017), 154–169. https://doi.org/10.1016/j.aeolia.2018.02.004

Schmidt, J. C., Topping, D. J., Grams, P. E., & Hazel Jr., J. E. (2004). System-wide changes in the distribution of fine sediment in the Colorado River corridor between Glen Canyon Dam and Bright Angel Creek, Arizona, (Final Report), 107. Retrieved from http://www.gcmrc.gov/library/reports/Physical/Fine_Sed/Schmidt2004.pdf

Strahler, A. N. (1952), Hypsometric analysis of erosional topography, *Bull. Geol. Soc. Am.*, *63*(November), 1117–1142, doi:10.1130/0016-7606(1952)63[1117:HAAOET]2.0.CO;2.

Topping, D. J., Rubin, D. M., & Vierra Jr., L. E. (2000). Colorado River sediment transport 1. Natural sediment supply limitation and the influence of Glen Canyon Dam. *Water Resources Research*, *36*(2), 515–542.

Tusso, R. B., Buscombe, D., & Grams, P. E. (2015). Using oblique digital photography for alluvial sandbar monitoring and low-cost change detection. In *Proceedings of the 3rd Joint Federal Interagency Conference on Sedimentation and Hydrologic Modeling, April 19-23* (pp. 79–85).

Water Quality History Derived From Diatom Communities in a Water Treatment Sediment-Settling Reservoir, Aztec, NM

Jeb Brown[1], Becky Bixby[2], Johanna Blake[1], and Christina Ferguson[1]

[1]U.S. Geological Survey, New Mexico Water Science Center, [2]University of New Mexico

jebbrown@usgs.gov 505-830-7915

Abstract

The Animas River and San Juan River watersheds in southern Colorado and northern New Mexico have a long history of anthropogenic land use activities. Some of these activities, including gold, silver, and uranium mining; lead, uranium, and vanadium milling; and oil and gas development, have resulted in adverse environmental impacts. Exposed geology of these watersheds can also contribute to naturally elevated constituents of concern (for example, lead and aluminum) in these rivers. Understanding historic effects of anthropogenic land use can inform future management decisions.

Diatoms are important single-celled photosynthetic protists in aquatic ecosystems that are useful for biomonitoring because they often live in a specific range of environmental conditions. Analysis of depositional layers of sediments in lakes and reservoirs for biological indicators such as diatoms can be used to reconstruct historic water-quality conditions of a watershed.

The U.S. Geological Survey collected bed sediments from four trenches within a drained settling reservoir maintained by the City of Aztec drinking water treatment plant. Analyses of bed sediments include sediment descriptions, chemistry, age dating, and diatom species identification, and provide a history of water quality (1947-2018) in the Animas River watershed upstream of Aztec, NM. This work explores the response of diatom taxa through the reservoir's history to changes in water-quality conditions (e.g. pH, nutrient concentrations, salinity, metals, etc.) that may have occurred in the watershed over the past 71 years.

Diatoms were identified and species composition delineated every 10 centimeters along the length of one sediment core. Diatom communities are characterized on the basis of the life history (e.g., cosmopolitan versus endemic, planktonic versus benthic, etc.) of community species. Chemical, physical, and particle size analysis of sediments are used to interpret drivers of the diatom community structure. These data inform the assessment of conditions of the settling reservoir in Aztec and may predict how upstream changes in water chemistry affect the local reservoir.

Wildfire in the West: Assessing the Detectability of a Post-fire Signal at the Watershed Scale

Aaron Heldmyer[1], Ben Livneh[1,2]

[1]Department of Civil, Environmental, and Architectural Engineering, University of Colorado Boulder, Boulder, CO, 80309.

[2]Cooperative Institute for Research in Environmental Sciences, University of Colorado Boulder, Boulder, CO, 80309.

Abstract

Wildfires are expected to increase in both size and severity in the western U.S. These disasters cause important, often lasting changes to watershed dynamics, particularly in sediment mobilization processes, and create problems for downstream reservoirs and water treatment facilities. Therefore, it is essential to improve our understanding of wildfire-driven changes in streamflow and suspended sediment loading (SSL) to mitigate damages. Previous efforts to model wildfire effects have often focused on a small subset of sites and a limited number of post-fire hydrologic processes changes such that the insights gained have generally lacked transferability due to regional variations in the drivers of these responses. Additionally, scarcity of observational sediment data provides a further challenge for finding generalizable influences on post-fire sediment response useful for modeling in areas with little to no available sediment data, which represent the vast majority of basins in the West. In this research, we seek to improve understanding of post-disturbance hydrology and sedimentation by first characterizing streamflow and sediment relationships through commonly used rating curve parameters at a diverse set of gaged locations across the western U.S. We combine this with basin topographical and water infrastructure development information from the GAGES-II dataset. We then select a relatively undeveloped basin from this dataset (the Rio Puerco near Bernardo, NM) that has been affected by five observed fire events between 1999 and 2014 as a testbed for measuring the viability of a set of increasingly data-intensive approaches for finding a detectable post-fire sediment response signal. We begin by applying a statistical model to pre-fire stream gage data and forecasting the post-fire season, comparing differences in suspended sediment loading (SSL) magnitudes between the forecast and observations. We subsequently add precipitation data from Daymet (basin-averaged, then gridded), and fire extent data from the Monitoring Trends in Burn Severity (MTBS) dataset to improve post-fire sediment signal strength. Future work will see further exploration of novel detection techniques, as well as the eventual application of these methodologies to other western basins in an effort to uncover regional influences on sediment response to wildfire. This study carries implications for post-fire sediment modeling, water management, and reservoir operations.

Introduction

Wildfires are expected to increase in both size and severity in the western U.S. Sankey et al. (2017) predicts that post-fire sedimentation rates will increase by over 10% for nearly 9/10ths of watersheds, and greater than 100% for more than 1/3rd of watersheds by the 2041-2050 decade. This is cause for concern, as these disasters instigate important and often lasting changes to watershed dynamics, particularly in sediment mobilization processes, and create problems for downstream reservoirs and water treatment facilities. Recent studies have shown that post-fire overland flow, discharge, and peak flows can increase by several orders of magnitude relative to pre-fire conditions, particularly in the first 1-3 years (Neary et al., 2011). Within streams, suspended sediment particles from fire-affected locations have been known to exhibit significantly higher settling velocities than unburned particles of similar diameter due to reduced organic content and pore space (Blake, et al., 2007, 2009). As a consequence, an increase in fine sediment loading in streams and reservoirs located downstream of affected areas may be observed (Smith et al., 2011). This can necessitate costly interventions such as reservoir dredging for downstream infrastructure (Jones et al., 2017), further underscoring the importance of understanding post-fire effects on hydrology and geomorphology.

From a hydrologic standpoint, destruction of vegetation and litter following an event affects canopy interception, evapotranspiration, and storage of rainfall, which can also influence the accumulation and melting of snow (Shakesby & Doerr, 2006). Wildfire-induced soil heating affects its physical and chemical properties, increasing water repellency and decreasing aggregate stability. Rain splash can disrupt and compact the soil, and fine sediments dislodged by this process can clog soil pores and lead to surface sealing. An abundance of fine sediments generated from the ash of combusted vegetation leads to further water repellency (Meyer & Wells, 1997). Infiltration is often reduced as a result of these changes (Moody & Martin, 2001), which in turn generates considerably higher overland flow, increased discharge, and peak flows orders of magnitude greater than pre-fire conditions, particularly in the first 1-3 years (Neary et al., 2011).

The geomorphology of a basin is also affected in a variety of ways. Numerous studies have documented increased erosion rates following a fire disturbance (Benavides-Solorio & MacDonald, 2001; Cerda & Doerr, 2005; Luis, et al., 2003; Emmerich & Cox, 1994; Fernandez, et al., 2011). Since erosion is largely dependent on overland flow, erosion rates are usually determined by factors that control runoff generation: soils, vegetation, and water input. Overland flow arises from either saturation-excess or infiltration-excess conditions, and it is the latter that is the dominant mechanism in arid and semi-arid regions where wildfires are commonplace (Wondzell & King, 2003). Easily erodible sediment becomes exposed when protective vegetation cover is burned away, and a combination of soil organics combustion and intense heating leads to decreased cohesiveness of surface soil and further ease of erosion (Johansen, et al., 2001).

In addition to the spatial component of wildfire disturbance, the temporal component of how wildfire effects manifest years or even decades into the future following an event is perhaps equally as important to characterize. The impact of wildfire disturbance can be quantified by measuring the post-fire change in process rates (discharge, hillslope and channel erosion, sediment transport, and deposition) and contrasting these with pre-fire conditions (Swanson, 1981). Some studies (Vieira, et al., 2015) characterize this difference

using a logarithmic response ratio, which expresses the proportional difference in a response variable between a "treatment" (burned area) and an unburned reference. This is a typical metric for meta-analysis of ecological data.

The relationship between pre- and post-fire process rates may be observed through time. Immediately following a wildfire event, during the "initial phase", process rates have been observed to increase with time before reaching a maximum. A recovery phase then takes place following this maximum where the rates decrease. The combined length of these two phases are what is known as the *relaxation time*, which can vary widely from one to three years for sediment fluxes, up to thirty years for discharge, and longer for regrowth of trees (Rowe, et al. 1949). Over long time intervals, the importance of wildfire as a geomorphic agent depends upon the ratio between this relaxation time, and the wildfire recurrence time: a ratio known as the *transient form ratio* (Brunsden and Thornes, 1979). Because wildfires lower the threshold of energy required for erosion to take place, even a low intensity storm event coupled with spatially heterogeneous wildfire effects can be an important agent for sediment mobilization, particularly in arid and semi-arid mountainous basins common across the West (Moody & Martin, 2001).

While many experiments document the effects of wildfire on erosion and overland flow magnitudes at the plot scale, few studies (Reneau et al., 2007; Pelletier & Orem, 2014) focus on post-fire sedimentation effects at the basin scale, which is significantly more important to quantify in order to avoid costly damages for downstream reservoirs and water treatment facilities. Unfortunately, predicting sediment delivery at the basin scale is a much more complicated process than predicting at the plot or hillslope scale, due to the addition of numerous processes, sources, and sinks that may hinder or help a sediment particle in reaching the basin outlet (Fryirs, 2013). For sediment transport, it is often noted that river systems act as 'jerky conveyor belts' (Ferguson, 1981), in that sediment is transported episodically through the catchment. Landforms in which sediment may be stored for long periods of time, such as slopes, floodplains, or terraces, may attenuate or even completely mask a sediment response signal (Fryirs & Brierley, 2001). The effects of a wildfire event on sediment loading may not make themselves known at the basin outlet until months, or even years after the fact.

To further complicate the issue, there are also limited resources available for the direct observation of sedimentation in the U.S. In the West, there are over 9,000 decommissioned or active gages measuring streamflow according to the USGS Geospatial Attributes of Gages for Evaluating Streamflow (GAGES-II) dataset (Falcone, 2017). Of these, 2,317 of the gaged basins are co-located with wildfire ignition points documented in the Monitoring Trends in Burn Severity (MTBS) dataset (Eidenshink et al., 2007), and only a small subset (n = 187) also contain direct measurements of suspended sediment concentration (SSC) at any point in their operational lifetime; that is, not necessarily when a wildfire event has taken place. This paper presents a preliminary analysis into the problem of detecting the post-fire hydrologic and sediment response from basins across the western U.S. in the context of this sparse data availability, and sets the stage for future work, which will more rigorously assess the detectability of wildfire signals at the basin scale using supplemental data derived from prior studies, remotely-sensed basin physiography, and meteorological observations. We first conduct a meta-analysis of gaged basins across the West as a top-down comparative measure, and subsequently focus on a

single basin to serve as a testbed for refining several analytical techniques with the aim of uncovering a robust post-fire sediment signal.

Study Domain and Data Products

The western U.S. was selected as the study domain for evaluation of regional variations in hydrologic and geomorphologic response to wildfire, as well as in relationships between streamflow and sediment transport (Figure 1).
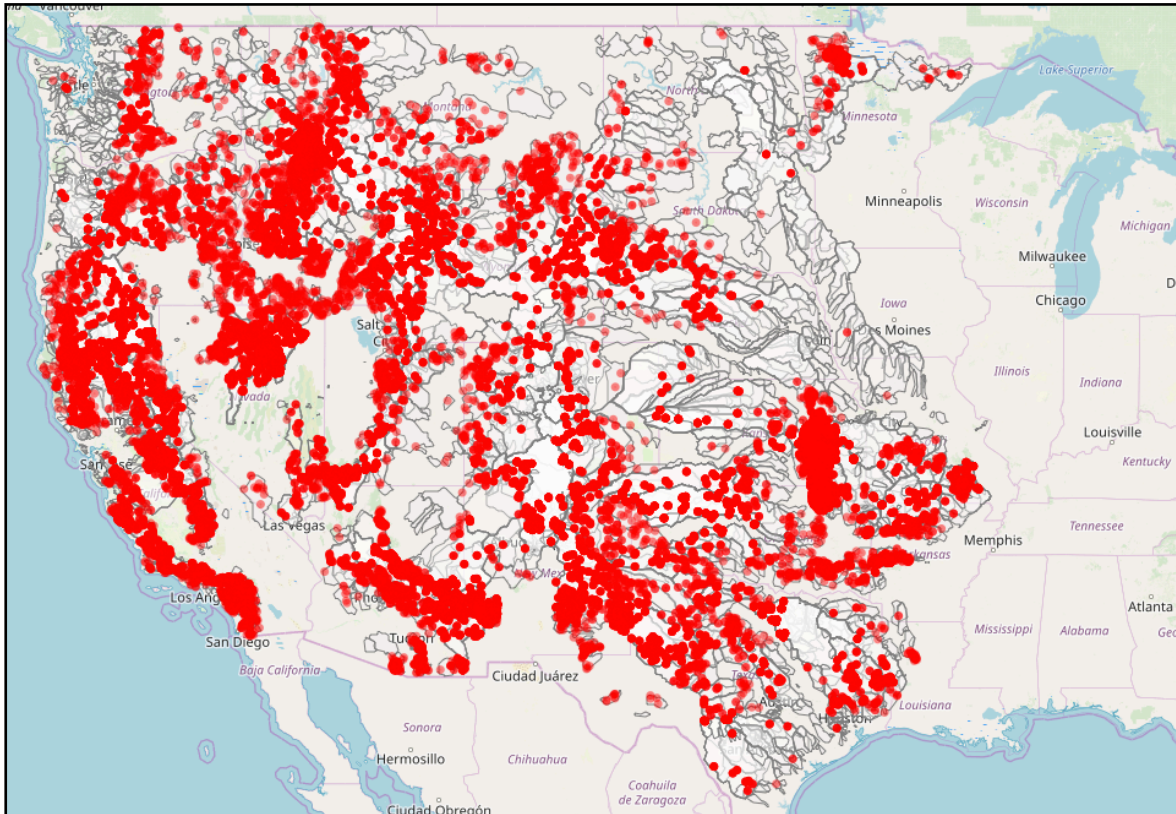

Figure 1. Western U.S. Study Domain: *All wildfire ignition points (recorded 1985-2016) are shown in red (Eidenshink et al., 2007). All GAGES-II basins are also displayed (Falcone, 2017). Note that some basins are nested.*

MTBS data were coupled with USGS GAGES-II basin information, and USGS National Water Information System (NWIS) stream gage data to support this regional analysis. Merging these datasets yielded a total of 255 wildfires across 187 gaged basins that have been observed for both streamflow and sediment, representing the wildfires and basins analyzed in the first section of this paper.

A single basin was isolated in order to evaluate and refine the methodology for quantifying post-fire sediment signals. This site was selected from the total 187 gaged basins based on several criteria that were established to identify a basin with the greatest likelihood of signal detection. These criteria include: minimal upstream regulation (e.g. dam density and storage) from GAGES-II, number of observed fires, size of observed fires as a percentage of basin size, and excluding non-snowmelt-dominated basins given
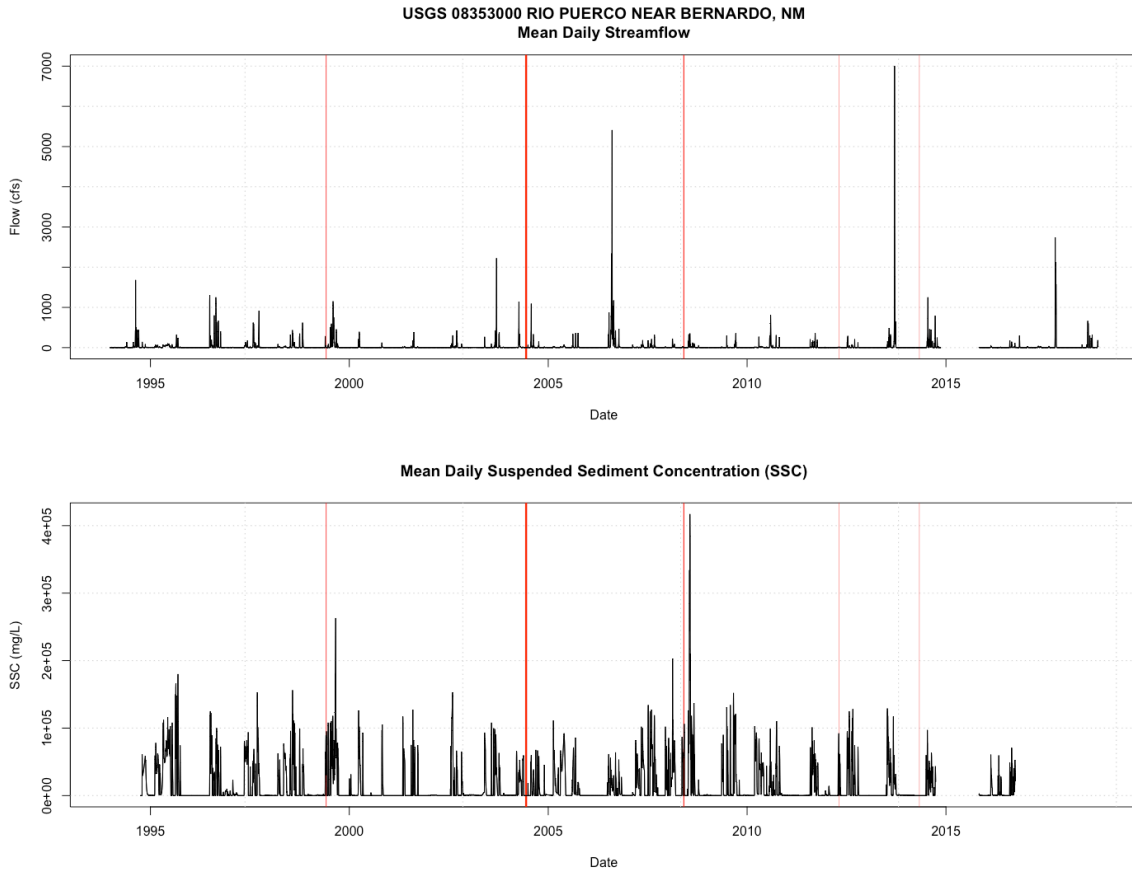
complexities associated with snowmelt timing and transport uncertainty. This selection process yielded the USGS Gage 08353000 for Rio Puerco near Bernardo, NM as the most suitable candidate. A plot of the study site is shown below in Figure 2. Located west of Albuquerque, NM, this location offers comparatively little infrastructure development, with a basin area of 15,724.93 km^2, 23 dams total (0.15 dams/km^2), and a dam storage density of 3.9 ML/km^2.
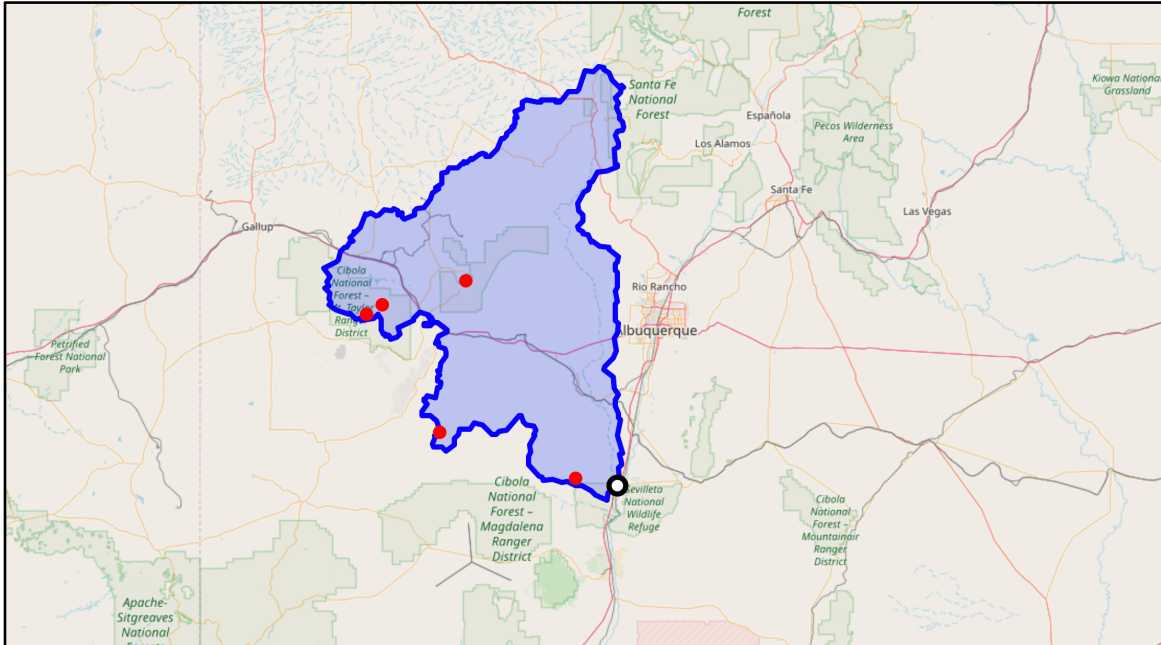
Figure 2. USGS Gage 08353000 (Rio Puerco near Bernardo, NM): *Basin extent is shown in blue. Fires observed for both sediment and streamflow are shown in red, and the gage location can be seen towards the south as a black and white circle.*

A total of 5 fires (2 prescribed burns and 3 wildfires) were observed within the drainage area during the period 1999-2014 when the gage was collecting both streamflow and sediment data. The largest fire, which occurred June 12th, 2004, consumed approximately 37.4 km^2 (0.23%) of the basin areal extent. The second and third largest fires occurred May 30th, 2008 and June 3rd, 1999, respectively, consuming 17.8 km^2 (0.11%) and 13.1 km^2 (0.08%) of the basin extent.

Streamflow and SSC data were available for the period between 1994 and 2016, with a brief period of streamflow only in 2015. A plot of observational data for the basin is shown below in Figure 3.

USGS 08353000 RIO PUERCO NEAR BERNARDO, NM
Mean Daily Streamflow

Mean Daily Suspended Sediment Concentration (SSC)

Figure 3. Mean daily streamflow (top) and mean daily SSC (bottom) data*. Vertical red bars denote wildfire ignition dates, with the thickness of the bars representing the relative size of the fires as a fraction of the total basin area.*

For the single site analysis, daily gridded 1-km precipitation data from Daymet (Thornton, et al., 2018) were utilized in addition to the gage data. These precipitation data were incorporated into the analysis in two ways: lumped over the basin areal extent to obtain a mean areal precipitation (MAP), and lumped individually over wildfire extents so as to only capture precipitation falling on fire-affected areas.

Methods

The Monovariate Rating Curve (MRC), also known as the sediment rating curve, is an empirical method for estimating sediment loading exclusively as a function of streamflow. The most common form is that of a power relationship:

$$SSL = aQ^b \tag{1}$$

where *SSL* is suspended sediment loading, *Q* is streamflow, *a* is a coefficient for the intercept, and *b* is an exponent for slope (Gray & Simoes, 2008). USGS daily streamflow

and sediment data were fitted to this model in order to create a summary relationship characterizing the expected sediment loading per unit streamflow for all 187 suitable basins with available data. This fitting process is demonstrated in Figure 4.
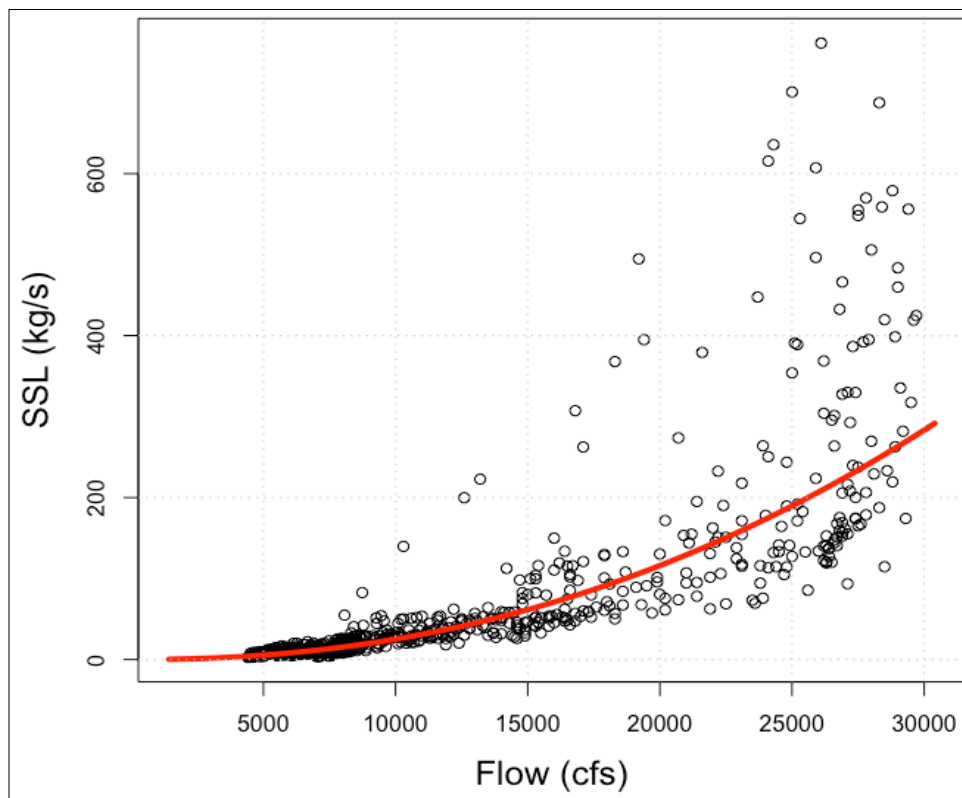
Figure 4. Sediment rating curve fitting: *An exponential relationship between SSL and Q is found and logged along with its correlation coefficient (R^2). The fitted coefficients are compiled along with GAGES-II basin properties for the wildfire analysis.*

Basin mean slope, relief ratio, drainage area, and total reservoir storage collected from the GAGES-II dataset were compiled along with fitted rating curve parameters to develop a profile for each basin, which were then used to select an appropriate study area for the single-site analysis.

A cascade of increasingly data-intensive techniques for detection of a post-wildfire signal was applied to the single site in New Mexico, with the intent of both *conclusively attributing*, and later *accurately predicting*, the presence and magnitude of a suspended sediment response at a basin outlet due to a wildfire event. The framework of this methodology is founded on two key motivations: the necessity for actionable post-fire sediment response information under conditions of data scarcity, and the need to identify influences on sediment response that may be generalized to the U.S. West region, such that inferences about post-fire sediment loading may be drawn for basins without an abundance of observational data. The most optimal technique would achieve an accurate prediction of sediment response magnitude due to a wildfire event using as little input data as possible.

The first method analyzes streamgage time-series data alone using a statistical technique called intervention analysis. Intervention analysis is commonly used to uncover the effects of an intervention, or an impactful event, on a time-series. Typically, an

AutoRegressive Integrated Moving Average (ARIMA) model (Box & Jenkins, 1976) is applied to pre-event time-series data and used to forecast theoretical post-event data. This essentially contrasts the actual post-event observations with the model scenario in which pre-event data are used to forecast post event response as if the event did not occur. An ARIMAX model is an extended version of ARIMA, and additionally includes one or more exogenous predictor variables. The equation for ARIMAX can be written as follows:

$$Y_t = C + v(B)X_t + N_t \qquad (2)$$

where Y_t represents the dependent variable, X_t is the independent variable, C is the constant term, N_t is the stochastic disturbance (i.e. the 'noise'), B is the backshift operator, and $v(B)X_t$ is the transfer function that allows X to influence Y through a distributed lag (Peter & Silvia, 2012). The transfer function can then be described as:

$$v(B)X_t = (v_0 + v_1 B + v_2 B^2 + \cdots)X_t \qquad (3)$$

This model was applied individually to each of the five wildfires at the study basin to train the model. The 'pre-fire' period used for training was defined as the start of the observational record up to the fire date of ignition. Determination of model parameters, including the lag order (number of lagged observations), degree of differencing (the number of times raw observations were differenced to remove nonstationarity), and the moving average order (the size of the moving average window), hereafter referred to as the variables (p, d, q), were made using the entirety of the observational record through step-wise Akaike Information Criterion (AIC) model ranking provided in the R function *auto.arima()* from the *forecast* package (Hyndman et al., 2019). A forecasted period of one year was selected to encapsulate a full post-fire season.

The second technique adds daily precipitation data from Daymet to create a basin mean areal precipitation as another predictor variable for the ARIMAX model. Several studies (Knapen, et al., 2007; Moody, et al., 2008; Momm, et al., 2018) identify precipitation intensity thresholds that must be overcome for the initiation of concentrated erosion and debris flows. Identifying this threshold may be particularly important for the prediction of suspended sediment following a fire, as a signal may not be readily detectable for storm events below these thresholds, whereas disproportionately high volumes of sediment may be transported during the first post-fire storm above the threshold. Initially, precipitation intensity was plotted against post-fire streamgage SSL to find evidence of this threshold by inspection. Then, precipitation data were used to filter out days during which no precipitation occurred (as it is assumed no overland flow was present to transport sediment into the channel), and subsequently added as a predictor variable for the ARIMAX model.

The third technique retains the spatial information of the precipitation data, rather than aggregating over the basin area. Fire extents from MTBS for the five events were compared against the gridded storm extents to find storms co-located with affected areas. A detectable signal may be more easily found and isolated when knowledge of whether a storm precipitated over a burned area is added. Thus, periods of time when no precipitation occurred over a wildfire-affected area were filtered out, and the remaining data were again modeled to detect pre- vs. post-fire differences in SSL.

Results

Regional Analysis

The results of fitting the MRC to observational data are summarized below. Figure 5 summarizes coefficient 'a' across the domain.
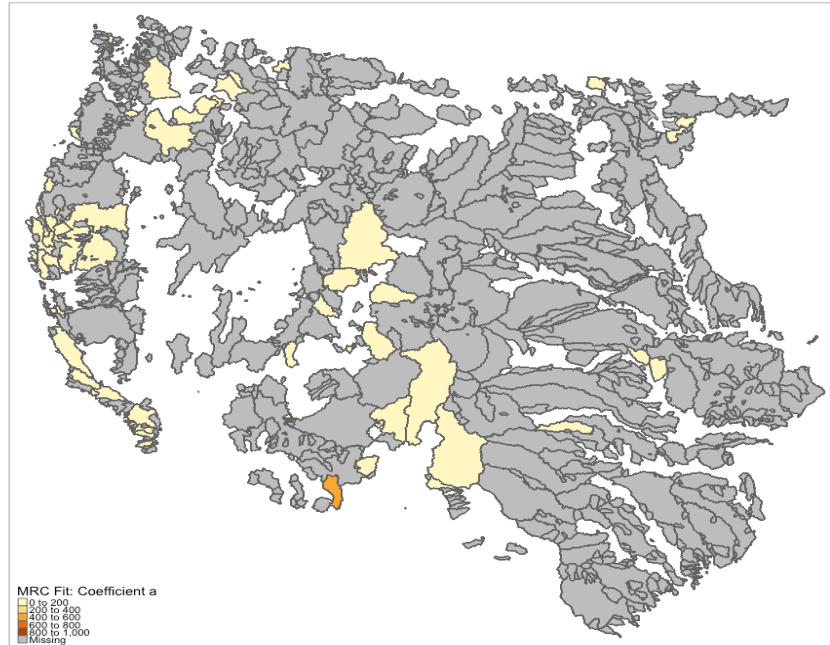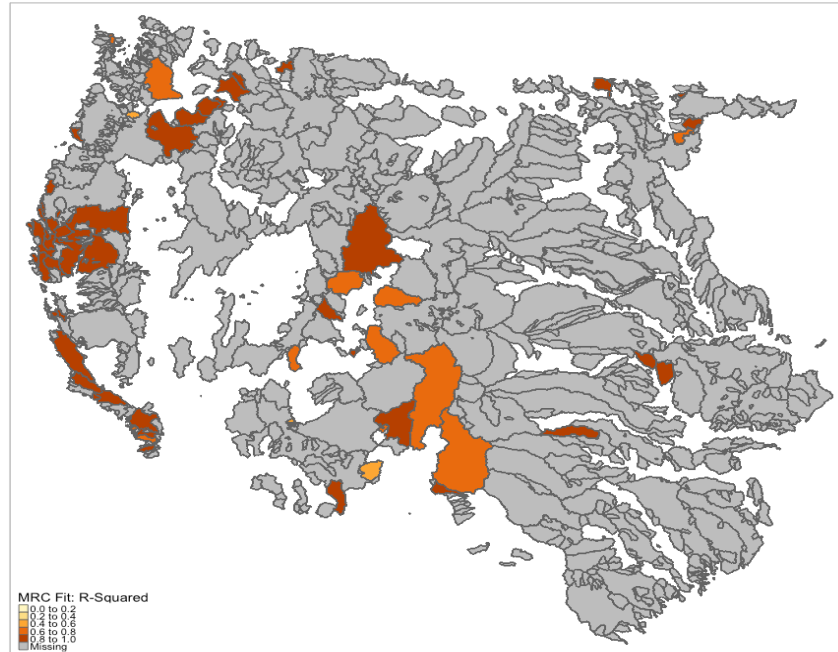

Figure 5. Spatial summary of coefficient 'a' from the MRC curve fitting process. *GAGES-II basins across the U.S. West are shown. Grayed-out basins are those with not enough available data.*

The spatial variation of exponent 'b' is shown below in Figure 6.
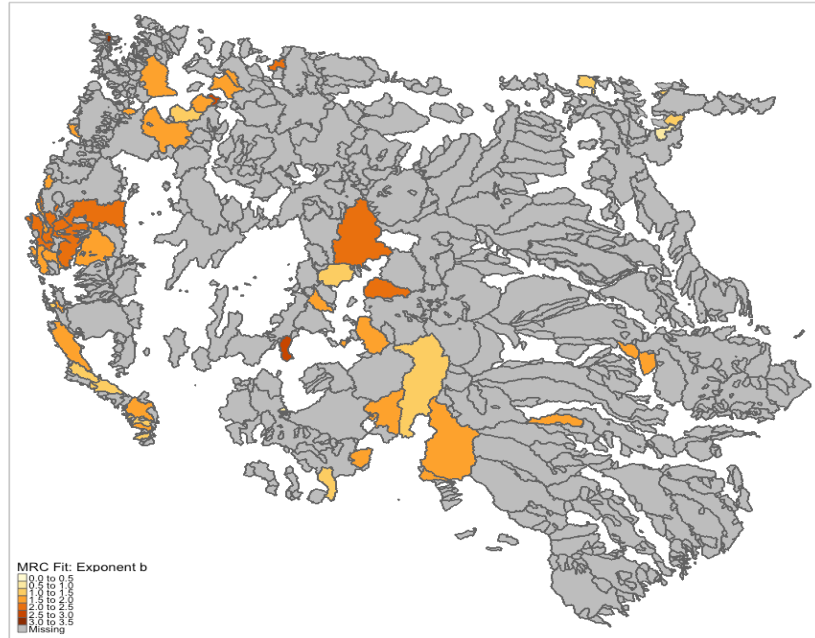
Figure 6. Spatial summary of exponent 'b' from the MRC curve fitting process. *GAGES-II basins across the U.S. West are shown. Grayed-out basins are those with not enough available data.*

Finally, the correlation coefficient, or R^2, of the fit between MRC-predicted and observed sediment is shown below in Figure 7.

Figure 7. Spatial summary of exponent 'b' from the MRC curve fitting process. *GAGES-II basins across the U.S. West are shown. Grayed-out basins are those with not enough available data.*

The MRC fit was largely skilled across the domain for all 187 basins, with 140 basins showing an R-squared greater than 0.75. Coefficient 'a' remained relatively low

across all basins, likely indicative of the 'flashy' nature of streams located in the arid West. Results for exponent 'b' are arguably the most interesting; high relative variability in its magnitude points towards basin-level differences that may be affecting its value. However, comparing 'b' against several basin metrics such as relief, mean slope, basin size, and mean flow (not shown) did not reveal any strong explanatory skill.

Single site analysis

For the single site analysis at Rio Puerco near Bernardo, NM, flow was multiplied with SSC to obtain SSL, which represents the volume of sediment flowing through the channel. Before fitting to an ARIMA model, these time-series were first examined for the presence of long-term trends and seasonality. An augmented Dickey-Fuller (ADF) test was applied to test for stationarity. The null hypothesis of non-stationarity over the time period was rejected with $p < 0.01$, indicating the absence of any longer-term trends that would need to be included in the model. To identify seasonal cycles in the data, plots of the auto-correlation function (ACF) and partial auto-correlation function (PACF) for SSL observations at the gage were examined (Figure 8).
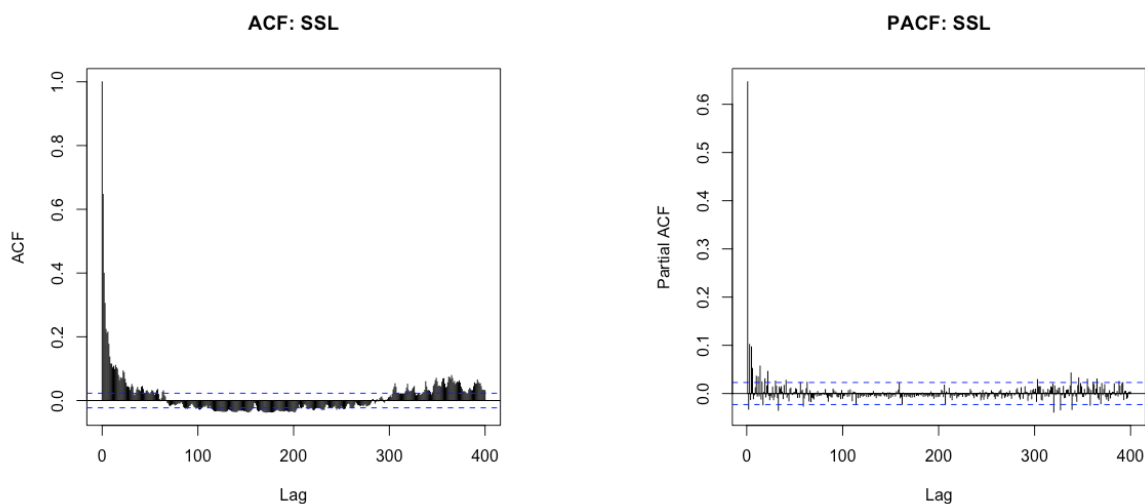
Figure 8. Autocorrelation function (left) and Partial autocorrelation function (right) for SSL. The horizontal axis shows lag in days, and the vertical axis shows correlation.

Significant auto-correlation exists for lags up to approximately one week, and, to a lesser extent, for a one-year lag, denoting the presence of an annual cycle for the time-series. A model optimization method using the R function 'auto.arima' was employed, which identifies a best model fit using the AIC method of ranking a model based on relative quality. Using the ARMIAX model with streamflow as an additional predictor, a non-seasonal AR order, degree of differencing, and MA order (p, d, q) = (2, 1, 2) was identified as the top performer through AIC best model selection, using the full record of observations.

For each wildfire, the model was fit to the pre-fire data and used to forecast the full year following the event. This was then compared against the true observed series for those 12 months, and the mean difference was taken to be the effect of the wildfire event. The results of this process are presented below in Figure 9.
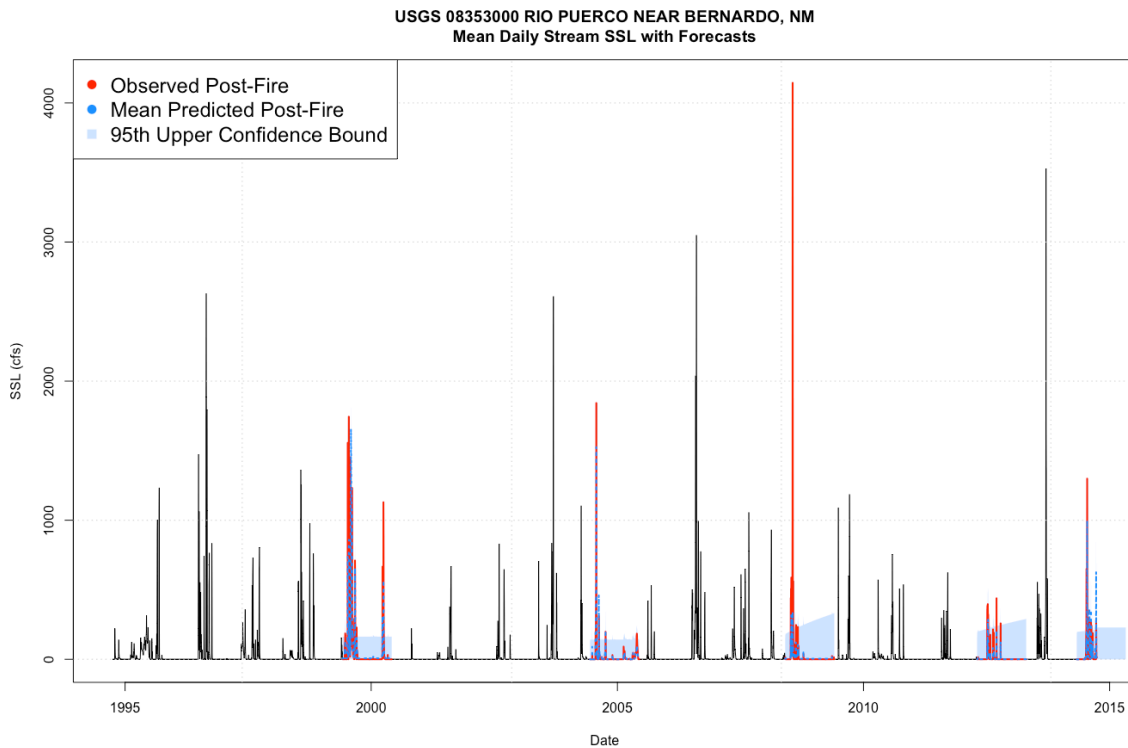
Figure 9. Model-predicted SSL versus observations following five observed wildfires at the study site near Bernardo, NM. *Pre-fire data used to inform the model is shown in black, the observed post-fire data is in red, model-predicted values are shown in blue, and the 95th percentile upper confidence bound is shown in light blue.*

Differences between post-fire observational and forecasted SSL during each post-fire year-long period are summarized below in Table 1.

Table 1. Summary of mean and maximum differences between forecast mean and observed SSL (in kg/s) during post-fire periods. *Ignition date and fire spatial extent are presented in the first column. Percent differences between forecasted and observed are also shown. An asterisk (*) denotes prescribed fires.*

Fire Event	Forecasted Mean SSL	Observed Mean SSL	Percent Difference	Forecasted Maximum SSL	Observed Maximum SSL	Percent Difference
1999-06-03 (13.15 km^2)	70.82	77.16	**8.22%**	1656.86	1744.32	**5.01%**
2004-06-12 (37.40 km^2)	20.02	20.63	**3.00%**	1525.73	1842.66	**17.20%**
2008-05-30* (17.83 km^2)	12.82	39.05	**67.17%**	340.74	4144.65	**91.78%**
2012-04-23 (6.4 km^2)	7.57	13.23	**42.78%**	288.75	439.03	**34.23%**
2014-05-02* (5.77 km^2)	49.07	56.83	**13.65%**	997.22	1299.03	**23.23%**

Next, the additional incorporation of precipitation data was tested to first determine if a specific post-fire erosion threshold could be found from the data, then added as a predictor to the ARIMAX model. First, a cross-correlation was applied between streamflow and precipitation, shown in Figure 10.
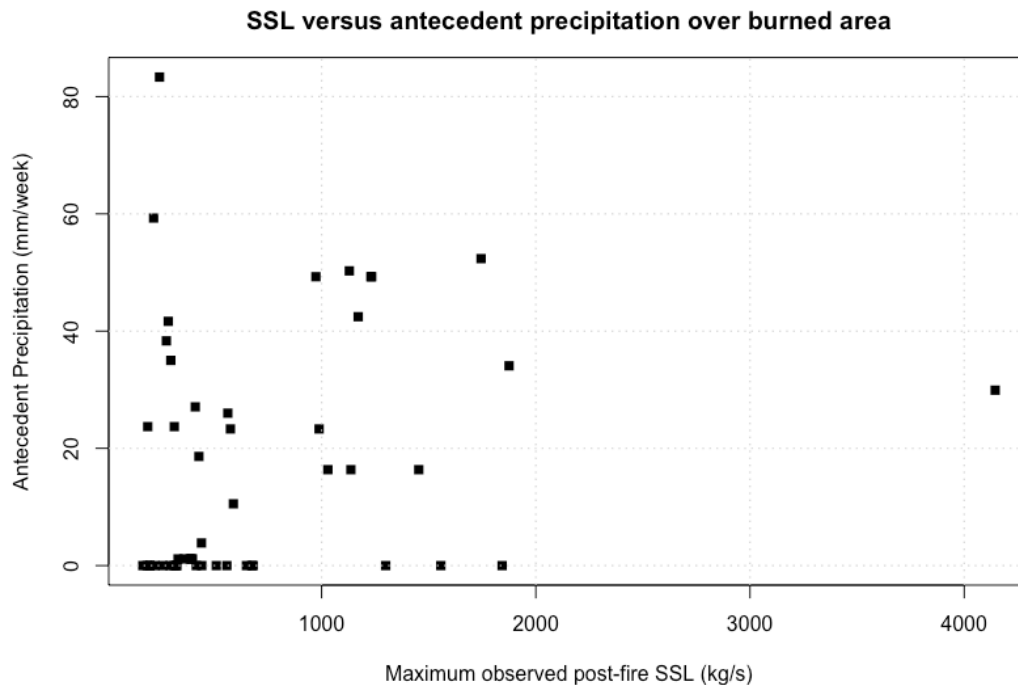
USGS 08353000 RIO PUERCO NEAR BERNARDO, NM
CCF between Flow and Precipitation
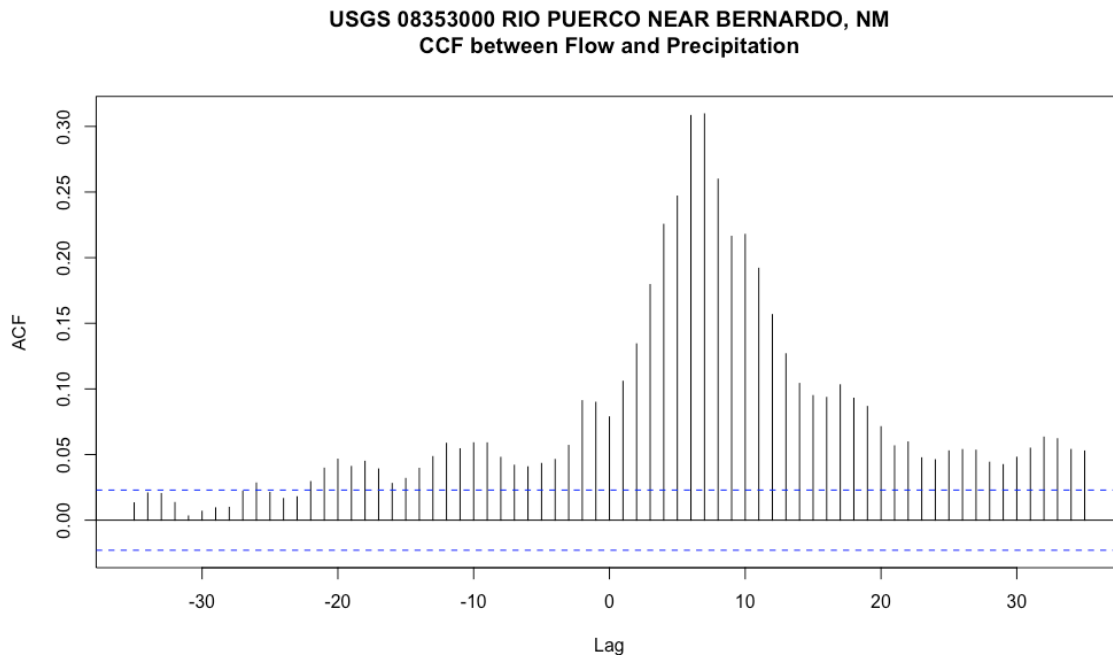
Figure 10. Cross-correlation between streamflow and precipitation. The horizontal axis shows the lag in days between the two series of streamflow and precipitation. The vertical axis shows correlation.

Prior literature, such as Valois et al. (2017), have taken the time of maximum correlation to be representative of the time of concentration for the watershed. The magnitude of the maximum correlation can also be taken as an indicator for the strength of the relationship between streamflow and precipitation. This basin shows a maximum lag time of 7 days, and a maximum correlation of 0.31, indicating a relatively slow concentration time and somewhat weak relationship between streamflow and precipitation. These initial findings point to the possibility of a predominantly groundwater discharge-fed watershed and/or the presence of other attenuating sub-basin processes that may store precipitation for a period of time before reaching the basin outlet.

Precipitation was fed into the ARIMAX model alongside streamflow as an exogeneous variable and used to forecast over the same post-fire periods. Adding precipitation as an additional parameter did not yield any significantly different forecast predictions, reflecting the weakness of basin-averaged precipitation as a predictor for SSL at the basin outlet. Among all fires, the largest difference between post-fire predicted mean SSL from the model with and without precipitation added was 0.71 kg/s. The largest difference in maximum SSL was 6.52 kg/s.

Finally, only precipitation that fell over a fire-affected area were analyzed. For each fire event, a unique time series of precipitation was used that represented precipitation falling within the extent of the fire perimeter provided by MTBS data. In order to determine if a sediment signal at the basin outlet could be attributed to sediment delivered from a burned area, the top 10 largest instantaneous SSL magnitudes were examined for

each post-fire period. Cumulative precipitation that had fallen within the prior week (based on the estimated 7-day time of concentration for this basin) were plotted against the largest SSL magnitudes during the post-fire seasons (Figure 11).

Figure 11. Cumulative precipitation over burned areas from the week preceding maximum observed SSL responses during post-fire periods. For each wildfire event, the top 10 post-fire SSL magnitudes were identified. For the week prior to these observations, precipitation over the burned area were summed. These SSL magnitudes and accumulated precipitation are shown.

Of the 50 maximum instantaneous sediment loadings (10 for each of 5 observed fires in the basin), 20 showed no prior precipitation over the burned area, indicating that at least 40% of these large sediment signals could not be attributed to sediment originating from burned areas.

Replacing precipitation over the entire basin with precipitation over burned areas alone again yielded few differences from the original model. Among all fires, the largest difference between post-fire predicted mean SSL from the model with and without burned area precipitation added was 1.28 kg/s. The largest difference in maximum SSL was 21.07 kg/s.

Preliminary Conclusions and Future Work

In this paper, we sought to characterize streamflow and sediment relationships through commonly used rating curve parameters at a diverse set of gaged locations across the western United States. We applied a statistical model to pre-fire streamgage data and forecasted the post-fire season, comparing differences in suspended sediment loading (SSL) magnitudes between the forecast and observations, and later adding data from

Daymet (basin-averaged, then gridded) and MTBS to improve post-fire sediment signal strength.

The regional analysis revealed trends in the rating curve exponent 'b' that may be worthwhile in future work to investigate further in order to identify correlations with additional basin characteristics not analyzed here. Future work will explore other predictive variables, such as land cover, geology, and climate, and their covariance with the value of 'b'.

For the single-site analysis, the gage-only method showed post-fire sediment signal for several of the fires, based on the difference between the observed and forecasted time series. The presence of these differences are encouraging, and reveal the potential for establishing an estimate of post-fire sediment response based on gage data alone. However, data limitations would make this method difficult, as most gages do not provide consistent sediment measurements. Including precipitation did not significantly affect the model; however, examining the link between cross-correlation in streamflow and precipitation versus sediment response may be worthwhile to investigate, as it could be posited that a shorter time of concentration, paired with a high correlation between precipitation and streamflow, may be indicative of a well-connected basin capable of delivering sediment with relative efficiency. Underpinning this hypothesis is the notion that a well-connected basin with little attenuation of streamflow from storm to outlet may also offer fewer obstacles for sediment as well. In these cases, strong post-fire SSL magnitudes may be more common.

Future work will focus on the development and application of a more sophisticated sediment routing model, which can explicitly take into account sediment traps and other sub-basin processes that may help or hinder the journey of a sediment particle from a burned area to the outlet.

References

Benavides-Solorio, J., MacDonald, L.H., 2001. Post-fire runoff and erosion from simulated rainfall on small plots, Colorado Front Range. Hydrol. Process. 15, 2931–2952. https://doi.org/10.1002/hyp.383

Blake, W.H., Droppo, I.G., Humphreys, G.S., Doerr, S.H., Shakesby, R.A., Wallbrink, P.J., 2007. Structural characteristics and behaviour of fire-modified soil aggregates. Journal of Geophysical Research 112, F02020.

Blake, W.H., Wallbrink, P.J., Droppo, I.G., 2009. Sediment aggregation and water quality in wildfire-affected river basins. Mar. Freshwater Res. 60, 653–659. https://doi.org/10.1071/MF08068

Box, G. E. P and Jenkins, G.M., (1976). "Time series analysis: Forecasting and control," Holden-Day, San Francisco.

Brunsden, D., Thornes, J.B., 1979. Landscape sensitivity and change. Transactions of the Institute of Geographers, New Series 4, 463 – 484.

Cerdá, A., Doerr, S.H., 2005. Influence of vegetation recovery on soil hydrology and erodibility following fire: an 11-year investigation. International Journal of Wildland Fire 14, 423. https://doi.org/10.1071/WF05044

Emmerich, W.E., Cox, J.R., 1994. Changes in Surface Runoff and Sediment Production after Repeated Rangeland Burns. Soil Science Society of America Journal 58, 199–203. https://doi.org/10.2136/sssaj1994.03615995005800010029x

Falcone, J.A., 2017, U.S. Geological Survey GAGES-II time series data from consistent sources of land use, water use, agriculture, timber activities, dam removals, and other historical anthropogenic influences: U.S. Geological Survey data release, https://doi.org/10.5066/F7HQ3XS4.

Ferguson, H.F., Hamel, J.V., 1981. Valley Stress Relief In Flat-lying Sedimentary Rocks. Presented at the ISRM International Symposium, International Society for Rock Mechanics and Rock Engineering.

Fernández, C., Vega, J.A., Jiménez, E., Fonturbel, T., 2011. Effectiveness of three post-fire treatments at reducing soil erosion in Galicia (NW Spain). Int. J. Wildland Fire 20, 104–114. https://doi.org/10.1071/WF09010

Fryirs, K., 2013. (Dis)Connectivity in catchment sediment cascades: a fresh look at the sediment delivery problem. Earth Surface Processes and Landforms 38, 30–46. https://doi.org/10.1002/esp.3242

Fryirs, K., Brierley, G.J., 2001. Variability in sediment delivery and storage along river courses in Bega catchment, NSW, Australia: implications for geomorphic river recovery. Geomorphology 38, 237–265. https://doi.org/10.1016/S0169-555X(00)00093-3

Gray JR, Simões FJM (2008) Estimating sediment discharge. In: Marcelo G (ed) Sedimentation engineering—processes, measurements, modeling, and practice. American Society of Civil Engineers Manual 110, Appendix D, pp. 1065–1086. http://water.usgs.gov/ osw/techniques/Gray_Simoes.pdf

Hyndman R, Athanasopoulos G, Bergmeir C, Caceres G, Chhay L, O'Hara-Wild M, Petropoulos F, Razbash S, Wang E, Yasmeen F (2019). *forecast: Forecasting functions for time series and linear models*. R package version 8.5, http://pkg.robjhyndman.com/forecast.

Johansen, M.P., Hakonson, T.E., Breshears, D.D., 2001. Post-fire runoff and erosion from rainfall simulation: contrasting forests with shrublands and grasslands. Hydrol. Process. 15, 2953–2965. https://doi.org/10.1002/hyp.384

Jones, K.W., Cannon, J.B., Saavedra, F.A., Kampf, S.K., Addington, R.N., Cheng, A.S., MacDonald, L.H., Wilson, C., Wolk, B., 2017. Return on investment from fuel treatments to reduce severe wildfire and erosion in a watershed investment program in Colorado. Journal of Environmental Management 198, 66–77. https://doi.org/10.1016/j.jenvman.2017.05.023

Knapen, A., Poesen, J., Govers, G., Gyssels, G., Nachtergaele, J., 2007. Resistance of soils to concentrated flow erosion: A review. Earth-Science Reviews 80, 75–109. https://doi.org/10.1016/j.earscirev.2006.08.001

Luis, M.D., González-Hidalgo, J.C., Raventós, J., 2003. Effects of fire and torrential rainfall on erosion in a Mediterranean gorse community. Land Degradation & Development 14, 203–213. https://doi.org/10.1002/ldr.547

Meyer, G.A., Wells, S.G., 1997. Fire-related sedimentation events on alluvial fans, Yellowstone National Park, U.S.A. Journal of Sedimentary Research 67, 776–791. https://doi.org/10.1306/D426863A-2B26-11D7-8648000102C1865D

Momm, H.G., Wells, R.R., Bennett, S.J., 2018. Disaggregating soil erosion processes within an evolving experimental landscape. Earth Surface Processes and Landforms 43, 543–552. https://doi.org/10.1002/esp.4268

Moody, J.A., Martin, D.A., Cannon, S.H., 2008. Post-wildfire erosion response in two geologic terrains in the western USA. Geomorphology 95, 103–118. https://doi.org/10.1016/j.geomorph.2007.05.011

Moody, J.A., Martin, D.A., 2001. Initial hydrologic and geomorphic response following a wildfire in the Colorado Front Range. Earth Surf. Process. Landf. 26, 1049–1070. https://doi.org/10.1002/esp.253

Neary, D.G., Koestner, K.A., Youberg, A., 2011. Hydrologic Impacts of High Severity Wilidfire: Learning from the Past and Preparing for the Future. 24th Annual Symposium of the Arizona Hydrological Society; Watersheds near and far: Response to changes in climate and landscape; September 18-20, 2010; Flagstaff, AZ. 8 p.

Pelletier, J.D., Orem, C.A., 2014. How do sediment yields from post-wildfire debris-laden flows depend on terrain slope, soil burn severity class, and drainage basin area? Insights from airborne-LiDAR change detection. Earth Surface Processes and Landforms 39, 1822–1832. https://doi.org/10.1002/esp.3570

Reneau, S.L., Katzman, D., Kuyumjian, G.A., Lavine, A., Malmon, D.V., 2007. Sediment delivery after a wildfire. Geology 35, 151–154. https://doi.org/10.1130/G23288A.1

Rowe, P. B., Influence of Woodland Chaparral on Water and Soil in Central California, California Department of Natural Resources, Division of Forestry, 70 pp., 1948.

Sankey, J.B., Kreitler, J., Hawbaker, T.J., McVay, J.L., Miller, M.E., Mueller, E.R., Vaillant, N.M., Lowe, S.E., Sankey, T.T., 2017. Climate, wildfire, and erosion ensemble foretells more sediment in western USA watersheds. Geophysical Research Letters 44, 8884–8892. https://doi.org/10.1002/2017GL073979

Shakesby, R.A., Doerr, S.H., 2006. Wildfire as a hydrological and geomorphological agent. Earth-Science Reviews 74, 269–307. https://doi.org/10.1016/j.earscirev.2005.10.006

Smith, H.G., Sheridan, G.J., Lane, P.N.J., Nyman, P., Haydon, S., 2011. Wildfire effects on water quality in forest catchments: A review with implications for water supply. Journal of Hydrology 396, 170–192. https://doi.org/10.1016/j.jhydrol.2010.10.043

Swanson, F J. 1981. Fire and geomorphic processes. Pages 401-420 in Proceedings of the Conference on Fire Regimes and Ecosys- tem Properties. USDA Forest Service Gener- al Technical Report WO-26, Washington, DC.

Thornton, P.E., M.M. Thornton, B.W. Mayer, Y. Wei, R. Devarakonda, R.S. Vose, and R.B. Cook., 2018. Daymet: Daily Surface Weather Data on a 1-km Grid for North America, Version 3. ORNL DAAC, Oak Ridge, Tennessee, USA. https://doi.org/10.3334/ORNLDAAC/1328

Valois, R., Vouillamoz, J.-M., Lun, S., Arnout, L., 2017. Assessment of water resources to support the development of irrigation in northwest Cambodia: a water budget approach. Hydrological Sciences Journal 62, 1840–1855. https://doi.org/10.1080/02626667.2017.1351030

Vieira, D.C.S., Fernández, C., Vega, J.A., Keizer, J.J., 2015. Does soil burn severity affect the post-fire runoff and interrill erosion response? A review based on meta-analysis of field rainfall simulation data. Journal of Hydrology 523, 452–464. https://doi.org/10.1016/j.jhydrol.2015.01.071

Wondzell, S.M., King, J.G., 2003. Postfire erosional processes in the Pacific Northwest and Rocky Mountain regions. Forest Ecology and Management, The Effect of Wildland Fire on Aquatic Ecosystems in the Western USA. 178, 75–87. https://doi.org/10.1016/S0378-1127(03)00054-9

Wildfires in the West: Characterizing Drivers of Post-Disturbance Hydrologic and Sediment Response through Laboratory Analysis

Carli Brucker, MS Student, Department of Civil, Environmental, and Architectural Engineering, University of Colorado Boulder, Boulder, CO, carli.brucker@colorado.edu

Aaron J. Heldmyer, PhD Student, Department of Civil, Environmental, and Architectural Engineering, University of Colorado Boulder, Boulder, CO, aaron.heldmyer@colorado.edu

Ben Livneh, Assistant Professor, Department of Civil, Environmental, and Architectural Engineering and Cooperative Institute in Environmental Sciences, University of Colorado Boulder, Boulder, CO, ben.livneh@colorado.edu

Fernando L. Rosario-Ortiz, Associate Professor, Department of Civil, Environmental, and Architectural Engineering, University of Colorado Boulder, Boulder, CO, fernando.rosario@colorado.edu

J. Toby Minear, Research Faculty, Cooperative Institute in Environmental Sciences, University of Colorado Boulder, Boulder, CO, tminear@colorado.edu

Abstract

Wildfires are a perennial problem across the western U.S. and internationally. By increasing watershed sedimentation rates to 25 times or more above non-wildfire base levels and raising concentrations of dissolved organic matter (DOM), fires create a major challenge for downstream water treatment plants. The overarching goal of this research effort is to test the response of sediment and runoff responses of soils at a range of burn severities, rainfall intensities, and terrain slopes. This paper will focus on the first phase of the project, exploring issues related to building the laboratory rainfall and wildfire simulators, and will discuss issues related to up-scaling of results to representative watershed scales to improve predictions of post-fire suspended sediment in streams.

Here we explore best practices for capturing burn, rainfall, and terrain related processes in the laboratory. The key experimental settings–burn temperature and duration, rainfall nozzle type and intensity–were determined based on published precedents and local historical observational data. Temperatures between 150 and 550°C, 30-minute burn duration, a *FullJet®* nozzle, and a maximum rainfall intensity of 2.5 in/hr were selected. We present synthetic results using a numerical model in order to anticipate how the soils will respond to the above settings to inform the subsequent laboratory testing. We have collected a series of soil samples from a steep mountain catchment with wildfire history: The Cache la Poudre (CLP) Basin near Fort Collins, CO that will form the basis of the laboratory experimentation. Samples will be exposed to burning and rainfall processes under combinations of burn temperature, rainfall intensity, and terrain slope, with differences in runoff sedimentation and DOM exports analyzed across these dimensions. A longer-term goal will be to apply up-scaling techniques of post-fire sedimentation prediction to entire catchments, in an effort to reduce uncertainty relative to either exclusively observational or model driven efforts to date.

1 Introduction

1.1 Post-Wildfire Sedimentation

Wildfires impact water supply and quality primarily by producing a large amount of ash and particulate, as well as increasing the hydrophobicity of soil (Scott & Van Wyk, 1990). This

combination results in increased runoff containing elevated levels of sediment in affected areas. The sediment in post-wildfire runoff poses a challenge for water treatment plants, not only because of the large volume, but also because of an increase in the concentration and reactivity of dissolved organic matter (DOM). DOM is the main substrate for the formation of carcinogenic disinfection byproducts during the water treatment process (Richardson et al., 2007). Therefore, there is a need for accurate predictions of sediment response due to wildfires to aid in treatment planning for these large influxes. Many studies have used observational data and simulation techniques (e.g. Kampf et al. 2016 and Larsen et al. 2009) to quantify the sedimentation response from soils after a wildfire event. However this study is unique in that it will enable a simultaneous evaluation of precipitation intensity, terrain slope, and burn severity on runoff and sediment response. This paper primarily describes construction of a laboratory scale rainfall and wildfire simulators to test sediment response under a range of precipitation intensities, terrain slopes, and burn severities. In addition, a discussion into up-scaling techniques using statistical and process-based approaches is included as a way to make much needed sediment response estimates at the catchment-scale.

According to Doerr et al. (2006) wildfires create a top layer of soil with low water repellency, consisting of combusted vegetation and charred soil, while increasing the water repellency of the soil directly beneath this layer. Post-fire rainfall events transport the loose sediment in the top layer and produce increased runoff, due to the increased water repellency of the lower layers of soil which allow less infiltration. This combination of effects causes a positive feedback in sedimentation rates in post-fire runoff (Benavides-Solorio & MacDonald, 2001).

Moody et al., (2009) report that a large number of field studies have attempted to quantify wildfire-sediment impacts across various regions and under different conditions, yet several key challenges exist with studying post-fire processes in the field. Most importantly, the highly variable conditions within any given catchment makes isolating the sedimentation responses solely from wildfires challenging. Moody et al. (2009) composed a meta-analysis of post-wildfire sedimentation across the western US and categorized basins on the basis of terrain slope and soil erodibility. A lack of correlation between sediment yield and these two factors suggested that other, less measurable factors, such as sediment supply, had a greater impact on the results. This finding underscores the challenges of developing a useful relationship between wildfire and sediment yield based on field measurements alone, in addition to the large time and costs associated with field analysis more broadly (Robichaud, 2005).

1.2 Context of this Study

This study is similar to other laboratory simulation studies that explore the effects of wildfire and rainfall intensity on runoff ratios, sedimentation, soil composition and water repellency, leachate, and other factors, with precise, quantitative results (Larsen et al. 2009, Cancelo-González et al. 2013, Keesstra et al. 2014, Kibet et al. 2014). However, few studies have taken a multivariate approach to the study of post-wildfire sedimentation response, studying multiple influencing factors and their interdependencies (e.g. Larsen et al. 2009). Our study is the first to incorporate specifically terrain slope, burn intensity, and rainfall intensity. When analyzing an area with consistent soil type and vegetation, these three variables cause the greatest amount of variability in sediment production (Yochum & Norman, 2015), suggesting that analyzing their variability simultaneously will offer key insights into the underlying processes and process interactions.

By using rainfall and burn simulation techniques in a controlled setting with laboratory-scale experiment, the impact on sedimentation from each variable–terrain slope, rainfall intensity, and burn intensity–in different combinations will give us a clearer understanding of how they affect sediment production towards the broader understanding of which characteristics make a

catchment most susceptible to increased sediment yield. The rest of this paper will detail the design processes and methods put into creating this comprehensive experiment, results, and future work.

2 Methods

2.1 Site Description

The study area is the CLP basin in the Arapahoe and Roosevelt National Forest near Fort Collins, CO. Draining 1915 mi^2 (4,960 km^2) above the canyon mouth west of Fort Collins, this watershed produces approximately 274,000 ac-ft (338 x 10^6 m^3) of water per year (Coalition for the Poudre River Watershed, n.d.). It supplies most of the water for Fort Collins and other nearby cities: Greenley, Timnath, and Windsor.

The CLP Basin has a wide range of topographic relief, vegetation, and soil types. According to the USDA Cache la Poudre Rapid Assessment (2009), the vegetation in the mountainous area of the CLP is mostly categorized as forest and rangeland, containing a wide array of grasses and pine and spruce trees. The geology of the area is comprised mostly of several types of gneisses and granitic rocks, topped with rich topsoil promoting abundant vegetation growth. The river itself is 126 miles long, stretching from the Rocky Mountain range past Fort Collins where it turns into a meandering river, finally culminating near Greenly where it joins the South Platte River (Columbia Gazetteer, 2000). The CLP Basin is primarily under the jurisdiction of the National Forest Services, the National Parks Services, and privately owned land (USDA, 2009).

Figure 1. The Cache la Poudre Basin overlain with the outline of the High Park fire.

In 2012, a wildfire affected 85,000 acres (34,498 ha) of the CLP (USDA, 2017). The High Park Fire, started from a lightning strike on June 9, 2012 (City of Fort Collins, n.d.), destroyed 259 homes, displaced hundreds of residents, and resulted in one fatality before it was contained on July 1. Most of the CLP basin was burned at a moderate-high severity (Kampf et al., 2016). In addition to the damage done to homes and property, High Park had severe implications for the city's water treatment plant. The large amounts of sediment produced by the wildfire inundated the water treatment plant, transported by the runoff from the basin. The plant responded by

increasing environmental monitoring, using multiple water supplies, and constructing a pre-sedimentation basin to continue delivering high-quality drinking water to its customers (Writer, 2014).

To simulate the effects of the High Park fire, soil samples for the laboratory experiments were taken from the CLP basin, near the edge of the burned area to obtain samples that are unburned, but have a similar soil composition. The samples were taken from a flat plot of land under tall, grassy vegetation. The soil was somewhat moist and black, rich with nutrients. There were very few rocks in the soil, making excavation less challenging. Sedimentation, chemical composition and runoff data collected in the CLP following the High Park Fire (Cotrufo et al. 2016, Kampf et al. 2016) will provide benchmark numbers to validate the results of this study.

2.2 Experimental Design

The major design elements in this study are of the rainfall and burn simulator structures, nozzle selection, burn method, sample tilting mechanism, and a subsequent runoff and infiltration collection system. The design of the rainfall simulator structure (Figure 2) was based on the protocol developed by Kibet et al. (2014), with a few alterations. A steel frame 91" tall was created, with a nozzle affixed to the top with a pressure meter, pressure gauge, flow meter and ball valve installed inline. The specifications of the simulator are more explicitly shown in the drawings in Figure 3.

Figure 2. Rainfall simulator created for a laboratory setting.
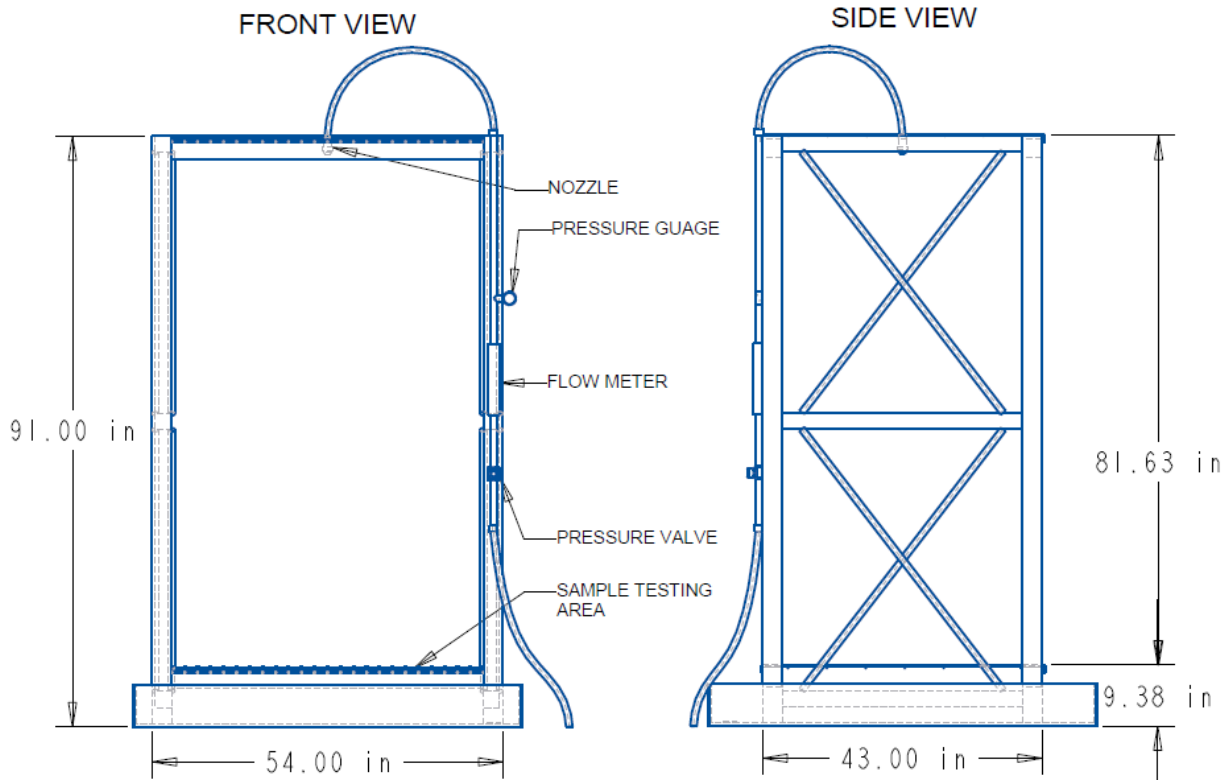
Figure 3. CAD drawing profiles of rainfall simulator.

Droplet size and kinetic energy, rainfall intensity, and rainfall distribution were all considered when designing the rainfall simulator. Natural rainfall droplets range in size from 0.5 mm to 4 mm (Perlman, n.d.), which was emulated by choosing a nozzle type rated to produce a natural rainfall at a specific pressure: the *FullJet®* nozzles, the same type as used by Kibet et al. (2014). Each size can accurately produce only a short range of rainfall intensities, thus four sizes—HH-4.3W, HH-8W, HH-17WSQ, and HH-20W—were purchased to achieve the full range of desired intensities. Target rainfall intensity rates were determined by analyzing historical rainfall data from the area of interest, the CLP basin, using a National Oceanic and Atmospheric (NOAA) Precipitation-Duration-Frequency database (NOAA, 2005). The minimum and maximum intensity for the simulator were chosen as the 2-year and 100-year rainfall events, 0.76 – 2.5 in/hr (1.93 – 6.35 cm/hr), respectively. A series of tests were performed to determine the relationship between the pressure of the water in the system and rainfall intensity, confirming that the target intensities range are achievable by the rainfall simulator. Similarly, the distribution of the rainfall was tested to identify a configuration that produces a relatively uniform intensity spatial distribution.

A temperature-based burn severity scale was chosen, where moderate to severe wildfires range in temperature from 200°C to 400°C, respectively (Chander et al., 1983), and where mild fires rarely exceed 200°C (Jian et al. 2018). A wider range of temperatures, 150°C to 550°C, were chosen to fully encompass the soil property-altering effects of fire. A simulator with eight 375W heat lamps will be used to achieve this desired range of temperatures, similar to the heating method described in Cancelo-González et al. (2012). The surface vegetation and organic matter within the soil will combust in the process, creating ashy particulate as the basis of the sediment. The temperature distribution through the depth of the soil will be measured with thermocouples inserted into the side of each sample. The apparati will be attached to a cart so the simulation can occur safely outside.

Soil sampling has been done toward the goal of collecting undisturbed, whole soil samples to the extent possible for laboratory experimentation to be representative of natural conditions. Sturdy sample collection containers were created from 4 x 12" (10.16 x 30.48 cm) steel tubing with ¼" thick walls, cut into 4" (10.16 cm) segments (Figure 4a). This material was selected due to its resistance to high temperatures and rigid structure to hold the shape and structure of the samples. Holes drilled in the side of the samples allow for thermocouples to track the soil temperature in the burn simulation.

Lastly, once the soil samples have been collected and subject to burning and rainfall, collection of runoff and infiltration from soil samples in the simulator required creation of custom funnels (Figure 4b) which separately collect the infiltration and runoff water through separate outlets that are diverted to individual 10 oz. bottles. These collection funnels will be situated in a gridded tilting mechanism which will simulate various terrain slopes in the rainfall simulator. The contents of the bottles will be analyzed for sediment concentration and composition.
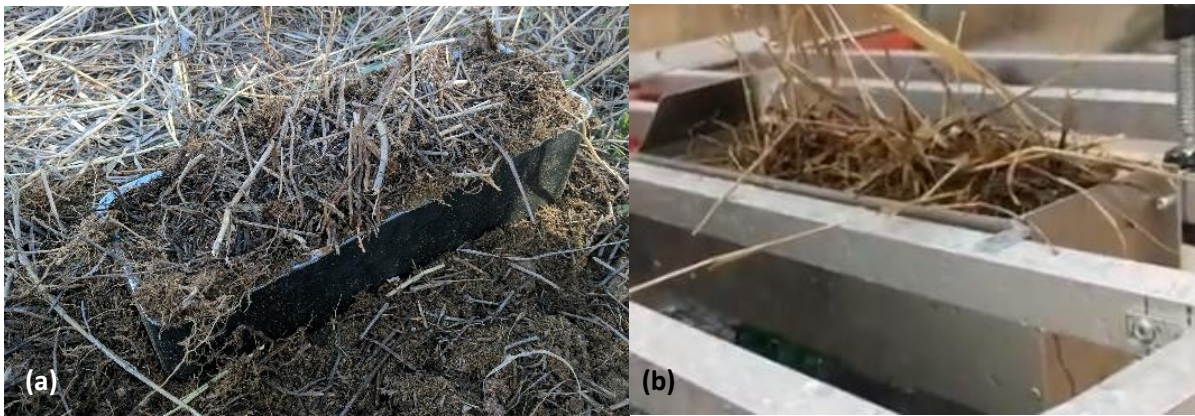
Figure 4. Soil sample in steel container (a) and custom funnel (b) created for collection rainfall infiltration and runoff from the soil samples, which are inserted inside, inserted in tilting mechanism.

2.3 Experimental Procedure

The first step in the simulation process is the selection of a location for soil sample collection. To ensure consistency in soil type, all samples were taken over a small footprint, a ¼ acre (0.101 ha) plot of land. Care was taken to obtain uniform and non-compromised soil structure following the method of the USDA NRCS South Dakota (2017). First, a rectangular outline slightly larger than the sample containers is dug into the plot of land with a spade, about 4" deep. Next, that rectangular piece of sod is gently lifted from the ground, trimming the vegetation roots connecting it to the ground, and placing the sample on top of a collection container. The edges of the sample are trimmed down with a hand saw to fit the form of the container, then pressed down gently until it is flush with the top and bottom of the sample container. This is repeated with enough samples to provide significant data points for the experiment.

Table 1 lists the experimental burn temperatures, precipitation intensities, and slopes. Samples are first placed in the burn simulator and burned to a certain temperature following the method used by Cancelo-González et al. (2012)—the heat applied just until the surface reaches the desired temperature, then turned off. Three thermocouples are placed into the sides of the samples at varying depths to track the temperature gradient throughout the soil.

Table 1. The range of experimental values for each variable.

Variable	Testing Values
Burn Temperature	100°C, 300°C, and 550°C
Precipitation Intensity	0.76 in/hr, 1.69 in/hr, and 2.50 in/hr
Terrain Slope	5°, 15°, 25°, 35°, and 45°

The burned and cooled samples are then placed in the rainfall simulator, to be run at varying rainfall intensities, with samples tilted at an angle reflective of terrain slope. The burned samples are tested in 1-hr runs in the rainfall simulator at all combinations of these variables. Testing of unburned samples provides an experimental control. Rain gauges placed in between the samples serve as references for the amount of rain applied to the samples, i.e. the rainfall intensity.

Runoff and infiltration waters flow into different sample bottles replaced at 10 minute intervals after samples are saturated, to capture the temporal change in sedimentation rates. Once the simulation is complete, the water-sediment solutions are run through a narrowly graded fiberglass filter to separate the sediment from water. Substrates are weighed to determine the ratio of sediment to liquid in the runoff and infiltration waters. The contents of the sediment are analyzed for the amount of dissolved organic material (DOM), total organic carbon (TOC), and grain size distribution through sieve analysis.

2.4 Synthetic Experiments

To complement the laboratory experiment, synthetic simulations of sediment rates and water fluxes in the samples were generated. Synthetic sediment data was generated via the Revised Universal Soil Loss Equation (RUSLE), chosen because it has the potential to incorporate the key dimensions of this study: burn-severity, slope, and rainfall intensity. RUSLE incorporates 6 soil and precipitation factors into its erosion estimate: the rainfall-runoff erosivity factor (R), the soil erodibility factor (K), the slope length factor (L), the slope steepness factor (S), the cover-management factor (C), and the support practice factor (P). These variables come together to form the following equation (Renard et al. 1997, Yochum et al. 2015):

$$A = R \; x \; K \; x \; L \; x \; S \; x \; C \; x \; P \qquad (1)$$

Where A is the estimated average soil loss in tons ac^{-1} yr^{-1}.

Terrain slope is represented in the L and S variables, the equations for which are below:

$$L = \left(\frac{\lambda}{22.13}\right)^m \qquad (1a)$$

$$m = \left(\frac{\beta}{1+\beta}\right) \qquad (1b)$$

$$\beta = \frac{\frac{\sin\theta}{0.0896}}{3(\sin\theta)^{0.8}+0.56} \qquad (1c)$$

$$S = 3(sin\theta)^{0.8} + 0.56 \qquad (1d)$$

Where λ is the horizontal slope length (m), m is the variable slope-length exponent, β is the mean slope angle, and θ is the slope angle (degrees).

Rainfall intensity is represented in the R variable, the equation for which is below:

$$R = \sum EI_{30} \tag{1e}$$

Where E is the energy for an individual storm (MJ ha^{-1}) and I_{30} is the maximum 30-minute rainfall intensity (mm hr^{-1}). R is the sum of the product of these two variables for every rainfall event in a year. For the purposes of our predictions, only the EI_{30} number for individual rainfall events is needed, which was calculated using an equation formulated by data collected in Wilson et al (2018):

$$y = 4.3654x - 6.1333 \tag{2}$$

Where y is EI_{30} (MJ ha^{-1} mm hr^{-1}) and x is total precipitation from a 30-minute storm event (mm). The rest of the variables in the RUSLE equation are constants determined by soil and vegetation properties. P is equal to 1 as no crop support practices are used in the majority of the CLP basin (Millward et al. 1999).

Though it was not originally intended for post-wildfire prediction, several studies have created alterations to the equation for this purpose. Yochum et al. (2015) used empirical data to derive multipliers for the soil erodibility factor, K, which reflect the effect of mild, moderate, and severe wildfires on soil permeability: 1.5, 1.75, and 2.0, respectively. Similarly, Miller et al. (2003) calculated cover-management factors, C, representative of the effects of mild, moderate, and severe fires on vegetation cover: 0.01, 0.05, and 0.2, respectively. These two studies used both of these modified RUSLE factors in their post-fire sedimentation calculations to represent the effect wildfires have on both soil erodability and vegetation cover. Therefore, using these equations and modified variables, RUSLE generated a synthetic sedimentation simulation following experimental values of terrain slope, rainfall intensity, and wildfire severity.

To generate synthetic runoff and infiltration rates in the soil samples, the modeling software HYDRUS 1D was used. Inputs reflecting actual experiment conditions were used to create the simulation: 4" (10.16 cm) soil samples comprised of sandy loam—a soil type common in the sampling area (Web Soil Survey, n.d.). A range of terrain slopes and rainfall intensities were then simulated using this setup. The effects of wildfires on the runoff and infiltration rates in the samples will be modelled by altering the hydraulic conductivity of the soil to reflect increased hydrophobicity, similar to the RUSLE simulations.

3 Results

3.1 Simulator Testing Results

The first project phase is complete—design and construction of the laboratory-scale rainfall simulator, but only partial construction of the burn simulator—so this section will focus primarily on the rainfall simulator testing. Intensity testing was performed to evaluate the simulator capability to consistently produce the minimum and maximum desired rainfall intensities, a 2-year and 100-year rainfall event: $0.76 - 2.5$ in/hr ($1.93 - 6.35$ cm/hr), respectively. A total of 12 configurations were tested: the four nozzle sizes at three different system pressures, the pressure the nozzle is rated to plus 2 psi higher and 2 psi lower. The trials show that the higher and lower pressures can vary the rainfall intensity produced, but the rated pressure produces the least amount of variance in rainfall intensity through time (Figure 5).
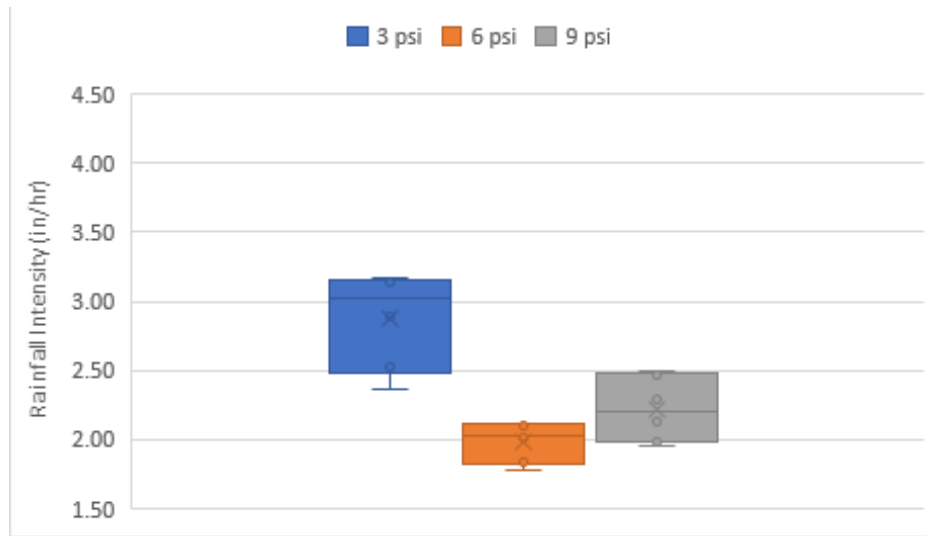
Figure 5. Example box-and-whisker plot of rainfall intensities at various pressures for the HH-17WSQ nozzle.

Rainfall distribution tests to evaluate spatial uniformity in the rainfall were also completed using the same configurations and recording the distribution by taking measurements from 6 graduated cylinders placed in the bottom of the simulator. These tests showed that the smaller nozzles, rated to produce a lower rainfall intensity, have a much more evenly distributed rainfall intensity than the larger nozzles (Figure 6).
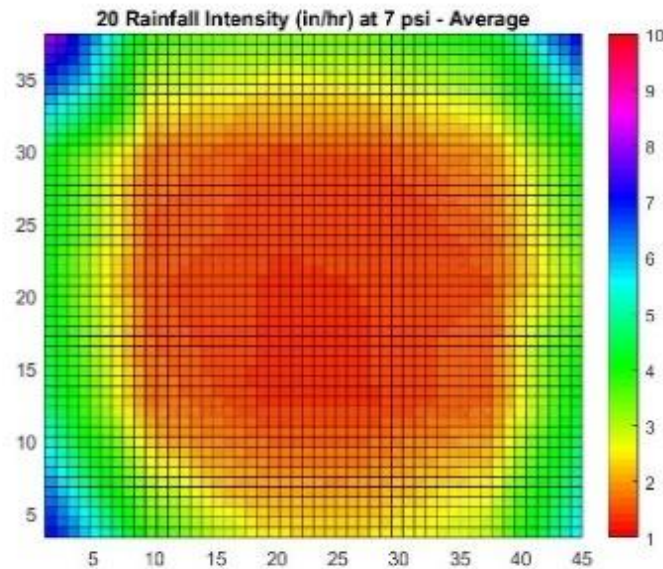
Figure 6. Example of distribution of rainfall in simulator at 7 psi averaged across measurement from 6 graduated cylinders, using the HH-20W size nozzle.

However, even the smaller nozzles produced a slight radial pattern in intensity distribution, indicating the importance of sample placement in the simulator to ensure desired intensities are reached. Overall, the nozzles had the most even distribution at their rated pressures, so these pressures were selected as the optimal operating pressures.

3.2 Synthetic Data Analyses

The RUSLE equation was applied to generate synthetic simulation data to provide insight into expected sedimentation response and for later comparison with laboratory scale results. With the altered *K* and *C* values to reflect the effects of wildfires (Yochum et al. 2013, Miller et al. 2003), sedimentation production was estimated for the same combinations of variables as will be done in the laboratory experiment. Figure 7 shows the RUSLE sedimentation rates for the variable combinations after a mild, moderate, and severe burn.
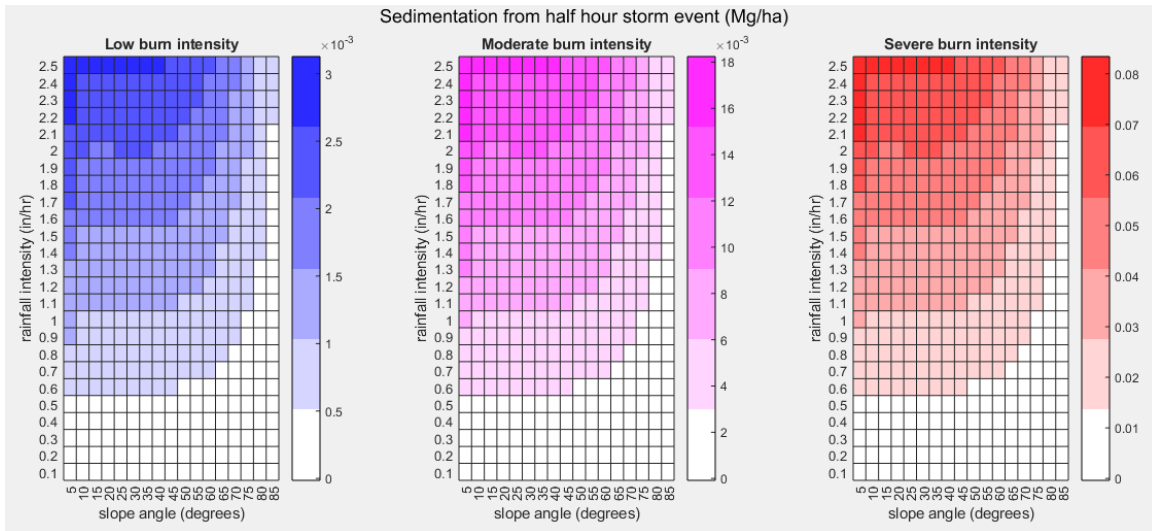
Figure 7. Sedimentation estimations by RUSLE for a (left) low, (center) moderate, and (right) severe burn intensity. Note the different labels on the color bar, indicating much larger sediment responses with increasing burn severity.

As expected, sedimentation varies monotonically in response to rainfall intensity, whereas it shows a sinusoidal relationship with slope angle. This is because the slope-dependent Equation 1c has the slope term in both the numerator and denominator. A key observation from these plots is that the largest increase in sedimentation relative to other factors results from increases in burn severity, due to increases in the *C* and *K* factors for each level of severity. This result is consistent with published findings (Benavides-Solorio et al. 2001) that report sedimentation increases more than 25 times.

To model the runoff and infiltration from the individual samples, a HYDRUS 1D model was implemented at a range of rainfall intensities and terrain slopes. Drainage from the bottom of the samples was modeled in addition to runoff and infiltration, since these targets for collection from the rainfall simulator (Figure 8). As expected, increasing the terrain slope produces increased runoff, and decreased drainage. The results show that at maximum rainfall intensity, runoff will start after 12 minutes and drainage after 24 minutes. These estimates will inform the design of the rainfall sampling protocols.
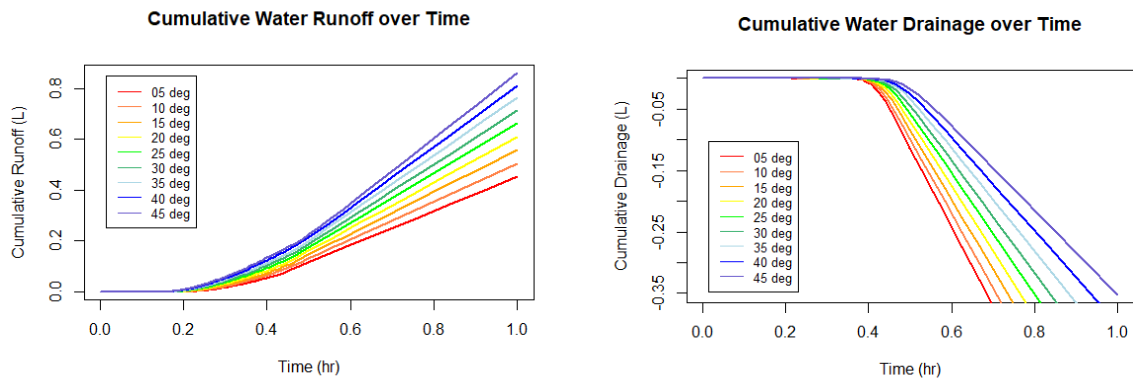
Figure 8. Simulated cumulative runoff (left) and cumulative drainage (right) from a single soil sample, produced from maximum rainfall intensity, 2.5 in/hr (6.35 cm/hr), where soil samples are at a range of terrain slopes.

4 Discussion

4.1 Future Work

The first phase of this project, the creation of a laboratory-scale rainfall simulator, has been completed, including a tilting mechanism to simulate varying terrain slopes and a system that collects and separates runoff and infiltration. Intensity and distribution test results show that the simulator is capable of emulating natural precipitation at the desired target intensity. The burn simulator structure and methods have been designed, and construction is underway. RUSLE results provided a synthetic simulation of the relationship between key variables and sediment response, and HYDRUS 1D provided predictions of runoff and infiltration. The next steps for this project are finishing the construction and testing of the rest of the equipment, then collecting additional soil samples, testing them in the burn and rainfall simulators, and finally analyzing the runoff and infiltration produced from the experiments.

Once sedimentation response has been analyzed across all variable combinations a broad goal is to up-scale these responses to entire basins. Each of these combinations of conditions can be associated with representative hillslopes within a given catchment to predict net sedimentation response. This concept was used by Yochum et al. (2015) to create a catchment-scale model of post-fire flood hazards. Notably, our study will use laboratory data instead of field data to inform the up-scaling.

This up-scaling analysis can be achieved in two different ways, using statistical analysis or applying a physically-based hydrologic model. A statistical model (regression, categorical, etc.) relating the three variables with sedimentation response can be up-scaled on the basis of the distribution of these three variables across a given catchment. Similarly, the parameters of an existing physically-based model (e.g. HSPF) of sedimentation response can be calibrated to the laboratory data and then applied to a given catchment.

Several studies exist forming a general relationship between the High Park Fire and its impact on the sedimentation in the CLP River, which will be compared to the net sedimentation prediction formed by the laboratory-scale experiment and subsequent up-scaling (Cotrufo et al. 2016, Kampf et al. 2016). In addition, the RUSLE analysis will be used to compare the sedimentation response due to each combination of the three variables to that observed in the

experimental analysis, determining whether the experimental data follows the same variable-dependent trends as RUSLE.

4.2 Uncertainty Analysis

Key sources of uncertainty in this analysis arise from the sampling process, as well as the instruments used to measure rainfall, the liquid/solute ratio in the runoff and infiltration, chemical composition and particle size distribution of the sediment. The largest source of uncertainty for the future analysis will come from assumptions needed to upscale the sediment response from the soil samples to the basin scale, as the length of hillslope in a sedimentation calculation greatly effects the results. Importantly, we expect that the sedimentation rate for an entire basin will be smaller than for a smaller segment of the basin, due to sediment trapping and deposition along the route to the catchment outlet (Le Bissonnais et al., 1998). To this end, an extra factor for length scaling will be implemented to account for up-scaling effects and sediment trapping.

5 Conclusion

The purpose of this study was to build a framework capable of addressing key knowledge gaps into the impacts of wildfires on sedimentation responses at catchment scales. This information will be valuable to water treatment planning efforts to anticipate the influx of sediment in water sources originating from catchments stricken by wildfire.

The post-wildfire sedimentation predictions from the models created in this experiment will be unique relative to extant research to date, most notably by simultaneously analyzing multiple sedimentation controls in a consistent framework. These results are expected to highlight the relationship between terrain slope, rainfall intensity, and burn severity and their effects on sediment production and chemical composition. In addition, the rainfall simulator and burn simulator will have the capacity to be used for future experiments, together or independently.

5 References

Adapting the RUSLE to model soil erosion potential in a mountainous tropical watershed - ScienceDirect [WWW Document], n.d. URL https://www.sciencedirect.com/science/article/pii/S0341816299000673 (accessed 3.24.19).

Benavides-Solorio, J., MacDonald, L.H., 2001. Post-fire runoff and erosion from simulated rainfall on small plots, Colorado Front Range. Hydrological Processes 15, 2931–2952. https://doi.org/10.1002/hyp.383

Cache la Poudre River. The Columbia Gazetteer of North America. 2000 [WWW Document], 2008. URL https://web.archive.org/web/20080830064047/http:/www.bartleby.com/69/15/C00215.html (accessed 3.24.19).

Cancelo-González, J., Barros, N., Rial-Rivas, M.E., Díaz-Fierros, F., 2012. Assessment of the impact of soil heating on soil cations using the degree-hours method . Spanish Journal of Soil Science 2. https://doi.org/10.3232/SJSS.2012.V2.N3.04

Cancelo-González, J., Rial-Rivas, M.E., Díaz-Fierros, F., 2013. Effects of fire on cation content in water: a laboratory simulation study. Int. J. Wildland Fire 22, 667–680. https://doi.org/10.1071/WF12178

Chandler, C., Cheney, P., Thomas, P., Trabaud, L., Williams, D., 1983. Fire in forestry. Volume 1. Forest fire behavior and effects. Volume 2. Forest fire management and organization. Fire in forestry. Volume 1. Forest fire behavior and effects. Volume 2. Forest fire management and organization.

Cotrufo, M.F., Boot, C.M., Kampf, S., Nelson, P.A., Brogan, D.J., Covino, T., Haddix, M.L., MacDonald, L.H., Rathburn, S., Ryan-Bukett, S., Schmeer, S., Hall, E., 2016. Redistribution of pyrogenic carbon from hillslopes to stream corridors following a large montane wildfire. Global Biogeochemical Cycles 30, 1348–1355. https://doi.org/10.1002/2016GB005467

Doerr, S.H., Shakesby, R.A., Blake, W.H., Chafer, C.J., Humphreys, G.S., Wallbrink, P.J., 2006. Effects of differing wildfire severities on soil wettability and implications for hydrological response. Journal of Hydrology 319, 295–311. https://doi.org/10.1016/j.jhydrol.2005.06.038

Foster, G.R., McCool, D.K., Renard, K.G., Moldenhauer, W.C., 1981. Conversion of the universal soil loss equation to SI metric units. Journal of Soil and Water Conservation 36, 355–359.

High Park Fire || High Park Fire [WWW Document], n.d. URL https://www.fcgov.com/highparkfire/ (accessed 3.24.19).

Jian, M., Berli, M., Ghezzehei, T.A., 2018. Soil Structural Degradation During Low-Severity Burns. Geophysical Research Letters 45, 5553–5561. https://doi.org/10.1029/2018GL078053

Kampf, S.K., Brogan, D.J., Schmeer, S., MacDonald, L.H., Nelson, P.A., 2016. How do geomorphic effects of rainfall vary with storm type and spatial scale in a post-fire landscape? Geomorphology 273, 39–51. https://doi.org/10.1016/j.geomorph.2016.08.001

Keesstra, S.D., Maroulis, J., Argaman, E., Voogt, A., Wittenberg, L., 2014. Effects of controlled fire on hydrology and erosion under simulated rainfall. Cuadernos de Investigación Geográfica 40, 269–294. https://doi.org/10.18172/cig.2532

Kibet, L.C., Saporito, L.S., Allen, A.L., May, E.B., Kleinman, P.J.A., Hashem, F.M., Bryant, R.B., 2014. A Protocol for Conducting Rainfall Simulation to Study Soil Runoff. J Vis Exp. https://doi.org/10.3791/51664

Larsen, I.J., MacDonald, L.H., 2007. Predicting postfire sediment yields at the hillslope scale: Testing RUSLE and Disturbed WEPP. Water Resources Research 43. https://doi.org/10.1029/2006WR005560

Larsen, I.J., MacDonald, L.H., Brown, E., Rough, D., Welsh, M.J., Pietraszek, J.H., Libohova, Z., de Dios Benavides-Solorio, J., Schaffrath, K., 2009. Causes of Post-Fire Runoff and Erosion: Water Repellency, Cover, or Soil Sealing? Soil Science Society of America Journal 73, 1393–1407. https://doi.org/10.2136/sssaj2007.0432

Le Bissonnais, Y., Benkhadra, H., Chaplot, V., Fox, D., King, D., Daroussin, J., 1998. Crusting, runoff and sheet erosion on silty loamy soils at various scales and upscaling from m2 to small catchments. Soil and Tillage Research 46, 69–80. https://doi.org/10.1016/S0167-1987(98)80109-8

Learn from the burn: The High Park Fire 5 years later, 2017. 18.

Miller, J.D., Nyhan, J.W., Yool, S.R., 2003. Modeling potential erosion due to the Cerro Grande Fire with a GIS-based implementation of the Revised Universal Soil Loss Equation. Int. J. Wildland Fire 12, 85–100. https://doi.org/10.1071/wf02017

Moody, J.A., Martin, D.A., 2009. Synthesis of sediment yields after wildland fire in different rainfall regimes in the western United States. Int. J. Wildland Fire 18, 96–115. https://doi.org/10.1071/WF07162

Perlman, H., Why raindrops are different sizes [WWW Document], n.d. URL https://water.usgs.gov/edu/raindropsizes.html (accessed 3.24.19).

PF Map: Contiguous US [WWW Document], n.d. URL https://hdsc.nws.noaa.gov/hdsc/pfds/pfds_map_cont.html?bkmrk=co (accessed 3.24.19).

Renard, K.G., USA, USA (Eds.), 1997. Predicting soil erosion by water: a guide to conservation planning with the revised universal soil loss equation (RUSLE), Agriculture handbook. Washington, D. C.

Richardson, S.D., Plewa, M.J., Wagner, E.D., Schoeny, R., DeMarini, D.M., 2007. Occurrence, genotoxicity, and carcinogenicity of regulated and emerging disinfection by-products in drinking water: A review and roadmap for research. Mutation Research/Reviews in Mutation Research, The Sources and Potential Hazards of Mutagens in Complex Environmental Matrices - Part II 636, 178–242. https://doi.org/10.1016/j.mrrev.2007.09.001

Robichaud, P.R., 2005. Measurement of post-fire hillslope erosion to evaluate and model rehabilitation treatment effectiveness and recovery. Int. J. Wildland Fire 14, 475–485. https://doi.org/10.1071/WF05031

Scott, D.F., Van Wyk, D.B., 1990. The effects of wildfire on soil wettability and hydrological behaviour of an afforested catchment. Journal of Hydrology 121, 239–256. https://doi.org/10.1016/0022-1694(90)90234-O

Stoof, C.R., De Kort, A., Bishop, T.F.A., Moore, D., Wesseling, J.G., Ritsema, C.J., 2011. How Rock Fragments and Moisture Affect Soil Temperatures during Fire. Soil Science Society of America Journal 75, 1133–1143. https://doi.org/10.2136/sssaj2010.0322

USDA, 2009. Cache la Poudre Rapid Assessment. https://www.nrcs.usda.gov/Internet/FSE_DOCUMENTS/nrcs144p2_061967.pdf

USDA, 2017. Learn from the Burn: The High Park Fire 5 Years Later. Science You Can Use Bulletin, (25). https://www.fs.fed.us/rm/pubs_journals/2017/rmrs_2017_miller_s003.pdf

USDA NRCS South Dakota, 2017. Rainfall Simulator: How to Properly Collect and Store Large Soil Samples.

USDA Web Soil Survey [WWW Document], n.d. URL https://websoilsurvey.sc.egov.usda.gov/App/WebSoilSurvey.aspx (accessed 4.20.19).

Wilson, C., Kampf, S.K., Wagenbrenner, J.W., MacDonald, L.H., 2018. Rainfall thresholds for post-fire runoff and sediment delivery from plot to watershed scales. Forest Ecology and Management 430, 346–356. https://doi.org/10.1016/j.foreco.2018.08.025

Writer, J.H., Hohner, A., Oropeza, J., Schmidt, A., Cawley, K.M., Rosario-Ortiz, F.L., 2014. Water treatment implications after the High Park Wildfire, Colorado. Journal - American Water Works Association 106, E189–E199. https://doi.org/10.5942/jawwa.2014.106.0055

Yochum, S.E., Norman, J.B., 2015. Wildfire-Induced Flooding and Erosion Potential Modeling: Examples from Colorado, 2012 and 2013. Unpublished. https://doi.org/10.13140/rg.2.1.4422.1923

Computer Modeling Session

Demonstration of the Automated Geospatial Watershed Assessment (AGWA) Tool

I. Shea Burns, Senior Research Specialist, Univ. of Arizona, Tucson Arizona,
shea.burns@ars.usda.gov
David C. Goodrich, Research Hydraulic Engineer, USDA-ARS, Tucson, Arizona,
dave.goodrich@ars.usda.gov
D. Phillip Guertin, Professor, Univ. of Arizona, Tucson, AZ, dpg@email.arizona.edu
Yoganand Korgaonkar, Graduate Student, University of Arizona, Tucson, AZ,
yoganandk@email.arizona.edu
Ben Olimpio, Graduate Student, University of Arizona, Tucson, AZ,
bolimpio@email.arizona.edu
Jane Patel, GIS Analyst, Tucson Water, Tucson, AZ, jane.patel@tucsonaz.gov
Carl Unkrich, Hydrologist, USDA-ARS, Tucson, AZ, carl.unkrich@ars.usda.gov

Extended Abstract

The Automated Geospatial Watershed Assessment (AGWA) tool is hydrological modeling tool designed to facilitate the setup and execution of a suite of hydrologic and erosion models (RHEM, KINEROS2, and SWAT). Leveraging GIS in ESRI ArcMap, AGWA uses geospatial data layers including a digital elevation model (DEM), polygon soils data, and classified, raster-based land cover data to delineate watersheds, discretize them into model elements, and parameterize the model elements as part of model setup. Precipitation inputs for the model are then prepared using AGWA, followed by writing of model input files and execution of the model. After model execution, AGWA can import model results for visualization and analysis in the GIS. For a more detailed description of AGWA and KINEROS2, including their histories, see Goodrich et al. (2019, these proceedings; 2015; 2010) and their respective websites (www.tucson.ars.ag.gov/agwa and www.tucson.ars.ag.gov/kineros). This poster and computer demonstration illustrates a sampling of the wide range of applications that are possible using the KINEROS2 - AGWA suite of modeling tools. Applications include:

- Core functionality including watershed delineation, discretization, parameterization, model execution, and results visualization (Figure 1);
- The Land Cover Modification Tool (LCMT), which allows users to simulate hydrologic effects of land cover change;
- Group watershed delineation, which allows users to delineate all watersheds within and draining a defined polygon boundary/area of interest (political, management, administrative, etc.);
- The Burn Severity Tool, which supports post-wildfire watershed assessment by using a burn severity map to adjust saturated hydraulic conductivity and hydraulic roughness as a function of burn severity and pre-burn land cover. See Guertin et al. (2019);
- The AGWA Urban Tool, which provides the capability to model urban hydrology at the lot level, including green infrastructure practices, using the KINEROS2 urban element;
- The Military Disturbance Tool, which is used to simulate on-site and downstream effects on runoff and erosion resulting from military training activities. See Levick et al. (2019);
- The Storage Characterization Tool, which uses high resolution DEM data to locate, characterize, and associate storage features (e.g. stock ponds, detention basins, etc.) and

their discharge characteristics with watershed discretizations in AGWA. See Guertin et al. (2019);

- The Riparian Buffer Tool, which is used to insert riparian buffer strips into an existing KINEROS2 discretization in AGWA, and simulate their effects;

- The Cross-Section Extraction Tool, which uses high resolution DEM data to characterize irregular channel cross-sections and insert them into KINEROS2 parameter files in lieu of channel width and side slope parameters for improved model representation of channel geometries;

- A real-time flash flood forecast version of KINEROS2, which ingests radar data or alert rain gauge data in near real-time or historical/archive modes;

- Use of dynamic erosion formulations of the RHEM (Rangeland Hydrology and Erosion Model) model;
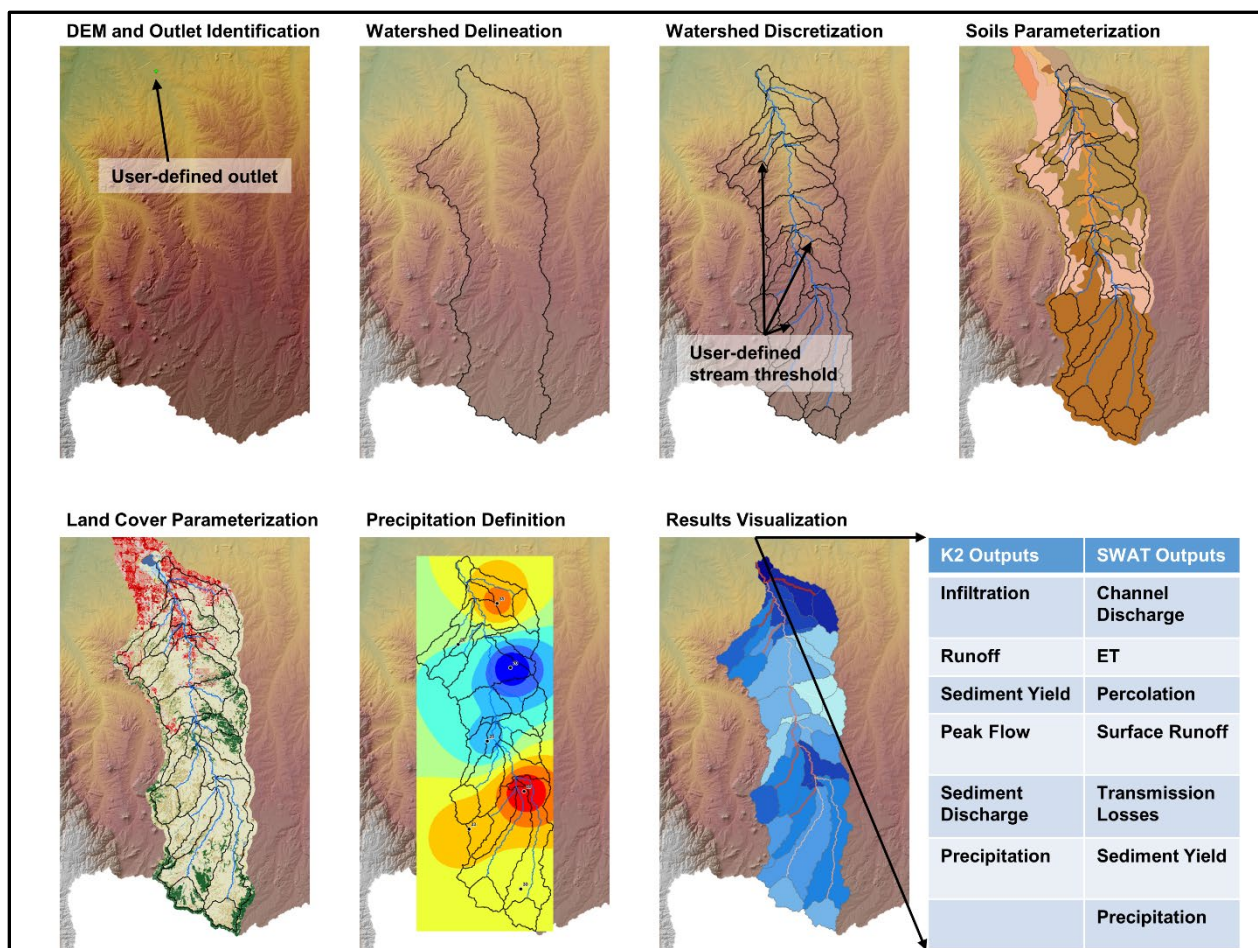
Figure 1. The required steps and core functionality in AGWA that are used to perform a watershed assessment. A DEM is used to delineate the watershed and subdivide it into model elements (i.e. hillslopes and channels for K2 and subwatersheds and channels for SWAT). The model elements are parameterized based on the DEM, soils, and land cover layers. The precipitation input is then selected from various sources. After the model is executed, the results are imported and visualized in the GIS.

References

Goodrich, D.C., Unkrich, C.L., Smith, R.E., Woolhiser, D.A., Guertin, D.P., Hernandez, M., Burns, S., Massart, J., Levick, L., Miller, S., Semmens, D., Keefer, T., Kepner, W., Nearing, M., Heilman, P., Wei, H., Paige, G., Schaffner, M., Yatheendradas, S., Gupta, H., Wagener, T., Troch, P., Brookshire, D., Guber, A.K., Pachepsky, Y.A., Boyd, J. 2010. The AGWA-KINEROS2 suite of modeling tools in the context of watershed services valuation. Proc. 2nd Joint Federal Interagency Conference, Las Vegas, NV, June 27 - July 1, 2010, 12 p. http://acwi.gov/sos/pubs/2ndJFIC/.

Goodrich, D.C., Unkrich, C.L., Korgaonkar, Y., Burns, S., Kennedy, J., Sidman, G., Sheppard, B.S., Hernandez, M., Guertin, D.P., Miller, S.N., Kepner, W., Heilman, P., Nearing, M. 2015. The KINEROS2-AGWA suite of modeling tools, Proc. of the 3rd Joint Federal Interagency Conference on Sedimentation and Hydrologic Modeling, April 19-23, 2015, Reno, Nevada, USA, p. 1759-1770. https://acwi.gov/sos/pubs/3rdJFIC/Proceedings.pdf.

Goodrich, D.C., Guertin, D.P, Burns, I.S., Unkrich, C.L., Levick, L., Korgaonkar, Y., Heilman, P., Hernandez, H., Olimpio, B., Wei, H., Patel, J., Kautz, M. 2019. The KINEROS2-AGWA suite of modeling tools, Proc. 2019 SEDHYD Conf., Reno, Nevada, June 24-28, 2019.

Guertin, D.P. Goodrich, D.C., I.S. Burns, Sidman, G., Sheppard, B.S., Patel, J., Clifford, T.J. Unkrich, C., Levick, L., 2019. Assessing the hydrological and erosional effects of wildland fire. Proc. 2019 SEDHYD Conf., Reno, Nevada, June 24-28, 2019.

Guertin, D.P., Patel, J., Levick, L., Wei, H., Goodrich, D.C., Burns, I.S., Unkrich, C. 2019. The impact of small ponds on streamflow response and sediment yield. Proc. 2019 SEDHYD Conf., Reno, Nevada, June 24-28, 2019.

Levick, L.R., Wei, H., Burns, I.S., Guertin, D.P., Goodrich, D.C., 2019. Military disturbance tool in the Automated Geospatial Watershed Assessment (AGWA) tool for management of military lands. Proc. 2019 SEDHYD Conf., Reno, Nevada, June 24-28, 2019.

Exploring Surface Processes Using the Community Surface Dynamics Modeling System Modeling Tools

Jordan Adams, Postdoctoral Research Associate, The Institute of Arctic and Alpine Research, University of Colorado, Boulder, CO, jordan.adams@colorado.edu
Irina Overeem, Associate Professor, Department of Geological Sciences, University of Colorado, Boulder, CO, irina.overeem@colorado.edu
Eric Hutton, Chief Software Engineer, Community Surface Dynamics Modeling System, University of Colorado, Boulder, CO, eric.hutton@colorado.edu
Gregory Tucker, Professor, Department of Geological Sciences, University of Colorado, Boulder, CO, gtucker@colorado.edu
Albert Kettner, Research Scientist II, The Institute of Arctic and Alpine Research, University of Colorado, Boulder, CO, albert.kettner@gmail.com

Extended Abstract

Hydrological and sediment transport processes operate over a range of temporal and spatial scales. Flood events can cause catastrophic erosion rates over short timescales, reshaping floodplains and catchments in hours or over days. Over longer timeframes, from decades to millennia, the cumulative effect of these erosional events sculpt watershed morphologies, driving changes in drainage area, density and relief. The feedbacks between hydrologic events and sediment transport can shape areas as small as millimeter-scale hillslope rills or as large as continental-scale river basins.

The unpredictable or unobservable nature of flood events makes it difficult to study the interaction between hydrologic and sedimentological proccesses. The stochastic nature of floods make it challenging to predict when an event will occur and how to best measure erosional and depositional changes. Morphological responses to climate change occur on timescales too long to make meaningful observations. Moreover, at many relevant natural hazard scales, hydrology and sediment transport are entangled with ecosystem and human dynamics, complex interactions that are even less understood.

Improved understanding, and ultimately, improved resiliency in the face of hydrologically-driven Earth surface change, require computational models that bridge boundaries and link process mechanics. Many hydrological models exist and have a variety of uses: forecasting floods or water resource availability (e.g. WRF-Hydro, Gochis et al., 2018); channel and floodplain engineering (e.g. HEC-RAS, Brunner, 2016) or groundwater resource assessment (SWAT, USDA ARS Grassland Soil and Water Research Laboratory, 2018). As computational resources become more efficient, more researchers are adding numerical modeling skills to their repertoire. Yet, as more models are built, questions remain: can the surface processes community work together to share these ever-improving tools? Is there a way to standardize both existing and new modeling components so that they can be coupled flexibly and effectively?

The Community Surface Dynamics Modeling System (CSDMS) is a NSF-funded initiative that supports the open software efforts of the surface processes community. CSDMS sets modeling standards and protocols, hosts a Model Repository to distribute models and modeling tools, and provides cyberinfrastructure to an interdisciplinary set of community members. The CSDMS Repository contains over 200 tools and models that simulate lithosphere, hydrosphere, atmosphere or cryosphere dynamics. The goal of CSDMS is simple: to expedite scientific discovery and eliminate duplication of effort by sharing computational resources.

As part of these efforts, CSDMS has designed a new tool for hypothesis-driven modeling; the CSDMS Python Modeling Tool (PyMT) provides a unified framework that allows users to interactively run and couple numerical models written in a variety of programming languages. These coupled models can operate on disparate time and space scales, which are then resolved by PyMT. Principally, the PyMT is three things: (1) a collection of Earth-surface models wrapped with a common interface, (2) an extensible plug-in framework into which new models can be incorporated, and (3) tools for coupling models that operate on a variety of spatial grids and time steps.

Currently, the PyMT model collection consists of several dozen Earth-surface models that cover a variety of process domains that range from land, to coast, to ocean. Each of these models were contributed by CSDMS community members to the CSDMS Model Repository as standalone models. There was no initial intent for these models to be part of a larger framework. The heterogeneity of the collection is represented not just in the variety of programming languages but also by idiosyncratic user interfaces (e.g. model specific input and output file formats).

All models within the PyMT collection are wrapped in a single, unified, interface within the Python programming language. An overriding tenet of the PyMT is: *if you know how to use one pymt model, you know how to use all pymt models*. The PyMT model interface allows users to interactively run models within a Python kernel such that they can advance models through time while dynamically changing their state variables. This allows users to become model composers by orchestrating different model functionality within a script, while being able to leverage the power of the Python programming language and its powerful collection of third-party packages (e.g. numpy, scipy, matplotlib, xarray, dask).

The PyMT provides an extensible plugin framework that allows additional models to be easily incorporated into the PyMT framework. This allows new models, written by domain experts, to become PyMT models usable by a broad community in potentially novel ways. To be incorporated into PyMT, new models must be written to expose a Basic Model Interface (BMI). At its core, the BMI is simply a specification that defines the necessary functions a model must provide to make it coupleable. These functions control how a model is initialized, updates through time, as well as how a model provides its output variables or ingests externally provided input variables. The CSDMS modeling stack additionally provides tools for automatically wrapping models written in several programming languages (currently C, C++, Fortran, and Python) into PyMT. These four languages cover a significant majority of the models in the CSDMS Model Repository.

The PyMT contains a collection of tools useful for model coupling (either model-to-model or model-to-data coupling). As mentioned previously, the CSDMS Model Repository is a heterogeneous collection of models that were not necessarily written with the intent of coupling to other models. As such, a significant obstacle when coupling models is transferring values from one model's solution grid to another. Included with the PyMT are a set of grid mappers, based on the Earth System Modeling Framework (ESMF) grid mapping library. This allows for efficient mapping of values between large grids. Other coupling tools include:

- Unit conversion utilities, which conform to the cfunits conventions, when models provide the same values but with different units,
- Time interpolators that estimate state variables between model timesteps,
- Output writers that write model output to standardized netCDF files that conform to the UGRID/SGRID specifications

PyMT is designed to expedite the process of exploring ideas, testing hypotheses, and comparing models with data, and make Earth-surface process models more accessible.

For proof of concept, we present an example of a coupled hydrodynamic and bedrock incision model in PyMT. This work uses two components from the Landlab model, OverlandFlow and DetachmentLtdErosion, as they are implemented in PyMT (Adams et. al, 2017; Hobley et al., 2017). The OverlandFlow component was originally developed to bridge the gap between fully hydrodynamic models used to model single hydrograph events and simplified 'steady-state' hydrology components used in long-term fluvial geomorphology models. Figure 1 illustrates the difference between these two model types: 'steady-state' models often simplify rainfall and runoff into steady, constant values that drive steady, constant incision rates (Figure 1a), while non-steady models can take rainfall stochasticity into account and drive individual event hydrographs and changing incision rates through time (Figure 1b). As computational efficiency and speed have improved over the last decade, more efforts have been made to bring hydrodynamics into models of landscape evolution. The Landlab OverlandFlow model is an open-source tool designed to achieve that goal.
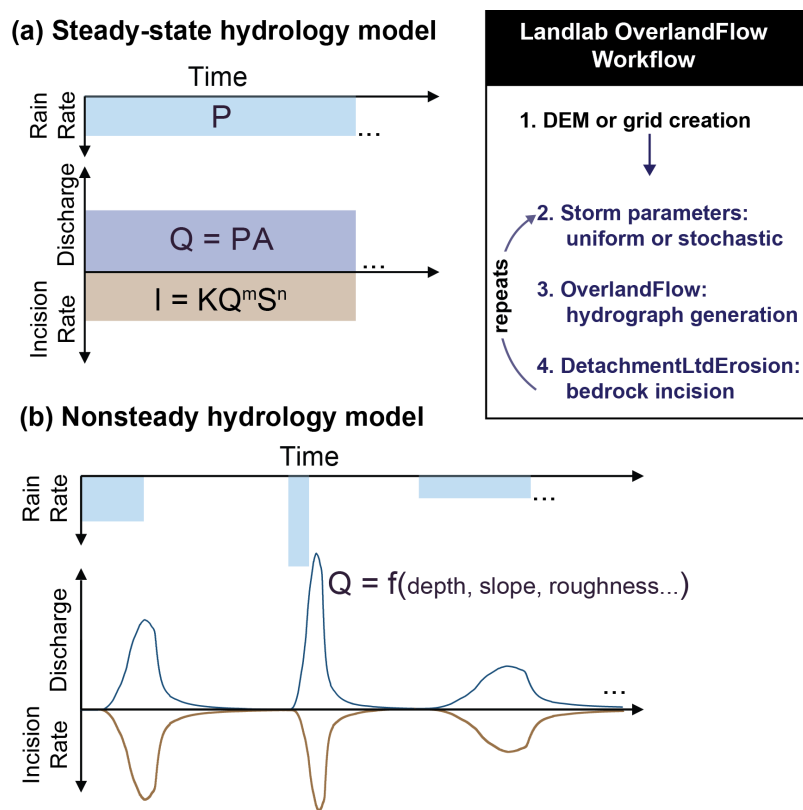
Figure 1. Comparison of steady (**a**) and nonsteady (**b**) hydrology models. The latter case illustrates how the OverlandFlow model is implemented. A sample OverlandFlow workflow is also shown.

In this presentation, we run several test cases in PyMT to illustrate landscape sensitivity to rainfall parameters, hydrograph shape and basin orientation. These results are compared against traditional steady-state model results. Landscapes eroded and evolved using nonsteady methods are characterized by greater relief and increased channel concavities when compared to steady results, suggesting that hydrodynamics should be considered when studying the impact of bedrock river incision on topographic evolution over long timescales.

The implementation of OverlandFlow and DetachmentLtdErosion is just one example of coupled hydrology-sedimentology modeling available through PyMT. This presentation will

provide detailed background on how models can be brought into the PyMT framework, how PyMT resolves grid and temporal differences across models, the existing hydrologic and sedimentologic tools in PyMT, and examples of model output from the OverlandFlow and DetachmentLtdErosion models.

References

Adams, J.M., Gasparini, N.M., Hobley, D.E., Tucker, G.E., Hutton, E., Nudurupati, S.S. and Istanbulluoglu, E., 2017. The Landlab v1.0 OverlandFlow component: a Python tool for computing shallow-water flow across watersheds. Geoscientific Model Development, 10(4).

Brunner, G. W. (2016). HEC-RAS river analysis system 2D modeling user's manual. US Army Corps of Engineers—Hydrologic Engineering Center, 1-171.

Gochis, D.J., M. Barlage, A. Dugger, K. FitzGerald, L. Karsten, M. McAllister, J. McCreight, J. Mills, A. RafieeiNasab, L. Read, K. Sampson, D. Yates, W. Yu, 2018. The WRF-Hydro modeling system technical description, (Version 5.0). NCAR Technical Note. 107 pages. DOI:10.5065/D6J38RBJ

Hobley, D.E., Adams, J.M., Nudurupati, S.S., Hutton, E.W., Gasparini, N.M., Istanbulluoglu, E. and Tucker, G.E., 2017. Creative computing with Landlab: an open-source toolkit for building, coupling, and exploring two-dimensional numerical models of Earth-surface dynamics. Earth Surface Dynamics, 5(1), p.21.

USDA ARS Grassland Soil and Water Research Laboratory; Texas A&M AgriLife Research, 2018. SWAT - Soil and Water Assessment Tool. USDA Agricultural Research Service; Texas A&M AgriLife Research. https://data.nal.usda.gov/dataset/swat-soil-and-water-assessment-tool

Physically-Based Hydrologic Modeling of Clear Creek Watershed

Marcela Politano, Research Engineer, IIHR – Hydroscience & Engineering, The University of Iowa, Iowa City, IA, marcela-politano@uiowa.edu

Antonio Arenas Amado, Ass. Research Engineer, IIHR – Hydroscience & Engineering, The University of Iowa, Iowa City, IA, antonio-arenas@uiowa.edu

Maral Razmand, PhD student, IIHR – Hydroscience & Engineering, The University of Iowa, Iowa City, IA, maral-razmand@uiowa.edu

Yong Lai, Hydraulic Engineer, Technical Service Center, U.S. Bureau of Reclamation, Denver, CO, ylai@usbr.gov

Larry Weber, Professor, IIHR – Hydroscience & Engineering, The University of Iowa, Iowa City, IA, larry-weber@uiowa.edu

Abstract

The Clear Creek Watershed covers about 270 km^2 with three headwater streams converging in Iowa Township. The watershed comprises 60% of agriculture, 23% pasture and other grasslands, 10% forest, and 7% urban areas. The hydrologic dynamic response of the Clear Creek Watershed was numerically simulated with the Generic Hydrologic Overland-Subsurface Toolkit (GHOST). GHOST includes specific models to properly predict water budgets for multi-year simulations in large basins. The numerical model takes into account interception, throughfall, infiltration, recharge, evapotranspiration, and infiltration, enabling discharge through the surface or subsurface into downstream water bodies or aquifers. The model considers the spatial distribution of land use and soil type. The model was calibrated and validated using 15 years of hourly climatological data with 4-km spatial resolution. Model results indicate that the model capture the watershed's hydrology and can be used to evaluate potential flood mitigation strategies.

Introduction

Devastating flooding caused by heavy rains brought economic, social, and environmental impacts in many watersheds across Iowa, USA. From 2011–2013, Iowa suffered eight Presidential Disaster Declarations, encompassing more than 70% of the state.

In Iowa's flood history, the events of 1993 and 2008 are on an entirely different scale than the others. These two events stand out from the rest when looking at the extent of the area impacted, recovery costs, precipitation amounts, and stream flows recorded (Bradley 2010; Smith et al., 2013). Figure 1 shows the extent of the flooding during the flood events of 1993 and 2008. In both years, flooding impacted the Clear Creek watersheds.

A hydrological model for the Clear Creek watershed was developed to better understand the hydrological response of the watershed and evaluate the potential impact of alternative flood mitigation strategies in the watershed. This paper presents model details of the hydrological model GHOST as well as calibration and validation against monitoring data from 2002 to 2017. A new watershed model SRH-W is under development, SRH-W will use several modules of

GHOST but the runoff engine is to be an implicit unstructured polygonal mesh. Efforts to model Clear Creek with SRH-W and preliminary results comparing both codes will be presented and discussed in the conference.
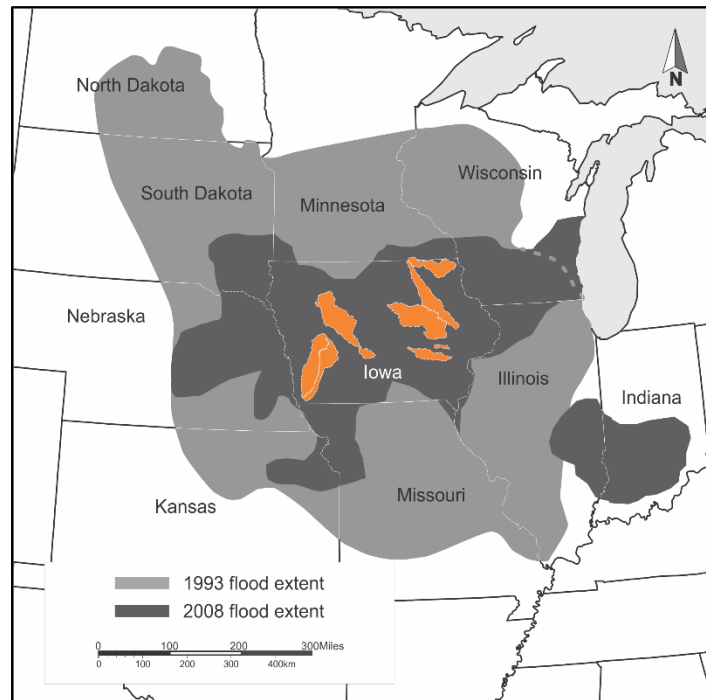

Figure 1. The extent of the flooding during the 1993 and 2008 floods (Bradley, 2010)

Hydrologic Model

The Generic Hydrologic Overland-Subsurface Toolkit (GHOST) is an integrated model able to represent the hydrologic response at watershed scale over time periods on the order of decades. GHOST is a physically-based model, based on physical laws and empirical correlations, that can be used for a wide range of applications and beyond the range of calibration. The model was developed to simulate watersheds ranging in area from 500 to 1,500 square miles, explicitly resolving Iowa's varied topography, soils, and land use.

GHOST is based on the open source hydrologic code MM-PIHM (Qu and Duffy 2007, Yu et al. 2013), which was developed to simulate fully coupled surface and subsurface water systems to predict streamflow and groundwater recharge for normal and extreme rainfall and snowmelt events. The watershed is conceptualized in three distinct zones: a surface region and two regions beneath the surface representing the unsaturated soil and groundwater (Kumar et al. 2009). The surface model consists of 2D overland flow and a 1D stream network. Overland flow is modeled using the diffusive wave approximation of 2D St. Venant equations. Channel flow is modeled using a 1D approach to properly capture the channel geometry and effect of flood mitigation structures without local grid refinement along the network. Water movement in the unsaturated zone is assumed to be vertical and the saturated groundwater region is modeled using the 2D Dupuit approximation.

Additional models were developed and incorporated into MM-PIHM to properly predict water budgets for long-term simulations in large-scale watersheds. Model development focused on improving efficiency while guaranteeing mass conservation. Figure 2 shows hydrological processes modeled in GHOST. The model uses meteorological data and vegetation characteristics to compute evaporation and plant transpiration. The form of precipitation, rain or snow, is determined by temperature. At above freezing temperature, accumulated snow melts contributing to net precipitation. The canopy can intercept rain, which then evaporates from the canopy or can reach the ground surface by canopy drip. Water from net precipitation at the ground surface can infiltrate to the unsaturated region or contribute to surface runoff. Infiltrated water can evaporate from the soil surface, be transpired by plants, or drain to the groundwater. Water stored in the groundwater can evaporate or discharge to a stream.
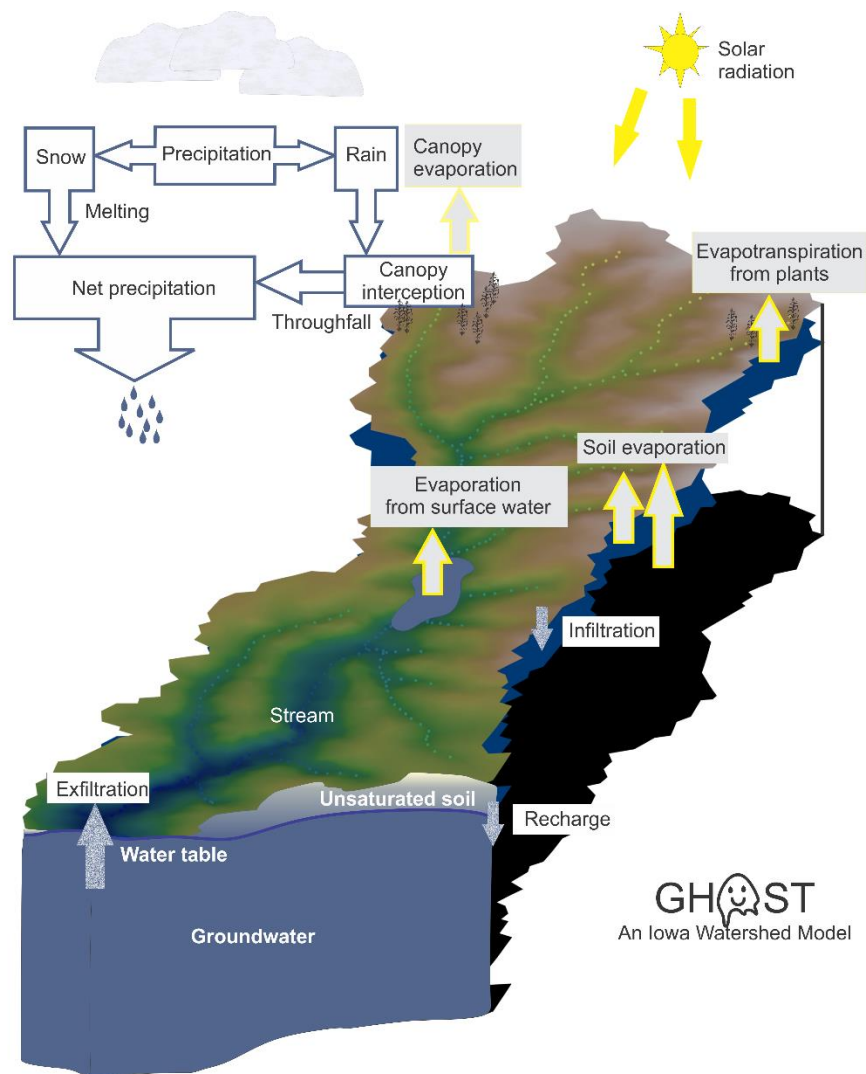
Figure 2. Schematic representation of GHOST

A finite-volume formulation is used to discretize the system of coupled equations. The ground surface of the watershed is discretized using a Delaunay triangulation and the subsurface is represented by vertical projection of each triangular element. Figure 3 shows variables and fluxes in the control volume i.
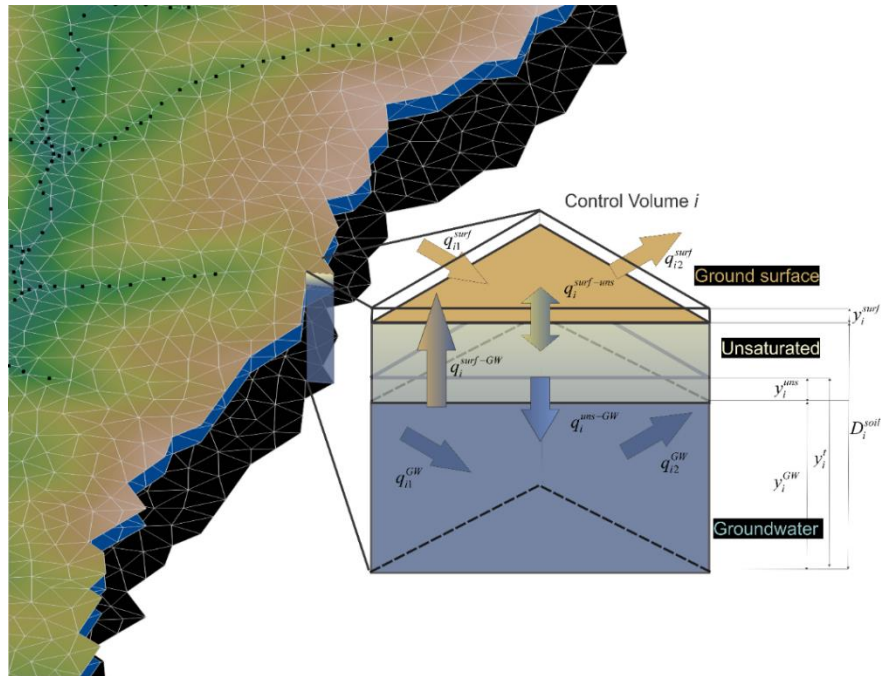
Figure 3. Numerical discretization

The resulting ordinary differential equation system is solved with using the library CVODE of SUNDIALS (SUite of Nonlinear and DIfferential/ALgebraic Equation Solvers) developed by Lawrence Livermore National Laboratory (Hindmarsh & Serban, 2016). The Backward Differentiation Formulas (BDFs) with Newton iterations recommended for stiffs problems are used in GHOST. A scaled preconditioned GMRES (Generalized Minimal Residual method) solver is used for the solution of the linear system within the Newton corrections.

The new watershed scale model SRH-W is an event based physically-based and distributed model for runoff and soil erosion simulation. Application targets include flood prediction and sediment delivery to streams and reservoirs caused by a large precipitation event. The code uses a finite-volume discretization method, explicit and implicit schemes, and diffusive wave routing equation.

Evapotranspiration

Interception and evapotranspiration are modeled following Panday and Huyakorn (2004). Available energy is first used to evaporate water intercepted by plant canopy and then surface water. If not depleted, available energy is used for soil evaporation and plant evapotranspiration.

Coupling between Regions

The driving force required for net mass flux from a 2D surface element i to the subsurface is modeled as:

$$\Delta h_i = \left[y_i^{surf} - max(y_i^t - D_i^{soil}, 0) \right] - \psi_i \tag{1}$$

Where y_i^{surf} is the water depth at the ground surface, y_i^t the total head in the soil, D_i^{soil} is the soil depth and ψ_i represents capillary head, which can be modeled following van Genuchten (1980).

Mass flux from the surface to the unsaturated region is modeled as:

$$q_i^{surf-uns} = \begin{cases} Z_i^{surf} \Gamma_i & \text{if } \Delta h_i > 0 \text{ (infiltration)} \\[2mm] \begin{cases} \dfrac{y_i^{uns}}{y_i^t} \Gamma_i & \text{if } |\Gamma_i^{uns}| < |\Gamma_i| \\[2mm] \Gamma_i & \text{if } |\Gamma_i^{uns}| > |\Gamma_i| \end{cases} & \text{if } \Delta h_i < 0 \text{ (exfiltration)} \end{cases} \tag{2}$$

where $\Gamma_i = \frac{k_i^v}{l_i^{exch}} \Delta h_i (1 + \delta_{ik} f_{ik})$ is the maximum mass flux, with k_i^v the vertical hydraulic conductivity and l_i^{exch} the coupling length. f_{ik} takes into account the area occupied by the channel and $\delta_{ik} \begin{cases} 1 & \text{if stream } k \text{ contiguos to element } i \\ 0 & \text{otherwise} \end{cases}$. Z_i^{surf} is a sigmoid function to reduce infiltration when ponded water is comparable to the depression storage. The model assumes preferential exfiltration from the unsaturated soil if water is available at that region. If the rate of water depletion in the unsaturated region is smaller than the maximum flux, exfiltration from the groundwater occurs and the flux from the unsaturated zone is proportional to the ratio of head in that region to total head in the soil.

Exfiltration or flux from the groundwater to the surface is:

$$q_i^{GW-surf} = -min\left(\Gamma_i - q_i^{surf-uns}, 0 \right) \tag{3}$$

Recharge or mass flux from the unsaturated region to groundwater is modeled as:

$$q_i^{uns-GW} = max\left(\left(\frac{s_{ni}^m}{s_{ni}^m + s_n^{*m}} \right) q_i^{surf-uns}, 0 \right) \tag{4}$$

Following Panday and Huyakorn (2004), the flux from the overland element i to the stream segment k is modeled using the equation for a broad crested weir:

$$q_{ik}^{surf-chan} \begin{cases} \dfrac{2}{3} \dfrac{C_i^d \sqrt{2|g|} L_{ik} \left(Y^{ups} - Y^{down}\right)^{3/2}}{sign\left((y_i^{ele} + z_i^{ele}) - (y_k^{chan} + z_k^{chan})\right)} & \text{if} & \dfrac{\left(Y^{down} - Y_i^{weir}\right)}{\left(Y^{ups} - Y_i^{weir}\right)} \qquad (5) \\[2em] \dfrac{2}{3} \dfrac{C_i^d \sqrt{2|g|} L_{ik} \left(Y^{ups} - Y^{down}\right)^{3/2}}{sign\left((y_i^{ele} + z_i^{ele}) - (y_k^{chan} + z_k^{chan})\right)} \left(\dfrac{\left(Y^{ups} - Y^{down}\right)}{\left(Y^{ups} - Y_i^{weir}\right)}\right)^{1/2} & \text{if} & \dfrac{\left(Y^{down} - Y_i^{weir}\right)}{\left(Y^{ups} - Y_i^{weir}\right)} \end{cases}$$

where upstream and downstream heads are:

$$\begin{cases} Y^{ups} = y_i^{surf} + z_i^{elem}; Y^{down} = y_k^{chan} + z_k^{chan} & \text{if} & y_i^{surf} + z_i^{elem} > y_k^{chan} + z_k^{chan} \\ Y^{ups} = y_k^{chan} + z_k^{chan}; Y^{down} = y_i^{surf} + z_i^{elem} & \text{if} & y_i^{surf} + z_i^{elem} < y_k^{chan} + z_k^{chan} \end{cases} \qquad (6)$$

It is assumed that $q_{ik}^{surf-chan} = 0$ if $Y^{ups} < Y_i^{weir}$. Figure 4 shows variable definition. $Y_i^{weir} = Z_i^{weir} + z_i^{elem}$ is the weir head with weir coefficient and weir elevation, C_i^d and Z_i^{weir}, model parameters.
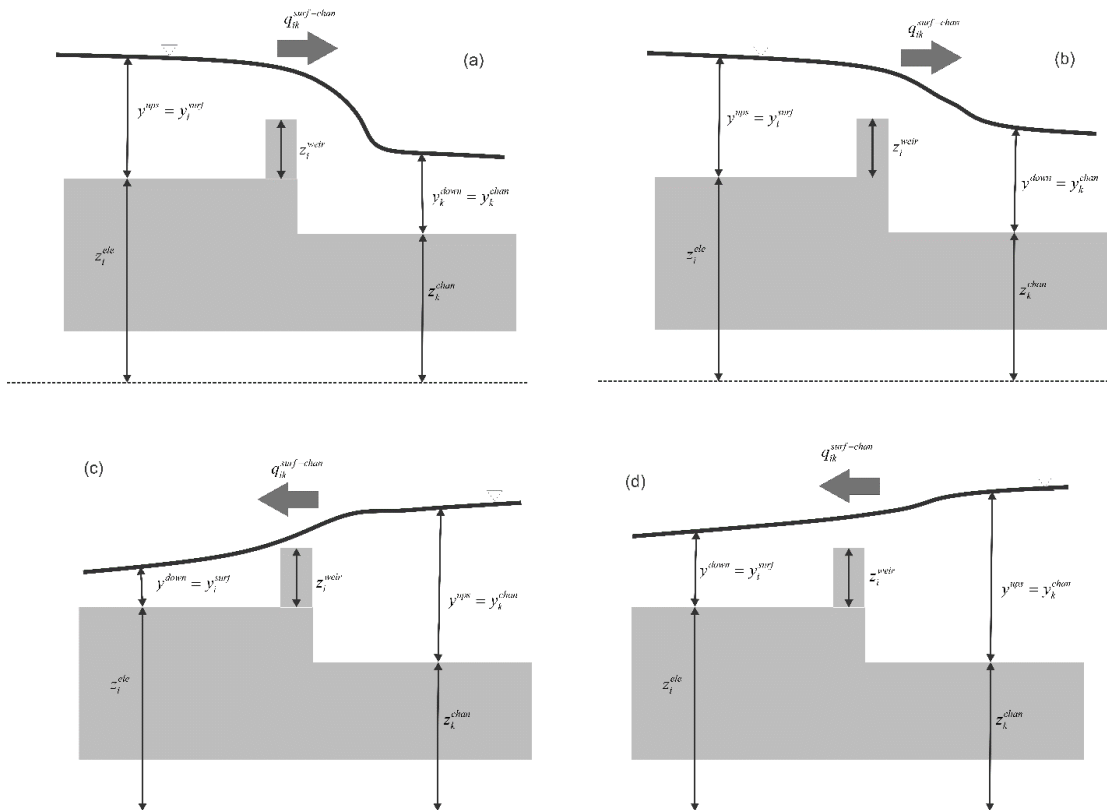
Figure 4. Schematic representation of coupling between 2D surface elements and channel. (a) and (c) free-flow conditions and (b) and (d) submerged-flow

Clear Creek Watershed

Hydrology

The Clear Creek Watershed (Figure 5), as defined by the boundary of ten-digit Hydrologic Unit Code (HUC10) 0708020904, is located in East-Central Iowa and encompasses approximately 104 square miles (mi2). Clear Creek flows west to east into the Iowa River at Coralville, Iowa. The Clear Creek Watershed boundary falls within two counties; Iowa and Johnson counties. For the region of East-Central Iowa, the annual precipitation ranges from roughly 21 to 55 inches. About 70% of the annual precipitation falls as rain during the months of April - September. During this period, thunderstorms capable of producing torrential rains are possible with the peak frequency of such storms occurring in June. The region has experienced increased variability in annual precipitation since 1975, along with a general increase in the amount of spring rainfall. Analyses of streamflow records at the USGS stations near Oxford and Coralville show that on an annual basis approximately 30% of the precipitation is transformed into streamflow and 60% of the streamflow is derived from groundwater.
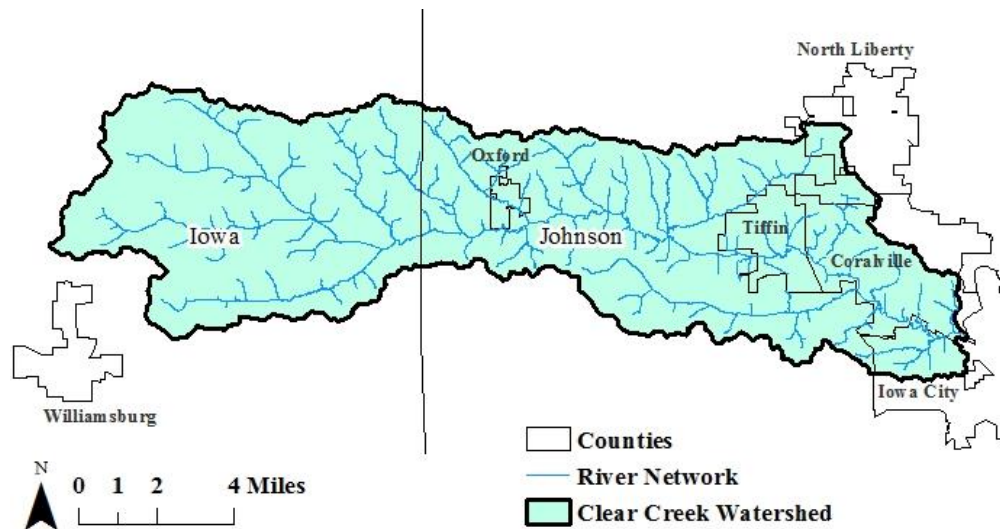
Figure 5. The Clear Creek Watershed

Topography

Figure 6 shows the topography of the Clear Creek Watershed. Elevations range from approximately 900 feet above sea level in the upstream and western part of the watershed to 500 feet above sea level in the downstream portion of the watershed in Coralville.
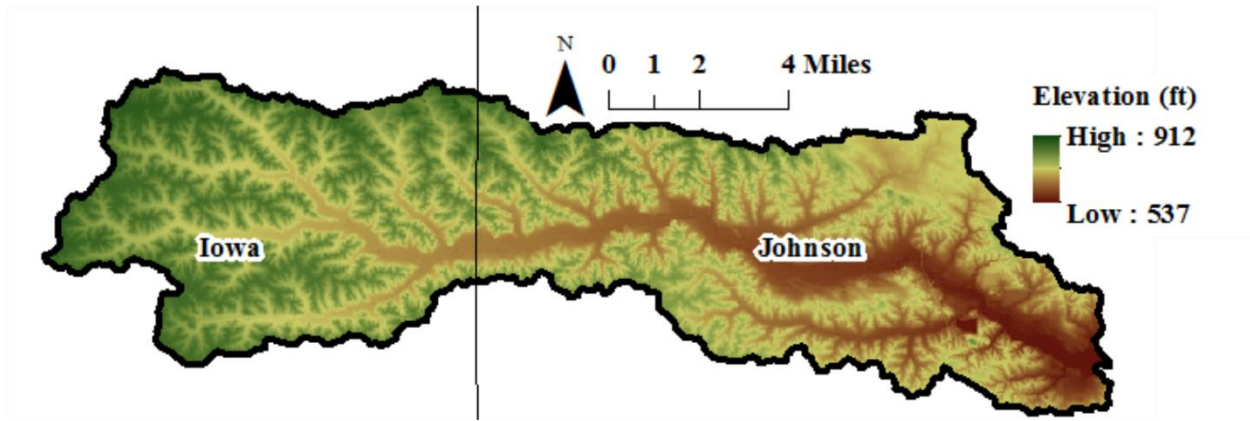
Figure 6. Topography of the Clear Creek Watershed

Forcing Data

Stage IV radar rainfall estimates were used as the precipitation input for the simulations. The Stage IV data set is produced by the National Center for Environmental Prediction by taking radar rainfall estimates produced by the 12 National Weather Service (NWS) River Forecast Centers across the Continental United States and combining them into a nationwide 4 km x 4 km (Figure 7) gridded hourly precipitation estimate data set. These data are available from January 1, 2002 – Current. Use of radar rainfall estimates provides increased accuracy of the spatial and time distribution of precipitation over the watershed and Stage IV estimates provide a level of manual quality control performed by the NWS that incorporates available rain gage measurements into the rainfall estimates. Other meteorological data such as air temperature, relative humidity, wind speed, shortwave/longwave radiation and surface pressure were obtained from North American Land Data Assimilation System Phase 2 (NLDAS-2) products. The temporal resolution of all the forcing data used was hourly.
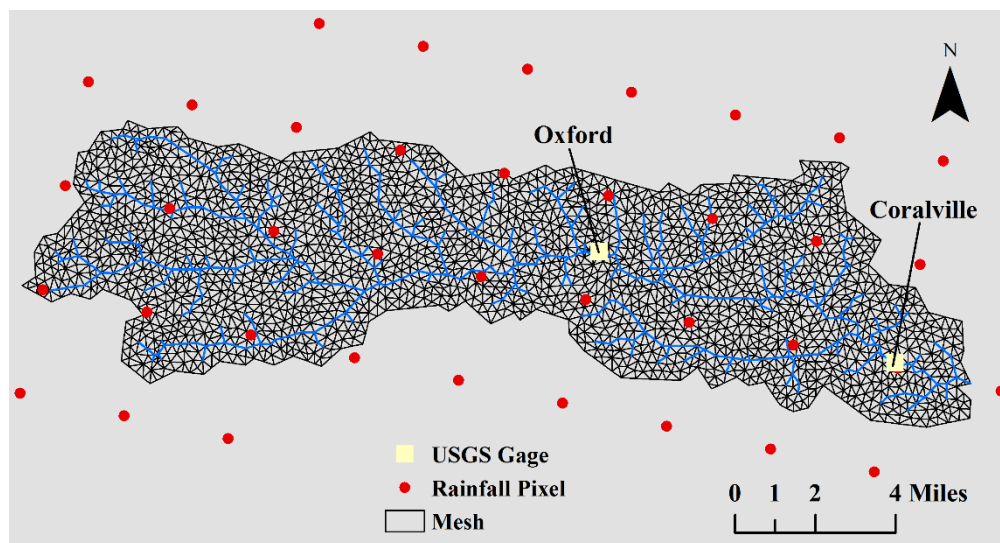
Figure 7. Stage IV rainfall data in the Clear Creek Watershed

Geology and Soils

The Clear Creek Watershed is located almost entirely within the Southern Iowa Drift Plain landform region. There is a very small area in the northeastern portion of the watershed that is part of the Iowan Surface landform region. The characteristics of each landform region have an influence on the rainfall-runoff potential and hydrologic properties of the watershed.

Soils are classified into four Hydrologic Soil Groups (HSG) by the Natural Resources Conservation Service (NRCS) based on the soil's runoff potential. The four HSG's are A, B, C, and D, where A-type soils have the lowest runoff potential and D-type have the highest. In addition, there are dual code soil classes A/D, B/D, and C/D that are assigned to certain wet soils. The soil distribution of the Clear Creek Watershed per digital soils data (SSURGO) available from the USDA-NRCS Web Soil Survey (WWS) is shown in Figure 8. Viewing the soil distribution at this map scale is difficult, but the map does illustrate the relative consistency of the HSG on this portion of the Southern Iowa Drift Plain landform region. The Clear Creek Watershed consists primarily of HSG B type soils (76.3%), which have a moderate runoff potential when saturated. Relatively small components of type B/D (16.3%) soils are present, occurring in the adjacent valleys. The remaining classes each comprise less than 4% of the total.
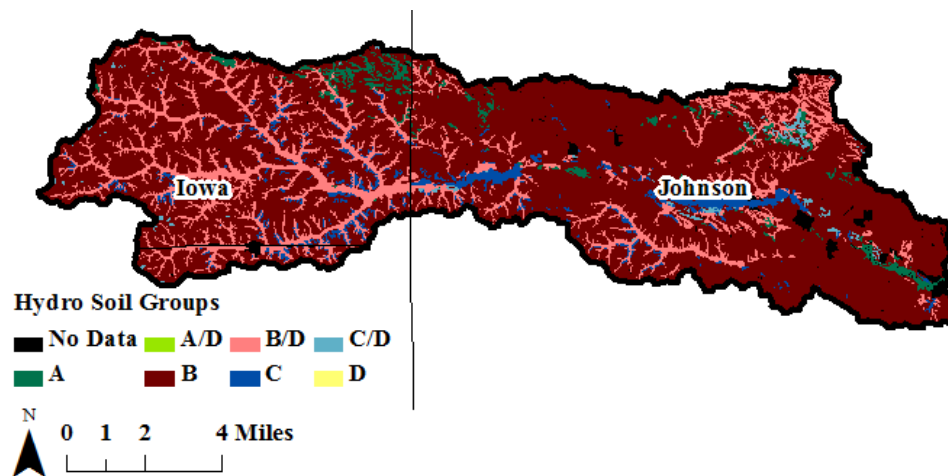
Figure 8. Distribution of Hydrologic Soil Groups in the Clear Creek Watershed

Land Use

Land use in the Clear Creek Watershed is predominantly agricultural, dominated by cultivated crops (corn/soybeans) at approximately 55% of the acreage, followed by grass/pasture at approximately 20% (Figure 9). The remaining acreage in the watershed is about 14% developed land, concentrated in the downstream part of the watershed, 7% forest, 3% crops other than corn/soy and 1% open water and/or wetlands, per the 2017 USDA/NASS Cropland Data Layer. For each land use, time series of crop coefficient, vegetation height and root depth are provided to compute actual plant evapotranspiration. Please refer to Krasowski (2019) for references on these model parameters.
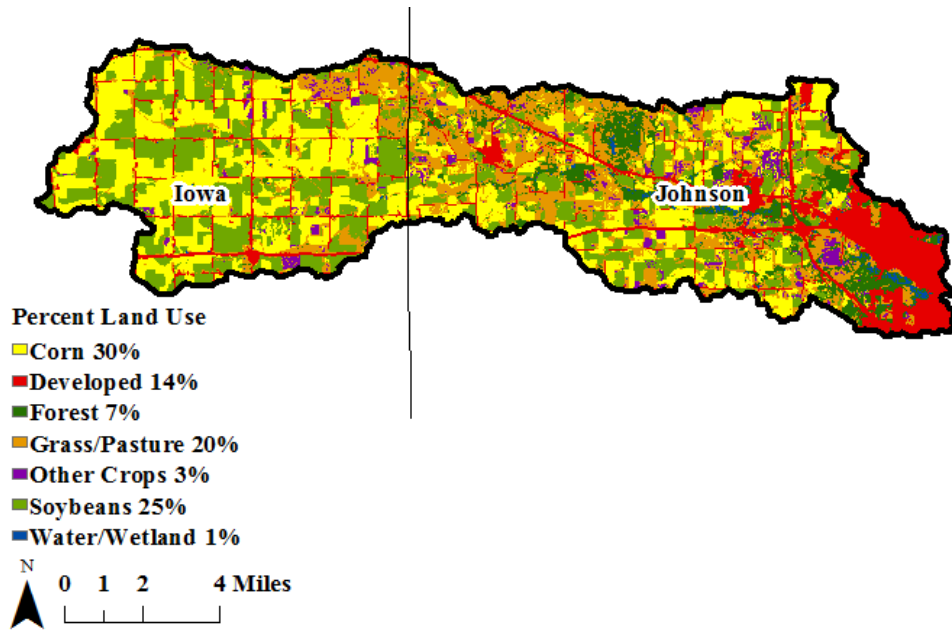
Figure 9. Land use composition in the Clear Creek Watershed

Instrumentation and Field Data

The Clear Creek Watershed has instrumentation installed to collect and record stream stage, discharge, and precipitation. There are two United States Geological Survey (USGS) streamflow gages and nine IFC stream stage sensors located within the watershed. There are also seven Rain Gage/ Soil Moisture Sensors owned by IFC (Figure 10).
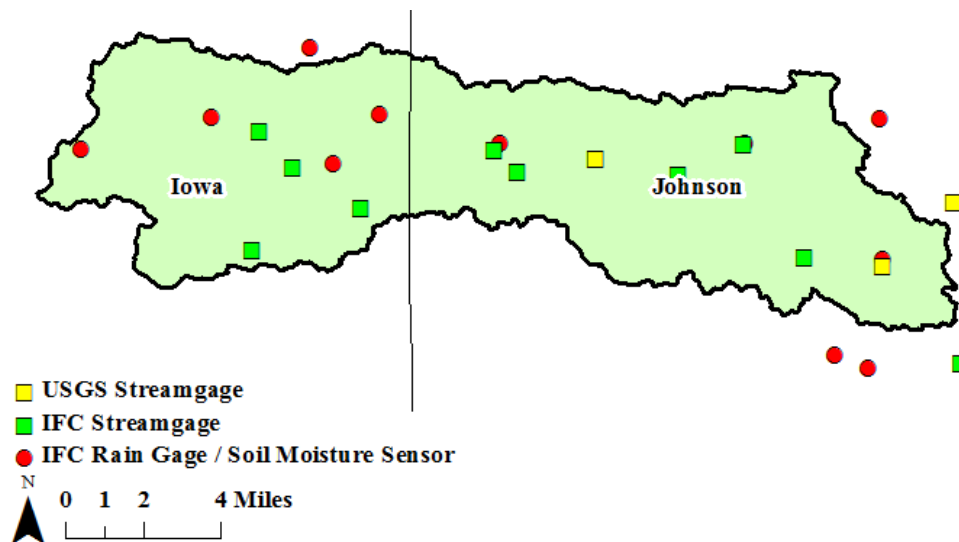

Figure 10. Hydrologic and meteorologic instrumentation in the Clear Creek Watershed

Model Calibration and Validation

Model calibration was carried out for an eight-year period (2002-2010) and during the validation process the model performance was evaluated using measurements taken between 2011 and 2016. Simulated flows were compared against observed flows at two USGS stream-gage stations: near Coralville: USGS 05454300, and near Oxford: USGS 05454220.

Figures 11 and 12 show the daily flow time series for both the calibration and validation periods. Overall, model predictions match well the measurements. These figures display both periods where the simulated values follow closely measured values, and others when it does not. Table 1 presents common metrics used in hydrologic model performance evaluation. Based on Moriasi et al. (2007), model simulations can be judged as satisfactory if Nash-Sutcliffe efficiency (NSE) > 0.50, Percent bias (PBIAS) ± 25% for streamflow, and the coefficient of determination (R^2) values are close to 1. Clear Creek model results for both the calibration and validation periods display metrics that meet those criteria.

**Table 1.** Hydrologic model evaluation metrics for both the calibration and validation periods

	NSE		PBIAS		R^2	
	Cal	Val	Cal	Val	Cal	Val
Coralville	0.64	0.67	3.30	22.46	0.82	0.82
Oxford	0.63	0.71	3.08	20.50	0.81	0.85
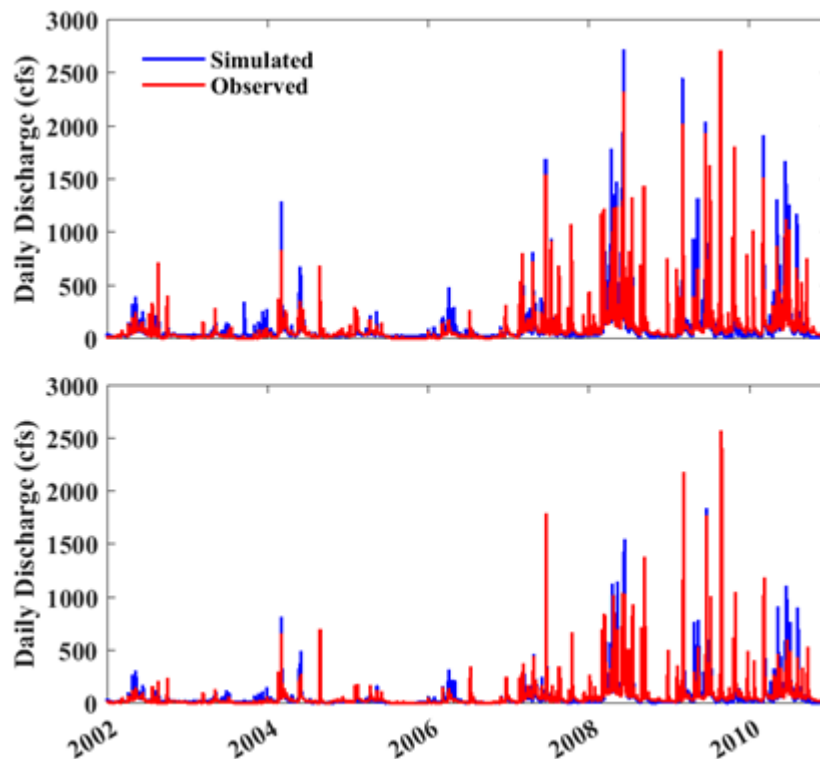
Figure 11. Observed and simulated daily flow time series. Calibration period. Top: Coralville, Bottom: Oxford
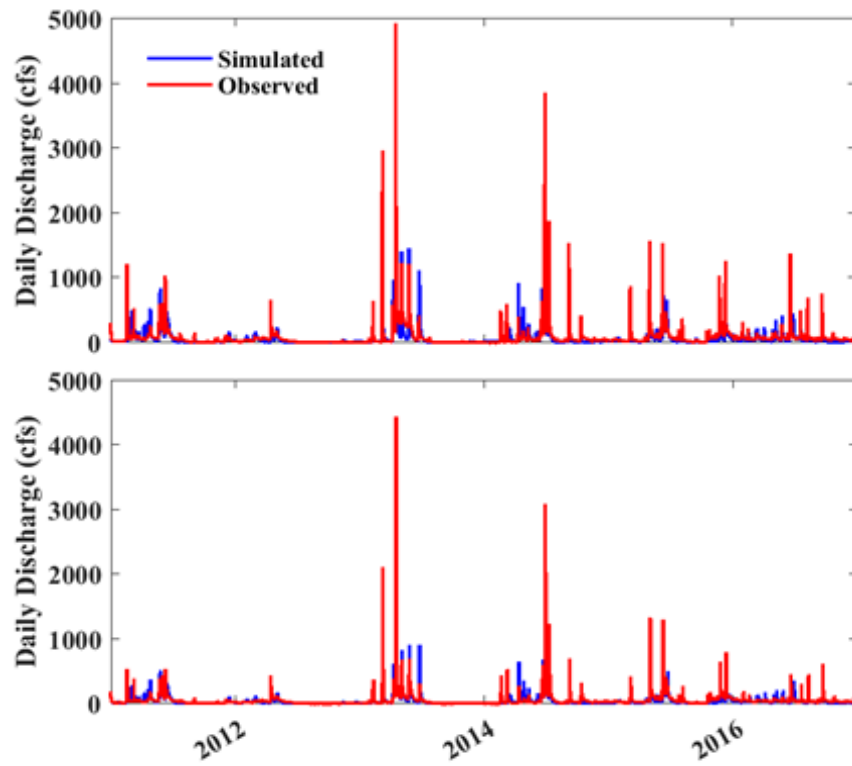
Figure 12. Observed and simulated daily flow time series. Validation period. Top: Coralville, Bottom: Oxford
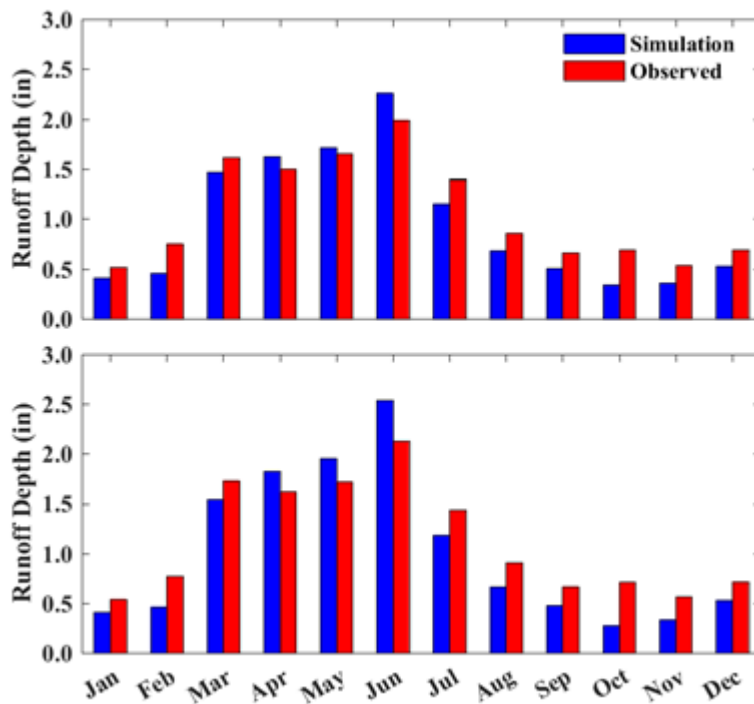
Figure 13. Observed and simulated average monthly runoff depth (in inches) for Clear Creek watershed. Results are shown for both the calibration and validation periods

To assess the model ability to predict flood characteristics in Clear Creek, simulated and observed annual peak flows were compared at Oxford and Coralville (see Figure 14). For values below 2,500 cfs the model shows no bias and annual peaks are both slightly under-predicted and over-predicted (data on both sides of the one-to-one line). For values above that threshold the model displays a slight tendency to underpredict extreme values with that behavior being more apparent at Oxford than at Coralville.

The flow duration curve shows the percent of the time that a given flow exceeded. For the entire record daily flows were ranked from smallest to largest and then plotted against the probability that a given flow will be equaled or exceeded (Figure 15). The observed and simulated flow duration curves show good agreement for flow values with exceedance probabilities lower than 10% (e.g. flood events).
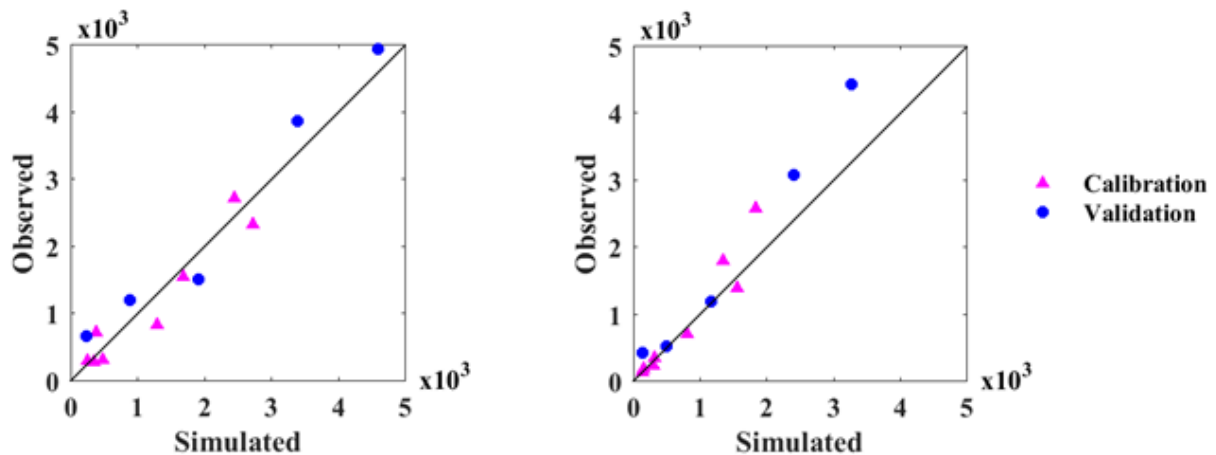

Figure 14. Simulated versus observed annual maximum peak daily discharges (cfs) for Clear Creek at Coralville (top) and Oxford (bottom)

Conclusions

A physically-based integrated model, based on the open source hydrologic code MM-pihm, was developed to simulate the hydrologic response at watersheds ranging in area from 100 to 2,500 square miles over time periods on the order of decades. Specific models were developed and incorporated into the code to properly predict water budgets for long-term simulations in large-scale watersheds. The model fully couples surface and subsurface domains to predict streamflow as well as groundwater movement for normal and extreme rainfall and snowmelt events. Model calibration and validation were performed using observed flows at two USGS stream-gage stations for an eight-year and two-year periods, respectively.
Clear Creek model results meet the criteria of Nash-Sutcliffe efficiency (NSE) > 0.50, Percent bias (PBIAS) ± 25% for streamflow, and the coefficient of determination (R2) values are close to 1. Annual peak flows were accurately predicted by the model. The model captures the statistic behavior of the historic record and therefore can be a useful tool to make flood impact reductions assessments. Future work involves the evaluation of best management practices

including increasing infiltration with native vegetation and with Cover Crops/Soil Health/No-Till, and distributed storage.
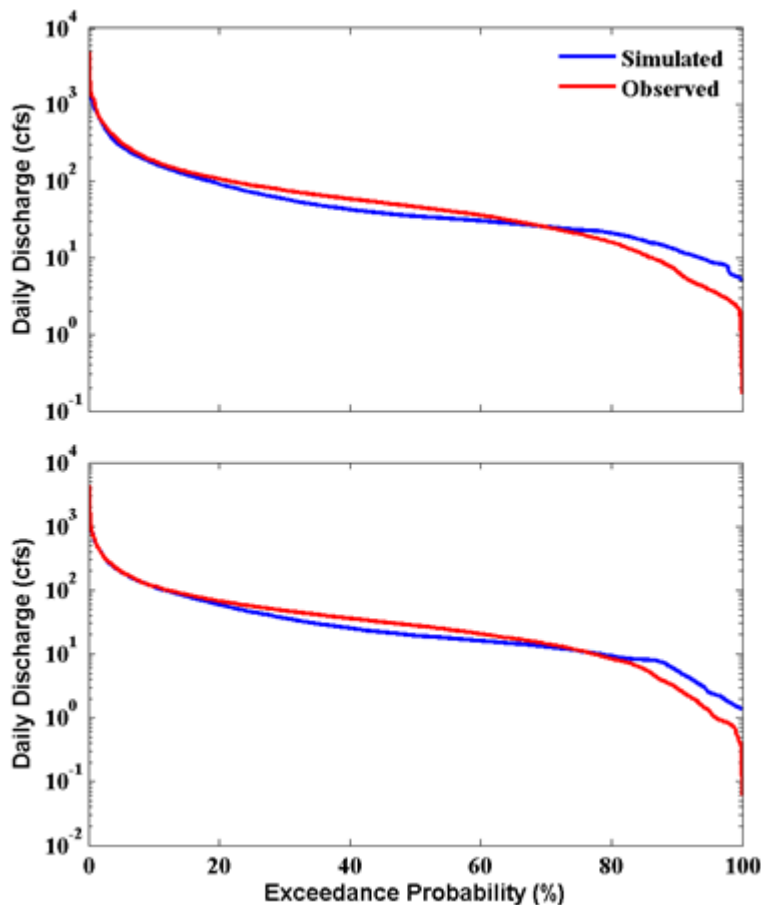
Figure 15. Daily flow duration curves for Clear Creek at Coralville (top) and Oxford (bottom)

References

Bradley, A.A. 2010. "What Causes Floods in Iowa?" A Watershed Year: Anatomy of the Iowa Floods of 2008, C. Mutel (editor), University of Iowa Press, Iowa City, Iowa. 7 - 17.

Krasowski, M. 2019. "Continuous Watershed-scale hydrologic modeling of conservation practices for peak flow reduction". Master's Thesis. The University of Iowa, Iowa City, IS, USA.

Kumar, M., Duffy, C., and Salvage, K. 2009. "A second-order accurate, finite volume–based, integrated hydrologic modeling (FIHM) framework for simulation of surface and subsurface flow," Vadose Zone 8.

Moriasi, D.N., Arnold, J.G., Van Liew, M.W., Bingner, R.L., Harmel, R.D., and Veith, T.L. 2007. "Model evaluation guidelines for systematic quantification of accuracy in watershed simulations," Transactions of the ASABE, 50(3), pp.885-900.

Panday, S. and Huyakorn, P.S. 2004. "A fully coupled physically-based spatially-distributed model for evaluating surface/subsurface flow," Advances in Water Resources 27.

Qu, Y., and Duffy, C.J. 2007. "A semidiscrete finite volume formulation for multiprocess watershed simulation," Water Resources Research 43.

Smith, J.A., Baeck, M.L., Villarini, G., Wright, D.B., Krajewski, W.F. 2013. "Extreme flood response: The June 2008 flooding in Iowa." Journal of Hydrometeorology. 14(6). 1810-1825.

Van Genuchten, M.T. 1980. "A closed-form equation for predicting the hydraulic conductivity of unsaturated soils," Soil science society of America journal 44.

Yu, X., Bhatt, G., Duffy, C., and Shi, Y. 2013. "Parametrization for distributed watershed modeling using national data and evolutionary algorithm," Computer and Geosciences 58.

RiverWare Interactive Scenario Explorer (RiverWISE) Demonstration

David Neumann, Senior Research Assistant, Center for Advanced Decision Support for Water and Environmental Systems, University of Colorado, Boulder, CO, david.neumann@colorado.edu

Edith Zagona, Research Professor and Director, Center for Advanced Decision Support for Water and Environmental Systems, University of Colorado, Boulder, CO, zagona@colorado.edu

Extended Abstract

The RiverWare Interactive Scenario Explorer (RiverWISE) is an easy to use tool that allows stakeholders and other interested parties to explore a RiverWare model, develop alternative scenarios, simulate those scenarios, and investigate and compare the results. RiverWISE is a tool built on top of RiverWare, which models the hydrologic response of a river/reservoir system given inflows and multi-objective operating policies. RiverWISE provides an intuitive, controlled environment for stakeholders to experiment with a special version of a RiverWare model called a WISE file. The RiverWISE tool is freely available; it only requires a downloadable license file from CADSWES and a WISE file to explore.

Using a utility in the RiverWare software, a model developer or author configures and exports a RiverWISE file from a RiverWare model; it includes the object network, baseline input data and operating rules, a set of input variables that can be modified by the stakeholder for scenario exploration, and a set of output variables that can be analyzed. Once exported, the WISE file can be shared with stakeholders who wish to explore the effects of alternative inputs on the outputs and compare with the baseline. This demonstration will touch on the export process but will focus on the stakeholder experience.

We will demonstrate how the stakeholder opens RiverWISE and loads the provided WISE file. RiverWISE allows the stakeholder to explore the model layout and see how features of the basin are represented and connected to other features. Figure 1 shows a screenshot of the RiverWISE interface with the model layout window, model description and scenario list. This tab provides a description, the model time range, and the names of the baseline file and other saved scenarios. Within the layout view, the stakeholder can zoom and pan the model to view the objects and the links. In addition, the stakeholder creates scenarios on this tab, copying the input data from the baseline scenario or any other saved scenario.
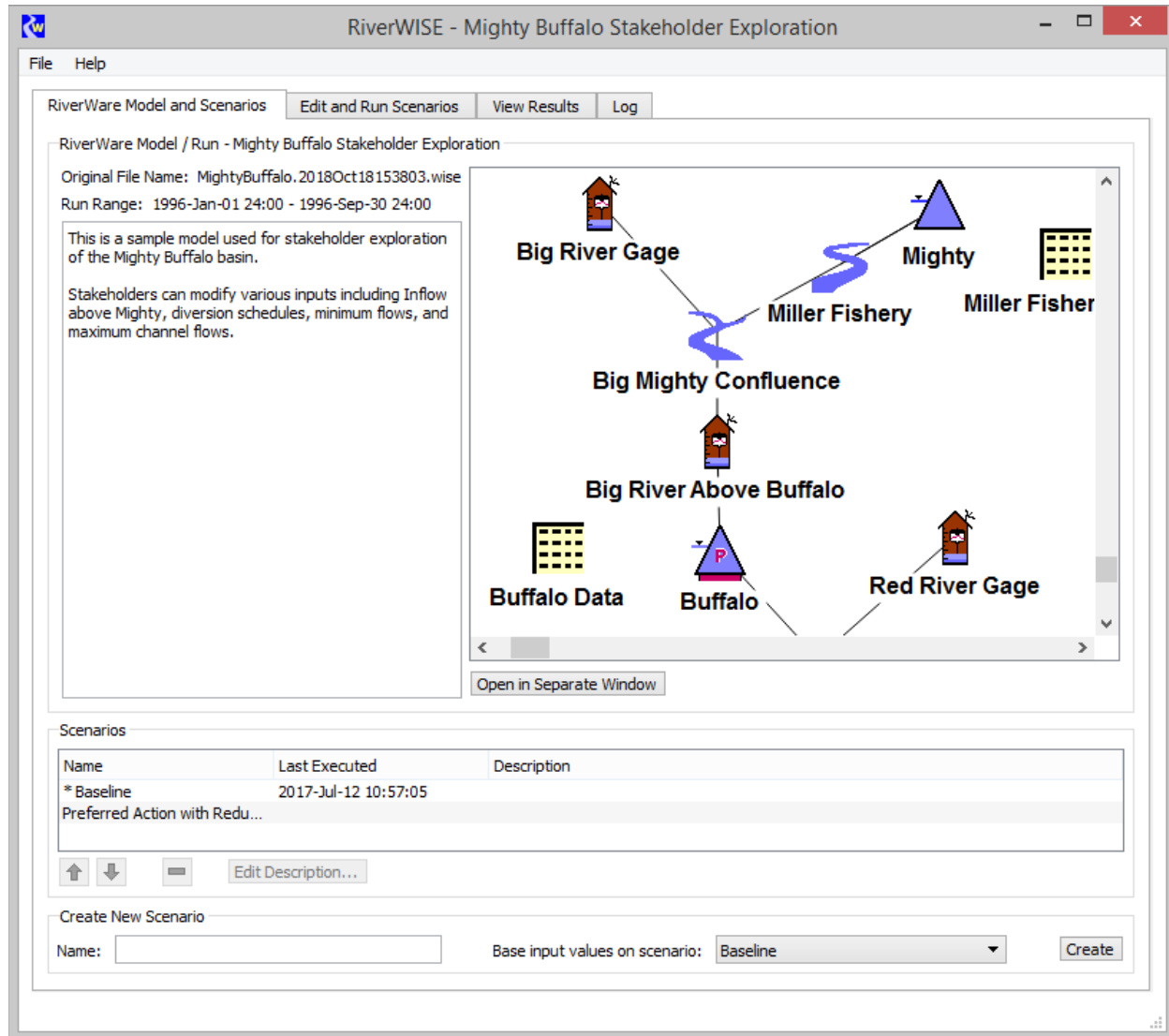
Figure 1. Screenshot of RiverWare Model and Scenario tab

We will show how the stakeholder modifies the input data for a scenario and makes a run on the Edit and Run Scenarios tab, as shown on Figure 2. The stakeholder selects one or more sets of input data and then edits the values either directly, by scaling, or by applying an offset. Values can be copied and pasted to external programs, like spreadsheets, for more complex data manipulation. Plots show how the scenario inputs differ from the baseline or other scenario's input data. The stakeholder uses this tab to make a run by clicking on the green run button.
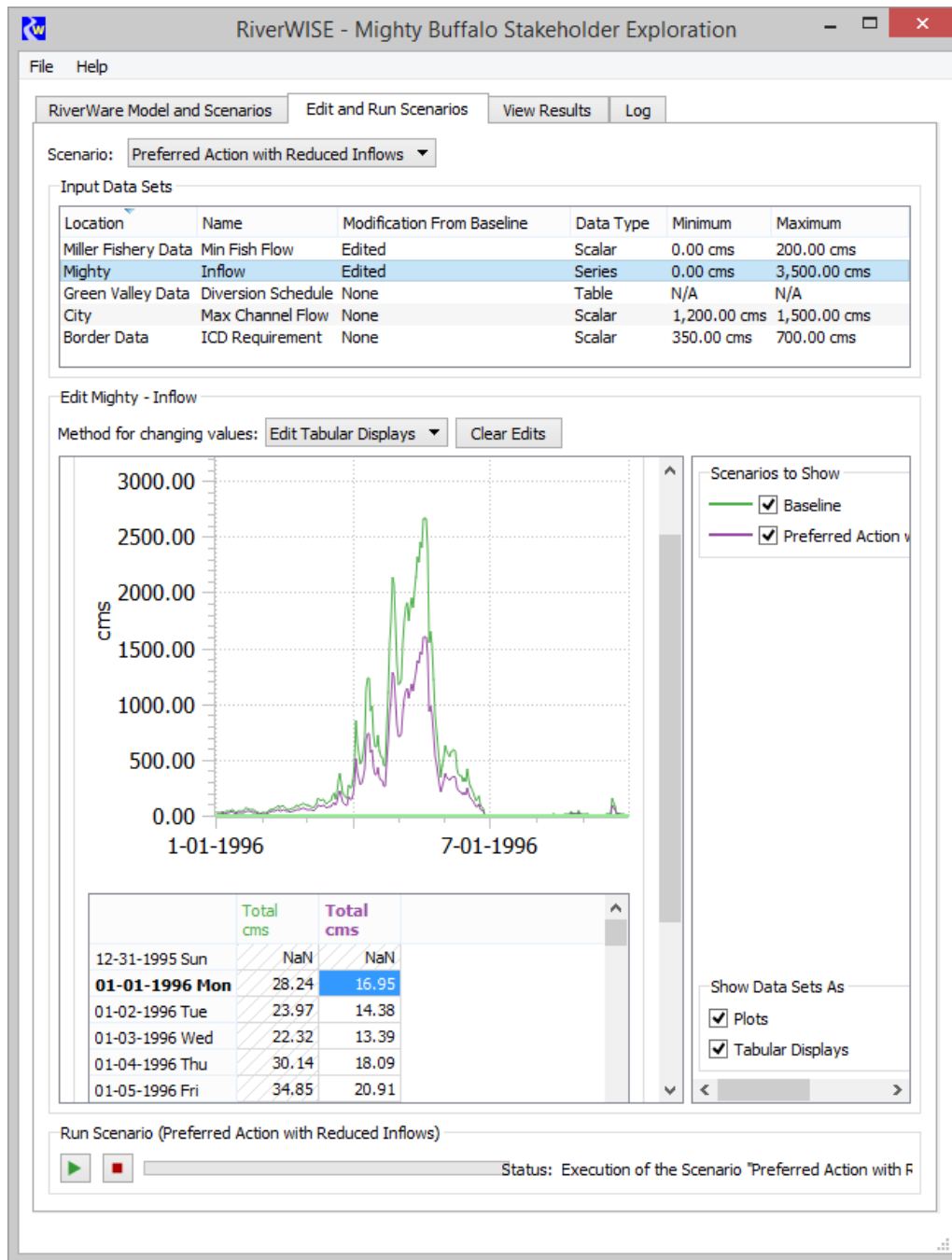
Figure 2. Screenshot of Edit and Run Scenarios Tab

We will show how to view the results of the scenarios, comparing one run to the next. Figure 3 shows a sample View Results tab. The results can be shown as either a plot or tabular data. The user can turn on or off display of different scenarios and data locations to compare the results of the runs. Tabular data and plots can be copied to the system clipboard for sharing results or including in documents or emails.

We will show how to save the resulting WISE file or export the developed scenario for sharing with other stakeholders and model developers. This allows communication among

stakeholders, model developers and other stakeholders; they can all be looking at the same results in the same tool.
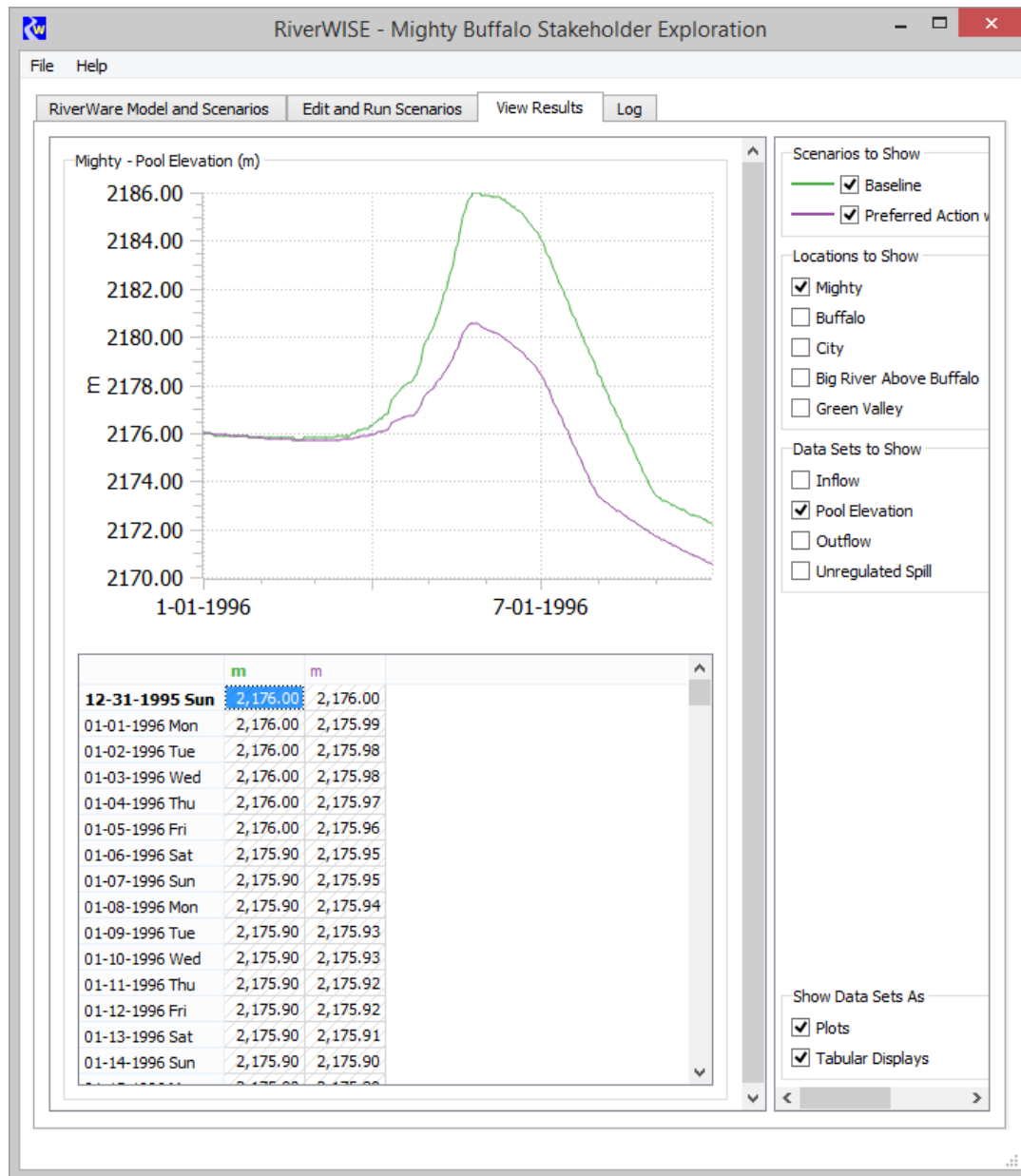
Figure 3. Screenshot of the View Results Tab

Finally, we will describe applications of RiverWISE on real basins, explaining the types of scenarios analyzed and presenting the experiences of the users. Free evaluation versions of RiverWISE and the RiverWare software with demo models will be given to interested visitors.

RiverWare is developed by the University of Colorado Center for Advanced Decision Support for Water and Environmental Systems (CADSWES) with sponsorship of the Tennessee Valley Authority, the Bureau of Reclamation and the U.S. Army Corps of Engineers and distributed by the University of Colorado Office of Technology Transfer.

Watershed-Scale Water Quality Modeling in HEC-WAT with CE-QUAL-W2 and HEC-RAS

Todd Steissberg, Ph.D., P.E., Hydraulic Engineer, U.S. Army Corps of Engineers, Institute for Water Resources, Hydrologic Engineering Center, 609 Second Street, Davis, CA 95616; 530-756-1104; todd.steissberg@usace.army.mil

Julia Slaughter, M.S., Hydrologic Technician, U.S. Army Corps of Engineers, Institute for Water Resources, Hydrologic Engineering Center, 609 Second Street, Davis, CA 95616; julia.b.slaughter@usace.army.mil

Zhonglong Zhang, Ph.D., P.E., P.H., Research Professor, Department of Civil and Environmental Engineering, Portland State University, Portland, OR 97207; zz3@pdx.edu

Mark Jensen, Hydraulic Engineer, U.S. Army Corps of Engineers, Institute for Water Resources, Hydrologic Engineering Center, 609 Second Street, Davis, CA 95616; mark.jensen@usace.army.mil

Ryan Miles, Software Engineer, Resource Management Associates, Inc. (RMA). 1756 Picasso Avenue, Suite G, Davis, CA 95618; ryanm@rmanet.com

Leila Ostadrahimi, Ph.D., P.E., Hydraulic Engineer, U.S. Army Corps of Engineers, Institute for Water Resources, Hydrologic Engineering Center, 609 Second Street, Davis, CA 95616; leila.ostadrahimi@usace.army.mil

Billy Johnson, Ph.D., Research Civil Engineer, U.S. Army Engineer Research and Development Center, Environmental Laboratory, 400 F Street, Suite 100, Davis, CA 95616; billy.e.johnson@usace.army.mil

Abstract

New software has been developed that facilitates watershed-scale water quality modeling. The U.S. Army Corps of Engineers' Hydrologic Engineering Center (HEC) has developed a CE-QUAL-W2 plug-in for HEC-WAT (Watershed Assessment Tool) that allows users to import and link multiple CE-QUAL-W2 water quality models with one another as well as with other hydraulic, hydrologic, and water quality models and external time series data. Modelers can create any number of model alternatives to stimulate system-wide water quality for various water management scenarios or time periods. The new software has been deployed by the U.S. Army Corps of Engineers for the Columbia River Treaty (CRT) study. Water temperature and Total Dissolved Gas (TDG) are the key parameters of concern in the Columbia River watershed. The large flows discharged over spillways at the high-head dams in the Columbia River system entrain significant amounts of atmospheric gases. Supersaturated TDG levels can persist for dozens of miles downstream, which can cause gas bubble trauma in fish, with chronic or acutely lethal effects, depending on TDG levels. TDG capability was added to HEC-RAS (River Analysis System) in support of the CRT study to enable existing HEC-RAS models to be linked with the CE-QUAL-W2 models to improve TDG management and impact assessments.

Introduction

Environmental watershed analyses are often performed using multiple water quality models, each of which is targeted to a particular location in the watershed or a particular capability, such as one-dimensional river hydraulics and temperature for a reach or two-dimensional stratified hydrodynamics and eutrophication for a reservoir. To enable efficient watershed-scale assessments, these models need to be integrated into a coherent system, linking flow and/or water quality outputs from one model to one or more downstream models, where appropriate, along with time series from other sources. The U.S. Army Corps of Engineers' Hydrologic

Engineering Center (HEC) developed the Watershed Assessment Tool (HEC-WAT) to provide a comprehensive systems-based approach to performing water resources studies (HEC 2017). The HEC-WAT software allows modelers to run a sequence of river, reservoir, and watershed runoff models, built for a particular location and purpose, to leverage each model's individual strengths at geographic scales ranging from a river reach to full coverage of the watershed. The models may be linked together, where one model provides the input for the next model in the computational sequence. For example, HEC-WAT allows a model that is specialized for simulating watershed runoff processes to provide runoff data to models specialized for river or reservoir modeling. Alternatively, any model can be run independently, where HEC-WAT only automates the compute sequence. Whether or not models share data with one another, HEC-WAT provides a common user interface that allows results from all of the models to be analyzed together. This improves the effectiveness of multi-disciplinary teams who need to efficiently analyze a watershed in a systems context.

To be able to compute a model in HEC-WAT and optionally link that model with other models, a plug-in must be developed for the computer simulation program that is used to build and run the model. The plug-in facilitates communication of each model's inputs and outputs with HEC-WAT. The HEC-WAT modeler controls communication between models using the Model Linking Editor by linking one model's inputs to the outputs from one or more separate models using each model's input and output locations. HEC-WAT is configured to connect time series data between models via the HEC Data Storage System (HEC-DSS). In general, users link models by selecting the model locations rather than the specific time series record in the DSS file. However, model inputs can be linked directly to external DSS time series data, which leverages the HEC-DSSVue user interface capabilities.

USACE Northwest Division (CENWD) provided funding and guidance to develop a system water quality model for the Columbia-Snake River watershed utilizing several CE-QUAL-W2 and HEC-RAS (River Analysis System) models. CE-QUAL-W2 (Cole and Wells 2016) is a two-dimensional (2D) laterally averaged hydrodynamic and water quality modeling program, which is widely used to simulate the water quality of reservoirs, lakes, rivers, estuaries, and river basin systems. Furthermore, CE-QUAL-W2 allows modelers to simulate basic eutrophication processes such as temperature, nutrient, algae, dissolved oxygen, organic matter and sediment relationships. HEC-RAS (HEC 2016) is a 1D and 2D river hydraulics model with 1D water quality capabilities. The U.S. Army Corps of Engineers (USACE) and U.S. Bureau of Reclamation (USBR) have developed CE-QUAL-W2 and HEC-RAS water quality models (USACE 2013) to assess the effect of reservoir operations on water temperature and Total Dissolved Gas (TDG) in the Columbia-Snake River watershed. These models are being used to support the Columbia River System Operations (CRSO) Environmental Impact Statement (EIS) and Columbia River Treaty (CRT) projects.

In collaboration with CENWD, Portland State University (PSU), the U.S. Army Engineers Research and Development Center's Environmental Laboratory (ERDC-EL), and Resource Management Associates, Inc. (RMA), HEC lead development of a CE-QUAL-W2 plug-in for HEC-WAT and updated HEC-RAS and its HEC-WAT plug-in to support water quality modeling within HEC-WAT. The updated software allows modelers to create a basin-scale water quality model, integrating several CE-QUAL-W2 (version 4.2) and HEC-RAS (version 5.0) models in a computational sequence. Moreover, the software allows the flexibility to integrate these models with other hydrologic and hydraulic models. Figure 1 shows the HEC-WAT software with several CE-QUAL-W2 water quality models displayed in an active map schematic to illustrate the ability to create an integrated basin-scale water quality model in HEC-WAT. This schematic shows the plan geometry of several of the Columbia-Snake River CE-QUAL-W2 models. Ongoing software

development is extending the existing water quality capabilities of HEC-RAS, and new water quality capabilities are in development for HEC-ResSim (Reservoir System Simulation) and HEC-HMS (Hydrologic Modeling System). The HEC-WAT plug-ins for these programs will enable integration of these new capabilities with CE-QUAL-W2 and other models within HEC-WAT.
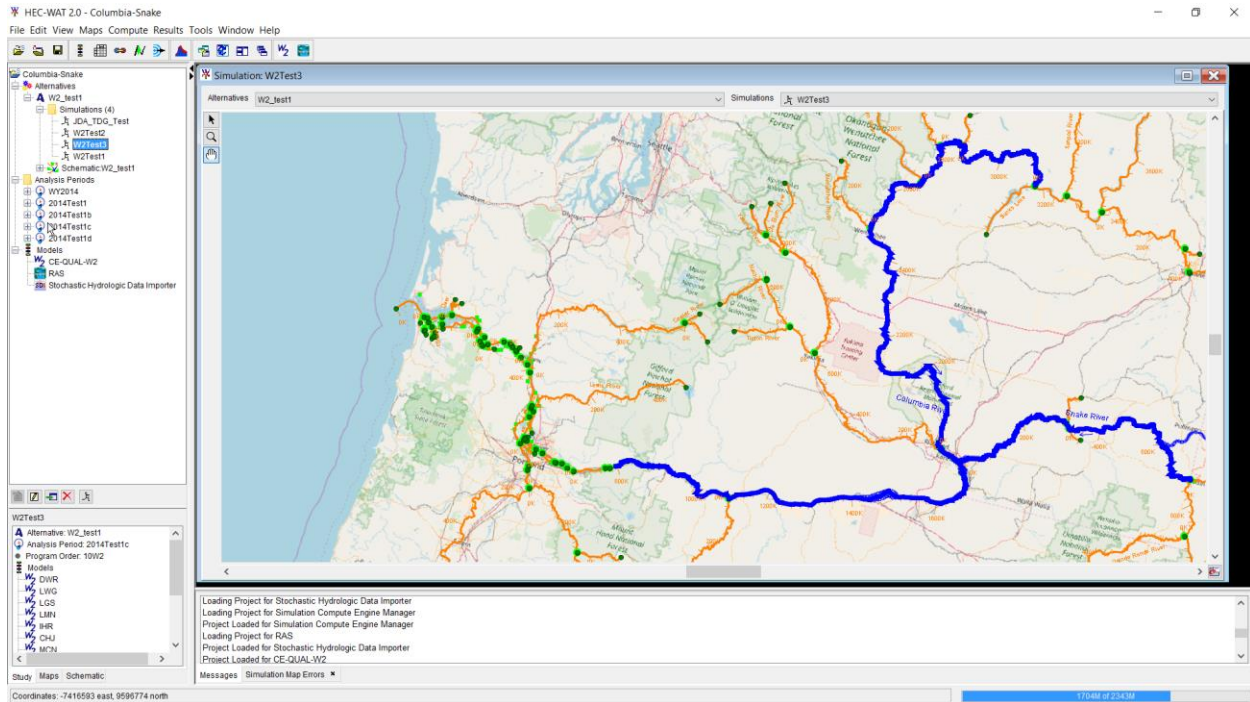
**Figure 1.** HEC-WAT user interface, showing CE-QUAL-W2 geometry of the ten Columbia-Snake River models

Integration of CE-QUAL-W2 with HEC-WAT

HEC-WAT plug-ins have been developed for HEC-RAS, HEC-ResSim, HEC-HMS, and HEC-FIA (Flood Impact Analysis). The plug-ins for the HEC software integrate the existing software in HEC-WAT and leverage the software's graphical user interface and capability to read and write DSS files. In contrast to HEC software, the majority of the CE-QUAL-W2 software's time series input and output is via ASCII files. Notably, the parameters and specifications for model setup are defined in an ASCII control file as well a set of ASCII bathymetry files (in fixed-width text or CSV format), one file per waterbody. Therefore, a unique plug-in was developed for CE-QUAL-W2 which included the ability to exchange data with DSS files. In addition, a graphical user interface was developed for the CE-QUAL-W2 plug-in to allow modelers to define initial conditions for flow, water surface elevation, water temperature, and constituent concentrations. The CE-QUAL-W2 software was also updated to generate geometry and geolocation information so the model could be displayed in the HEC-WAT map schematic (Figure 2).
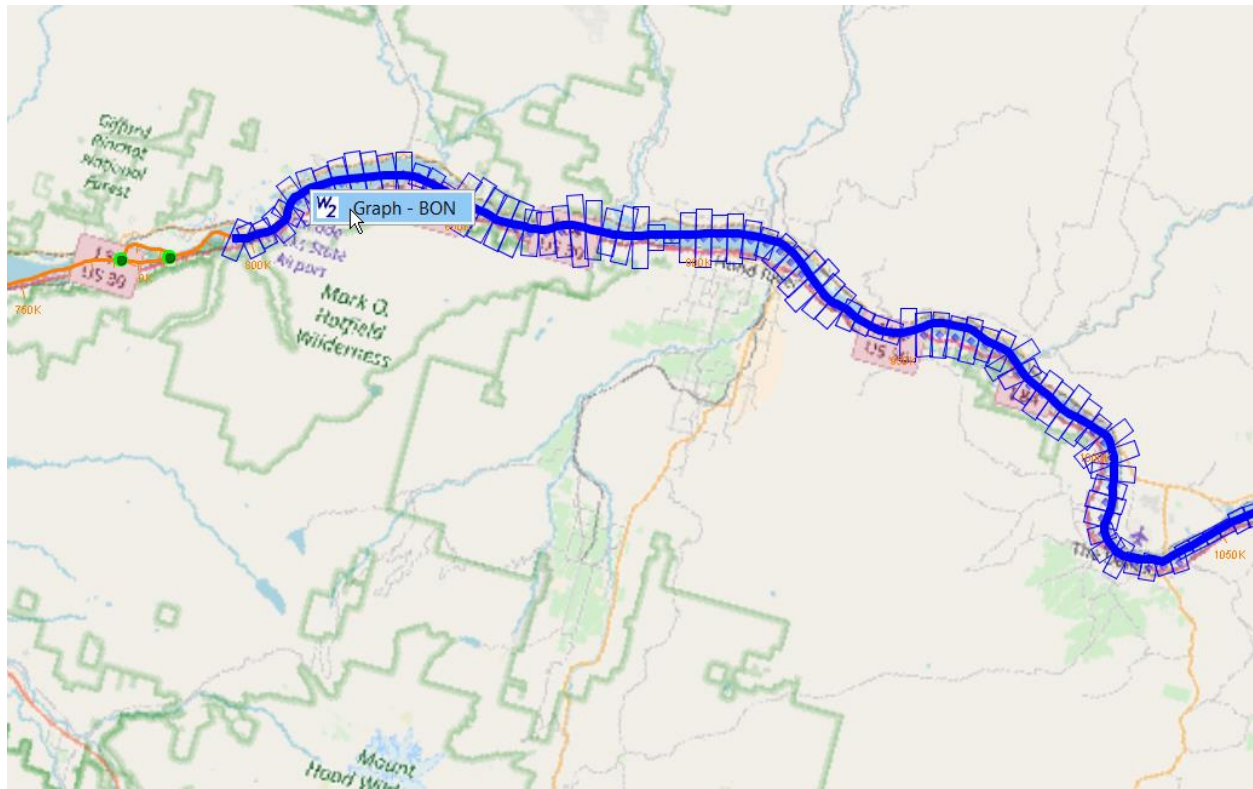
Figure 2. CE-QUAL-W2 model schematic for Lake Bonneville, showing option to plot the results

Two components of the plug-in, the Parser and the Data Transformation Tool (DTT), were developed to facilitate communication between individual CE-QUAL-W2 models, the HEC-WAT analysis framework, and other models imported into the HEC-WAT study. The Parser was designed to read and update any setting in the imported CE-QUAL-W2 model's control file. The Parser provides extensive information for the imported model to HEC-WAT which includes parameter names, units, and filenames. The information provided by the Parser is used to initialize the settings in the CE-QUAL-W2 user interface provided by the plug-in and assist with the exchange of data between the CE-QUAL-W2 ASCII input and output files and the HEC-DSS database used by HEC-WAT. When modelers enter new information in the user interface, the Parser communicates this new information to the CE-QUAL-W2 model's control file. When the model is computed, any input data linked (using the Model Linking Editor) with an upstream model is first exported (by the DTT) from the upstream model's DSS output file to ASCII input files using the filenames provided by the Parser. **Figure 3** shows a schematic of the compute order. **Figure 4** shows a model being computed with the CE-QUAL-W2 software in control of the simulation in progress. Once the CE-QUAL-W2 simulation completes, the DTT imports the time series data from the ASCII output files to the current model's DSS output file, which can be used by the next model in the computation sequence. The CE-QUAL-W2 plug-in also provides a platform to view the time series data written to DSS, which is plotted by selecting a CE-QUAL-W2 model location in the map schematic. The opened plotting dialog provides options to select and plot multiple time series in one or more sub-plots (**Figure 5**).
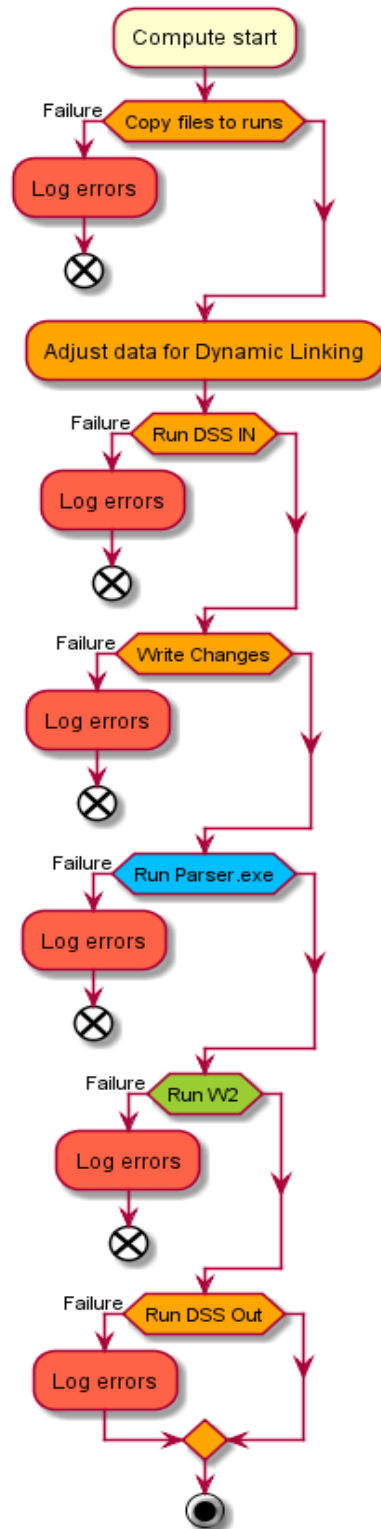
Figure 3. Compute order for the CE-QUAL-W2 plug-in for HEC-WAT. The plug-in processes are shown in orange and blue. The CE-QUAL-W2 executable program is shown in green. Red indicates logging errors and exiting with unsuccessful status.
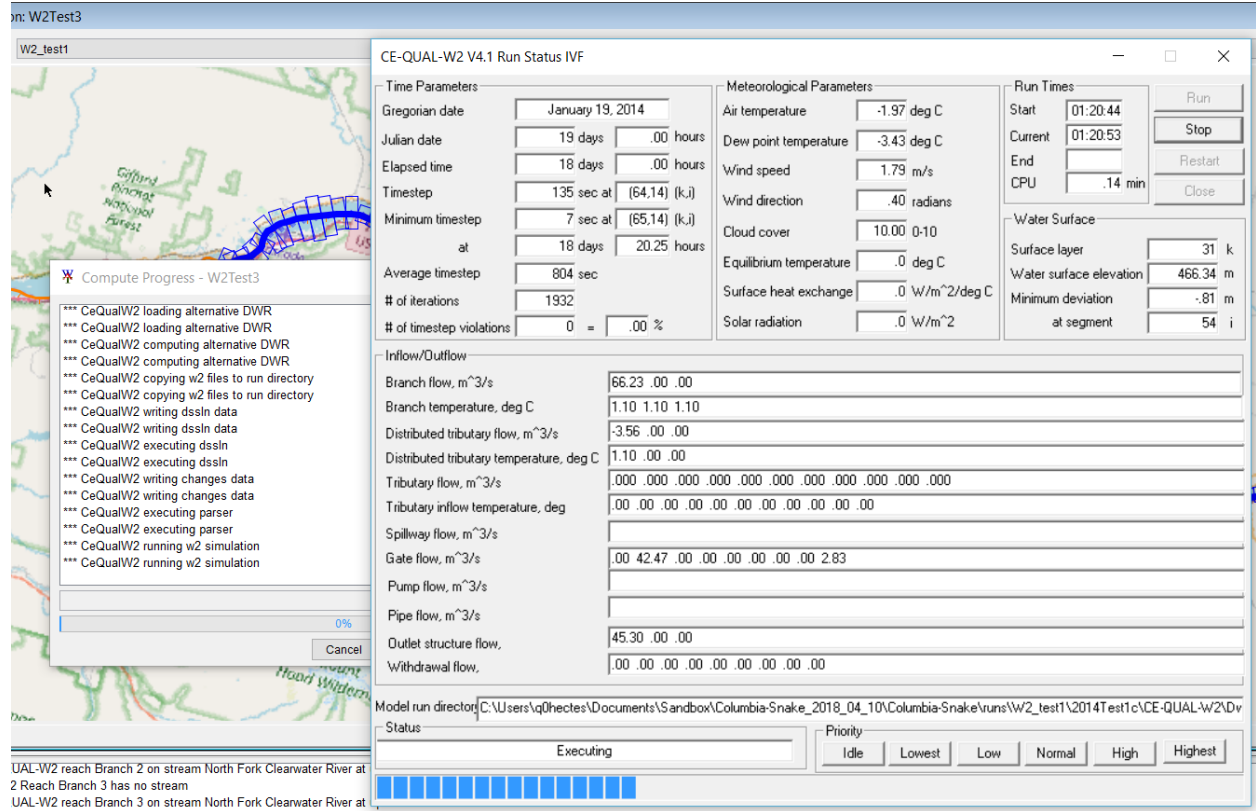
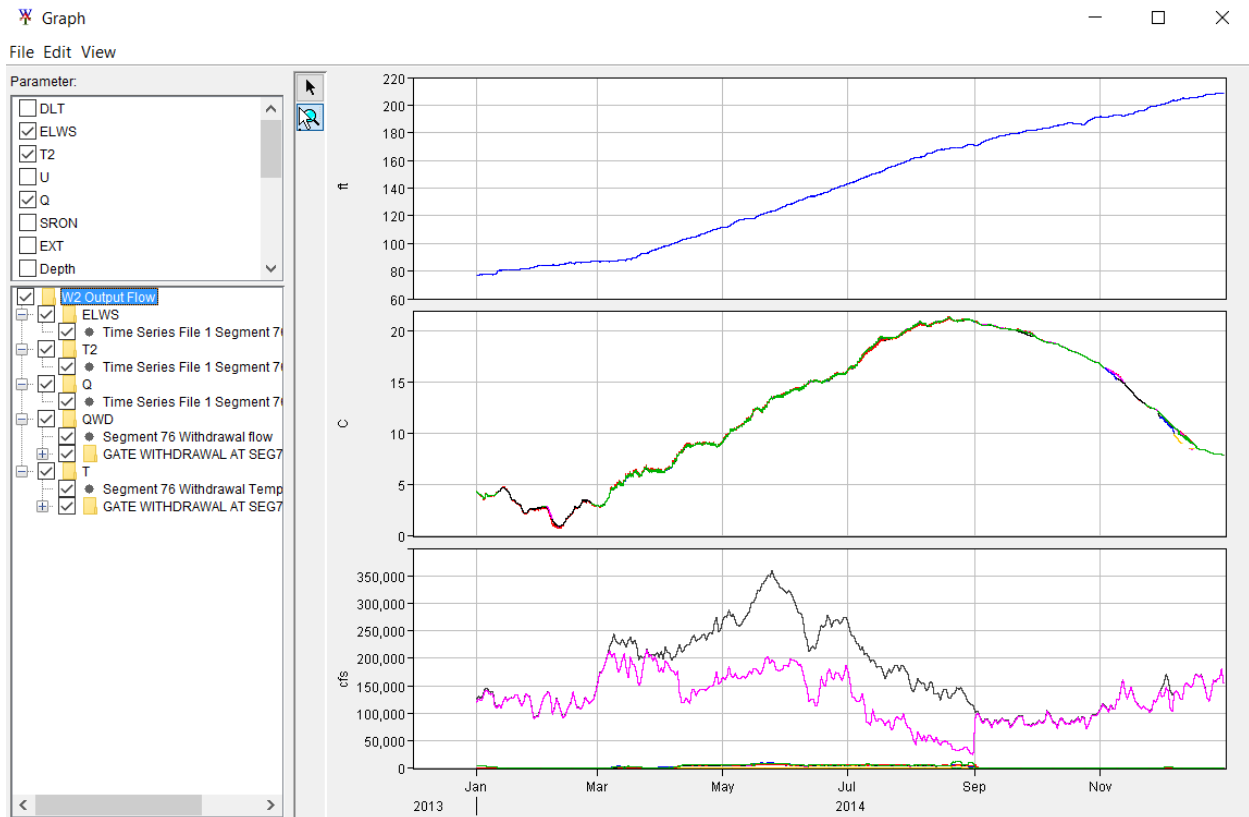**Figure 4.** CE-QUAL-W2 simulation in progress

Figure 5. CE-QUAL-W2 time series plot dialog

Integration of HEC-RAS Water Quality with HEC-WAT

To support the water quality modeling capabilities of HEC-RAS within HEC-WAT, the existing HEC-RAS plug-in and HEC-RAS software were modified. HEC-RAS runs unsteady flow and water quality simulations as separate processes, each manually initiated by the user. To automate this process in HEC-WAT, an option was added to HEC-RAS to trigger a water quality simulation after the unsteady flow simulation has completed. A water quality checkbox was added the HEC-RAS software interface in the "Program to Run" section of the "Unsteady Flow Analysis" dialog to select this option. Second, the capability of HEC-RAS to write water quality output to HEC-DSS was extended to provide the necessary water quality outputs to HEC-WAT so they can be linked with other models. Finally, the HEC-RAS plug-in for HEC-WAT was extended to handle the necessary communication of water quality information, such as providing the list of HEC-RAS water quality parameters to the Model Linking Editor.

TDG Capabilities

In support of the CRSO and CRT projects as well as real-time TDG modeling capabilities, algorithms from the SYSTDG (Schneider and Hamilton 2016a; 2016b) model were incorporated into CE-QUAL-W2 Version 4.2 for "source generation" of TDG at twelve Columbia-Snake River dams. Table 1 lists the five regression equations for calculating spillway flow TDG that were added to CE-QUAL-W2. A number of datasets were used to test and validate the new TDG capabilities. Consequently, the enhancements provide CE-QUAL-W2 modelers with the ability to evaluate the impacts of spill operations and mitigation measures on the tailwater TDG.

Table 1. List of spillway flow TDG production equations in SYSTDG

1. $TDG_{sp} = P_1 * \left(1 - e^{P_3 * Q_{sp}}\right) + BP$
   $\Delta TDG_{sp} = P_1 * \left(1 - e^{P_3 * Q_{sp}}\right)$

2. $TDG_{sp} = P_1 * (E_{tw} - E_{ch})^{P_2} * (1 - e^{P_3 * q_s}) + P_4 + BP$
   $\Delta TGP_{sp} = P_1 * (E_{tw} - E_{ch})^{P_2} * (1 - e^{P_3 * q_s}) + P_4$

3. $TDG_{sp} = P_1 * (E_{tw} - E_{ch})^{P_2} * q_s{}^{P_3} + P_4 + BP$
   $\Delta TGP_{sp} = P_1 * (E_{tw} - E_{ch})^{P_2} * q_s{}^{P_3} + P_4$

4. $TDG_{sp} = P_1 * (E_{tw} - E_{ch}) + P_2 * q_s{}^{P_3} + P_4 + BP$
   $\Delta TGP_{sp} = P_1 * (E_{tw} - E_{ch}) + P_2 * q_s{}^{P_3} + P_4$

5. $TDG_{sp} = P_1 * (1 - e^{P_2 * q_s}) + P_3 * (Temp_{tw} - P_4) + BP$
   $\Delta TDG_{sp} = P_1 * (1 - e^{P_2 * q_s}) + P_3 * (Temp_{tw} - P_4)$

TDG_{sp} = spillway discharge total gas pressure (mmHg)
ΔTGP_{sp} = spillway discharge gas pressure (mmHg)

BP = observed barometric pressure (mmHg)
E_{tw} = observed project (dam) tailwater elevation (feet)
E_{ch} = project specific tailwater channel elevation (feet)
E_{tw} - E_{ch} = tailwater channel depth (feet)
$Temp_{tw}$ = tailwater temperature (ºC)
Q_{sp} = total project spillway discharge (kcfs)
q_s = flow weighted specific spillway discharge (kcfs)
P_1 - P_4 = project specific coefficients (unitless)

In SYSTDG, the entrainment of powerhouse flows is computed as a simple linear function of spillway flows. The TDG pressures generated from a project (dam) are computed from the flow-weighted average TDG pressures of the spillway and the powerhouse using the following equation:

$$TDG_{rel} = \frac{TDG_{sp}(Q_{sp} + Q_{ent}) + TDG_{ph}(Q_{ph} - Q_{ent})}{Q_{ph} + Q_{sp}},$$

where TDG_{rel} = project release TGP (Total Dissolved Gas Pressure) after mixing (mmHg), TDG_{sp} = spillway TGP (mmHg), TDG_{ph} = release TGP through the powerhouse turbines (mmHg), Q_{sp} = Total project spill (kcfs), and Q_{ph} = total flow through powerhouse turbines (kcfs).

Similarly, TDG capabilities were also incorporated into HEC-RAS version 5.0 by adding new algorithms to the existing Nutrient Simulation Module I (NSMI, Zhang and Johnson 2016). The following equation was incorporated into NSMI to leverage its existing dissolved oxygen (DO) and dissolved nitrogen gas (N₂) simulation capabilities to compute TDG saturation as a derived water quality constituent, which is then reported in the HEC-RAS model output.

$$TDG\% = \left[79\frac{N_2}{N_{2_s}} + 21\frac{DO}{DO_s}\right]$$

In this equation, $N2$ = dissolved nitrogen gas (mg L^{-1}), $N2_s$ = nitrogen gas saturation (mg L^{-1}), DO = dissolved oxygen (mg-O$_2$ L^{-1}), and DO_s = dissolved oxygen saturation (mg-O$_2$ L^{-1}). Version 5.0 of HEC-RAS does not have the capability to compute TDG source generation. However, a future version of the HEC-RAS software will allow modelers to compute advection, diffusion, and reaeration processes for a river reach using input TDG concentrations, such as are currently being provided by the CE-QUAL-W2 program.

Columbia-Snake River System Model

The Columbia-Snake River dams and associated water regulation policies have a significant impact on water temperature and TDG. The reservoirs in this watershed typically stratify from the late summer to the early fall and delay the flow of water downstream, altering the spatial-temporal thermal regime of the watershed. Water temperature can affect the timing and survival of adult and juvenile salmon and steelhead migrating through the main-stem Snake and Columbia rivers (NMFS, 2014). The State Departments of Oregon and Washington have identified the Columbia and Snake Rivers as not achieving their temperature standards (EPA 2019a; 2019b).

In addition, the physical characteristics of the dams and the operational procedures can have substantial impacts on the downstream ecosystem. For example, non-turbine releases allow more juvenile salmon to safely pass downstream over spillways (voluntary spill) or during high flow events when turbine capacity is exceeded (involuntary spill). Conversely, dams that allocate large quantities of flow plunging over tall spillways, or other non-turbine outlets, can result in significantly elevated TDG concentrations in the downstream river reaches. High enough TDG concentrations (115% to 120% TDG saturation in shallow water, measured by the twelve highest hours in a 24-hour period) can cause gas bubble trauma or gas bubble disease in aquatic organisms. Above 120% TDG saturation, death occurs before symptoms are shown.

The Oregon State Department of Environmental Quality and Washington State Department of Ecology have developed a Total Maximum Daily Load (TMDL) for TDG for the lower Columbia River (Pickett and Harding 2002), middle Columbia River (Pickett et al. 2004), and lower Snake River (Pickett and Herold 2003). For these river reaches, the measured TDG levels have frequently exceeded TMDL standards. Operational and structural TDG abatement measures (USACE 2016) have been extensively investigated and subsequently implemented, which have reduced TDG levels. Nevertheless, TDG levels frequently remain too high. TDG modeling can help refine reservoir operations and help identify areas for improvement.

In order to further improve the water quality of the Columbia-Snake River watershed, a system water quality model has been built using HEC-WAT to link ten CE-QUAL-W2 and three HEC-RAS models together. This system model includes the main-stem Columbia River from the U.S./Canadian border to downstream of Bonneville Dam, the Snake River downstream of Hells Canyon, and the Clearwater River from Dworshak Reservoir to the confluence with the Snake River. Each CE-QUAL-W2 model represents one of the ten reservoirs in the Columbia-Snake River system, and each model is being used to simulate temperature and TDG for the reservoir, where both the vertical and horizontal dimensions are important. HEC-RAS is being used to represent riverine reaches where a two-dimensional, laterally averaged model is more prone to instability and long run times. HEC-RAS has also been used to represent non-federal dams in the middle Columbia River (the main-stem river reach from the international border with Canada to the confluence of the Columbia and Snake Rivers near Pasco, Washington).

The Columbia-Snake River system model will represent the physical processes that control temperature and TDG in the Columbia-Snake River watershed. Each individual CE-QUAL-W2 or HEC-RAS model has been constructed using measured bathymetry, meteorology, flow, and water quality data to set the initial and boundary conditions. Each of these models has been calibrated and validated, ensuring that the model adequately represents the Columbia-Snake River system. Through the HEC-WAT interface the HEC-RAS and CE-QUAL-W2 models can be used individually or collectively to evaluate water quality changes induced by changes to water management plans.

Conclusions

The new CE-QUAL-W2 plug-in and updated HEC-RAS plug-in for HEC-WAT allow users to import and link multiple CE-QUAL-W2 water quality models with one another as well as with other hydraulic, hydrologic, and water quality models and external time series data. Modelers can create any number of model alternatives to simulate system-wide water quality for various water management scenarios or time periods. The CRT study team is using this software to evaluate the impacts on water temperature and TDG due to system operations and configuration of fourteen multiple purpose and related facilities that are operated as a coordinated system within the interior Columbia River basin in Idaho, Montana, Oregon, and Washington. The software can also be used to evaluate watershed-scale eutrophication processes (DO, nitrogen, phosphorus, and algae) and evaluate alternative system operations to improve water quality and ecosystem management in watersheds of varying size and complexity.

References

Cole, T.M. and Wells, S.A. 2016. CE-QUAL-W2: A Two-Dimensional, Laterally Averaged, Hydrodynamic and Water Quality Model, Version 4.0, Department of Civil and Environmental Engineering, Portland State University, Portland, Oregon, June 2016.

Environmental Protection Agency (EPA). 2019a. Water Quality Standards Regulations: Oregon. Retrieved from https://www.epa.gov/wqs-tech/water-quality-standards-regulations-oregon

Environmental Protection Agency (EPA). 2019b. Water Quality Standards Regulations: Washington. Retrieved from https://www.epa.gov/wqs-tech/water-quality-standards-regulations-washington

Hydrologic Engineering Center (HEC). 2016. HEC-RAS River Analysis System Version 5.0 User's Manual. Davis, CA.

Hydrologic Engineering Center (HEC). 2017. HEC-WAT Watershed Analysis Tool Version 1.0 User's Manual. Davis, CA.

National Marine Fisheries Service (NMFS). 2014, Endangered Species Act (ESA) Section 7(a)(2) Supplemental Biological Opinion, Consultation on Remand for Operation of the Federal Columbia River Power System. http://www.westcoast.fisheries.noaa.gov/publications/hydropower/fcrps/2014_supplemental_fcrps_biop_final.pdf

Pickett, P.J. and Harding, R. 2002. Total Maximum Daily Load (TMDL) for Lower Columbia River Total Dissolved Gas. Oregon Department of Environmental Quality and Washington State Department of Ecology. https://www.oregon.gov/deq/FilterDocs/Coltmdlwqmp.pdf

Pickett, P.J. and Herold, M. 2003. Total Maximum Daily Load for Lower Snake River Total Dissolved Gas. Washington Department of Ecology. https://fortress.wa.gov/ecy/publications/SummaryPages/0303020.html

Pickett, P.J., Rueda, H., and Herold, M. 2004, Total Maximum Daily Load for Total Dissolved Gas in the Mid-Columbia River and Lake Roosevelt. Washington Department of Ecology. https://fortress.wa.gov/ecy/publications/SummaryPages/0403002.html

Schneider, M. and Hamilton, L. 2016a. SYSTDG User's Manual, US Army Corps of Engineers, Northwest Division, Reservoir Control Center.

Schneider, M., and Hamilton, L. 2016b. SYSTDG Developer's Manual, US Army Corps of Engineers, Northwest Division, Reservoir Control Center, updated February 2016.

U.S. Army Corps of Engineers (USACE). 2013. HEC-RAS Water Temperature Model Development Report, a Supplement to the Water Quality Report Technical Appendix, Columbia River Treaty, 2014/2024 Review Program, December 2013.

U.S. Army Corps of Engineers (USACE). 2016. Update to the Total Dissolved Gas Abatement Plan, Lower Columbia River and Lower Snake River Projects, August 2016.

http://www.nwd-wc.usace.army.mil/tmt/wqnew/gas_abatement/2016/USACE_update.pdf

Zhang, Z. and Johnson, B. 2016. Aquatic Nutrient Simulation Modules (NSMs) Developed for Hydrologic and Hydraulic Models. Technical Report, Environmental Laboratory, U. S. Army Engineer Research and Development Center. http://acwc.sdp.sirsi.net/client/en_US/search/asset/1048348

WEPPCloud Beyond the Horizon

Peter R. Robichaud[1], Roger Lew[2], Marianna Dobre[2], William J. Elliot[1], Erin Brooks[2]

[1]USDA-Forest Service, Rocky Mountain Research Station, Moscow, Idaho, [2]University of Idaho, Moscow, Idaho. probichaud@fs.fed.us; rogerlew@uidaho.edu; mdobre@uidaho.edu; welliot@fs.fed.us; ebrooks@uidaho.edu

The Water Erosion Prediction Project (WEPP) model has been modified for the assessment of forestry and rangeland management applications for predicting surface runoff, water yield, soil erosion, and sediment delivery over the last 30 years. WEPP is a complex process-based hydrology and erosion model that utilize large climatic and soils databases. During the past decade, hillslope-based decision support tools were developed with streamlined user input requirements and simple, clear output (https://forest.moscowfsl.wsu.edu/fswepp/). These simplified hillslope scale tools include road erosion estimation (WEPP:Road), the post-fire Erosion Risk Management Tool (ERMiT), pre-fire Fuel Management Erosion (FuME), and timber harvest impacts with Disturbed WEPP. These tools have been widely applied to single hillslopes and in batch model runs to evaluate large networks. The ERMiT tool has been used over 138,000 times in 2018 alone. Recent improvements to subsurface lateral flow, baseflow, and elevation-variable climate allowed for small watershed modeling with reliable agreement with observed streamflow and sediment load using online and GIS versions of the WEPP model. One watershed-scale decision support tool for Post-fire Erosion Prediction is called WEPP-PEP (http://129.101.152.143/baer/) which provides both hillslope and watershed outlet predictions based on actual soil burn severity maps uploaded to the interface by users. This tool allows managers to assess the impact of targeted post-fire mitigation efforts (e.g. mulching) on hillslope erosion and watershed response.

Over the last two years considerable efforts have been invested in developing a broader online platform (WEPPCloud; https://wepp1.nkn.uidaho.edu/weppcloud/) to house a wide range of decision support tools including a watershed-scale applications of WEPP. WEPPCloud automates the acquisition and processing of climate, soil, management, and topographic inputs for WEPP from publically available datasets with national coverage (USGS National Elevation Dataset, the NRCS Soil Survey Geographic Database (SSURGO), USGS National Landcover, PRISM, DAYMET) and allows users to delineate and perform a watershed analysis within a user-friendly mapping interface. WEPPCloud allows users tremendous flexibility in climatic input files ranging from historic daily climate input files dating back to 1980 using NASA DAYMET gridded data products, long-term stochastically generated climate inputs using spatially-explicit PRISM corrected CLIGEN products, or future downscaled climate projections. The ability to apply a process-based spatially-distributed hydrology and erosion model online using daily observed climate and current soil burn severity maps make this a unique and powerful tool for watershed assessment and management. Demonstrations and applications for various forest management scenarios will be taught.